ISSN 1880-8468

Technical Report of
International Development Engineering

国際開発工学研究報告

TRIDE-2023-02 March 31, 2023

Abstracts of Bachelor Theses Presented from September 2016 to March 2022

Department of International Development Engineering,
Graduate School of Science and Engineering,
Tokyo Institute of Technology
http://www.ide.titech.ac.jp/TR

Preface

This technical report consists of the abstracts of Bachelor theses presented in the Department of International Development Engineering, Tokyo Institute of Technology, on August 2, 2016, February 28, 2017, August 1, 2017, February 23, 2018, August 8, 2018, February 22, 2019, August 19, 2019, February 20, 2020, February 18, 2021, August 23, 2021, and February 17, 2022.

Technical Report of International Development Engineering
TRIDE-2023-02

Table of Contents

(Completeng in September 2016)

(Completeng in March 2017)

(Completeng in September 2017)

(Completeng in March 2018)

(Completeng in September 2018)

(Completeng in March 2019)

(Completeng in September 2019)

(Completeng in March 2020)

(Completeng in March 2021)

(Completeng in September 2021)

(Completeng in March 2022)

Parameter selection of Support Vector Machine with Variable Kernel Function

Student Number:12_07140　Name:Akira Shiozuka　Supervisor:Yukihiko Yamashita

1 Introduction

Kernel method is a data analysis methodology which has been rapidly developed in the field of computer science in recent years. For example, support vector machines (SVM) based on on kernel method have demonstrated very high performance in classification and regression. The central idea of kernel method is mapping an original input vector into a high dimensional feature space to change the nonlinear classificclassification functions to linear classification functions. However to realize such excellent performance, the proper selection of feature mappings is very important. For the purpose, The variable kernel method (VKM) was researched. VKF can change the kernel parameter according to the position, although all sample patterns have the same parameter in the standard kernel method.

In this paper, I propose methods to fix parameter for VKF to improve recognition performance. I explain the framework of VKF, VKF-SVM, and propose a new parameter for selection method and 3 types of sample number selection method. I also show experimental results by using a toy problem and UCI datasets.

2 Framework for VKF

2.1 Mercer's Theorem

Let (x_n, y_n) $(n = 1, \cdots N)$ be a set of sample, where each x_n is a sample patter and y_n is its label (± 1). The inner product between x and z is denoted by $\langle x, z \rangle$. In this paper, a liner discriminant model for a binary problem is discussed. In case of the standard kernel method, a Marcer kernel function $k(x, z)$ is fixed and the kernel parameter σ is constant. The discriminant function is given by

$$d(x) = \sum_{n=1}^{N} \alpha_n k(x_n, x) + \theta, \qquad (1)$$

where α_n are coefficients and θ is a threshold. From Mercer's theorem, we can consider there exists a feature mapping $\Phi(x)$ that can satisfy

$$k(x, z) = \langle \Phi(x), \Phi(y) \rangle. \qquad (2)$$

Then eq.(1) can be written as

$$d(x) = \langle w, \Phi(x) \rangle + \theta, \quad w = \sum_{n=1}^{N} \alpha_n \Phi(x_n). \qquad (3)$$

2.3 Framework for VKF

As an example of kernel method several feature mapping $\Phi_j(x)$ $(j = 1, \cdots J)$ of which inner product can be calculated analytically are prepared.Their kernel functions are denoted by

$$k_{i,j}(x, y) = \langle \Phi_i(x), \Phi_j(x) \rangle. \qquad (4)$$

In VKF, nonlinear feature mapping Φ_n for each leaning pattern x_n and only one feature mapping Φ_0 for an unknown pattern x are prepared. The model of w in eq.(3) can be denoted by

$$w = \sum_{n=1}^{N} \alpha_n \Phi_n(x_n). \qquad (5)$$

Then, the discriminant function is given by

$$d(x) = \langle w, \Phi_0(x) \rangle + \theta,$$

$$= \sum_{n=1}^{N} \alpha_n k_{n,0}(x_n, x) + \theta. \qquad (6)$$

In VKF, we can change the kernel parameter σ_i of x_i according to the distances to the adjacent samplig points.

3 VKF with SVM

SVM can be summarized as minimizing

$$\|w\|^2 + C \sum_{n=1}^{N} \xi_n. \qquad (7)$$

subject to (for any $n = 1, 2, \cdots, N$)

$$y_n d(x_n) - 1 + \xi_n \geq 0, \quad \xi_n \geq 0. \qquad (8)$$

where C is a constant

VKF is applied to SVM. It is denoted by VKF-SVM. In the previous work, VKF parameter σ_i was selected by average of the distances from

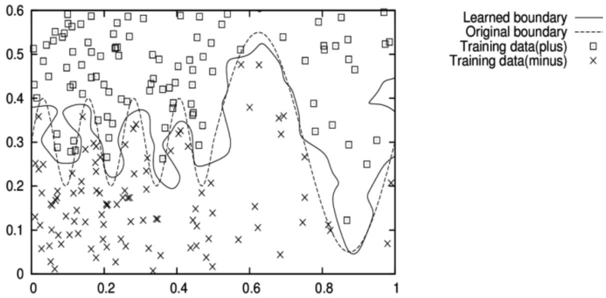

(a)SVM

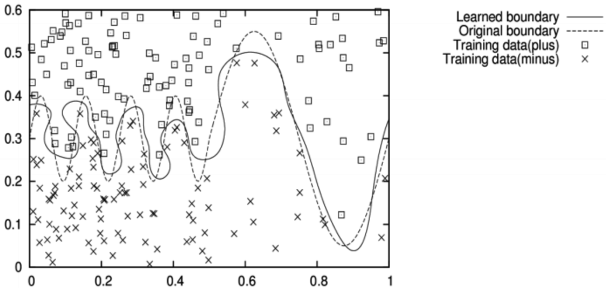

(b)VKF-SVM with Density selection and Area regular

Figure 1 : Results of toy problem

x_i to its nearby points (DIS-select).

I propose to decide σ_i by an inverse density of nearby points. (DEN-select) In the previous work , the number of samples for the selection is fixed. I propose to change it and three sample

number selection (SNS) method. r is a SNS parameter and $d_{i,n}$ is distance from x_i to nearest n-th

points.

(1) Distance SNS (DIS-SNS)

$$d_{n+1}/d_n < r . \tag{9}$$

(2) Averaged distance SNS (AVE-SNS)

$$\left(\frac{1}{n+1}\sum_{l=1}^{n+1} d_l\right) \Big/ \left(\frac{1}{n}\sum_{l=1}^{n} d_l\right) < r . \tag{10}$$

(2) Density SNS (DEN-SNS)

$$\left(\frac{n+1}{d^2_{n+!}}\right) \Big/ \left(\frac{n}{d^2_n}\right) < r . \tag{11}$$

4 Experiment Result

In the experiment , I used the Gaussian kernel function (GKF) for a feature mapping

Table 1: Error rates for UCI datasets (DIS-select)

	No SNS	Distance	Average	Density	SVM
Ba	10.9±0.6	**10.7±0.6**	10.8±0.5	10.9±0.7	10.8±0.5
He	16.5±3.8	**16.4±3.4**	16.9±3.6	**16.4±3.2**	17.8±3.6
Th	4.5±2.2	**4.0±1.6**	4.5±1.6	4.4±2.2	5.7±2.4
Ti	22.3±0.3	**22.2±0.4**	22.4±0.3	22.3±0.3	22.4±1.2
x	10.1±0.4	10.1±0.4	**10.1±0.4**	10.1±0.4	10.2±0.3

Table 2 : Error rates for UCI datasets (Den-select)

	No SNS	Distance	Average	Density	SVM
Ba	10.7±0.5	**10.7±0.5**	10.8±0.4	10.7±0.5	10.8±0.6
He	16.5±3.6	16.7±3.7	17.1±3.7	**16.4±3.6**	17.8±3.7
Th	**4.9±2.8**	**4.9±2.7**	6.1±3.7	5.1±2.7	5.7±2.5
Ti	**22.4±0.6**	22.8±0.9	23.4±1.5	22.7±0.6	22.5±1.3
Wa	10.3±0.4	**10.3±0.4**	10.3±0.4	10.3±0.4	10.3±0.4

and the smallest σ_i as σ_0. From eq.(4), the kernel function for VKF is given by

$$k_{i,j}(x,z) = \left(\frac{2\sigma_i\sigma_j}{\sigma_i^2+\sigma_j^2}\right)^M \exp\left(-\frac{\|x-z\|^2}{\sigma_i^2+\sigma_j^2}\right) \tag{12}$$

Then, I apply VKF-SVM to a toy problem and 5 types of UCI datasets. For the toy problem, the error rate for SVM is 7.58%. And the rates for SVM-VKF with DIS-select without SNS , DIS-SNS, AVE, DEN are 7.20%, 7.18%, 7.20 %, and 7.06%. On the other hands the rates for SVM-VKF with DEN-select under there are 6.20%, 6.21%, 6.14% and 6.00%. DEN-select with DEN-SNS is the best with parameter : $\sigma = 0.178, C = 178, r = 1.005$. Fig.1(a) shows result with SVM, and Fig.1(b) shows results of VKF –SVM with the best method. We can see clearly that Fig.1(b) is more smooth. Tables 1 and 2 show error rates for UCI datasets. From the tables, we can see VFK -SVMs with SNSs outperform SVM those no-SNS.

5 Conclusion

In this paper, I proposed new parameter and sample number selection methods. For future work, I have to use a wide range of parameter and propose a new parameter selection method to suit VKF.

References

[1] Naoya and Yukihiko Yamashita, "Simultaneous learn- ing of localized multiple kernels and classifier with,wighted regularization" Structural , Syntactic and Statistical Pat- tern Recognition, pp,543-362, Springer Berlin

Selective Catalytic Reduction by C_3H_6 over CeO_2-ZrO_2

Student Number: 09-09638 Name: Takumi Komori Supervisor: Hirofumi HINODE

1. Introduction

Nitrogen oxides (NOx) is general term for NO, NO_2 and N_2O. NOx causes several environmental problems, such as photo- chemical smog, acid rain and global warming. Main sources of NOx are factories, power plants and automobiles. Especially more than half of NOx are emitted from automobiles. So this is important to develop catalysts for NOx reduction.

Nowadays, three-way catalysts (TWC) are generally used to reduce NOx in automobiles. This catalyst can reduce NOx high efficiency at specific air to fuel (A/F) ratio. However, the development of lean-burn engines (A/F = 20~60) that have higher fuel economy and cleaner emissions requires another type of catalyst for NOx reduction. One common method to reduce NOx in exhaust gas is selective catalytic reduction of NO using hydrocarbon as reducing agent (HC-SCR of NO) [1].The main reactions of HC-SCR are the following:

$$2NO+O_2 \rightarrow 2NO_2 \quad (1)$$

$$3NO+3NO_2+C_3H_6 \rightarrow 3N_2+3CO_2+3H_2O \quad (2)$$

Previous Studies showed that CeO_2-ZrO_2 catalysts have potential of HC-SCR [2][3]. However in those studies, catalysts were made only 1 to1 ratio. Therefore in this study, I decided to prepare some CeO_2-ZrO_2 catalysts by changing the ratio, and compare each catalytic activity to reduce NOx.

2. Experimental

In this study, CeO_2-ZrO_2 catalysts were prepared by manual mixing method using CeO_2 (JRC-CEO1) and ZrO_2 (JRC-ZRO6) as precursors. CeO_2 and ZrO_2 were mixed together manually with ethanol, then dried, and calcined at 550℃ in air for 4 hours. Then the catalysts were crushed and sieved to 0.71-1.00 mm [4].

The HC-SCR activity experiments were carried out in a fixed-bed flow reactor. The reactant gas was composed of 1500 ppm NO, 10% O_2, 1500 ppm C_3H_6 and He as a balance gas. Catalyst was used with a corresponding space velocity of 13000h^{-1}. The temperature was changed stepwise from 150℃ to 550℃.

The NO and NO2 concentrations were analyzed by NOx analyzer (Shimadzu, NOA-7000) while CO2 was analyzed using gas chromatograph with thermal conductivity detector (GL Science, GC-3200). The catalysts were characterized by TG-DTA, XRD.

3. Results and Discussion

Fig.1 shows the results of catalytic activity tests of each catalyst. By adding CeO_2, the peak of the activity shifted to lower temperature. In this study 30wt% CeO_2-ZrO_2 catalyst shows the highest activity at 400℃.

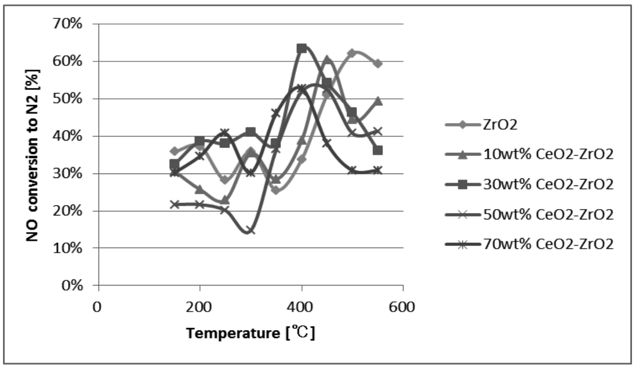

Fig.1 Catalytic activity of ZrO_2 and 10wt%, 30wt%, 50wt%, 70wt% CeO_2-ZrO_2 for the reduction of NO to N_2 using C_3H_6 as a reductant

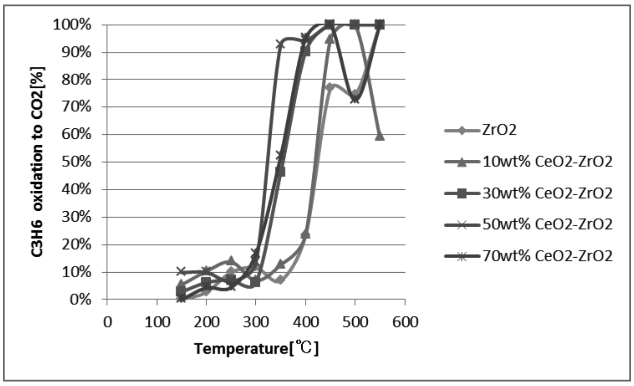

Fig.2 Catalytic activity for the oxidation of C_3H_6 to CO_2

Fig.2 shows the catalytic activity of each catalyst for the oxidation of C_3H_6 to CO_2. By adding CeO_2, the oxidation ability of the catalyst became higher. It can be considered that CeO_2 helps oxidation in HC-SCR.

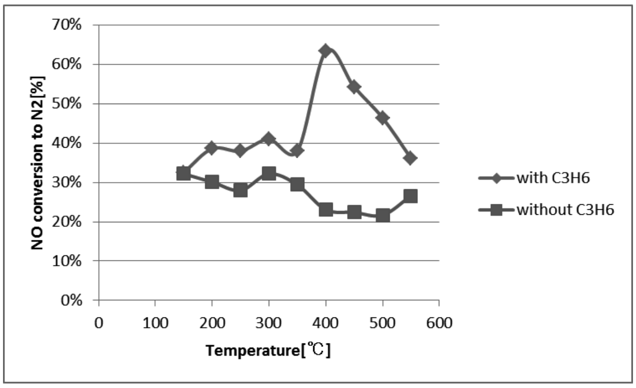

Fig.3 Effect of C_3H_6

To make sure HC-SCR, I compared reduction activity of 30wt%CeO_2-ZrO_2 in case that there is C_3H_6 or not. The result of this test is Fig.3. It shows that catalyst activity without C_3H_6 is lower. From this test we can see that NO was reduced by HC-SCR in this study.

XRD patterns of each catalyst are shown in the Fig.3. It can see that by adding CeO_2, CeO_2 peaks become stronger and ZrO_2 peaks become weaker. From this figure, it can say that CeO_2 exist as crystal in these catalysts.

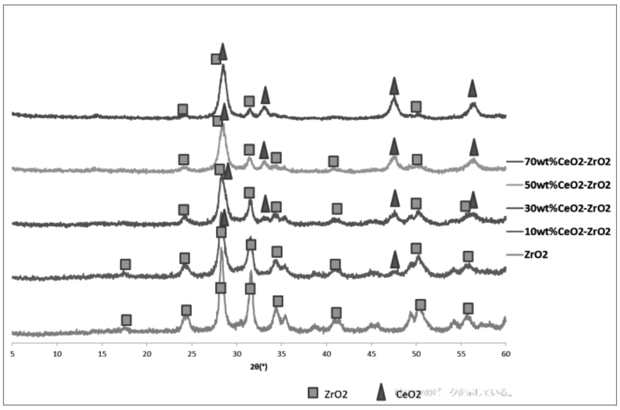

Fig.4 XRD patterns of the catalysts

4. Conclusion

In this study, the peak of catalytic activity shift to lower temperature by mixing CeO_2 to ZrO_2. And 30wt% CeO_2-ZrO_2 showed the highest activity at 400℃ in prepared catalysts. And I made sure NO reduction by HC-SCR, and CeO_2 helps oxidation.

Reference

[1]R.Burch et al, Appl.Catal.B, 11, (1997)

[2]「いまセリウムがおもしろい」,(株)ティー・アイ・シー, 初版 (2005)

[3]Bantan Furat; bachelor thesis, Tokyo institute of technology (2013)

[4]yang wang; master thesis, Tokyo institute of technology (2010)

Microbial community analysis in anaerobic digestion of oil-containing wastewater

Student Number: 12-12767 Name: Jou FUJITA Supervisor: Kiyohiko NAKASAKI

1. Introduction

Lipid is one of the major organic matters in wastewater from food processing factory. Lipid can be a good substrate for anaerobic digestion as in theoretical value, 850 mL of methane gas can be produced from 1 g of lipid, while the methane production from protein and carbohydrate are 500 and 395 mL/g respectively [1]. However, the anaerobic digestibility of lipid is not satisfactory due to the low biodegradability. To solve the problems, lipid is often pre-hydrolyzed by reagent or enzyme. Moreover enzyme pretreatment is more lower-cost than chemical treatment. So there is possibility of improving anaerobic digestion from pretreated oil by microorganism producing surfactant.

Anaerobic digestion of organic matter is a complex process which is governed by distinct microbial community. To achieve anaerobic digestion of a new substrate, the sludge needs to be adapted to new substrate. This adaptation generally involves a significant change in the microorganisms present in the sludge. An understanding of these changes in the microbial community would allow us to know which microorganisms contribute to higher methane production during anaerobic digestion, which would allow the development of system to monitor the presence and abundance of relevant microorganisms.

This study analyzed the changes in the microbial community during the adaptation of sludge to soybean oil after an increasing the concentration of soybean oil to feed in anaerobic digestion process. Furthermore, the microbial community in the reactor with soybean oil feeding was compared to the one with pretreated soybean oil feeding.

2. Materials and methods

An yeast strain, *Pseudozyma rugulosa* NBRC 10877 was used to pretreat the soybean oil. The yeast was precultivated in 20 mL of YM broth at 25 ºC for 2 days 150 spm. Then yeast was inoculated to 10 mL of Yeast oil broth and cultivated at 25ºC for 7 days. After 7 days cultivation, the culture was supplied to anaerobic digestion reactor.

The mixture of glucose, sodium acetate, lactic acid (GAL) and soybean oil were used as substrates for anaerobic digestion and two experiments, Run A and Run B were conducted. In Run A, the reactor was fed with untreated Yeast oil broth, and in Run B, the reactor was fed with pre-treated oil broth. In both of Run, the ratio of soybean oil against amount of carbon increased to 0%, 25% and 50% (O-0, O-25 and O-50) for each step. Those substrates were supplied to each reactor in a stepwise manner: day 0-20 with O-0, 21-95 with O-25 and day 96-370 with O-50.

For the startup of the experiment, distilled water, 200 mL of O-0 substrate and 65 g of granular sludge were mixed in two of the anaerobic sequencing batch reactor (ASBR). These reactors had a working capacity of 2.5 L, and operated 39℃ with agitation at 100 rpm. In these experiments, 200 mL of supernatant was extracted from the reactor and the same volume of fresh substrate was fed every day.

The pH in the supernatant was measured by the pH meter. A sample of the exhaust gas was captured into a sampling bag and gas compositions were measured by GC-TCD. Gas volume was measured using dry test gas meter.

The microbial community in the sludge was determined by denaturing gradient gel analysis, and bacterial 16S rRNA gene fragment was used. Characteristic bands in the DGGE gel were excised and base sequences of the DNA contained in the bands were determined. Also to determine the distribution of bacterial community, next generation sequence method using MacQIIME was used.

3. Results and discussion

The pH values of Run A and B are around optimum value, 6.3-7.4 for whole period of fermentation.

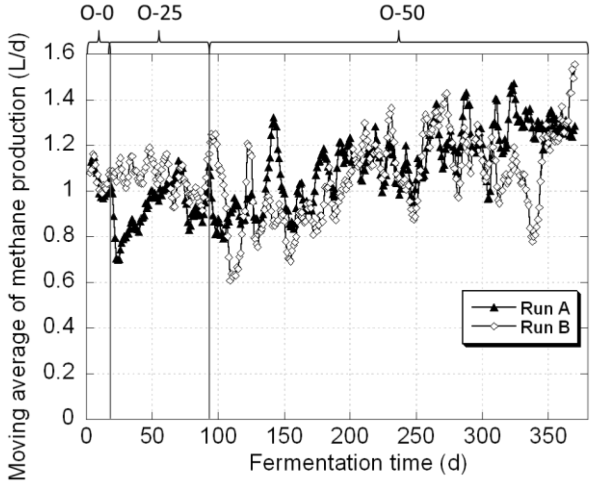

Fig. 1 Course of moving average methane gas production of Run A and Run B

Fig. 1 shows the courses of methane gas volume in Run A and Run B. During day 1 to 20 of fermentation the gas productions of both Runs were stable at around 1.07 L. After changing the substrate to O-25 at day 20, the gas volume of Run B during day 21 to 95 was almost the same volume with that before day 21. This result indicated that pretreated oil could be completely degraded and converted to

CH_4 and CO_2 since in total amount of carbon in the substrates of O-0 and O-25 were the same. By contrast, the gas volume of Run A decreased to around 0.80 L at day 21. Then, the gas volume of Run A gradually increased from day 24 and reached at around 1.09 L on day 74.

After changing the substrate to O-50 at day 95, the gas volume of Run A and Run B decreased to around 0.65 L, After the pretreatment, O-50 was considered to contain higher amount of long chain fatty acid (LCFA) that was produced in the degradation of soybean oil than that in O-25. It is considered that LCFA produced in the degradation of soybean oil in O-50 caused decrease of the methane gas production of Run B.

Around day 155, the gas volume of Run A and Run B gradually increased and reached to 1.09 L on day 175 that is almost the same volume observed before day 21. Also after day 175 we could observe increasing methane gas volume.

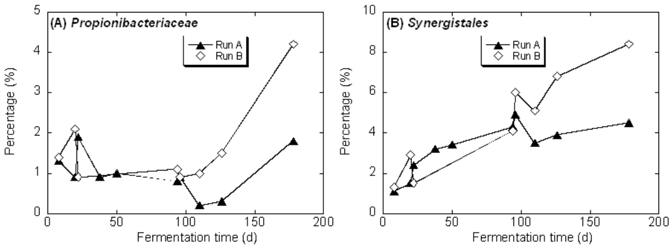

Fig. 2 Changes of key bacteria in Run A and Run B

The distribution of bacteria and archaea population in Run A and Run B was analyzed by using next generation sequencing (NGS). Fig. 2 shows the changes of the key bacteria which seem striking difference between Run A and Run B. Among the all microorganisms, these bacteria which close to *Propionibacteriaceae* and *Synergistales* were more dominant in Run B than in Run A after day 100. And it is known that *Synergistales* is obtained from oil-degrading enrichment [3]. In Fig. 2(A), the population of the microorganisms in Run A was twice higher than in Run B, on the other hand in Fig. 2(B), the population in Run A was also twice higher than in Run B. The results indicated that in Run B these two microorganisms played important roles in LCFA rich environment and supported methane production in the period when the methane production increase after day 120.

Fig. 3 shows the DGGE pattern for bacteria of Run A and Run B. In both Runs, it was observed that the increase of band 13, which was close to *Actinomycetaceae*. This microorganism was considered to be able to degrade LCFA, because during gradual increase of methane gas in day 120-220 the density of the band 13 also increased and it was considered to be rich-LCFA environment in both Runs. In Run B after day 96, The disappearance of band 7 was observed. And the increasing of band 4, 5, 6 and 10 were observed in only Run A. Since Run A was fed with untreated soybean oil and Run B was fed with pretreated soybean oil, it is implied that these microorganisms degrade the soybean oil.

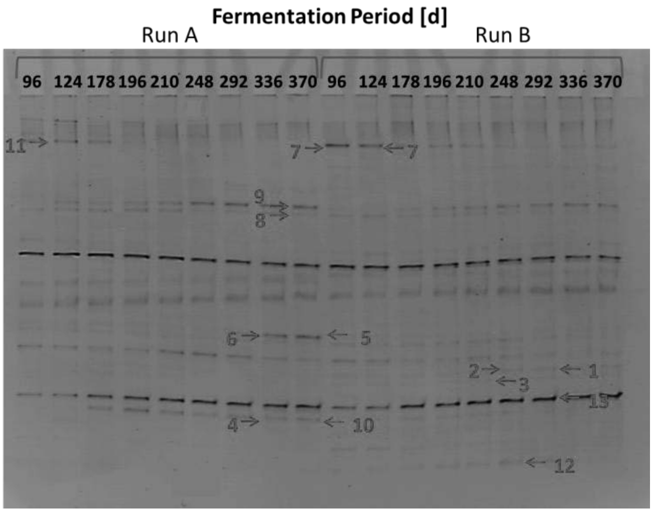

Fig. 3 DGGE pattern for bacteria of Run A and Run B

4. Conclusions

The methane production of Run B was recovered after day 120 and *Synergistales* and *Propionibacteriaceae* was candidate of bacteria which can support increasing methane production.

There is possibility that bands 4, 5, 6, 10 in DGGE pattern for bacteria of Run A are significantly important microorganisms.

Reference

[1] N. Kataoka et al. : Studies on a Methane Fermentation Process for Treating Oil and Fat Containing Food-processing Wastewater, Ebara engineering review, 212, 3-9 (2006).

[2] I. Angelidaki et al. : Effects of free long-chain fatty acids on thermophilic anaerobic digestion, Appl Microbial Biotechnol, 37, 808-812 (1992).

[3] Lisa M. Gieg, Irene A. Davidova, Kathleen E. Duncan and Joseph M. Suflita : Methanogenesis, sulfate reduction and crude oil biodegradation in hot Alaskan oilfieldse, Environmental Microbiology, 11, 3074-3086 (2010)

Prediction of future population distribution of Jakarta on the basis of global warming scenario

ID : 13B08154　　Name : Takakuwa Shun　　Supervisor : Prof. Kanda and Alvin C. G. Varquez

1. Introduction

Data such as urban parameters and anthropogenic heat emissions is necessary in order to study future urban climate using meteorological models. It is already known from previous research that these data can be derived from the high resolution population distribution of urban.1) In other words, if the future population distribution of urban is known, future urban climate can be studied. The objective of this research is to predict future population distribution in Jakarta based on two types of SSP scenarios.

2. Methodology

Three inputs are needed to predict future population distribution. First is gridded distribution of probability for urbanization derived from an urban growth model. Second is the trend of future total population in Jakarta based on a Shared Socioeconomic Pathways Scenario (SSP). Third is present-day population distribution by LandScan^{TM}. Using a logistic model which utilizes these inputs, future population distribution can be obtained.

SLEUTH model is a cellular automata model which can estimate future horizontal urban growth (Urbanization Probability Map) by using different input data such as Slope, Excluded region, Urban extent, Transportation, and Hill shade2). I used the model to predict two types of urban growth, Historical and Compact Growth. Historical Growth is the urban growth which follows the historical trend. Compact Growth represents a restricted urban growth by strict economic and urban planning policies.

SSP and the growing ratio of Jakarta's population to Indonesia's defines the decadal changes of total population in Jakarta from the present to the future. In this study, two types of SSP were used, SSP1 and SSP33). SSP 1 is based on the future assumption that education, governance and technology are of highest level and the rate of population increase is restricted. On the other hand, SSP3 is business as usual condition, suggesting higher rate of population increase and uncontrolled growth. Based on this assumption, SSP1 (SSP3) is paired with Compact (Historical) Growth. Then final population distribution scenarios were referred to "Historical Scenario" and "Compact Scenario".

LandScan^{TM} provides past and latest (2013) population distribution and was used as a base of population distribution prediction; and to validate the estimated population distribution.

Future population distribution was calculated annually from the base year using a discretized form of the logistic function as follows.

$$\mathrm{Pop}_{i,j}^{t+1} = \frac{\left(\mathrm{A}_{i,j}^{t} + 1\right)\mathrm{Pop}_{i,j}^{t}}{1 + \mathrm{B}_{i,j}^{t} \times \mathrm{Pop}_{i,j}^{t}} \qquad (\mathrm{Eq.}\,1)$$

$$\mathrm{Pop}_{i,j}^{t+1} = 10 \ \left(\mathrm{Pop}_{i,j}^{t} = 0 \ \& \ \mathrm{Pro}_{i,j}^{t+1} \geq 0.5\right) \ (\mathrm{Eq.}\,2)$$

; where

$$\mathrm{A}_{i,j}^{t} = \ exp\left(\mathrm{r}_{i,j}^{t}\right) - 1 \qquad (\mathrm{Eq.}\,3)$$

$$\mathrm{B}_{i,j}^{t} = \ \frac{\mathrm{A}_{i,j}^{t}}{\mathrm{K}^{t}} \qquad (\mathrm{Eq.}\,4)$$

$$\mathrm{r}_{i,j}^{t} = \begin{Bmatrix} \mathrm{a}^{t} \times \mathrm{Pro}_{i,j}^{t+1} & \left(0 < \mathrm{Pop}_{i,j}^{t} < 100\right) \\ \mathrm{b}^{t} \times \mathrm{Pro}_{i,j}^{t+1} & \left(100 \leq \mathrm{Pop}_{i,j}^{t}\right) \end{Bmatrix} \qquad (\mathrm{Eq.}\,5)$$

i, j and *t* refer to the spatial and temporal coordinates. *Pop* and *Pro* refer to the population and urbanization probability. K^{t}, a^{t} and b^{t} are coefficients obtained by minimizing the difference between the estimated population distribution and the actual values from

LandScan^{TM}. SSP was used as an additional constraint,

$$\left|SSP^t - sum\left(\mathrm{Pop}^t_{i,j}\right)\right| \leq 1000 \quad (\mathrm{Eq.}\,6)$$

to optimize K^t, a^t and b^t.

3. Result

Fig.1 shows the result of SLEUTH. From Fig.1, it can be seen that urbanized area is so different between Historical and Compact Growth.

Fig.2, 3, and 4 reveal the future population of Jakarta. From Fig.2, it can be seen that trends of total population are almost the same in Compact Scenario and SSP1, Historical Scenario and SSP3 respectively. From Fig.3, it can be seen that future population based on SSP is well distributed by this estimation procedure. In Fig.4, red region shows population increasing significantly in the Historical Scenario than in the Compact Scenario. On the other hand, blue region shows an opposite condition. From this figure, it can be seen that population is expected to increase at the central area in the Compact Scenario than in the Historical Scenario.

4. Conclusion

Future population distribution in Jakarta based on the SSP scenarios is introduced. This method can be expanded to other cities, and can potentially useful for urban planners and weather modelers.

Reference

1) Manabu Kanda, et al ; A new aerodynamic parametrization for real urban surfaces *Boundary-Layer Meteorol* (2013), vol148 : 357-377

2) PROJECT GIGALOPOLIS http://www.ncgia.ucsb.edu/projects/gig/index.html

3) 藤森 真一郎（2011 年 11 月 22 日）; IPCC 第 5 次評価報告書に向けた将来シナリオの検討 日本からの貢献とその意義 http://2050.nies.go.jp/sympo/111122/file/1_fujimori.pdf

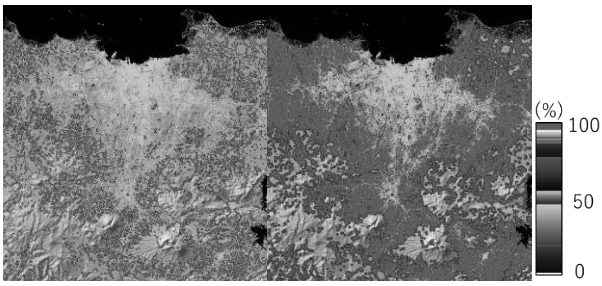

Fig.1 Urbanization Probability Map by SLEUTH model. Compact Growth (left) ; Historical Growth (right)

urban area in 2014 : ▨

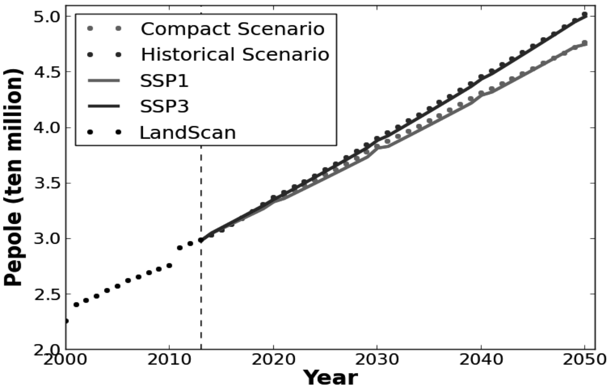

Fig.2 Trends in the total population of Jakarta.

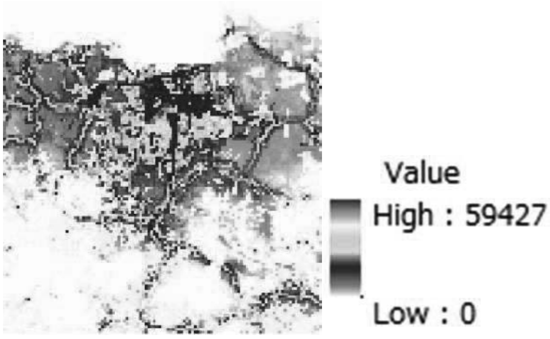

Fig.3 Population distribution of Jakarta in 2050 in "Historical Scenario"

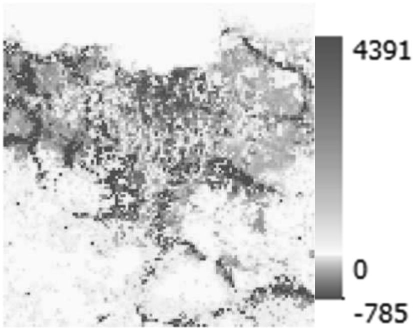

Fig.4 Population distribution difference between Historical and Compact Scenario in 2050

Exploring the Optimal Number of Days in East China Sea Cruise Tourism from/to Shanghai

Student Number: 13_09484 Name: Zhonghui Zheng Supervisor: Shinya HANAOKA, Tomoya KAWASAKI

1. Introduction

In 2015, nearly 1.91M Chinese passengers took a cruise vacation, growing 66 percent annually since 2012[2]. Shanghai as the main port of the cruise tourism products, it is developing rapidly in recent years. However, Shanghai in the process of further development of cruise tourism also met with some bottlenecks, for instance, how to attract more and more new users and repeaters to join cruise tourisms.

According to the survey of International Cruise Tourism in Shanghai (Costa Cruise 2009), 58% of people selected the number of cruise days is the most important factor they emphasize when choosing a cruise tour. Because for Chinese people, the most concentrated holiday are three Golden Weeks and the longest holiday is also less then 10 days. For most of the Chinese office workers, they still have not enough time to participate in a longer voyage cruise travel. Therefore, this study mainly concentrated on cruise days and other two factors, destinations and price that the most tightly connected with cruise days.

Based on the background, objectives of this study are 1) Using SP Survey to analyze the main factors influence tourists' decision making, and to clarify when they change how people's satisfaction change. Also consider the interaction of other factors with days.2) By using the estimated parameter result to find the utility function and find out its saturation point. Also, we analyze the change of maximum utility by the optimum number of days and clarify the characteristics by individual attribute.

2. Methodology

2.1 Stated Preference (SP) Survey Design

1) Overview of Web-based Questionnaire

Table 1 shows the overview of web-based questionnaire. According to *Asia Cruise Trends (CLIA, 2016)*, Japan and South Korea mixed cruise lines is the most popular to Shanghai cruise tourists. The ports of call are top 6 of destinations most popular to Chinese cruise tourists. The reason why this study did not consider other factors may influence people's decision making is that due to limitation of vacation time, Chinese tourists will give priority to consider how long and where they want to cruise to, after that, they consider what kind of service they want to enjoy and how much is it. Therefore, cruise days is most concerned at first when choosing cruise tour.

Table 1 Overview of Web-based Questionnaire

Contents								
Survey Area	Shanghai, China							
Survey Target	New users, Repeaters, Captive users							
Survey contents	I. Attributes (gender, age, occupation, monthly income) II. Preference of Days and Ports of call III. Intention to join the cruise tourism (existing & fictitious)							
Sample Size	648*15 (number of cruise lines)							
Origin(port of departure)	Baoshan Port, Shanghai							
Destination Region	East China Sea (West Japan & South Korea)							
Ports of call	Nagasaki JP	Fukuoka JP	Kumamoto JP	Okinawa JP	Jeju KR	Busan KR		
Periods (Days)	3	4	5	6	7	8	9	10
Number of Cruise Lines	1	2	2	2	2	2	2	2
Class of Cruise ships	Casual/Standard							
Ordinal Scale (4 grade)	1.Like to join	2.Slightly like to join	3.Slightly don't like	4.Dislike				

2) Existing & Fictitious Lines (Orthogonal Design)

Table 2 shows the Existing (fill color) and Fictitious (non color) cruise lines made by orthogonal design. Price setting refers to the actual price of Casual/Standard cruise ship ticket; because we only can cruise to Jeju for a travel within 3 days realistically, the Day 3 just has 1 line.

Table 2 Existing & Fictitious Cruise Lines

Day / Port	3	4		5		6		7		8		9		10	
Line Number	1	2	3	4	5	6	7	8	9	10	11	12	13	14	15
Nagasaki （JP）		■				■			■	■			■		■
Fukuoka （JP）				■				■			■		■	■	■
Kumamoto （JP）			■			■		■		■			■	■	
Okinawa （JP）					■		■		■		■	■		■	
Jeju （KR）	■						■			■		■	■		■
Busan （KR）				■				■			■	■		■	■
Price （CNY/person）	2200	3000	3200	3800	4000	4500	5000	5500	6000	6500	7000	8000	7500	9000	8500

2.2 Mixed Ordered Logit Model

In this study, *StataSE 1.4* is used to analysis Ordered Logistic Regression for panel data. Because it is random-effects OLM, methods and formulas are shown as the following:

for i=1,…,n panels, where t=1,…, n_i , ν_i are independent, identically distributed $N(0,\sigma_\nu^2)$, also called panel-level random effects and κ is a set of cutpoints, K is the number of possible outcomes. So derive the probability of observing outcome k for response y_{it} as:

$$p_{itk} = \Pr(y_{it} = k|\kappa, x_{it}, \nu_i)$$

$$= \frac{1}{1+exp(-\kappa_k + x_{it}\beta + \nu_i)} - \frac{1}{1+exp(-\kappa_{k-1} + x_{it}\beta + \nu_i)}$$

Where κ_0 is taken as $-\infty, \kappa_K$ is taken as $+\infty$.

2.3 Method of estimating the optimal cruise days

Step 1: Analysis ordered logistic regression for panel data by using *StataSE 1.4,* confirm main independent variables that can influence significantly and using appropriate coefficients to define the utility function.

Step 2: Differentiate U(x_i) with respect to Day ($dU/dDay$), plug the known values and check out the extreme point of the function(i.e, when ($dU/dDay$)=0, calculate value of Day).

Step 3: Plot the obtained optimal Days and the days of existing & fictitious Lines(line 1~20). Except lines mentioned in 2.2, other existing lines that provide by Cruise Company are added into analysis.

3. Result and Discussion

3.1 Overview of Survey Data

Gender: The number of total answerers is 648, female is 52.78% (342); male is 47.22% (306). Age: Proportion of less than 40 years and over 40 years is almost 1:1. Occupation: 50% are company clerks. Monthly Income: Over 50% are in the range of 5000~15000 CNY. Experience of cruise tourism: 527 answerers want to join cruise tourism if they have chance. Preferences of Cruise

Days: from figure 1, it can be said that 5 days tour is the most popular without regarding for the influence of price and ports, the answerers just were asked " How many days do you expect to take a cruise? "

3.2 Cross Analysis

In this part, cross analysis include gender (male, female), age groups (18~29, 30~39, 40~49, 50~) and monthly income (0~8000, 8001~15000, 15001~25000, 25001~, unit CNY), experience of cruise tourism (yes & no). Figure 2 and 3: the shapes of curves are almost the same; the peak is 5. Monthly Income (figure 3): the preference of cruise days for each group is 5; but for short trip (2~3), there are some differences that the proportion of the low-income people is higher than others, maybe because short trips are not so expensive that they can be able to afford. Age groups (figure 4): age groups shows some differences that 18~29 is prefer to 5 days; 30~39 and 40~49 are all most expected 5 days; relatively, the most expected cruise days for old people is longer than young people. It can be said that because old people (include retiree) have time and considerable economic condition, they would like to travel long days for relax [3].

Figure 1 Preference of Cruise Days

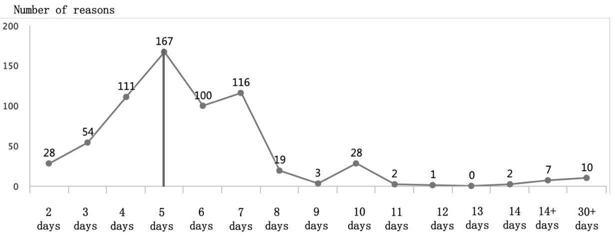

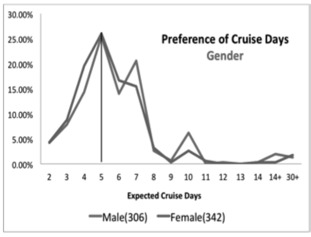

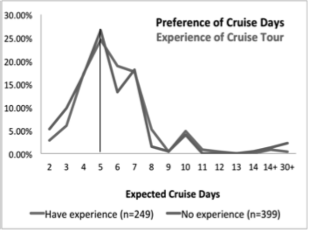

Figure 2 Gender

Figure 3 Experience of Cruise Tour

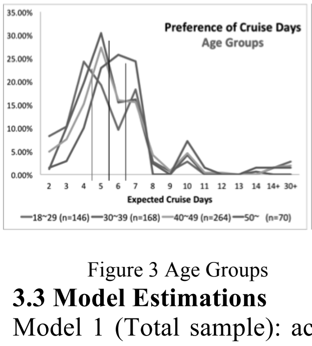

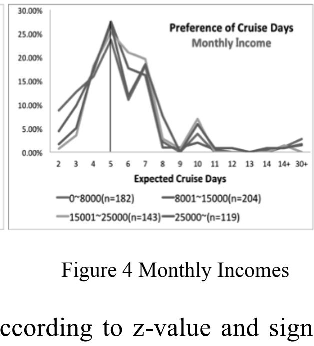

Figure 3 Age Groups

Figure 4 Monthly Incomes

3.3 Model Estimations

Model 1 (Total sample): according to z-value and signs of coefficient (+&-), it indicated that young people like to cruise than old people and the probability join the cruise tour of repeater is higher than new user; number of Days is longer better, but from sign of Day square is negative, we can obtain maximum value, and people refer to cheap tours. From sign of Fukuoka is negative, it means people not so like to go to Fukuoka for a travel. Model 2 and 3 (Male & Female): Age influences the female satisfaction negatively, but experience is positive;

Table 3 Summary of parameter estimation results

Explanatory variables		Model 1 (Total)		Model 2 (Total Estimate D*)		Model 3 (Male)		Model 4 (Female)		Model 5 (No experience)		Model 6 (Experienced)	
		Coef.	z-score	Coef.	z-score	Coef.	z-score	Coef.	z-score	Coef.	z-score	Coef.	z-score
Gender		-0.003	-0.01	-	-	-	-	-	-	0.109	0.34	-0.116	-0.42
Age		-0.036	-3.05	-	-	-0.019	-1.14	-0.054	-3.26	-0.060	-3.46	-0.005	-0.31
Monthly Income		0.000	0.81	-	-	0.000	1.80	0.000	-0.75	0.000	-0.27	0.000	2.40
Experience(dummy)		0.746	3.40	-	-	0.589	1.74	0.901	3.18	-	-	-	-
Days		9.846	5.16	9.850	5.16	8.791	3.04	10.800	4.24	10.622	4.59	8.641	2.63
Price		-0.006	-5.45	-0.006	-0.54	-0.006	-3.26	-0.007	-4.46	-0.007	-5.13	-0.005	-2.52
Port dummy	Nagasaki (p1)	-2.470	-3.27	-2.472	-3.27	-1.884	-1.71	-2.984	-2.86	-2.991	-3.27	-1.712	-1.32
	Fukuoka (p2)	-4.762	-3.20	-4.768	-3.21	-3.949	-1.83	-5.487	-2.66	-4.798	-2.58	-4.697	-1.90
	Kumamoto (p3)	-1.009	-1.19	-1.012	-1.20	-0.570	-0.46	-1.400	-1.19	-1.264	-1.20	-0.615	-0.44
	Okinawa (p4)	-0.168	-0.12	-0.175	-0.13	0.656	0.33	-0.883	-0.47	-0.548	-0.32	0.431	0.19
	Jeju (p5) Busan(p6)	0 omitted	-	0 omitted	-	0 omitted	-	0 omitted	-	0 omitted	-	0 omitted	-
Cross Terms interaction	D^2	-1.418	-5.36	-1.418	-5.36	-1.272	-3.23	-1.549	-4.32	-1.536	-4.75	-1.237	-2.75
	P*D	0.001	4.99	0.001	4.99	0.001	3.08	0.001	3.96	0.001	4.60	0.001	2.38
	p1*D	0.375	3.70	0.374	3.70	0.258	1.70	0.475	3.47	0.414	3.14	0.328	2.03
	p2*D	0.662	4.60	0.662	4.60	0.554	2.67	0.758	3.78	0.638	3.52	0.698	2.93
	P3*D	0.090	1.47	0.090	1.46	0.010	0.11	0.160	1.89	0.095	1.15	0.089	0.94
	p4*D	-1.112	-1.45	-1.112	-1.45	-0.230	-2.00	-0.130	-0.12	-0.125	-1.30	-0.85	-0.65
	p5*D	0.055	0.60	0.054	0.59	0.029	0.21	0.761	0.62	0.029	0.25	0.100	0.65
	P6*D	0.061	0.44	0.060	0.44	0.021	0.10	0.93	0.51	0.032	0.18	0.115	0.50
sigma2_u		7.202	10.48	7.528	10.44	8.317	7.23	6.136	7.79	9.584	8.27	4.095	6.72
Sample Size		9630 (642*15)		9630 (642*15)		4545(303*15)		5085(339*15)		5895(393*15)		3735 (249*15)	
Adjusted McFadden's R2		0.27		0.27		0.28		0.26		0.29		0.24	

For male, it seems that except Days, Price, Day square, Price*Day, others not affect significantly.

Model 4 and 5 (New user & Repeater): young and new users more like to cruise, and high-income repeaters probably prefer join again. Using the result of Model 1, confirm the utility function and plot:

$$U(D2, Day, Pd, \sum_{i=1}^{6} p_i d\ , \sum_{i=1}^{6} port_i), calculate\ \frac{dU}{dDay} = 0$$

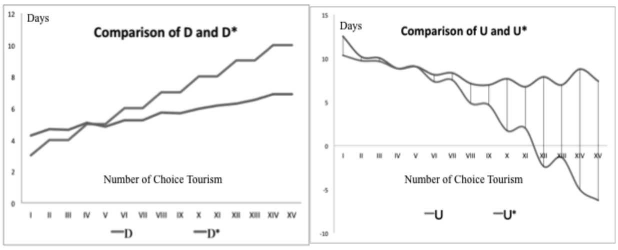

Figure 5 Comparison of D and D* , U and U*

From figure 5, When D=D*, it means the days (D) of choice tourism become the optimal days(U*) and the utility of this choice tourism will be the U* maximum utility. In this case, D* of choice tourism IV is nearly 5.0677, comparing to other D* of choice tourism, it is the closest approach. From the figure 4.3.3, it indicated that it is better to extend for less than 5 days of intersection and shorten after 5 days. It is realistically possible by adjusting the sailing date, calling area sightseeing, shopping time etc. If pay attention to the magnitude relation between U and U * for the same choice tourism, the difference between U and U * of each tour increases as the number of days increases and the rate of increase in utility also increases.

4. Conclusion

Age, experience, number of days, price, port of calling are the main factors for passenger decision making, but the most important are days, prices, port of call. Generalization cannot be done because the optimal number of days is changed according to other factors, but substituting the estimated optimum days into the utility function increases the utility.

References

[1] Kam Huang James F. Petrick, "Why do you cruise?", Tourism Management, No 32, 286-393, pp.4-6 (2011)

[2] Cruise Lines International Association (CLIA), "Asia Cruise Trends", 2016 Edition, pp.6-13, pp.29-30

[3] Kawasaki, T. Todoroki, T. Komatsu, G., "Preferences of the Potential Cruise Ship Users in Japan, International Association of Maritime Economics (IAME) 2016 Conference, Hamburg (2016)

Raspberry Pi による低コストな屋内位置推定システムの構築

学籍番号: 13B04920　氏名: 姜　竣銘　指導教官: 高田　潤一、 Azril Haniz

1　はじめに

近年、スマートフォンとコミュニケーションネットワークの普及に伴い位置情報サービス（Location based service）の需要が高まってきている。位置情報サービスに用いられている技術は屋外位置推定技術と屋内位置推定技術に分けられている。屋外位置推定技術では、GPS による位置取得が主流である。しかし，GPS 衛星の電波が届かない屋内では、取得した位置情報には誤差がある。屋内位置推定では、研究者は様々な技術を検討しているが、まだ市場に決定打が出ていない状況である。

様々な技術の中に、最近では省電力無線通信である BLE(Bluetooth Low Energy) が注目されている。BLE は消費電力が少ないことから長時間稼動に適しており、近年スマートフォンをはじめ BLE 機能を備えているデバイスが増えており、屋内位置推定システムとしての利用は期待されている。さらに、低価のシングルボードコンピュータである Raspberry Pi は BLE 信号を送信したり受信したりすることができて、容易に屋内位置推定システムを構築できる。

本研究では Raspberry Pi で BLE 受信信号強度（Received Signal Strength:RSS）に基づいて位置指紋法（Location Fingerprinting）を使いデバイスフリー屋内位置推定システムを提案する。そして、提案したシステムの初期的検証として実験を行い、その結果と考察を報告する。

2　原理

2.1　デバイスフリー位置推定システム

Aly の調査 [1] により、屋内位置推定システムは主に二つに分かれて：デバイス依存システム（Device-based System）とデバイスフリーシステム。従来のデバイス依存システムはユーザーが無線の端末を持つ必要がある。しかし、デバイスフリーシステムでユーザーは無線の端末を携帯する必要はなく、ユーザへの負担は軽減できるというメリットがある。

Figure 1 に示したように、デバイスフリーシステムは複数の送信機と受信機により構成される。屋内環境の様々の場所に、送信機と受信機を適切に設置し、複数の送受信機のペアを作る。人が屋内環境に現れる場合、人体による電波の遮蔽や反射により、屋内の電波伝搬環境が大きく変化すると考えられ、送受信機間の通信路も変化する。人が立つ場所によって影響を受ける送受信機のペアが異なり、場所依存性があるため、その特徴を位置推定に利用できる。デバイスフリーシステムの事例として高齢者の遠隔介護支援が挙げられる [2]。

2.2　位置指紋法に基づく位置推定技術

位置指紋法に基づく位置検出技術は、受信信号の伝搬特性を利用する [3]。Figure1 が示してように、２つの段階があり、一つは「Offline Phase」で、もう一つは「Online Phase」である。Offline Phase では事前に設定した場所で一定時間に取得した信号の特徴量をデーターベースに格納する。Online Phase では未知の場所で取得した信号の特徴量を利用して、パターンマッチング手法により位置を推定する。人体の指紋と同じように、ある場所の指紋がデータベースにある指紋が一致すれば、場所を特定することができる。本研究では信号の特徴量として受信信号強度を利用する。

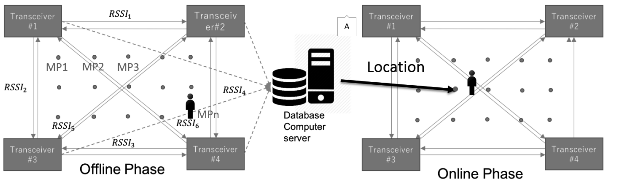

Figure 1: Raspberry Pi を利用したデバイスフリーシステムのイメージ

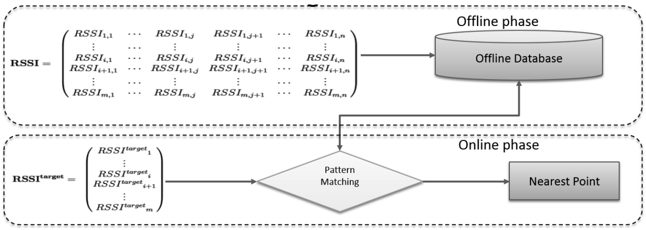

Figure 2: 位置指紋法の全体図

位置指紋位置検出技術の利点として、マルチパスが多い屋内環境は適しており、データベース作成時と同じ環境下では高い位置推定精度が期待できることである。しかし、精度を維持するためには環境変化に合わせてデータベースを再作成する必要がある [5]。

Figure2 が示しているのは位置指紋法の全体図である。$RSSI_{i,j}$ とは i 番目の送受信機ペアの j 番目の計測ポイントにおける RSS であり、$RSSI'_i$ は online phase で測定した i 番目の送受信機ペアの RSS である。n は計測ポイントの個数で,m は送受信機ペアの組合せの数である。

パターンマッチングアルゴリズムとして、本研究ではユークリッド距離を用いた最近傍法を採用した。データベースに各計測ポイントの指紋と Online Phase のユーザの指紋とのユークリッド距離は式 1 で表す。それで式 2 によって、ユークリッド距離が最小の計測ポイントを絞り出し、この点は推測した場所である。

$$d_j^2 = \sum_{i=1}^{m} (RSSI_{i,j} - RSSI^{target}{}_i)^2 \tag{1}$$

$$\hat{j} = \arg\min_j d_j \tag{2}$$

3　システムの構築

3.1　Raspberry Pi

Figure3 は本研究使っている Raspberry Pi である。Raspberry Pi はシングルポードコンピュータで、LINUX などの OS をインストールすることができる。そして、自分で書いたプログラミングによって、自由に Bluetooth、Wi-Fi などのハードウェアを操ることができる。BLE　USB ド

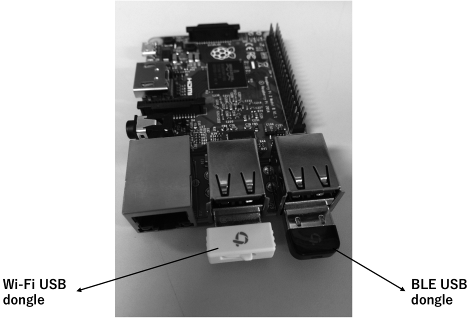

Figure 3: Raspberry Pi の写真

ングルを装着することによって、BLE 信号を送受信することが簡単にコントロールすることができる。本システムでは、コマンドで複数の Raspberry Pi を受信機と送信機の間切り替えて、システムの送受信機関の通信路を変化させる。

3.2 ネットワークの説明

屋内に各場所で設置した Raspberry Pi の送受信をコントロールしたり、Raspberry Pi が受信したデータをパソコン・サーバーに送信したりするためにネットワークを構築すべきである。本システムは Wi-Fi ルーターによって、ローカルエリアネットワークを構築することで実現した。サーバーパソコンを使って SSH と VNC(Virtual Network Computing) プロトコルで Raspberry Pi を遠隔操作する。UDP 送信プログラムを書いて Raspberry Pi とサーバー間のデータの通信を行う。

4 実験

4.1 実験説明

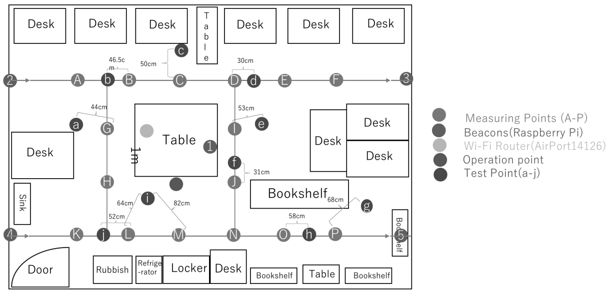

Figure 4: テストベッドの設置

提案した屋内位置推定システムを初期検証するため東工大南６号館２１４室で実験を行った。Figure4 は実験のテストベッドである。５個の Raspberry Pi は一定の順序によって送受信を切り替えて、様々な送受信機の組み合わせを作り、RSSI を測定する。送信側は送信強度が 0dbm で、送信間隔が 100ms である。実験実施者は各計測ポイントに立ち、受信機は各送受信パターンで 40 秒間の RSSI データの平均値を記録する。 Offline phase が完了したら、Figure 2 に示す $\mathbf{RSSI}$ のようなデータベースを作る。そのとき m ＝ 20 で、n=16 である。

Online Phase では、１０個のテストポイントを取り（緑の丸）、各テストポイントで受信して Figure 2 に示す $\hat{\mathbf{RSSI}}$ のような行列を作る。そして、式 1 と式 2 を使って、推測位置を決める。

4.2 結果と考察

提案した屋内位置推定システムで実験し、結果はユーザの実際の位置と推定位置の間の距離（誤差距離：error distance）で評価する。テストポイントは計測ポイントと同じではないから、理想的な推測位置はテストポイントと空間的に距離が一番近い計測ポイントである。つまり理想的な場合でも、誤差距離はゼロではないわけである。

Fig5 は結果を示した。赤線は理想的な場合の誤差距離で、青線は実際の場合の誤差距離である。a,b,d,e,i 点は誤差距離は１メートル以内であったが、他のテストポイントは誤差距離が大きかった。その原因は大きく２つ考えられる。

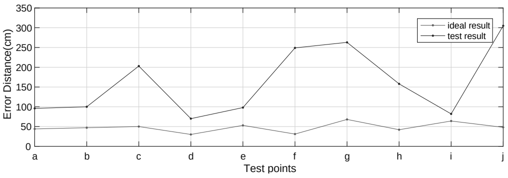

Figure 5: 屋内位置推定実験の結果

まず、今回の実験では一つのポイントで２０個の RSSI データが指紋としてデータベースに格納され、同じく式 1 によって計算された。人が立つ場所によって必ずしも全ての送受信機間の通信路に影響を与えているわけではない。例えば、A 点の近くに人が立っても Raspberry Pi♯4 と ♯5 の間の通信路への影響は少ない。すべての送受信機ペアではなく、有効な送受信機ペアのみを適切に選択することで、より高い推定精度が得られると考えられる。

そして、屋内環境における障害物によるシャドウィングとマルチパスによるフェージングにより、場所の変動が小さくても、位置指紋の変動は大きい。その問題を解決するために、計測ポイントが多く増やして、データーベースにより多くの位置指紋を保存する。それでより高い推定精度が得る事ができると考えられる。

5 おわりに

今回の研究では、Raspberry Pi で BLE 受信信号強度（RSS）に基づいて位置指紋法（Location Fingerpriting）を使いデバイスフリー屋内位置推定システムを提案した。検証実験によって、その結果を分析し、その可能性を探った。

今後の課題として、次のようなことに関する研究を進めていく必要がある。提案したシステムにふさわしいパターンマッチングアルゴリズムを研究する。またスマートフォンで表示できるリアルタイムな屋内位置推定システムを構築する。

References

[1] H.Aly and M.Youssef,“An analysis of device-free and device-based wifi-localization systems”, Ambient Computing and Intelligence(IJACI), vol.6, no.3, January 2014.

[2] 杉野恭兵, 大囿忠親, 新谷虎松: “複数の Bluetooth ビーコンに基づくデバイスフリーな屋内測位におけるキャリブレーションについて”，信学技報，115(381)，pp1-6, 2015.

[3] 辻広之,“アレーアンテナを用いた屋内外の無線局位置推定の実験的検証” 信学論（B），vol.J90-B, no.9, pp-784-796, Sep.2007.

[4] 大槻知明, “位置推定技術”, 2009: “http://www.ohtsuki.ics.keio.ac.jp/theme/localization.pdf”.

[5] A.Dempster,B.Li,and I.Quader, “Errors in determinstic wireless fingerprinting systems for localization”, 3rd International sysmposium on Wireless Pervasive Computing (ISWPC), pp.111-115, May 2008.

A system of extracting common form in multiple natural scene images and reading form-data

Student Number : 13_05405 Name : Yuhang HUANG Supervisor : Yukihiko YAMASHITA

1 Introduction

With the development of computer, most of tasks of data processing are done in computer, although there are still many paper forms, such as business reports, business cards, and invoices, which are still being used. To process both paper-based data and digital data at the same time, studies on form document recognition and understanding based on document images have been done, and a method for form-type identification and form-data recognition was proposed [1].

Nowadays, with the increase of portable camera devices such as camera in smart phone or car, text understanding in natural scene images has become a key task that can change our everyday lives by novel applications such as automated vehicle system. With portable camera and computer processing unit, now people can process data without desktop computer or scanner. A need of processing document easily from images in natural scene background has appeared in recent years.

To solve the situation where the original form image is lost or form media can not be scanned like car number plate, in this study I propose a system of extracting unknown common form in multiple natural scene images by analyzing the differences of the contents of images to find out the text region and reading form-data.

2 Form extracting and reading system

The proposed system consists of three parts. A. Extract same-form template image target t from input image data set $I = \{i_1, i_2, \ldots, i_n | i_k, k = 1, 2, \ldots, n\}$. B. Analyze the difference between template t and each image i_k and mark different text region in mask image m. After processes A and B, template image t and mask image m are obtained. C. Execute template matching between template image t and each image q_j in test image set $Q = \{q_1, q_2, \ldots, q_m | q_j, j = 1, 2, \ldots, m\}$ and extract the result of text region set $R = \{r_1, r_2, \ldots, r_m | r_j, j = 1, 2, \ldots, m\}$ using mask image m.

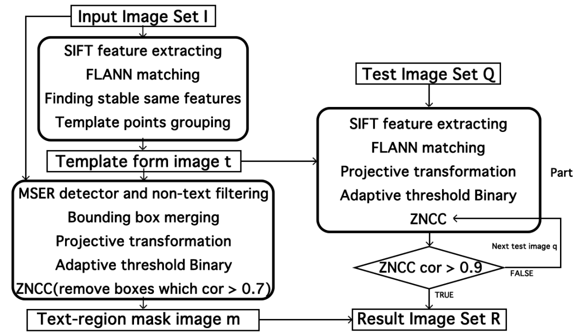

Figure 1: Flow chart of proposed system

A. Extract template image target t

Firstly, we change all the images i_k in I to gray scale and execute Scale-Invariant Feature Transform (SIFT) [2] to each image i_k to get their feature keypoint descriptors $D = \{d_1, d_2, \ldots, d_n | d_k, k = 1, 2, \ldots, m\}$. A matching method of Fast Library for Approximate Nearest Neighbors (FLANN) is done for feature matching [2]. By matching i_1 to i_2, i_2 to i_3, $\ldots$,i_{n-1} to i_n, and finally i_n to i_1, we make a matching cycle of the input image set I, which can provide a map set $\{f | f_k : d_k \to d_{k+1}, f_n : d_n \to d_1, k = 1, 2, \ldots, n-1\}$. Secondly, we pick up the feature points $p \in P_{\text{target}l}$ which meet $P_{\text{target}l} = \{p | p \in d_l, f_{l-1} \circ f_{l-2} \circ \ldots \circ f_1 \circ f_n \ldots \circ f_l(p) = p\}$, which can find a set of stable features among images in I. Finally, we group points $p \in P_{\text{target}l}$ with rectangle as target image region, and find out the best $P_{\text{target}l}$ of which rectangle is the most nearly parallel with horizon, in order to find a good template for text extracting. And then we clip a template image t from the original image i_l by using the rectangle region.

B. Mark different text regions

After process A, we can get the template image t and its original image i_l. We apply Maximally Stable Extremal Regions (MSER) method that performs well in extracting character candidates [3]. Firstly, we execute the MSER detector to the template image t and find the candidates of character. Using geometric properties of text to filter out non-text regions with thresholds [4], we can get text regions with rectangle boxes. After expanding this bounding boxes and merging the connected boxes, we finally get text regions. Secondly, we transform the template image t and the images in image set I to binary images using the adaptive threshold method. And then we execute projective transformation from each image $\{i_k \in I, k = 1, \ldots, l-1, l+1, \ldots, n\}$ to template image t. By calculating the Zero-mean Normalized Cross Correlation (ZNCC) coefficients with each block image clipped by text regions after blurring them by a Gaussian function, we can find differences between template image t and i_k.We remove the text region results if not all the correlation coefficients of the corresponding region among the images are lower than 0.7. Finally, we save all the results of text regions that remain as the mask image m.

C.Read form-data from test image set Q

First, we execute SIFT both to template image t and to test images $q_j \in Q$, and match each test image q_j to template t. Then we calculate the parameters of homography and execute projective transformation from each test image q_j to template t. Finally, we calculate the ZNCC coefficient between q_j and t. If coefficient is higher than 0.9, we extract the text from mask image m. If not, we turn to the first step to calculate q_{j+1}.

3 Experimental Result

We examined the system by setting I with four input images and Q with two test images. We implemented the procedure A, B and C using Eclipse C++ in Linux with OpenCV3.1 library, which contains SIFT feature extracting tools. And we implement the algorithm of ZNCC and MSER text extracting based on [3], [4].

The results of procedure A, B and C are shown in Figure 2.

Even though most of test data sets run successfully, we found that error occurs when using ZNCC to measure natural scene images because of lighting and displacement, which will get coefficients lower than 0.5 although two images are almost similar. MSER will miss some candidates. Grouping by margin will group all the form as one region.

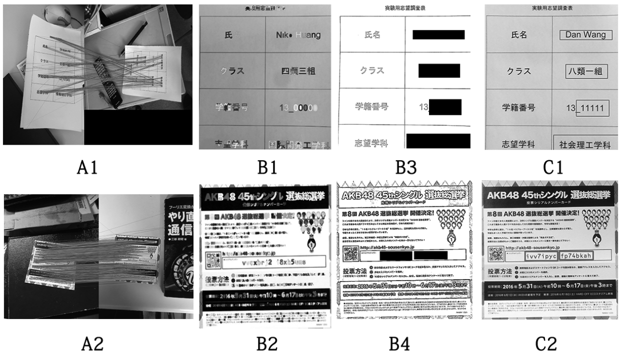
A1 B1 B3 C1
A2 B2 B4 C2

Figure 2: Experimental results. A1 and A2:SIFT feature matching, B1 and B2: text regions after removing non-text regions based on geometric properties, B3 and B4: text-region mask image m, and C1 and C2: result image r

4 Conclusions

In this study, I proposed a system of extracting common form and form-data from natural scene background text images with portable camera devices. By experiment, we confirmed that we can extract simple form and process form data simply with camera devices in a smart phone.

Performance could be improved, by using other feature extracting method to increase stable matched points in procedure A. Comparing not ZNCC coefficient but the contents of text, adding logical structure analysis, and using improved natural scene image text recognition methods can also improve procedure B.

References

[1] Sako H., Seki M., Furukawa N., et al, "Form reading based on form-type identification and form-data recognition." Proceedings of the 7th International Conference on Document Analysis and Recognition, Vol.3, pp.926-930, 2003.

[2] Lowe,D.G.,"Distinctive Image Features from Scale-Invariant Keypoints." International Journal of Computer Vision,Vol.60,No.2,pp.91-110,2004.

[3] CHEN, Huizhong, et al, "Robust text detection in natural images with edge-enhanced maximally stable extremal regions." Image Processing, 2011 18th IEEE International Conference, pp.2609-2612, 2011.

[4] Neumann, L. and Jiri M., "Real-time scene text localization and recognition." Computer Vision and Pattern Recognition, pp. 3538-3545, 2012.

A study on travel behavior and characteristic of residential zone in satellite metropolitan cities for urban function attraction
-Case study of Kashiwa city and surrounding cities

Student Number: 13B07172   Name: Yiting JIANG
Supervisor: Shinya HANAOKA, Kumiko NAKAMICHI

1 Introduction

In addition to the urban problems caused by rapid urbanization in Japan, a number of new problems has arisen such as decline of productive population and aging problems. On the other hand, local government will face financial difficulties if they try to maintain all the public facilities especially in sprawl areas. And the quality of resident's life will also decrease. Therefore, government realized that it is essential to reconsider the urban structure. According to this background, the Act on Special Measures Concerning Urban Renaissance was revised, and Location Optimization Plans has been created since 2014[1]. This means that local government should draw where is resident-attracting districts and where is urban function area specifically around core area to attract residents and urban functions to promote compact city. There are about 300 cities starting to set this plan as of 2016.

However, it is risky and unreliable to set Location Optimization Plans without clear current status of each core areas [2]. To avoid any possible risks, it is essential to evaluate the utilization conditions of each stations and facilities in core areas, which could be achieved by analyzing the travel behavior of the residents.

This paper aims to analyze the current situation of target city from residential zone type and resident's travel behavior from the view of urban function attraction.

2 Data and Methodology

2.1 Introduction of the target city

Kashiwa City is one of the satellite cites in the Tokyo Metropolitan Area. Like other cities around Tokyo, population increased rapidly around stations with the improvement of access to metropolis and housing developments in Kashiwa since 1970s. Furthermore, with a new train route opened in 2005, population of such satellite cities as Kashiwa will still increase in the future, although the population of most of cities in Japan is decreasing now. Under the financial pressure, local government need to reconsider urban structure and improve convenience of life of residents by improving urban function.

2.2 Analysis of residential zones

In order to grasp the basic urban structure of the target city, all residential districts in Kashiwa were classified by population density, land use regulation type, distance to city center and distance to the nearest railway station. Based on the national residential zone type classified by Nakamichi et al. (2016) [3], smaller number of zone types means higher national average value of fuel consumption per person per day, is used as a reference

2.3 Analysis of travel behavior

In this paper, the 5th Person Trip (PT) Survey in Tokyo Metropolitan Area conducted in 2008 is used to analyze resident's travel behavior in small zone unit. 1.4 million households are randomly chosen from 16 million households living in the Tokyo Metropolitan Area to answer this survey. Valid response rate is about 24%. Target zone of this research is the small zone that includes station in Kashiwa and surrounding cities. There are 16 small zones in total.

The methodology is shown as figure1.

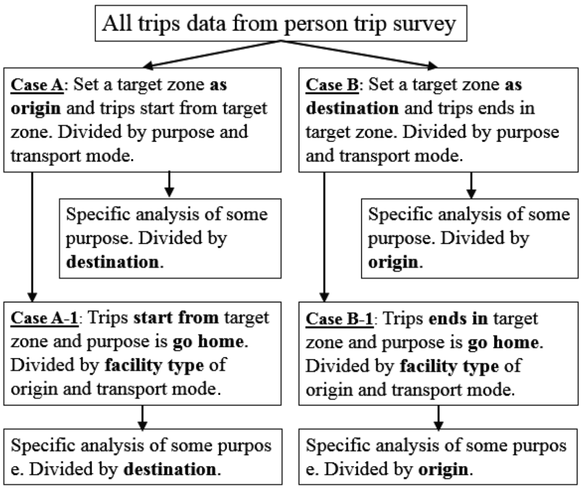
All trips data from person trip survey

Case A: Set a target zone **as origin** and trips start from target zone. Divided by purpose and transport mode.

Case B: Set a target zone **as destination** and trips ends in target zone. Divided by purpose and transport mode.

Specific analysis of some purpose. Divided by **destination**.

Specific analysis of some purpose. Divided by **origin**.

Case A-1: Trips **start from** target zone and purpose is **go home**. Divided by **facility type** of origin and transport mode.

Case B-1: Trips **ends in** target zone and purpose is **go home**. Divided by **facility type** of origin and transport mode.

Specific analysis of some purpose. Divided by **destination**.

Specific analysis of some purpose. Divided by **origin**.

Figure 1: Flow of travel behavior analysis

3 Results and Discussion

3.1 Results of residential zone type

Figure 2 is the final result of residential zone type.

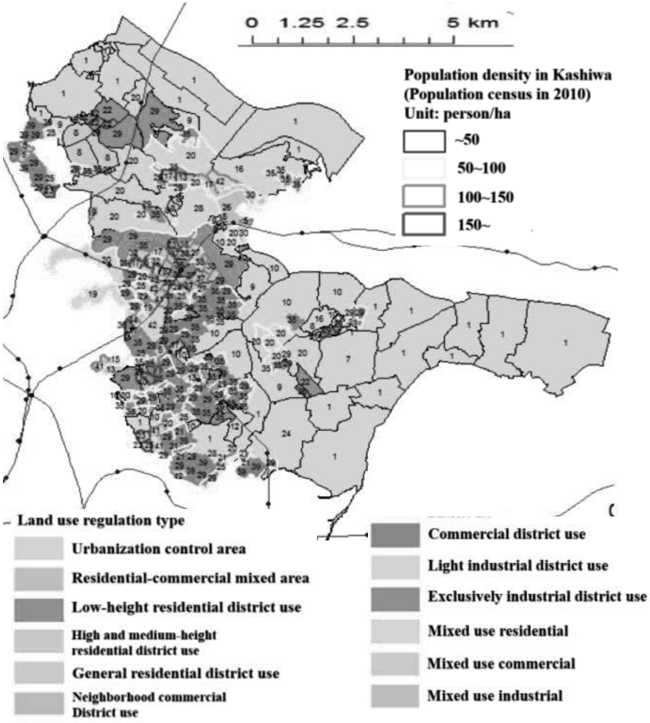

Figure 2: Kashiwa residential zone type

The results showed that most of towns are low-height residential district use, especially in southern Kashiwa and the fuel consumption around Kashiwa Station is lower than other stations surrounding the area. There are several densely populated areas far from railway stations and fuel consumption showed different tendency, so travel behavior analysis was used to find out the reason.

3.2 Results of travel behavior

The analysis of two typical zones are shown here.

The first is small zone 42211, which is in the center area of Kashiwa and includes west side of Kashiwa Station.

Figure 3 is the result of "Case A" that people depart from target zone. Each purpose has two cases, they are inner-inner (I-I) trip and inner-outer (I-O) or outer-inner (O-I) trip. The largest number of trips is the case that people go home from target zone to the others zones.

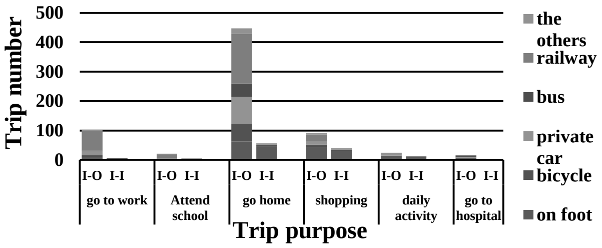

Figure 3: Case A (Trips from zone 42211 divided by purpose)

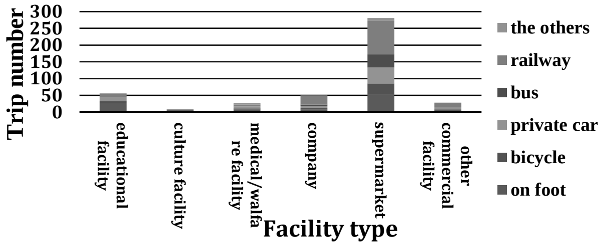

Figure 4: Case A-1 (Trips from zone 42211 for go home divided by type of facility that people last visited)

Figure 4 is "Case A-1" that people visit the facility in target zone and depart from target zone to home eventually. Use of commercial facilities is the highest in this zone and most people go home by public transportation or on foot from this zone.

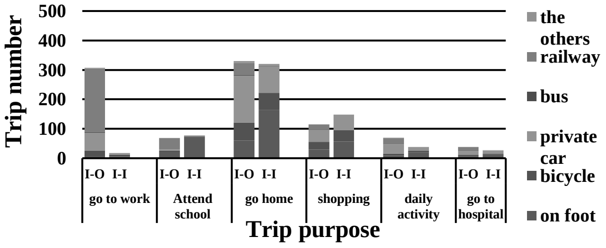

Figure 5: Case A (Trips from zone 42221 divided by purpose)

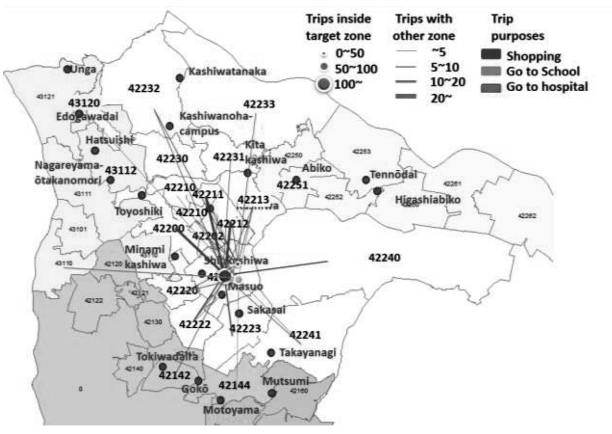

Figure 6: Trip flow from zone 42211 with 3 purposes

The second is small zone 42221, which is in the southern area and includes Shinkashiwa Station and Masuo Station.

Figure 5 is also the "Case A" situation. It shows that the number of OD trips for going home and shopping is much higher than other zones such as the zone 42211. Furthermore, share of private car is much higher than 42211 zone.

Figure 6 is an example of a specific analysis of " Case A" in which trips start from 42221 zone. This figure shows that a majority of the trips are from southern area to northern area. Especially when people go shopping they usually choose nearby places or the city center.

3.3 Summary

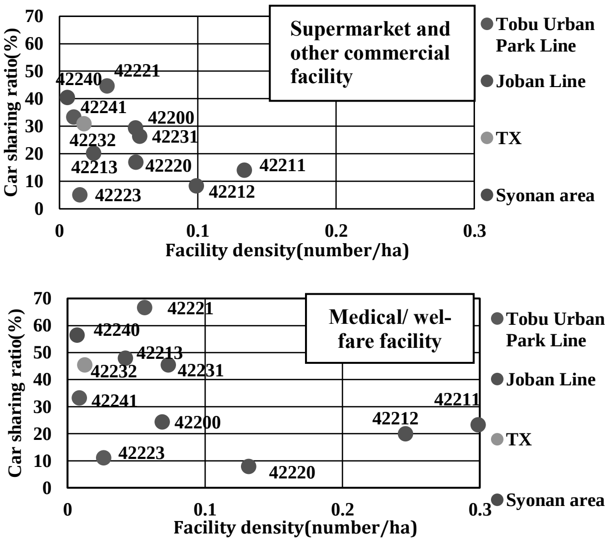

Figure 7: Facility density and private car share

Figure 7 shows the relationship between facility density and car share divided by railway line. It shows that areas along Joban Line have more facilities and lower car share. The area along Tobu Urban Park Line has lower facility density and higher car share.

4 Conclusion

People who live around Kashiwa Station and Minamikashiwa Station (Joban Line) are more likely to use public transportation since the number and frequency of buses is much higher than other station. Areas along Tobu Urban Park Line still need to be equipped with more public facilities especially the area around Sakasai Sation, most people living in this area drive private cars to other small zones for shopping. Takayanagi area has same situation with Sakasai Station area. But it has much fewer bicycle users.

In this research, the relationship between public facility and travel behavior and usage of each type of facilities in each core areas was made clear by arranging data from PT survey with a focus on the type of facilites that people last visit before they go home. This methodology could also be applied to other cities.

References

[1] 国土交通省—立地適正化計画制度: http://www.mlit.go.jp/en/toshi/ city_plan/ compactcity_network.html

[2] 肥後洋平, 森英高, 谷口守:「拠点へ集約」から「拠点を集約」へ－安易なコンパクトシティ政策導入に対する批判的検討,都市計画論文集,Vol49, No3,2014

[3] 中道久美子,呂田子,花岡伸也: 大都市圏及び地方圏都市における住宅地タイプと交通行動特性の変化,土木計画学研究・講演集, Vol.53, 2016.

高速コンポスト化に寄与する新規な好熱性酢酸分解菌の特定

学籍番号:13_02074　氏名: 氏家大祐　指導教官:中崎清彦

1 はじめに

近年、大量に発生する廃棄物の効率的な処理が大きな関心を集めている。廃棄物の中でも家庭・飲食店等から廃棄される生ごみはコンポスト化処理により有機肥料として有効利用が可能である[1]。しかしながら、生ごみはコンポスト化の過程で多量の有機酸が発生し、pHが低下することによって微生物の活性が阻害されコンポスト化に長い時間がかかることが知られている。

コンポスト化の過程で有機酸を分解する微生物の研究がおこなわれてきた。40℃付近の中温条件で有機酸を分解する酵母はすでに報告されている[2]。一方で、コンポスト化の高温期にあたる 60℃付近で有機酸を分解する微生物の存在はこれまでのところ知られていなかった。60℃付近で酢酸を分解できれば微生物の活性を促し、コンポスト化の時間を短縮できる。

当研究室の平井は 60℃のコンポスト化で活発な酢酸の分解がおこる事象を偶然に見いだしている(Run D-1)[3]。本研究では、Run D-1 のサンプル中に存在すると考えられる、高温条件下で酢酸を分解する新規な微生物の特定を目的とした。

2 実験方法

2-1 コンポスト化操作

モデル的な生ごみはラビットフードと米を乾燥重量比で 7:3 に混合して調整した。モデル生ごみにおがくずを通気性改良材として、また市販の微生物資材(オーレスG, (株)松本微生物研究所)を種菌として乾燥重量比で 10:9:1 に混合しコンポスト混合原料とした。コンポスト混合原料を 30L のコンポスト装置中に湿重量で 3 kg 投入し、底部より通気量を増減させて温度を制御しながらコンポスト化をおこなった。サンプル 15g を経時的に取り出し、コンポスト化過程で変化する温度、CO2 発生速度、pH、含水率、有機酸濃度、微生物濃度を測定した(Run D-1)[3]。

2-2 酢酸分解菌の推定

Run D-1 のコンポスト化過程で経時的に取り出したサンプルに対しては 2 種類のインデックスプライマー(Nextera XT Index 1 (N7xx), Nexteea XT Index 2 (S5xx))を用いて 16S rRNA の V4 領域を増幅して、NGS(Next Generation Sequence)を用いた解析をおこなうことによりサンプル中に存在する微生物の種類と相対的な存在度の経時変化を求めた。これをもとに好熱性酢酸分解菌を推定した。

2-3 酢酸分解菌の単離

酢酸分解菌の培養には酢酸を唯一の炭素源とする液体および寒天培地(CH_3COOH 1g/L, Na_2HPO_4・$12H_20$ 12.362g/L, $(NH_4)_2SO_4$ 2.0g/l, KH_2PO_4 2.0g/L, $MgCl_2$・$6H_2O$ 0.34g/L, $FeSO_4$・$7H_2O$ 2.8mg/L, $MnSO_4$・$4H_20$ 2.23mg/L $CoCl_2$・$6H_2O$ 2.4mg/L, $CaCl_2$・$2H_2O$ 1.7mg/, $CuCl_2$・$2H_2O$ 2.8mg/L, $ZnSO_4$ ・ $7H_2O$ 0.287mg/L, $NaMoO_4$ ・ $2H_2O$ 0.242mg/L and agar 15g/L for agar plate) を用いた。Run D-1 のコンポスト化 8 日目のサンプルを滅菌水で 100 倍希釈し、液体培地 50mL に接種して 60℃, 150rpm で 3 日間集積培養した。集積培養の後、培養液 100μL を寒天培地に塗沫して 60℃で 5 日間培養した。その後、寒天培地上に現れたコロニーを純化して好熱性酢酸分解菌を単離した。単離した微生物を液体培地で純粋培養し、HPLC を用いて酢酸の分解能を確認した。

好熱性酢酸分解菌として単離した微生物の解析では 357F プライマーと 907R プライマーを用いて 16S rRNA の V3, V4 領域を増幅し、塩基配列を測定した。これにより単離した微生物を同定した。

3 結果と考察

Run D-1 ではコンポスト化 6 日目から 9 日目にかけて 60℃の高温条件下で酢酸が分解され、pH が 5.2 から 8.6 まで上昇した[3]。

図 1 に NGS を用いた Run D-1 中の菌叢解析の結果を示す。NGS によって 80 種類を超える微生物群の存在が確認され、各微生物群の相対的な存在度が明らかになった。先に述べたように Run D-1 ではコンポスト化 6 日目から 9 日目にかけて酢酸が分解されているので、好熱性酢酸分解菌の相対的な存在度はこの時期に高くなっていることが推測される。コンポスト化 6,8 日目の微生物叢では Ureibacillus (#18), Geobacillus (#60), Symbiobacterium (#57), Bacillus (#4), Bacillales (#2) が主な微生物であった。

Geobacillus(#60)の相対的な存在度に注目して Run D-1 中の酢酸濃度と比較した結果を図 2 に示す。コンポスト装置中の温度が 60℃に達した 4 日目以降、Geobacillus(#60)の相対的な存在度は酢酸濃度の増減と同じ傾向の変動をしていた。このような傾向を持つ微生物は Geobacillus(#60)のみであったことから、Geobacillus(#60)が酢酸を分解することで増殖している、好熱性酢酸分解菌であることが推定された。

Run D-1 コンポスト化 8 日目のサンプルを接種して得られた液体培地を塗沫した寒天培地の写真を図 3 に示す。この寒天培地から 8 種類の異なるコロニー形状を示

す微生物（uj1～uj8）を単離した。これらの微生物は高温条件下で酢酸を唯一の炭素源とする寒天培地上に増殖したので、好熱性酢酸分解菌であると考えられた。

これらの微生物を液体培地で純粋培養したときの、酢酸濃度の変化のうち uj1 と uj8 を図 4 に示す。uj1 と uj8 は 60℃で酢酸を分解するために、これらは好熱性酢酸分解菌であることが確かめられた。なお、塩基配列に基づいて uj1～uj8 を同定したところ、uj1 から uj7 は *Geobacillus* spp. の近縁であり、uj8 は *Aeribacillus pallidus* と相同性が高いことがわかった。

引き続いて、これらの微生物と Geobacillus（#60）の塩基配列を比較したところ、uj1, uj3, uj4, uj5, uj6 が Geobacillus（#60）に含まれることを確かめた。以上の結果、高温条件下での酢酸分解能を持つ uj1, uj3, uj4, uj5, uj6 が Run D-1 のコンポスト化においても高温で酢酸を分解するという重要な役割を担っているものと考えられた。

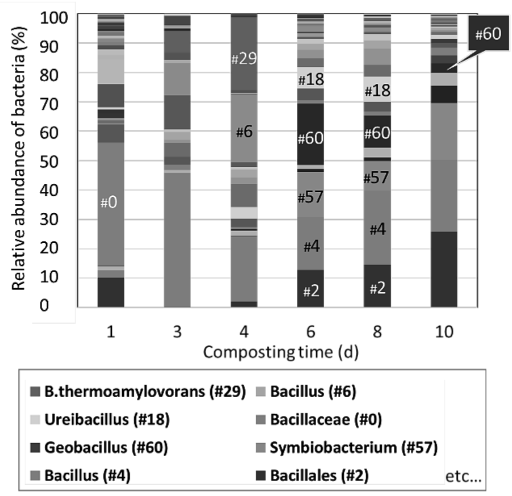

図 1 Run D-1 サンプル中の微生物叢変化

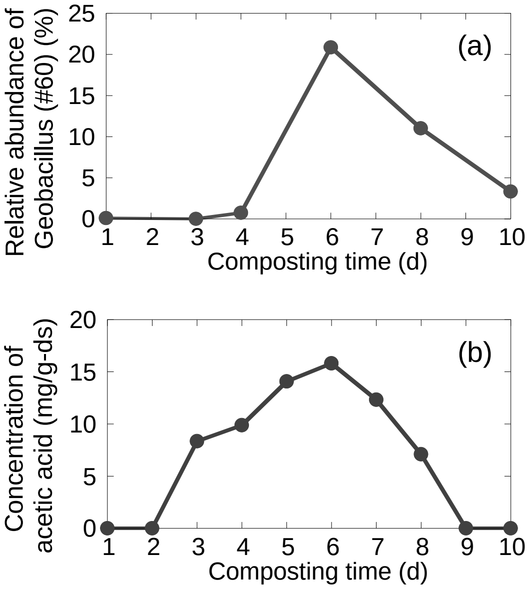

図 2 Run D-1 における (a) Geobacillus（#60）の相対的な存在度および (b) 酢酸濃度

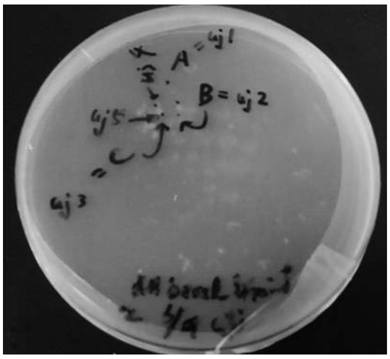

図 3 寒天培地上のコロニー

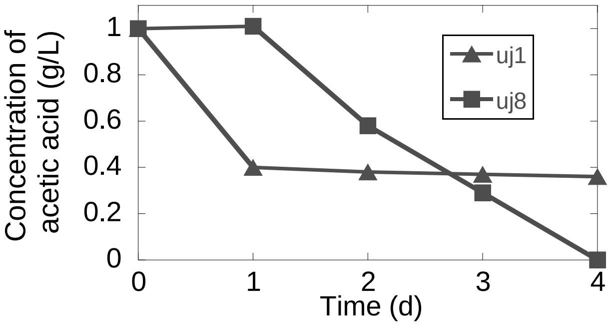

図 4 単離した微生物の培養にともなう酢酸濃度の変化

4 結論

60℃のコンポスト化で酢酸が活発に分解されているコンポスト中の微生物叢を NGS を用いて解析することにより、高温条件下で酢酸分解に寄与する微生物として Geobacillus 属細菌を推定した。また、そのコンポストサンプルから Geobacillus 属細菌を単離し、60℃で酢酸を分解できる新規な微生物の存在を確かめた。

5 参考文献

[1] Al-jabi, L. F., Halalsheh, M. M., & Badarneh, D. M. (2008) Conservation of ammonia during food waste composting. Environ. Technol. 29, 1067-1073.

[2] Nakasaki, K., Araya, S., & Mimoto, H. (2013) Inoculation of Pichia kudriavzevii RB1 degrades the organic acids present in raw compost material and accelerates composting. Biores. Technol. 144, 521-528.

[3] 平井秀平（2015） 酵母 RB1接種と温度制御による高速コンポスト化 東京工業大学 修士論文.

Clarification of Paratransit industry and driver's life satisfaction analysis considering social capital in Sri Lankan cities

Student number:13-06110 Number: Yuri Saito Supervisor: Shinya Hanaoka, Tomoya Kawasaki

1. Introduction

In many developing countries where public transport is poor, paratransit, which is middle transport mode between public transport and private transport, have important role for people's life. However, many of them are informal and not controlled by government and research about paratransit industry are not conducted much.

Sri Lanka is one of the countries where public transport is poor and many paratransit called "3-whleer" (3W) exist. Although 3W is not only necessary transport mode for people but also cause of several problems, research about 3W industry are not conducted much. Therefore, Sri Lanka is selected as a target country to clarify paratransit industry in developing country.

First objective of this research is to clarify the 3W industry in Sri Lanka. From first objective research, it is revealed that 3W driver's life is influenced by government policy and driver's group. Generally, "social capital" is defined as features of social organization, such as trust, norms, and networks. In this case, a relationship with government and driver's group is social capital for 3W drivers. Therefore, based on first objective results, second objective is to conduct driver's life satisfaction analysis considering social capital and compare the results among cities. The results help government to keep good relationship with 3W drivers when they make or introduce their policy.

2. Methodology

Two field surveys were conducted in this study. First one is interview survey with stakeholders of 3W industry to clarify the actual condition of 3W industry in October 2016. The second one is questionnaire survey in target four cities (Colombo (city area), Moratuwa (urban area), Padukka (rural area) in western province and Kandy (urban area) in central province) in December 2016. The questionnaire sheets including personal information, general social capital questions and 3W driver's social capital questions were made. Based on this questionnaire, ordered logit model is developed to clarify the factors which affect 3W driver's life satisfaction for each city.

3. The results of Interview survey

3.1 Stakeholders in 3W industry

National institution, provincial institution, Municipal Council/Local Council, and 3W association relate to 3W industry in urban area. Ministry of Transport (MOT), National Transport Authority (NTC), and Department of Motor Traffic (DMT) are national level stakeholders. Under the instruction of MOT, NTC are considering to replace 3W of electric environmental friendly vehicle in the future to solve air pollution problems caused by 3W. DMT are planning to make new 3W driver license considering age limitation and start stricter 3W driver training system from 2017 in order to reduce accident rate related to 3W.

Provincial Passenger Authority is provincial level stakeholder. Western Provincial Passenger Authority are introducing policy to control 3W in western province. Municipal Council or Local council make 3W parking space in a proper area. There are largest 3W authority, called "All Island 3W Drivers and Owner Association" and provincial 3W trade unions in some area. All Island 3W Drivers and Owner Association is consist of each province's 3W director and they are able to talk with political people and present their opinion about nation and provincial policies. On the other hands in rural area, Police have responsibility of 3W. They have role to build 3W parking space, register 3W vehicle and conduct training of 3W drivers.

3.2 About 3W drivers

3W drivers form local 3W driver group consisting 20-30 drivers called "Society". A society provides several welfare services to drivers and are important role for 3W drivers. There are two types of 3W drivers, one belongs to society (society driver) and the other do not belong to society (free driver). Generally, society limit the number of members by themselves so that free driver is difficult to belong to society even though they want to belong to it. Society has their own parking space given by Municipal Council and wait passengers in a line. Each society have their own rules and welfare services. Society drivers are not allowed to catch passengers except their society's parking space. On the other hands, although free drivers do not have parking space, they can catch passengers everywhere except society's parking spaces. The role of society is different among areas. The rate of societies which have relationship with nearby residents is 37% and 33% in Colombo and Kandy (urban area), respectively. However, Moratuwa is 53% and Padukka is 60%. In addition, the rate of societies which have relationship with other societies is only 13%, 14% in Colombo, Kandy and Moratuwa are 20%, respectively. However, Padukka is 77%. From the results, it is revealed that the farther from city area (that mean the lower power of provincial government), the stronger of connection between the societies and the area.

4. The results of questionnaire survey

4.1 Questionnaire sheet and sample numbers

459 samples in Colombo, 457 samples in Moratuwa, 510 samples in Padukka, 500 samples in Kandy, total about 1900 samples were gathered. However, Padukka questionnaire sheets have many no answer parts. Hence the models of 3 cities except Padukka are developed. After the descriptive analysis, ordered logit model was developed. Dependent variable is satisfaction of life (1 is extremely unsatisfied, 10 is extremely satisfied), and high number of each independent variable mean high satisfaction, high trust or strongly agree the question.

4.2 City comparison of the analysis results

Table 1 shows significant variables in Moratuwa, Colombo and Kandy. Although worthwhile and satisfaction of 3W is significant in Moratuwa and Colombo, importance of family and friends, which are general social capital variables, are significant in Kandy. Therefore, it is revealed that compared to Colombo Moratuwa, 3W driver job do not have big impact on driver's life satisfaction in Kandy. Justification of bribe is significant in only Moratuwa and Colombo therefore it might be western provincial specific characteristics. However, clear characteristics of western province have not obtained yet, therefore more deeper consideration is needed.

In Moratuwa, interesting job as a reason to still continue 3W driver job and satisfaction of 3W vehicle is significant. Therefore, life satisfaction of Moratuwa drivers who can enjoy their job comfortably is high. In Colombo, although driver can earn as he wants and interesting job as a reason to start 3W driver job are significant, trust of trade union is significant and coefficient is minus. Generally, 3W driver trade union take actions since they are not satisfied with government or provincial government. Therefore, high trust of trade union means low satisfaction with government. In Kandy, the variables which is significant in 2 cities are not significant. Not only general social capital parameters but also importance to have friendly relationship with other 3W drivers and have reliable 3W driver friends, which are 3W driver's social capital parameters, are also significant. Therefore, Kandy driver's life satisfaction is influenced by social capital more than Moratuwa and Colombo.

Table 1 Each city's significant variables

Independent variables	Moratuwa	Colombo	Kandy
Average Satisfaction of life (1Unsatisfied⇔Satisfyied10)	**7.00**	**7.33**	**8.36**
3W driver job is worthwhile and fulfilling	○	○	—
Driver are proud of his job.	○	○	—
Satisfaction of 3W driver job	○	○	—
How much you want to justify bribe?	○	○	—
Satisfaction of salary as 3W driver	△	○	○
Interesting job as a reason to still continue 3W driver job (1: Yes,0: No)	○	—	—
Unsatisfaction of the quality of your 3W vehicle	−○	—	—
Satisfaction of fuel cost and maintenance cost.	△	—	—
Interesting job as a reason to start 3W driver job (1: Yes,0: No)	—	○	—
Driver can earn as he wants	—	○	△
Trust of trade union	—	−○	—
Importance of family	—	—	○
Importance of friends	—	—	○
Trust of dealer	—	—	○
Importance to have friendly relationship with other 3W drivers	—	—	○
Driver have reliable 3W driver friends	—	—	○
Trust of press	—	—	○

(○:1% significance level, △:5% significance level)

▨ : General social capital parameters

▨ : 3W driver's social capital parameters

▨ : Personal information (3W driver)

Table 2 shows significant variables of society driver and free driver in 3 cities. In Moratuwa and Colombo, worthwhile and satisfaction of 3W job is significant in both drivers. Monetary variables, which are satisfaction of salary and fuel cost, is significant in both society drivers in Colombo and Kandy. Passenger variables, which are importance to communicate with passengers and like to communicate with passenger, are significant in both Moratuwa and Kandy. In Kandy, social capital variable is more significant in free driver than society driver.

Table 2 Significant variables of society driver and free driver

Independent variables	Moratuwa		Colombo		Kandy	
	S	F	S	F	S	F
3W driver job is worthwhile and fulfilling	○	○	○	○		
Driver are proud of his job.	○	○	○	○		
Satisfaction of 3W driver job	○	○	○	○		
How much you want to justify bribe?	○					
Importance to communicate with passengers		○				
Satisfaction of Municipal Council and Provincial Government		△	△			
3W driver is easy job			○			
Satisfaction of salary as 3W driver			○		○	
Trust of trade union			−○			△
Driver can earn as he wants			△			
Importance of family					○	
Satisfaction of fuel cost and maintenance cost.					○	
Trust of press					○	
Importance of friends					△	○
Importance to have friendly relationship with other 3W drivers						○
Driver like to communicate with passengers		△				○
Driver has 3W driver friends who help him when he faces some trouble						○
Driver have reliable 3W driver friends						○

(○:1% significance level, △:5% significance level)
S: Society driver F: Free driver

5. Conclusion

This study clarifies 3W industry situation by interview survey and conducted 3W driver's life satisfaction analysis by questionnaire survey considering social capital to clarify factors which affect their life satisfaction. From interview survey, it is revealed that now 3W industry is not under control of government and government is introducing or making new policy in order to control 3W. 3W drivers form local 3W driver groups and make their own rules and welfare services. From questionnaire survey, it is revealed that although the same province cities have common significant variables, different province city have different significant variables. In addition, there is different significant variables between society driver and free driver. As a future work, more models should be developed.

References

[1] JICA: Urban transport system development project for Colombo metropolitan region and suburbs:2014

[2] Johannes Orlowskil, PamelaWicker: The monetary value of social capital: *Journal of Behavioral and Experimental Economics*:2014

[3] Amal S. Kumarage, Mahinda Bandara, Darshini Munasinghe: Analysis of the economic and social parameters of the Three-Wheeler Taxi service in Sri Lanka: *Research in transportation economics*:2010

Simulation of forest fire using a coupled weather-fire model WRF-Fire

13B15384 Name : Kohei YAMASHITA Supervisor : Manabu KANDA

1. Introduction

When fire occurs, it triggers modifications to its surrounding meteorology. In investigations of neighborhood-scale fire incidents, it is necessary to consider the interaction between the fire and weather. Until now, a lot of research of wildland fire has been condicted internationally. However, this has never been conducted in Japan. The aim of this study is to test the applicability of a coupled weather-fire model in investigating Japan forest fire events.

2. Numerical Setting

2.1 WRF-Fire Model

The regional weather model Weather Research and Forecasting (WRF) which is widely used to calculate the weather field is capable of local and wide interconnection by the nesting method. WRF-Fire is an additional component of the model which couples the weather model with a fire-sread model. WRF calculates the surface wind field and is inputted to the fire spread module which calculates spread rate and feedbacks heat flux from the fire (Rothermal, 1972; Coen et al., 2012).

2.2 Target Forest Fire Event

We applied WRF-Fire to a forest fire incident that occurred in Japan. Figure 1 shows Takamikurayama forest fire in Hyogo Prefecture, the center of the nested domains. The fire occurred early in the morning of January 24th, 2011. 117 ha of forest area was burned.

To determine the fuel category of the forest, 13 fuel model (Anderson 1982) is commonly used. In the simulation, the forest was set to a category of 10(timber). Objective analysis data of the National Center for Environmental Prediction (NCEP) was used for the initial and lateral boundaries.

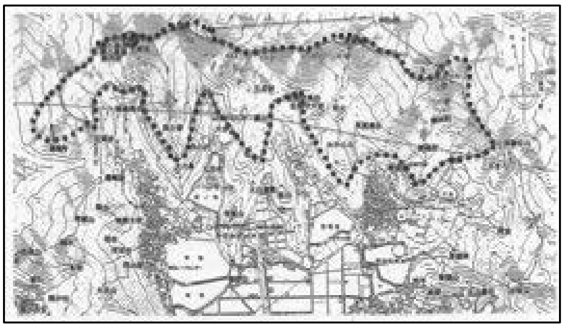

Fig.1 Burned area. Dotted line represents actual burned line

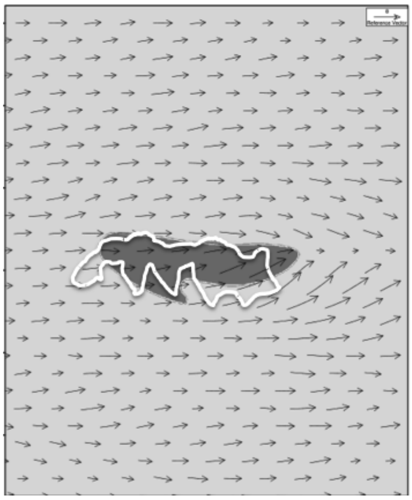

Fig.2 Simulated fire spread (orange area) corresponding to the actual burnt area (white line) in fig. 1. Arrows represent simulated 10-m wind velocity.

3. Results

Fig.2 shows the simulation result of fire spread area. The simulation captured the areal sequence of spread. Fire spread to eastwards following the wind. Fig.3 shows the temperature difference due to latent heat release from fire. Arrows in figures mean wind velocity. Figures show wind is affected by causing plume at fire front line.

In the first simulation, it was found that fire spread rate was overestimated although the pattern matches with the observed fire spread. The spread rate was improved by correcting the fuel category (from category 10 to 9) and limiting the fire spread based on fire-fighting activity (i.e. setting no fuel category to the fire-protected area) (Fig. 4). Simulation result is Fig.5. Simulation result area is similar to actual burned area.

Conclusion

The result of simulation showed feedback effect from fire. The result of simulation confirms that WRF-Fire can be applied to forest fires in Japan. The next step of this research is to improve the model to consider urban fire.

Acknowledgment

This research was funded by Promotion Program for Scientific Fire and Disaster Prevention Technologies.

Reference

Rothermal, 1972: A mathematical model for predicting fire spread in wildland fuels

Anderson, 1982: Aids to Determining Fuel Models For Estimating Fire Behavior

Coen et al., 2012: WRF-Fire Coupled Weather-Wildland Fire Modeling with the Weather Research and Forecasting Model

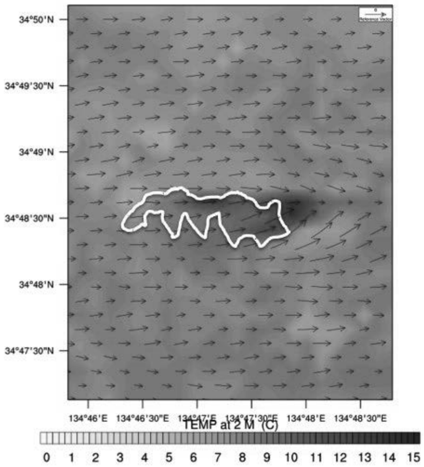

Fig.3 Change in 2-m. temperature (°C) due to forest fire.

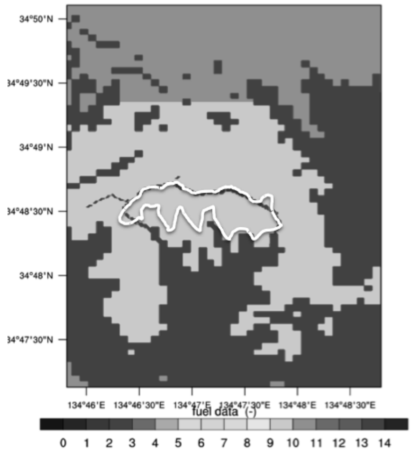

Fig.4 Forest fuel category based on the classification by Anderson (1982). Yellow and red area corresponds to fuel category 9 (litter) and no fuel category, respectively.

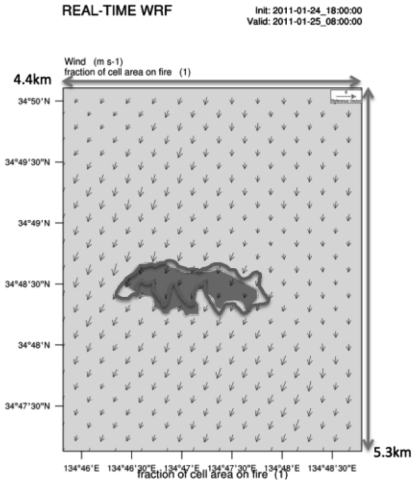

Fig.5 New simulated fire spread (orange area) corresponding to the actual burnt area (red line). Arrows represent simulated 10-m wind velocity.

Design of a Rectangular Patch Antenna for Radio Propagation Measurement

Student Number: 13B09596 Name: Xin Du Supervisor: Jun-ichi TAKADA

2017/2/21

1 Introduction

The antenna is an essential part in the wireless communication systems. A channel sounder is an important equipment to predict performance of advanecd systems such as MIMO [1]. There are numerous researches about evaluation of propagation mechanism for the MIMO systems at 2.4GHz and 60GHz frequency band [2]. In the next generation 5G systems, higher frequency band will be used and our group is focusing on measurement of the channel characteristics at 5GHz frequency band by using USRP channel sounder systems. Lightweight antenna is desired in a channel sounding equipment. Therefore, a patch antenna with 5GHz center frequency will be designed for both transmitter and receiver of USRP channel sounder.

2 Patch Antenna

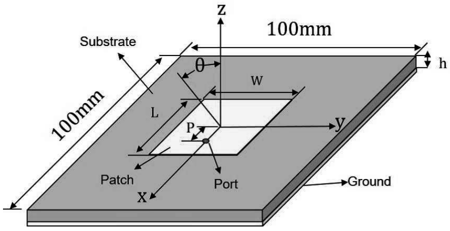

(a) Perspective view

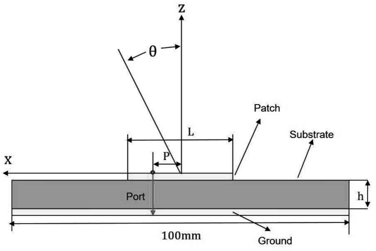

(b) Cross-sectional view

Figure 1: Configuration of a rectangular patch antenna

Figure 1 shows the configuration of a rectangular patch antenna. Here, an FR-4 substrate with 1.6mm-thick is used. The dielectric constant of FR-4 around 5 GHz is ϵ_r = 4.3. The thickness of the copper is 18μm. The resonance frequency of a rectangular patch antenna can be approximately expressed by Eq.(1)– Eq.(4) [3].

$$f_r = \frac{c_0}{2L_e\sqrt{\epsilon_r}} \tag{1}$$

$$L_e = L(1+\Delta)\frac{\sqrt{\epsilon_{re}(L)\epsilon_{re}(W)}}{\epsilon_r} \tag{2}$$

$$\Delta = \frac{h}{L}[0.882 + \frac{0.164(\epsilon_r - 1)}{\epsilon_r^2} + \frac{\epsilon_r + 1}{\pi\epsilon_r}\{0.758 + \log(\frac{L}{h} + 1.88)\}] \tag{3}$$

$$\epsilon_{re}(x) = \frac{\epsilon_r + 1}{2} + \frac{\epsilon_r - 1}{2}(1 + 12\frac{h}{x})^{-\frac{1}{2}} \tag{4}$$

Where, f_r is resonant frequency. c_0 is speed of light. L and W are the length and width of the patch, respectively.

3 Simulation and Design

The finite integration technique (FIT) based simulator CST Studio Suite was used in analysis and design. Discrete port, which is used for simple modeling, with 50Ω impedance is set at P. To adjust center frequency at 4.85GHz, $L(= W)$ is determined according to the Eq.(1)–Eq.(4) as the initial value. The feed offset P was set by 1.9mm tentatively. $L(= W)$ is changed to adjust center frequency and $L = W = 13.2$mm was determined by the simulator. Then, L and W are changed individually for fine tuning. Figure 2 shows frequency characteristic of reflection coefficient S_{11} with variations of L ($W = 14.0$mm). Fine adjustment of resonance frequency can be controlled by changing the values L and W. Finally, $L = 13.6$mm and $W = 14.0$mm was determined for the antenna with center frequency of 4.85GHz.

Next, the SMA, which is used in the measurement, connector is introduced in the simulation as feed structure to validate the discrete port feed modelling. It was found that the shift of resonant frequency is negligible. Figure 3 shows frequency characteristic of reflection coefficient S_{11} with variations of P. When $P = 2.1$mm, the best matching can be realized. The relative bandwidth is 2.45% (for $|S_{11}| < -10$ dB) and 4.94% (for $|S_{11}| < -5$ dB).

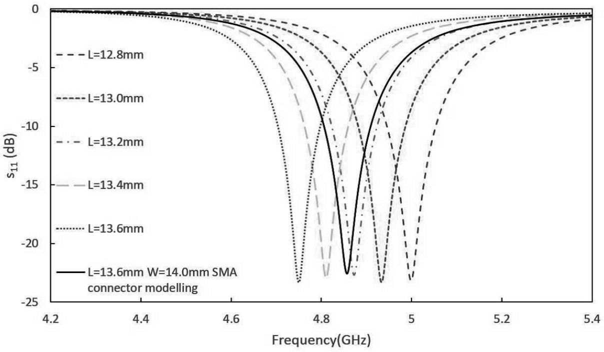

Figure 2: Frequency characteristic of S_{11} with L

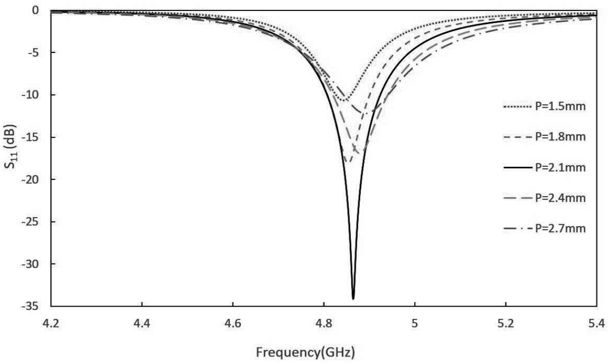

Figure 3: Frequency characteristic of S_{11} with P

In order to make the lightweight patch antenna, it is necessary to miniaturize the substrate size. The simulation shows the influence is not large until substrate size is larger than 50mm-length square. Therefore 50mm-length square substrate is used for fabrication. Figure 4 shows gain pattern with lengths of substrate ($L = 13.8$mm $W = 14.0$mm $P = 2.1$mm). Here, the angle theta (θ shown in Fig. 1) is the angle from z axis.

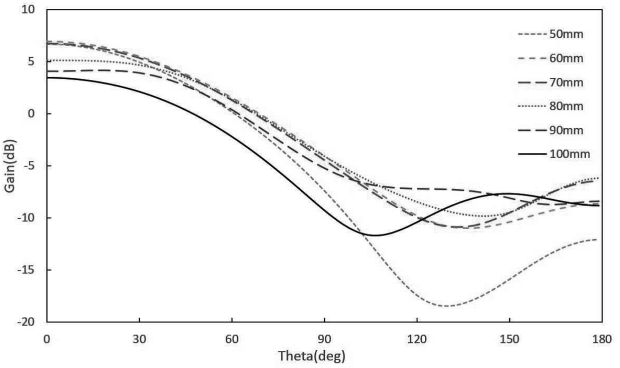

Figure 4: Gain pattern with lengths of substrate (x-z plane)

4 Measurement and Results

A CAD software EAGLE and milling machine were used for fabrication of the antenna. An SMA connector was soldered after drilling and milling the substrate as shown in Fig. 5.

(a) Front view (b) Back view (c) After soldering

Figure 5: Fabrication of Patch Antenna

Figure 6 shows the measured and simulation result of frequency characteristic of S_{11}. Vector network analyzer ROHDE&SCHWARZ ZVA 40 was used in measurement. The shift of center frequency was observed. The measured center frequency is about 5.1GHz.

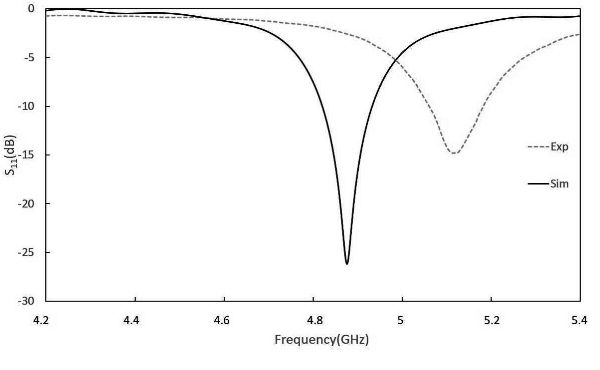

Figure 6: Measured and simulated S_{11}

According to Eq.(1)– Eq.(4), the reasons for frequency shift were considered. The thickness and permittivity of substrate may cause frequency shift. In fabrication, length and width of the patch will also affect the center frequency. Precision of the dimensions of the patch was enough. It is difficult to control thickness of substrate with milling machines while in-plane pattern can be precisely controlled. The measured thickness of the fabricated antenna was 1.4mm. The simulation was conducted to check the influence of thickness of the substrate. Figure 7 shows frequency characteristic of S_{11} for two kinds of thickness (1.4mm and 1.6mm). The center frequency of 1.4mm-thick substrate is higher than that of 1.6mm-thick one.

Another potential possibility of frequency shift is estimation error of the substrate dielectric constant. In the simulation, dielectric constant of 4.3 is used for the FR-4 substrate. However, it is known that the FR-4 has dispersive characteristic around GHz band and dielectric constant become small as the frequency becomes higher [4]. For example the dielectric constant of substrate is about 4.0 at 5.94 GHz [5]. Figure 7 also shows that the difference of frequency characteristic of S_{11} between two different dielectric constant, 4.3 and 4.0 (h=1.4mm). The center frequency is about 5.1GHz when dielectric constant is 4.0. There is a high possibility the thickness and dielectric constant factors cause the center frequency shift.

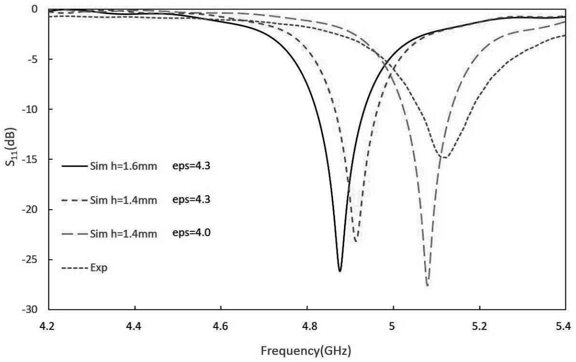

Figure 7: Comparison between different thickness and dielectric constant

5 Conclusion

A rectangle patch antenna was designed for channel sounder at 5GHz band. An antenna was fabricated and measured. Frequency shift was observed from simulation. The frequency shift may due to the estimation error of dielectric constant of the substrate. Frequency adjustment is future study.

References

[1] Ezio Biglieri, Robert Calderbank, Anthony Constantiniades, Andrea Goldsmith, Arogyaswami Paulraj and H.Vincent Poor “*MIMO Wireless Communications*” isbn.13-978-0-521-87328-4, pp.1-7, publisher.Cambridge University Press, 2007.

[2] Tianyang MIN, Kentaro SAITO, Minseok KIM and Junichi TAKADA “*Channel Sounding in 2.4GHz and 60GHz band for Multi-band Wireless LAN System*” IEICE Technical Report SRW2016-39 pp.37-41, 2016-08.

[3] G. A. Deschamps “*Microstrip Microwave Antennas*” 3rd USAF Symposium on Antennas, 1953.

[4] Shingo INOUE and Futoshi KUROKI “*Measurement on Dielectric Properties of FR-4 Substrate at Millimeter-wave Frequency*” IEICE Technical Report, vol.111, no.351, MW2011-126, pp.5-8, 2011-12.

SFM-AKAZEによる3D点群再構築に関する研究

学籍番号:13B04506　　名前:魏　嘉昊　　指導教員:山下　幸彦　準教授

1　はじめに

現在、コンピュータービジョンの分野において、複数の画像から対象物の3次元情報を取得する3次元再構築手法に関する研究が数多く行われている。最近は動画像解析（SFM）に基づいた3次元情報の取得に関して世界の人々が研究を行っている。

SFMでは、まず3枚以上の複数の画像間の対応点を、各画像の特徴点の特徴量に基づいてマッチングによって探す。マッチングした対応点からエピポーラ幾何（Epipolar Geometry）の理論を用いてカメラの内部パラメーターと外部パラメーターを計算し、Bundle Adjustment手法で誤差を抑えることで各カメラの位置及び対象物の3次元位置を推定する。本研究では、従来多数のSFMソフトウェアに使われているSIFT（Scale-Invariant Feature Transform）の代わりに、最近注目されているAKAZE（Accelerated KAZE）の特徴量を用いて対応点をマッチングすることを試みる。

2　カメラモデル及びエピポーラ幾何

カメラで撮影した画像は、3次元空間の物体をカメラを通して2次元平面に射影したものである。最終的には、ある物体に対し、行列をかけて3次元空間の点から2次元平面の点に変換できる。エピポーラ幾何とは、3次元空間に存在する点をステレオ視から観察する際の相対的なカメラ位置や姿勢などの情報を記述できる幾何である。

2.1　カメラの内部パラメーター

まず、3次元カメラ座標系上の点(X_C, Y_C, Z_C)、2次元画像平面上の点(x, y)はカメラの焦点距離fを用いて、以下の関係を満たす。

$$\begin{pmatrix} x \\ y \end{pmatrix} = \frac{f}{Z_C}\begin{pmatrix} X_C \\ Y_C \end{pmatrix} \tag{1}$$

また、点の位置の次元を一つ上げた同時座標で表す。すなわち(x, y)の代わりに$(x, y, 1)$で表す。

さらに、画像座標(x, y)からディジタル画像座標(u, v)への変換が必要である。その関係式は以下となる。

$$\begin{pmatrix} u \\ v \\ 1 \end{pmatrix} = \begin{pmatrix} k_u & -k_u \cot\theta & u_0 \\ 0 & \frac{k_v}{\sin\theta} & v_0 \\ 0 & 0 & 1 \end{pmatrix}\begin{pmatrix} x \\ y \\ 1 \end{pmatrix} \tag{2}$$

今までの式を以下のようにまとめる。

$$s\begin{pmatrix} u \\ v \\ 1 \end{pmatrix} = K\begin{pmatrix} X_C \\ Y_C \\ Z_C \\ 1 \end{pmatrix} \tag{3}$$

ここで、行列Kはカメラの内部行列である。

2.2　カメラの外部パラメーター

一般には、世界座標系とカメラ座標系は独立である。3D再構築する際には一つの固定した世界座標系と複数のカメラ座標系が必要となる（一般には最初のカメラ座標系を世界座標系にする）。

$$\begin{pmatrix} X_C \\ Y_C \\ Z_C \\ 1 \end{pmatrix} = D\begin{pmatrix} X_W \\ Y_W \\ Z_W \\ 1 \end{pmatrix} \tag{4}$$

外部パラメーターはワールド座標系内のカメラ座標系の位置t（平行移動Translationを表す3x1ベクトル）と姿勢R（回転Rotationを表す3x3行列）によって決定できる。Rとtを用いて座標間の関係を式で表すと以下となる。ここで、Dと0_3は次式で定義される。

$$D = \begin{pmatrix} R & t \\ 0_3^t & 1 \end{pmatrix}, 0_3 = [0, 0, 0]^T \tag{5}$$

2.3　カメラ行列

上述のカメラ内部パラメーターと外部パラメーターを合わせた関係式は以下のようになる。

$$s\begin{pmatrix} u \\ v \\ 1 \end{pmatrix} = K\begin{pmatrix} X_C \\ Y_C \\ Z_C \\ 1 \end{pmatrix} = KD\begin{pmatrix} X_W \\ Y_W \\ Z_W \\ 1 \end{pmatrix} = P\begin{pmatrix} X_W \\ Y_W \\ Z_W \\ 1 \end{pmatrix} \tag{6}$$

ここで、行列Pはカメラ行列（または新たな透視投影行列）と呼ばれる。世界座標とディジタル画像座標の関係を表す大事な行列である

2.4　エピポーラ方程式

仮に、3次元ワールド座標系のある点Pに対し、$p = (x, y, 1)^T$と$p' = (x', y', 1)^T$は2つの画像座標からなる同次座標とする。pとp'は以下の関係を持つ。

$$p' = Rp + t \tag{7}$$

同一平面上の三つのベクトルp、p'、tから二つのベクトルの外積と残る一つのベクトルの内積は0という性質を用いて以下の方程式が成り立つ。

$$p'^T[t \times (Rp)] = 0 \tag{8}$$

$$p'^T Ep = 0 \tag{9}$$

ここで、行列Eは基本行列（Essential Matrix）と呼ばれる。基本行列はベクトルtの歪対称行列$[t_x]$と回転行列Rから構成される。また、上述したカメラ同次座標における点p、p'に対する2次元画像平面のディジタル

画像座標系の 2 次元点を $x = (u, v, 1)^T$、$x' = (u', v', 1)^T$ に変換する。関係式は以下のようになる。

$$x = Kp, x' = K'p' \tag{10}$$

上述したエピポーラ方程式は以下のように変わる。

$$\begin{aligned} p'^T Ep &= 0 \\ x'^T (K'^{-T} EK^{-1})x &= 0 \\ x'^T Fx &= 0 \end{aligned} \tag{11}$$

ここで、行列 F は基礎行列 F（Fundamental Matrix）と呼ばれる。基礎行列 F はカメラの内部パラメーター K と外部パラメーター E 両方を含んでいる。

3 AKAZE 法

SIFT 法ではガウシンフィルターの等方性により勾配強度の大きい方向に対しても平滑化してしまうため、局所的な特徴及び輝度値が曖昧になってしまう。AKAZE ではエッジを保存するために非線形拡散フィルターを用いる。さらに、AKAZE では特徴記述子として独自の記述子を使用する。

3.1 非線形拡散フィルター

AKAZE 法は非線形拡散フィルターを用いることでエッジを保存することができる。

$$\frac{\partial L}{\partial t} = \mathrm{div}(c(x, y, z) \cdot \nabla L) \tag{12}$$

$$c(x, y, t) = g(|\nabla L_\sigma(x, y, t)|) \tag{13}$$

$$g_2 = \frac{1}{1 + \frac{|\nabla L_\sigma|^2}{k^2}} \tag{14}$$

3.2 非線形スケールスペース

対数ステップの離散化スケールスペースはオクターブ o とサブレベル s で書かされ、スケール σ と次式のように対応する。

$$\sigma_i(o, s) = \sigma_0 2^{\frac{o+s}{S}} \tag{15}$$

拡散フィルターは時間軸で定義されているため、下式でピクセル軸から時間軸へ変換する。

$$t_i = \frac{1}{2}\sigma_i^2, \ (i = 0, 1, \cdots, N) \tag{16}$$

3.3 特徴点検出

特徴点を検出するために、非線形スケール空間におけるフィルタリングされた画像 L の各点で、ヘッセ行列の行列式を計算する。下式は標準化する際に用いる微分演算子である。

$$L^i_{\mathrm{Hessian}} = \sigma^2_{i,\mathrm{norm}}(L^i_{xx}L^i_{yy} - L^i_{xy}L^i_{xy}) \tag{17}$$

3.4 特徴量記述

AKAZE 法は KAZE 法のように各特徴点ごとに半径 σ_i ごとに $6\sigma_i$ までの範囲を探索することで特徴量発見し、各特徴点の一次導関数 L_x と L_y を特徴点のガウス関数によって重み付けする。特徴点の方向は $\frac{\pi}{3}$ の角度のベクトルの総和になる。その総和のベクトルのオリエンテーションが特徴点の方向となる。

4 実験結果

今回の実験は fountain-P11、Herz-Jesu-P8、entry-P10 三つの画像データを用いて、SFM-SIFT と SFM-AKAZE を比較して、その結果を検討する。

Table 1: 実験結果

	fountain		Herz-Jesu		entry	
	SIFT	AKAZE	SIFT	AKAZE	SIFT	AKAZE
画像数	11	11	8	8	10	10
合計点数	8188	4497	4501	4431	9936	8570
BA 前誤差 [pixel]	4.04	3.99	3.50	3.28	7.08	8.80
BA 後誤差 [pixel]	1.45	1.95	1.40	1.73	3.88	5.20
抽出時間 [s]	36.40	25.05	25.77	18.19	34.66	24.79
マッチング時間 [s]	5.99	3.80	3.36	2.25	11.09	15.74
合計時間 [s]	47.51	31.15	31.48	22.70	51.09	44.02

SFM-AKAZE 法は SFM-SIFT 法より再構築した点群数が少なかった。しかしながら、計算時間に関しては SFM-AKAZE 法は SFM-SIFT 法より明らかに短縮できた。リアルタイム 3D 点群再構築や 3D 顔認識などの様々な方面の応用は期待できる。

5 結論

本研究では、対応点マッチング法の AKAZE 法を用いた 3D 点群再構築手法を提案した。実験の結果、再構築した点群数は一般の SFM-SIFT 法より少なかったが、時間を短縮できることがわかった。対応点マッチングした後の誤差を減らすステップの改善により再構築する点群数の増加が今後の課題である。

参考文献

[1] Alcantarilla, Pablo F., and T. Solutions. ”Fast explicit diffusion for accelerated features in nonlinear scale spaces.” IEEE Trans. Patt. Anal. Mach. Intell 34.7 (2011): 1281-1298.

[2] Alcantarilla, Pablo Fernandez, Adrien Bartoli, and Andrew J. Davison. ”KAZE features.” European Conference on Computer Vision. Springer Berlin Heidelberg, 2012.

[3] Hartley, Richard, and Andrew Zisserman. Multiple view geometry in computer vision. Cambridge University press, 2003.

[4] Perona, Pietro, and Jitendra Malik. ”Scale-space and edge detection using anisotropic diffusion.” IEEE Transactions on pattern analysis and machine intelligence 12.7 (1990): 629-639.

Fe交換ゼオライト触媒によるC_3H_6を用いたNO選択還元

学籍番号:13_09159　名前:譚　楊　指導教員:日野出洋文

1 背景

今日、自動車は産業社会や日常生活において不可欠な存在となっている。一方で排気ガスが工場の排煙とともに大気汚染源の一つとなっている。近年、特に発展途上国において大気汚染問題が深刻で、WHOがPM2.5など大気汚染による死者が2012年に推計700万人超だったとの報告を出した。自動車排ガス中の主要な大気汚染物質は、CO、HC、NO_X、SO_2、パティキュレート（未燃焼すす）である。NO_Xの除去が重要であることが明白である。

NO_X除去の有効な方法の一つは触媒技術で、その中に炭化水素によるNOxの選択的接触還元（HC－SCR）がある。これは排ガス中の未燃焼のプロピレンなどの炭化水素または含酸素有機化合物をNOxの還元剤に使用する技術である。

これまでゼオライト系、金属酸化物触媒、貴金属系触媒においてNOx選択還元能が見出されている。ゼオライト特にZSM-5（MFI）、モルデナイト（MOR）、ベータ（BEA）などにCuを担持した触媒によるHC-SCRを扱った報告が多いが、実用に至っていないのも事実である。またゼオライト結晶内部での拡散の効果が検討され、細孔内の反応物、生成物、水蒸気などの活性抑制物質の拡散が容易であるため、酸素の12員環からなる比較的大きな細孔を持つCo-ベータは、活性が高いことが報告されている[1]。

さらにFe交換ベータ型ゼオライトは、CO還元能を有すると共にN_2O分解活性を併せ持つことが報告されている[2]。

本研究では上で述べた既存研究のもとにFe交換ベータ型ゼオライトのNO選択還元活性について検討した。

2.実験

本研究ではベータ型ゼオライトにJRC-Z-B25(1)を使用した（以下はBetaと呼ぶ）。また比較的細孔径の大きなメソポーラスベータゼオライト（以下Betamesoと呼ぶ）を水熱合成法[3]で合成した。

Betaと水熱合成法により合成したBetamesoをイオン交換法でFeイオンを導入した。イオン交換過程での上澄み液を回収し、回収した液をすべて集め、イオン交換量を誘導結合プラズマ原子発光分析（ICP-AES）で測定した。

Fe交換ゼオライトを乾燥、550℃で6時間焼成し、触媒を調製した。当該触媒をFe-beta、Fe-betamesoとし、また比較として、Beta、Betamesoの選択還元活性を測定した。

炭化水素によるNO_Xの選択還元実験は常圧固定床流通式反応装置を用いた。一回の測定に0.4gの触媒を用い、NO（1500ppm）、O_2（10%）、C_3H_6（1500ppm）というガス組成（バランスガス:He）で実験を行った。空間速度は約$1.3\times10^4h^{-1}$である。

NOとNO_2の定量にはNO_X分析計（島津製作所NOA-7000）を使用した。CO_2の定量にはガスクロマトグラフ（GL Science社製GC－3200、TCD detector）を用いた。触媒のキャラクタリゼーションを熱重量分析・示差熱分析法（TG-DTA）、X線回折法（XRD）、ICP-AES、窒素吸着法（Nitrogen adsorption method）で行った。

3. 結果および考察

Fig.1で示したようにFeイオン交換ベータ型ゼオライト(Fe-beta)は300℃から500℃の間で他の触媒と比べて高い活性示した。350℃付近では一番高い活性（NO転化率63.6%）を示した。Fe-betamesoはFe-betaと同じ傾向を示し、350℃で一番活性（NO転化率52.6%)を

示すも、Fe-beta より低いことがわかった。Fe イオンを導入していないゼオライト触媒 Beta と Betameso はある程度活性を示したが、Fe イオンを導入したものと比べると活性が著しく低い結果となった。

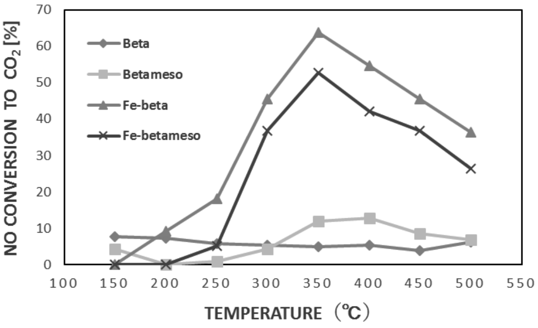

Fig.1 NO から N_2 の転化率[%]

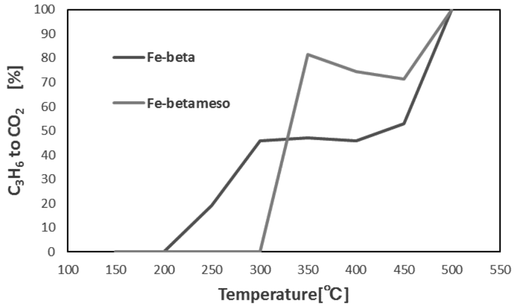

Fig.2 C_3H_6 から CO_2 転化率[%]

Fig.2 から触媒 Fe-beta と Fe-betameso は 300-450℃で高い CO_2 への転化率を示した。活性実験で 300-450℃で高い活性がでたことと一致したことから、この温度域で NO 選択還元反応が行われることがわかった。

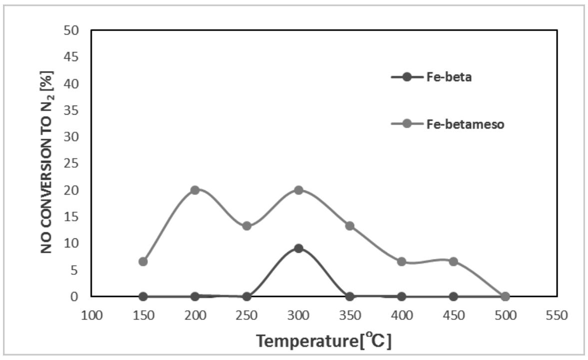

Fig.3 C_3H_6 の無い状態の転化率

Fig.3 から C_3H_6 の無い状態では活性が低いことから還元剤 C_3H_6 の存在は NO の還元分解に不可欠であることがわかった。

Table1 触媒の比表面積

	比表面積(m^2/g)
Fe-beta	733.9
Fe-betameso	405.6

Table1 の比表面積の結果から Fe－betameso より Fe-beta 比表面積が大きいことが Fe-beta の活性の高いことと一致したことから、比表面積が活性点の分散に影響していることが考えられる。

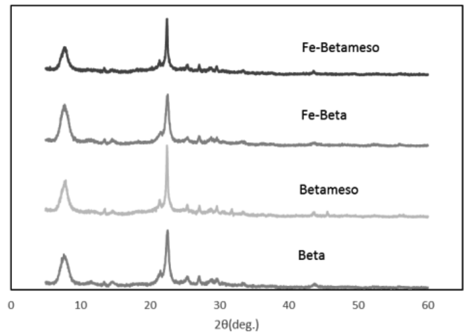

Fig.4 触媒 XRD パータン

Fig.4 に合成したベータ型ゼオライトや Fe-beta、Fe-betameso の XRD パータンを示した。結果はゼオライトの結晶構造はイオン交換のあとでも保たれ、またイオン交換量が少ないため、鉄の酸化物結晶相は検出されなかった。

TG-DTA の結果から各種の触媒は900℃まで熱的に安定しているが確認できた。

ICP-AES でイオン交換量を測定した結果 Fe-beta と Fe－betameso のイオン交換率はそれぞれ 0.69%、1.14%で Fe－beta の交換率(鉄含有量)が低いのにもかかわらず高い活性を示した。

4. 結論

Fe 交換ゼオライト系触媒は HC－SCR で高い活性示した。また比表面積は反応活性に関係していることがかわった。更に、実用化には水蒸気、SO_2などの反応阻害物質の影響と長時間運転時の耐性を検討する必要がある

参考文献:

[1]T.Tabata et al.,Catal.Today,27,91

[2]M.Rutkowska et al.,Applied Catalysis B(2013)

[3]Van Obers et al.Microporous and mesoporous Materials120(2009)

地方自治体の水道事業体の経営効率性と国際活動の関係

学籍番号：13_15556　氏名：山田 優志　指導教官：阿部 直也

1.研究の背景と目的

近年、我が国の地方自治体の水道局の一部は、開発途上国における水道事業の運営体制改善や人材育成、さらには技術協力などに関して積極的に活動を行っている。一方、開発途上国における水道事業は、地域やコミュニティーによっては、依然としてインフラとして十分に整備されていない状況があり、インフラとして上水道が整備されている地域においても、水質・水量ともに不十分な状況がしばしば指摘されている。具体的には、水道事業を担う組織の不十分なマネジメント体制や能力不足により、盗水や漏水問題、さらには水質汚染に伴う感染症などが指摘されている。

開発途上国の水道局職員の人材育成を怠ると、水道職員は、世界からの ODA により建設された高機能な水道施設を効率的に使用できない。また、開発途上国の無収水率は高く、供給した水を料金として効率よく回収できていない。このような問題を解決するために、現地の水道職員に日本の水道事業のノウハウを伝えるべきであると考える。国際活動に関する現状は、平成 20 年から平成 27 年の八年間にかけて 2,000 近くある水道事業体の中からわずか 23 事業体と活発であるとは言い難い。さらに、国際活動を直接的にはやっていない水道事業体も国際活動に貢献しようとしている。堺市と仙台市がそれにあたる。堺市水道局は公式に国際活動に乗り出すことを発表しており、仙台市は 2003 年から札幌市水道局の国際活動を一部引き受けている。

以上を踏まえ本研究の目的は二点である。第一に、国際活動の活発度に注目し、水道事業体の規模と経営率性の間に関係性があるかを明らかにする。第二に、国際活動の実績の有無に着目し、水道事業体の経営効率性に差があるのか明らかにする。

2. 研究の枠組み

国際活動に従事したことある水道事業体、政令指定都市の水道事業体、中核都市の水道事業体を対象(合計 64)に、各水道局の需要の大きさ[給水人口(人)]、施設の能力の大きさ[年間配水量(m3)]、技術力の大きさ[有収率(%)]、施設の規模の大きさ[職員数(人)]、水道料金(円)、事業収入(円)、事業支出(円)を知るために、それらの過去五年間(平成 23 年~平成 27 年)の平均値をデータとした。まずクラスター分析を行い水道事業体の規模と、国際活動の関係性を調べた。効率の面を調べる際には、DEA(BCC モデル)を用い、変数を DEA に投入する組み合わせを、すべての変数、技術的な変数、経済的な変数の三通りに分け、どの側面の効率値が国際活動に関係するのかを明白にした。そこで、国際活動に関係すると判明した側面の効率値をいくつか求め、クラスター分析を再度行うことで、効率値と国際活動に関係があるかを観察した。

3. 各水道局の規模と効率値

前述の全ての変数を投入し水道事業体の規模についてのクラスターを図.1 に挙げた。

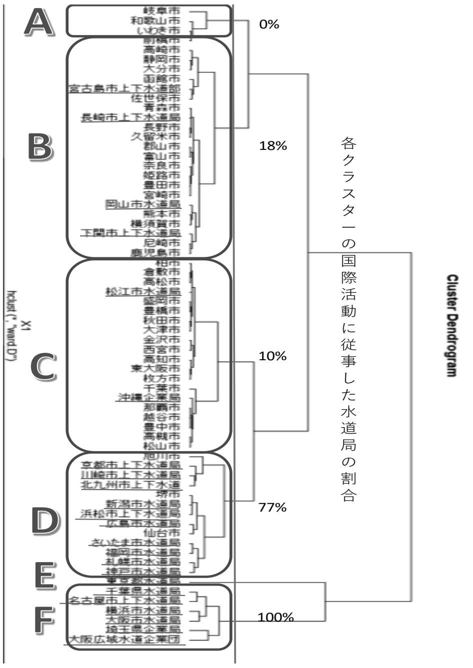

図.1 規模のクラスター分析

また、クラスターの各変数の平均値を表.1に挙げた。

表.1 各クラスターの平均値

	給水人口(人)	年間配水量(m3	有収率(%)	水道料金(円)	事業収入(円)	事業支出(円)	職員数(人)
Cluster A	3.65E+05	4.59E+07	8.78E+01	5.18E+09	5.49E+09	4.75E+09	1.28E+02
Cluster B	4.06E+05	5.14E+07	8.85E+01	6.94E+09	7.57E+09	6.75E+09	2.12E+02
Cluster C	3.85E+05	4.47E+07	9.25E+01	6.45E+09	7.02E+09	6.44E+09	1.73E+02
Cluster D	1.10E+06	1.29E+08	9.29E+01	2.09E+10	2.36E+10	2.24E+10	4.45E+02
Cluster E	3.86E+06	4.30E+08	9.24E+01	5.01E+10	5.64E+10	4.98E+10	1.15E+03

国際活動に貢献したことがある水道事業体の割合が多いクラスターほど、各変数の平均値が高いことが見受けられた。ここから、規模が大きいほど国際活動に貢献していることが確認できた。また、DEAでは、全体の効率値、技術的効率値、経済的効率値を観測した。技術的な変数を入れた時にだけ、国際活動に貢献したことある水道局の効率値とそうでない水道局の効率値に有意性を確認できた(図.2)。経済的効率値で二つの間に有意性が見られなかった背景は、国際活動をする際にJICAによる財政補助があり、各水道事業体で国際活動の費用を負担しなくてもいいことが考えられる。

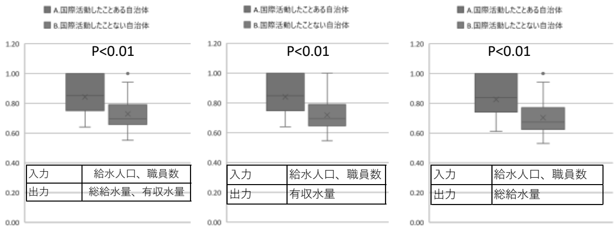

図.2 技術的効率値の有意性

技術的な変数をいくつか組み合わせて各々効率値を出し、クラスター分析を行った。クラスターβとγには国際活動に貢献した水道局の割合が高く(α=17%, β=75%, γ=39%)、各々のクラスターの効率値の平均を見ると、クラスターβとγが全体の効率値の平均よりも高いことを確認した(図.4)。ここから技術的効率と国際活動にも関係があることを確かめた。

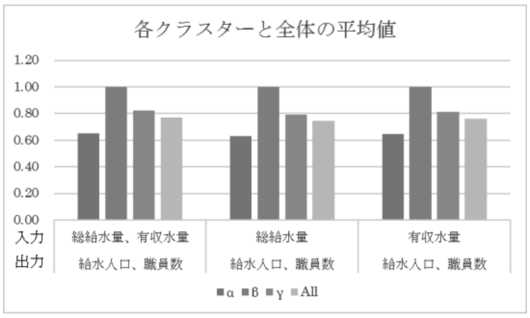

図.3 各クラスターと全体の平均値

4. おわりに

以上より本研究の結論をまとめる。第一に、地方自治体の水道事業体による国際活動の活発度に注目すると、水道局の事業規模と技術的効率性の間に正の関係性があることを確認した。第二に、経営効率性の間には、統計的に有意な差を確認できなかったが、両者の技術的効率性に注目すると統計的な有意差を確認した。

そこから得られる提案として大きな規模かつ高い技術的効率性を持っている水道局は国際活動に貢献できる可能性を持っている。前述した仙台市と堺市の規模は大きく技術的効率性の高いため、研究結果に沿った形となった。

今後の課題として、技術が高い故、国際活動に貢献しているだけでなく、国際活動を通じて、日本の職員の技術が高まっていることを解明することが挙げられる。また、実践的な国際活動に貢献する理由を調べることが挙げられる。規模、効率性と国際活動の関係性から、論理的には国際活動に貢献できる水道局を特定することができる。しかし、実際にメリットがないと多くの水道局は国際活動に踏み出すことができない。ステークホルダーを整理し、23の水道局が実際なぜ国際活動を始めたのかをまとめていくことでより多くの水道局が国際展開していけると考えられる。

参考文献

[1] 東京都水道局(2016), https://www.waterworks.metro.tokyo.jp/ (閲覧日：2017年2月10日)

[2]各地方自治体の水道局

[3]奥沢英一,濱田篤郎(2000) 開発途上国における水系感染症とその実態

[4] 公益社団法人日本水道協会 (2016), http://www.jwwa.or.jp/ (閲覧日：2017年2月10日)

Concept study of a deployable atmospheric reentry vehicle with Waverider effect

Student Number : 13-16478   Name : Tomohiro Watanabe   Supervisor : Daisuke Akita

1 Introduction

A sounding rocket is an instrument-carrying rocket designed to perform scientific observations during its suborbital flight(50〜1500km). The recovery of the payload on the final stage of the sounding rocket opens up new possibilities. The recovered equipment can be reusable and it is cost-effective. The Sample-return mission, whose goal is collecting and returning samples from high altitude to ground, also becomes possible.

This paper proposes the recovery of the payload with a deployable reentry vehicle with Waverider effect. The feasibility is investigated by designing the shape and the aerodynamics performance of the vehicle.

2 Mission and System concept

Figure. 1 shows the mission concept.

1. The sounding rocket carrying the recovery vehicle on the final stage is launched
2. The rocket reaches the target altitude, releases the final stage and opens the nose cone. The recovery vehicle separates from the final stage and is deployed.
3. The recovery vehicle controls its attitude. During on-design Mach number, the lift to drag ratio increases by Waverider effect.
4. The vehicle reaches near the launch site. Before the vehicle falls into the sea, the parachute is deployed.

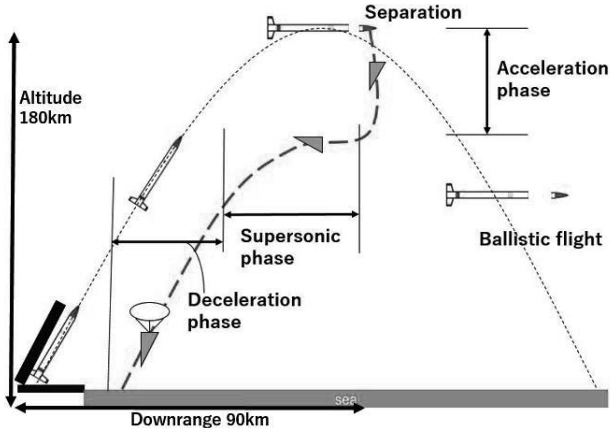

Figure 1: Mission Concept

Figure. 2 shows the model of the recovery vehicle. It is the "Caret-Wing Waverider", which has the simplest shape in all the Waveriders. In Fig. 2, the black line shows the shape of vehicle and the blue line shows the shock wave attaching the leading edge of the vehicle. The lower surface of the vehicle receives high pressure by the attached shock wave and results in the increase in the high lift to drag ratio. This is the Waverider effect.

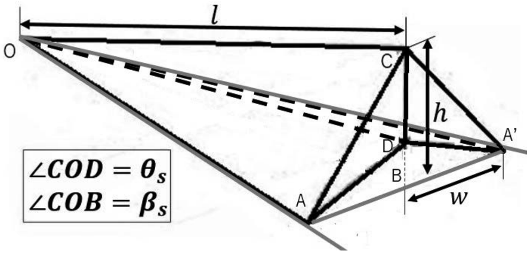

Figure 2: Vehicle Configuration

3 Trajectory calculation

The motion equations of the vehicle are given in polar coordinates. The forces on the vehicle are only the Earth gravity force and the aerodynamic force. The equation is numerically calculated by 4th order Runge-Kutta method. Initial velocity is 0.01[m/s], initial altitude is 180[km], initial path angle is 0[deg], initial longitude is 0[deg].

The heat flax $q[W/m^2]$ is estimated by Detra-Kemp-Riddell equation[1]. The surface temperature of the vehicle is calculated by Stefan-Boltzmann equation using the result of heat flax. The curvature radius of the leading edge is 2.0[cm].

4 Required aerodynamic characteristics

The vehicle must meet the following three requirements to realize the mission.

(i) The temperature of the vehicle surface is less than 1550[K].

(ii) The downrange of the vehicle is more than 90[km].

(iii) The vehicle can be installed inside the rocket nose cone of 20[cm] radius.

As the lift to drag ratio is 1.0, the ballistic coefficient is less than 170[kg/m^2] to meet Req. (i).

The lift to drag ratio was determined by the following procedure.

1. The lift to drag ratio gained by Waverider effect is determined, and then the vehicle wedge angle θ_s is determined by Eq. (1)[2].

$$\frac{L}{D} = \frac{1}{\tan\theta_s} \tag{1}$$

2. On-design Mach number is determined by the trajectory calculation for the long downrange, and the shock wave angle β_s is determined by Eq. (2). The heat capacity ratio κ is 1.4.

$$\theta_s = \tan^{-1}\left(2\cot\beta_s \frac{M^2\sin^2\beta_s - 1}{M^2(\kappa + \cos 2\beta_s) + 2}\right) \quad (2)$$

3. In this study, off-design lift to drag ratio is determined by assuming the shape of the triangular pyramid (triangular pyramidOAA'C in Fig. 2) in the supersonic flow[3]. Table. 1 shows the height h and the width w of this triangular pyramid.

Table 1: Triangular pyramid size

Hight h[cm]	20
Width w[cm]	20

The length l is calculated by the equation($h = l\tan\beta_s$).

As on-design lift to drag ratio is 2.3 and the Mach number is 5.0, the vehicle meets Req. (i). Table. 2 shows the lift to drag ratio of this vehicle.

Table 2: Aerodynamic characteristics of Waverider

Lift to drag($4.25 \leq M \leq 5.75$)	2.3
Lift to drag(otherwise)	1.8

As the vehicle has the lift to drag ratio such as Tb. 2, the ballistic coefficient is less than 175[kg/m^2] to meet Req. (i).

Figure. 3 shows the flight trajectory of the vehicle that has the aerodynamic characteristics above.

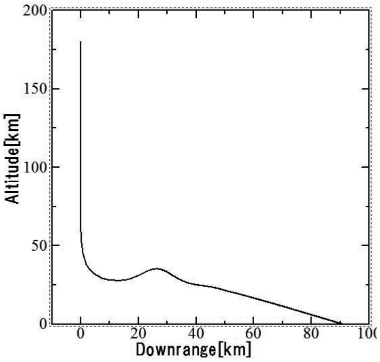

Figure 3: Trajectory of the recovery vehicle

5 Deployable vehicle and Non-deployable vehicle

Figure. 4 shows non-deployable vehicle inside the nose cone of the sounding rocket. Figure. 5 shows deployable vehicle. The span of this vehicle is maximized by deployment. The size of the vehicle needs to be large to decrease the ballistic coefficient of the vehicle. The ballistic coefficient is determined by the requirement for the aerodynamic heating.

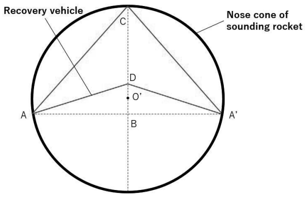

Figure 4: Cross-section drawing of non-deployable vehicle inside the nose cone of sounding rocket

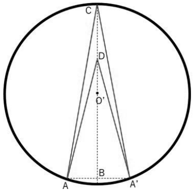

Figure 5: Cross-section drawing of deployable vehicle inside the nose cone of sounding rocket

The condition for maximizing the projected area was determined. The projected area($S = lw$) is the function of only the width.

Table. 3 shows the size of deployable and non-deployable vehicle which has the maximum projected area.

Table 3: Size of deployable and non deployable vehicle

	Deployable	Non-deployable
Length $l[cm]$	51.7	54.4
Height $h[cm]$	28.6	30.0
Width $w[cm]$	28.0	17.3
Projected area $S[cm^2]$	1449	941

6 Conclusions

This study shows that the recovery reentry vehicle is able to withstand the aerodynamic heating and reach near the launch site. However, the estimation of aerodynamic characteristics isn't sufficiently accurate. The estimation of the aerodynamic characteristics is necessary to model the effect of viscosity and non-linearity of the compressible flow. The future work is to estimate the accurate aerodynamic characteristics of the vehicle by wind tunnel experiments and CFD.

References

[1] N. H. Kemp, F. R. Riddell "Heat Transfer to Satellite Vehicles Re-entering the Atmosphere", Journal of Jet Propulsion, Vol. 27, No. 2, 1957, pp. 132-137

[2] Goro Kamimoto, Yoshitaka Uenaka, "Measurements of the Hypersonic Aerodynamic Characteristics for Several Kinds of Wave Riders", The Japan Society for Aeronautical and Space Sciences, Vol.17, No.184, 1969

[3] L. C. Squire "A comparison of the lift of flat delta wings and waveriders at high angles of incidence and high mach number", Archive of Applied Mechanics, Vol. 40, Issue 5, 1971, pp. 339-352

地域特性がエコツーリズムの特徴に与える影響

学籍番号：13B03599　**名前**：**海宝 慎太郎**　**指導教員**：**阿部 直也**

1.　研究の背景と目的

エコツーリズムとは地域が主導して、自然を保護しつつも観光資源として利用しようとする新しい形態の観光である（敷田・森重 2001）。1970年代に欧米で広まり、日本においては1990年代後半から主に地域活性化の目的から注目を浴びるようになる。欧米のエコツーリズムが希少な自然を対象とするなど比較的統一された定義が存在するのに対し、日本では広義の定義から狭義のものまで様々ある。希少な自然のみでなく里山などの身近な自然も含み、さらに地域文化や農業・漁業のような地域産業も観光対象としている地域も多く見られる。このような「日本型エコツーリズム」の多様性は先行研究でも指摘されているが、定量的な指標を用いて説明したものはない。

本研究では、多様性の背景を理解するために、エコツーリズムの特徴に影響を与える地域特性を明らかにすることを一つ目の目的とする。そしてクラスター分析による類型化で、エコツーリズムの多様性を明らかにすることを二つ目の目的とした。

2.　現状把握のためのヒアリング調査

どのような地域特性がエコツーリズムの特徴に影響を与えるか把握するため、地域特性の異なる6件の市町村において、自治体もしくは観光協会へのヒアリングを実施した（表2)。ただし調査の幅を広げるため、比較的広義のエコツーリズムを対象に行った。

表 1　ヒアリング調査地域の一覧

市町村名	都道府県	訪問日*	インタビュー対象組織	観光スタイル
檜原村	東京	11月8日	檜原村観光協会	森林セラピー
			檜原村観光産業課	エコツーリズム
青梅市	東京	11月15日	青梅市観光協会	-
奥多摩町	東京	11月23日	奥多摩観光協会	森林セラピー
山口市阿東町	山口	12月6日	NPOあとう観光協会	スローツーリズム
周南市	山口	12月6日	周南観光コンベンション協会	-
美祢市	山口	12月7日	美祢市観光協会	ジオツーリズム
			秋吉台地域エコツーリズム協議会	エコツーリズム

*調査は全て2016年に行った。

調査の結果、特に興味深い発見としてエコツーリズムを行う目的が自治体によって様々であることが浮かび上がった。筆者はここから、『エコツーリズムを行う自治体は経済的な利益を期待する「観光振興」と地域の外部との交流を促進する「地域活性化」の2つの目的を持ち、優先度の高さはもともと観光地であるかどうかに依存する』という仮説を設定したい。観光地性の高さを観光発展度と定義した。ヒアリング調査から知見を得て、本研究では特にこの観光発展度を重要な地域特性として考えた。

3.　分析枠組み

本研究は以下の手順に沿って行われた。

1) ヒアリング調査による影響要因の推測
2) 分析対象の自治体の絞り込み
3) 地域特性を記述する変数の収集
4) 主成分分析を行い変数の情報を縮約
5) 得られた合成変数を用いた階層的クラスター分析によるエコツーリズム推進自治体の類型化

分析対象の絞り込みは、環境省が公開するデータベースの中から行った。エコツーリズム推進協議会といったネットワーク型の団体を持ち、行政として取り組みを行う自治体であることを条件として36自治体に絞り込んだ。次に、エコツーリズムに関連する6つの変数区分を定め、それらを表現する変数を集めた。各指標区分を選択した理由は、人口・財政は都市の持つ力を表し、観光はその地域の観光発展度を、自然・一次産業・史跡はエコツーリズムの対象となる観光資源の充実性を表すためである。

表 2　変数一覧

区分	変数名	単位	出典	調査年
人口	人口総数	人	国勢調査	2010
	老年人口率	%	国勢調査	2010
	昼夜人口比	-	国勢調査	2010
財政	財政力指数	-	総務省*注1	2013
自然	林野面積率	%	国土交通省*注2	2014
一次産業	農業従事者率	%	H26経済センサス	2014
	林業従事者率	%	H26経済センサス	2014
観光発展度	宿泊業従事者率	%	H26経済センサス	2014
	飲食業従事者率	%	H26経済センサス	2014
	道路旅行運送業従事者率	%	H26経済センサス	2014
史跡	仏教系宗教従事者率	%	H26経済センサス	2014

*注1：総務省自治財政局「地方財政統計年報」,「市 町村別決算状況調の結果」

*注2：国土交通省国土地理院測図部「全国都道府県市 区町村別面積調の結果」

4.　データおよび分析結果

主成分分析を行った結果は表3の通りである。各変数の因子負荷量から主成分の意味付けを行えるものとして第三主成分までを選択した。第三主成分までの累積寄与率が58%と低いのは、本研究が着目した変数では捉えきれていない特徴がまだ残っている可能性を示しており、今後の課題である。第一主成分（PC1）は人口総数、財政力指数に正の影響を受けるため、「都市度」とした。PC2は宿泊業従業者率、昼夜人口比に正の影響を受けるため、「観光発展度」とした。PC3は史跡を代替的に表す仏教系従事者率に正に影響されるため、「歴史価値度」とした。特にPC2については、ヒアリング調査で確認した観光発展度に相当する評価軸であると捉えた。したがってPC2はエコツーリズムの目的に影響を与える変数とみなした。

表 3　主成分分析の結果

	PC1（都市度）	PC2（観光発展度）	PC3（歴史価値度）
標準偏差	1.69	1.39	1.25
寄与率	26%	18%	14%
累積寄与率	26%	44%	58%

次に階層的クラスター分析を行った結果、36 の自治体は 4 つの主要類型へと分類が出来た。PC1、PC2 のスコアで自治体をプロットしたものが図 1 である。都市度と観光発展度に両指標によって大きく 4 つの類型が特徴付けられることが明らかになった。主要類型はさらに 11 の小類型に分かれる。分析対象の自治体を類型別に整理したものが表 4 である。

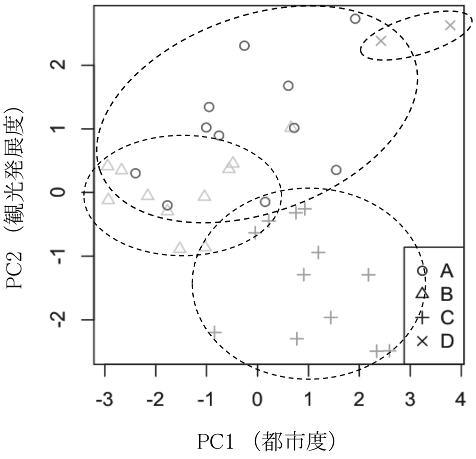

図 1　エコツーリズム推進自治体の主要類型

表 4　類型後の分析対象の自治体

	1	2	3	4	5
類型A [11自治体] **小規模観光地型**	北塩原村 座間味村	小笠原村 標津町 東川町 国頭村	屋久島町 弟子屈町 宮古市	竹富町	東村
類型B [11自治体] **中規模都市** **低観光発展型**	南丹市 美祢市 鳥羽市 宮津市 みなかみ町 東伊豆町 佐渡市	西目屋村 信濃市 串間市 川根本町			
類型C [12自治体] **都市非観光発展型**	名張市 東近江市 飯能市 斜里町 阿蘇市 三条市 茅野市 飯田市	松川村	松本市 米子市 佐世保市		
類型D [2自治体] **財政成功的** **高観光発展型**	軽井沢町 山中湖村				

次に、11 小類型の分類図を図 2 に示した。簡略化のため、各小類型の PC1、PC2 の平均値をプロットした。円の大きさは小類型内の自治体の数に対応する。図 2 により、自治体の多様性がより視覚的に把握できる。小類型の中の A2、A3、A5、C1、C2 は PC1 と PC2 だけでは分類できないことが図 2 からわかった。これらの類型は PC3（歴史価値度）によって区別できた。よって図 2 より歴史価値度も自治体の分類に重要なことがわかった。

すでに述べたように、PC2 はヒアリングで確認した観光発展度に相当する。すなわち図 2 において縦軸はエコツーリズムの目的に対応するため、各類型で行われるエコツーリズムの目的を、図 2 を用いて推測可能だと考えた。

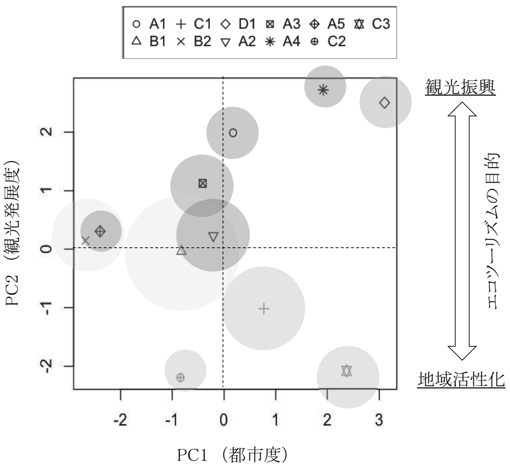

図 2　エコツーリズムの目的に関するモデル

5.　結論と今後の課題

本研究が設定した目的であるエコツーリズムの多様性を示すため、本研究は図 2 で示すように都市度と観光発展度の 2 指標でエコツーリズム推進自治体を細かく分類できることを明らかにした。そしてエコツーリズムの特徴に影響を与える地域特性については、観光発展度がエコツーリズムの目的に影響を与え、多様性を生む要因の一つであるとヒアリングを通して結論付けた。

本研究の意義は、エコツーリズムの全体像を都市度と観光発展度の 2 軸で示したことにある。自治体の観光発展度による分類化の試みは古村（2015）も行っている。しかし本研究では、高い低いといった序数的な類型化でなく、定量的な指標を用いて類型間の差異をより明確にした測距的な類型を行った点に意義がある。類型化によって、自治体は自らと比較的似た地域特性を持つ自治体を知ることができる。本研究は、類型の似た自治体間の交流促進を促せると期待する。今後の課題として主にモデルの検証が挙げられる。エコツーリズムの目的が実際に観光発展度にどの程度影響されるかを類型ごとに調べて明らかにする必要がある。また、都市度のような他の指標がエコツーリズムにどのような影響を与えるのかに関しては、都市度の異なる類型についてそれぞれ調査することが必要である。

6.　参考文献

[1]　敷田麻実, 森重昌之, 新広昭, & 佐々木雅幸. (2001). エコツーリズムの発展過程と構造モデル.

[2]　古村学（2015).『離島エコツーリズムの社会学--隠岐・西表・小笠原・南大東の日常生活から』, 吉田書店, 296.

[3]　沓掛博光, & 敷田麻実. (2008). エコツーリズム推進における適地性と発展プロセスの比較研究. 日本観光研究学会全国大会学術論文集, 23, 201-204.

Numerical analysis of storm surge inundation in Tacloban City caused by the 2013 Typhoon Haiyan − analysis of evacuation and effectiveness of the embankment

Student Number：12_05514　Name：Shota Kurobe　Supervisor：Hiroshi Takagi

1. Introduction

Typhoon Haiyan (referred locally as "Yolanda") struck the Philippines on 8 November 2013, which induced severe damages to Leyte, Samar, and several other more islands and provinces. It was the strongest storm ever recorded in terms of one-minute sustained wind speed [Takagi *et al.*, 2015]. According to the National Disaster Risk Reduction and Management Council (NDRRC), it was reported that 6,300 people died, 28,688 people were injured, and 1,062 people were still missing by April 2014.

On November 8, Typhoon Haiyan made landfall in Leyte, Samar and other islands causing a catastrophic destruction. According to the previous studies, a large storm surge occurred along the coastline of Leyte Gulf, causing particularly large damages to the sea front of Tacloban City, which is the biggest city in Leyte Island located at the north western end of Leyte Gulf.

This paper aims at revealing the characteristics of storm surge caused by Haiyan, focusing on Tacloban City where the largest number of casualties took place. In order to do so, based on a prior research conducted in 2014, an analysis of evacuation behavior among local people and the effectiveness of the newly proposed coastal embankment were investigated.

2. Field survey

In the previous study carried out in 2014, the model accuracy was calibrated from the flow velocity at one observation point while the water depths were calibrated at 14 observation points [Takagi *et al.*, 2016]. However, according to other studies, damage to buildings and structures are not solely attributed to flood water level but rather more connected to the water depth-velocity products [Cox *et al.*, 2010]. In this research, a field survey was carried out from December 13 to December 17, 2015, to investigate how accurately water depth-velocity products can reproduce the actual damages happened during the passage of the typhoon.

In the field survey, the flow direction of storm surge was confirmed by the interview survey in which the interviewees were asked whether or not they observed if any humans were being drifted along with the surge flow. Besides, analyzing a captured video that shows the storm surge flow velocity confirmed the findings through the present study.

We surveyed 38 households, while only 22 of these households observed physical damages to properties outside. Using these survey results, the calibrated model utilized in the prior research in 2014 was verified (Figure1).

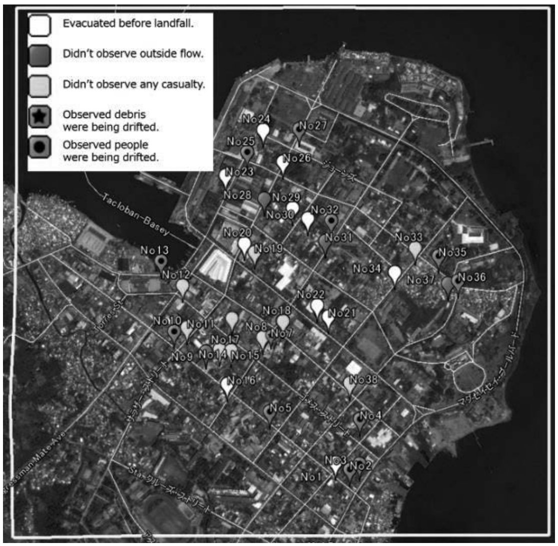

Figure 1. Interview result, indicating what they observed during TY Haiyan

3. Numerical analysis

The fluid dynamics model Delft3d-FLOW coupled with a typhoon model [Takagi *et al.*, 2016] was employed for the simulation. Calculation settings is as below (Table 1).

Table 1. Calculation settings

Item	Outline	
Mesh size	Domain1:Philippines wide area(3000m)	
	Domain2:Leyte bay area(100m)	
	Domain3:Tacloban area(10m)	
Cause of storm surge	Typhoon Haiyan(central pressure895hpa), 50 years period typhoon(Central Pressure 905hpa)	
Time step	Δt=0.005 min	
Tide level	Mean Lower Low Water	
Computation time	Domain1	2013/11/8 6:00～2013/11/8 9:40
	Domain2・3	2013/11/8 6:00～2013/11/8 9:40
Data of sea level	Domain1	GEBCO_08 Grid
	Domain2	Chart
	Domain3	The data which measured in 2014
Data of ground level	Domain1	ASTER GDEM
	Domain2	ASTER GDEM
	Domain3	The data which measured in 2014
Roughness coefficient	Domain1	Sea area : 0.025　Land area : 0.06
	Domain2	Sea area : 0.025　Land area : 0.06
	Domain3	Sea area : 0.025　Land area : 0.04

It was confirmed that there is a plan to construct coastal embankments along the coastline of Leyte Island in response to the damage from Typhoon Haiyan. However the detail of the embankment in Tacloban downtown area has not been decided yet.

The simulation incorporating the dyke construction plan was performed with the assumption that a 2d-weir tide embankment would be installed (Figure 2), and thereby the effectiveness of the tide embankments as a coastal protection structure was evaluated.

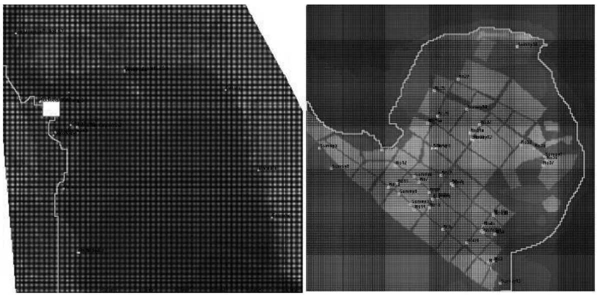

Figure 2. Calculation area of downtown Tacloban and the assumed a thin weir along the coastline

4. Results

It was found that even if the embankment height is raised, the inundation depth is not linearly decreased. The water depth was changing greatly depending on whether the embankment height is above or below the maximum storm surge height (Table 2, Figure 3).

Simulation results of inundation depth showed drastic changes if the water level exceeds the 4.3m-high embankment, whereas the inundation depth exhibited a constant depth if the embankment height exceeds 4.9m (Figure 4).

Table 2 Classifications of flood damage according to water depth

Color	Group of water depth	Meanings of the group
■	2m～5m	Most of wooden house will be collapsed.
▩	1m～2m	If people get invovled, people will die.
░	0.3m～1m	People can not move and evacuate from that point.
▒	0.01m～0.3m	Flood damage will be negligible.
□	less than 0.01m	Flood damage will be nothing.

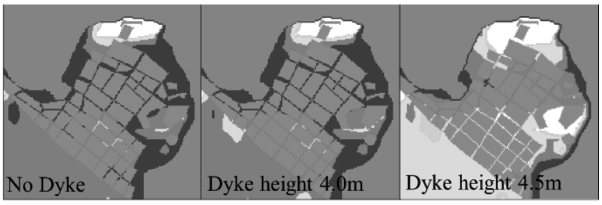

Figure 3. Contour figure of water depth.

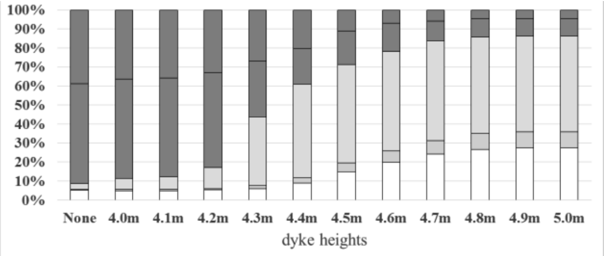

Figure 4.Distribution of the maximum water depth in downtown Tacloban, classified by dyke heights

A report states that evacuation activities during when the water depth exceeds 0.3 [m/s] or when the water depth-velocity products exceeds 0.6 [m/s^2] would be likely difficult to perform with safety [Cox *et al.*, 2010, Ministry of Land, Infrastructure and Transport, 2012]. Using the index of this report as a basis, the time for people to safely travel to evacuation areas from each observation points was computed. Calculation revealed that if the embankment was raised, the margin for a safer evacuate could be created at a linearly increasing trend. This is due to the fact that for the case where there is no embankment, flooding in Tacloban City will start soon after storm surge occurs. On the other hand, for the case where there is the embankment, the arrival time of floodwater will be delayed (Figure 5).

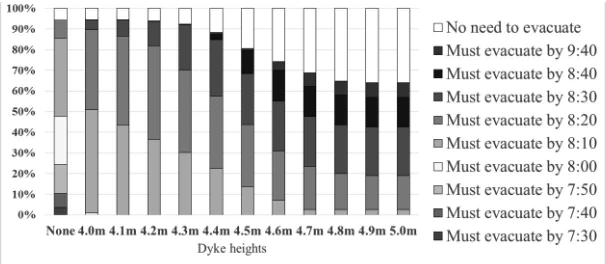

Figure 5. Transition of the time when people have to start their evacuations in downtown Tacloban

5. Conclusion

If embankments do not have a sufficient height, a reduction effect on inundation depths cannot be expected. Nonetheless, a marginal time for enabling people to get themselves a safer evacuation can be created by constructing the dykes along the coastline.

References

1)Takagi, H., Esteban, M., 2015.：Statistics of tropical cyclone landfalls in the Philippines unusual characteristics of 2013 Typhoon Haiyan. Nat. Hazards.

2)Takagi H., Li S., de Leon M., Esteban M., Mikami T., Matsumaru R., Shibayama T., Nakamura R. (2016) Storm surge and evacuation in urban areas during the peak of a storm, Coastal Engineering.

3) Cox R.J., Shand T.D.,and Blacka M.J. (April 2010)：Australian Rainfall & Runoff Revision Projects Project10 Appropriate Safety Criteria for People STAGE1 REPORT,19p.

4) 国土交通省（Ministry of land, Infrastructure and Transport, 2012）：津波浸水想定の設定の手引き　Ver.2.00,P45

A STUDY ON CONTINUITY OF UTILIZING A CLOSED SCHOOL FOR EXCHANGE FROM THE VIEWPOINT OF TRAVEL INFLOW

Student Number: 11_18181 Name: Haruyoshi NAGAFUNE Supervisor: Naoya ABE

1 Introduction

From 2002 to 2013, 2,208 public schools were closed and re-used for the other purposes except school. Many re-used schools are for neighbors, but Ministry of Education, culture, sports, science and technology (MEXT) has recently introduce utilizing closed schools for exchange (UCSEs) (Fig.1), so I think the number of UCSEs will increase in the future. Compare with utilizing closed schools for the other purposes, UCSEs have three features: high repairing cost, highly dependence on support from government and company, and many users come from far. These three features show that it is necessary to obtain consensus from many stakeholders, so it is an important problem to grasp the amount of travel inflow (TI) in the area of UCSEs.

In order to analyze continuity of UCSEs, I classify regional zones as similarity and type of TI, and consider the relation between the amount of TI and the number of UCSEs, users per year (UPY), and years of a UCSE.

Figure 1: One of the utilizing closed schools (Akitsuno Garten)

2 Classifications

At first, principal component analysis evaluate 207 zones by eight local indexes, which are "population", "ratio of population increase", "area", "rate of under 15 years old", "rate of over 65 years old", "rate of population of primary industries", "rate of forest area", and "financial index". Second, principal component scores classify 207 zones by cluster analysis under three regional groups: urban group, middle group, and rural group. Urban group has 54 zones, middle group has 95 zones, and rural group has 58 zones.

207 zones are also classified by the relation between a travel inflow zone and a top residence zone of travel inflow under three groups: "From urban zone inflow group (UIG)", "From similar zone inflow group (SIG)", and "From rural inflow group (RIG)" (Table.1). "From urban inflow group" has 109 zones, "From similar inflow group" has 77 zones, and "From rural inflow group" has 21 zones.

52 zones that belong to three metropolitan areas and a center area of Hokkaido exclude travel inflow from same that area. So, in 155 zones excluding 52 zones from 207 zones, I also consider the relation between the amount of TI and the number of UCSEs, UPY, and years of a UCSE.

Table 1: The definition of type of travel inflow

		From regional group (Top)		
		Urban	Middle	Rural
To regional group	Urban	SIG	RIG	RIG
	Middle	UIG	SIG	RIG
	Rural	UIG	UIG	SIG

3 Relations

I confirm the correlation coefficient and the scatter diagram between TI and the number of UCSEs, UPY, and years of a UCSE.

In the relation between TI and the number of UCSEs, there are two weak correlations on "urban group in 207 zones" and "rural group in 155 zones". In the scatter diagram (Fig.2), "rural group in 155 zones" has few unique zones far from coordinate origin and has many zones near to coordinate origin.

In the relation between TI and the number of UPY, there are three weak correlations on “urban group in 207 zones”, “from similar in 207 zones” and “from similar in 155 zones”. In the scatter diagram (Fig.3), “from similar in 207 zones” has few unique zones far from coordinate origin and has many zones near to coordinate origin.

In the relation between TI and the number of years of a UCSE, there are two correlations on “urban group in 207 zones” and “urban group in 155 zones”, and four weak correlations on “rural group in 207 zones”, “rural group in 155 zones”, “from similar in 207 zones” and “from similar in 155 zones”. In the scatter diagram (Fig.4), “urban group in 155 zones” has one unique zone far from coordinate origin and has the others close to each other.

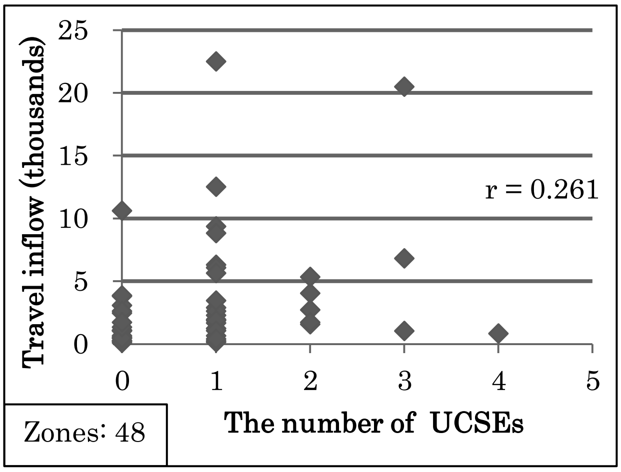

Figure 2: TI-No. Of UCSE scatter diagram on rural group in 155 zones.

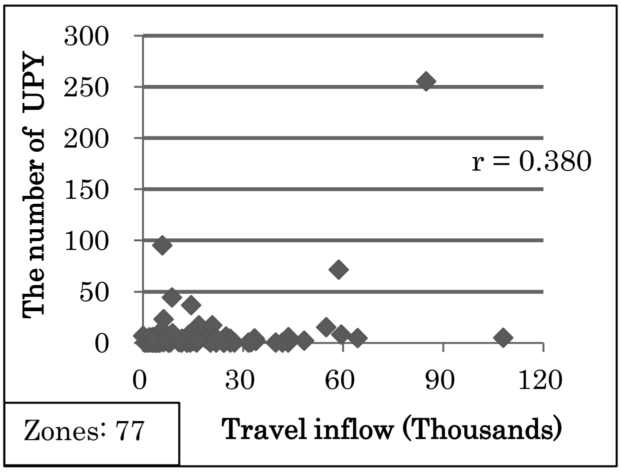

Figure 3: TI-No. Of UPY scatter diagram on “from similar in 207 zones”

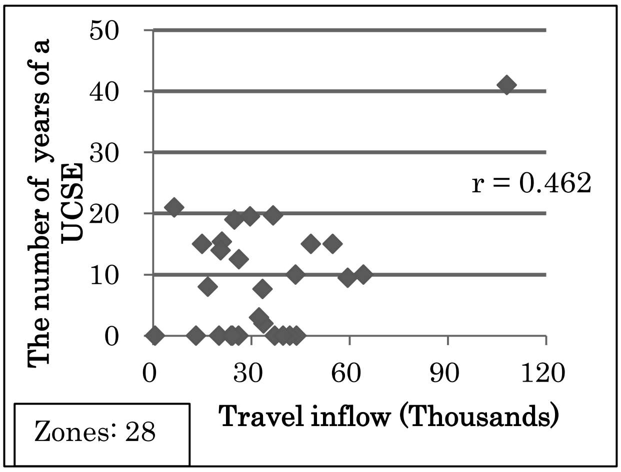

Figure 4: TI-No. Of YR Of UCSE scatter diagram on “urban group in 155 zones”

4 Conclusions

This study has following conclusions.

In the two relations between TI and the number of utilized closed schools, and UPY, there are a few weak correlations. In the scatter diagram which has the largest correlation, there are few unique zones far from coordinate origin and many zones near to coordinate origin.

In the relation between TI and the number of years of a UCSE, there are two correlations and four weak correlations. In the scatter diagram which has the largest correlation, there is one unique zone far from coordinate origin and are the others close to each other.

References

[1] 文部科学省，廃校施設活用状況実態調査，2014.

[2] Ministry of Land, Infrastructure, Transport and Tourism Government of Japan, “2010 Inter-Regional Travel Survey in Japan”, 2010.

[3] Hideki Nozawa, Gen Taniguchi, Kazuhisa Tsunekawa, and Eisuke Tabata, “A Study on The Feature of Regions that Have Closed Public Schools and Reuse – In case of Aichi, Gifu, and Mie prefecture -”

Effects of AC voltage on Asymmetric Capacitor Thruster

Student number: 13-15496 Name: Shunnosuke Yamada Supervisor: Daisuke Akita

1.Introduction

Titan is Saturn's 6th satellite. Presence of some kind of life is expected on titan because of the following factors. [1]

(1). Titan has dense atmosphere (about 1.5atm) mainly consists of nitrogen and methane.
(2). Methaneis circulating like water on earth.
(3). There is ammonia water inside the crust.

We think Titan exploration is very important. But Titan can't be observed from an orbit due to methane sol.[2] So we need send a spacecraft inside Titan atmosphere. Figure 1 is a blimp-type explorer proposed by NASA.The reasons to use a blimp are as follows.

(1). Blimp can observe the atmosphere directly.
(2). Blimp is not affected by terrain, so it can work also over the lakes.
(3). Titan has dense atmosphere.

We propose a blimp-type probe that is propelled by Asymmetric Capacitor Thruster (ACT) shown in Fig 2, because of the following reasons compared with the propeller and the motor.

(1). Simple structure and easy to fold and deploy.
(2). No driving part and high reliability.
(3). High thrust-to power ratio.

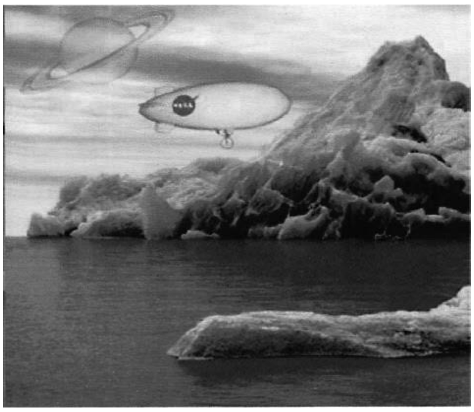

Figure 1 Blimp-type explorer proposed by NASA [3]

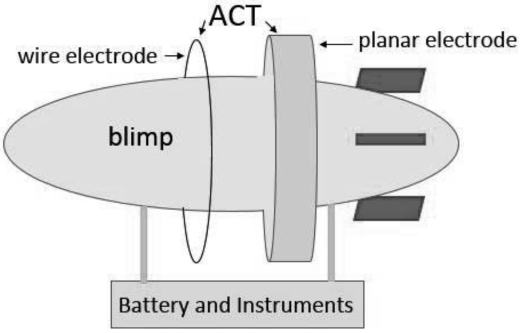

Figure 2 Blimp type explorer's image

2. Asymmetric Capacitor Thruster

The asymmetric capacitor thruster is a simple thruster, which consists only of hairline wire and aluminum foil. [4] When a high DC voltage, say 10kV, is applied to the ACT of 20cm span, the ACT produces a force of a few milli Newtons. However, to get a sufficient force by the thruster, a high voltage power supply is required. In the most previous works, a DC voltage is applied to the ACT. In this study, effects of AC voltage on the ACT is investigated.

3. Experimental method

As shown in Fig 3, the ACT for this experiment is composed of a thin wire electrode (anode) of copper and a planar electrode (cathode) of aluminum foil. The diameter of the wire is 0.05 mm, 0.2 mm, 0.5 mm. The width of the electrode is approximately 180 mm, the distance between the electrodes is 12 mm and 20 mm. Table 1 shows the experimental conditions.

Table1 Experimental conditions

	DC	AC(square wave)	AC(sine wave)
Applied Voltage	<15kV	<11kVp	13.5kVp
Frequency	—	4.3-20kHz	5.5kHz
Electrodes Distance	12 mm, 20 mm	12 mm	20 mm

The thrust is measured by electronic balance. The experimental system is shown in Fig 4.

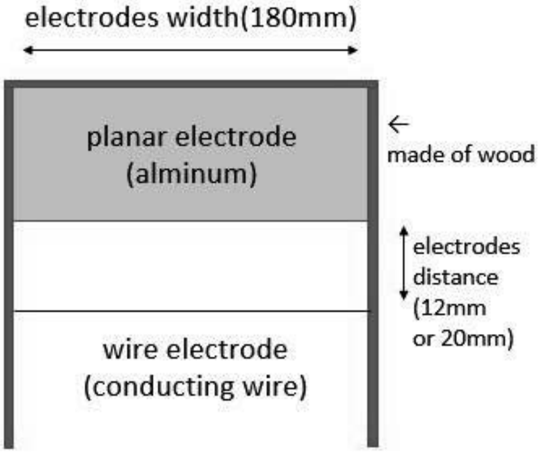

Figure 3 Structure of AC

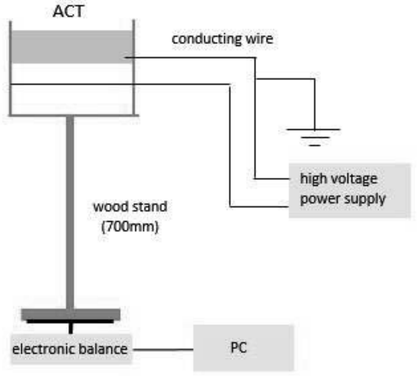

Figure 4 Experimental system

4. Results

Figure 5 shows the applied voltage vs the thrust. Electrodes distance is 12 mm. The wave shape of the applied AC voltage is square. DC produces stronger thrust than that of AC. High frequency square wave produce stronger thrust than that of low frequency square wave. Any gradient in case of AC is lower than that of DC.

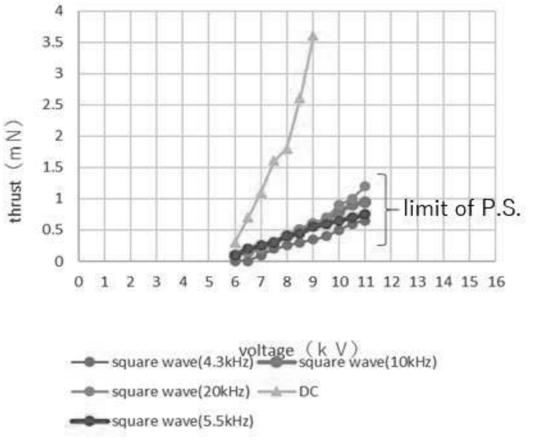

Figure 5 voltage vs thrust (square wave)

Figure 6 shows the voltage vs current in the same case of Fig. 5. The current in the case of AC-applied is higher than that of DC applied. The current increases with the applied AC frequency.

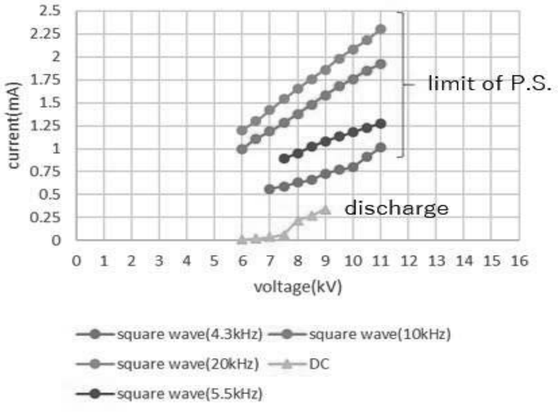

Figure 6 voltage vs current (square wave)

Figure 7 also shows the applied voltage and the thrust. The wave shape of the applied AC voltage is sine.Electrode distance is 20 mm. The thrust in the case of AC applied is lower than that of DC applied when the applied voltage is evaluated as a RMS's value.

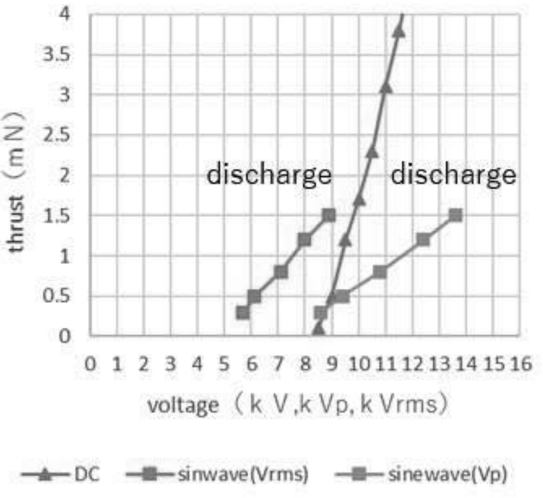

Figure 7 voltage vs thrust(sine wave)

5.Conclusions

In this study, the effects of AC voltage on asymmetric capacitor thruster is investigated to apply it for Titan exprolation.In all the cases of this experiment, the thrust is increased with the applied voltages.Basically the thrust and the thrust-to-power ratio in the case of AC is lower than that of DC. Current in the case of AC is higher than that of DC. The future work is to investigate the effects of dielecrics around the electrode in the case of AC.

Reference

[1] Cassini Celebrates 10 Years Exploring Saturn [https://www.nasa.gov/jpl/cassini/10-years-20140625] access 2017/02/21
[2] Kensei Kobayashi,2011 "タイタンのアストロバイオロジー探査" 日本惑星科学会誌 Vol20,No.2
[3] NASA Ames Research Center NASA Jet Propulsion Laboratory [https://www.jpl.nasa.gov/missions/?type=future] access 2017/2/21
[4] Francis X. Canning, Cory Melcher and Edwin Winet, "Assymmetrical Capacitors for Propulsion", NASA/CR-2004-213312,2004.

Outdoor-to-Indoor Radio Propagation Measurement by using an Unmanned Aerial Vehicle in 2.4GHz band

Student Number: 13B11890 Name: Qiwei Fan Supervisor: Jun-ichi TAKADA, Kentaro SAITO

1 Introduction

Owing to the wide spread of smart phones and tablet computers, the user traffic in mobile communication systems is increasing rapidly. Especially, in the urban environments, it is a significant issue to accommodate many users in office buildings in the network. Therefore, 3-dimensional(3D) service area planning is recently investigated. 3D service area planning is a method to achieve frequency reuse by arranging some micro cell base stations. Therefore, we need to analyze the radio propagation characteristics in Outdoor-to-Indoor(O2I) propagation scenario.

The O2I radio characteristics have been investigated in [1] [2], and it showed that the dominant penetration loss was the shielding of Fresnel region and the diffraction of waves by the window of building. Therefore the spatial relation between the transmitter, and the window position is important to understand the propagation

However, the variations of actual measurement settings are limited because transceiver is set on the ground or on the floor of a building. Because surrounding environment and window position in high altitude is totally different from that on the ground, we use Unmanned Aerial Vehicle(UAV) to achieve high altitude environment. Moreover, we can get propagation characteristic while changing the altitude of the transmitter smoothly by using UAV.

2 Radio Propagation Measurement by using UAV

2.1 Measurement System

The transmitter in the measurement was a WIMAX Mobile router which was set on the plastic box under an UAV type DJI F550 with NAZA M V2, as shown in Fig.1. During the measurement of O2I radio propagation, the mobile router was placed outside the building, which acted as the outdoor base station, and the receiver was a laptop with a USB dongle. The receiver received Beacon signal which is a signal sent by a wireless hardware regularly to all clients within wireless network coverage and logged Received Signal Strength Indication(RSSI) data.

Figure 1: UAV used in measurement

2.2 Transceiver and Measurement course

The transmitter and receiver is introduced in Section 2.1, the detailed information of transceivers are summed up in Table 1

Table 1: Measurement parameters

item	detail
Transmitter	pocket wifi WX02
Receiver	FUJITSU laptop with IODATA WN-AC876U
Software	Homedale
UAV	DJI F550 with NAZA M V2
Height of Receive Antenna	1.6m (from 6th floor)
Carrier Frequency	2.4GHz
measurement interval	one data per second
Transmit Course	p0-p11 (distance interval 2m)
Receive Course (Distance from window)	Rx1(0.4m), Rx2(2.4m), Rx3(4.4m)

The measurement was conducted in the Suzukakedai campus, Tokyo Institute of Technology, and measurement place was a lawn in front of a tall building. The horizontal distances between the building and measurement points were 15m. p0 was the starting point of the measurement as shown in Fig. 2. The distance between subsequent points was 2m, p11 was the final snapshot in which it was 22m away from p0.

The receiver was set on the 6th floor of the building, and outside the window there was a metal fence. The

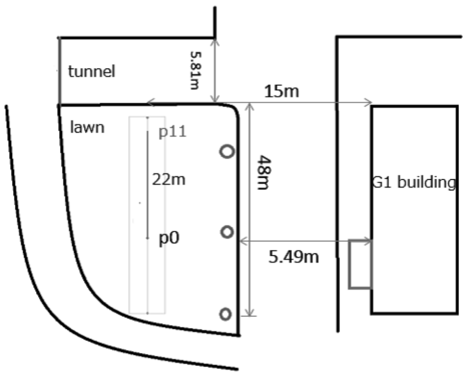

Figure 2: Top view of course outside

receiver was placed at the distance of 0.4, 2.4, 4.4m away from window which was denoted by Rx1, Rx2 and Rx3. The receiver antenna hight was 1.6m.

2.3 Process of the Measurement

We put the UAV on p0, and used the controller to make UAV gain altitude. After the UAV height reached 20m above the lawn, we lowered it down until it landed. During the measurement, we tried to make UAV's speed constant. After we finished measurement at p0, we moved UAV to next point, and repeated this process again. When finished measuring p11, we moved the receiver to the next position in order of Rx1, Rx2, Rx3. We took notes of the elapsed time at three locations: (1) the starting point, (2) at the maximum altitude, (3) the ending point.

3 Results

In Fig. 3, and Fig. 4 , the vertical axis the excess loss (which means the loss increased comparing to free space loss), if it is close to 0dB, it means the propagation is almost the same as free space propagation. The horizontal axis is altitude of UAV.

For Rx1 as shown in Fig. 3, there was a LOS(line-of-sight) while altitude was higher than 10m, and excess loss increased about 5dB while transitioning to non-LOS(line-of-sight). Moreover, in non-LOS the excess loss increased following the decrease of altitude.

For Rx3 as shown in Fig. 4, there was a LOS while altitude was higher than 14m, and excess loss increased significantly while transitioning to non-LOS. Excess loss in Rx3 is larger than that in Rx1, it can be considered as the increase of penetration loss following the increase of penetration distance.

The result is that, the excess loss increased while transitioning from LOS to non-LOS scenario, because of diffraction loss. In LOS case, the excess loss became higher as the penetration distance increases because of penetration loss. In the case of non-LOS, excess loss became higher as diffraction angle increased.

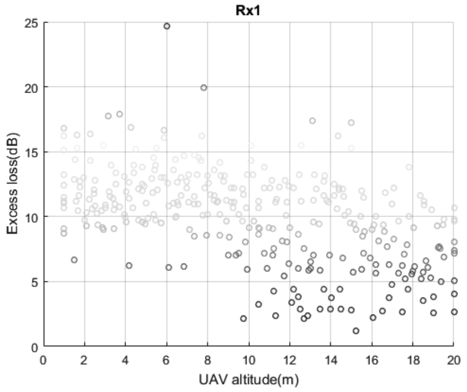

Figure 3: Excess loss of Rx1 in vertical

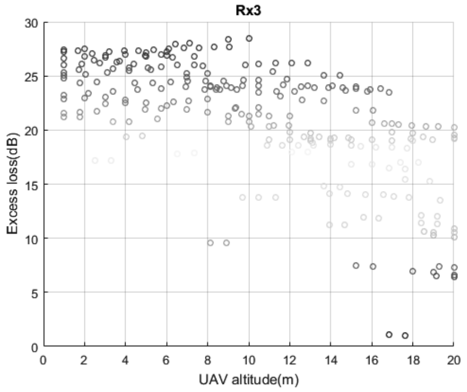

Figure 4: Excess loss of Rx3 in vertical

4 Conclusion

In this thesis we introduced an O2I radio propagation measurement system at 2.4 GHz band by using UAV. The objective of this paper is to use the UAV to send the signal at a high altitude. The result shows some characteristics of diffraction and penetration loss in measurement

References

[1] H. Omote, M. Miyashita ”Analysis of Arrival Angle Characteristics between Indoors of Difference LOS Buildings in Mobile Communications” , IEICE Society Conference, B-1-6, Sept.2016

[2] R. Eguchi, D. Furuishi, S. Araki, S. Ichitsubo, ”Frequency Characteristics of Penetration Loss Caused by Window”, IEICE Society Conference, B-1-8, Sept.2016

改良されたクラスタリングによるウェーブレット画像符号化の線形予測

学籍番号:13_16165　名前:李　然　指導教員:山下　幸彦

1　はじめに

離散ウェーブレット変換（DWT）は，データや関数などを異なる周波数成分に分解するための方法の一つである。ウェーブレット画像符号化は，DWTを用いる画像符号化の方法で，変換係数を算出することでデータ圧縮を実現している [1][2]。予測符号化は，予測を利用してデータ圧縮を行う手法である。この研究では，予測符号化で利用する k-means の計算時間や初期値問題を解決するために，従来の k-means の代わりに，最近注目されている k-means++[3] を用い，更に交差検定に基づくアルゴリズムでデータセットに合うクラスタ数を算出し，時間削減と予測精度の向上を試みる。

2　クラスタリングによる線形予測

2.1　線形予測

元々の線形予測は以下の式で表される。

$$\hat{s}(n)=\sum_{i=1}^{p} a_i s(n-i), \tag{1}$$

$\hat{s}(n)$ は実際の信号 $s(n)$ の p 個の信号値の係数 a_i の線型結合による予測値である。予測値と実際値の差で生じた誤差 $e(n)$ は次の式で表される。

$$\begin{aligned} e(n) &= s(n)-\hat{s}(n) \\ &= s(n)-\sum_{i=1}^{p} a_i s(n-i), \end{aligned} \tag{2}$$

線形予測係数 a_i は, 次の平均予測誤差

$$E=\sum_{n} e^2(n). \tag{3}$$

を最小にするように決める。

2.2　k-means クラスタリング

k-means クラスタリングは n 個のデータを距離に基づき k 個のクラスタに分類する方法である。この実験では，その距離にユークリッド距離を用いる。

ここで $(x_1, x_2, ..., x_n)$ をデータセットとし，それぞれのデータは d-次元の実数ベクトルとする。 k-means のアルゴリズムは以下の通りである。

Algorithm 1 k-means アルゴリズム

```
ランダムに $k$ 個の点を選んで，中心点初期値とする。
repeat
    1. データセットの各データを最も近い中心点のクラスタに割り当てて，$k$ 個のクラスタを形成する。
    2. 新しく割り振られたクラスタから中心点を再計算する。
until 中心点が変化しなくなる。
```

2.3　クラスタリングによる線形予測

この研究では，画像の特徴値を抽出し，k-means でクラスタリングし, カテゴリー $\boldsymbol{\Omega}_c$ $(c=1,2,...,C)$ に作成する. $\boldsymbol{\Omega}_c$ に対する予測モデルは以下の通りである。

$$q=\langle \boldsymbol{a}_c, \boldsymbol{v}\rangle, \tag{4}$$

ここで $\boldsymbol{a}_c$ は線形予測の係数ベクトルである。 学習データ $\boldsymbol{v}_i$ と q_i $(i=1,2,...,N_c)$ は $\boldsymbol{\Omega}_c$ に属し， $\boldsymbol{a}_c$ はクラスタ内の平均予測誤差

$$\sum_{i=1}^{N_c} |q_i-\langle \boldsymbol{a}_c, \boldsymbol{v}_i\rangle|^2. \tag{5}$$

を最小にするように決める。

3　k-means ++とクラスタリングの改良

3.1　k-means++法

k-means++法により，クラスタリングの時間短縮とクラスタ構成の安定化が可能になる。$D(x)$ は各データ点から最も近い既存のクラスタ中心との距離と定義する。本論文の実験では，客観的にクラスタ数を評価するために，ランダム要素を取り除く必要性があり，k-means++法の最初の中心点をデータ数 n をクラスタ数 k で割った $\frac{n}{k}$ の整数部分番目のデータに固定する。k-means++のアルゴリズムを以下に示す。

Algorithm 2 k-means++ アルゴリズム

```
ランダムに最初の中心点 $c_1$ を $X$ から選出する。
repeat
    次の中心点 $c_i$ は，$\frac{D(x')^2}{\sum_{x \in X} D(x)^2}$ を最大にする $x'$ とする。
until $k$ 個の中心点が選出される。
普通の k-means 法でクラスタリングを行う。
```

3.2 改良されたクラスタリング法

k-means 法の最大の問題点は，クラスタ数 k を事前に決めなければならないことである。特に本実験では，クラスタ数は線形予測の精度に甚大な影響を及ぼす。ここで，クラスタリング法を改良するために，予め用意された複数の学習画像データを使い予測し，予測データと元データを比較することで学習データに対して一番適切なクラスタ数を推定する。クラスタ数 k の取り得る範囲を $\{k_{\min}, k_{\max}\}$ とし，m 個の学習画像データを合わせたデータセットを二組に分け、その中で N_1 をクラスタリングで利用するデータセットとし，N_2 を線形予測用データとする。最良クラスタ数を k_{best} と記す。アルゴリズムは以下の通りである。

Algorithm 3 線形予測による最良クラスタ数の推定

```
最初のクラスタ数 $k$ は $k_{\min}$ から始める。
repeat
    1. 普通の k-means++法で $N_1$ をクラスタリングする。
    2. $N_1$ のクラスタリング結果で算出した係数で線形予測用データ $N_2$ を予測する。
    3. 予測結果からクラスタ数 $k$ ごとに平均平方二乗誤差 $RMSE_k$ を計算する。
    4. $k = k + 1$。
until クラスタ数 $k$ が 最大クラスタ数 $k_{\max}$ に達する。
    $RMSE_k$ が最小値となる $k$ を $k_{\mathrm{best}}$ とする。
```

4 実験結果

今回の実験は画像電子学会が頒布した JIS X 9201:1995「高精細カラーディジタル標準画像 (CMYK/SCID)」の自然画像から 8 つの画像データを学習データとし，その中の一番目の画像データをクラスタリング用データ N_1 とし、他の画像データを線形予測用データ N_2 とする。そして、予め用意した別の画像データ (Intersection, Lenna, Barbara) をテストデータとする。従来の方法とクラスタ数と $RMSE_k$ と比較しながら，クラスタリングに必要な時間と計算ループ数も測定する。今回のデータセットで算出された最良クラスタ数 k_{best} は 104 となった。従来手法のクラスタ数をその両側の 64 と 128 とする。なお，RMSE は小さいほど精度が高いことを意味する。実験結果から，本研究の方法で，予測精度の向上やクラスタリングに必要な時間の短縮，ループ数の消減を実現した。

表 1: $RMSE_k$ の比較 (括弧中の数はクラスタ数)

実験データ	提案法 (104)	従来法 (64)	従来法 (128)
Intersection	**9.22**	9.67	9.61
Lenna	**5.79**	6.02	6.30
Barbara	**21.30**	21.95	22.47

表 2: クラスタリング時間

手法＼クラスタ数	64	104	128
k-means 法	2789.79s	4895.63s	7416.46s
提案法	**1372.79s**	**3156.13s**	**5951.62s**

表 3: クラスタリング計算に必要なループ数

手法＼クラスタ数	64	104	128
k-means 法	795	965	1075
提案法	**331**	**589**	**801**

5 結論

本研究では，ウェーブレット画像符号化の線形予測のためのクラスタリングの改良方法を提案した。実験の結果，予測精度の向上とともに，クラスタリングに必要な時間とループ数も短縮できた。しかし，最良クラスタ数の算出には，ある範囲内のクラスタ数の予測誤差を調べ尽くす必要があり，そのため大量な時間が必要で，アルゴリズムのさらなる高速化が今後の課題である。

参考文献

[1] Marc Antonini, Michel Barlaud, Pierre Mathieu and Ingrid Daubechies, ”Image Coding Using Wavelet Transform”, IEEE Transactions on Image Processing, Vol. 1, No. 2, April 1992.

[2] Dan Wang, Yukihiko Yamashita, ”Wavelet Based Image Coding via Linear Prediction and Improved Clustering”, Master Thesis, Jan 2017.

[3] D.Arthur, S.Vassilvitskii, ”k-means++: The Advantages of Careful Seeding”, Stanford University, 2007.

Pretreatment of Feed Oil for Biodiesel Fuel Production

Student ID:13B16171 Name: Zhuoheng LI Supervisor: Ryuichi EGASHIRA, Hiroaki HABAKI

1. Introduction

Biodiesel fuel is a kind of alternative diesel fuels and made from renewable biological sources such as vegetable oils and animal fats. Although biodiesel fuel has attracted much attention as environmentally friendly fuel, it is difficult to be popularized due to the high cost of the feed oil and the limitation on feed supply. The cost of feed oil frequently shares more than 80 % of its total production cost, and then, low quality feed oils, such as crude plant oils, used frying oil and so on, have come into utilization, which generally contain some impurities, such as phospholipids, free fatty acids (FFA), and so on. The impurities reduce biodiesel fuel product yields and contaminate biodiesel fuel products. Therefore, the removal of phospholipids and free fatty acid from feed oil before transesterification is so important as the feed pretreatments(FP). Whereas the ordinary method to remove phospholipids in the feed oil by sulfuric acid solution and water washing was inefficient to remove FFA, the removal of FFA with sodium hydroxide solution could separate FFA and some parts of phospholipids simultaneously[1)]. On the other hand, the removal of FFA by sulfuric acid and menthol has inadequately been studied on the removal of phospholipids.

In this dissertation, the simultaneous separation of the phospholipids and FFA was studied in terms of the phospholipid reduction and yield of the treated oil.

2. Experimental

2.1 Feed oil

Triolein (C18:0) was selected as the major component in feed oil because it was a major component in the vegetable oils generally used for biodiesel fuel production. Oleic acid and lecithin were added as impurities as model FFA and phospholipids, respectively. Generally, two types of phospholipids are contained in the plant feed oils, such as hydratable and non-hydratable phospholipids. Lecithin is one of the plant-derived phospholipids, which include both hydratable phospholipids, such as phosphatidylcholine and phosphatidylinositol, and non-hydratable one such as phosphatidylethanolamine, respectively.

2.2 Feed oil treatment methods

2.2.1 Sulfuric acid solution treatment with water washing

The experimental conditions of sulfuric acid solution treatment with water washing (treatment 1) were summarized in **Table 1**[1-3)].

Table 1 Experimental conditions

Feed oil	
Phosphorous/Feed oil mass fraction[-]	0.001
Sulfuric acid solution treatment	
H_2SO_4/H_2O solution mass fraction[-]	0.25; 0.4
H_2SO_4 aq/Oil mass fraction[-]	0.0008; 0.001
Reaction temperature[k]	343
Reaction time[h]	0.33
Water washing	
H_2O/Oil mass ratio[-]	0.1
Reaction temperature[k]	343
Reaction time[h]	0.33

The initial mass fraction of phosphorous of phospholipid in the feed oil was adjusted to 0.001. Sulfuric acid was used as catalyst to convert non-hydratable phospholipids into hydratable ones. The reaction was carried out in flask with a magnetic stirrer, with temperature-controlled water bath. The feed oils were mixed with sulfuric acid and kept at 343K for 0.33 hour. After reaction, the hydratable phospholipids were removed by repeating water washing with a specified amount of water for total five times. After each water washing, the mixture was separated by centrifuge to obtain the aqueous and organic phases. Then the aqueous phases after each separation were analyzed by ICP-AES (SPS 7800, Seiko Instruments Co. Ltd.) for determination of the mass fraction of phosphorous in the aqueous phase.

2.2.2 Sodium hydroxide solution treatment

The experimental conditions of sodium hydroxide solution treatment (treatment 2) were summarized in **Table 2**[3-6)]. The neutralization of FFA to form soap by sodium hydroxide solution was expressed as the following reaction.

$$RCOOH(org) + NaOH(aq) \rightleftarrows RCOONa(aq) + H_2O \qquad (1)$$

The mass fraction of phosphorous of phospholipid in the feed oil was adjusted to 0 or 0.001, and the mass fraction of FFA in feed oil was adjusted to 0.15. The specified amounts of feed oil and sodium hydroxide solution were contacted in flask with a magnetic stirrer in the temperature-controlled water bath. After completing reaction, the mixture was separated into the aqueous and organic phases by centrifuge. The obtained aqueous phases also were analyzed by ICP-AES to determine the mass fraction of phosphorous in aqueous phase. This method should require no water washing to remove sodium hydroxide because sodium hydroxide generally was used as alkali catalyst in transesterification reaction for biodiesel production,

Table 2 Experiment conditions

Feed oil	
Phosphorous/Feed oil mass fraction[-]	0.001; 0
FFA/Feed oil mass fraction[-]	0.15
Sodium hydrate solution treatment	
$NaOH/H_2O$ solution mass fraction[-]	0.095
NaOH aq/Oil molar fraction[-]	1.15
Reaction temperature[k]	353
Reaction time[h]	0.083

2.2.3 Sulfuric acid and methanol treatment with water washing

The experimental conditions of sulfuric acid and methanol treatment with water washing (treatment 3) were summarized in **Table 3**[3-6)]. The esterification of FFA into fatty acid methyl ester (FAME) by methanol with catalyst of sulfuric acid was expressed as the following reaction.

$$RCOOH(org) + CH_3OH(aq) \overset{H_2SO_4}{\rightleftarrows} RCOOCH_3(org) + H_2O \qquad (2)$$

The composition of the feed oil was the same as in the cases of treatment 2. The specified amounts of feed oil, concentrated sulfuric acid and methanol were contacted and the reaction was carried out in a two-necked flask, which was equipped with reflux condenser, and temperature-controlled water bath. After esterification, the water washing should be required to remove sulfuric acid because sulfuric acid may neutralize the alkali catalyst in transesterification. The water washing with a specified amount of water was repeated twice. The aqueous and organic phases also were separated by centrifuge after the treatment. The obtained aqueous phases also were analyzed by ICP-AES to determine the mass fraction of phosphorous in aqueous phase.

Table 3 Experiment conditions

Feed oil	
Phosphorous/Triolein mass fraction[-]	0.001; 0
FFA/ Triolein mass fraction[-]	0.15
Sulfuric acid and methanol treatment	
MeOH/Oil molar ratio[-]	7.5
H_2SO_4/Oil mass fraction[-]	0.03
Reaction temperature[k]	333
Reaction time[h]	1.5
Water washing	
H_2O/Oil mass ratio[-]	1.5
Reaction temperature[k]	333
Reaction time[h]	0.33

3. Results and Discussion

3.1 Definitions of yields

The fractional removal of phosphorous after *k*-th time water washing from the aqueous phases by *j* operation, $Y_{P,j,k}$, was defined as,

$$Y_{\mathrm{P},j,k} = \sum_{l=1}^{k} M_{\mathrm{aq},j,l}\, y_{\mathrm{P},j,l} \Big/ M_{\mathrm{org},j,\mathrm{F}}\, x_{\mathrm{P},j,\mathrm{F}} \qquad (3)$$

Here, $M_{\mathrm{org},j,\mathrm{F}}$, $x_{\mathrm{P},j,\mathrm{F}}$, $M_{\mathrm{aq},j,l}$ and $y_{\mathrm{P},j,l}$ indicate the mass of feed oil, mass fraction of phosphorous in the feed oil, mass of the aqueous phase obtained at the k-th time water washing and mass fraction of phosphorous in the k-th aqueous phase, respectively. The j stands for the operation of three types treatment methods.

The total mass of obtained aqueous phase until k-th treatment was defined as,

$$W_{\mathrm{aq},j,k} = \sum M_{\mathrm{aq},j,k} \qquad (4)$$

Here $M_{\mathrm{aq},j,k}$ means the mass of the aqueous phase obtained at the k-th time washing treatment. The j stands for the operation of three types treatment methods.

The yield of the organic phase by those three types treatment methods was defined as $Y_{\mathrm{org,j}}$.

$$Y_{\mathrm{org},j} = M_{\mathrm{org},j} \Big/ M_{\mathrm{org,F}} \qquad (5)$$

Here $M_{\mathrm{org,j}}$, $M_{\mathrm{org,F}}$ means the mass of the organic phase obtained after j operation and the mass of feed oil. The j stands for the operation of three types treatment methods.

3.2 Removal of phospholipid by different treatment methods

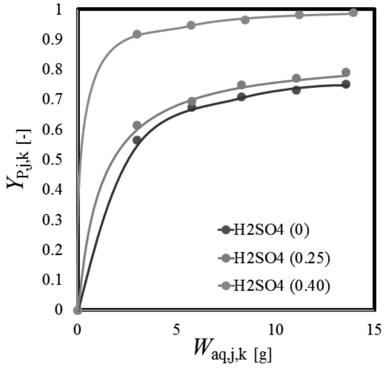

Figure 1. The effects of different sulphuric acid differernt during sulphuric acid solution treatment with water wash on $Y_{\mathrm{P,j,k}}$ [-]

Figure 1 shows the plots of $Y_{\mathrm{P},j,k}$ against $W_{\mathrm{aq},j,k}$ in the case of sulfuric acid solution treatment with water washing, treatment 1. The $Y_{\mathrm{P},j,k}$ increased as $W_{\mathrm{aq},j,k}$. When water containing no sulfuric acid was used, $Y_{\mathrm{P},j,k}$ was more than 0.55 at the first time water washing and raised to 0.75 after total five time operations. The $Y_{\mathrm{P},j,k}$ with sulfuric acid solution of 0.25 mass frac. was almost same as that with water washing. The treatment with sulfuric acid of 0.4 mass frac. enhanced $Y_{\mathrm{P},j,k}$ significantly, and $Y_{\mathrm{P},j,k}$ was 0.85 after first time water washing and raised to 0.99. The higher sulfuric acid treatment should effectively convert non-hydratable phospholipids into hydratable ones to enhance $Y_{\mathrm{P,j,k}}$, after water washing the mass fractions of phosphorous in organic phase could be reduced to 0.00001

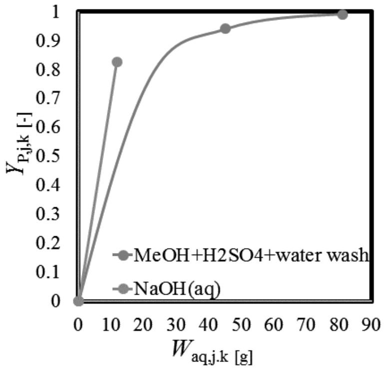

Figure 2. The effects of Sodium hydrate solution treatment method and sulphuric acid and methanol treatment with water wash method on $Y_{\mathrm{P,j,k}}$ [-]

Figure 2 shows the plots of $Y_{\mathrm{P},j,k}$ against $W_{\mathrm{aq,j},k}$ during sodium hydroxide solution treatment, treatment 2, and sulfuric acid and methanol treatment and with water washing, treatment 3. In all cases, white colored high-viscous substance was obtained. The phospholipids should work as surfactant and some emulsion might be generated. For both cases, $Y_{\mathrm{P},j,k}$ increased with $W_{\mathrm{aq,j},k}$. In the case of treatment 2, the aqueous solution of sodium hydroxide could extract phospholipid compounds and $Y_{\mathrm{P},j,k}$ increased less than 0.82. The mass fractions of phosphorous in the feed oils could be reduced to 0.00018, and still some part of non-hydratable phospholipids might have remained in the organic phase. In the case of treatment 3, $Y_{\mathrm{P},j,k}$ attained more than 0.93 at the first time water washing, and $Y_{\mathrm{P},j,k}$ raised to 0.99 at the second water washing. It meant that treatment 3 could favorably reduce the phospholipid even if FFA and methanol existed in the system. The mass fraction of phosphorous in the organic phase after water washing could be reduced to 0.00001.

3.3 Comparison of organic phase yields

Table 4 shows the comparison of $Y_{\mathrm{org,j}}$s by three kinds of treatment methods. In the case of treatment 1, $Y_{\mathrm{org,1}}$ increased as the concentration of sulfuric acid used. The $Y_{\mathrm{org,j}}$s were larger with the treatment 3 than those with treatment 2. Sodium hydroxide should react with FFA to be removed as soap. On the other hand, treatment 3 should convert FFA to FAME, to keep higher $Y_{\mathrm{org,j}}$ than treatment 2. With the feed oils containing phospholipids, $Y_{\mathrm{org,j}}$s decreased for both cases because emulsification of the oil phase should be enhanced, as mentioned above, and the effects of the emulsification must be larger with treatment 2. Accordingly, FFA and phospholipid could be removed simultaneously by treatment 3 in the feed pretreatment with higher oil yield. Thus, this method might have possibility to simplify the feed pretreatment process. The treatment 3 might keep the final biodiesel fuel yield high even if the crude plant oils containing phospholipid and FFA by higher level.

Table 4 Comparison of organic phase yields

Treatment methods	H_2SO_4/H_2O solution mass fraction [-]	$H_2SO_{4(aq)}$/Oil mass fraction [-]	Phosphorous/Feed oil mass fraction [-]	Organic phase yields [-]
Sulfuric acid solution treatment with water washing (treatment 1)	0	-	0.001	0.68
	0.25	0.0008	0.001	0.69
	0.40	0.001	0.001	0.72
Sodium hydroxide solution treatment (treatment 2)	0	-	0	0.61
			0.001	0.41
Sulfuric acid and methanol treatment with water washing (treatment 3)	≥ 0.98	0.03	0	0.93
			0.001	0.76

4. Conclusion

The treatment of feed oil to remove phospholipid and free fatty acid was studied. In the case of sulfuric acid and methanol treatment with water washing, the sulfuric acid could effectively convert non-hydratable phospholipids into hydratable ones. This treatment could improve the phospholipid removal, even if free fatty acid and methanol existed in the system. Furthermore, this treatment attainted higher fractional yield of the feed oil. Therefore, this treatment could be expected to remove phospholipids and free fatty acids simultaneously with the higher yield of the biodiesel fuel product.

Literature Cited

[1] Sinthupinyo Patima "Comparative Study of Biodiesel Production by Alkaline Transesterification from Low- valued Feed" Master Thesis, Tokyo Tech (2007)

[2] K. T. Liu, S. Gao, T. W. Chung, C. M. Huang, Y. S. Lin "Effects of process conditions on the removal of phospholipids from Jatropha curas oil during the degumming process" Chemical Engineering Research and design, 90 (2012) 1381-1386

[3] Hayashi Tomoki "Effects of Operating Conditions in Biodiesel Fuel Production from Low-valued Feed" Bachelor Thesis, Tokyo Tech (2008)

[4]-B. Freedman, E. H. Pryde, T. L. Mounts, "Variables Affecting the Yields of Fatty Esters from Transesterified Vegetable Oils." J. Am. Oil Chem. Soc., 61, (10), 1638-1643, (1984)

[5]-G. Vicente et al. "Integrated biodiesel production: a comparison of different homogeneous catalysts systems" Bioresource Technology, 92, 297-305, (2004)

[6]-G. Vincente et al. "Optimization of integrated biodiesel production." Bioresource Technology, 98, 1724-1733, (2007)

Effects on landing aircrafts by wind around the hangars at Haneda Airport

Student number：13_14746　Name：Yuhei Morita　Supervisor：Daisuke Akita

1. Introduction

At Haneda Airport in Tokyo , there're four runways. At near the edge of one runway of four, four hangers are placed in parallel to the runway. When wind is going over the hangers, it can be stirred and after that, it can affect to aircrafts which is landing at the runway. Details of disposition of these buildings are shown in Fig.1.

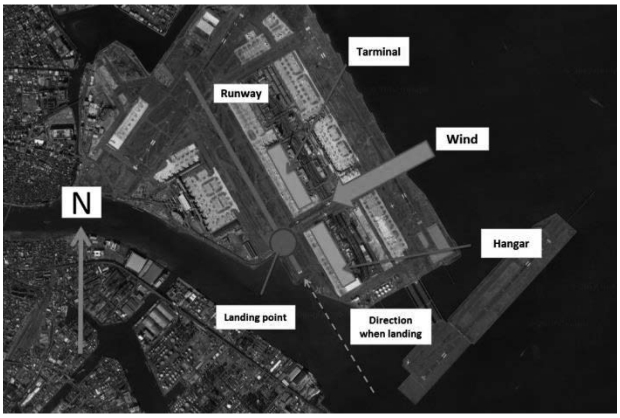

Figure 1 Disposition of hangers and runway

Figure 2 shows the details the touchdown point on the runway and the route of landing aircrafts.

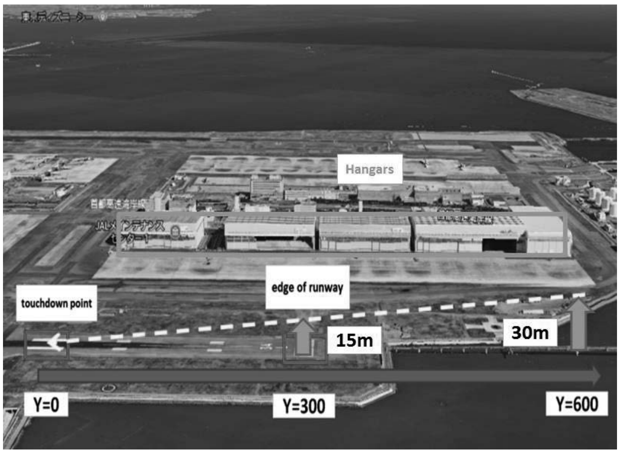

Figure 2 Touchdown point and the route of landing aircrafts

In this paper, I investigate the effects on landing aircrafts caused by the wind going over the hangars. In order to simulate the flow field around the hangar, a open source CFD software called OpenFOAM was used. The validation of the CFD method was performed through simulations of flow field around a cylinder.

2. Simulation Model

Figure 3 shows the simulation model.

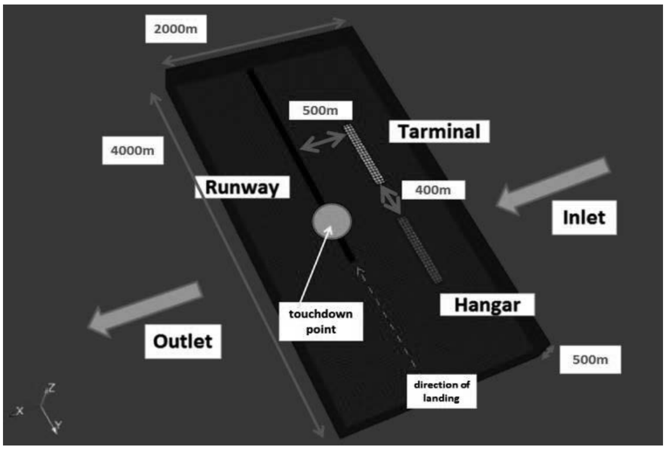

Figure 3 Simulation model

3. Results

Although the flow must be turbulent considering the Re number, turbulence models are not used in this simulation.

Figure 4 shows a velocity distribution at 15m high.

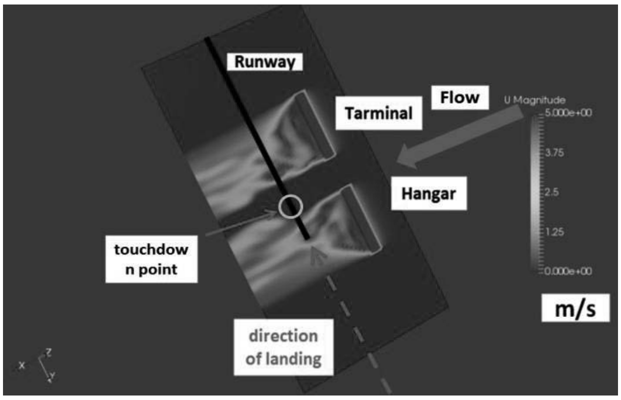

Figure 4 Velocity distribution

In Fig.4, the angle between the wind and the runway is 90°. The table 1 shows the wind parameters used in the simulation.

Table 1 Parameters

wind direction		wind velocity			
45 deg	90 deg	5m/s	10m/s	15m/s	20m/s

The effect on the landing aircraft by wind is evaluated with the following equation [1].

$$\frac{\Delta L}{L} = -\frac{2}{V_a}\Delta u + \frac{1}{V_G}\cdot\frac{1}{C_L}\cdot\frac{\partial C_L}{\partial \alpha}\cdot\Delta \mathrm{w} \quad \cdots (3.1)$$

- L: Lift
- V_a, V_G: airspeed, ground speed
- Δu: a change of tail wind
- Δw: a change of vertical wind
- C_L: coefficient of lift
- α: angle of attack

Figure 5 shows a change in lift force along the trajectory of aircrafts. The wind direction is 90 deg to the runway in Fig 5.

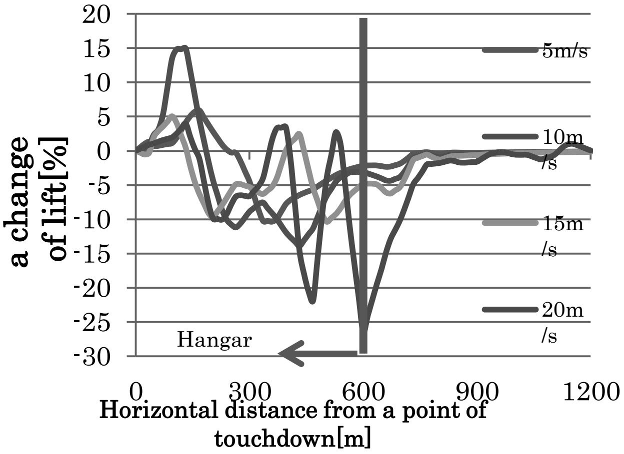

Figure 5 Lift change along aircrafts trajectory

In Fig 5, the change in lift increases with the velocity. Even when the velocity is 5m/s, the lift seems to be drastically changed.

Figure 6 shows the comparison of the wind direction.

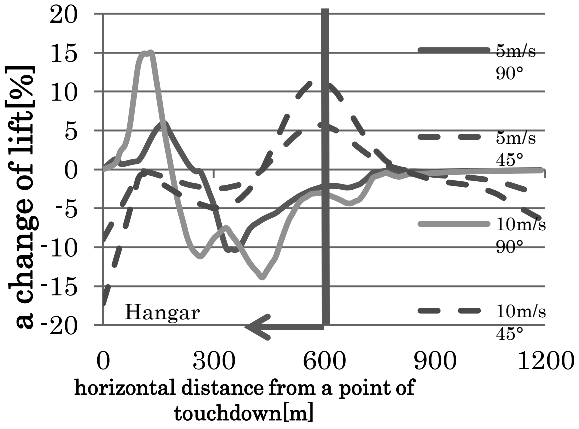

Figure 6 Effect of wind direction

In Figure6, when the angle is not 90°, a change of lift just before touchdown can be lower than zero. It means it must be more dangerous because decreasing lift may lead an airplane to touchdown strongly, unsafely.

A change of vertical component of acceleration was calculated using the following equation[2].

$$\Delta n = \frac{\rho V C_{L\alpha}}{2(W/S)} \times \Delta w \cdots (3.2)$$

- ρ: density of atmosphere[kg/m^3]
- V: ground speed[m/s]
- $C_{L\alpha}$: lift slope
- W/S : wing loading[kg/m^2]
- Δw: a change of vertical velocity[m/s]

This change of acceleration stands for how much passengers can feel the change of lift. Figure 6 shows the results.

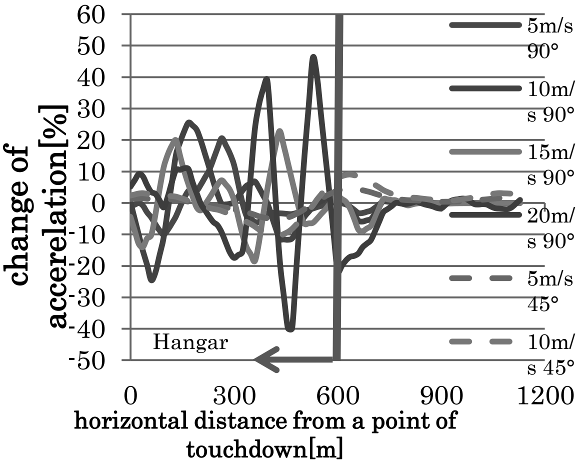

Figure 7 change of acceleration

When the wind velocity is 20m/s, and the direction is 90°, passengers can feel the maximum acceleration.

Both maximum and minimum of a change of a lift is shown in figure7. The duration is from 0[s] to 3000[s]. The wind velocity is 5 m/s and wind direction is 90deg.

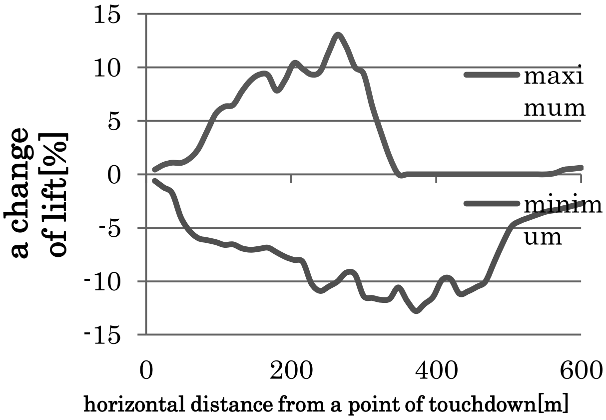

Figure 8 a change of lift

Till an aircraft reaches at the edge of the runway, a change of lift can be decreased at any time. But after passing at the edge of the runway, lift can be increased.

4. Conclusion

In this study, the wind flow field around the hangars was simulated to investigate its effects on landing aircrafts. The effect on landing aircrafts is evaluated by change in lift force of the aircrafts using the simulation results. Although the hangars are distant from the runway, the lift force of the aircrafts is affected by the wind behind the hangars. The touchdown point should be changed for safe aircrafts operation.

Reference

[1] Akira Nakayama, Humio Watanabe, 1981年5月12日に羽田空港に発生したLaw Altitude Wind Shear(LAWS)の解析, 1987

[2] JAPAN AIRCRAFTS ASSOCIATION

https://www.japa.or.jp/wp-content/uploads/2016/05/2010no4.pdf#search=%27%E6%8F%9A%E5%8A%9B%E5%A4%89%E5%8C%96+%E4%B9%99%E5%AE%A2%27 17/07/2017

Effects of electrode tip curvature and distance between electrodes on electric field

Student number: 12B11325 Student name: Gota Nurishi Supervisor: Kunio Takahashi

1. Introduction

Electrical breakdown can occur and current can flow through the air if large voltage is applied between electrodes. This is called discharge phenomenon. Arc welding and argon plasma therapy are very famous application examples. It is known that electrode tip curvature greatly effects on electrical breakdown [1].

The problem is that the way to calculate electric field isn't accurate although electric field greatly effects on electrical breakdown. Electric field isn't always equal to voltage over distance between electrodes. Therefore, charge density on the surface of electrode should be calculated.

2. Model treated in this research

Two parabola-shaped electrodes shown in Fig.1 are treated in this research.

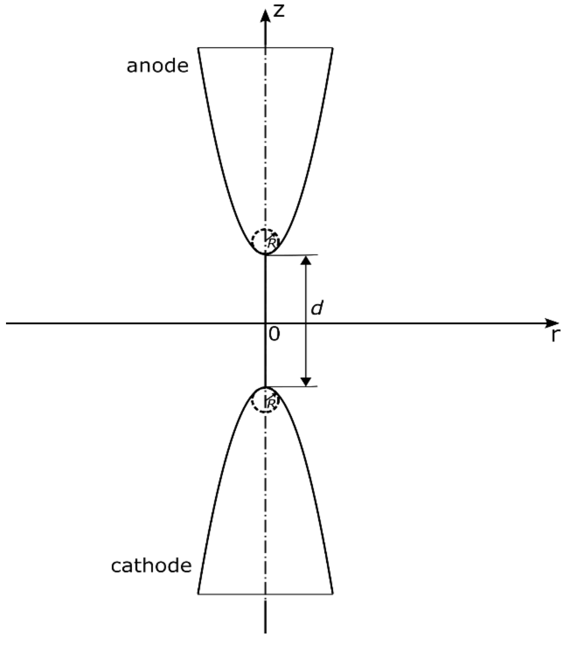

Fig.1 Model of electrodes

The electrodes for anode and cathode have a same material and form. The surface and the interior of them are seen as conductors, so potential on the surface of each electrode is constant and there is no electric field distribution inside the surface. Considering symmetry between anode and cathode, potentials at anode and cathode are set to $\frac{V}{2}$ and $-\frac{V}{2}$, respectively. Electric field in each point of the surface is in proportion to voltage under the condition that both electrode tip curvature and distance between electrodes are constant. So effects of electrode tip curvature and distance between electrodes on electric field should be tested with voltage fixed.

3. Procedure to calculate electric field

2*N* lattice points are arranged on the surface of electrodes — Each of anode and cathode has *N* lattice points. As Fig.2 shows, (*N*—5) lattice points are arranged on each curve, but the closer to electrode tip, at shorter intervals lattice points are required. On straight lines which correspond to cutting planes, 5 lattice points each are arranged. *N* is set to 50 in this research.

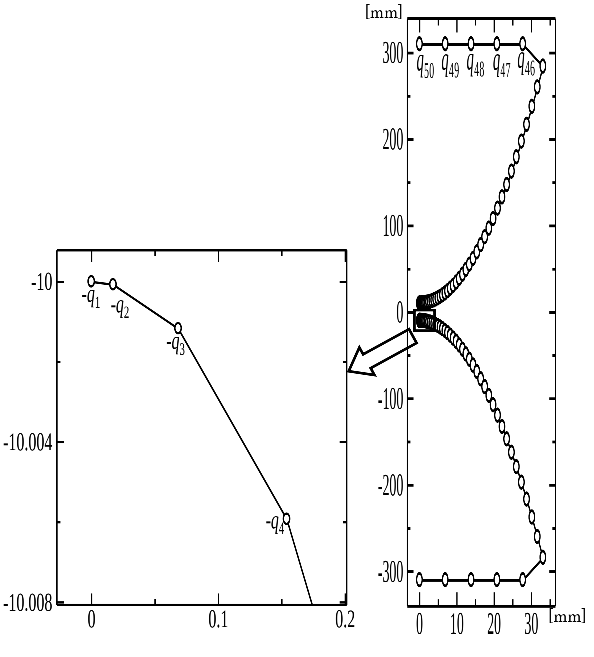

Fig.2 lattice points plotting — In case that distance between electrodes is 20mm and radius of curvature is 2mm—

Electric field is equal to charge density over permittivity on each point of surface, so electric field will be clear if charge density is calculated on each point of surface. Charge density everywhere can be calculated by using BEM(boundary element method) and considering that potential on the surface of each electrode is constant($\frac{V}{2}$ everywhere at anode, and $-\frac{V}{2}$ everywhere at cathode) [2]. Electric field not only on electrodes but also on neutral axis$\left(-\frac{d}{2} < z < \frac{d}{2}, r = 0\right)$ will be clear if charge density is calculated on each point of surface. Superposition principle of coulomb's law enables to solve electric field distribution on neutral axis easily [3].

4. Simulation Result

2 kinds of diagrams are shown below. Voltage is 1[V].The ratio of 'radius of electrode tip curvature' (*R*) to 'distance between electrodes' (*d*) greatly effects on electric field. The intensity of electric field itself isn't so significant.

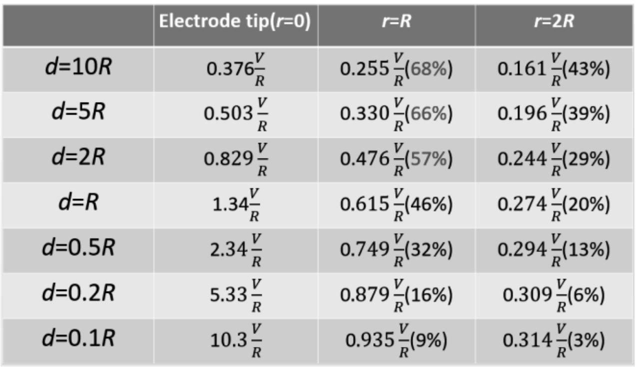

	Electrode tip(*r*=0)	*r*=*R*	*r*=2*R*
d=10*R*	$0.376\frac{V}{R}$	$0.255\frac{V}{R}$(68%)	$0.161\frac{V}{R}$(43%)
d=5*R*	$0.503\frac{V}{R}$	$0.330\frac{V}{R}$(66%)	$0.196\frac{V}{R}$(39%)
d=2*R*	$0.829\frac{V}{R}$	$0.476\frac{V}{R}$(57%)	$0.244\frac{V}{R}$(29%)
d=*R*	$1.34\frac{V}{R}$	$0.615\frac{V}{R}$(46%)	$0.274\frac{V}{R}$(20%)
d=0.5*R*	$2.34\frac{V}{R}$	$0.749\frac{V}{R}$(32%)	$0.294\frac{V}{R}$(13%)
d=0.2*R*	$5.33\frac{V}{R}$	$0.879\frac{V}{R}$(16%)	$0.309\frac{V}{R}$(6%)
d=0.1*R*	$10.3\frac{V}{R}$	$0.935\frac{V}{R}$(9%)	$0.314\frac{V}{R}$(3%)

Fig.3 The ratio of charge density to electrode tip

R is fixed in Fig.3. The smaller *d* is, the easier it is that the ratio of charge density to the tip decreases with respect to displacement as Fig.3 shows. Whether *d* is big or small, charge density at the place horizontally more than 2*R* away from electrode tip is sufficiently smaller than that at the tip.

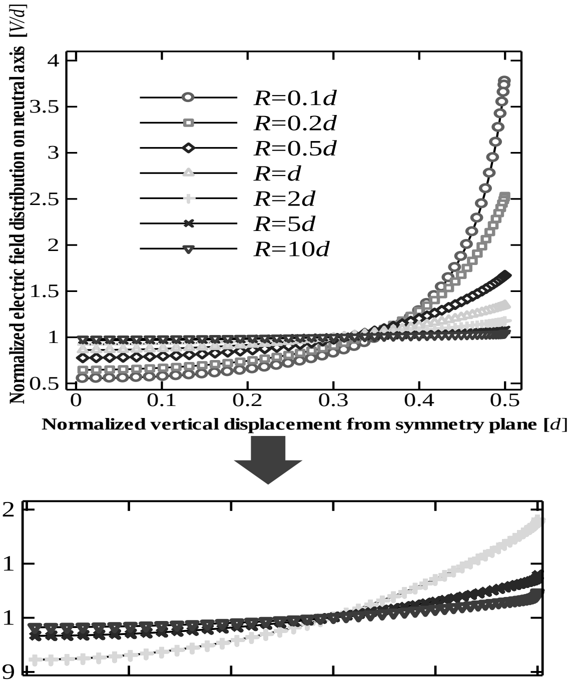

Fig.4 Diagram of electric field distribution on neutral axis

d is fixed in Fig.4. In case that *R* is small, electric field near the tip (*z*≒0.5*d*) is much bigger than it on symmetry plane. In case that *R* is big enough, electric field is almost constant with respect to displacement.

5. Conclusion

The ratio of radius of electric tip curvature to distance between electrodes greatly effects on electric field distribution. The intensity of electric field can't be defined as voltage over distance between electrodes unless radius of electrode tip curvature is sufficiently bigger than distance between electrodes. In case that distance between electrodes is bigger than radius of electrode tip curvature, electrical breakdown doesn't always occur at electrode tip.

6. Reference

[1] Japan Welding Society, Vol.12, No.4, 1994 "Phenomena of micro-discharge across the gap of sub-micrometer" by Hiroshi Maruo, Yoshinori Hirata and Kimihiro Ozaki

[2] Journal of applied physics, Vol.90, No.1, 2001 "Voltage required to detach an adhered particle by Coulomb interaction for micromanipulation" Kunio Takahashi, Hideaki Kajihara, Masataka Urago, Shigeki Saito, Yoshihiro Mochimaru, and Tadao Onzawa

[3] "電磁気学" by 浅田雅洋 and 平野拓一

財務的内部収益率から見た大型ショッピングモールにおける太陽光発電システムの導入可能性：上海（中国）を事例として

学籍番号：13_05322　　氏名：顧　任遠　　指導教官：阿部　直也

1. はじめに

「パリ協定」の採択でエネルギー構造の調整が中国の一大課題となっていた。その中の一つとしては1950年代から発展し始まった中国太陽光発電事業であり，近年都市部における太陽光発電システム設置の推進も始まっていた。しかしながら，都市部における太陽光発電システムの設置は場所がないという問題が残されていた。そこで政府が分散型太陽光発電システム(電力需要側が建設し，電圧レベル35kVかつ容量6MW以下であり，自己消費を主とする同時に余剰電力を地域ネットワークに輸送する太陽光発電システムが分散型に分類すると中国国家電網会社が定義している)の推進を国戦略として提示し，都市部における太陽光発電の推進を図った。

太陽光発電システムの設置候補施設の中で、日射量を確保しやすい屋上面積が広く、自己消費電力量が比較的多いショッピングモールは、発電設備の設置施設として望ましい条件を有していると思われる。しかし、中国において、現時点では、分散型太陽光発電システムを設置しているショッピングモールの事例が大変限られている。そこで、本研究は、発電及び施設設置のために比較的好条件を兼ね備える施設と想定されるショッピングモールに分散型太陽光発電システムの設置が必ずしも進んでいない背景を、(1)投資の収益性という観点と(2)日本におけるショッピングモールにおける同システムの設置方針と比較して検討することを目的とした。具体的には、設備設置を投資とみなし、その財務的内部収益率の視点から，検討を行う。

2. ショッピングモールにおける太陽光発電システム普及の実態

2-1. 上海（中国）における太陽光発電システム普及の実態と関連制度

本研究が着目している上海における太陽光発電システムの累積設置容量は確認できなかったが，2016年に補助金を受けて設置されたシステムの建設状況は表1の通りである。同表からわかる通り、ショッピングモールにおける設置容量は全体の１％未満である。また、上海に立地するショッピングモール（127箇所）のうち、太陽光発電システムを導入しているところは、0箇所である。(2016年12月BAIDU衛星画像で確認した結果)

表1　上海市分散型太陽光発電システム建設状況概要(2016年)

投資企業	容量(kW)	割合(%)	設置場所	容量(kW)	割合(%)
エネルギー関係	1,573	2.93	公共施設	2,394	4.46
設備関係	37,182	69.21	住宅施設	2,126	3.96
建築関係	6,153	11.45	政府関係	323	0.60
その他	8,817	16.41	その他	2,055	3.82
合計	53,724	100.00	企業屋上↓	46,826	87.16
			ショッピングモール	**503**	**0.94**
			合計	53,724	100.00

上海（中国）において、太陽光発電システムを設置しようとする事業者が、所定の条件を満たした場合、受け取ることができる補助金制度は表2の通りである。

表2　上海（中国）における太陽光発電システム設置に対する補助金制度(単位：RMB/kWh)

中央政府から	地方政府から	最大合計
0.42	0.25	0.67

2-2. 日本のショッピングモールにおける太陽光発電システム普及の実態

本研究では、日本におけるショッピングモールにおける太陽光発電システム普及の背景を理解するため、関連資料の収集とヒアリング調査を行った（I-M社を訪問してヒアリング調査を行った、2017年）。その結果、まず日本の立地する全147箇所のショッピングモールでは、71箇所が容量太陽光発電システムの設置が行われていることを確認した。設置の際、どのような基準に基づきシステムの設置を判断するのか、I-M社の担当者に確認したところ、基本的には財務的収益性を確保できるか否かによって判断しているとのことであったが、特に同社はグループ会社全体として、環境に配慮するポリシーを明確に掲げているため、その点もシステム導入を決める大きな要因となっていることが確認された。また、政策的要因、すなわち、補助金の有無は収益性を大きく左右するため、結果的に政策面の動向も大きく導入を決める際に影響を及ぼしていることが確認された。

3. 財務的内部収益率

企業は投資プロジェクトを遂行するか否かを意思決定するために使われる評価指標の一つは、プロジェクトがもたらす費用と便益の時間価値に基づき計算する内部収益率である。内部収益率は、社会的費用と便益も計算に入れる経済的内部収益率と純粋にプロジェクトの投資費用と収益を計算する財務的内部収益率がある。本論では，財務的内部収益率を適用した。

内部収益率の具体的な概念と算出手順は以下の通りである。実施期間がn年のプロジェクトから得られる財務的収益の現在価値の合計と、プロジェクトの為に要する財務的費用の現在価値の合計と等しくなるような割引率と定義されるのが財務的内部収益率であるI_0を初期投資額，CF_tをt年度目にプロジェクトから得られる収入にその年の投資費用を引いた数値，rを割引率，nをプロジェクトの想定期間とすれば，

$$NPV = -I_0 + \frac{CF_1}{(1+r)} + \frac{CF_2}{(1+r)^2} + \cdots + \frac{CF_n}{(1+r)^n}$$

$$= -I_0 + \sum_{t=1}^{n} \frac{CF_t}{(1+r)^t} = 0$$

この等式が成り立つようなrを財務的内部収益率と呼ぶ。本研究ではこれを求める。

4. 収益分析とシナリオ別の検討

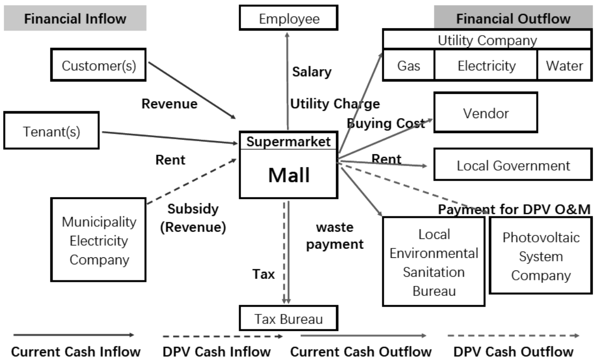

図1 ショッピングモールと太陽光発電システムのビジネスモデル

上海に立地するショッピングモールに太陽光発電システムを設置する場合、どのような費用と便益が発生するのか、関連資料およびヒアリング調査（2016年8月実施）により図示したものが、図1である。 この調査では，ショッピングモールのビジネス規模を考察するための各収支データを揃えた。同図にある通り、太陽光発電システムの主な収益は売電収入と補助金であり、主な費用は O&M 費用と税金である。本論では、太陽光発電システムの収益分析を、全量売電する場合と全量自己消費する場合の二通りに分けて行う。

虚線部分の太陽光発電システムを単独で分析する結果，全量売電の場合内部収益率は 12.66%、全量自己消費の場合は 9.57%になる。また，太陽光発電事業とショッピングモール本来の事業と比較すると，ショッピングモール事業の収入が太陽光発電事業の収入の何十倍もあることが判明し，両者の収入の額が桁違うことがわかった。ここまでの分析結果から二つがわかる：(1)現在システム全量売電の場合は全量自己消費にするより内部収益率が高い；(2)太陽光発電事業はショッピングモール本来のビジネスと比べると無視できるほど微々たるである。

太陽光発電事業の収益性は様々な要因で内部収益率が影響される。本論では人間行動、補助金、買取り価格、初期投資費用による内部収益率の変化に着目し、検討した。各シナリオの試算結果は表3でまとめている。

表3 シナリオ別の収益性試算結果（単位：％）

シナリオ	全量売電	全量自己消費
人間行動		最大 9.57%
補助金(国)(↓)	12.66%から 3.51%	
補助金(地方)(↓)	12.66%から 10.35%	
買取り価格(↓)	12.66%から 6.25%	
初期投資費用(↓)	12.66%から 22.86%	

4-1. 人間行動に着目する場合

発電することで多少電力を余計に使用しても良いと考え，電力消費量が逆に増える可能性がある。施設利用者が太陽光による発電電力を過剰に消費した場合，財務的内部収益率がどのように変化するかに着目する。過剰に消費される電力は総発電量の 1(%)から計算し始め、1(%)刻みとし、内部収益率が計算できなくなるまで電力消費量を増加した。結果的に人間の過剰電力消費で仮想プロジェクトの財務的収益率が確実に減少する。また，過剰消費の程度と比例して財務的収益率の減少が激しくなる。

4-2. 補助金に着目する場合

現在太陽光発電コストがまだ高く，補助金は事業に欠かせない。補助金額が下がる場合，全量売電の時に内部収益率がどのように変化するかに着目した。国の補助金を現在の 0.42(RMB/kWh)、地方の補助金を 0.25(RMB/kWh)から計算し始め，0.1(RMB/kWh)刻みとし，0になるまでの財務的内部収益率の変化に着目した。結果的に内部収益率が 12.66%からそれぞれ 3.51%と 10.35%まで減少した。また，両方の補助金が無くなると，財政収支が負になる。

4-3. 買取り価格に着目する場合

中国では太陽光発電事業主が全量売電を選択する場合，所在地域買取り価格で電力を買取られている。上海の買取り価格は現在 0.85(RMB/kWh)である。買取り価格が下がる場合，全量売電の時に財務的内部収益率がどのように変化するかに着目した。買取り価格を 0.85(RMB/kWh)から計算し始め，0.1(RMB/kWh)刻みとし，現在火力発電コストの 0.39(RMB/kWh)までの財務的内部収益率の変化に着目した。結果的に内部収益率が 12.66%から 6.25%まで減少した。

4-4. 初期投資費用に着目する場合

太陽光発電設備の価格は近年低下傾向にある。初期投資費用が下がる場合，全量売電の時に財務的内部収益率がどのように変化するかに着目する。初期投資費用を現在設定している 750(万 RMB)から計算し始め，10(万 RMB)刻みとし，初期設定の三分の二の 500(万 RMB)までの財務的内部収益率の変化に着目した。結果的には財務的内部収益率が 12.66%から 22.86%までに上昇した。

4. 結論および今後の課題

本論の結論として，以下の2点を確認した。(1)現時点中国では太陽光発電事業への民間投資を促進する政策が実施されているため，ショッピングモールにおける太陽光発電事業の投資の収益性がある程度確保できることがわかった。また，(2)政策面と収益性両方が整えている中，現在中国におけるショッピングモールにおける太陽光発電システムの投資の実績は限定的である事実が，会社全体として環境に配慮するポリシーを明確に掲げていないためと考えられる。

今後の研究課題としては，ショッピングモールへの太陽光発電システムの導入による社会的便益の考察が考えられる。ショッピングモールのような人が多く集まる場所での再生可能エネルギーの導入によって，人々の環境意識はどれだけ喚起されるか，またその際に用いる補助制度はどうあるべきかについて研究が考えられる。

参考文献

[1]中国国家発展改革委員会（2016） 可再生能源発展“十三五”規劃

[2] Antonio Colmenar-Santos et al. (2016) An assessment of photovoltaic potential in shopping centres

[3]蜂谷豊彦・中村博之（2001） 企業経営の財務と会計 第7章 戦略的投資の評価と決定

Analysis of microbial flora in canned Shirasu heat-sterilized under reduced pressure

Student Number: 13-13155 Name: Tatetsu MAEDA Supervisor: Kunio TAKAHASHI

1. Introduction

Boiled Shirasu (whitebait) is a highly perishable food, so that it can be preserved for only up to 4 days at 10℃. Therefore, it is necessary to develop the technologies, such as packing in a can, to preserve boiled Shirasu for a long period of time.

Sterilization is necessary for the long-term preservation of Shirasu. During heat sterilization of canned Shirasu, the internal pressure increases and causes dripping, which results in the decrease of amino acid content by 51 to 60%. Therefore, canned Shirasu is heated at reduced pressure to avoid dripping. Because canned Shirasu is distributed at 10°C, it needs to be confirmed that psychotropic and/or psychrophilic micro-organisms do not grow in a can after sterilization. These microorganisms may increase during a long-term storage period, although the microbial concentration is low at immediately after the sterilization. The existence of microorganisms would be examined in a short period of time by growing the microorganisms under their favorable growth conditions and by applying molecular biological techniques. The present study investigated the microbial community of canned Shirasu heated at reduced pressure, in order to confirm the long-term stability of canned Shirasu.

2. Materials and methods

2-1. Enrichment culture

Two cans of Shirasu (Lots 1 and 2) were sterilized at 85℃, -20 kPa for 60 min. Microorganisms in canned Shirasu were enriched under two different temperatures. Approximately 2 g of sterilized Shirasu was added in a 200 mL sterilized trypticase-soy (TS) liquid medium. Each medium was flushed with nitrogen gas at 50 mL/min for 8 min to ensure anaerobic environment. The culture flask was incubated at 10 or 30℃, 120 rpm, for 30 days. To confirm the growth of microorganisms, turbidity of the medium was observed.

2-2. Microbial community analysis

Total DNA was extracted from microorganisms grown after enrichment culture, and the DNA region encoding 16S rRNA was amplified by PCR using TaKaRa EX Taq® Hot Start Version (Takara Bio Inc., Japan). After confirming the amplification, the PCR products obtained were purified using Wizard® SV Gel and PCR Clean-Up System (Promega Corp., USA). The purified PCR products were sequenced using BigDye® Terminator v3.1 Cycle Sequencing Kit (Perkin Elmer, Applied Biosystems Division, Japan).

3. Results and discussion

3-1. Enrichments at different temperatures

During enrichment culture under anaerobic conditions, the growth of microorganisms in sterilized canned Shirasu was different depending on incubation temperatures (Fig. 1). The liquid medium incubated at 30℃ became turbid within 2 days, indicating the rapid growth of microorganisms. On the other hand, no microbial growth was observed at 10℃ even after 30 days. These results suggest that some microorganisms remain in canned Shirasu after sterilization, but they do not grow at 10℃.

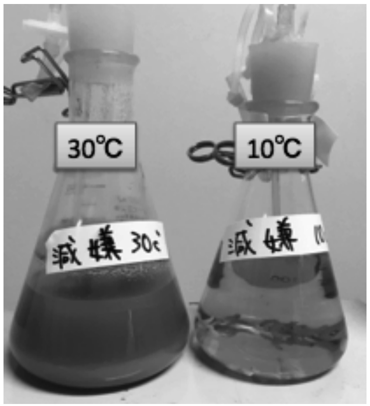

Fig. 1. Comparison of turbidity in TS liquid media enriched at two different temperatures

3-2. Microbial community analysis

Figures 2 and 3 summarize the results of microbial community analysis of the sterilized canned Shirasu enriched at 30℃. In Lot 1 can, two kinds of microorganisms were detected; *Paenibacillus qingshengii* strain S1-9 and *Bacillus subtilis* subsp. *inaquosorum* strain BGSC 3A28. These identified strains were both spore-forming bacteria [1,2]. In Lot 2 can, a spore-former *Bacillus amyloliquefaciens* subsp. *plantarum* strain FZB42 [3] was also detected. Their spores are known to be tolerant against high temperature so that they often survive after heating sterilization [3]. Thus it was suggested that the spores of these microorganisms survived after heating of canned Shirasu at 85℃. On the other hand, no microorganism was found at 10℃ (Fig. 1), suggesting that the growth of these microorganisms enriched at 30℃ is very slow at low temperature. From these results, it is suggested that the heating sterilization adopted in this study efficiently disinfects psychotropic and/or psychrophilic microorganisms of canned Shirasu.

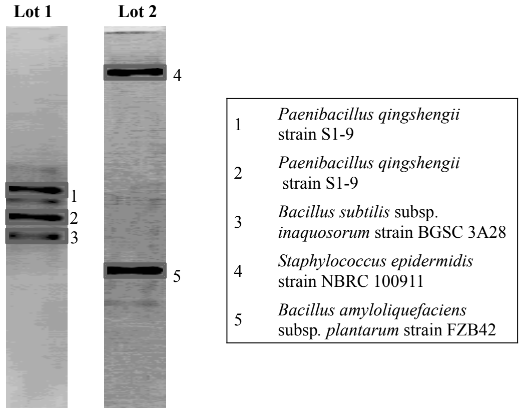

Fig. 2. DGGE profiles of sterilized canned Shirasu enriched at 30℃

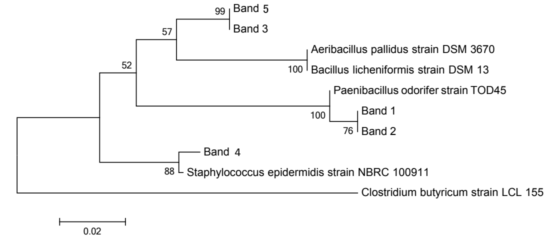

Fig. 3. Phylogenic tree of the bacteria found in sterilized canned Shirasu enriched at 30℃

4. Conclusions

Three spore-forming bacteria were observed in heat-sterilized canned Shirasu after enrichment at 30℃, while no microbial growth was observed at 10℃. It is suggested that the heating sterilization disinfects psychotropic and/or psychrophilic microorganisms of canned Shirasu.

5. References

[1] Chen, L., et al., 2015. *Int. J. Syst. Evol. Microbiol.*, 65, 2161–2166.

[2] Setlow, P., 2005. *J. Appl. Microbiol.*, 101, 514-525.

[3] Rajan, S., et al., 2006. *J. Food Prot.*, 69, 853–860.

Assessment of Technical Feasibility of Jakarta's Giant Seawall Project

Student ID: 14B15849 Name: Yi Xiong Supervisor: Hiroshi Takagi

1 Abstract

Jakarta is the capital of Indonesia. This megacity is located on the northwest coast of Java, the most populous island in the world. Jakarta metropolitan area is the second largest urban agglomeration and second largest city in the world after Tokyo **[1]**. However, this megacity is suffered from the flood almost every year. Jakarta is located at the mouth of many rivers which are connected with Jakarta Bay. The land subsidence caused by overexploitation of groundwater makes the city more vulnerable to flood hazard **[1]**. In order to save the city and thousands of residents against the annual floods from sea and rivers, Jakarta government decided to promote a project named ***The Master Plan "National Capital Integrated Coastal Development"***, collectively called as NCICD, which incorporates the multi-phases of a Giant Seawall and large storage basins. The project activities were changed several times due to political or economy reasons. And it will be still changing in the future considered that the technical feasibility is inadequate **[2]**. There are a number of grave concerns relating to such an ambitious project. In the event that the great seawalls fail to shut out seawater or the project is suspended or postponed due to economic turmoil, engineering difficulties, environmental impact, or political decisions, and assuming that efforts to reduce land subsidence are not carried out, downtown Jakarta would eventually become submerged **[3]**.

It is not clear how the project will look like in the future. Other studies have concluded that the huge storage will turn into a receptacle of waste water if the government does not prioritize a parallel development of structural treatment of sewage**[4]**. The effects on the fishery industry cannot be ignored neither. This study mainly focused on protecting Jakarta from flood hazard. The aim of this research is to find out the appropriate height of coast dyke and discuss the technical feasibility of constructing the outer sea wall.

Fig. 1 strengthening dykes in northern Jakarta

2 Numerical analysis using Delft3D according to NSICD scenarios

Land subsidence rate in Jakarta is assumed at 7.5cm/year on average along the coastline **[2]**. According to Deltares, an independent institute, the worst area's land subsidence rate in north Jakarta is up to 18cm/year, urging the government to proceed the Master Plan promptly. The future land subsidence rate depends on the decrease in groundwater extraction and the implementation of piped water supply as alternative drinking water source.

The master plan NCICD has three phases including flood protection and urban development. Phase A consists of short-term measures for strengthening the existing coastal dykes **(Fig.1)**. Phase B includes the western part of outer sea wall (total length 31km) and land reclamation for urban development. Phase C is an optional construction of a sea wall depending on the development on the land subsidence in the eastern part of Jakarta bay. This paper attempts to find out the feasibility and effects mainly on flood protection part of Phase A and B by simulating scenarios using Delft3D Flow.

The following approach was assumed based on construction schedule of NCICD. For simulation, every 5 years of time interval has been considered from 2020 to 2050. And the average land subsidence rate was considered to create each year's depth file in Delft3D. In this study, three situations have been examined where the dyke's height considered as 1m, 3m and 5m, respectively. Sea level was imposed based on astronomical tide level considering an abnormal high tide occurred in 2007 **[5]**. Considering the storage lake that collects all the flows from many rivers, the sea level inside the seawall will quickly rise unless discharged water is released into the sea accordingly. Thus pump stations need to be constructed in order to lower sea level inside the sea wall. The capacity and number of pump stations need to be determined by considering river discharges and other water inflows to control sea level inside.

The result showed in each case, flooded area was almost same. Although 1m high dyke is enough to protect the city from flood **(Fig 2, Fig 3)**. However, it should be noted that dyke must be heightened as the land subsidence continues. It also should be noted that dyke was not affected by land subsidence in the simulation. In fact, seabed can also be affected by land subsidence but not as fast as coast area. In this study, although the subsidence rates were assumed to be constant, in real situation the sea level rise is slightly faster than simulation condition.

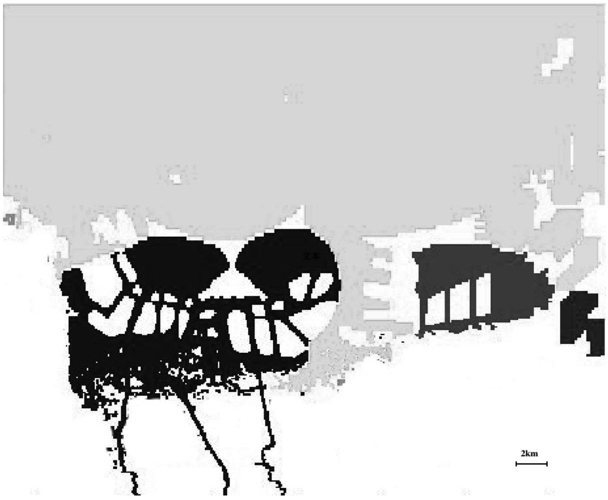

Fig. 2 Flood area without coastal dykes in 2050

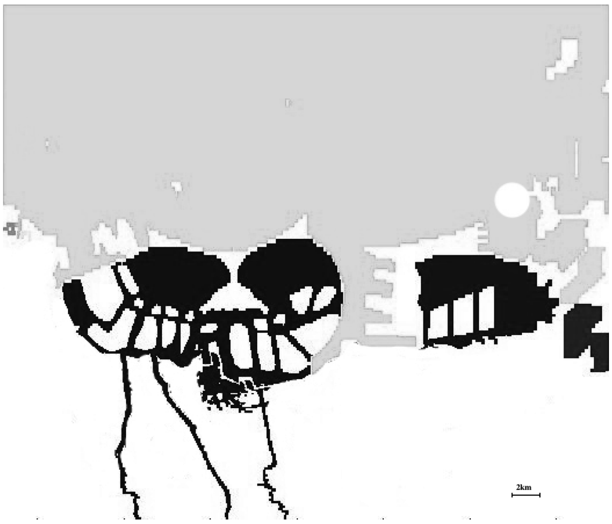

Fig. 3 Flood area with 1m high coastal dykes in 2050

3 Investigation on Outer Seawall System

According to the information from Jakarta's government officer, there is a plan to construct a 300m-wide opening on the outer sea wall which enables ships to access the existing ports. Based on this information, another simulation scenario has been carried out. The gate is needed in order to keep alive fishing activities even after Master Plan is being implemented. In this study, two types of access between inner and outer seas have been considered. One type is free-access opening and the other is a canal lock type that can keep the water out of the seawall. The result showed that the giant seawall might fail to protect the city from flood even if they can limit the opening part as short as 100m wide **(Fig4).** On the other hand, canal locks type gate can prevent the sea level inside the seawall from rising of water effectively, although the operation appears to be very complicated and the associated cost, including construction, operational, and maintenance costs, should be very expensive.

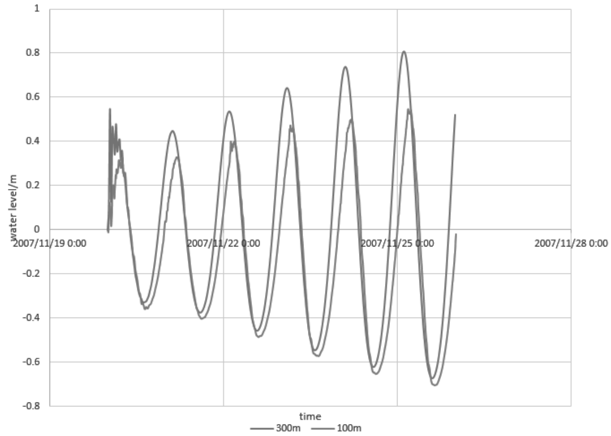

Fig.4 Sea level inside with 100m and 300m opening

4 Conclusions

Theoretically, the proposed Phase A of NCICD can protect Jakarta from flood hazard. According to the simulation result, the whole system including pump station, sea wall, dyke, storage basin, land reclamation and gate system is proved as effective. However, according to the analysis of this study, in Phase B, free-access sea wall was effective only if the opening is shorter than 100m. This small opening should limit the capacity of accessing ships. As an alternative solution, canal-lock type gate can both keep sea level from rising and provide a fluent access for ships. However, expensive cost needs to be managed by the local government. It also should be noted that no matter how the sea wall would be built, the massive pump system would continuously require a plenty of electricity and financial resources.

References

[1] NCICD, "Master Plan, National Capital Integrated Coastal Development", 2014

[2] Deltares, "Pump schemes, NCICD Phase A Retention", 2016

[3] Takagi H., Fujii D., Esteban M., Yi X. Effectiveness and Limitation of Coastal Dykes in Jakarta: The Need for Prioritizing Actions against Land Subsidence. Sustainability, 9, 619, 2017.

[4] van der Wulp, S.A., et al., "Master Plan Jakarta, Indonesia: The Giant Seawall and the need for structural treatment of municipal waste water", Marine Pollution Bulletin (2016)

[5] Takagi H., Esteban M., Mikami T., Fujii D. Projection of coastal floods in 2050 Jakarta, Urban Climate, 17, pp.135-145, 2016.

[6] NCICD, "Construction strategy stage B", 2014.

Numerical Modeling for Predicting River Flow in the Mekong Delta
メコンデルタの河川流予測のための数値シミュレーション

Student Number : 13B00543　Name : Mizuho Arai　Supervisor : Hiroshi Takagi

1. Introduction

The Mekong Delta is formed by the accumulation of sediment carried by the Mekong River in southern Vietnam. It is one of the areas where the influence of sea-level rise is concerned due to its extremely low elevation. Major flood events are occurring almost every year in the Mekong Delta. Especially, in September 2000, remarkable flood damage which caused more than 400 casualties, manifesting lack of effective countermeasures against flood issues. Can Tho, the largest city in the Mekong Delta, is situated 80 km inland where tide has dominant influence on the river level. In other words, it is clear that rising of sea surface elevation will increase the risk of flooding in Can Tho. Therefore, it is essential to understand the combined influence of tide and river discharge in order to evaluate the flooding risk of Can Tho and other Mekong Delta's cities. The prediction of river flows is also important in assessing the flood risk. However, it appears that the river flow characteristics and patterns in the delta system have been overlooked and have not been sufficiently studied in the previous flood risk studies.

This study attempt to develop a practical procedure to predict a combined river flow in Can Tho, using a hydrodynamic model, Delft 3D-FLOW.

2. Numerical Modeling

There is a significant difference in rainfall between dry season and in rainy season. Therefore, this study uses two methodologies to examine river flows in Can Tho, as described in this section.

(1) Dry season (2010/4/15～4/30)

Due to the low-lying nature of the Mekong Delta, the tidal current is dominant in the Mekong Delta during the dry season. In the dry season when rain rarely falls, the influence on the river flow from the upstream is extremely small. Therefore, the dry season model can ignore the flow rate due to rainfall as well as freshwater discharging from the upstream river. By applying tidal constituents along the ocean-side boundary, river flow and water level in the dry season can be simply reproduced.

(2) Rainy season (2009/7/24～7/30)

In the rainy season, the flow from upstream due to rainfall needs to be considered in addition to tidal-induced currents. Therefore, it is necessary to obtain the flow rate that can reproduce the observation value. For the sake of simplicity of calculation, in this study we assumed an artificial source term, which reproduces total river discharge in the middle stream of Can Tho. The discharge at the source point is determined by a trial method, which finds the discharge that best describes water levels observed by the Southern Regional Hydro-Meteorological Centre in Can Tho.

3. Analysis result and consideration

Figs. 1 and 2 show the reproducibility of the water level and flow velocity in the dry season. Peak values during maximum and lowest tidal phases are extracted, and coefficient of determination is calculated by regression analysis. Fig-1 (a) shows that simulated water levels overestimate when tidal level is relatively low (= neap-tide phase), whereas those agree well with the observed data during the spring tide. Fig-2 shows that the flow velocity in the dry season can be simulated with relatively high accuracy. Nevertheless, it is confirmed that in Fig-2 (a) numerical results significantly overestimate particularly when flow velocity is low. This is likely because the river flow in this model neglected complex mechanisms of river-flow attenuations due to the tidal current that travels upward.

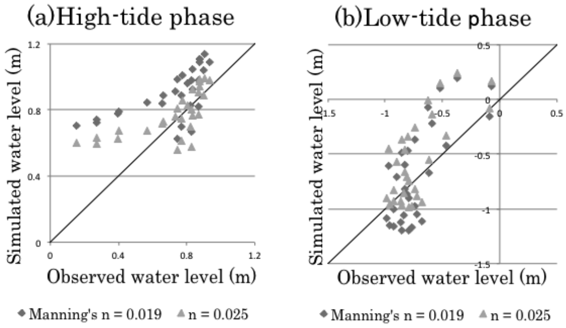

R²	High-tide phase	Low-tide phase
Manning's *n* = 0.019	0.3919	0.5276
n = 0.025	0.4516	0.5158

Fig-1 (a), (b) Model verification for high-tide level and low-tide level in the dry season

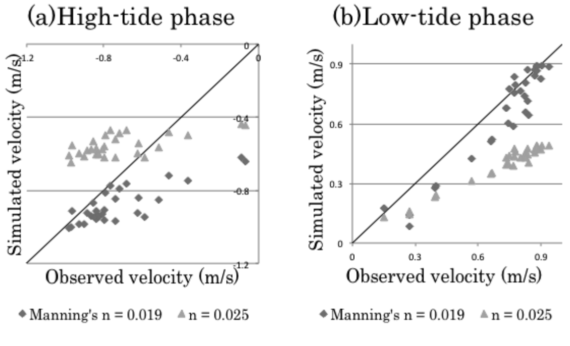

R²	High-tide phase	Low-tide phase
Manning's *n* = 0.019	0.7055	0.9092
n = 0.025	0.435	0.9602

Fig-2 (a), (b) Model validation for High-tide velocity and low-tide velocity in the dry season

Table 1 shows the coefficients of determination of the water level and the velocity for three different flow rates due to total rainfall. Overall, the average flow rate with 18,000 ㎥/s seems to best reproduce velocity and water level among three assumed discharges.

Table 1. Coefficients of determination of water level and velocity according to three discharge scenarios

		n = 0.019		*n* =0.025	
R²	Flow(m3/s)	Rising tide	Falling tide	Rising tide	Falling tide
Velocity	12,000	0.6873	0.9205	0.7181	0.973
	18,000	0.7438	0.9326	0.8308	0.8842
	24,000	0.5952	0.8786	0.7996	0.8678
Water level	12,000	0.9724	0.8157	0.9601	0.8957
	18,000	0.9674	0.8881	0.96	0.8671
	24,000	0.9688	0.9017	0.9643	0.7472

Fig-3 (a), (b), Fig-4 (a), (b) show the reproducibility of the water level and flow velocity in the rainy season respectively. Peak values of rising and falling tides are extracted, and each coefficient of determination is calculated by regression analysis.

From the above results, it was found that the influence of the tide is dominant to the river flow, and by using a model with high roughness coefficient, it is possible to predict the maximum water level and flow velocity which are important for the evaluation of flooding risk in rainy season. On the other hand, in order to avoid overestimation of the water level in the dry season, it is necessary to evaluate the influence of river flow in the dry season on the tidal current.

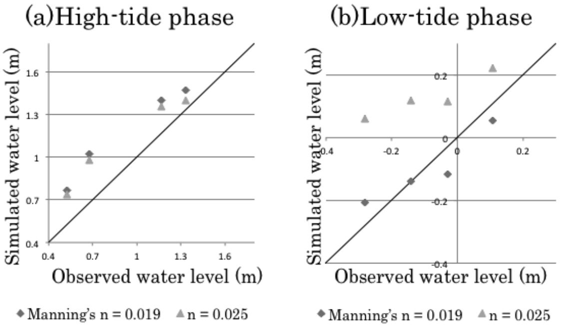

R²	High-tide phase	Low-tide phase
Manning's *n* = 0.019	0.9674	0.8881
n = 0.025	0.96	0.8671

Fig-3 (a), (b) High-tide phase level and low-tide phase level in the rainy season

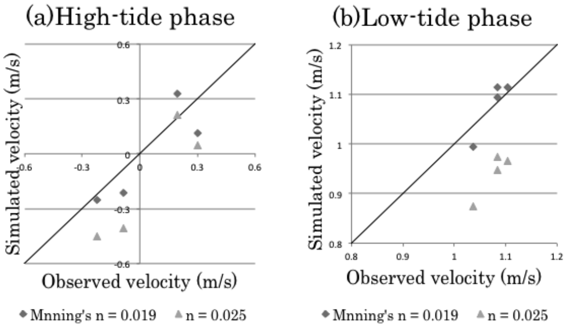

R²	High-tide phase	Low-tide phase
Manning's *n* = 0.019	0.7438	0.9326
n = 0.025	0.8308	0.8842

Fig-4 (a), (b) Model verification for high-tide phase velocity and low-tide phase velocity in the rainy season

4. Conclusions

Can Tho is densely populated city in the Mekong Delta over low land, and is considered to be the world's most vulnerable region to climate change. This study constructed a practical simulation model that took into consideration river discharge as well as tide, and investigated the possibility of predicting the river flow in the Mekong River.

As a future task, it is necessary to advance research on the following things: Improving the proposed method to be applicable for a longer period of the data. Considering detailed land geometries to investigate flooding risks in urban and agricultural areas.

5. References

1) 高木泰士, Tran Van Ty, Nguyen Danh Thao, Esteban Miguel, 高橋勇人: “メコンデルタ都市の洪水の研究―潮汐と海面上昇の影響―”,土木学会論文集 B3(海洋開発), 69(2), pp.988-993, 2013.
2) Mekong River Commission: “Overview of the Hydrology of the Mekong Basin”
3) 高木泰士: 途上国防災の現実と課題―土木と国際開発の２つの視点から, 土木技術, 68 (3), pp. 85-88, 2013.
4) Hiroshi Takagi, Nguyen Hong Quan, Le Tuan Anh, Nguyen Danh Thao, Van Pham Dang Tri, Tran The Anh: “Practical modelling of tidal propagation under fluvial interaction in the Mekong delta (under review)

Trial Production of Self-rechargeable Drone

Student number: 13B02306 Name: SIQI YUAN Supervisor: Kunio Takahashi

1 Introduction

Drones(Unmanned aerial vehicle) have been widely used in multiple different applications[1]. Due to safety reasons, battery has become the main energy source for drones. However the operation time of drone is relatively short[2]. Drones have to stop for charging, then can continue operating[3]. Multiple methods have been tried to solve this problem. One of them is building a charging platform and developing algorithm to let drones charge as efficiently as possible[5]. However the operation area has been limited by this.

This research focus on designing a system which do not require any additional charging platform and do not need to change drone's original size. Two following method have been used. (1)On-board solar panel that absorb solar energy for powering the drones. (2)Boost Converter to higher the voltage the drones require.

2 Design of the boost converter

Model of the boost converter have been thought as fig.1[4]. Here by setting $R_{\mathrm{L}} + R_{\mathrm{DS}} + R_{\mathrm{MP}} = R_{\mathrm{on}}$, and $R_{\mathrm{L}} + R_{\mathrm{D}} + R_{\mathrm{MP}} + R_{\mathrm{DR}} = R_{\mathrm{off}}$, $V_{\mathrm{D}} + V_{\mathrm{DR}} = V_{\mathrm{C}}$ and set V_{MP} as power source's maximum power point(MPP) voltage, I_{MP} set as power source's MPP current, $R_{\mathrm{MP}} = \frac{V_{\mathrm{MP}}}{I_{\mathrm{MP}}}$, We can figure out

$$2V_{\mathrm{MP}} - R_{\mathrm{on}} i_{\mathrm{on(t)}} = L\frac{di_{\mathrm{on(t)}}}{dt} \tag{1}$$

$$2V_{\mathrm{MP}} - R_{\mathrm{off}} i_{\mathrm{off(t)}} - V_{\mathrm{C}} = L\frac{di_{\mathrm{on(t)}}}{dt} \tag{2}$$

Therefore the general solution for (1) and (2) is shown respectively as (3) and (4). Here C_1 and C_2 are random constant.

$$i_{\mathrm{on(t)}} = \frac{2V_{\mathrm{MP}}}{R_{\mathrm{on}}} + C_1 e^{-\frac{R_{\mathrm{on}}}{L}t} \tag{3}$$

$$i_{\mathrm{off(t)}} = \frac{2V_{\mathrm{MP}} - V_C}{R_{\mathrm{off}}} + C_2 e^{-\frac{R_{\mathrm{off}}}{L}t} \tag{4}$$

We can set $\frac{2V_{MP}}{R_{on}} = A$ and $\frac{2V_{MP}-V_C}{R_{off}} = B$ temperately.

$$I = i_{\mathrm{on[1]}},\ i_{\mathrm{off[2]}},\ i_{\mathrm{on[3]}},\ i_{\mathrm{off[4]}},\ \ldots,\ i_{\mathrm{on[2n-1]}},\ i_{\mathrm{off[2n]}} \qquad n = 1, 2, 3, \ldots \tag{5}$$

End current of each period is defined as I_n. eq(5) shows the switching pattern. fig.2 shows the image of it.

$$\lim_{n\to\infty} i_{\mathrm{off[\infty](t)}} = \frac{(B-A)(e^{-\frac{\mathrm{R_{on}T_{on}}}{\mathrm{L}}} - 1)}{1 - e^{-\frac{R_{\mathrm{on}}T_{\mathrm{on}}+R_{\mathrm{off}}T_{\mathrm{off}}}{L}}} e^{-\frac{R_{\mathrm{off}}t}{L}} + B \tag{6}$$

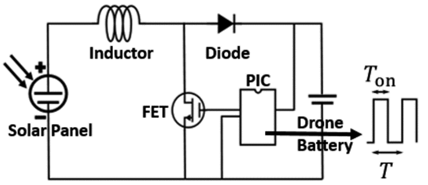

(a) Boost converter design

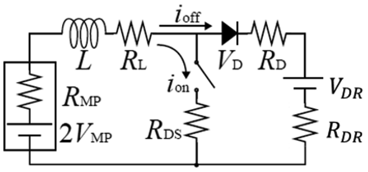

(b) Equivalent circuit of boost converter

Fig. 1: Finding the basic character of solar drone

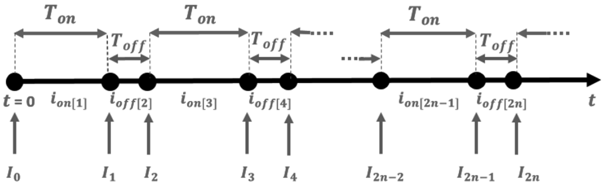

Fig. 2: Current combination of the switching circuit

When $f \to$ inf, the influence L brings to i_{off} becomes negligible.

$$\lim_{f\to\infty} E_{1\mathrm{s}} = V_{\mathrm{DR}} \frac{2V_{\mathrm{MP}} - V_{\mathrm{DR}}}{R_{\mathrm{off}}} (1-r) \tag{7}$$

Then we can use the result from [4] that the optimal duty ratio is shown in eq(8) and the setting is $\widetilde{g}_{\mathrm{C,D}} = \frac{V_{\mathrm{DR}}+V_{\mathrm{D}}}{V_{\mathrm{MP}}}$. Also need to under the condition that $\frac{R_{\mathrm{off}}}{R_{\mathrm{on}}} \to 1$.

$$d_{\mathrm{g}} = 1 - \frac{1}{\widetilde{g}_{\mathrm{C,D}}} \tag{8}$$

3 Experiment

After figuring out the maximum power point by fig.4, insert to eq(8). Assembling design following the fig.1a, and the model is shown in fig.3. The biggest obstacle of this research was designing a light system. The element which had a significant impact on the total system weight is the coil. Due to the comprehension of the switching circuit charging system, higher the inductance therefore the higher

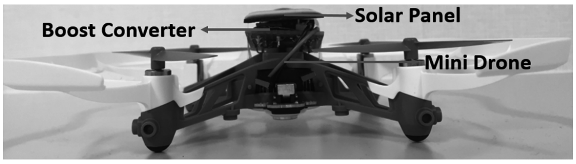

Fig. 3: Final assembly

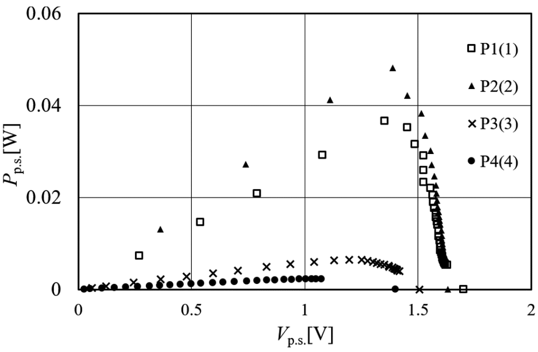

Fig. 4: Maximum Power Point Tracking
(1)$V_1 = 1.701V$ (2)$V_2 = 1.632V$
(3)$V_3 = 1.505V$ (4)$V_4 = 1.400V$

(a) Out of battery (b) Halogen Lamp for charging

(c) Remove Halogen Lamp (d) Start operation

Fig. 5: 4 hours results of in-door simulation charging

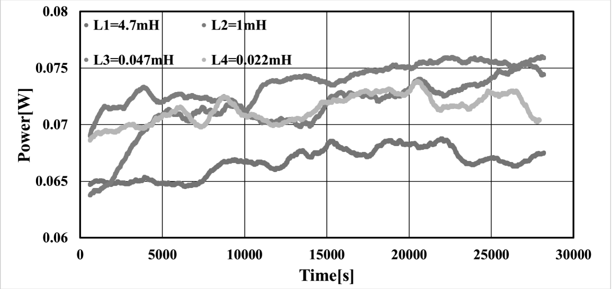

Fig. 6: The result of four different coils

the current follows through the battery. Therefore higher the charging power. But to figure out whether by setting a high frequency will keep the system light, 4 different coils have been used to calculate the charging power under f = 400kHz. During 8 hours recording, voltage between testing resistance and drone battery has been recorded. Eventually, whole charging system routine have been checked. For indoor experiment, Halogen lamp have been used. After checking solar panel under Halogen lamp, shown to provide average 1.6V(original voltage 1.5V), continued the experiment. Experiment drone can fly after 10% charging.

4 Result and Discussion

The first result shows in fig5d that after 4hours charging, the drone successfully charge the battery from 4% to 13%. After recording the 8 hours charging power, the hypothesis which by setting high frequency will weaken the influence of inductance are found to be true. As is shown in fig6 the charging power order was found by $L_3 > L_2 > L_4 > L_1$.

5 Conclusion

In this research, prototype production of self-rechargeable drone has been completed. By using both solar panel and boost converter, an on-board system successfully enabled drones to charge. However due to the calculation of the current format, it was found that if setting the frequency to a high magnitude, the current will be less influence by the inductance. This hypothesis have been proved through the experiment by using different inductance coils. Therefore when aiming to provide a light on-board system, it is found that using lower inductance coil which have a reduced weight impact will require setting the frequency to the maximum frequency PIC available in the system.

References

[1] Jinyong Kim, Jinho Lee, Jaehoon Jeong, Hyoungshick Kim, Jung Soo Park, and Taeho Kim. SAN: Self-adaptive navigation for drone battery charging in wireless drone networks. *Proceedings - IEEE 30th International Conference*, pages 248–251, 2016.

[2] Chenchen J. Li and Hao Ling. An Investigation on the Radar Signatures of Small Consumer Drones. *IEEE Antennas and Wireless Propagation Letters*, 16:649–652, 2017.

[3] Chiuk Song, Hongseok Kim, Youngwoo Kim, Donghyun Kim, Seungtaek Jeong, Yeonje Cho, Seongsoo Lee, Seungyoung Ahn, and Joungho Kim. EMI Reduction Methods in Wireless Power Transfer System for Drone Electrical Charger using Tightly-coupled Three-phase Resonant Magnetic Field. *IEEE Transactions on Industrial Electronics*, 0046(c):1–1, 2018.

[4] Masanori Tanaka. Optimization of circuit and control parameters of a boost converter for energy harvesting. 2010.

[5] Chungki Woo, Sanha Kang, Hojin Ko, Hochan Song, and Jae Ook Kwon. Auto charging platform and algorithms for long-distance flight of drones. *2017 IEEE International Conference on Consumer Electronics, ICCE 2017*, pages 186–187, 2017.

日本全域における大気境界層水平風速の年間スペクトル特性

学籍番号：14_03770　氏名：何暁卿　指導教官：神田学

1. はじめに

スペクトル解析は様々な気象現象の、時空間スケールの特性を知るのに役に立つ。過去の長期地上観測データから、時間スケール約1時間の所にスペクトル強度の著しく低いスペクトルギャップが存在し、その高周波側については Kaimal らによるカンザスでの微気象観測実験から、Monin-Obukhov 相似則に従う普遍的性質を実証されている。一方、スペクトルギャップの低周波側では慣性小領域と似た一定勾配でエネルギーが減少する帯域があることが指摘されているが、観測及び解析事例の少なさからよく分かっていない。また、この二つのスケール間での相互作用なども検討されていない。これに対し本研究では、日本全国に散在する 155 地点の地上気象観測 1 分値データを用いて、風速に関する長期スペクトルの低周波側の特性について検討した。

2. 理論背景

スペクトルギャップより高周波数側では地表面の三次元乱流に支配される。慣性小領域において、Kolmogorov は次元的な考察から

$$E(k) = C\epsilon^{2/3}k^{-5/3} \quad (1)$$

という式を導いた。いわば Kolmogorov の-5/3 乗則である。E(k)はエネルギースペクトル、C は定数、ϵは乱流エネルギーの散逸率、k は波数である。空間スペクトルを周波数スペクトルに変化するため、Taylor の仮説

$$k = 2\pi f/u_0 \quad (2)$$

を用い、f の重みをつけ、下の周波数スペクトルに変換できる。

$$fS(f) = af^{-2/3} \quad (3)$$

この式は両軸対数スケールで、直線になり、元の指数の-2/3 は傾きの値になる。

より低周波数側では、大気流れの水平スケールに比べ、鉛直スケールは非常に小さいため、二次元的な流れが支配的になると考えられており、そのスペクトル強度は周波数の-3 乗に比例して減少することが理論的に示されている。

3. データ

使用したデータは 2014 年から 2016 年まで、三年間の日本全国 155 地点の気象官署および特別地域気象観測所で観測した風速の 1 分値データである。これは地域気象観測システム（アメダス）の一部であるが、データの品質管理が施された状態で配布されている。155 地点はほぼ日本全域をカバーしており、各地方の代表的な風速スペクトルが得られていると考えられる。

4. 結果と考察

4.1 地上観測データの長周期スペクトル特性

図 1 は 155 地点で計測された風速スペクトルの平均値であるが、いくつかの特性が見られる。周期約 4 日に最大値、1 日と半日に帯域の極大値があり、それぞれ移動性の高・低気圧の通過、地球の自転及び大気潮汐などによるものとされている。さらに、周期約 1h~10min の間に

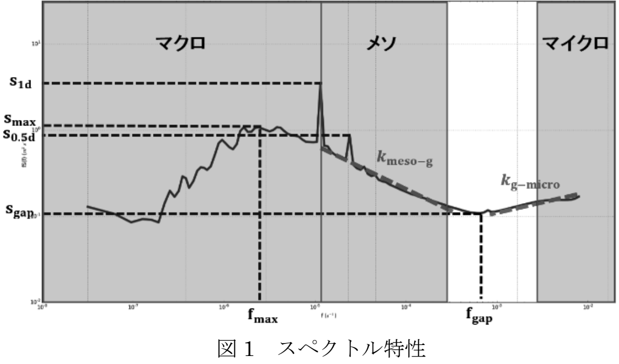

図１　スペクトル特性

スペクトル強度が非常に低い領域があり、これがスペクトルギャップである。以上から、地上1分データにおいても地上風速に見られる代表的な傾向を捉えられることが分かる。

4.2 メソスケール領域のスペクトル特性

Kraichnan (1967)によると、メソスケールにおいて、二つ領域があり、二つ式で表せる。

一つ目はエンストロフィー慣性領域で下の式

$$\mathrm{E(k)} = \mathrm{C'}\eta^{2/3}\mathrm{k}^{-3} \qquad (4)$$

で表す。$\mathrm{C'}$は定数、ηはエンストロフィーの散逸率である。前述したように、

$$fS(f) = \mathrm{a'}f^{-2} \qquad (5)$$

に変化できる。両軸対数スケールで、-2の傾きが得られる。もう一つはエネルギー慣性領域であり、式(1)で示され、周波数の-5/3乗でエネルギーが減少する。つまり、メソスケールにおいても次々とより小さなスケールの場にエネルギーは受け渡されるエネルギーカスケードが生じている。

以上について検討するため、155地点の風速スペクトルから読み取られる、メソスケールにおけるスペクトル強度の傾き$\mathrm{k_{meso-g}}$と、年間平均風速$\overline{\mathrm{U}}$の散布図について見てみた（図2）。まず、-2の傾きは確認できなかった。-2/3に近いことが分かった。

ただし、この傾きは常に理論の-2/3になっているのではなく、$\overline{\mathrm{U}}$と負の相関性を持っていることが分かった。これに加え、世界各地の観測事例の値もプロットしてみたところ、概ね分布の範囲内に収まっており、同様の風速依存性を見ることができる。この傾きが他の要素に対する依存性を見たところ、それほど強い相関が見られなかった。

次にこの傾きの地域性について見てみる。得られた傾きの値と-2/3との差をパーセンテージで表し、日本マップにプロットしたのが図3である。図から明らかなように、北海道、太平洋側沿岸、島及び平野のような平坦地では-2/3に近い値を示している。$\overline{\mathrm{U}}$も地形影響を受けることから、図2の分布は地形に依存していることが示唆される。

5. 結論

地上気象観測1分値データを用い、日本全域の155地点の風速スペクトルを算出し、スペクトルギャップの低周波側のスペクトル形状の特性について検討し、その傾きが局所的な風速、あるいは地形の影響により変化することを示した。

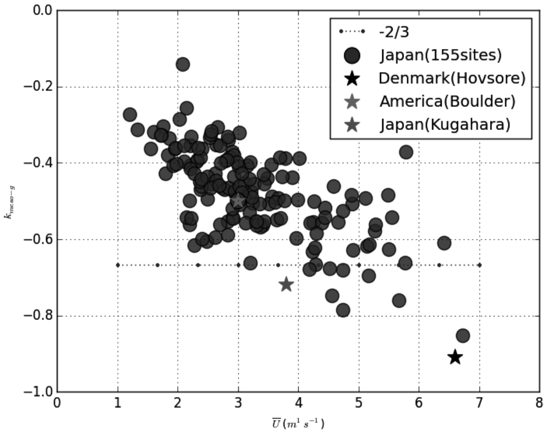

図2　メソスケールにおける傾き$\mathrm{k_{meso-g}}$と年間平均風速$\overline{\mathrm{U}}$の関係図

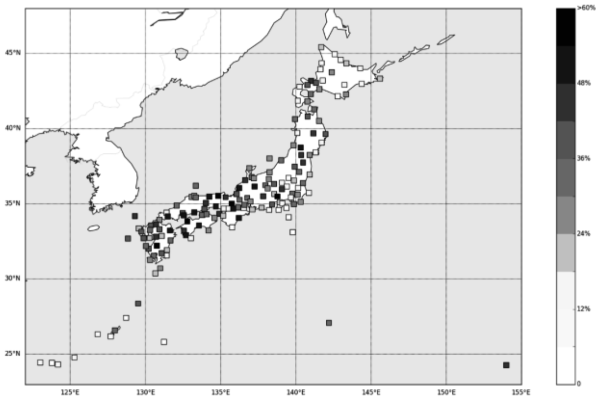

図3　−2/3傾きとの差(x%)

k_{meso-g} ＝ (-2/3)*(1±x%)

参考文献

1)野口（2011）東京工業大学卒業論文

2)Kraichnan R (1967) Phys. Fluids, 10, 1417-1423

3)Larsen XG et al. (2016) Boundary Layer Meteorol, DOI:10.1007/s10546-016-0129-x

4)Kang S et al. (2017) J.Geophys.Res:Atmospheres, 121(20),11946-11967,DOI: 10.1002/2016JD025289

The effect of consolidation and privatization of ports in proximity
― Case study in Osaka and Kobe ports ―

14_08683：Hoshi TAGAWA Supervisor: Shinya HANAOKA, Tomoya KAWASAKI

1. Introduction

In Japan, growth rate of transshipment container volume and the number of trunk lines are substantially lower than other East Asian countries. In order to strengthen the competitiveness of Japanese container port, Japanese Government launched the policy for "International Container Strategy Port". The prominent characteristics of this policy is "consolidation" and "privatization" of container ports in proximity (i.e. Osaka and Kobe port). However, the effect of consolidation and privatization of the ports are not well discussed. Thus, this study aims to explore the effects of the four cases such as "consolidation or non-consolidation" and "private or public" for Osaka and Kobe ports. These effect is examined by using indicators such as container volume and social welfare estimated from the agent-based model. As a case study, competition between Hanshin (Osaka and Kobe) and Busan port is analyzed.

2. Methodology

2.1 Effect of consolidation

By executing the consolidation, "Integrated terminal management" become possible. As a result, cargos to North America from Osaka and Kobe are aggregated to one place. It enables to reduce of waiting time due to concentration of ships and attain economics of scale.

2.2 Effect of privatization

In the case of private, port management company aims to maximize own profit. On the other hand, in the case of public, it aims to maximize social welfare. And also in the case of private, efficient operations are possible. Cost is cut by 10% from public.

2.3 Behavior of stakeholders

Stakeholders involved to port can be divided into five. "Local government", "Port management company", "Terminal operator", "Shipping company", and "Shipper". Agent-based model can simulate the relations of those five stakeholders.

A) Local government

In Japan, it is decided by Port and Harbor Act that Port management body is local government. And, local government must decide "Ship's harbor charges (e_i)". Local government is public, so e_i is decided to maximize social welfare. (Equation (1))

$$\max_{e_i} SW_i = \Pi_i + Pt_i + Ps_i + CS_i \tag{1}$$

$$CS_i = \sum_k \frac{1}{2}\left(q_{ik}^0 + q_{ik}^t\right)\left(GC_{ik}^0 - GC_{ik}^t\right) \tag{2}$$

q_{ik}^t is total cargo from port k and transship at port i in year t. GC_{ik}^t is generalized cost cargo from port k and transship at port i in year t.

B) Port management company

a) public

Port management company is considered to be same subject as local government since executive committee members are comprised by local and central government officers and stock share of this company is mostly shared by governments.

$$\max_{e_i} \Pi_i = \mu\cdot(52\cdot f_i)\cdot e_i gt_i + r_i - mc_p K_i \tag{3}$$

Π_i is profit of Port management company. gt_i is gross tonnage of ship. r_i is charges of berth lease. mc_p is maintenance cost of port. K_i is capacity of port. μ is parameter. In the case of public, $\mu = 1$.

b) private

Port management company is outsourced by local government. Port management company and local government are different subject. Port management company decide r_i to maximize own profit Π_i. (Equation (3)) In the case of private, $\mu = 1/10$. (Interview result)

C) Terminal operator

Terminal operator is subject of lease berth and loading and unloading. Terminal operator is private. They decide port service charge (w_i) to maximize own profit. (Pt_i)

$$\max_{w_i} Pt_i = (w_i - mc_t)Q_i - r_i \tag{4}$$

mc_t is marginal cost. Q_i is total cargo in port i.

D) Shipping company

Shipping company is subject of cargo transport by ship. They decide frequency of ships (f_i) and freight rate (τ_i) to maximize own profit. (Ps_i)

$$\max_{\tau_i, f_i} Ps_i = (\tau_i - w_i)Q_i - \varepsilon\cdot 52 f_i \frac{y_i N_i}{V_i} - 52 f_i e_i gt_i \tag{5}$$

y_i is fuel surcharge of ship. N_i is distance from port i to North American port. ε is parameter.

E) Shipper

Shipper is owner of cargo. They choose using port based on generalized cost. (GC_{ik}) Generalized cost is consist of "frequency", "lead time" and "freight rate."(Equation (7)) The choice model are represented in Equation (6).

$$Q_i = \sum_k QO_k \frac{\exp(-\theta\cdot GC_{ik})}{\sum_i \exp(-\theta\cdot GC_{ik})} \tag{6}$$

$$GC_{ik} = \alpha\left[\frac{N_i}{V_i} + \frac{n_{ik}}{v_i} + \beta\cdot\frac{7}{f_i}\right] + \gamma\cdot\frac{QB}{K_i} + \tau_i + \frac{z_i n_{ik}}{s_i v_i} \tag{7}$$

QO_k is total cargo from port k. QB is cargo volume at berth. α is time value. $N_i/V_i + n_{ik}/v_i$ is total shipping time. $7/f_i$ is waiting time in berth. V_i is shipping speed. n_{ik} is distance from port k to port i. v_i is shipping speed of transship. z_i is fuel surcharge of transshipment ship. s_i is capacity of transshipment ship. θ ,β and γ are parameter.

2.4 Solution algorithm

The shipper of hinterland in target 10 ports chooses using port based on own generalized cost. (GC_i) Other stakeholders determine each variables based on each objective. In order to solve this calculation, this study adopt Hooke-Jeeves pattern search. Figure 1 shows the solution algorithm of this study. (Public-case)

3. Case study

3.1 Target cargo

Target cargo is from Western Japan 10 ports to North America. MLIT forecasts future cargo volume for two cases; middle and high increase. This study simulates the two cases and trend case which is expected from least squares method.

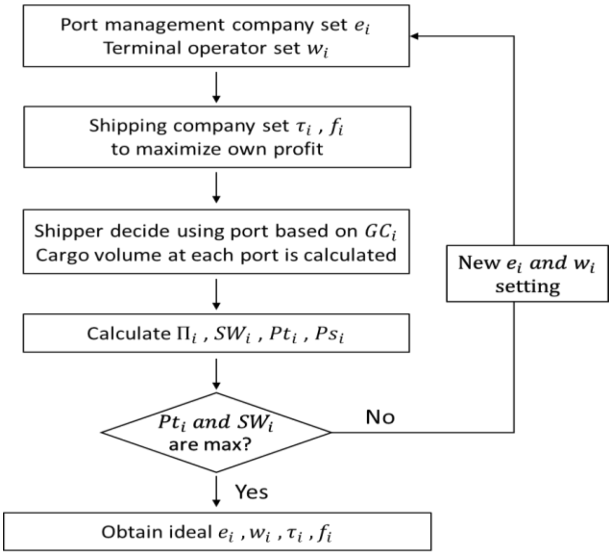

Figure 1 Solution algorithm (Public)

3.2 Inputs for the simulation

A) trend case

In trend case, total cargo volume are decreasing. As table 1 total cargo shows, when total cargo is decreasing, the difference in effect between consolidation and non-consolidation becomes smaller. In 2030, as table 1 shows, the total cargo of Pub-Non are largest and social welfare is high as well. From this result, in case total cargo will decrease, Pub-Non is efficient in terms of social welfare maximization.

Table 1 Result of trend case

		2015	2020	2025	2030
	Pub -Non	94.83	89.37	85.8	**82.6**
total cargo	Pub -Con	**100.27**	**94.55**	**86.88**	80.33
(’000TEU)	Pri -Non	93.22	88.83	84.8	80.75
	Pri -Con	99.04	93.85	86.09	79.53
	Pub -Non	**14.43**	12.36	**10.5**	8.43
social welfare	Pub -Con	12.03	10.4	8.19	6.17
(million$)	Pri -Non	14.29	**12.45**	**10.5**	**8.45**
	Pri -Con	12.65	11.19	8.75	6.65

B) middle and high increase case

As for middle and high increase case, total cargo and social welfare in case of consolidation are higher than non-consolidation case. (Table 2) But, there is little difference between private and public. This implies that the effect of consolidation is higher than privatization. If total cargo is increasing, consolidation is important to achieve cargo volume and social welfare.

Table 2 Result of high case

		2015	2020	2025	2030
	Pub -Non	127.05	144.19	165.51	179.67
total cargo	Pub -Con	**147.68**	**167.54**	**189.21**	**212.45**
(’000TEU)	Pri -Non	140.05	161.74	178.24	196.77
	Pri -Con	146.6	167.26	186.78	207.34
	Pub -Non	27.06	33.11	38.71	44.09
social welfare	Pub -Con	29.37	37.74	**46.48**	**54.68**
(million$)	Pri -Non	27.07	32.87	37.55	42.34
	Pri -Con	**30.13**	**38.31**	46.37	54.43

C) transshipment cargo

As for transshipment cargo, transshipment cargo volume of Pri-non is the largest. (Table 3) This is because, freight rate is lower than other case. Pri-Non is effective as a hub port.

Table 3 Result of transshipment cargo (high case)

		2015	2020	2025	2030
	Pub -Non	8.56	9.39	10.91	11.31
transshipment	Pub -Con	8.3	9.29	10.46	11.77
(’000TEU)	Pri -Non	**11.95**	**13.63**	**13.67**	**14.49**
	Pri -Con	8.19	9.27	10.27	11.37
	Pub -Non	403	408	407	403
freight rate τ_i	Pub -Con	**381**	402	420	436
($/TEU)	Pri -Non	397	**398**	**395**	**389**
	Pri -Con	395	416	436	454

3.3 Competition between Osaka, Kobe and Busan

Table4 shows that changing port style makes it possible to strengthen international competitiveness. But, compared with Busan international they are weaker. Only changing port style cannot get stronger international competitiveness than Busan.

Table 4 International competitiveness (high-2030)

freight rate τ_i [$/TEU]					
Busan	No-Change	Pub-Non	Pub-Con	Pri-Non	Pri-Con
270	403	403	436	389	454

frequency f_i [times/week]					
Busan	No-Change	Pub-Non	Pub-Con	Pri-Non	Pri-Con
38	14	14	16	14	16

4. Conclusion

This study construct the agent-based model to explore the effects of the four cases such as “consolidation or non-consolidation” and “private or public” for Osaka and Kobe ports.

The most efficient management form of port is different from the situation. It is important choose suitable style to their objective.

Changing the port style makes it possible to strengthen the international competitiveness, but even the most strength style, the competitiveness is inferior to Busan.

In this study, cost of land transportation and transshipment are not considered. To make model closer to real, thinking such things is future work.

References

[1] Matsushima and Takuchi (2014) ‘Port privatization in an international oligopoly’ Transportation Research Part B 67 382–397

[2] Hooke, R., Jeeves, T. A., 1961. Direct search solution of numerical and statistical problems, Journal of the ACM, 8, 212–229

[3]渡部富博ら(2011)「国際間の貿易・産業構造を考慮した輸出入港湾貨物量推計モデル構築」国土技術政策総合研究所研究報告(49)

Study on Wave Pressure exerted on Piles installed in Swash Zone

Student Number: 14_07726 Name: Takayuki Sugiu Supervisor: Hiroshi Takagi

1. Introduction

In developing countries such as Vietnam, coastal cities often experience rapid economic growth because of their geographical advances. However, many environemental issues triggered by the development are left behind. One of such examples is coastal erosion.

Phan Thiet, which is the city located in southern Vietnam, is famous as a tourist destination and a number of resort hotels has been built along the coastline. Recently, many coastal communities are suffering from severe coastal erosion caused by adjacent coastal development such as land reclamation and jetties. Local people has installed wooden piles by themselves as a coastal-protection countermeasure to prevent the retreat of coastline. Although these community-based wooden piles are commonly installed in a very shallow water, extensive research has yet to be conducted to investigate *e.g.* wave pressures exerted on the piles or characterisitcs of waves in swash zone.

The purpose of this research is to verify the accuracy of numerical analysis and thereby discuss the applicability of it for wooden piles design. For this purpose, a physical experiment was carried out using a wave flume, and it was compared with results from numerical simulation. Applicability of existing formulas is also discussed.

Fig.1. coastal erosion in Phan Thiet city, Vietnam (January,06,2012)

2. Experiment and numerical analysis

In order to reproduce a similar situation as Phan Thiet, an experiment was carried out using the wave flume at a Vietnam's governmental institute, SIWRR. Figs. 2 and 3 show the geometry of the flume and dimension of the piles installed. The water-pressure gauge was placed on the surface of the center pile, 9 cm above the bottom. This experiment was carried for six cases, as shown in Table 1. The condition was determined based on tidal condition (High Water Level (HWL), Middle Water Level (MWL), and Low Water Level (LWL)) and target wave height (Ht=10, 20 cm). Channel 1, 2, 3, and 4 in Fig.2 indicate the locations where wave gauges were installed.

Numerical simulation was performed using IhFoam, which is one of the solvers of OpenFOAM. OpenFOAM is an open-source software, and IhFoam is a three-dimensional two-phase flow solver using Volume of Fluid (VOF) method. Table 2 shows the settings of this model. In order to acquire the same waves with those in experiment at channel 1, the incident wave height and the depth of the flume in the numerical model were slightly modified by trial and error, resulting in the conditions as shown in Table 1.

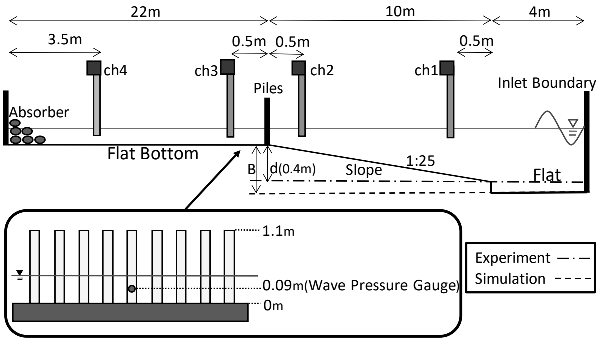

Fig2. Geometry of experiment and simulation (cross-shore direction)

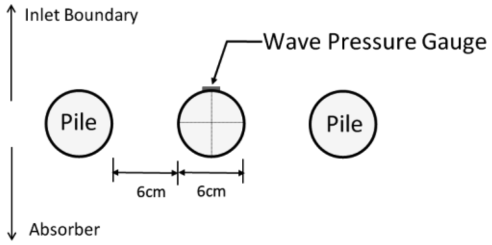

Fig3. Wave pressure gauge point and the piles

Table1. Numerical settings for each cases

cases	Initital Water Level [cm]	Ht [cm]	B [cm]
①HWL・Ht=10	26	10	40
②HWL・Ht=20	26	20	55
③MWL・Ht=10	16	10	40
④MWL・Ht=20	16	20	47
⑤LWL・Ht=10	10	10	55
⑥LWL・Ht=20	10	20	55

Table2. Calculation settings

Item	outline
Mesh size	0.015～0.3m cube mesh
Time step	⊿t = 0.05sec
Wave period	T = 2.0sec
Wave theory	Stokes theory
Turbulance model	LES model
LES SGS	smagorinsky

3. Previous research

There are many previous research about wave pressure exerted on objects. In this research, three of them were applied. Table 3 indicates each of three theories along with assumed conditions.

Table3. Summary of previous research

	Object	assumed types of conditions		
		wave	flow	breaking wave pressure
Hiroi's Wave pressure	pile	○	−	○
Wave Pressure Distribution by Goda	wall	○	−	○
Small amplitude wave theory	−	○	−	−

4. Assessment of wave pressure exerted on the pile

There are two factors that determine wave pressures. One is flow which occurs subsequently induced by wave-breaking and the other one is wave height. When wave-breaking occurs, wave motions turn into mass flows, which are transformed into flow towards the shore. The closer the wave-breaking points to the pile, the more energy exerts on water-pressure gauge. Figure 4. shows the comparison between experiment results and calculation results of the previous research. Figure 5 indicates ratio of errors of each theories to experimental results. In this experiment, waves broke before they approach to the piles in case ④ ⑤ and ⑥. Particularly, wave-breaking can be observed multiple times immediately in front of the piles in case ⑤. As a result, larger pressure was instantaneously exerted in case ⑤ than other cases. When the broken wave stroked the piles, splash of water rising was observed. In general, after a wave-breaking happens, its wave height and velocity of the flow will be attenuated as the wave proceeds forward. Wave height is the other factor which is critical to the wave pressure. Thus, in case ④, water pressure is relatively lower even though the wave broke before it arrived at the pile.

Nevertheless, some of preceding research can predict the value of the pressure in particular cases, but the limitation of their accuracy can be explained as they assume wave as hydrodynamic phenomena. In addition, Hiroi's and Goda's formulas are commonly used for designing constructions, and therefore they take into account safety factors to incorporate a certain margin into the design.

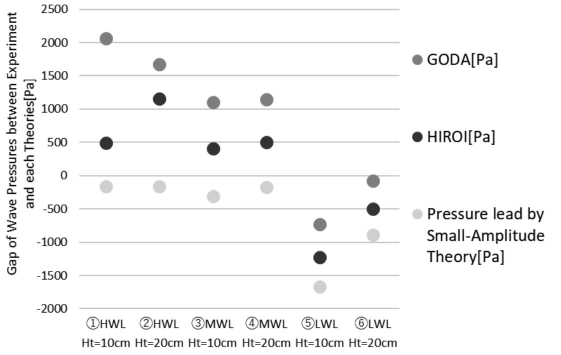

Fig4. Comparison between the experimental and three theoretical formulas

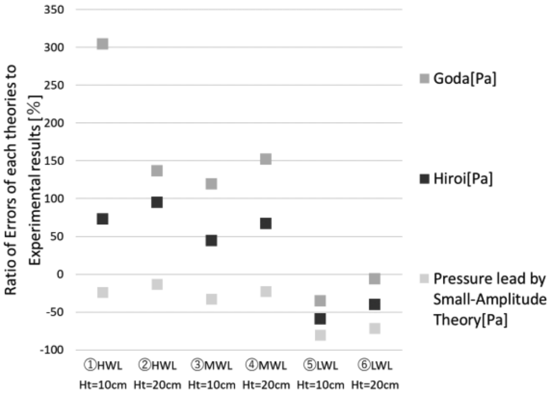

Fig5. Ratio of errors of each theories to experimental results

Figure 6, 7 and 8 indicate the comparison of maximum water pressure observed in experiments and OpenFOAM in cases HWL, MWL, and LWL, respectively. In the case of ① and ③, the results from the OpenFOAM analysis show a good agreement with the experimental result. However, overall, Openfoam tends to underestimate wave pressures. This underestimation can be explained that it is difficult to calculate an impulse force induced by wave breaking. In case ⑤, there is relatively large gap between experiment and OpenFOAM result and OpenFOAM estimated lower maximum water pressure by more than 2500 Pa. This is because in the model of OpenFOAM, it is much more complicated to reproduce the impulse exerted on the pile because of the limitation of mesh sizes. In addition, inaccuracy of reproductively of wave-breaking points also affect wave height.

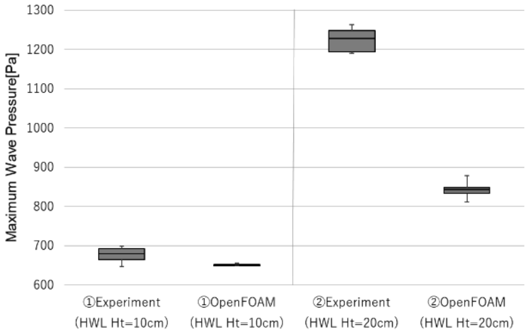

Fig6. Maximum wave pressure in case HWL

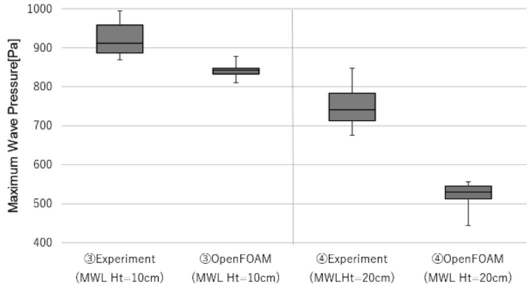

Fig7. Maximum wave pressure in case MWL

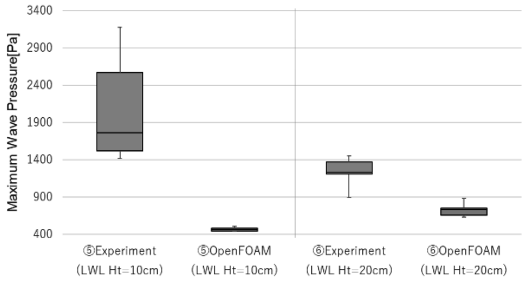

Fig8. Maximum wave pressure in case LWL

5. Conclusion

By comparing results of preceding research, a certain level of analysis could be carried out. Also, by analyzing the experimental model using OpenFOAM, the limitation and the validity of IhFoam were proved. It should be noted that OpenFOAM tends to underestimate breaking wave impact pressure in terms of design of wave suppressors piles. Although it has some limitation in terms of accurate calculation, IhFoam can reveal better analysis other than previous methods and more precise data can be observed.

References

[1] Takagi H. et al., Coastal Vulnerabilities in a Fast-Growing Vietnamese City, *Coastal Disasters and Climate Change in Vietnam, Elsevier,* pp157-171, 2014

[2]広井勇，波力の推定法に就きて，土木学会誌，第 6 巻，第 2 号, 1920

[3]合田良実, 防波堤の設計波圧に関する研究, 港湾技術研究所報告書， 第 12 巻， 第 3 号， 1973

[4]合田良実， 砕波指標の整理について， 土木学会論文報告書， 第 180 号， 1970

Recovery of Acetonitrile from Pharmacy Factory Wastewater by Distillation Process

Student Number:14B07488 Name: Jierui XU Supervisor: Ryuichi EGASHIRA, Hiroaki HABAKI

1. Introduction

Acetonitrile is one of the important substances in the chemical industry and is widely used in the pharmaceutical industry as a solvent or reactant. Although it is industrially obtained as a by-product in the production of acrylonitrile, acetonitrile is demanded more than acrylonitrile, and recycle method of acetonitrile in the wastewater from pharmaceutical factory has attracted attention. However, acetonitrile and water form azeotropic mixture, and it is difficult to completely separate them in ordinary distillation. Then, pressure swing distillation[1] and extractive distillation[2] have been studied to separate acetonitrile and water.

This study aims to propose efficient separation of acetonitrile and water by pressure swing and extractive distillation processes. First, the vapor-liquid equilibrium (VLE) was estimated to examine the effects of the conditions on the azeotrope point. Then, the separation was computationally simulated and energy consumptions by both processes were compared.

2. Vapor–Liquid Equilibrium and Distillation Process

2.1 Estimation of Vapor–Liquid Equilibrium

Table 1 shows the calculation conditions for the VLE estimations with binary system of acetonitrile and water, and ternary system of acetonitrile, water and dimethyl sulfoxide (DMSO). DMSO was selected as the third compound because it has been proved that is a suitable solvent[3]. The UNIFAC model was used to estimate the activity coefficients in the liquid phase, one of the thermodynamic estimation methods with interaction parameters between functional groups composing the molecular. Then, the effects of the pressure and DMSO on the VLE was studied.

2.2 Pressure Swing Distillation

Figure 1 shows vapor-liquid equilibrium of a binary system. It can be seen that the azeotropic composition changed when pressure is changing. **Figure 2** shows azeotropic composition with different pressure and it can be known that the azeotropic composition changes rapidly when the pressure was around 10kPa to 100kPa and change slowly when the pressure is rising over 300kPa.

Pressure swing distillation is a distillation method that relies on the phenomenon that the azeotropic composition changes with the change in pressure. The process of pressure swing distillation is shown in **Figure 3**, distillations of D1 and D2 are used as the low-pressure distillation and the high-pressure distillation respectively.

2.3 Extractive Distillation

Figure 4 shows vapor-liquid equilibrium of a ternary system after adding the solvent. It can be seen that as the solvent concentration increases, the azeotropic composition increases. And the minimum required amount of solvent can be calculated from **Figure 5**.

The process of extractive distillation is shown in **Figure 6**. It consisted of an extractive distillation(D3) and distillation for a solvent recovery(D4).

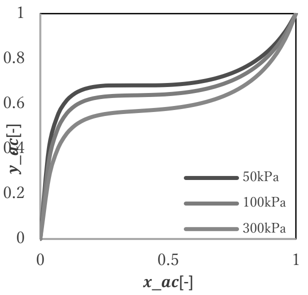

Figure 1 VLE diagram of binary system

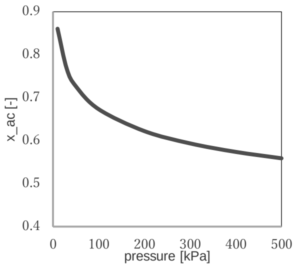

Figure 2 Azeotropic composition with different pressure

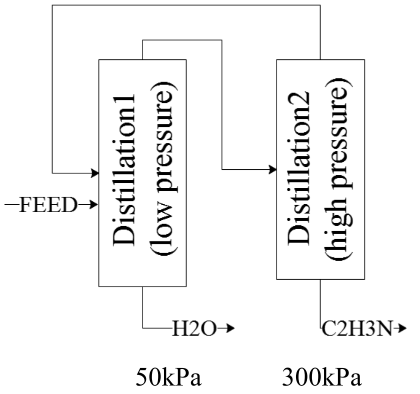

Figure 3 Process of pressure swing distillation

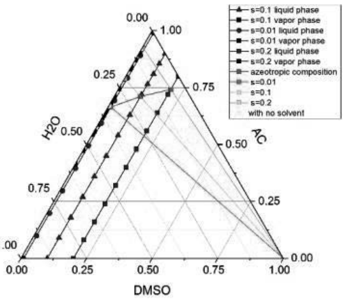

Figure 4 VLE diagram of ternary system

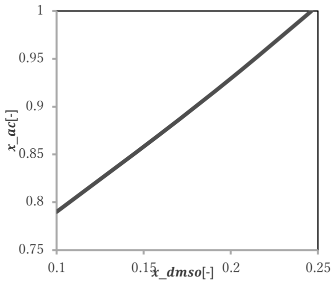

Figure 5 Normalized azeotropic composition of acetonitrile with different mole fraction of solvent

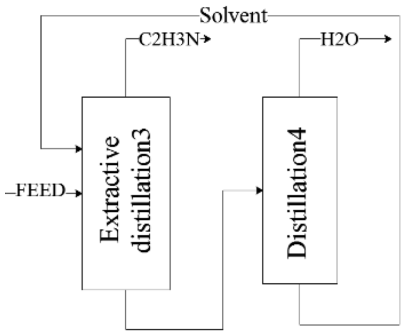

Figure 6 Process of extractive distillation

Table 1 Conditions for VLE estimation

Binary system		acetonitrile, water
Pressure	[kPa]	10-500
Ternary system		acetonitrile, water, DMSO
Pressure	[kPa]	100
Mole Fraction of DMSO	[-]	1-30

3. Comparison of Distillation Process

3.1 Simulation Conditions

Table 2 shows the calculation conditions of pressure swing and extractive distillations. The composition of the feed consisted of acetonitrile and water and the mole fraction of acetonitrile was 0.4 because actual factory wastewater has such a composition. The specification of the product was that the mole fraction and yield of acetonitrile was set as 0.999. In the case of pressure swing distillation, the operating pressure was set at 50kPa and 300kPa. The low-pressure column operated lower than 30kPa should be vacuum distillation and the energy consumption will increase rapidly. When the pressure of high pressure column is higher than 300kPa, the azeotrope point changed unremarkably. And from **Figure 4**, when the molar ratio of acetonitrile and water is 4:6, the minimum required amount of solvent can be known. The process simulation was conducted with the general process simulator of PRO II.

Table 2 Conditions of the simulation

Feed and Product		
Feed Mole Flow rate	[kmol/h]	1000
Temperature	[K]	298
Mole Fraction of Acetonitrile in Feed	[-]	40
Yield	[-]	0.999
Mole Fraction of Acetonitrile in Product	[-]	0.999
Pressure Swing Distillation		
Feed Stage (D1)	[-]	10-20
Number of Stages (D1)	[-]	10-20
Number of Stages (D2)	[-]	20-30
Pressure (D1)	[kPa]	50
Pressure (D2)	[kPa]	300
Reflux Ratio (D1)	[-]	1.0-2.0
Reflux Ratio (D2)	[-]	0-1.0
Extractive Distillation		
Pressure (D3 and D4)	[kPa]	100
Number of Stages (D3)	[-]	1-100
Number of Stages (D4)	[-]	1-20
Feed Stage (D3)	[-]	1-100
Solvent Stage (D3)	[-]	1-10
Reflux Ratio (D3)	[-]	0.1-1.0
Reflux Ratio (D4)	[-]	0.1-1.0

3.2 Result and discussion

Operating conditions and heat duty for pressure swing distillation and extractive distillation are shown in **Table 3**. In this research, heat duty of two reboilers in the process has been decided as the approximate value of the total energy consumption.

Table 3 Condition and heat duty of distillation

Distillation column	Pressure [kPa]	Stage number	Feed-in stage	Reflux ratio	Heat duty of reboiler[kJ/mol]
D1	50	15	10	1.8	115.4
D2	300	30	13	0.9	58.2
D3	100	58	52	0.9	28.8
D4	100	19	8	0.1	34.1

The total energy consumption by the reboiler after two distillations is shown in **Table 3**. Therefore, extractive distillation is more efficient than pressure swing distillation in acetonitrile-water system. The reasons leading to such results were considered to be related to latent heat of water. With the data of the overall flow rate in the two processes, in the pressure swing distillation, the flow rate of mixture with water and acetonitrile refluxed is as high as 822kmol/h, so a large amount of heat is necessary to evaporate mixture which contains 42.7% of water again in distillation column D1. However, in the case of the extractive distillation, since there is no mixture except solvent is refluxed, less energy is required to evaporate mixture again. Otherwise, trace amounts of solvent may be contained in the product depending on the state of the distillation facility, so there is a risk of affecting quality while using extractive distillation.

4. Conclusion

By making the VLE diagram of binary system and ternary system. Conditions of the simulation such as selection of operating pressure in pressure swing distillation and minimum required amount of solvent in extractive distillation can be decided.

After running simulation and optimizing operating conditions, both pressure swing distillation and extractive distillation proved that can separate acetonitrile and water into target concentrations.

Among comparing the energy consumption of two reboilers in the process, extractive distillation is more efficient than pressure swing distillation.

References

[1]Zhou Jinbo, Cui Xianbao, et al. Separation of acetonitrile-water mixture by batch extractive distillation[J]. Chemical Industry and Engineering,26(6):482-486, (2009).

[2]Repke J U, Klein A, et al. Pressure swing batch distillation for homogeneous azeotropic separation[J]. Chemical Engineering Research and Design,85(4):492-501, (2007).

[3]Zhang Zhigang, Lv Ming, et al. Isobaric vapor-liquid equilibrium for the extractive distillation of acetonitrile-water mixtures using dimethyl sulfoxide at 101.3kPa[J]. Chem.Eng.Data,58,3364-3369(2013).

FUTURE PRECIPITATION PREDICTION BASED ON CLIMATE CHANGE & URBANIZATION SCENARIOS IN A MEGACITY—JAKARTA

Student Number: 14_07608 Name: Ouran Sinn (Yinglan QIN) Supervisor: Manabu KANDA, A.C.G VARQUEZ

1 Introduction

Climate change affects the intensity and duration of rainfall which is directly related to our daily lives. In climate change studies, future precipitation is widely investigated using general circulation models (GCM), or downscaling of future climate scenarios. Besides climate change, the effect of urbanization to precipitation has also been proven. In spite this, the effect of future urbanization to the future precipitation in addition to global climate change is uncertain. This research aims to understand the effect of urbanization scenarios in the future to precipitation and the mechanisms behind them while experiencing various climate change scenarios.

This study is a pioneering work initially applied to Jakarta, Indonesia which is a large developing megacity. The periods cover months of extreme levels of precipitation, drought and oversupply months.

2 Numerical Setting

In this study, we utilized a downscaling method called pseudo-global warming (PGW, [3]; see 2.1) to investigate future climate and developed a tool (see 2.2) which can consider social scenarios as inputs to estimating distributions of urban morphological changes.

The main model used is a modified version of the Weather Research Forecasting Model (WRF). WRF is a non-hydrostatic weather model initially developed by NCAR and was improved to accommodate distributions of urban parameters [1] to show different urban morphology. 135 by 115 grids were allocated for the final domain to cover Jakarta. Grid spacing was set to 1200 meters. The same physical settings were used as in [1].

2.1 Setting of Climate change

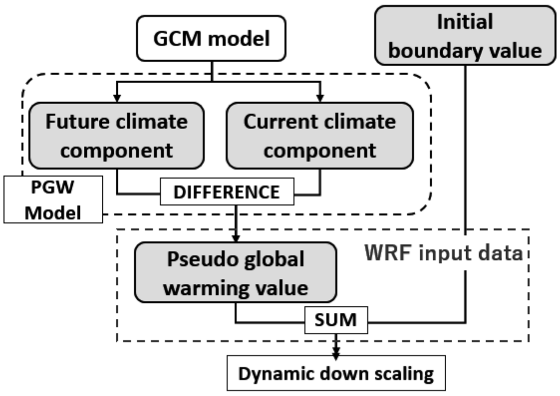

Figure 1 Future climate downscaling

In PGW, the lateral boundary condition of WRF which uses the present climate is modified by adding the temporal change (2010s to 2050s) of climate parameters (temperature, wind velocity, humidity, geopotential height) estimated from a GCM (Fig.1). 5 GCMs providing two climate pathways, RCP2.6 (conservative) and RCP8.5 (worst-case) scenarios were ensemble and used.

2.2 Setting of Urbanization

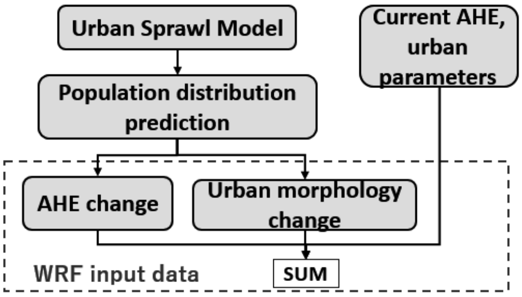

Figure 2 Estimate future urbanization

Urban areas in WRF can be represented in more detail by anthropogenic heat emissions (AHE) and urban parameters (e.g. average building height, plant area index). According to [2], urbanization which considers spatial change of both AHE and urban parameters can be estimated using a model which can predict future population distribution and empirical relationships between population and the said parameters. These changes are added to the present AHE [4] and urban parameters [5]. The process is showed by Fig.2. To predict both population and AHE distribution, future social conditions (e.g. country-level population, energy consumption, consumption) are needed as inputs. These social pathways can be derived from SSPs. Here, we focus on SSP1 (compact) and SSP3 (business-as-usual).

2.3 Cases of simulation

Table 1 Information of current & future cases

Name of case	year	RCP	Weather component described by RCP	SSP	Urbanization component described by SSP
Current case	2010s	FNL	Current weather	—	Current urban
RCP2.6 case	2050s	2.6	Low greenhouse gas(GG) emission	—	Current urban
RCP8.5 case	2050s	8.5	High GG emission	—	Current urban
RCP2.6+SSP case	2050s	2.6	Low GG emission	1	Compact city
RCP8.5+SSP3 case	2050s	8.5	High GG emission	3	Urban sprawl

The simulation cases are shown in Table 1. RCP scenario and SSP scenario are paired to indicate both and separate effects of global climate change and local urbanization. RCP2.6 with SSP1 show the best future that have environmental awareness and good urban planning. On the contrary, RCP8.5 with SSP3 represents a worst future society.

3 Results and Discussion

3.1 Future climate change effect

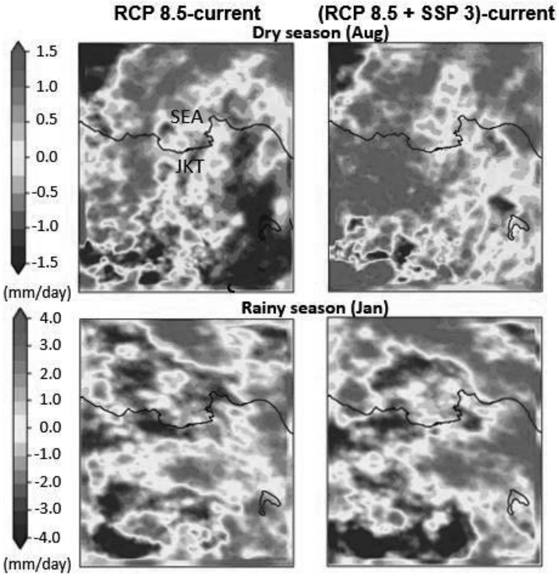

Figure 3 Increase precipitation in RCP, RCP+SSP case

Figure 3 shows the difference in precipitation between RCP8.5 case with current case and RCP8.5+SSP3 case with current case. The difference shows the pure effect of background climate change in left side figure and background climate with urbanization effect in right side figure. Precipitation increase appeared in west side in dry season, but in east side in rainy season. Furthermore, precipitation increase was found when urbanization was included both in RCP2.6+SSP1 and RCP8.5+SSP3 cases. Temperature increase caused by global warming is around 1.23℃ in RCP8.5 case. 1.30℃ in RCP8.5+SSP3 case. This temperature increase is also evidence that heating will trigger more moisture from the surface to advected above leading to more precipitable water vapor in the atmosphere. The seasonal dependence can also be seen. Dry seasons show increase at the northwestern part, while in wet seasons (RCP 8.5) at the Southwestern side. This is brought about the differences in dominant wind directions (monsoon).

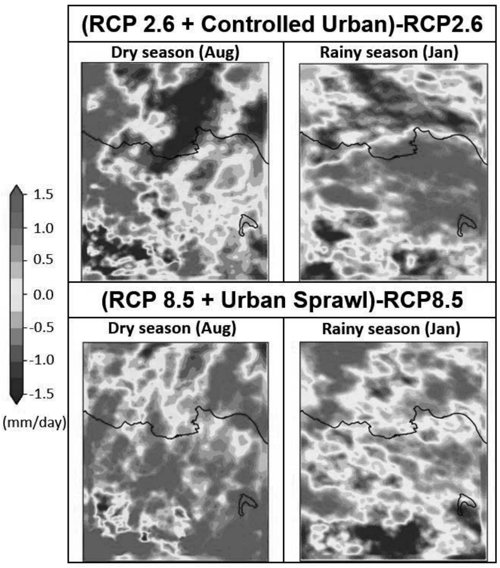

Figure 4 Increase precipitation by urbanization

3.2 Future urbanization effect

Figure 4 is the subtraction between RCP+SSP case with RCP case. Increase of urbanization case additional temperature change around 0.05~0.07 ℃ than RCP cases. Urbanization lead to more precipitation around the city.

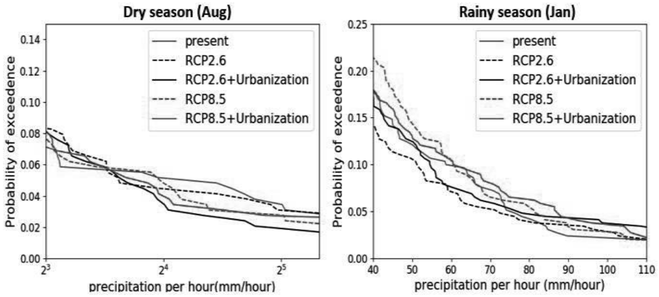

Figure 5 Extreme value of each cases

In terms of extreme rainfall, levels of urbanization show various effects depending on the background climate being considered (Fig. 5). RCP+SSP cases (solid line) have lower probability than RCP cases (dotted) during the dry season but the situation is reversed during the rainy season.

4 Conclusions

The research findings are summarized as follows:

(1) Global climate change trigger precipitation increase. Because of the dominant direction of monsoonal winds shift the rainfall, precipitation increase appears in the west side of Jakarta in the dry season(August), and east side in the rainy season(January).

(2) Urbanization causes additional temperature increase and evapotranspiration decrease in the city lead to precipitation increase. Compare to the pure effect of climate change, rainfall increase due to urbanization is more concentrated around the urban area.

(3) Simulated future extreme rainfall in Jakarta decreased in dry season but increased in rainy season. Extreme drought events in dry season and flood events in rainy season could occur in the future.

References

[1] VARQUEZ, A.C.G., et al., (2015) "The Effects of Highly Detailed Urban Roughness Parameters on a Sea-Breeze Numerical Simulation" Boundary-Layer Meteorol, 154:449–469

[2] VARQUEZ, A.C.G., et al., "Future population distribution of an urban agglomeration given climate change scenarios", Journal of Japan Society of Civil Engineers, accepted

[3] Kimura, F., and A. Kitoh (2007) "Downscaling by pseudo global warning method" ICCAP final report, 43–46

[4] Y. Dong et al., (2017) "Global anthropogenic heat flux database with high spatial resolution" Atmospheric Environment, volume 150, 276-294

[5] N.S.Darmanto et al., (2017) "Urban roughness parameters estimation from globally available datasets for mesoscale modeling in megacities" Urban Climate, volume 21, 243-261

Simultaneous measurement of liquid surface tension and contact angle

Student number : 14B11722 Name : Keiichiro HAMADA Supervisor : Kunio TAKAHASHI

1. Introduction

Super-hydrophilic glass applies the concept of surface tension as one of the important elements to evaluate the wettability of the solid surface, and improve the function for eliminating dimness.

Measurement of liquid surface tension is important. In most of wettability phenomena, contact angle is formed between solid and liquid surface. Therefore, it's necessary to measure contact angle for measurement of accurate liquid surface tension. In present, sessile drop method is familiar to the measurement. This method estimates liquid surface tension by measuring the surface profile of an axisymmetric liquid drop on a solid surface. However, this method uses spherical approximation, and ignored gravitational force.

In Bakker's study, the analytical solution exists about 2-demensional catenary liquid surface model [2]. From this model, liquid surface tension and contact angle are calculated by measurement of liquid surface profile. Due to the analytical solution, high accuracy calculation of liquid surface tension can be expected.

2. Model

Figure 1 shows a model of 2-dimensional catenary liquid surface made by semi-infinite solid surface and liquid which wet to solid surface. From Laplace pressure equation, the following equation consists of curvature radius ρ_m and angle ε of a point on liquid surface.

$$\Delta p(\varepsilon) = \frac{\gamma_l}{\rho_m} = -\rho g z(\varepsilon) \qquad (1)$$

where γ_l is liquid surface tension, ρ is liquid density, and g is acceleration of gravity. And, eq.(1) is result of solving the eq.(2).

$$x(z) = \frac{1}{\sqrt{a}}\Big(\tanh^{-1}\sqrt{1-\frac{az^2}{4}} - 2\sqrt{1-\frac{az^2}{4}}$$

$$-\tanh^{-1}\sqrt{1-\frac{a{z_c}^2}{4}} + 2\sqrt{1-\frac{a{z_c}^2}{4}}\ \Big) \qquad (2)$$

$$a = \frac{\rho g}{\gamma_l}, \qquad z_c = \frac{2}{\sqrt{a}}\cos\frac{\theta_c + \frac{\pi}{2}}{2} \qquad (3)$$

where z_c is the height, to which the liquid goes up wet on the solid surface, θ_c is the contact angle. This is the analytical solution about 2-demensinal catenary liquid surface profile. Parameter a and z_c is obtained by fitting the curve of eq.(2) using known ρ, g. Therefore, γ_l, θ_c is obtained from a and z_c.

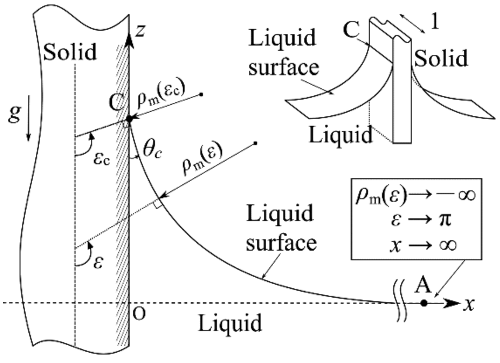

Figure 1. 2-demensional catenary liquid surface model

3. Experiment

3-1. Experiment apparatus

A camera equipped with telecentric lens is used for observing the reflected light from the target, which is parallel to glass slide as a solid (Figure 2).

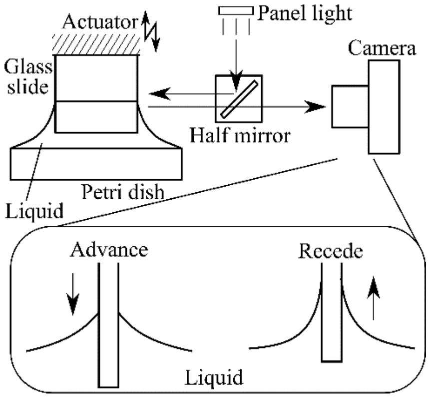

Figure 2. Equipment apparatus

Solid material is borosilicate glass (Matunami glass, C024601), and liquid material is pure water.

Experiments are done for two types of measurement of liquid profile after a glass slide has moved to advancing or receding enough as a control experiment.

3-2. Analyze experiment result

Table 1 shows γ_l, θ_c calculated from the fitted result. Compared with physical property value of liquid surface tension : γ_l=73.1(mJ/m^2) at 17.8℃, each γ_l corresponds to the degree of the physical property value.

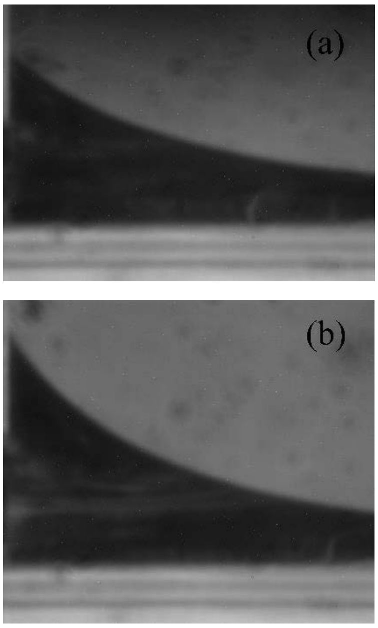

Figure 3. Observation of liquid surface
(a)Advancing (b)Receding

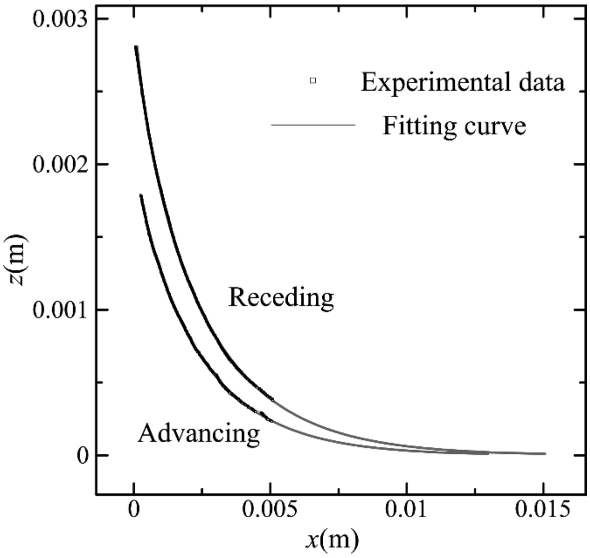

Figure 4. Fitting curve representative

Table 1. Fitting Results

	Advancing		Receding	
	γl	θc	γl	θc
No.1	61.31	48.16	74.31	28.70
No.2	31.11	19.12	77.26	9.898
No.3	31.99	20.02	58.37	5.047
No.4	32.02	20.02	63.28	3.054

γ_l(mJ/m^2), θ_c(°) (Tempreture:17.8℃)

Each measured result of γ_l between advancing and receding is not almost consistent in each number of data. Since γ_l is the characteristic value and is not changed by different operations. It is not considered about deviation of the z-axis direction occurred in a processing picture. It is possible that the deviation of z-axis direction affect the different values of γ_l.

There is a tendency that γ_l of data of latter number is smaller. Experiments are performed in the order of number. It's considered that surface tension of water is changed because water is mixed with the dust in the air.

4. Conclusion

Simultaneous measurement of liquid surface tension and contact angle by 2-demensional catenary liquid surface model is verified in this research.

It is possible that a deviation of z-axis direction of processing pictures affects to a calculated value.

It is considered that physical property is rapidly changed as time goes by.

Reference

[1] 中島章，固体表面の濡れ性（2014）
[2]G.Bakker, Handbuch der Expeimentalphysik (1928)
[3] 小野周，表面張力（1980）

Design method of angle of beams to maximize gripping force of multi-beam structure

Student number：14_15507 Name：Hiroaki Yamashita Supervisor：Kunio Takahashi

1. Introduction

Multi-beam structure, i.e. two dimensional array of inclined beams, can be used as a manipulation device since it not only generates adhesion force to grip object but also absorbs the roughness of object's surface.

In preceding study, multi-beam structure was investigated [1], and it is found that the geometry of the beams affects the strength of the gripping force. However, an optimal angle of beams necessary for maximizing gripping force has not been clearly studied. This study investigates the design method of angle of beams to maximize gripping force, i.e. gripping stress, considering the density of beams.

2. Gripping force of single beam based on elastic beam theory

2.1 Model of the contact between elastic beam and rigid surface

Multi-beam structure is composed of inclined beams fixed as two dimensional array on rigid substrate and operated by the process shown in Figure 1. (a) the multi-beam structure approaches an object by applied displacement and the edge of the beams contact with the object's surface. (b) After sufficiently approaching, the beams alter to area contact, and the adhesion force occurs between the interface. (c) the multi-beam structure is then receded and it detaches the object. The detaching force is called gripping force.

Figure 2 shows the contact between two elastic beams and rigid surface, which is the unit model of this study. The intervals of the beams are δ_x and δ_y. The beams have a length L, a width W, a thickness H, an angle $\theta (0 < \theta < \pi/2)$, Young's modulus E and the geometrical moment of inertia I. The gripping force, work of adhesion, displacement between surface and beams, length of the contact area are F, $\Delta\gamma$, d, a, respectively.

Considering maximizing gripping stress of the multi-beam structure, the beams should be fixed as densely as possible but they can't overlap with each other. Therefore, it is assumed that the beams don't contact each other when the maximal gripping force occurs during the contact process.

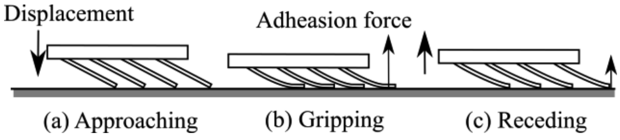

Figure 1. The process of contact between multi-beam structure and surface of object

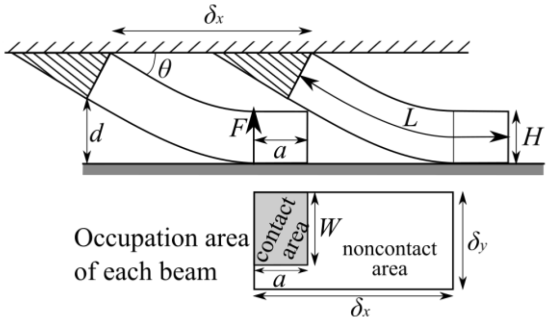

Figure 2. The model of contact between elastic beams and rigid surface

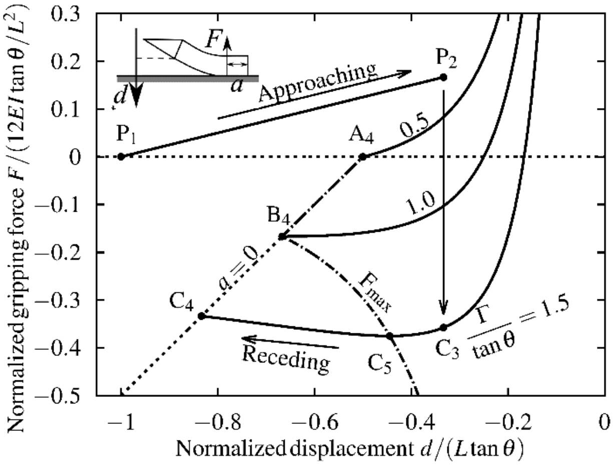

Figure 3. Relation between displacement and gripping force of single beam

2.2 Relation between displacement and gripping force of a single beam

The gripping force and deformation of a single beam are estimated by using elastic beam theory [2]. Figure 3 shows the relation between the displacement and the gripping force. According to Figure 3, the gripping force occurs when $\Gamma/\tan\theta > 0.5$, where Γ is introduced as

$$\Gamma = \sqrt{\frac{\Delta\gamma W L^2}{2EI}}.$$

The maximal gripping force of a single beam occurs at line A_4B_4 and curve B_4C_5 in Figure 3.

3. Design method of multi-beam structure

3.1 The area in which parameters for design multi-beam structure

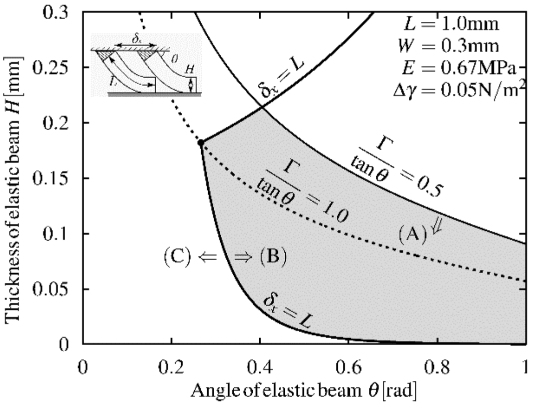

Figure 4. The area that allows multi-beam structure to generate gripping force and absorb surface roughness

The area filled with gray in Figure 4 indicates the area in which (A) the gripping force occurs, and (B) the multi-beam structure can absorb the roughness of object's surface. The condition (A) is expressed $\Gamma/\tan\theta > 0.5$ as shown in Figure 3. On the other hand, the condition (B) explained as $\delta_x < L$ absorb the roughness better than (C) as shown in Figure 5. Therefore, the parameters for the design of multi-beam structure should be determined within this area.

Condition	Multi-beam structure
(B) $\delta_x < L$	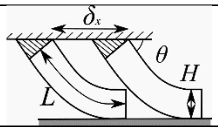
(C) $\delta_x > L$	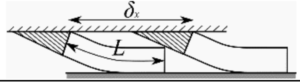

Figure 5. The multi-beam structures which have different conditions of interval δ_x

3.2 Angle of beams which maximize the gripping stress of multi-beam structure

The gripping stress of multi-beam structure σ is estimated as

$$\sigma = \frac{F_{\max}}{\delta_x \delta_y},$$

where $F_{\max}$ is the maximal gripping force of a single beam and $\delta_x\delta_y$ is the occupied area of the single beam as shown in Figure 1.

Figure 5 shows the relation between the angle of beams and the gripping stress of the multi-beam structure. The parameters on line $\alpha_1 D_1$ ($\alpha_2 D_2$ or $\alpha_3 D_3$) in Figure 5 meet the conditions (A) and (B) discussed in chapter 3.1. M_1 (M_2 or M_3) is the point at which the maximal gripping stress occurs. Therefore, the angle of beams at M_1 (M_2 or M_3) should be selected for maximizing the gripping stress of multi-beam structure.

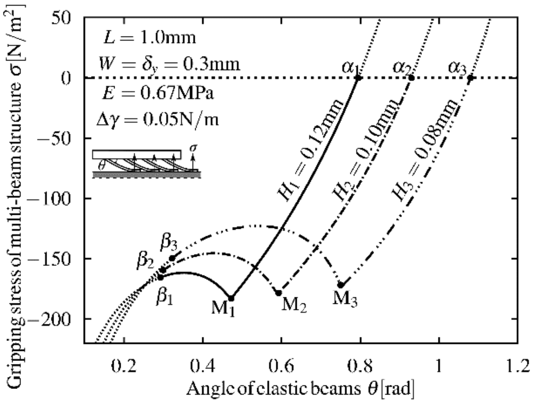

Figure 6. Relation between angle of beams and gripping stress of multi-beam structure

3.3 Procedure to determine the angle of beams

Angle of beams is determined in the following process (1)~(2). In this process, it is assumed that the length *L*, width *W*, thickness *H*, Young's modulus *E*, interval δ_y and the work of adhesion $\Delta\gamma$ are already known.

1. Choose the angle which maximize gripping stress of multi-beam structure. In figure 6, gripping stress at the neighborhood of zero radian or M_1 (M_2 or M_3) is maximized.
2. Then, choose the angle for absorbing the roughness of object's surface. According to Figure 5, M_1 (M_2 or M_3) should be used for gripping rough surface.

4. Conclusion

The angle of beams which maximize the gripping stress of multi-beam structure is estimated. The procedure to determine the angle of beams is obtained.

Reference

[1] Mikhail Salyukov, et al, Development of a Multy-Beam Structure by Stacking Comb-Shaped Rubbers", Mate2018, vol24 pp. 261-264, 2018

[2] Yu Sekiguchi, et al., "Adhesion between side surface of an elastic beam and flat surface of rigid body", Journal of Adhesion Science and Technology, 26:23, 2615-2626, 2012

Utilization of Bio-oil Derived from Wood Residues in Rubberwood Process

Student Number:14-09139 Name:Haruka TANAKA Supervisor:Ryuichi EGASHIRA, Hiroaki HABAKI

1. Introduction

Rubberwood furniture manufacturing is an important industry in Southeast Asian countries, and the sawmilling process has been studied to be improved by the utilization of wood residue, as shown Fig.1 [1]. The operations expressed by white-colored boxes were additional ones to be proposed. The products from the thermal treatment of the wood residue, such as pyroligneous acid, activated carbon, and off-gas, were used as preservatives, adsorbent, and heat energy. However the utilization of bio-oil has not been studied.

In this study, rubberwood sawdust was thermally treated, and the yields and characteristics of the bio-oil obtained under various conditions were examined. Then, utilization of the bio-oil as heat source in the process was studied.

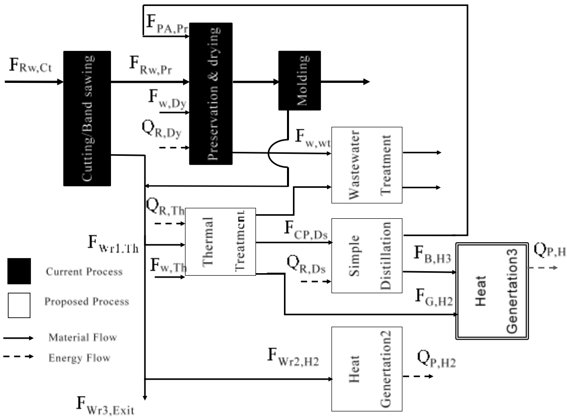

Fig.1 Current and proposed process of sawmilling: material and energy flow[1]

2. Thermal treatment of rubberwood

2.1 Experimental

The rubberwood sawdust (RW), provided from manufacturing company in Malaysia, was used as pyrolysis feed.

The experimental equipment is as stated in previous study [1]. Table1 shows the conditions of thermal treatment. The RW was dried at 373 K for 24 hours before the treatment. The dried RW was heated by a commercial electric furnace under nitrogen atmosphere in a stainless tube (I.D. 0.0384 m × 0.70 m) and pyrolyzed to crude pyroligneous acid (CPA), char and off-gas. The sample of off-gas were taken at the exit of apparatus along time, until the furnace cooled down to 313K.

The CPA was collected by the condensation of the effluent gas. CPA was separated into pyroligneous acid (PA) and bio-oil by simple distillation. The final temperature of the liquid was varied from 393 K to 433 K. The obtained CPA, PA and bio-oil were analyzed to determine the moisture content and pH by Karl Fischer titrator and pH meter, respectively. The elemental analysis of bio-oil were conducted by MICRO CORDER JM10.

Table1 principal conditions for thermal treatment

Feed		rubberwood sawdsut
Mass of feed	[kg]	0.020-0.030
Atomosphere		N_2
Flow rate	[L/min]	0.5
Temprature	[K]	713, 903, 1093
Holding time	[hour]	0.5
Ice bath temprature	[K]	275-278

2.2 Result and discussion

The yield of CPA, Char and Off-gas based on the RW, and those of PA and bio-oil based on the feed CPA were defined as,

$$Y_i = \frac{W_i}{W_{RW}} \quad (1)$$

where W_{RW} and W_i were the mass of the feed RW and product i (i = CPA, Char, or Off-gas). $Y_{Off\text{-}gas}$ was estimated by material balance.

Fig.2 showed the yield of CPA, Char, and Off-gas of thermal treatment of RW together with previous data in dried condition [2]. T_T was temperature of thermal treatment and T_S was the final temperature of the liquid. The yield of CPA and Off-gas gradually increased with T_T, and the yield of Char decreased as T_T decreased. Although these trends were the same as the previous data, the yield of CPA of this study was a little higher than those in the previous study.

Fig.3 showed the yield of PA and bio-oil. The yield of bio-oil increased as T_T increased and T_S decreased. The higher T_T enhanced yield of CPA and heavier compounds should be generated more in the higher T_T range.

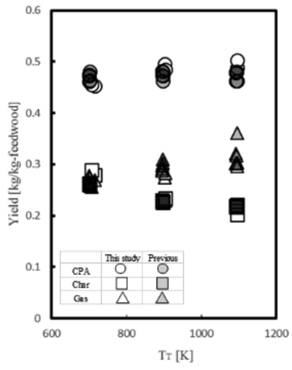

Fig.2 Yield of each component in thermal treatment

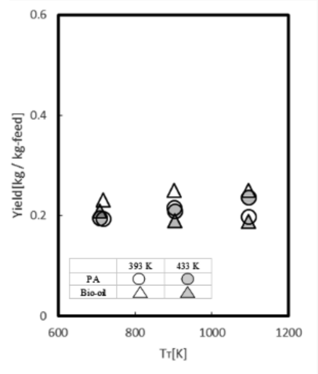

Fig.3 Yield of each component in simple distillation

Fig.4 showed pH of CPA, PA, and bio-oil and **Fig.5** showed moisture content of them. Bio-oil had no moisture content, and pH of each bio-oil was almost constant to be 2.1. Moisture content of CPA was 0.40

and pH of CPA was in the range from 1.9 to 2.4. Moisture content of PA was 0.70 and pH of CPA was the range from 2.1 to 2.3.

Table2 also showed characterization of bio-oil. The element of composition in bio-oil was almost constant independently of condition. To determine heating value of bio-oil, the empirical equation estimate higher heating value, HHV, of bio-oil derived was reported as [4],

$$\mathrm{HHV} = 35.2x_C + 99.4x_H + 10.5(x_S - x_O) \quad (3)$$

where x_i was the mass fraction of element i in the bio-oil (i is C, H, S or O). Generally plants should contain S by so low level and it was assumed $x_s = 0$. Then, the HHV was estimated as 19.8 MJ / kg-bio-oil, and lower heating value, LHV, was as 19.7 MJ /kg-bio-oil. Here it was assumed that all hydrogen be should be converted water and the latent heat was taken into consideration.

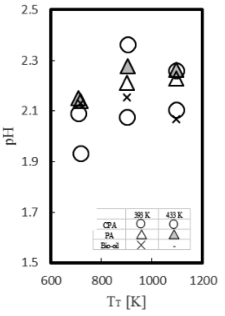

Fig.4 pH of CPA, PA, Bio-oil

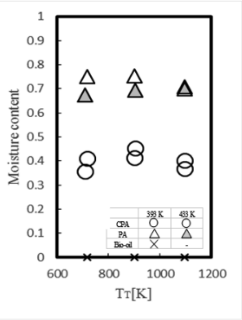

Fig.5 Moisture content of CPA, PA Bio-oil

Table2.Result of elementary analysis

T_T[K]	T_S[K]	H	C	N	O	Moisture contnent	pH
713	393	0.059	0.485	0.001	0.398	0.00	2.13
903	393	0.061	0.507	0.001	0.402	0.00	2.15
1093	393	0.062	0.502	0.000	0.414	0.00	2.18
713	433	0.062	0.545	0.001	0.385	-	-
903	433	0.062	0.539	0.001	0.387	-	-
1093	433	0.062	0.530	0.000	0.398	-	-

3. Heat recovery from bio-oil

Fig.1 showed was proposed to improve the process to use bio-oil. $Q_{P,H2}$, $Q_{P,H3}$, $Q_{R,Dy}$, $Q_{R,Dh}$ and $Q_{R,Ds}$ were estimated from the enthalpy of inlet and outlet materials. $Q_{R,Th}$ and $Q_{R,DS}$ were the heat energy used in thermal treatment and simple distillation respectively, that RW and water were the inlet materials at room temperature and AC, CPA, and off-gas were outlet materials at T_T and PA and bio-oil ware outlet materials at T_S. Total heat required heat is the synthesis of these added $Q_{R,Dy}$, heat of drying RW. This study was used previous data because of getting overall process and data for thermally treatment process [5]. $Q_{P,H3}$ was the heat energy produced by off-gas and bio-oil, used previous data and estimated from Eq.(3) respectively. $Q_{P,H2}$ was the heat energy combusted wood residues.

Now, it was changed the ratio of residue from rubberwood feed for thermal treatment, and calculated each flow rate, when the required heat of whole process is equivalent value to the produced heat of whole process. To evaluate heat energy produced by off-gas and bio-oil, Heat recovery A, QPH3 was divided the required heat of whole process, was defined as,

$$\text{Heat recovery A} = \frac{Q_{P,H3}}{Q_{R,Dy}+Q_{R,Th}+Q_{R,Ds}} \quad (4)$$

Fig.6 showed maximum heat recovery A of only off-gas or off-gas and bio-oil when all wood residues were used in thermal treatment and heat generation2. When T_T was 697 and 897 K, the heat energy produced by bio-oil was higher than off-gas and The heat quantity of bio-oil was occupied 30% of the required heat at maximum.

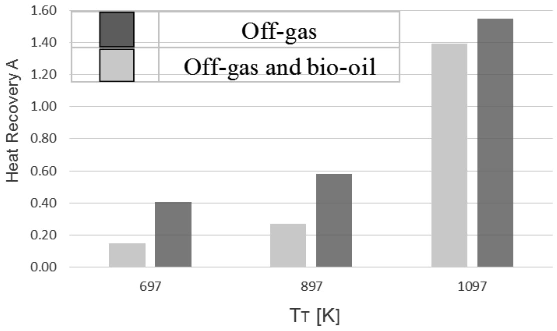

Fig.6 Maximum heat recovery

4. Conclusions

To propose rubberwood process to use bio-oil in this study, and the following conclusions were drawn from the results.

The effect of thermal treatment temperature had little difference the elemental yield of bio-oil.

HHV of bio-oil was decided 19.8 MJ/kg, and LHV of bio-oil was decided 19.7 MJ/kg by Eq. (3).

The heat quantity of bio-oil occupied 30% of the required heat at maximum when all wood residue was used.

Acknowledgement

Author would also like to express my gratitude to Hock Chuan Enterprise for providing rubberwood sawdust.

References

[1] Rizafizah OTHAMAN, Kean Giap LIM, Shunsuke KONISHI, Masayuki SATO, Nan SHI and Ryuichi EGASHIRA, “Thermal Treatment of Wood Residues and Effective Utilization of Its Products to Improve Rubberwood Manufacturing Process,” Journal of Chemical Engineering of Japan, pp. 1149–1158 (2008)

[2] K.G. Lim, Master Thesis, Tokyo Institute of Technology, 2004

[3] K. Chaiwong, T. Kiatsiriroat, N. Vorayos, C. Thararax, Study of bio-oil and bio-char production from algae by slow pyrolysis, Biomass and Bioenergy, Pages 600-606, 2013

[4] S.A. Channiwala, P.P. Parikh, "A unified correlation for estimating HHV of solid, liquid and gaseous fuels", Fuel, Pages 1051-1063, 2002

[5] Sayuri MITANI, Bachelor Thesis, Tokyo Institute of Technology, 2009

Feasibility Study of Mars Orbit Insertion by Aerocapture Using Solar Sail

Student Number : 14_09659 Name : Yuichiro Tsukamoto Superviser : Daisuke Akita

1. Introduction

One of the problems in manned Mars exploration in the future is transportation of a lot of payload to Mars. By conventional propulsion methods, however, only a small amount of payload mass can be carried in spite of huge total mass due to the specific impulse (I_{sp}).

Solar sail is a space propulsion system, which does not require propellants and obtains thrust by reflecting photons. JAXA launched solar sail IKAROS (Interplanetary Kite-craft Accelerated by Radiation Of the Sun) in 2010 and it has successfully demonstrated photon acceleration. The solar sail membrane is deployed by centrifugal force with weights attached to the sail tip. Figure 1 shows the configuration of the solar sail IKAROS.

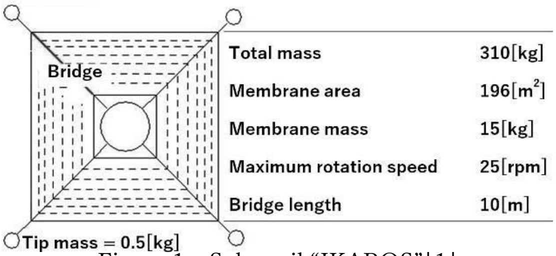

Total mass	310[kg]
Membrane area	196[m^2]
Membrane mass	15[kg]
Maximum rotation speed	25[rpm]
Bridge length	10[m]

Figure 1 Solar sail “IKAROS”[1]

2. Mission Concept

The solar sail, which has an infinite I_{sp}, could be useful as an in-space propulsion system for an interplanetary logistics from Earth to Mars. Solar sail can’t produce impulse propulsion, hence deceleration at Mars is impossible. In this paper, solar sail is inserted into Mars orbit by aerocapture. Aerocapture is an orbit insertion method that the spacecraft is decelerated by drag during atmospheric entry. For acceleration at apoapsis, photon acceleration is used. Fig. 2 and 3 shows the mission concept.

In this study, in order to estimate the possibility of successful insertion into Mars orbit, the flight path angle range (corridor) is investigated. In current technology it is feasible if corridor is 0.1 [deg] or more.

In this study, the orbit of the solar sail is calculated until the second entry into the atmosphere after aerocapture. The solar sail is square shaped. The parameter are membrane area, membrane mass, and rotation speed. The ratio of membrane area density to rotation speed in IKAROS is used as a reference for the rotation speed and membrane mass of the solar sail considered here.

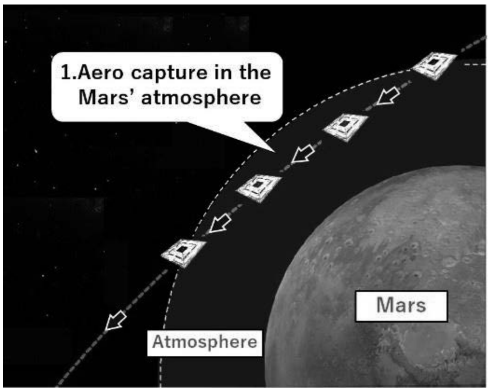

Figure 2 The sequence of Mars orbit insertion by aerocapture using solar sail (Aerocapture phase)

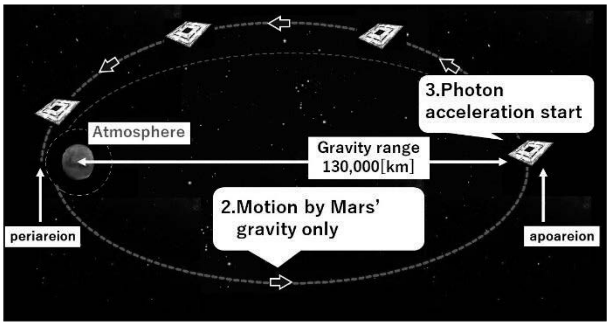

Figure 3 The sequence of Mars orbit insertion by aerocapture using solar sail (Photon acceleration phase)

3. Trajectory Calculation for Aerocapture

Figure 4 shows the model for calculating the trajectory during aerocapture. The motion equation of solar sail is represented by Eq. (1).

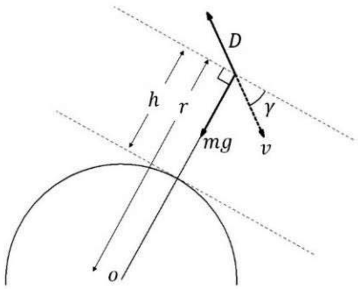

Figure 4 Motion equation model

$$\begin{cases} \dfrac{dv}{dt} = \dfrac{\mu_m}{r^2}\sin\gamma - \dfrac{1}{2}\rho v^2\dfrac{1}{\beta} \\ \dfrac{d\gamma}{dt} = \left(\dfrac{\mu_m}{vr^2} - \dfrac{v}{r}\right)\cos\gamma \\ \dfrac{dr}{dt} = v\sin\gamma \end{cases} \qquad (1)$$

t[s] : time from entry
v[m/s] : velocity
γ[deg] : flight path angle
r[m] : distance from the center of Mars
ρ[kg/m^2] : density of Mars
μ_m[m^3/s^2] : a product of Mars mass and gravitational constant
β[kg/m^2] : ballistic coefficient

Equation (1) is numerically calculated by 4th order Runge-Kutta method with time step of 0.1 [s]. Initial velocity v_0 is 5.6[km/s]. The initial altitude h_0 shown in Figure 4 is 125[km]. [2]

As aerodynamic heating during aerocapture, the heat flux to the membrane surface is calculated by the Tauber’s formula. The temperature limit of the membrane surface is 660 [°C] which is the melting point of aluminum deposited on the membrane surface, If the membrane surface exceeds this temperature during aerocapture, it is assumed that the solar sail is burn out.

Fig. 5 shows the corridor based on each ballistic coefficient and initial Flight path angle. If the velocity of solar sail exceeds the second astrnomical velocity at Martian altitude of 200 [km], it will escape from the Mars gravitational zone and can’t enter the elliptical orbit. If the velocity of the solar sail does not exceed the fist astrnomical velocity at Martian altitude of 200 [km], it will descent to the surface of Mars. Also, $\beta < 5.0[\mathrm{kg/m^2}]$ is necessary to complete the aerocapture in terms of aerodynamic heating.

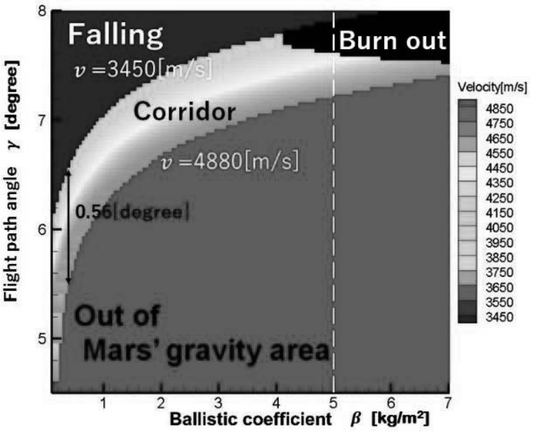

Figure 5 Corridor led by temperature condition and ballistic coefficient

Free molecular flow calculation is performed for getting aerodynamic characteristics of the rotating solar sail. In the free molecular flow calculation, the drag coefficient is determined only by the angle of the membrane surface with respect to the flow, and accordingly the ballistic coefficient during atmospheric entry changes. The angle of the membrane surface to the flow is calculated from the balance of forces in the symmetrical cross section of the solar sail.

For the tensile strength of the membrane, only the diagonal line component (bridge) is evaluated. The force acting on the membrane surface of the solar sail is decomposed into components along this diagonal component and the tensile load is calculated.

4. Trajectory Calculation for Elliptical Orbit

The elliptical orbits after aerocapture is calculated by using the 4th order Runge-Kutta method. The gravity range of Mars is considered to be a sphere with a radius of 130,000 [km]. If the solar sail goes beyond that, it is assumed to be affected by the gravity of other objects and the solar sail can't return to Mars. It is assumed that the sun's position, the apoareion, and the periareion are all on the same axis.

The thrust bythe photon reflection is considered to be given by the following formula with 1.12 [mN] at 1AU of IKAROS being regarded as a reference. [4]

$$F_s = 1.12 \times 10^{-3} \times d_0 / (d_1 - x) \times S_s / 196 \qquad (2)$$

F_s[N] : photon reflection thrust of solar sail
d_0[km] : distance between Sun and Earth (1AU)
d_1[km] : distance between Sun and Mars
x[km] : distance between Mars and solar sail
S_s[m^2] : solar sail membrane area

The membrane surface of the solar sail is assumed to be perpendicular to the velocity vector, and the thrust acts in the velocity vector direction. At that time, the area subjected to photon acceleration decreases by change in attitude of the solar sail with respect to the sun. The motion of solar sail is dominated only by Mars gravity until fly to the apoapsis. After that, photon acceleration is applied from the apoareion to the regression periareion.

5. Results of Trajectory Calculations

On elliptical orbit, it is judged to be successfully inserted into Mars elliptical orbit if the energy obtained by photon acceleration exceeds the energy loss due to the second entry into the atmosphere. If the rotation of the solar sail is stopped, the membrane is deformed by aerodynamic force during entry. The membrane deformation increases the ballistic coefficient and thus keeps the orbit energy. The altitude at the second entry into the Mars atmosphere is about 200 [km] and the velocity is about 4800 [m/s].

The corridor with the membrane area is calculated so that solar sail can insert into an elliptical orbit. The ballistic coefficient at first entry into the Mars atmosphere is less than 5.0[kg/m^2], and withstands the aerodynamic heating. Corridor is 0.1 [deg] or more when the total membrane area is more than 4,800 [m^2] as shown in Fig.6. If the total membrane area is 4,800 [m^2], the rotation speed is 125 [rpm] and the tensile load applied to the bridge is 461 [MPa]. It is necessary to use a material having a tensile strength higher than this value for the bridge.

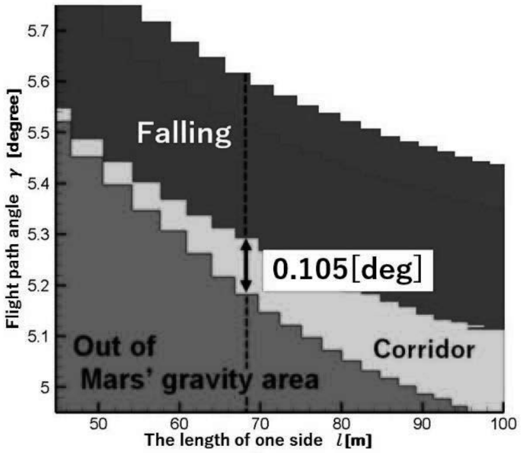

Figure 6 Aerocapture corridor with solar size

6. Conclusion

If the solar sail has a total membrane area of 4,800 [m^2], the solar sail has a sufficient corridor for aerocapture. Although there remain tasks in the development of the large membrane surface, this study would be the first step toward the interplanetary logistics using the solar sail.

Reference

[1] "Japan Aeronautic Association Aerospace and Culture", Available at:< http://www.aero.or.jp/web-koku-to-bunka/2017-03-mori/2017-03-mori.html>[Accessed 29 January 2018]

[2] Prasun N(2008), "Entry, Descent, and Landing Performance of the Mars Phoenix Lander", Journal of Spacecraft and Rockets, Vol. 48, No. 5, pp. 798-808.

[3] Lobbia Marcus(2003),"A Framework for the Design and Optimization of Waverider Derived Hypersonic Transport Configurations"JPh.D.thesis,University of Tokyo.

[4] "JAXA Small Solar Power Sail Demonstrator 'IKAROS' Confirmation of Photon Acceleration " Available at<:http://www.jaxa.jp/press/2010/07/20100709_ikaros_j.html> [Accessed 29 January 2018]

Global exploration of asteroid by numerous microlanders

Student Number : 14_15884, Name : Seonghwan YEO, Supervisor : Daisuke AKITA

1 Introduction

Asteroids are celestial bodies that have not had much process to become planets and may have primitive substances for the solar system formulation. At the same time, "space guard", which prepares for the asteroid colliding with the earth, has significance.

A lander is a spacecraft which descends toward on the surface of an astronomical body. In this paper, I propose a method to disperse microlanders on the surface of asteroids in large quantities. This mission has the merit of being able to explore many points simultaneously.

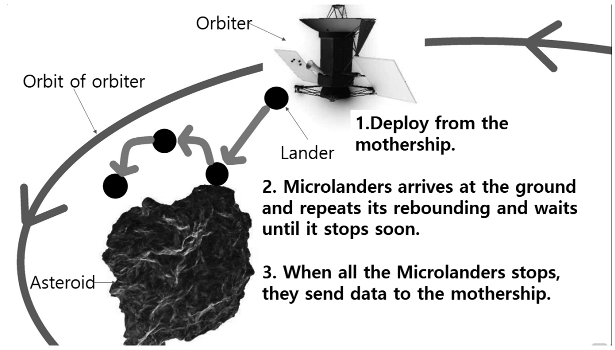

Figure 1: Mission scenario overview

Figure 1 shows the mission scenario. When a mother ship carrying many microlanders runs around the asteroid, it scatters the microlanders and collects data at that position when the microlaner bounces off and sends it to the mother ship.

The specification of one exploration lander is assumed as follows.

- Mass : 0.01[kg] or less
- Size : 0.01[m]×0.01[m]×0.01[m]
- Communication : It is possible to communicate with the mother ship and other landers.

In this paper, we have four types of possible parameter, such as inital position and initial velocity, coefficient of restitution and friction coefficient, collision condition, initial arragement. In order to evaluate each parameter, those other than the relevant parameter are fixed.

2 Physical modeling

In this paper, only the gravitational field is considerd, shall ignore the influence of other forces such as air resistance. Focusing on Lander, the basic operation of a single lander is to let it fall from the mother ship, repeat the rebound, and to distribute on the asteroid. According to the law of Conservation of Energy, Eq.(1) and Eq.(2) are established. and *h'* can be obtained in Eq.(3). The universal gravitational constant $G[\mathrm{m}^3/(\mathrm{kg}\cdot\mathrm{s}^2)]$, the mass of the asteroid M[kg], the mass of microlander m[kg], the radius of the asteroid R[m], the dimensionless constant coefficient of restitution e, the initial height h[m], the maximum height after collision *h'*[m]

$$\frac{GMm}{R+h} = \frac{1}{2}mv^2 - \frac{GMm}{R} \quad (1)$$

$$\frac{1}{2}m(ev)^2 - \frac{GMm}{R} = -\frac{GMm}{R} \quad (2)$$

$$h' = \frac{e^2h(Rv^2-2)}{(R(ev)^2-2)} \quad (3)$$

Lander bounces with the horizontal kinetic energy at the time of collision and moves horizontally until its total kinetic energy can be regarded as almost zero.

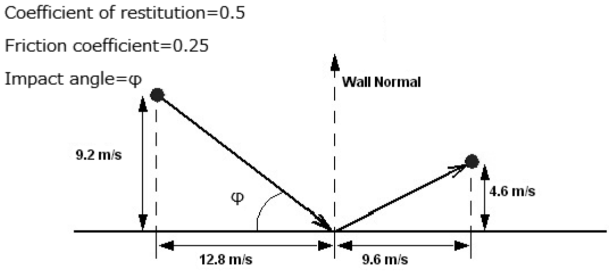

Figure 2: Example of collision situation

The friction coefficient μ is define as shown in Eq.(4). For expressing the definition of the coefficient of friction in this study by the formula, I denote the dimensionless constant coefficient of restitution e, the dimensionless constant friction coefficient μ, the vertical component to the collision plane of the velocity before collision $V_{n,o}$[m/s], collision velocity before collision Supposing that the horizontal component to the surface is $V_{t,o}$[m/s], the vertical component to the collision surface of the collision velocity is $V_{n,i}$[m/s] as shown in Eg.(5).

$$V_{t,i} = (1-\mu)\cdot V_{t,o} \quad (4)$$

$$V_{n,i} = e\cdot V_{n,o} \quad (5)$$

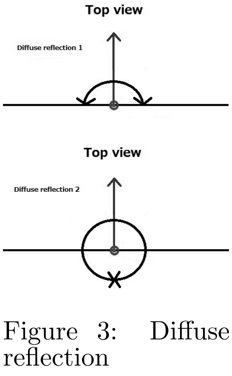

Figure 3: Diffuse reflection

In this paper, there are three kinds of collision conditions, which consider two kinds of diffuse reflection and a specular reflection. In this paper, two situations of (Diffuse reflection 1)$(-90°, 90°)$ and (Diffuse reflection 2)$(-180°, 180°)$ as (Min, Max) of the rotation angle around the vertical component against the collision surface are considered. When examining the friction coefficient, the coefficient of restitution, and the characteristics of the collision condition, each parameter follows the normal distribution with (-3σ, 3σ) as (Min, Max)(Figure. 3).

I thought four types of possible arrangements that were expected when orbiter shots(Figure. **??**). When examining other three parameters, initial arrangements are fixed except for other three parameters not-fixed.

3 Evaluation of scattering

For visual evaluation on the plane, I take the obtained spherical coordinate r, ϕ, θ to find the coordinates A[m] and E[m] as apply map projection. Consider ellipsoid asteroid. The simulation of this research is done 500 times. Therefore, take the average and perform coordinate transformation from the following equation.

$$\begin{aligned} r(range) &= \sqrt{x^2+y^2+z^2} && (6) \\ \theta(azimuth) &= \arccos\left(\frac{z}{r}\right) && (7) \\ \phi(elevation) &= sgn(y)\arccos\left(\frac{x}{\sqrt{r^2-z^2}}\right) && (8) \\ A &= r \cdot \theta && (9) \\ E &= r \cdot \phi && (10) \end{aligned}$$

4 Result of simulation

All of the simulation in this paper performed 500 times of 100 landers. Consider the influence of various initial positions and initial velocity. While changing the initial position and initial velocity, the arrangements is (Arrangement1) with an interval of 10[m]. The coefficient of restitution is fixed at 0.9, and the friction coefficient is fixed at 0.1. The initial velocity is given from 0[m/h] to 300[m/h] at intervals 50[m/h] in the axial direction(Table. 1)."Distance of the table means the distance from the center of gravity of the asteroid.

Table 1: Effect of initial posistion and initial velocity (optimum value)

Velocity[m/h]	Coordinate[m]	Distance[m]
(0,0,0)	(-9.7, 32.1, 100.7)	106.137
(0,0,-50)	(-17.9, 44.1, 99.5)	110.297
(0,0,-100)	(-0.8, 4.4, 103.4)	103.497
(0,0,-150)	(2.2, -11.0, 104.0)	104.603
(0,0,-200)	(2.2, -12.0, 105.0)	105.706
(0,0,-250)	(-21.4, 48.0, 99.1)	112.173
(0,0,-300)	(12.8, -21.3, 106.0)	108.874

From Table. 1, it seems that (50, 0, 0) is the condition that is most difficult to be uniformly, but because it does not move with respect to the axis, it is difficult to be even more uniform as a result of moving a little with respect to the axis (0, 0, 500) [m] to (0, 0, -100) [m / h] does not exceed the escape speed of the asteroid, the distance from the center of gravity of the asteroid is the closest. Understanding with only a single ladder The best simulation in the future will use the results of this condition to examine the characteristics of the other conditions.

Consider the influence of various coefficient of restitution and friction coefficient. When the initial position (0, 0, 500) [m], give the initial velocity (0, 0, -100) [m / h]. For the simplicity (restitution coefficient (average value), friction coefficient (average value)), the standard deviation is 0.1, (Min, Max) is set to (-3σ, 3σ). Possible combinations are (0.3 ～ 0.7, 0.7 ～0.3). Simulation is performed 500 times2, Table. 3).

Table 2: $(e, \mu) = (0.6, 0.7 \sim 0.3)$

(e,μ)	Distance[m]
(0.6,0.7)	76.62776
(0.6,0.6)	73.75840
(0.6,0.5)	67.09725
(0.6,0.4)	65.79947
(0.6,0.3)	69.42426

Table 3: $(e, \mu) = (0.7, 0.7 \sim 0.3)$

(e,μ)	Distance[m]
(0.7,0.7)	51.40219
(0.7,0.6)	49.22597
(0.7,0.5)	54.22401
(0.7,0.4)	43.37022
(0.7,0.3)	36.78452

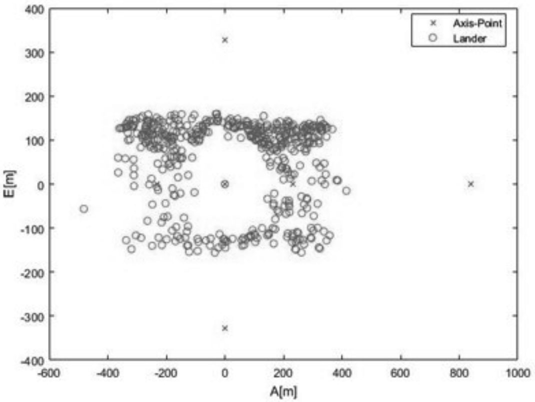

Figure 4: Specular Reflection

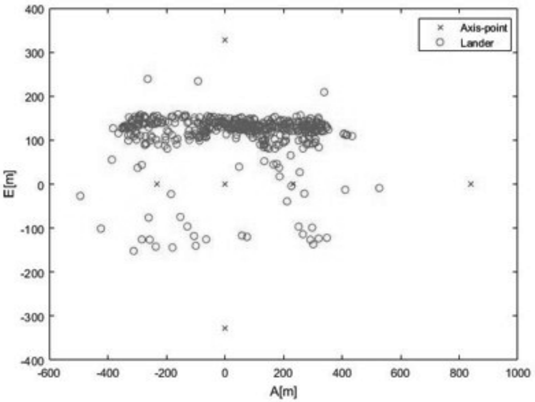

Figure 5: Specular Reflection

Consider three kinds of collision condition influences. There are three kinds of collision conditions, and consider specular reflection and two kinds of diffuse reflection. When the initial position (0, 0, 500) [m], give the initial velocity (0, 0, -100) [m / h]. The coefficient of restitution and coefficient of friction shall be (0.9, 0.1). The simulation performed 500 times (table .4).

Table 4: Collision condition

Collision condition	Distance[m]
(specular)	33.89221
(diffuse1)	81.22123
(diffuse2)	83.43120

5 Conclusion

In this research, investigated the asteroid exploration by numerous microlanders. Various problems are obvious in using the conventional Lander's method. Thus, I proposed a new asteroid exploration method and explored the possibility.

- Depending on the initial position and initial speed, there are conditions that are difficult to spread.
- In the case of a spherical shape, it is easier to disperse than in the case of an ellipssoid。
- The efficiency decreases when a collision that often bounces back in the direction of collision occurs often.
- The higher the coefficient of restitution, the higher the scattering efficiency increases as the friction coefficient decreases.

References

[1] 吉田，浅井：“微小重力環境において跳躍する探査ロボットの設計”，ロボティクス・メカトロニクス講演会’99 講演論文集 1p206044, 1999.

[2] 吉光徹雄. “Musesc プロジェクトと小惑星探査ロボット minerva 構想”. jSAIRAS’98, 1998.

Effect of ions generated between electrodes on breakdown voltage

Student Number:14_12124 Name : Masaki Hira Supervisor : Kunio Takahashi

1. Introduction

Discharge phenomena is a phenomena in which a current flows in gas between electrodes to which the voltage is added between the electrodes. Arc welding is one of the applications of the discharge phenomena. Arc welding uses discharge as a heat source. As a feature of the discharge phenomena, the breakdown voltage is higher than re-ignition and arc voltage [1].

There are various research to lower breakdown voltage. One of the studies suggests that ions between the electrodes may lower the breakdown voltage [2]. However, since these are speculation, they need to be examined experimentally. In this research, the effect of ions generated between electrodes on breakdown voltage is investigated experimentally.

2. Experiment Equipment

2.1 Calibration experiment

Ioncounter (NKMH-103) is used to measure ion concentration(Number/cc). A dryer (Panasonic) accessories is used as an ionizer. The ionizer is covered by a glass tube. The ion concentration was measured by changing the distance from the inlet port of the ioncounter to the ionizer.

2.2 Experiment of breakdown voltage

Electrode rods used in this study are tungsten containing 2% ThO_2. The diameter is 1mm. In figure 1, R is the resistor to limit the current (1500Ω). Ions are blown into the air between the electrodes by the ionizer. E is the DC power supply.

2.2.1 Voltage-current characteristic

After d was fixed at 1 μm, the voltage of power supply is increased gradually. The current and voltage are continuously measured until the discharge start.

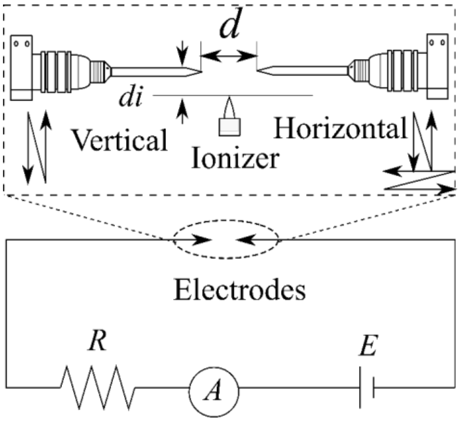

Figure 1 Schematic lustration of measurement experiment system

2.2.2 Breakdown voltage

After d was fixed, I increased the voltage between electrodes. Then switch off the power at the discharge starts. The voltage at this time is measured as the breakdown voltage. After the experiment was repeated 5 times under the same conditions, Change d and repeat this procedure.

3. Experiment Result and discussion

3.1 Calibration experiment

Figure 2 shows the relation between the ion concentration and the distance between the ionizer and the inlet port. According to the figure 2, the ion concentration drops sharply when the distance exceeds 2cm. Therefore, di = 3mm , 1cm was selected in this research.

3.2 Experiment of breakdown voltage

3.2.1 Voltage-current characteristic

Figure 3 shows the measurement of current flowing between the electrodes and the power supply voltage waveform in case of d_i= 3mm, d =1 μm, with ions, and no ion. In Figure3, current flowing between the electrodes was

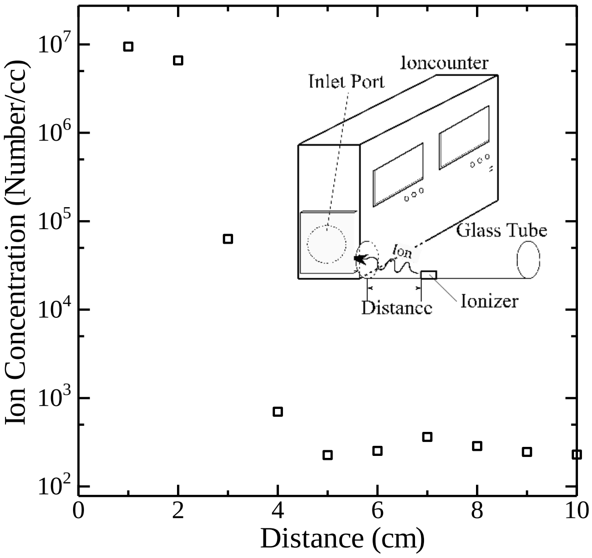

Figure 2 The experimental result of relation between ion concentration and distance

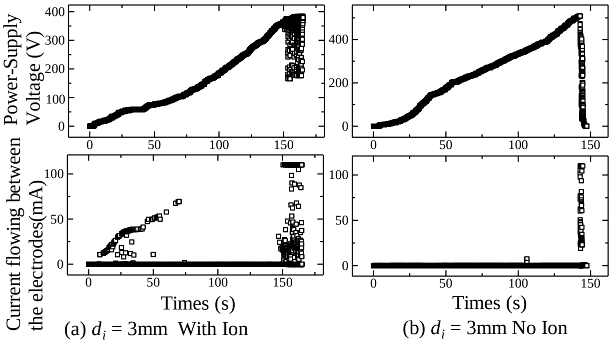

(a) d_i = 3mm With Ion (b) d_i = 3mm No Ion

Figure 4 Current flowing between the electrodes and Power-supply voltage measured before breakdown

observed in the region of 150V or less and wasn’t observed in the region from 150V to the start of discharge. It was found that the current observed in the region of 150V or less was not tunnel current but the possibility of the current flowing by the ions generated between the electrodes.

3.2.2 Breakdown voltage

Figure 4 shows the relation between the breakdown voltage and *d*. The graph on the left shows with ions and the graph on the right shows no ions. ○ and × represent breakdown voltage. ◇ represent average breakdown voltage. Comparing the graph on the left with the graph on the right, the graph on the left shows small variations and the average breakdown voltage is low. On the other hand, the graph on the right shows large variations and high average breakdown voltage. Therefore, it is found that the ions generated between the electrodes qualitatively affect the breakdown voltage.

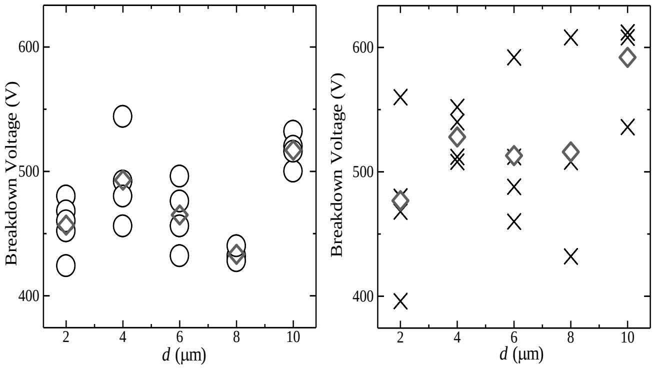

(a) d_i = 3mm With Ion (b) d_i = 3mm No Ion

Figure 5 The experimental results of relation between the breakdown voltage and the distance between electrodes

Conclusion

- ✓ The effect of the ions generated between the electrodes qualitatively on the breakdown voltage was found
- ✓ In case of ‘Ionizer on’, it was observed that a current was flowing in a region of 150V or less. It was also found that the current is not the tunnel current but the possibility that it is the current flowed by the ions generated between the electrodes.
- ✓ For the phenomenon that current does not flow in the region from 150 V or more to the start of discharge, the mechanism is unknown and further research is needed.

4. Reference

[1] 原雅則,酒井洋輔, 気体放電論. 東京: 朝倉書店, 2011.

[2] 元木幹雄,小野雅章,上出諭吉”放電加工のギャップ現象”,電気加工学会誌,Vol8,No15,1974

Abnormal tides caused by storm surges in Tokyo Bay

Student Number: 13B08237 Name: Atsuhei TAKAHASHI Supervisor: Hiroshi TAKAGI

1. Introduction

Storm surge is an abnormal rise of water generated by developed low pressure system such as typhoon, over and above the predicted astronomical tides. Along with strong wind, low air pressure system is mainly caused by difference in air pressure between center of typhoon and outside the storm center [1]. Japan is affected by typhoon mostly every year. The typhoon that caused the most devastating damage at Tokyo Bay in recorded history was occurred in October 1, 1917. Number of casualties and destroyed houses caused by this typhoon reached up to 1,301 and 43,083, respectively [2].

The coastal protection around Tokyo Bay has been much improved over the last century. However, excessive ground water use during the period of rapid economic growth caused land subsidence about 4 m, inevitably increasing flood risks. Also less attention has been paid to the disaster risk associated with storm surges. Storm surges are amplified by geographical features of Tokyo Bay and further complicated by multiple mechanisms associated with ocean, river, and meteorological dynamics.

The purpose of research is to numerically investigate characteristics of abnormal high tides induced by typhoon storm surges in Tokyo Bay.

2. Numerical Analysis

In this study, parametric typhoon model coupled with the fluid dynamics model Delft3D-FLOW has been used in order to estimate the extent of storm surges inside Tokyo Bay due to the passage of recent major typhoons. Nested grid system where the simulation was firstly carried out for a wide area which encompasses coasts of Tokyo, Kanagawa and Chiba Prefecture. Then, with finer grid, detailed simulation was carried out for low lying areas of Tokyo bay. Table 1 shows the model settings. Past typhoons that have been reproduced in this study are Phanfone (2014) and Lan (2017).

Terrain data	The Geospatial Information Authority of Japan (GSI)
Roughness	sea area: 0.025
	land area: 0.08
Time step	0.05 (min)
Mesh size	Wide area: 250-1000 (m)
	Narrow area:25-100 (m)
Dyke height	The Breau of Construction, Tokyo Metropolitan Government
Typhoon Track	Japan Meteorological Agency (JMA)

Table 1. Calculation settings and Data sources

Typhoon Phanfone and Lan developed as a tropical storm on September 29, 2014 and October 16, 2017, respectively. Finally they took similar route to each other and eventually passed over Tokyo on October 6, 2014 and 23 October 2017, respectively.

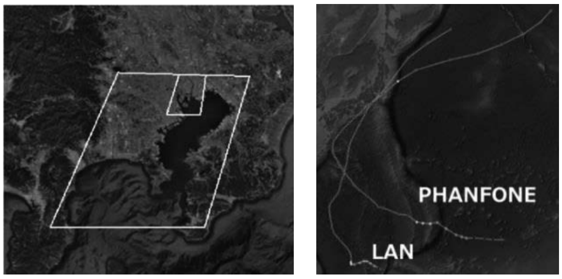

Fig 1. (left) Grid area (outer and inner domains) and (right) Typhoon Track

3. Result

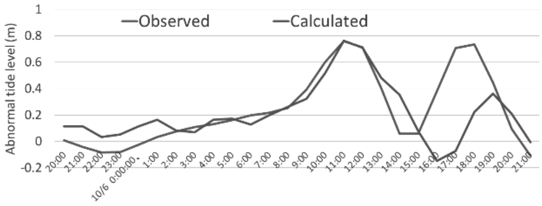

Fig 2. Calculated and observed abnormal tidal level at Harumi during Phanfone

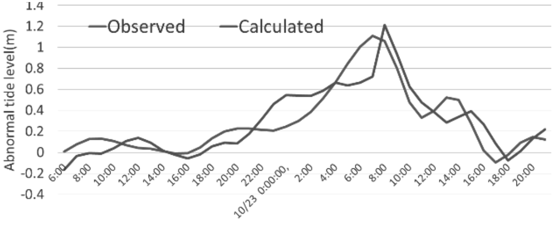

Fig 3. Calculated and observed abnormal tide level at Harumi during Lan

Figs 2 and 3 compare the calculated and observed tide level deviation in Harumi tidal station (St.), Tokyo.

For both cases, the first peak of water-level rise is well reproduced by the typhoon model, demonstrating that storm-surge component is predominant among many others. However, second peak which occurred around six hours later from the first peak did not show well agreement with observed value. The reason for this will be discussed in the following section.

3.1 Seiche effect in Tokyo Bay

Tokyo Bay is a semi-enclosed bay surrounded by both Miura and Boso Peninsula. As a result, behavior of seawater inside is significantly confined by the shape of the bay. Therefore, a secondary oscillation called “seiche” can also be induced by an abnormal atmospheric event. In general, seiche happens in Tokyo Bay around 6 hours later of typhoon passage [3], and this could be one of the reasons for secondary high tide found in Fig3.

3.2 Effect of river discharge

Generally typhoon brings much rainfall than any other normal atmospheric conditions. As a result, water volume in the river system connected directly with Tokyo Bay should also increase. There is no available data which contains a pure river discharge because river flow near the river mouth is highly influenced by storm surges as well as tides that propagates in the opposite direction of river flow. Thus it is difficult to estimate accurate water discharge from the data measured at upstream observatories. Nevertheless, this study tried to explain river discharge effect by comparing available water level information along Sumida River.

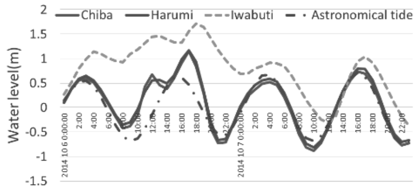

Fig 4. Observed water level during PHANFONE

[

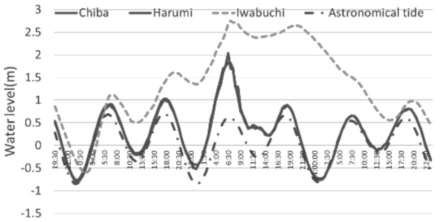

Fig 5. Observed water level during LAN

Figs. 4 and 5 compare observed water level at Iwabuchi St. (23.5km upstream along Sumida river) with those at tidal station located at Harumi and Chiba. Tidal stations at Harumi and Chiba both are far away from each other. Iwabuchi St. is located relatively close to Harumi St., whereas Chiba St. is far away from Iwabuchi St.. Therefore, water level should also be different between Harumi and Chiba St. if there is any significant effect of river discharge. However, both are almost identical. And secondary peak observed water level at Iwabuchi did not match well with secondary high tide during Typhoon Lan.

3.3 Atmospheric pressure and wind velocity after typhoon passes

In parametric typhoon model, the shape of typhoon approximates as a circle. Therefore, after a typhoon passed Tokyo Bay, atmospheric pressures and wind velocity rapidly becomes normal. But in some cases, even when typhoon travels far away from Tokyo Bay, low-pressure system and associated strong winds may remain. Such wake of meteorological condition is important in predicting water levels, but it could not be precisely evaluated by the present model.

4. Conclusion

This study confirmed that the numerical model can well predict the first peak of the high tide during typhoons, which is mainly induced by storm surges. However, the second peak of water level did not necessarily show a good agreement with observed tide water levels. This could be explained due to the effect of seiche and residue of winds and low pressures after the typhoon, which cannot be precisely model with the present typhoon model. Second peak of tide during typhoon period could also be dangerous if it coincides with high tide. In order to reproduce secondary high tide, further studies are needed to improve the storm surge model.

Reference

[1] 気象庁 台風に伴う高潮
http://www.jma.go.jp/jma/kishou/know/typhoon/4-1.html
[2] 北原糸子ら『日本歴史災害事典』吉川弘文館, 2012
[3] 宇野木早苗『東京湾の 6 時間周期の振動』海洋学会秋季大会講演要旨集, 1987

PHOSPHATE RECOVERY USING CALCIUM SILICATE HYDRATE SYNTHESIZED FROM COAL FLY ASH

Student Number: 14-00701 Name: Yu Ando Supervisor: Hirofumi Hinode, Winarto Kurniawan

1 Introduction

Phosphorus (P) is one of the indispensable elements for human life. It is used in agriculture as fertilizer, has a wide range of applications in industry and is one of the main components in our bones and DNA. Phosphorous can be sourced from phosphate rocks and at present, the recoverable reserves are decreasing at a fast rate because of human consumption. About 70% of the rocks are mined mainly in 3 countries: China, Morocco, and USA. These countries impose high tariffs and strict restrictions on exports of phosphate rocks. Japan rely heavily on this imported resource but about half of the volume that is imported ends up in waste. Therefore, Japan needs a viable phosphorous recovery system. Usually, P is removed from the sewage to prevent eutrophication. There are two most common methods which can recover P and converted into some value-added chemical such as fertilizers: first, in the sewage treatment plant, P is recovered through precipitation method using chemicals such as polyaluminium chloride to recover chemical phosphorus from wastewater and excess sludge. This method needs another process to remove other components and to adjust the pH and requiring large amount of chemicals; the second method is alkaline extraction in which P in incineration ash of sludge is extracted by alkali solution. This method needs high temperature, therefore initial cost and running cost of this method are high. For these reasons alternative P recovery system which can reduce recovery cost is needed.

Calcium silicate hydrates (CSH) are formed in hyper-alkaline, hydrothermal environments with silica and calcium. CSH have high specific surface area and can adsorb heavy metal ion and anion. In previous study, it was reported that CSH has high P adsorption and sedimentation ability. Moreover, its ability is not influenced by CO_3^{2-}, thus P recovery by CSH do not need decarboxylation and pH adjustment processes [1]. However previous research used mineral as silica resource and only recover P from simulated water (SW). There is some hypothesis about this adsorption mechanism but This was not thoroughly studied. In this research to reduce the synthesis cost of CSH, CSH was synthesized from coal fly ash which is industrial waste, P recovery test was done using actual sewage and the mechanisms were studied using by X-ray diffraction (XRD) and FT-IR analysis.

The research objectives in this research are as follows. 1) To synthesize CSH from coal fly ash for phosphate recovery and; 2) To explain the mechanism of P-adsorption on CSH

2 Experimental methods

2.1 CSH synthesis

The coal fly ash used in this research was from Ishinomaki, Miyagi. To extract silica, fly ash was mixed with 5 mol/L of NaOH solution and was stirred at 300 rpm for 3 hours at 80℃. After filtration, Ca/Si ratio was adjusted through the addition of $Ca(OH)_2$ and the CSH was synthesized by hydrothermal method. After the reaction, the solid phase was washed by deionized water and dried under vacuum condition at 60℃. To find the optimum condition for P recovery, CSH which were synthesized at different reaction times, reaction temperatures and molar ratios of Ca/Si were tested. The name of samples are assigned as X-Y-Z (X: reaction temperature, Y: reaction time, Z: Ca/Si molar ratio)

2.2 Batch test

Phosphate recovery test was carried out by using simulated wastewater (SW) which was prepared from deionized water and KH_2PO_4. The final concentration of P in SW was 150 ppm. 0.112 g of samples was added to SW and stirred at 300 rpm at 25℃. The contact time was 24 hours. In this study, adsorption isotherm and the influence of pH and CO_3^{2-} was investigated. Actual sewage recovery test was also conducted by using excess sludge from “Naruse Clean Center” in Machida, Tokyo.

2.3 Characterization studies

XRD analysis was carried out to identify the crystal phase. Surface functional groups were identified by FT-IR analysis. XRF analysis was carried out to identify and quantify the elements on the surface. The properties of pore of samples were analyzed by N_2 adsorption methods. Chemical compositions and concentrations of the solution was analyzed by ICP-AES.

3 Results and discussion

CSH samples labelled ② and ③ in the XRD diagram showed in Fig. 1 exhibited peaks at around 7, 29, 32, 50 and 55°, which are specific peaks of CSH. Samples ② and ③ in Fig. 2 also exhibited specific FT-IR peaks of CSH at 500, 650, 970, 1450 and 1640 cm^{-1}[2]. From this results, it can be concluded that CSH was successfully synthesized from coal fly ash.

Figure 3 shows the amount of P recovery and the amount of Si release. The adsorption of P is thought to be accompanied by the release of Si. It is considered that CSH adsorb P by ion exchange between phosphate and silicate.

Figure 4 shows influence of pH on P adsorption. Initial pH of SW was adjusted to around 3.0, 7.0, 9.0 and 11.0 using NaOH and HCl solution. CSH showed high P recovery ability at low pH and ability stayed almost constant value at high pH. The amount of P recovery was in proportion with Si release at pH range of 5.0-11.0. However, at pH range of 3.0-5.0, the amount of P recovery was increased in spite of decreasing Si release. This is because when pH is high, phosphorus ion is in the form of $H_2PO_4^{1-}$, so P could be recovered even with low Si release compared to high pH conditions when P exist as HPO_4^{2-}.

Figure 6 shows the result of recovery from actual sewage wastewater sample. CSH could recover about 90% of P in actual sewage sample[4]. However, compared to the results of P-recovery from SW, the amount of Si released was lower. In excess sewage, most of P exists as organic phosphorus or condensed phosphoric acids. Condensed phosphoric acids has multiple P in an ion so CSH can exchange multiple P by only one silicate ion.

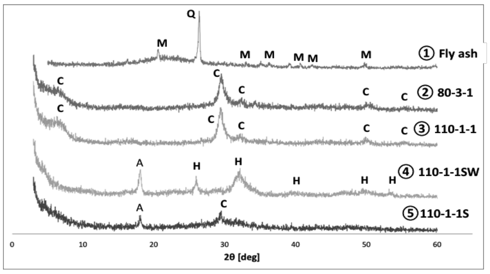

Q: Quartz(SiO_2), M: Mullite (MgO-Al_2O_3・$2SiO_2$)
C: CSH, H: hydroxyapatite($Ca_{10}(PO_4)(OH)_2$, A: $Ca(OH)_2$

Figure 1. X-ray diffraction patterns

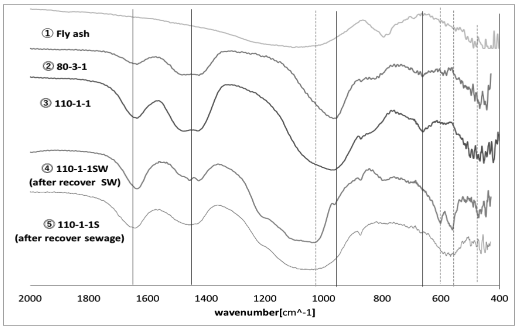

Figure 2. FT-IR patterns

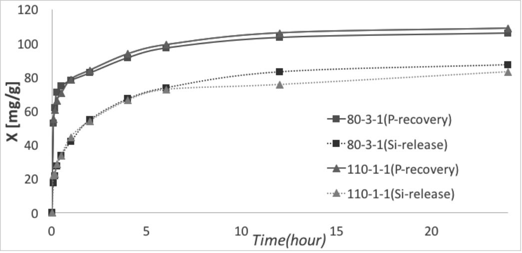

Figure 3. Result of adsorption from simulated wastewater

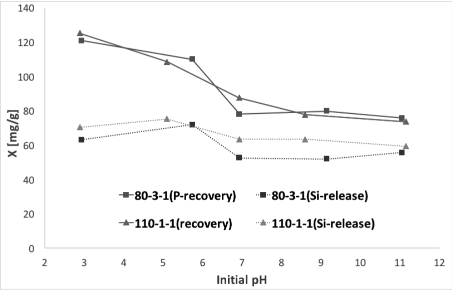

Figure 4.　Influence of pH on P adsorption

Sample ④ in Fig. 1 shows hydroxyapatite (HAP) is crystalized. The sample after P recovery from sewage do not show peaks of HAP. This is because there are different forms of P in the actual sewage wastewater sample.

Samples ④ and ⑤ in Fig. 2 shows that after P recovery, peaks of Si-O (around 500, 650 and 970cm^{-1}) disappeared and peaks of phosphate (around 450, 560, 600 and 1025cm^{-1})[3] were generated. This showed that silicate in sample was replaced by phosphate by ion exchange.

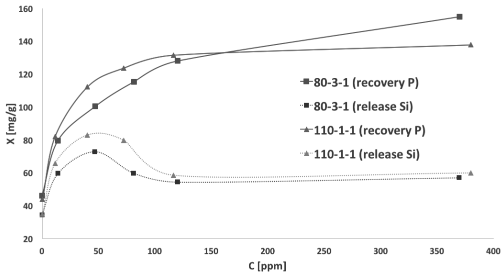

Figure 5. Adsorption isotherms

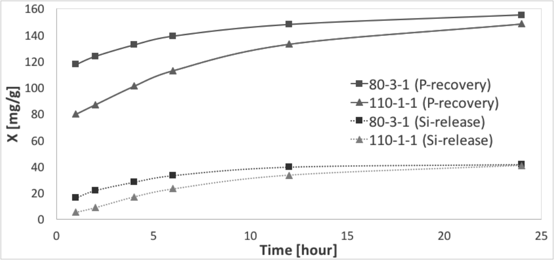

Figure 6. Result of adsorption from actual sewage

Table 1. XRF results

	Si (atm/%)	Ca	P	Al	Mg	C/S
80-3-1	52.6	43.7		2.35		0.83
110-1-1	57.3	40.2		2.47		0.70
80-3-1 S	18.3	28.0	40.8	3.41	11.2	
80-3-1SW	22.1	31.4	36.9	2.30		
110-1-1S	25.1	28.3	42.5	2.25	7.48	
110-1-1SW	28.8	33.0	35.1	3.17		

Table 1 shows the amount of elements (atomic % composition) on the surface of samples by XRF analysis. This indicates that P was recovered on the surface and the amount of silica on the surface decreased. Therefore, it can be concluded that P ion exchange occurred on the surface.

4　Conclusion

CSH was successfully synthesized from coal fly ash by hydrothermal method and could recover about 90% of P from actual sewage sample that was studied. Results of FT-IR, XRD and composition analysis indicated that CSH recovers P by ion exchange between phosphorus and silicate. Result of XRD and XRF also indicated that CSH recover phosphorus as hydroxyapatite on the surface. The amount of Si released was influenced by ionic phase of P and the amount of P recovered.

Accordingly, the synthesis of CSH from coal fly ash is considered to be a new way to recover phosphate from sewage.

References

[1] Kenji Okano, et al,’’Novel technique for phosphorus recovery from aqueous using amorphous calcium silicate hydrate(A-CSHs)’’, Water Research 47, pp.2251-2259, 2013

[2] Wei Guan, et al, “Synthesis and Enhanced Phosphate Recovet Property of porous calcium Silicate Hydrate Using Polyethylenglycol as Pore-Generation Agent”, materials 2013,6(7), 28462861

[3] Hisao Otake, ‘’リンの事典’’, 朝倉書店, 2017

Clarification of Public Transport Usage Conditions in Ahmedabad, India

Student number: 14-12147　Name: Takashi Hiraide　Supervisor: Shinya Hanaoka, Tomoya Kawasaki

1. Introduction

The population of Ahmedabad is increasing with economic growth, and becomes the fifth largest city in India in 2011. The number of registered vehicles has also increased rapidly and it cause economic loss and environmental problems due to the severe traffic congestion. In order to solve those problems, the bus transport network Ahmedabad Municipal Transport Service, AMTS has started since 1947 and Bus Rapid Transport System, BRTS has also started since 2007. Nevertheless, these public transport accounts for only 12% of modal share in the city and private vehicle accounts for no less than 36% in 2011. [1] The traffic congestion has not been resolved yet and the various problems are remained. This city has the paratransit called "Auto-rickshaw, Auto", which is expected to play a role as a feeder of public transport.

Previous studies on public bus transport services at national and local levels focused on various contents, but there is scant literature on residents' impression of public transport with its feeder in Indian cities and none for Ahmedabad. Thus, this study is aimed to clarify conditions to use public transport of private vehicle user.

2. Methodology

Two field surveys were conducted in this study. First one is interview survey with stakeholders of urban transportation in Ahmedabad to clarify the actual condition of each mode in July 2017. The second one is questionnaire survey of private vehicle users, who live in northwest side of the city in December 2017. Survey area is divided into Area A and B. The former is inside the station area of the AMTS and outside that of BRTS, and the latter is within 500m from the BRTS route, which means inside the station area of BRTS. The questionnaire sheet includes personal information and the impression of AMTS, BRTS and Auto. Using collected samples, the model of impression structure towards nonuse of public transport is developed based on Technology Acceptance Model 2, TAM2, which is a model for explaining the usage behavior of information systems based on Structural Equation Modeling, SEM. [2]

3. Model development

The conceptual structure of TAM 2 assumes that the belief of "perceived usefulness" and "perceived ease of use" is fundamentally important in explaining the behavior of using service. Perceived usefulness is the degree to which a person believes that using a particular system would enhance his/her job performance. Perceived ease of use is the degree to which a person believes that using a particular system would be free from effort. When thinking about behavior of nonuse of transportation modes, the degrees to which a person believes that the mode has no advantage and that it is needed too much cost are fundamentally important. It is also needed the degree to which a person believes that he/she would use a particular system with adverse effects and loads. Based on these assumptions, that models how users not to use a public transportation with auto is created as Figure1. In this path diagram, it is assumed the impression of Auto has influence on the use of Bus service.

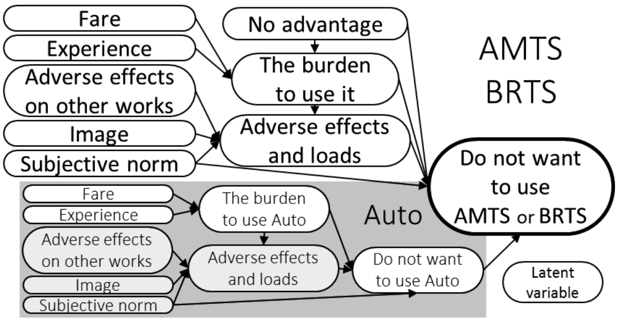

Figure 1 Path diagram

Direct path coefficients are calculated by the following equations.

The measurement equation

$$x_{ij} = \alpha_{ij} \cdot y_i + \zeta_{ij} \qquad (1)$$

The structural equation

$$y_i = \textstyle\sum_n \beta_{ni} \cdot y_n + \xi_i \qquad (2)$$

Where, x_{ij} is observed variable, y_i is latent variable, α_{ni} and β_{ij} are direct path coefficient, and ζ_{ij} and ξ_i are error variable. Total effect is the sum of direct and indirect path coefficients. It shows the influence between observation variables.

4. The results of questionnaire survey

4.1 Questionnaire sheet and number of samples

297 samples in Area A and 295 samples in Area B were collected. Respondents were asked to answer each question, which are the variables of nonuse of public transport including Auto by 4 point scale. 4 and 1 indicates "strongly agree" and "strongly disagree", respectively. After the descriptive analysis, the model is developed based on TAM2 and analyze it by SEM.

4.2 Results

The results of analysis for each area are addressed. All the model obtained are less than 0.9 of Root Mean Square Error of Approximation, RMSEA. Based on developed models, the conditions not to use public transport with Auto are discussed.

4.2.1 Area A AMTS - Auto

First, AMTS in Area A is discussed. Figure 2 shows the amount of total effect of latent variables to the nonuse of AMTS in Area A. "No advantage" has the greatest influence on nonuse of AMTS. It means the residents recognize that owned vehicles are more convenient or comfortable, and might not take road congestion and air pollution seriously. Moreover, "The burden to use AMTS" also has an influence on this means of transport. According to its observed variables, AMTS is necessary to make it easy to interchange with other transports and to choose route. It also shows residents consider the operating hour and frequency are not appropriate.

Next, feeder of AMTS is discussed. The impressions related to Autos also affect AMTS, and "Subjective norm" has the greatest influence on it. , The decision making of the surrounding people affects to that of himself/herself greatly. The influence of "The burden to use Auto" and "Adverse effects and loads" has also great influence on nonuse of Autos. According to their observed variables, discontent with the performance of the car body and the attitude of the drivers have an influence from them.

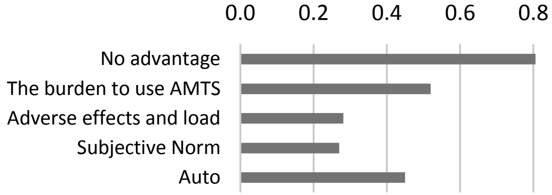

Figure 2 The amount of total effect of latent variables to the nonuse of AMTS in Area A

4.2.2 Area B AMTS-Auto

AMTS in Area B is discussed. Figure 3 shows the amount of total effect of latent variables to the nonuse of AMTS in Area B. The nonuse of AMTS is affected by the impression of its feeder, rather than the evaluation of itself. The influential latent variable on the nonuse of Auto is "Subjective norm" as with Area A. "The burden to use Auto" is also as influential as "Subjective norm". According to its observed variables, the residents are dissatisfied with the driver's attitude when making routing and negotiating fare. It leads to not using Auto and buses. "Adverse effects and loads" has not a little influence as well. "Autos tend to get involved in harassments at times." has greatest influence of this latent variable. In the analysis of Area A, where the same transport is operated, the path coefficient toward this observed variable was smaller than other pass. From these results, it can be said that the residents of Area B are sensitive to the risk of being involved in crimes. It is convincing, because Area B has order residents with higher income and education level compared to Area A.

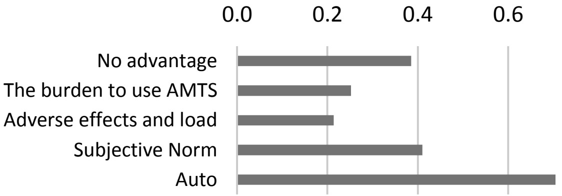

Figure 3 The amount of total effect of latent variables to the nonuse of AMTS in Area B

4.2.3 Area B BRTS-Auto

BRTS in Area B is discussed. Figure 4 shows the amount of total effect of latent variables to the nonuse of BRTS in Area B. “The burden to use BRTS" has the greatest influence on the nonuse of BRTS. The observed variables, such as difficultness to purchase tickets, get on and off the bus, and determine the route has a large influence from it. Thus, it is required to make it easier to use the bus for these contents. Furthermore, since the value of the path coefficient of "It does not operate in early morning or midnight." is also large, residences have the impression, that the operating hour is not appropriate. Next, it is noted that the feeder of BRTS is considered. The impressions of Auto also affects BRTS and “The burden to use Auto” and "Subjective norm" had great influence on it. One of the influential latent variables is "The burden to use Auto". According to their observed variables, it is required to raise the quality of driver’s service. The impression that Autos are hard to catch is also making people feel hard to use. "Subjective norm" is influential as much as "The burden to use Auto". Thus, the decision making of the surrounding people is greatly related to that of himself/herself. The amount of path coefficient of "Adverse effects and loads" is also large. Thus, the residents of Area B are sensitive to the risk of being involved in crimes from this result as well.

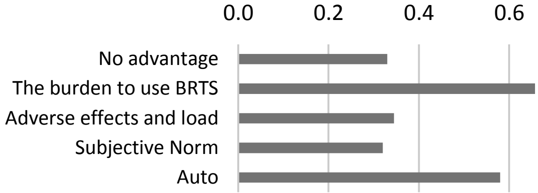

Figure 4 The amount of total effect of latent variables to the nonuse of BRTS in Area B

5. Conclusion

In this study, the impression on public transportation with its feeder of owned vehicle user in Ahmedabad is analyzed. It is revealed from the model that the feeling of ‘no advantage to use’ of owners of private vehicles has the highest effect on non-use of AMTS among the latent variables, followed by ‘burden to use’ as the second highest effect. Observed variables of ‘effort to transfer’ and ‘effort of route choice’ largely affect latent variable of ‘burden to use’. ‘Burden to use’ of ‘auto-rickshaw’ is observed to have a relatively high effect on non-use of AMTS. This implies that the improvement of feeder service i.e. auto-rickshaw and connectivity between auto-rickshaw and AMTS are important to enhance the use of AMTS. As for BRTS, ‘burden to use public transport (i.e. ticketing system)’ and ‘auto-rickshaw’ have the highest effect among the latent variables. Several negative impressions towards auto-rickshaw as a feeder service are observed in both AMTS and BRTS. Particularly, subjective norms such as ‘family and friends do not use auto-rickshaw’ is identified as one of the influential conditions of non-use of public transport.

Those findings would be utilize in the process of planning and implementing measures to realize more efficient and less burdensome city traffic in the future. Nevertheless, it is unknown how much residents will modally shift by improving the contents mentioned in this research. Therefore, it is necessary to make policy based on the results of this research and to conduct a demonstration experiment.

Reference

[1] CoE, Urban Transport-CEPT University and Ahmedabad Urban Development Authority (AUDA), Integrated Mobility Plan for Greater Ahmedabad Region. 2013

[2] 中村雅章 情報システム利用の人間行動モデル-TAM (技術受容モデル) に関する研究-, 中京経営研究 10 (2), p.51-77, 2001-02-01

3D model construction of indoor environment using photogrammetry

Student Number: 14B02679 Name: Shan Wang Supervisor: Jun-ichi TAKADA, Azril Haniz

1 Introduction

To predict and clarify how radio waves from wireless communication systems propagate in the environment, it may be useful to perform simulations. Surrounding environment has a great influence in wireless communication systems, and particularly in indoor environments, the arrangement of the room may be very complex and difficult to be modeled accurately. However it is not easy to construct a 3D model of a whole room from the beginning using software such as CAD. In order to reduce the cost of construction, we can use photos to get a rudimentary 3D model by photogrammetry.

Photogrammetry is a technique to obtain geometric characteristics of objects from photos. It is as old as modern photography. By photogrammetry, we can get information about 3D coordinates, image coordinates of views and so on [1].

The objectives of this research are summarized below: Examine the feasibility of utilizing photogrammetry to construct 3D models of indoor environments. Investigate parameters which may affect the quality of the constructed 3D models.

2 SfM

One of the most commonly used techniques of photogrammetrical is called structure from motion(SfM), where 3D models are generated using overlapping photos taken from lots of locations and orientations.

The process of SfM can be simply summarized into four steps. Firstly, detect feature points in each photo. Then, match feature points in pairs, and estimate camera movement. Next, according to feature points matched and camera movement estimation, construct 3D model. Finally, optimize to have least error between all matching feature points, view point movement estimated with real ones.

To detect feature points, Scale-Invariant Feature Transform(SIFT) is used. SIFT is an algorithm which adds smoothing filter in different scales, and detect feature points according to the difference between smoothed photos. Feature points are matched by each pairs of photos and matching is refined using Random Sample Consensus(RANSAC), which to ignore ostracized samples in matching. According to pairs of feature points, fundamental matrix can be calculated by Epipolar constraint equation which includes information to estimate camera movement. Finally, model is constructed by using Triangulation method. Figure 1 shows the algorithm of SfM [2].

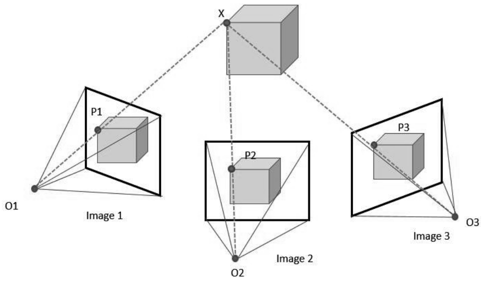

Figure 1: Algorithm of SfM

3 Factors which influence 3D model accuracy

Before constructing a whole room, it is necessary to clarify what factors influence the construction and examine how accurate the models are. Thus we tested six reasonable factors: texture, color, number of photos, masking background, quality of photos and camera positions by modeling objects using software Agisoft Photoscan.

Color

The influence of color was investigated by changing the color of a black box, results show that dark or light color does not influence the construction.

Texture

The influence of color was investigated by wrapping a black box with newspaper, as distinct texture strongly helps construction. This is because distinct texture has many feature points that can be easier found by Photoscan.

Number of photos

The influence of the number of photos was also examined. This is related to the overlapping rate. We found that more photos with high overlapping rate helps the matching of feature points.

Masking background

Masking the background may help improve the model because only the object parts will be used in construction. However, in our experiments, we found that masking does not have obvious influence on the results.

Quality of photos

Photoscan can calculate the image quality of photos by sharpnessm Image quality does not have influence on the accuracy of modeling but affects the clarity of texture construction.

Camera positions

Camera positions have great effect on the construction. This is also related to the overlapping rate.

Figure 2: Flyers put on objects without texture

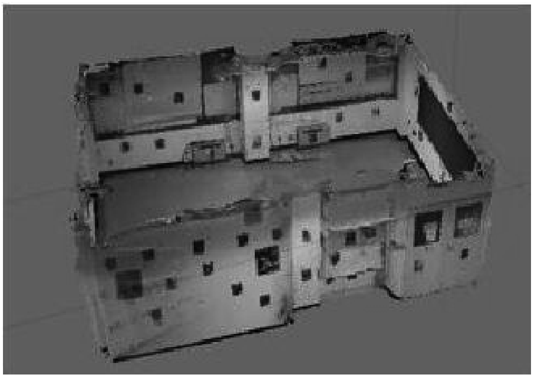

Figure 3: Room model

A quantitative analysis of accuracy was investigated by comparing the actual dimensions of a simple object with the modeling results. Results show error within 2%, which indicates that photogrammetry can achieve high accuracy on modeling simple objects.

4 3D model construction of seminar room

For the whole room modeling, we divided the room into two parts and rebuilt each part respectively then connected them to a whole model. We put flyers on the walls, blackboards, cabinet and other objects without texture like Figure 2. We stood at several positions spaced 20cm along the middle line of the room, and at every position, we took photos continuously while rotating the camera 180 degrees. And about the blind spots like the side part of cabinet, heaters and others, we took photos focusing on them. Finally, we took 246 photos with average image quality 0.9.

The textured room model is shown in Figure 3. Cabinet and blind spots could not be modeled well. Places without texture or flyers were blank especially high places. Floor has a big hole on the middle. We consider that photos taken from blind spots were not continuous with other photos, so the overlapping rate is low. And the shadow and light reflect of metallic objects influence the construction of cabinet and blind spots.

About the accuracy of the room model, we compared the dimensions of the blackboard, door and the whole room in the generated model with the actual dimensions measured using Cloud Compare. Although the errors are larger compared to the simple box, it is within 6% error. Figure 4 shows the roughness of the room model. For each point, the ’roughness’ value is equal to the distance between this point and the best fitting plane computed on its nearest neighbors. Because we do not know the actual surface roughness, we could not calculate the absolute error. But the surface of the blackboard is smooth, an its roughness should be less than 1cm. We can see from the Figure 4 that color green indicates the roughness of 1.7cm, which is much larger than 1cm. The surface of the blackboard is not smooth. Thus, the accuracy of the roughness is low.

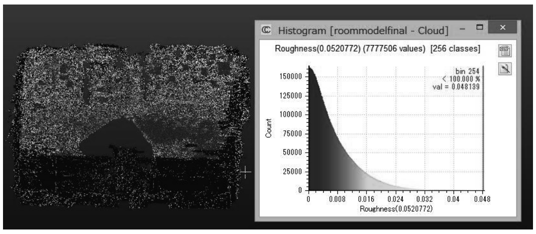

Figure 4: Roughness of the room model

By photogrammetry, the scale of the room can be constructed accurately, so it can be used in radio wave propagation simulation like ray tracing which will not be influenced by the surface roughness error. But simulations which are highly dependent on roughness can not be applied. For example, simulations of radio wave scattering from object surfaces, and power attenuation caused by surface roughness. Thus further processing is needed to improve the accuracy of the roughness.

5 Conclusion

In this thesis, we examined factors that have influence on the modeling and we used the findings to build a 3D model of a seminar room. The results show that for a simple object, the accuracy of model is quite high. For a whole room, the scale can be constructed correctly, but the roughness shows large error. Thus the model can be used in simulations that are not influenced by surface roughness, such as simple ray tracing simulations.

References

[1] W. Elhassan ”3D Modeling of Indoor Building Geometry Using Unmanned Aerial Systems” , Concordia University, March 2016

[2] Linda G. Shapiro and George C, ”Computer Vision. Prentice Hall”, ISNE 0-13-030796-3, B-1-8, 2001

[3] Joanna A,S “Evaluation of algorithms and tools for 3D modeling of laser scanning data”,Norwegian University, June 2014 .

都市におけるミツバチプロジェクトが地域に与える環境・社会的影響

学籍番号：13_04475　氏名：神田大樹　指導教員：阿部直也

1. 研究の背景

ポリネーターが人類に与える恩恵は様々であるが、近年の都市の拡大が原因の一つとなりポリネーターの減少が懸念されている。しかし、都市環境内でもミツバチをはじめとするハチはポリネーターとしての恩恵を、都市環境内の植物、都市農業にもたらしうることが多くの研究で確認されている（Colla, Willis, & Packer, 2009)。これにより、都市内でミツバチを飼育することでハチミツの生産以外にも、都市農業や屋上緑化の恩恵の向上、都市環境の改善が期待される。実際にニューヨークやロンドンなどの世界各都市内で、ビル屋上などでミツバチを飼育しハチミツなどを生産する養蜂活動が確認されている。日本では趣味養蜂の他にミツバチプロジェクトと呼ばれる「都市域において、団体が実施する環境保全活動などの目的を持つ継続的な養蜂プロジェクト」が確認されている(山田，曽根，古谷，2011)。この活動は 2006 年に銀座で始まり、日本各地の都市へ広がりを見せている。

2. 研究目的

本研究は、第一にミツバチプロジェクトへボランティアや会員として参加している社会人、実施団体へのアンケート調査を通じて、ミツバチプロジェクトへ参加した動機、ミツバチプロジェクトによる都市への恩恵（環境的影響)、参加者の意識変化（社会的影響）を調査し、第二にその実態を把握するとともに今後新たに発足するミツバチプロジェクトの実施方向性を提示することを目的とした。

3. 研究手法

本研究では 2006 年に開始した銀座の「銀座ミツバチプロジェクト」に参加している同プロジェクトの参加者と実施団体を、2008 年に開始した自由が丘の「丘バチプロジェクト」の参加ボランティアと実施団体を研究対象としてアンケート調査を行った。銀座ミツバチプロジェクトでは全会員数が不明であるため 2017 年 12 月 8 日に紙パルプ会館で行われた菜の花交流会にて集まった会員ならびにスタッフ 24 名中 18 名にアンケート票を配布、丘バチプロジェクトでは 2017 年 12 月 19 日に参加している全ボランティア 9 人と実施団体の自由が丘商店振興組合の職員 10 人にアンケート票を配布し、回収を郵送形式で実施した。本研究のアンケート票では養蜂活動の参加頻度(Q1-1)、農業・緑地活動の参加頻度(Q1-2)、参加動機「ミツバチの保全(Q2-1)」「環境貢献(Q2-2)」「地域貢献(Q2-3)」「食べ物づくり(Q2-4)」「地域交流(Q2-5)」、ミツバチとの接触の頻度(農業緑地活動場所：Q3-1、地域内の公園：Q3-2、地域の街中：Q3-3)、ミツバチプロジェクトの都市への恩恵の認識「植生の向上(Q4-1)」「農業・緑化活動の活性化(Q4-2)」「地域のブランド化(Q4-3)」「地域の注目度の増加(Q4-4)」、ミツバチプロジェクト参加後の意識変化「生物や植物(Q5-1)」「地域の活性化(Q5-2)」「地元で取れた食べ物(Q5-3)」を回答してもらい、調査結果を分析した。

4. アンケート調査結果並びに分析結果

アンケート票の回収結果は 2018 年 1 月 9 日時点で、23 件であった（回収率：23/37、自由が丘 13、銀座：10)。そのうち無効票は 1 件、欠損値が含まれているものは 4 件であった。図 1 はアンケート調査結果のうち参加動機の集計結果であるが、図 1 では、ミツバチの保全や環境への貢献が参加を後押ししている動機であると答えた回答が多いことが確認できる。このことから参加動機の観点から環境的活動の側面が強いことがわかる。またアンケート調査結果からアンケート票の各質問事項 2 つを選択して作成したクロス集計表で、フィッシャーの正確検定を行ったところ、「ブランド化(Q4-3)」が養蜂活動（Q1-1）と農業・緑地活動（Q1-2）の活動頻度、多くの参加動機と強い関係性を示し（表 1)、養蜂活動の頻度（Q1-1）と公園や街中でミツバチを見ること（Q3-2、Q3-3）が生物や植物への意識変化（Q5-1）と強い関係性があった(表 2)。図 2 は農業・緑地活動の参加頻度(Q1-2)、農業・緑地活動場所におけるミツバチとの接触の頻度（Q3-1)、農業・緑化活動の活性化(Q4-2)を係数とした多重対応分析の結果であるが、他の質問項目と比較して高い農業・緑地活動の参加頻度（Q1.2.1)、高いミツバチとの接触頻度（Q3.1.1)、実感を伴った都市農業の活性化（Q4.2.1)が互いに近くにプロットされていることが確認できる。

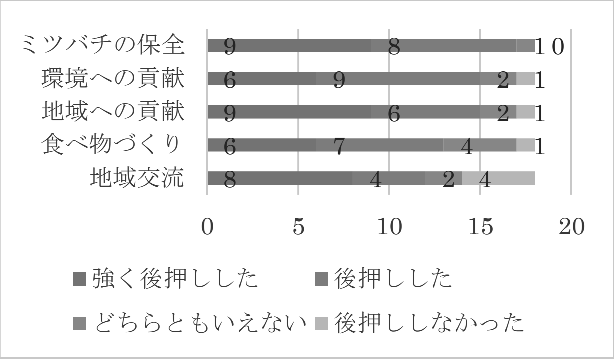

図 1　参加動機

表 1　参加動機とブランド化、注目度の認識

変数 1	変数 2	P 値
Q1-1	Q4-3	0.08
Q1-2	Q4-3	0.002
Q2-3	Q4-4	0.02
Q2-4	Q4-3	0.01
Q2-4	Q4-4	0.005
Q2-5	Q4-3	0.008

表 2　ミツバチと生物、植物への意識変化

変数 1	変数 2	P 値
Q1-1	Q5-1	0.07
Q3-2	Q5-1	0.04
Q3-3	Q5-1	0.01

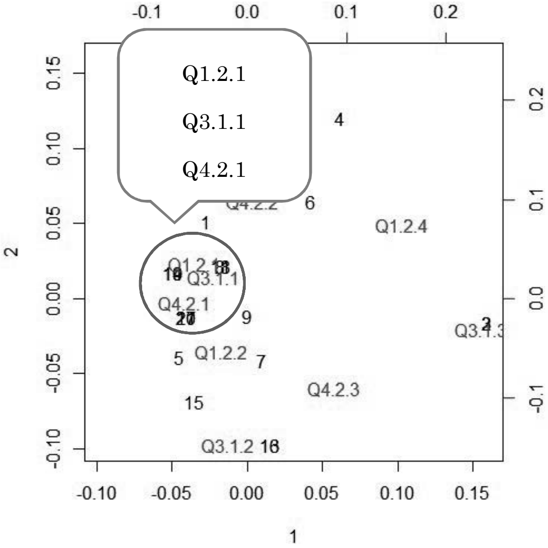

図 2　多重対応分析の結果

5. 結論

研究対象としたミツバチプロジェクトでは、第一に、ミツバチプロジェクトへ参加したことによる意識変化において、ミツバチとの接触や養蜂活動への高い頻度の参加が、生物や植物への関心を高めていると解釈できた。また第二にアンケート集計結果から参加動機においては環境的思考が確認できた、が参加者が認識する恩恵の中で地域ブランドの向上と地域の注目度の上昇が多くの参加動機と有意な関係性があり、かつ認識する恩恵の中で養蜂活動と活動頻度と有意な関係性、または比較的強い関係性があったのは地域ブランドの向上だけであったことを確認した。このことから、都市内におけるミツバチプロジェクトが都市のイメージや独自性を向上しているといえよう。

6. 提言

商業都市のミツバチプロジェクトにおいて、第一に養蜂活動のみならず、都市域でミツバチを観察できる環境を整えることで、啓もう的効果をより大きくすることができる。第二に、都市域においてミツバチプロジェクトは環境的活動として開始し、その後地域ブランドに関連する人々が潜在的な参加者となることを本研究の提言とする。

謝辞

アンケート調査にご協力居てくださったミツバチプロジェクトの皆様に感謝申し上げます。

参考文献

Colla, S. R., Willis, E., & Packer, L. (2009). Can green roofs provide habitat for urban bees (Hymenoptera: Apidae)? *Cities and the Environment (CATE), 2*(1), 4.

Riza, M., Naciye , D., & Mukaddes , F. (2012). City branding and identity. *Procedia-Social and Behavioral Sciences, 35*, 293-300.

愛甲哲也, 庄司康, 栗山浩一. (2016). 『自然保護と利用のアンケート調査―公園管理・野生動物・観光のための社会調査ハンドブック―』. 築地書館.

山田順之, 曽根佑太, 古谷勝則. (2011). 都市域の自然体験活動としてのミツバチプロジェクトに関する研究. ランドスケープ研究, 74(5), 585-590.

Visualization Of Indoor Radio Wave Propagation By Using Augmented Reality Technology

Student Number: 14B09889 Name: JIAYUE CHENG
Supervisor: Supervisor: Jun-ichi TAKADA Assistant Professor: Kentaro Saito

2018/2/23

1 Introduction

The wireless communication is playing an essential role in information transmitting nowadays. While because of the radio wave is invisible, it is difcult for users to estimate the radio wave distribution in the room without device.[1] The focusing point of this thesis is to visualize the radio wave by using the mobile device, and enables the user know about the distribution situation of the radiowave in the surroundings. The augmented technology is utilized in this thesis. Augmented reality technology overlays the digital object onto a persons perceived reality, and integrates the virtual world with reality.[2] In this thesis, an augmented reality (AR) application is developed to exhibit the radio wave distribution in the indoor environment. The research divides into two parts: the establishment of the application, and the conduction of the demonstrate experiment. For the establishing part, in an indoor environment, the radio wave propagation is calculated by ray tracing method and then show the distribution detail in the vertical view graph. Then using the result data, and develop an AR application by Unity 3D software. After the establishment, an experiment is conducted in the S6-102 room in Tokyo Institute Technology University to demonstrate whether the application is running successfully. Moreover, using augmented reality in the application, accuracy errors may occur. Finding the accuracy errors in this AR application is another target of the experiment.

2 Analysing And Design

The ray tracing method is used in analyzing the radio wave propagation. The Fig.1 shohws the vertical view of the room S6-102 in Tokyo Institute Technology University. In Fig.1 Tx indicates transmitter, Rx indicates the location of the receiver, and the distance between them is 3m. The width, length, and height of the room are 4.8m, 7.6m and 3.0m respectively. The room S6-102 is considered as a simplied indoor environment with only direct ray and rays reected once off the walls are considered.

The next step is to establish the AR application by unity 3D. As the invisible radio wave signal propagates in straight direct rays, arrows can be used to represent the rays. The direction of the arrows shows the propagating direction of the rays. Then insert the pose information of the 'rays into the Unity 3D.

The Unity 3D software creates a virtual world in the computer, tracking the characteristic points of the environment and create a 3D model of the environment. Then add the 3D model of the object, which does not exist in the environment, to the environment model. This process is the way augmented reality works. To develop an application in Unity, though the reality pose of the rays is calculated by ray tracing method, the information should match to the virtual information in Unity. To coincide the scale of the virtual world and the reality, experiments are needed to test the direction of each axis. As a result of an experiment, it can be found that in the x-axis, the left is the positive direction, y positive is up direction, and z position is from the real environment to the camera direction.

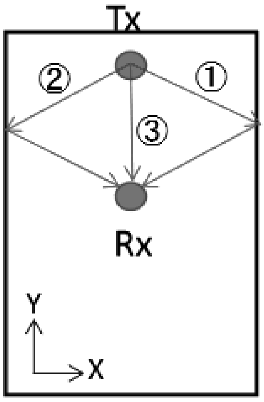

Figure 1: Vertical view of the radio wave propagation in room S6-102

Another topic is that in the unity 3D, units is used as a measurement, but it is reference. [3] However, the position of the rays needs to be input into the unity in units. So another experiment is established to test the matching relation between the real distance and virtual distance. In this experiment, a sphere is put in the tracking point, and at the same time an arrow is put in the unity position of (200, 0, 0) then conduct the application in room S6-102. The distance between the sphere and the camera is decided to be 3m. The result is showing in Fig.2.

Test the real distance between the sphere and the arrow, and the distance is about 0.46 m. In another word, by calculating, we can found the relation between unity units and meters is about 1 meter $\approx$ 434.8 units.

3 Result

In the experiment, if the transmitters position is considered as the zero point, the position of the rays (I named

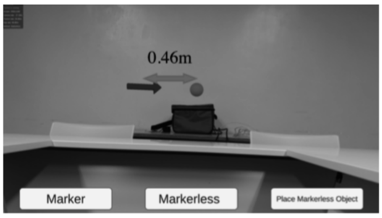

Figure 2: Experiment of reality distance to camera distance

them from 1 to 4)are(1.25, 0, 0.75), (1.25, 0, 2.25), (-1.25, 0, 0.75), (-1.25 ,0 ,2.25) respectively. Using the result from the last experiment that 1 meter ≈ 434.8 units, we can decide the virtual position of each ray, the virtual position is showing in the below Fig.

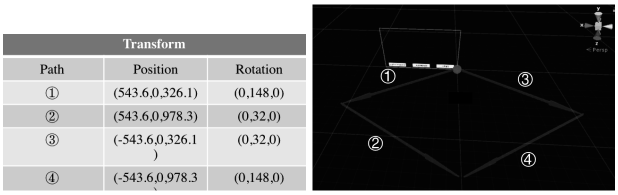

Transform		
Path	Position	Rotation
①	(543.6,0,326.1)	(0,148,0)
②	(543.6,0,978.3)	(0,32,0)
③	(-543.6,0,326.1)	(0,32,0)
④	(-543.6,0,978.3	(0,148,0)

(a) Unity pose information of rays (b) Names of the rays

Figure 3: Information of rays

Then create the radio wave model(arrow model) in the unity, the name of each ray is shown in the Fig.3.

Finally, main experiment is conducted in room S6-102, and the result is showing in the Fig.4. below.

(a) Front view (b) Left view (c) Right view

Figure 4: Main experiment result

4 Analyse

However, in the experiment, the rays are not correctly fixed to the point where it should be. As it said above, accuracy errors occur. When moving around in the environment, the ray model shows the trend of unstable. After changing the direction of the camera to observe the rays in other angle views and then moves it back towards the original direction, position shifting of the receiver can be observed in the application. To analyze the phenomenon further, two attempts are tried to make the phenomenon concrete. First running the application, and record position of the receiver, then rotate the camera to other angles, and move it back, then record the position shifting of the recevier again. Next, try the experiment again after moving the camera in parallel.

Record the results of the receiver shifting before and after the camera rotation and movement. It can be found that the receiver position changes respectively. To analyze the shifting in detail, the shifting data CDF is shown as bellow Fig.5.

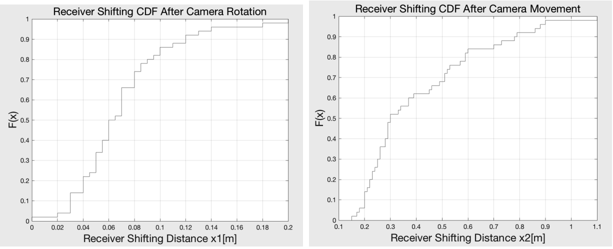

(a) Receiver shifting CDF after camera rotation (b) Receiver shifting CDF After camera movement

Figure 5: Receiver shifting before and after the movement of the camera

In these two attempts of the experiment, it can be found that the position of the receiver changes indeed after rotating the camera but 90 percent of the shifting is under 0.12m . However, after the moving of the camera for some distance, the 90 percent of recevier shifting is under 0.8m, and which is much bigger than that after the rotation. It can be conrmed that the movement of the camera influent the stability of the receiver, and the form of the camera movement inuence the receiver shifting in different degree. This occurs because of the usage of the gyro sensor. The gyro sensor measuring the orientation and react to the rotation of the camera, while it doesn't correspond well to the translation.

5 Conclusion

An AR application aiming at the visualization of the indoor radio wave propagation is developed. In the final experiment, the radio propagating distribution showed successfully on the screen, but some accuracy errors are observed in the process as well. After the camera moves, the shifting of the receiver can be observed in the application. Because of the distance between the transmitter and the recevier is 3 m, the shifting after camera movement is so significant and cannot be ignored. In the future, other sensor like distance sensor can be tried to improve the accuracy of the application.

References

[1] Cem Sahin, Danh Nguyen, Simon Begashaw *"Wireless communications engineering education via Augmented Reality Frontiers"* Education Conference (FIE), 2016 IEEE

[2] H Ridho Rahman, Darlis Herumurti, Imam Kuswardayan *"Location basedaugmentedrealitygameusingKudanSDK"* Information CommunicationTechnologyandSystem(ICTS),201711thInternational Conference on

[3] Cem Sahin, Danh Nguyen, Simon Begasha *"Unity Technologies* https://unity3d.com/cn/

WAVELET BASED IMAGE CODING VIA PREDICTION USING NEURAL NETWORKS

Department of International Development of Engineering
Student Number: 14B08878 Name: Takuma TAKEZAWA Supervisor: Yukihiko YAMASHITA

1 Introduction

Recently, by the development of multimedia terminals, a large amount of information is produced every day. It causes the problems such as the shortage of memories. Thus, the methods to reduce the data redundancies have been investigated. For example, image compression technique such as JPEG and JPEG2000 have been developed.

JPEG is one of the most popular methods for image compression. It is useful but still has a problem called block distortions. As a method to solve the problem, the wavelet-based image coding was invented. Zhou, *et al.* proposed to introduce the predictive coding into wavelet-based image coding [1]. They used linear prediction with clustering as a prediction method.

In this research, I propose to apply the artificial neural network to the prediction part and conduct experiments to evaluate the proposed method.

2 Image Coding

2.1 Wavelet Based Image Coding

Wavelet-based image coding is one of the image compression methods using discrete wavelet transform (DWT). Wavelet transform is a method to analyze signals and divide them into different frequency components. Because digital images are discrete signals, the DWT is applied and the amount of data can be reduced by encoding the coefficients.

Since this method treats the target signals as one of the waveforms, it is usually called waveform coding.

2.2 Predictive Coding

Predictive coding focuses on the correlations between adjacent signals. For example in natural images, neighboring pixels tend to be positively correlated because natural image shapes extend over finite spatial regions [2]. And the goal of predictive coding is to reduce redundancy by removing the predictable components from original signals.

2.3 Prediction using Neural Networks

The artificial neural networks (ANN) is a learning system inspired by the biological neuron structure in natural animals' brains. The main goal of ANN is to learn a model between inputs and outputs. A standard ANN consists of many simple, connected processors called neurons, and each produces a sequence of real-valued activations [3]. Input neurons get activated through sensors perceiving the environment, and other neurons get activated through weighted connection from previously active neurons. The learning of ANN is to find weights that make the network exhibit desired behavior.

In this research, ANN is used to predict the true value of target pixels. That is, the goal of this task is to make a function which outputs the desired true value from inputs. In this research, outputs are the values of target pixels, and inputs are the values of their neighboring pixels that have been decoded.

In order to solve this problem, I applied the feedforward neural networks (FNNs). It consists of a number of neurons and several layers. Each unit among the layers is connected one by one, and each connection has its weight. Generally, these units are called nodes.

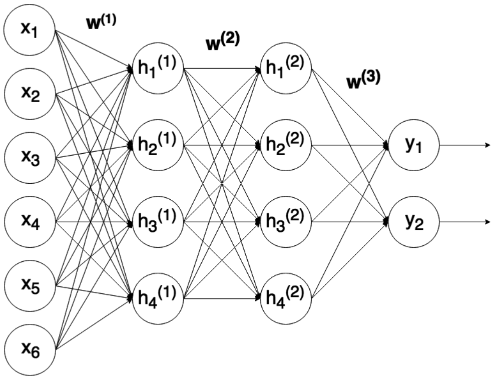

Figure 1: Feedforward neural networks

Figure 1 illustrates a feedforward neural network. In this system, information is inputted from the layer of the leftmost (input layer), and it gets activated with weights in each connection and propagates among the layers from left to right. The model is validated by errors between the calculated outputs and desired values. Usually, the error is expressed by so-called loss function. For the loss function, mean squared error (MSE) or cross entropy error (CEE) is used in general. They are applied depending on the problem to be solved. A learning process is continued until the loss function outputs the desirable results.

3 Experimental Results

I used 3 standard images as test data (Fig 2), and 14 standard images as training data. To evaluate the data size of compressed images, bit rate, the amount of bits per one pixel is used. Then, the less the value is, the more effective the method is.


Lenna Barbara Intersection

Figure 2: Test Data

For prediction, I extracted blocks of the pixels, whose size is 6 × 3, from the training images. And I iterated the calculation 10,000 times for every learning process.

Table 1: Bit rates for different training data

Training Data	Lenna	Barbara	Intersection
w/o Prediction	1.861	2.298	2.169
n1	2.221	2.569	2.334
n2	3.085	3.391	2.947
n3	2.952	3.269	2.862
n4	2.930	3.273	2.889
n5	2.741	3.091	2.731
n6	2.364	2.743	2.480
n7	2.981	3.324	2.916
n8	3.249	3.506	3.012
n1-n8	2.773	3.117	2.705
n1-n14	2.184	2.519	2.277

Table 1 shows the results of this experiment. Those values express bit rates for compressed images when the same quantized factor is used. And Figs 3, 4 and 5 show the coding efficiency. But obviously, the best result is given by without prediction. It implies that the prediction is not precise.

Among the results except without prediction, the best one is produced when 14 images are used as training data at the same time. That is, by using several images for learning, the generalizing ability of ANN was improved.

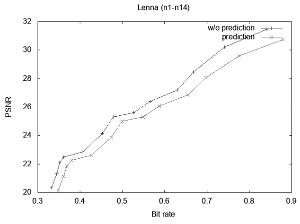

Figure 3: Rate-distortion curve for Lenna

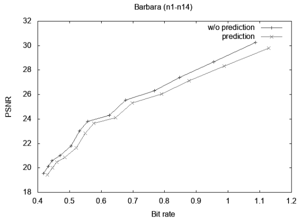

Figure 4: Rate-distortion curve for Barbara

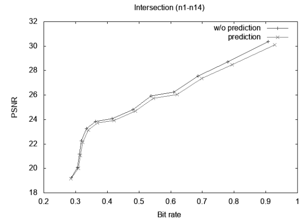

Figure 5: Rate-distortion curve for Intersection

4 Conclusions

In this research, I proposed to use ANN for a prediction part of wavelet-based image coding via prediction. And the desired goal of this research was the reduction of the amount of data by using prediction. However, as a result, any type of ANN just increased the amount of data.

As a future work, it is necessary to enhance the generalizing ability of ANN. In order to improve ANN, I considered the following attempts. For example, I change the hyperparameter of the network such as the number of hidden layers, nodes, and iterations have to be changed. To confirm the validity of the network, cross-validation have to be applied, more images have to be used for training data.

References

[1] Shiyu Zhou, Yukihiko Yamashita, "Image Coding using Discrete Wavelet Transform Decomposition with Prediction of Half-pixel Line Segment Matching", Proceedings of Picture Coding Symposium of Japan, no.27, 2013

[2] Yanping Huang, Rajesh P.N. Rao, "Predictive coding", Wiley Interdisciplinary Reviews: Cognitive Science, vol 2, pp.580-593, 2011

[3] Jrgen Schmidhuber, "Deep learning in neural networks: An overview", Neural Networks, vol 61, pp.85-117, 2015

Equilibrium Adsorption of Manganese Using Mordenite

Student Number: 10_18887, Name: Shunya Hattori, Supervisor: Ryuichi EGASHIRA and Hiroaki HABAKI

1. Introduction

The acid mine drainage is acidic wastewater containing heavy metal sulfates, generated through the oxidization of metal sulfides at the surface of mineral deposit with water or air, and polluting the ecological systems. To improve this environmental issue, the treatment of the acid mine drainage with natural zeolites has been studied. However, natural zeolites generally contained several metal ions and so on as impurities to make adsorption equilibrium more complicated. [1] [2]

In this study, commercially available synthetic zeolite of Mordenite was used as adsorbent and the adsorption equilibrium was measured to treat with the model acid mine drainage containing manganese ion.

2. Experimental

The synthetic zeolite of Mordenite was used, purchased from Wako Pure Chemical Industries (HS-690, Powder, Hydrogen Mordenite). To measure the cation exchange capacity (CEC) of the zeolite, 4g of zeolite was contacted with 30mL of 1M aqueous ammonium acetate (NH_4OAc) solution and shaken for 5 minutes. After phase separation using centrifuge, fresh 30mL NH_4OAc solution was added to the solid phase and this operation was repeated 10 times, based on the Method-9801 by the US Environmental Protection Agency. **Table 1** shows the conditions of adsorption equilibrium measurement. In advance, the zeolite was kept at 383K for more than 24 hrs in order to dehydrate. The solutions were prepared by dissolving $MnSO_4 \cdot 5H_2O$ and deionized water. The specified amounts of zeolite and solution were contacted at 300 K for 240 hrs to be equilibrated.

The liquid phases were analyzed by *p*H meter(Horiba,F-74) and ICP-AES(SPS7800, SII Nano Technology) to determine the *p*H and metal concentration, respectively.

Table.1 Experimental condition of Batch adsorption

*p*H of feed solution	[-]	2-5
Volume of feed solution	[L]	50×10^{-3}
Initial concentration of Mn	[mol/L]	9.1×10^{-4}-1.8×10^{-2}
Mass of zeolite	[g]	2.5
Contacting time	[hours]	240
Temperature	[K]	300

3. Results and discussion

Material balance of batch adsorption is shown as,

$$C_{i,0}V_0+q_{i,0}\,S_0 = C_iV+q_iS \quad (1)$$

where C_i V, S, and q_i are the concentration of component *i* , volume of the solution, mass of zeolite and adsorbed amount of component *i* per unit mass of zeolite. The subscript of 0 stands for the initial conditions. It was assumed that there was no change in the volume of the solution and mass of zeolite before and after the experiment.

Fig. 1 shows the result of XRD analysis. It was confirmed that the zeolite used was pure mordenite, and there was no other component.

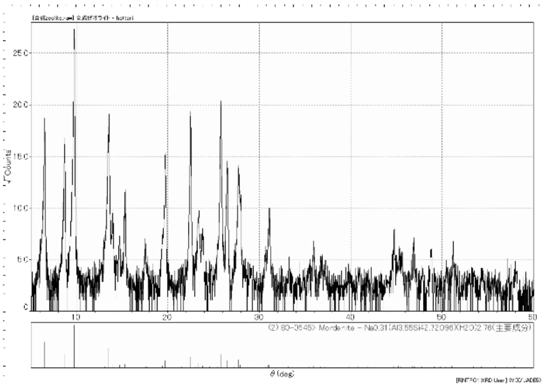

Fig. 1 Result of XRD analysis

Table 2 shows the result of CEC measurement. The CEC of the pure mordenite was lower than that of Bogor natural zeolite. Compared with theoretical CEC of ideal pure mordeite(23×10^{-4}mol/g-zeo),it was lower too [4]. The zeolite was originally treated by acid solutions, and this should lower the CEC of the zeolite [5].

Table 2 cation exchange capacity

	Pure mordenite	Bogor natural zeolite
CEC[mol/g-zeo]	6.94×10^{-4}	8.42×10^{-4}

Fig. 2 shows the changes in *p*H before and after adsorption equilibrium measurement of pure mordenite and Bogor natural zeolite [1] [2]. For the Bogor zeolite, the *p*H at equilibrium become 7-8 which was higher

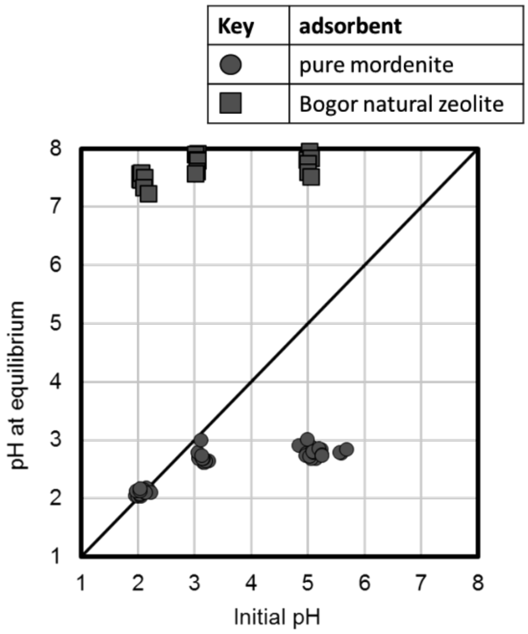

Fig. 2 Change of pH at initial and equilibrium

than initial. For the pure mordenite, the *p*H at equilibrium become lower than initial when intial *p*H were 3 and 5. The *p*H at equilibrium were almost constant, ranged from 2.6 to 2.8 in the cases that the initial *p*H were 3 and 5. The hydrogen ion in the mordenite might have been exchanged with Mn^{2+} ion and this made the *p*H lower. When the initial *p*H was set at 2, the equilibrium *p*H was the same as the initial one. The H^+ concentration was so high that the amount of the H^+ desorbed was negligible.

Fig. 3 shows the molar concentrations of the metal ions at equilibrium, desorbed from the zeolite. Although Na, K, Mg and Ca were detected, their concentrations were much lower than those of H^+ or Mn^{2+} and the effects of these ions on H^+ or Mn adsorption must be small.

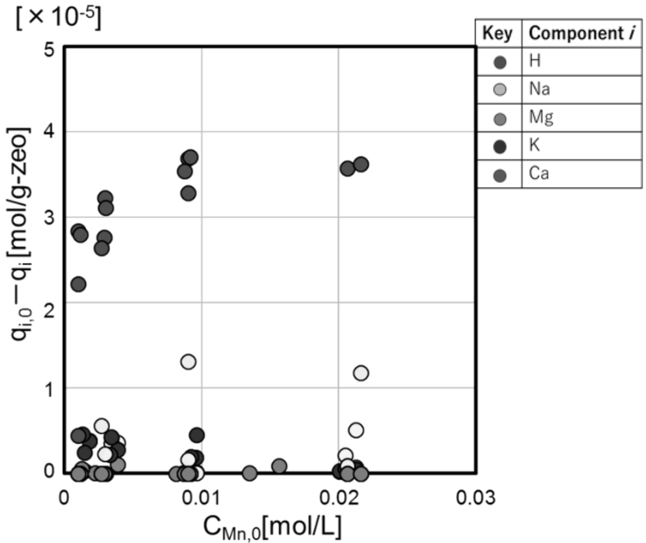

Fig. 3 Concentrations of cations at equilibrium

Fig. 4 shows the charge numbers of the cations due to adsorbed on and desorbed from the zeolite. The charge numbers of adsorbed ion, Mn^{2+}, were almost balanced with those of desorbed ions, H^+, Na^+, K^+, Mg^{2+} and Ca^{2+}. However when initial *p*H=2, the charge numbers were not balanced. This might be because when initial *p*H=2, the concentration changes of H^+, Na^+, K^+, Mg^{2+} and Ca^{2+} were so small, the amount of the desorbed ion could not be appropriately calculated.

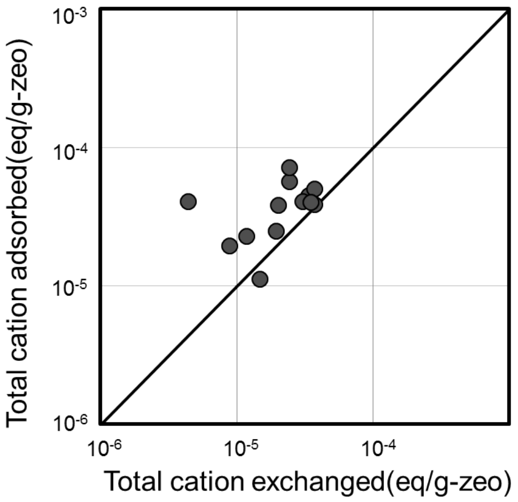

Fig. 4 cation balance of the batch adsorption

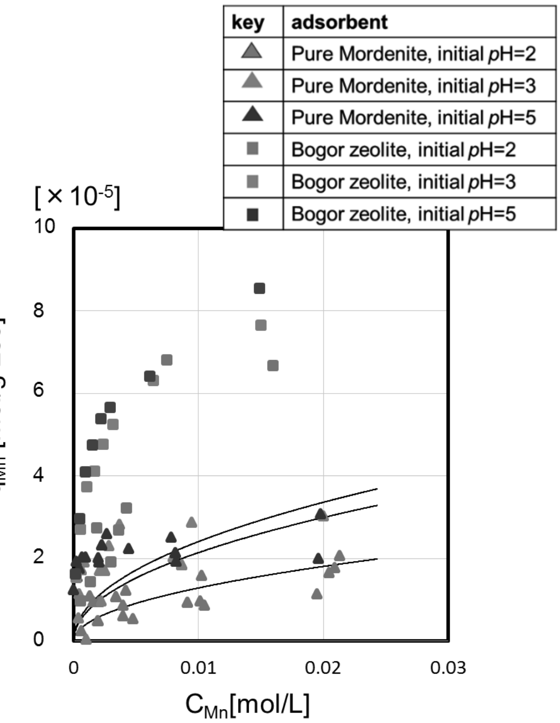

Fig. 5 Adsorption isotherms of manganese

Fig.5 shows the adsorption isotherms of Mn with mordenite and natural zeolite from Bogor[1][2]. The q_i of Mn increased as C_{Mn} and *p*H increased. The q_i of Mn with mordenite were much lower than those with Bogor zeolite. The equilibrium *p*H was much lower with mordenite and H^+ should be competitively adsorbed. In the cases of low initial *p*H, adsorption amount of Mn was lower.

4, Conclusion

XRD pattern showed that the zeolite was pure mordenite and the cation exchange capacity was measured as 6.94×10^{-4} mol/zeo-g. Mordenite could remove the manganese in the solution and it lowered the *p*H. Manganese in the solution was exchanged with H^+ in the zeolite to reduce the *p*H. The initial *p*H of the solution affected the adsorption of Mn and the amount of Mn adsorbed decreased as *p*H decreased. The *p*H at the equilibrium affect the adsorption of Mn due to the competitive H^+

References

[1]Fernando, master Thesis ,Tokyo technology of Institue(2015)

[2]Hasegawa, master Thesis ,Tokyo technology of Institute(2017)

[3]Chapman, H. D.; Chemical and Microbiological Properties, C. A. Black ed., pp. 891–900, U.S.A. (1965)

[4]Nishimura, Journal of the Clay Science Society of Japan, vol13, No1, p23-34(1975)

[5]Sakamoto , The chemical Society of japan,p.874-882(1994)

オセアニア島嶼諸国における水道事業の効率性分析

学籍番号:14B05785　氏名:国分 紘一郎　指導教員:阿部 直也

1.　序論

1.1.　背景

水道事業の整備と運営は世界的に重要なテーマの一つであり、持続可能な開発目標（SDGs）の目標 6「すべての人に水と衛生へのアクセスと持続可能な管理を確保する」に象徴されている通りである。全ての地域[1]で飲み水と衛生施設へのアクセス率が伸びているなか、オセアニアの島嶼諸国だけはその状況が悪化している。2000 年から 2015 年へ、飲み水へのアクセス率は（56%→52%）低下し、衛生施設へのアクセスは(35%→35%)変化していない [1]。オセアニアは島嶼諸国という大きな特徴を持っており、一般的な開発途上国とは性質が異なる。1 つ 1 つの島が小さいことによる資源や人材の不足をはじめ、激しい気候変動による大きな被害、複雑な統治などで、水道事業の整備と運営は様々な困難に直面している。近年はIWRM（統合的水資源管理）という水以外のあらゆる要素を組み込んだ統合的な水資源管理の枠組みが注目されており、限られた資源を有効に活かしながら人々の水へのアクセスを高める必要がある。そのため、各島嶼国の水道事業の実態について、相対的な優位性や課題を客観的に把握することが重要になっている。

1.2.　目的

上記の背景を踏まえ本論の目的は以下 2 点である。

- 各島嶼国における水道事業の運営効率性を比較・評価すること
- 各国の水道事業の実態を定性的な側面から水道事業の発展に必要な方策を提案すること

本稿では、主に第一の目的について記載する。

2.　方法

2.1.　分析対象および使用データ

本研究の分析対象はオセアニア 13 か国とそれらの国における 18 の水道事業者である。各国の情報として①面積②人口③一人当たりの GNI④水の普及率⑤一人当たりの水の消費量を使用した。各水道事業者の情報としては①一人当たりの水の生産量②接続数③1000 接続当たりの従業員数④水の生産コスト⑤NRW[2]率を使用した。

2.2.　分析の手順

水道事業者の効率性を以下の 3 段階で分析する。①と②は定量的に、③では定性的に分析する。

① 主成分分析（PCA）とクラスター分析を用いて対象となる水道事業者が存在する国を分類
② DEA を用いて各水道事業者の効率性を算出
③ ①と②で得られた結果と各種報告書による社会文化的側面を組み合わせてオセアニアの水道事業者をより大局的に評価

2.3.　DEA について

本研究が適用する DEA（Data Envelopment Analysis：包絡分析法）は、複数の入力と複数の出力を伴う財やサービスの生産・提供事業体(Decision Making Unit：DMU)の効率性を評価するための分析方法である。各 DMU の相対的優位性を取り入れた評価が可能である。本研究では最も基本的な CCR モデルを使用した。以下の分数計画問題を解くことでそれぞれの DMU の効率値が得られる。$v_i(i = 1,2,\cdots m)$と$u_r(1,2,\cdots,s)$はそれぞれ入出力につけるウェイトであり、記号 o は n 個の事業体のどれかを指す。式(2)はウェイトv_iとu_rによる入出力の比を全ての DMU について 1 以下に抑えるという意味の制約式である。

$$\max(\theta,u,v)\ \theta = \frac{u_1 y_{1,o} + u_2 y_{2,o} + \cdots + u_s y_{s,o}}{v_1 x_{1,o} + v_2 x_{2,o} + \cdots + v_m x_{t,o}} \qquad \text{式(1)}$$

制約式 $$\frac{u_1 y_{1,i} + u_2 y_{2,i} + \cdots + u_s y_{s,i}}{v_1 x_{1,i} + v_2 x_{2,i} + \cdots + v_m x_{m,i}} \leq 1 \qquad \text{式(2)}$$

$$(j = 1, 2, \cdots, n)$$

$$v_1, v_2, \cdots v_m \geq 0 \qquad \text{式(3)}$$

$$u_1, u_2, \cdots u_s \geq 0 \qquad \text{式(4)}$$

水道事業は多くの場合そのコスト削減に関心があるため本研究では出力を固定した、入力指向型を採用した。

---

[1] 国連によって分類された地域分けに基づく。

[2] NRW（Non-Revenue Water）：収入が得られない水。

3. 結果と考察

対象国を国の規模と水道事業の発展度合いの 2 つの基準で分類した〈図 1〉。PCA で使用した面積と人口が国の規模を示す軸として、またその他 3 つの要素はその国の水道事業レベルを示す軸として解釈ができた。

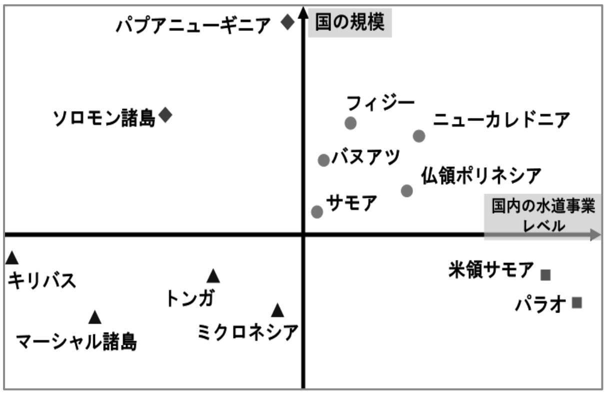

図 1 各国の分類

表 1 各水道事業者の効率値と優位集合

水道事業者	効率値	優位集合
フィジー	1.00	-
バヌアツ	1.00	-
ニューカレドニア	1.00	-
サモア	0.74	Mic.1,Fiji,Van
仏領ポリネシア	0.32	Van, Mic.1, Fiji
米領サモア	0.56	Van, Mic.1
パラオ	043	Mic.1, Mic.3, Fiji
パプアニューギニ 1	0.57	Van, Fiji, Mic.1
パプアニューギニ 2	0.37	Mic.1, Fiji, Mic.3
ソロモン諸島	0.37	Van, Mic.1, Fiji
マーシャル諸島 1	1.00	-
ミクロネシア 1	1.00	-
ミクロネシア 4	1.00	-
ミクロネシア 3	1.00	-
ミクロネシア 2	0.33	Van, Mic.1
トンガ	0.25	Van, Mic.1, Fiji
キリバス	0.08	N.C,Mar.1,Mic.1.
マーシャル諸島 2	0.04	N.C

表 2 グループことの効率値の主要値

	平均値	最小値	最大値
A) 規模大・先進	0.81	0.32	1.00
B) 規模小・先進	0.50	0.43	0.56
C) 規模大・途上	0.44	0.37	0.57
D) 規模小・途上	0.59 (0.18*)	0.04 (0.04*)	1.00 (0.33*)

(*)効率値の高い上位 4 水道事業者を除いたときの値

〈表 1〉は、各 DMU の効率値とその優位集合を示している。フィジーやバヌアツを含む 7 社で効率値 1 を取り、ミクロネシア 1 は 5 社中最も多い 10 社に優位とされ、次いでフィジー・バヌアツは 7 社に優位とされた。ミクロネシア 3 とニューカレドニアは 2 社と、あまり優位にされていないことから個性的な DMU であることが分かった。優位集合の共通点としてどの 5 社も NRW 率が良いことが挙げられる。入力においてミクロネシア 1 とフィジーが NRW に強みを示す一方、バヌアツは従業員数でも強みを持っていた。出力においてはフィジーだけが接続数に強みを持っていた。同じ国でも効率値が著しく異なる DMU について、ミクロネシアは 4 つの州に分かれており、ミクロネシア 1 と 4 は同じ州に存在するが、1 のほうが規模の面でははるかに大きい事業である。4 が他者に参照されない理由もそこにあると考えられる。2 では水道料金を徴収しておらず、水道メーターの故障も頻繁に見られる。2 の効率値が低い理由もそこにあると考えられる。

〈表 2〉は各 DMU をより大局的に見たときの結果である。この表から各 DMU の効率値は国の規模とその国の水道事業レベルの両方に正の相関があることが分かった。理由として面積や人口が大きいと人材や水資源が豊富になることが考えられる。ミクロネシアとマーシャルの効率的な 4 社を除くとその値はより顕著になった。

4. 結論

DEA の結果、全ての水道事業者が NRW を改善する必要があることが分かった。さらに各社で異なるが、従業員数、接続数あるいは水の生産量を改善することでそれぞれの効率値は向上する。DEA 効率値は相対的な効率値である。オセアニア内で効率的であっても、先進国と比べれば効率的と言うことはできない。各社はより効率的な事業を目指すと同時にオセアニア全体としてさらなる効率化に努める必要がある。また、水道事業は技術的側面が全てではない。オセアニア地域は社会文化的な面で他国にはない固有な特徴があり、それが発展の障壁になっていることも事実である。本研究では多くは扱えなかったが、それらを統合したより包括的な分析も必要である。

参考文献

[1] WHO., UNICEF. (2017). Progress on Drinking-Water, Sanitation and Hygiene. UN-Water.

Influence of Speed of Gate Opening in Dam-break Experiment

Student Number: 14_12880 Name: Fumitaka Furukawa Supervisor: Hiroshi Takagi

1 Introduction

The aim of this study is to examine the influence of speed of gate opening in a dam-break experiment. “Dam-break” is a simplistic method to generate a rapid water flow which is induced by releasing water column in the reservoir being held with a gate. This type of experiment is often applied to an experiment with the aim of generating tsunami-like waves. By pulling the gate in a short time, an intensive flow can be generated. However, little attention has been given to the mechanism of the gate in dam-break analysis. In this study, how the gate can affect the flow of water was examined.

2 Numerical Analysis with OpenFOAM

In this study, two types of gate opening were reproduced using OpenFOAM analysis. The first method (Case 0) is to make the gate disappear instantaneously (i.e., without consideration of the transition of opening), and the second one (Case 1) is to control the rate of gate’s opening in accordance with seven different scenarios as shown in Table 1.

In OpenFOAM analysis, interFoam and interDyMFoam were used as solver for two incompressible fluids. The interFoam solver is applied to the model without gate control, while interDyMFoam is applied to the model with gate control. These two solvers are made for analysis of two phase fluid and VOF (Volume of Fluid) method is used for tracking and locating the free surface. The interDyMFoam was adopted because it enables computational meshes to be modified as the time step advances, which is suitable for reproducing the transition of gate opening.

Figs 1 and 2 are the schematic diagrams of each models.

The pulling speed of the gate was calculated using the following sinusoidal function.

$$v = v_0 \sin(\frac{\pi t}{T}) \qquad (1)$$

In the simulation for “with gate model”, totally seven cases have been used, and for each case has unique parameter v_0 and T from (1). The following table shows the combinations of (v_0 , T).

OpenFOAM was also used to calculate water pressure and water velocity for all cases.

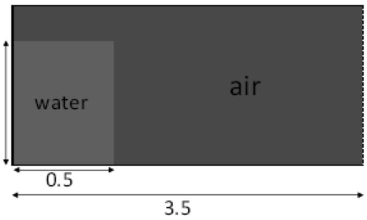

Figure 1 without gate model (unit: m)

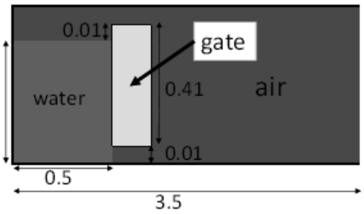

Figure 2 with gate model (unit: m)

Table 1 simulation models

case		(v_0(cm), T(s))	T_{gate}(s)	V_{gate}(cm/s)
w/o gate	case0	-	0	-
with gate	case1-A	(32.5,1.75)	0.9	21.02
	case1-B	(30.0,2.0)	0.95	18.52
	case1-C	(27.5,2.25)	1.05	16.8
	case1-D	(25.0,2.75)	1.1	14.7
	case1-E	(22.5,2.75)	1.2	13.15
	case1-F	(20.0,3.0)	1.25	11.32
	case1-G	(8.2,6.0)	2.3	4.37

3 Results

3.1 The gate condition

In Table 1, T_{gate} indicates the duration for pulling the gate from a static condition till a position high enough. The mean rate of the gate opening, v_{gate}, is calculated by

$$v_{gate} = \frac{x_{gate}}{T_{gate}} \qquad (2)$$

where x_{gate} is the vertical distance over the time of T_{gate}.

3.2 Water velocity

Figure 3 shows the peak velocities at 2.5 m and 3 m from the front of the water column. The difference of water velocity among six cases, 1-A to 1-F, is within ±1%, which are remarkably small compared to those differences with case0. Thus it is considered that a slight difference in the opening speed of the gate does not significantly cause change in flow velocity in the flume. However, compared with 1-G whose gate is opened relatively slow, water velocity of 1-G is about 10% less than the other with gate control cases. Furthermore, velocities differ considerably between with and without gate controls. Water velocity of 1-A to 1-F is reduced by about 15% and that of 1-G is reduced by about 25% in comparison with the scenario without gate control.

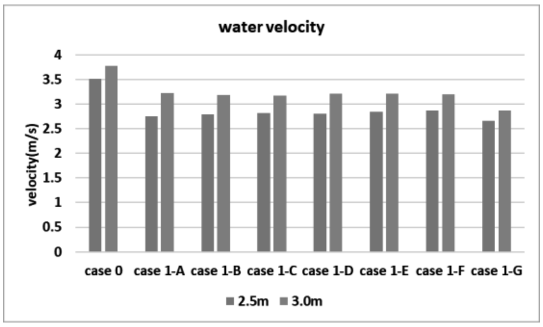

Figure 3 peak of water velocity

3.3 Water pressure

Figure 4 shows the peak of water pressure at every 0.5m point from the front of the water column. Here the horizontal axis and vertical axis denotes the horizontal distance from the gate and the peak water pressure, respectively.

Figure 5 shows the peak pressure without gate control that intersect those of with gate control, focusing on the range from 1.6 m to 2.3 m in Figure 4. The peak pressure of case 1-A to 1-F intersect that of case 0, but pressure peak of 1-G does not intersect it as far as observed in this 3m geometry.

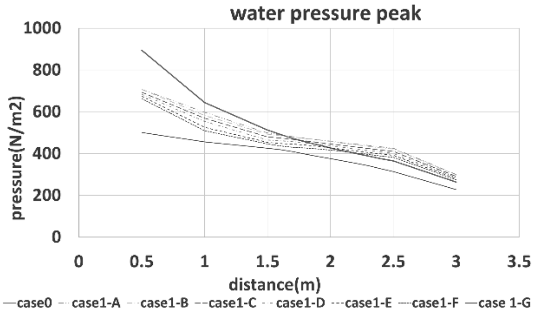

Figure 4 water pressure peak

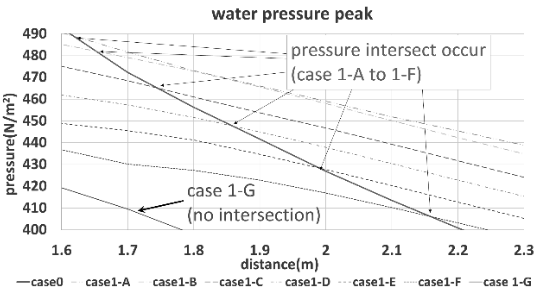

Figure 5 peak of water pressure (extract)

4 Observation

Figure 6 shows the comparison between T_{gate} and X_{equal}. X_{equal} denotes the distance from the front of the water column to the point where the pressure curve without gate control intersects with a pressure curve with gate control.

This figure demonstrates a strong relationship between T_{gate} and X_{equal}, which is confirmed by a high value of R^2 (=0.956). The relationship is represented as

$$X_{equal} = 1.4907T_{gate} + 0.2359 \qquad (3)$$

Although it should have to do with various other conditions such as flume geometry, bottom friction, and discharge volume, these simple fomulas will be beneficial in carrying out a dam-break experiment because water pressures monitored in the experiment can be converted to those without gate control, which is commonly assumed in a numerical modelling of dam-break test.

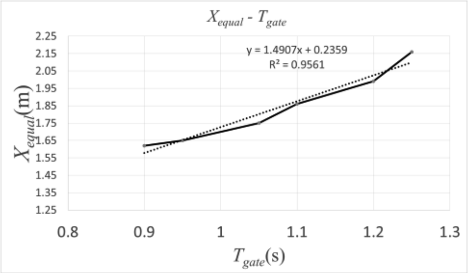

Figure 6 T_{gate}-X_{equal}.

5 Conclusion

It was confirmed that the speed of gate control is one of the influential factors in a dam-break experiment. If the gate speed is considered, water velocity is reduced by about 20% and the pressure become larger than that of without gate control.

References

[1] J.C.Martin and W.J.Moyce “Part V An Experimental Study of the Collapse of Fluid Columns on a Rigid Horizontal Plane, in a Medium of Lower But Comparable, Density” The Royal Society,1952

[2]松田信彦、千田優、岩本浩明、江口三希子、武田将英“電動式スルースゲートを用いた段波造波特性”海洋開発論文集 vol.33,2017

Characteristics of the Users of Residential Photovoltaic and Energy Storage Systems in Japan

Student Number: 14_14146 Name: Hiromichi MITANI Supervisor: Naoya ABE

1. Introduction

Renewable energy is defined as "Energy derived from natural processes (e.g. sunlight and wind) that are replenished at a faster rate than they are consumed" [1], and solar power, wind power, hydropower, geothermal, and biomass are common as renewable energy. The utilization of those energies has become more important as the importance of combating climate change by reducing the consumption of fossil oils has become critical. It is, however, well-know that some of the renewable energy system have their inherent limitations in terms of stable generation of energy, notably electricity. For example, photovoltaic (PV) system highly depends on weather conditions. It is also critical for a grid as a whole to maintain the balance between demand and supply simultaneously. Even for a consumer of electricity, it has become more important to have means to control his/her consumption pattern of electricity as the retail market has been liberalized and now there are more and more options of how people use electricity. Therefore, while we need to defuse more renewable energy systems in a society, we also need to implement some measures to keep grids stable and functional as well as to provide means to consumer who wish to enjoy more flexibilities of how they could use electricity.

Energy Storage System (ESS) is a good measure to promote renewable energy because it can make up for shortcomings renewable energy has. ESS can store surplus electricity that renewable energy generates excessively, and it can release the electricity inside when renewable energy plants cannot generate enough electricity. ESS could provide back-up power when the distribution of electricity is cut due to natural disaster such as earthquakes. Through those functions, ESS will contribute to renewable energy diffusion, mainly for PV systems. However, ESS for households is still too expensive and it diffusion is still at an early stage. Little is known about the motivation of the users who have already purchased or used PV and/or ESS.so that it is important to understand who actually purchased and how they find the systems.

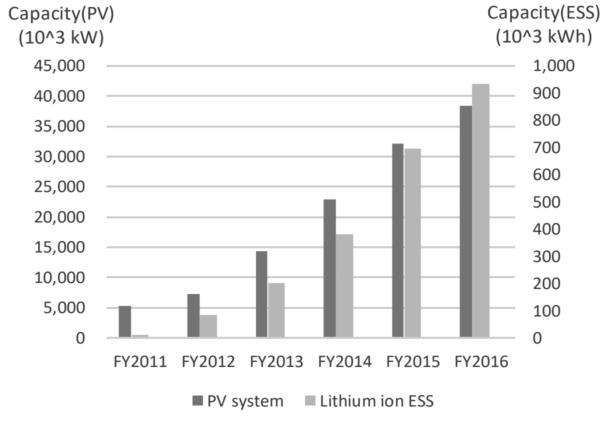

Fig.1: Cumulative capacity of PV and ESS system in Japan (Source; [2], [3])

2. Objective

The objectives of this study are,

1. to clarify how the users of residential PV and ESS systems recognize their own systems
2. to find out any obstacles for further diffusion of PV and ESS at household level

For those ends, the interviewees are selected through an internet-based question, followed by group interviews.

3. Methodology

Internet-based inquiry was sent to the registered tester of a Japanese marketing firm to recruit the interviewees for the group interviews to those who have already installed PV and/or ESS. The flow of the selection of the interviewees was conducted as shown in Fig.2.

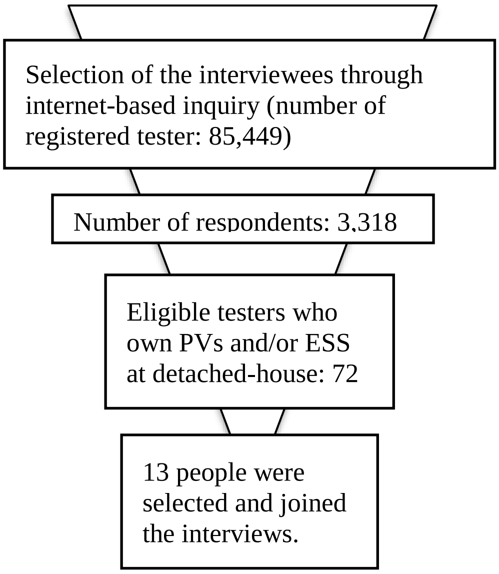

Fig.2: The flow of the selection of interviewees

To clarify the similarity of the invited interviewees, cluster analysis was conducted for the 72 eligible testers. Multiple correspondence analysis was also conducted to clarify the common attributes of the interviewees. By combing the results of the two analyses and the group interviews, this study will obtain findings according to the objectives.

4. Findings

Fig.3 and 4 show the results of cluster analyses of 72 testers who have installed PV and/or ESS system based on the Internet-based questions, and correspondence analysis of interviewees of group interviews who have installed ESS based on paper-based questions in Table.1.

Table 1: Variables used for analysis

Types of Analysis	Variables used for analysis
Cluster Analysis	• Age… (1) • The number of children… (2) • Commute time (one-way) • Working time per day • The number of working days per week… (3) • Annual household income
Correspondence Analysis	• (Variables above) • Economic benefits from PV/ESS… (4) • Degree of satisfaction toward PV/ESS… (5) • Awareness of saving electricity • Sensitivity to electricity rate … (6) • Degree of satisfaction toward current life… (7)

The general findings of the group interviews were summarized as in the following. As for economic benefits from PV/ESS, 9 out of 13 answered they had economic benefits. As for degree of satisfaction toward PV/ESS, 10 out of 13 answered they were satisfied with their own system. Regarding awareness of saving electricity and sensitive to electricity rate, younger interviewees answered they felt it burden more than older interviewees.

As a result of the cluster analysis, the testers were classified into three groups. The interviewees of the group interviews were circled with colors. Seeing the colored circle, it is found that the interviewees were scattered into all groups, not distributed biased. It means that the interviewees of the group interviews were not so biased group. Group I is the group that most of the testers are in the thirties and forties and the average of commuting time and working time per day is very high among three groups, and that all of the testers in this group have their PV system. Group II is the group that the age of the testers in this group is scattered, and that the average annual household income is the lowest, the average number of children is the highest of three groups. Group III is the group that most of the testers are in their fifties and sixties and the average annual household income is quite higher than other two groups.

As a result of correspondence analysis, it was found that the degree of satisfaction toward PV system/ESS, age, the number of children, and attitude to electricity rate was plotted nearly and that the degree of satisfaction towards current life and economic benefits from PV system/ESS were also plotted nearly.

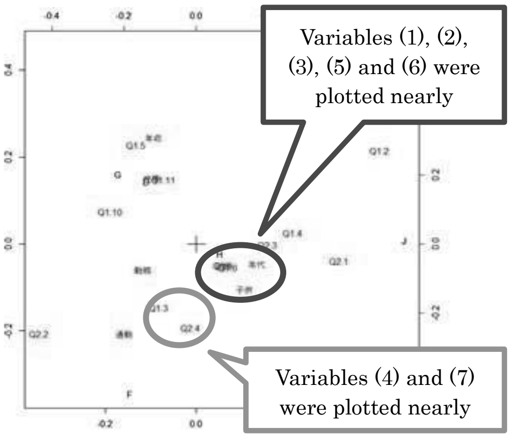
Variables (1), (2), (3), (5) and (6) were plotted nearly

Variables (4) and (7) were plotted nearly

Fig.4: Result of correspondence analysis

5. Conclusion

This study obtained the following conclusions.

1. The users of residential PV/ESS recognized their own systems as good systems, but the benefits they can get from ESS were not so well known as that of PV among those who didn’t have ESS.
2. It was found that the expectation for PV/ESS was different from person’s age, life stage, having children or not, and commuting or not. Thus, for further diffusion of PV/ESS, measures taken it into consideration would be necessary.

References

[1] International Energy Agency. IEA website, FAQs, Renewable energy.

[2] 資源エネルギー庁. (2017). なっとく！　再生可能エネルギー　固定価格買取制度　情報公表用ウェブサイト.

[3] 一般社団法人　日本電機工業会 (JEMA). (2017). 定置用リチウムイオン蓄電システムの出荷実績 2011 年度～2016 年度

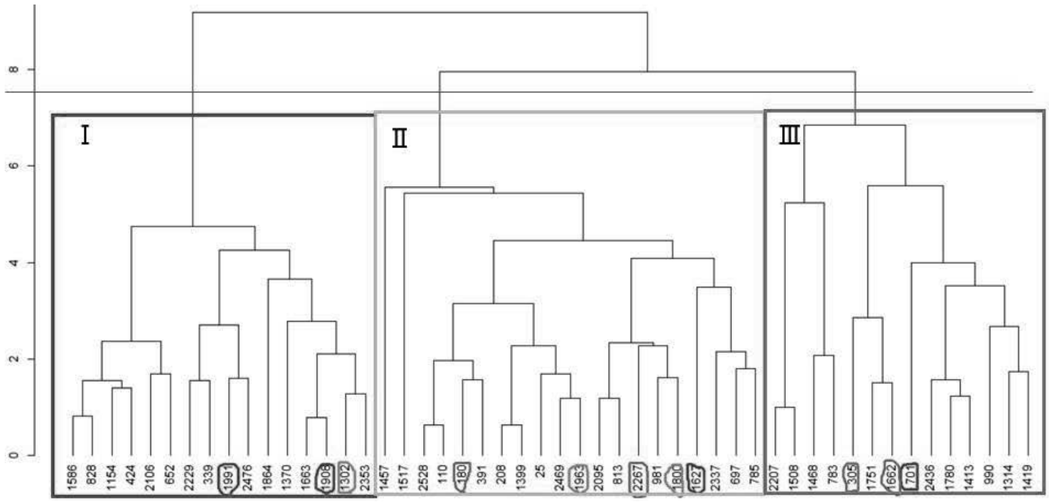

Fig.3: Result of cluster analysis

Possibility of Tethered Aerocapture for direct orbit insertion

Student Number : 14_04099 Name : Saho Kato Supervisor : Daisuke Akita

1 Introduction

Payload mass of a spacecraft is limited by performance of a rocket. The spacecraft has many observation instruments and a lot of fuel to enter into an orbit of planet. In case of Magellan spacecraft, the fuel and thruster occupied 30% of total mass of the space craft[1].

A new way to enter into an orbit around a planet, in stead of a thruster system, is Aerocapture has been studied. Aerocapture uses aerodynamic drag to enter into the orbit. Spacecraft must be equipped with heat shield to protect the payload from heating and force. However, method needs acceleration at apoapsis.

Tethered aerocapture is an alternative way to enter into orbit by using atmospheric drag. This system has an aero-device at the end of tether. In this way, spacecraft needs neither the heat shield nor the thruster.

2 Mission Concept

Figure 1 shows the mission scenario.

① The aero-device is separated from the orbiter with deployment of the tether before entry.

② Deployment of the tether is finished before entry enter into Venus atmosphere.

③ Aerodynamic force begins to affect the aero-device.

④ The orbiter is decelerated by tension of the tether.

⑤ The orbiter cuts off tether when the orbiter finishes deceleration.

⑥ The orbiter goes on elliptical orbit around Venus.

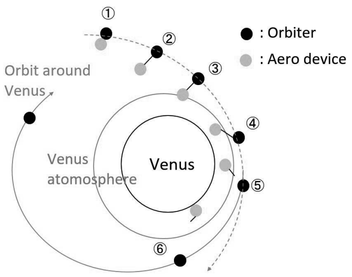

Figure 1: Mission scenario

The purpose of this study is to verify the tethered aerocapture for planetary orbit insertion.

3 Motion Equation and Initial Condition

Motion of the orbiter and the aero device are considered in cartesian coordinate system as shown in Figure 2. Venus gravity, aerodynamic force and tension from the tether act on the orbiter and the aero-device. The motion equation of the orbiter and the aero-device are given by Eq.(1)-(5).

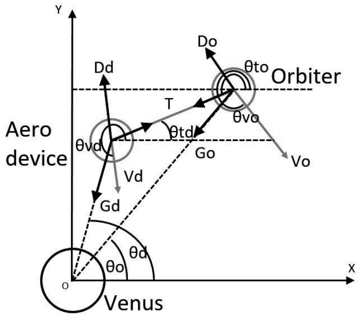

Figure 2: Motion equation model

$$\frac{d^2x}{dt^2} = -\frac{\mu_v}{r^2}\cos(\theta) - \mathrm{D}\cos(\theta_\mathrm{v}) - \frac{\mathrm{T}\cos(\theta_\mathrm{t})}{\mathrm{m}} \tag{1}$$

$$\frac{d^2y}{dt^2} = -\frac{\mu_v}{r^2}\sin(\theta) - \mathrm{D}\sin(\theta_\mathrm{v}) - \frac{\mathrm{T}\sin(\theta_\mathrm{t})}{\mathrm{m}} \tag{2}$$

$$D = \frac{\rho(r)v^2}{2\beta} \tag{3}$$

$$T = k(l - L) \quad (l \geq L) \tag{4}$$

$$T = 0 \qquad (l \leq L \text{ or after tether cut off}) \tag{5}$$

t [s] : time from entry
v [m/s] : velocity of point
μ_v [m^3/s^2] : standard gravitational parameter of Venus
r [m] : distance from center of Venus
θ [deg] : point angle from the X-axis
γ [deg] : velocity angle from the X-axis
α [deg] : tether angle from the X-axis
m [kg] : mass of point
ρ [kg/m^2]: atmosphere density
β [kg/m^2 : ballistic coefficient
k [N] : spring constant
l [m] : distance between orbiter and aero device
L [m] : initial tether length

The equation is numerically calculated by 4th order Runge-Kutta method to estimate trajectory of the orbiter and the aero-device. Initial condition of the orbiter is following values.

m_o [kg] : mass of orbiter, 1000[kg]
H_o [km] : initial altitude of the orbiter, 230 [km]
v_o [m/s] : initial velocity of the orbiter
θ_o [deg] : initial angle of the orbiter, 90[deg]
γ_0 [deg] : initial velocity angle of the orbiter
α_0 [deg] : tether angle of orbiter[deg]

Mass of the aero-device is m_d [kg]. Initial γ_0 of aero-device is same one. Initial condition of the aero-device is given by L, γ, α_0. In this study L, γ, α_0 and m_d are parameters.

4 Trajectory Results

Characteristics of α_0, L, d and m_d are evaluated. In this study, the evaluation criteria are m_{total}(tether mass + aero-device mass)[kg] and corridor $\Delta\gamma$. It is preferred that m_{total} is low and $\Delta\gamma$ is high in their values. In this study, standard parameter are given in Table1.

Table 1: Standard Parameter

parameter		value
α_0	[deg]	90
L	[km]	40
d	[mm]	2.0
m_d	[kg]	100
β	[kg/m^2]	1

When α_0=90 [deg], γ_{min}(γ_{min} means requisite minimum path angle) is the lowest. Because apparent tether length for orbit is the longest when α_0=90 [deg]. It is used that α_0=90 [deg] in following part.

L is changed from 30 [km] to 50 [km] in this part. $\Delta\gamma$ increases with increase of L as shown in Figure 3. Because the longer L is, the lowest aero-device can be got aerodynamic force in initial path angle. But the longer L is, the stronger aerodynamic force is. So γ_{max} is decrease with increase of L. Compared of decreasing of γ_{min} and γ_{max}, γ_{min} decreases more than γ_{max}. And $\Delta\gamma$ increases with increase of L.

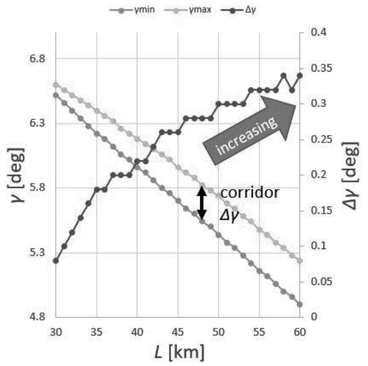

Figure 3: L vs γ and $\Delta\gamma$

d is changed from 1.5 [mm] to 2.5 [mm] in this part. $\Delta\gamma$ increases with increase of d as shown in Figure 4. Because increasing of d, tether can endure strong tension in higher initial path angle as shown in change of γ_{max}. When d is low, tether can't endure tension. So d must be high above a certain value. In conclusion, L and d must be high for getting larger corridor.

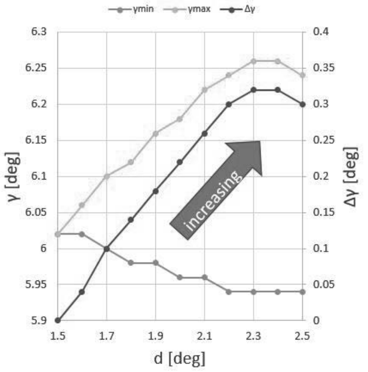

Figure 4: d vs γ and $\Delta\gamma$

m_d is changed from 0 [kg] to 200 [kg] in this part. When L is high, $\Delta\gamma$ doesn't increase effectively with increase of m_d as shown in Figure5. Because Compared of decreasing of γ_{min} and γ_{max}, the change is same. The higher m_d is, the larger S(surface area of aero-device) is. But The higher m_d is, the stronger tension is. In conclusion, m_d isn't effective when L is longer.

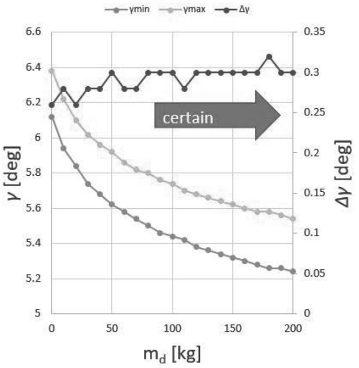

Figure 5: m_d vs γ and $\Delta\gamma$:L=50[km]

In summary, optimum point of α_0 is 90 [deg]. L should be long and d sholud be thick within the limited total mass. m_d isn't effective for getting larger corridor when L is long.

Three limiting conditions on trajectory calculating are considered.

- Minimum altitude of orbiter is above 160 [km] [2].
- Total mass(m_t + m_d) is 363 [kg] or less [1].
- Corridor is 0.1 [deg] or more.

Based on estimation the parameters are set to be α_0=90[deg],m_d=0 [kg] . Figure6 shows corridor with change in L and d. Red area means total mass is above 363 [kg].

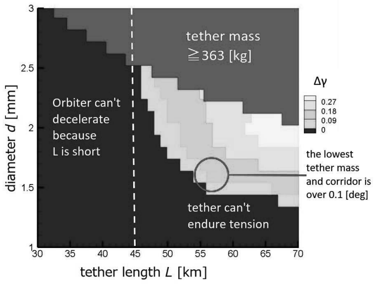

Figure 6: Corridor with changing L and d

Green area means that corridor is over 0.1 [deg]. Tether mass in Figure6 is the lowest when L=57 [km] and d=1.6 [mm]. Tether mass is 176 [kg] which is below that of thruster system.

5 Conclusion

It is shown that tethered aerocapture is able to entry orbit around Venus. Tethered aerocapture may provide mass reductions over thruster systems. A problem of this method is aerodynamic heating on tether. The aero-device could be used as a heat sink to reduce the temperature of the tether.

References

[1] Charles D. Brown. "Elements of Spacecraft Design Charles". AIAA Education Series, 2003, 615p.

[2] Toshio Kawasaki. " 宇宙航行の理論と技術". Tijinshokan, 1986, 347p.

[3] Mary Kae Lockwood and Brett R. Starr. "System Analysis for a Venus Aerocapture Mission". NASA/TM-2006-214291, L-19237, https : //ntrs.nasa.gov/search.jsp?R = 20060010899, (cited 2018-1-17)

TIV APPLICATION TO SIMULTANEOUS MULTIPLE SURFACE OBSERVATION

Student Number: 14B01327 Name: Yoji ISHIBASHI Supervisor: Manabu KANDA, Atsushi Inagaki

1 Introduction

Air flow at the near surface has influence on human lives in terms of pollutant transport or thermal comfort. It is important to understand how the wind blows in pedestrian levels or in urban canyons. However, complex urban building structures make the wind field so complicated. To observe this spatial wind distribution, several observation methods are developed.

PIV (particle image velocimetry) has great contribution to observe 2D wind structure in the building canyon.[1] While PIV should disperse small particles as tracer and using laser to illuminate particles, and it limit to do PIV out or daytime observation.

TIV (thermal image velocimetry) is one of the methods measuring wind field. It can estimate wind velocity at the near surface by tracking the temperature perturbation region from thermal images. This methods applied to wind field on the wall of building or schoolyard covered with artificial turf.[2] Although these observation has great contribute to develop TIV, air flow structure surrounding the building will be limited by the viewing angle of the thermal camera.

TIV has potential to observe real wind flow in the urban canyons. In order to overcome this, simultaneous TIV measurements should be conducted on multiple surfaces.

Objective of this research is to build an inexpensive simultaneous observation system, evaluate its applicability, verify the system by comparisons with numerical simulations or previous PIV observation results, and investigate wind flow around a cube block.

2 COSMO Observation

The observations were implemented at the outdoor urban scale model, COSMO on 13th of December 2017, from 1055 JST. The target block is a cube with a $1.5-\mathrm{m}$ side and made of concrete and covered with styrofoam board with $20-\mathrm{mm}$ thickness(Fig.1). Styrofoam board make the temperature perturbation on the surface large due to its low heat capacity. It becomes easier to catch by the thermal infrared cameras.

The equipments which used in this experiments were thermal infrared cameras, sonic anemomteter and thermocouples.

The thermal infrared cameras which used in this study were Lepton 3 (FLIR Systems, Inc), SC5200-AIT (FLIR Systems, Inc) and FSV-1100-L8 (Apiste Corporation). In order to obtain several thermal image of target from different directions, we need to construct an inexpensive system of thermal cameras, an added originality of this study. Lepton 3 is a core module of infrared camera which adopts uncooled microbolometer. Although it has only lower sensitivity and frame rate than SC5200, it is nuch cheaper and enough for this system. Already tested in TIV, SC5200 adopts cooled Indium Antimonde (InSb) can provide high sensitinity and accuracy with high frame rate but it costs much. FSV1100 is mid-grade of two and it adopts uncooled microbolometer with high resolution. This experiment use 11 Lepton 3 cameras to shoot the target from different directions. SC5200 and FSV1100 were installed to validate the TIV velocity from Lepton 3.

The sonic anemometer MODEL 81000 (R.M. Young Company) was installed at 3 m above ground and 3 m downwind from the leeward facet. 13 thermocouples (Type-E) were attached to the center of each surfaces and floors surrounding the block. Both observations were recorded at 10 Hz.

Fig. 1 Appearance of target block in COSMO

3 Analysis Method

3.1 Data preprocessing

Preprocessing multiple thermal infrared images taken by the thermal cameras were necessary. In particular, filling lacking data and correcting lens distortions were conducted.

Temperature data lacking from the Lepton 3 measurements were complemented by linear interpolation of the nearest valid frames. Then, lens distortion due to close distance from the target was eliminated. Finally, homographic transformation was done to normalize each camera.

3.2 TIV

Multiple thermal infrared cameras provide thermal images of each surfaces. TIV process can be divided into two parts; extracting temperature perturbation and correlation analysis. Averaging time to extract temperature perturbation was set to 0.5 s. Integration domain size is 7×7px(0.26×0.26 m) and search domain size is 8×8px(0.30×0.30 m).

4 Observation Results

The wind was around 3 m s^{-1} northwesterly at the height $2H$. Stability parameter z/L was around 1.39 derived from the data obtained from sonic anemometer, and it indicates stable.

4.1 TIV Vectors

Temperatrue perturbation at the north-facing surfaces was too little to extract perturbation by wind because the intensity was almost same as noise. TIV vectors were derived for southern and top surfaces.

Each surfaces had been taken by two types of thermal infrared camera. TIV wind vectors obtained from one thermal camera shows good correlation with each

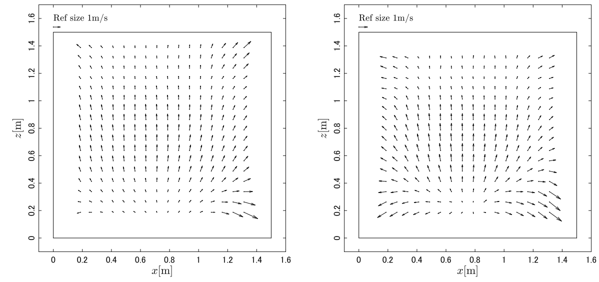

(a) FSV1100 (b) Lepton3

Fig. 2 Wind distribution on leeward surface obtained from FSV1100 and Lepton3

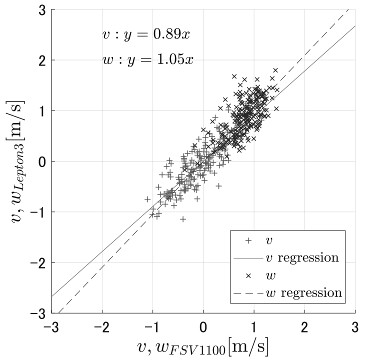

Fig. 3 Correlation of v and w component at the center of leeward surface with 5 s averaging

other (Fig.3).

On the top surface, TIV wind velocity tend to correspond to those obtained from the sonic anemometer. The delay between measurements was about 3 s calculated from cross-correlation. This lag occurs because observed position differed by 3 to 4.5 m. While mean wind speed was about 3 m s^{-1} at the height $2H$, different lag times were observed above the block; wind speed changes above the block at $2H$ propagate surface wind speed with 2 to 3 seconds delay.

On the southeast-facing leeward surface, updraft motion due to the cavity circulation was observed. Largest updraft motion was observed almost center of the surface (Fig.2). According to Uehara[3], under neutral and unstable condition, it appears at or a little above the center of the surface. In general, this shows TIV was successfully implemented using the inexpensive system.

4.2 Sweep and Ejection

In this section, we discuss two patterns in the cavity flow observed by the TIV influenced by sweep and ejection. Sweep and ejection modes can be detected using a sonic anemometer (Fig.4).

Sweep condition ($uw < 0$ $with$ $u' > 0, w' < 0$) occurs in case wind speed above the block become faster. Under this condition, leeward surface updraft is enhanced (Fig.5(a)) and surface temperature decreased (Fig.5(c)). Ejection condition ($uw < 0$ $with$ $u' < 0, w' > 0$) occurs with slower above wind speed. Updraft motion on the leeward surface become little slower (Fig.5(b)) and surface temperature becomes higher (Fig.5(d)).

This is considered that cavity circulation is mainly dominated by the wind speed above the canyon for accelarating or decelarating the circulation speed. Faster circulation enhance heat exchange between the block surface and the air in the cavity, on the other hand, slower circulation doesn't exchange the heat so much, then surface temperature get higher and become unstable condition.

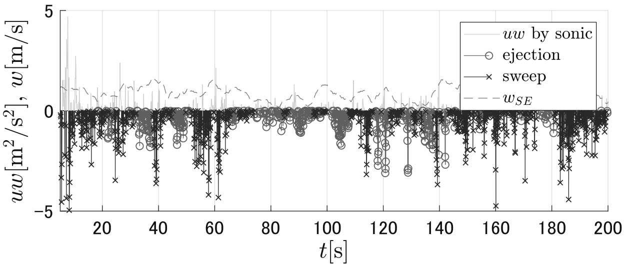

Fig. 4 w and uw obtained from sonic anemometer

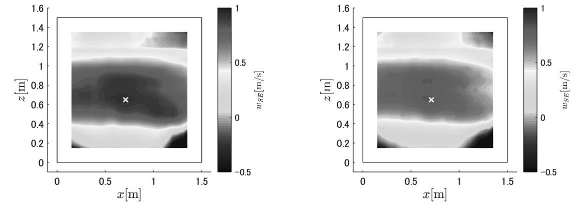

(a) w_{SE} under Sweep mode (b) w_{SE} under Ejection mode

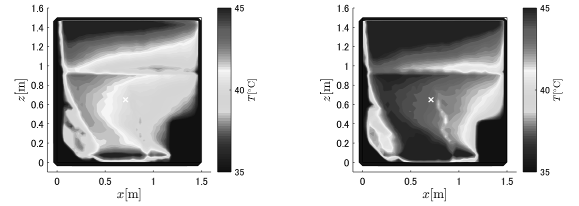

(c) T_{SE} under Sweep mode (d) T_{SE} under Ejection mode

Fig. 5 TIV estimated ensamble averaged vertical motion and temperature distribution on the leeward surface. The 'x' marker indicates the point of the maximum w_{SE} value.

5 Conclusions

This study is the first-ever attempt of a simultaneous TIV application across multiple facets. Here, reliability of TIV velocity estimated from multiple qualities of thermal images and its application to instantaneous phenomena around a block were conducted.

In this paper, we discussed about reliability of TIV velocity from multiple thermal images and instantaneous phenomena.

Multiple thermal images shows similar TIV vectors and wind speed. Under dim conditions, temeperature perturbation wasn't obtained because of the lack of sensitivity of thermal cameras.

Sweep and ejection motion are caused by the large structure above urban canopy layer. TIV confirmed that these motions affect the stability in the cavity.

References

[1] 瀧本浩史, 森脇亮, 津國眞明, 神田学. 屋外都市スケールモデルにおける piv 計測. 水工学論文集, Vol. 52, pp. 259–264, 2008.

[2] Atsushi Inagaki, Manabu Kanda, Shiho Onomura, and Hideaki Kumemura. Thermal image velocimetry. *Boundary-Layer Meteorology*, Vol. 149, No. 1, pp. 1–18, Oct 2013.

[3] Kiyoshi Uehara, Shuzo Murakami, Susumu Oikawa, and Shinji Wakamatsu. Wind tunnel experiments on how thermal stratification affects flow in and above urban street canyons. *Atmospheric Environment*, Vol. 34, No. 10, pp. 1553 – 1562, 2000.

Phytoremediation of aquatic environment polluted by antibiotics

Student number: 14B02692 Name: Shuyang WANG Supervisor: Ryuichi EGASHIRA Hiroaki HABAKI

1. Introduction

Various kinds of antibiotics have been widely used for both human beings and animals to get rid of the bacteria. However, in India, pharmaceutical company discharged wastewater produced during production process with high concentration antibiotics [1-4]. This may cause 2 main problems: the increase of antibiotic-resistant bacteria and the sediment in animals (especially in aquatic animals) and plants through irrigation and soil [5]. Antibiotics being accumulated in animals and plants will enter human body and will lead to the ineffectiveness during a surgery or cure.

Since the last decades, ponds of duckweed(Lemna minor) has been utilized in the removal of nutrients and organic compounds successfully. Then, the utilization of duckweed has been studied in the removal of the organic compounds in water.

This study aimed the treatment of aqueous solution contaminated by antibiotics with duckweed. First, removal of antibiotics in the aqueous solution by the duckweed was measured. Then, the effects of operating conditions on the antibiotics removal was studied to discuss the mechanism of antibiotics removal.

2. Experimental

2.1 Experiment materials

Two kinds of antibiotics were selected, ciprofloxacin (CIP), and sulfamethoxazole (SMX), which are detected in the polluted water in India. Ciprofloxacin is a member of fluoroquinolone that share a bicycle core structure related to the 4-quinolone. Sulfamethoxazole belongs to sulfonamide group. In this research, antibiotics are purchased from Wako Pure Chemical Industries. Ltd. The structure and other chemical data are shown as below in Table 1.

Table 1 Structure and molar mess for each antibiotic

	Ciprofloxacin	Sulfamethoxazole
Formula	$C_{17}H_{18}FN_3$・HCl・H_2O	$C_{10}H_{11}N_3O_3S$
Molar mass	385.82	253.28

Duckweed were purchased and grown under a specific condition. Temperature of water was monitored and controlled at 24±0.5C°(297.15±0.5K). Illumination was supplied by a metal halide lamp (Eye HID LAMP, 400W IWASAKI ELECTRIC CO. LTD.), which could provide 680μmol/m^{2}s. Illumination was provided 16 hours per day. In order to reproduce duckweed, aeration was provided by an air pump (4.5W NISSO CORPORATION) for 24 hours per day. Duckweed cultures were grown for 4 weeks before experiments.

2.2 Methods

The wet mass of duckweed was measured after wipe off the surface of random amount of duckweed. Then the duckweed was dried in a dryer at 110C°(383.15K) for 24 hours, and the dried mass was measured, too.

Three mechanisms are connected with the remove: hydrolysis, photo-degradation and uptake by duckweed. Through Experiment A~D we could investigate the efficiency of each mechanism and the efficiency of duckweed in the removal process. Experiment conditions were set as described in Table 2. C_0 was the concentration of feed solution. By scanning the sample from each flask, C_A ~C_C (concentration of antibiotic in sample) could be calculated.

Hydrolysis was conducted in experiment A, hydrolysis and photo-degradation were conducted in experiment B. Uptake, hydrolysis and uptake were conducted in Experiment C. Under a condition with light, mechanisms conducted in the removal will be hydrolysis, photo-degradation and sorption with uptake by plant. This condition was considered as L group (Light).

As a hypothesis of this research, we consider there is no connection between these mechanisms. For example, in Experiment B, both hydrolysis and photo-degradation conducted. The hypothesis means the participation would not affect the efficiency of hydrolysis.

Therefore, we could calculate the efficiency of each mechanism by counting the D-value between the remained concentration. C_0 - C_A (mol/L) is the amount that hydrolysis worked. The rest can be done as the same: C_A–C_B is the work by photo-degradation, and C_B–C_C is the work by duckweed.C_A-C_D is the work by plant under no-light condition.

Experiment D was set to investigate the effectiveness of hydrolysis and plant under the condition without light. In this case, the mechanisms related to the removal will be hydrolysis, sorption and uptake under no-light condition(NL group). By comparing these two groups, we could find out the difference between the efficiency of duckweed under light and no-light condition.

All experiments were set triplicate to avoid accidental mistake, and calculation were based on the average of each kind of data. Relationship between each experiment and the mechanism conducted was shown in Table 3.

2.3 Experiments and analytic methods for the removal mechanisms investigation

Table 2 Experiment conditions for experiment A~D

	A	B	C	D
Weight of duckweed(g)	×	×	3.00	3.00
Illumination	×	○	○	×
Antibiotics in feed	CIP/SUL	CIP/SUL	CIP/SUL	CIP/SUL
Concentration of feed (C_0 mol/L)	5.00×10^{-5} /1.00×10^{-5}	5.00×10^{-5} /1.00×10^{-5}	5.00×10^{-5} /1.00×10^{-5}	5.00×10^{-5} /1.00×10^{-5}
Amount of feed (mL)	80	80	80	80
Growth medium (amount mL)	4.00×10^{-3}	4.00×10^{-3}	4.00×10^{-3}	4.00×10^{-3}
Time(hrs)	168	168	168	168

Table 3 Mechanism involved in each experiment and the calculation method for their effectiveness

	A	B	C	D
Hydrolysis	○	○	○	○
Photo-degradation	×	○	○	×
Uptake by plant	×	×	○	○*

3. Results and Discussion

3.1 Moisture content of Duckweed

The moisture content of duckweed was estimated with the following equation:

$$Moisture\ content = 1 - \frac{Dried\ mass}{\text{Wet mass}}$$

Experiment were conducted 9 times. Data is shown below in Table 4.

Table 4 Experiment result for moisture content

Group	Wet mass (g)	Dried mass (g)	Moisture content
1	5.61	0.63	0.89
2	4.15	0.43	0.90
3	3.88	0.41	0.89
4	4.20	0.42	0.90
5	4.01	0.43	0.89
6	2.94	0.33	0.89
7	3.51	0.40	0.89
8	2.66	0.33	0.88
9	3.20	0.37	0.88

By calculating the average of all the moisture content, the average moisture content is around 89%.

3.2 Removal Mechanisms

All results of efficiency is based on the formula described below.

Table 5 Formula for the calculation of efficiency

	E $_{\text{hydrolysis}}$	E$_{\text{photo-degradation}}$	E $_{\text{plant}}$	E $_{\text{plant(NL)}}$
Formula	$C_0 - C_A$	$C_A - C_B$	$C_B - C_C$	$C_A - C_D$

When the concentration of feed (C_0) is 5×10^{-5}mol/L, the result is shown in Table 6.

Table 6 Experiment result (C_0=5×10^{-5}mol/L)

L	CIP	SUL
$C_0 - C_A$	0.51	0.00
$C_0 - C_A$	1.49	0.06
$C_B - C_C$	1.30	1.22
NL	**CIP**	**SUL**
$C_0 - C_A$	0.51	0.00
$C_A - C_D$	2.52	2.43

At this concentration, both the ciprofloxacin and the sulfamethoxazole group, part of the duckweed died after 2 weeks. At this concentration, duckweed's metabolism was influenced.

In the case of ciprofloxacin, hydrolysis and photo-degradation showed their effectiveness in the removal process. Together, hydrolysis and photo-degradation occupied 60% of the ciprofloxacin being removed. Uptake by plant did benefit the removal by taking up 40% of the work.

On the other hand, in the case of sulfamethoxazole, duckweed showed its effectiveness in the process. Uptake and sorption by plant maintained 95% of the decrease in concentration. Sulfamethoxazole is stable towards hydrolysis and photo-degradation but could be removed by plants during a period, mainly because sulfamethoxazole has sulfonic acid as a part of it, which can make sulfamethoxazole stable towards hydrolysis.

In condition 2, we could find out no matter what the antibiotics is in the feed, plant could still remove antibiotics from water. Though the effect is somehow weaker than under condition 1.

When the concentration of feed is 1×10^{-5}mol/L for both antibiotic, the result is as described in Table 5.The calculation is based on the formula described in Table 5, results are showed as the ratio of work done by each mechanism (D-value) and the concentration of feed.

Table 7 Experiment result (C_0=1×10^{-5}mol/L)

L	CIP	SUL
$C_0 - C_A$	0.23	0.00
$C_0 - C_A$	0.32	0.22
$C_B - C_C$	0.19	-0.45
NL	**CIP**	**SUL**
$C_0 - C_A$	0.23	0.00
$C_A - C_D$	0.23	0.33

Ciprofloxacin tends to collapse under hydrolysis and photo-degradation, and could be removed by duckweed. Compared to former experiment, the antibiotic remained in the solution is less, decreased from 0.34 to 0.26. In condition 2, hydrolysis share the same efficiency with sorption and uptake. But obviously, plant showed a low efficiency under no-light condition.

The result of sulfamethoxazole at this concentration is complex. Again, sulfamethoxazole was stable towards hydrolysis. Sulfamethoxazole collapsed under photo-degradation, account for 21% of the sulfamethoxazole been removed. Data for E $_{\text{uptake}}$ could not be calculated, because the concentration 'increased', which is normally impossible. The reason is that in condition 2, sulfamethoxazole decreased from 1×10^{-5}mol/L to 0.67×10^{-5}mol/L . Based on experience in this research, the 'increase' may be considered as no change in concentration.

There are several reasons for this result. The first reason is about the metabolite from duckweed during the experiment. As mentioned in 2.5, to avoid the influence from the metabolite, we have set a control group. And in the calculation, data from this group were being subtracted from the absorbance of group C. But still, individual difference of plant may exist. Furthermore, the spectrometer could only measure the absorbance of sample but not distinguish compounds in the sample as a Liquid Chromatography, which means is the sample is a mixture, the absorbance may lead to a 'increase' in the signal and in the data.

4. Conclusion

In this research, we observed and calculated the effectiveness for each mechanism in the removal of antibiotics from water. Ciprofloxacin could be removed by hydrolysis, photo-degradation and uptake by duckweed in both concentration. On the other hand, remove of sulfamethoxazole is difficult. Because it showed stability towards these 3 mechanisms. Among all the mechanisms, the participation of duckweed displayed its potential in removing sulfamethoxazole. However, at feed concentration 1×10^{-5}mol/L, effect is still questionable, which may need new analytical methods or different analyze machine based on other theory like LC(liquid chromatography).

References

[1] Carolin Rutgersson, Jerker Fick, Nachiket Marathe, Erik Kristiansson, Anders Janzon, Martin Angelin, Anders Johansson, Yogesh Shouche, Carl-Fredrik Flach, and D. G. Joakim Larsson Fluoroquinolones and qnr Genes in Sediment, Water, Soil, and Human Fecal Flora in an Environment Polluted by Manufacturing Discharges

[2] Carl-Fredrik Flach, Anna Johnning, Ida Nilsson, Kornelia Smalla, Erik Kristiansson and D. G. Joakim Larsson Isolation of novel IncA/C and IncN fluoroquinolone resistance plasmids from an antibiotic-polluted lake

[3] Sivanandham Vignesh, Krishnan Muthukumar, Rathinam Arthur James Antibiotic resistant pathogens versus human impacts: A study from three eco-regions of the Chennai coast, southern India

[4] Johan Bengtsson-Palme, Fredrik Boulund, Jerker Fick, Erik Kristiansson and D. G. Joakim Larsson Johan Bengtsson-Palme, Fredrik Boulund, Jerker Fick, Erik Kristiansson and D. G. Joakim Larsson

[5] Xiaoqin Wu, Laurel K. Dodgen, Jeremy L. Conkle, Jay Gan, Plant uptake of pharmaceutical and personal care products from recycled water and biosolids: a review

チェルノフ距離に基づく局所フィッシャー線形判別分析

学籍番号：14_10020　　氏名：湯韻佳　　指導教員：山下幸彦

1　はじめに

コンピュータによるパターン認識は，前処理，特徴抽出と識別の3つの過程で行われる，その中で特徴抽出とは，対象を区別できるような情報を観測パターンから取り出す処理である。その方法は多岐にわたるが，本論文では最も基本な手法の1つであるフィッシャー線形判別分析 (FDA) とその関連研究に基づいて，判別性能を高める手法を提案する。

局所線形判別分析 (LFDA) は，FDA を局所性保存射影 (LPP) と組み合わせることによって，データ構造を保存しながら，FDA の認識率を高めた。しかしながら，FDA と同様に各クラスの分散共分散行列が異なる場合，識別のために最適な特徴を抽出しないという問題が残されている。一方，チェルノフフィッシャー線形判別分析 (CFDA) は，FDA に補正項を加え，分散共分散行列の形が異なる場合に，分類の認識精度を高めるための手法である。論文では，LFDA に，CFDA で使われたチェルノフ距離に基づいた補正項を加えることによって，形が異なる分散共分散行列を持つデータに対して認識精度を高めることができる特徴抽出法を提案する。そしてその効果を評価するため，トイデーターと UCI データセットのデータを用いた実験を行う。実験で求めたエラー率から，その判別性能を既存手法と比較し，評価する。

2　チェルノフ局所線形判別分析

フィッシャー線形判別分析とは，多変量に基づく2クラスのパターンの分布からこの2クラスを識別するために適した1次元軸を求めるための手法である。クラスの中の情報を表すクラス内変動行列 S_W とクラスの間の関係を表すクラス間変動行列 S_B はそれぞれ：

$$S_B = (\mu_1 - \mu_2)(\mu_1 - \mu_2)^T, \tag{1}$$

$$S_W = \Sigma_1 + \Sigma_2. \tag{2}$$

と書ける。ここで μ_c は，クラス c の平均ベクトル，Σ_c はクラス c の分散共分散行列である。次元を落とした平均ベクトル m_c と分散共分散行列 σ_c^2 を用いて，FDA におけるフィッシャーの評価基準関数を定義すると次のようになる。

$$\mathrm{argmax}\ _w \quad J(w) = \frac{|m_1 - m_2|^2}{{\sigma_1}^2 + {\sigma_2}^2} = \frac{w^T S_B w}{w^T S_W w}. \tag{3}$$

ここで，w は特徴ベクトルである。式の分母を小さくすると同時に分子を大きくする w を定める。このことによって，変換後は，クラスの分離が可能になる。w は，S_W と S_B に関する一般化固有値問題によって得られる。

FDA をベースに CFDA は，誤認識率の定義から提案されたチェルノフ距離を用いて，S_W と S_B の計算に補正項を加えることで FDA に汎用性を与えた。一方，LFDA は，局所性保存射影のアイデアを取り入れ，S_W と S_B に親和性行列を導入したものである。その効果は，より離れているサンプルのペアはクラス内変動行列 S_W により小さい影響を与えることであり，多数のクラスターを持つデータも非常に高い精度で分類することができる。しかし各クラスの分散共分散行列が異なる場合，識別のために最適な特徴を抽出しないという問題がある。そのため CLFDA 特徴抽出モデルを導入することを提案する。

既存のクラス間変動行列 S_B とクラス内変動行列 S_W は，データの平均と分散のみを用いて計算されたものであるが，ここでは，それを親和性行列と組み合わせた $\tilde{S_B}$ と $\tilde{S_W}$ に置き換えることによって，同じクラスに所属するデータを近づけ，離れたデータ間の影響を抑える。ただし LFDA と CFDA において，平均値と分散の定義の方法が異なっているため，係数を補正し，変動行列を算出できるようにする必要がある。

3　特徴抽出精度検証のための実験

本節では，提案モデルの有用性を検証するために行った実験について述べる。プログラムによって生成した AB 型 (図 1) と ABA 型 (図 2) のトイデータと，機械学習のための UCI データ (表 1) を 2 つ使い，4 つの手法 (CLFDA，LFDA，CFDA，FDA) による特徴抽出を行う。そして，認識法として最近傍法を用いて，エラー率を出力する。さらに，それぞれのデータセットに対して，どの方法が適する手法であるか検証する。

次に各データとパラメータについて述べる。図 1，2 はトイデータであり，図 1 ではクラスごとのデータ数は 100 であり，図 2 では 200 である。交差検定を 100 回行ってエラー率を評価し，各データセットにおいて学習のために使うデータは全体の 70%とし，テストデータには残りの 30%を使った。

トイデータの実験結果を表 2，表 3 で，UCI データの

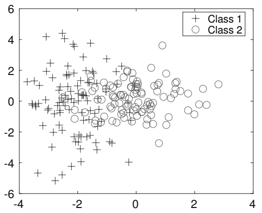

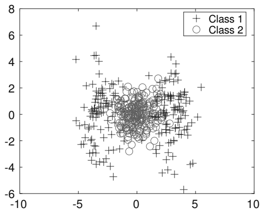

表 1: UCI データセットの情報

Data Type	特徴量	データ数	クラス数	使うデータ
Iris	4	150	3	クラス 2，3
Wine	13	178	3	クラス 1，2
Transfusion	4	748	2	1,2
Haberman	9	569	2	1,2

実験結果は表 4 で示す。ただし，各データタイプにおいての最もエラー率が低い結果の前に「O」を付けている。

表 2: AB 型データの認識エラー率 (平均 ± 標準偏差)

Data Type	CLFDA	LFDA	CFDA	FDA
1	O 14.53±0.14	34.07±0.26	27.85±0.19	28.87±0.26
2	O 9.97±0.13	23.90±0.24	14.82±0.17	13.83±0.23
3	O 10.10±0.12	23.08±0.18	19.10±0.12	20.83±0.24
4	O 11.85±0.19	49.16±0.22	25.17±0.27	23.70±0.25

表 2 では，すべてのデータに対し，CLFDA が最も低いエラー率を達成している。そのエラー率は FDA の約 1/2 である。表 3 からは，クラスターが 3 つある場合，中心のクラス 2 が両側のクラス 1 と分散が明らかに異なるとき，CLFDA の特徴抽出精度が最も高い。ただし，そうでないときは LFDA の結果が一番良い。原因としては，補正項のモデルは，AB 型分布とデータの形が明らかに異なる場合に適するため，他のデータでは補正項の本来の機能を実現できなかったためと考えられる。最後に表 4 では，CFDA と LFDA が最も良い結果を出している。CLFDA は，2 クラス 2 クラスターのトイデータの場合とほとんど変わらず，補正項の機能を実現することができていないと考えられる。すなわち高次元ベクトルに対する抽出精度は，既存の方法より劣っている。この問題の解決のためには，パターン間距離の評価法に工夫が必要と考えられる。

表 3: ABA 型データの認識エラー率 (平均 ± 標準偏差)

Data Type	CLFDA	LFDA	CFDA	FDA
1	O 10.83±0.06	13.85±0.05	33.90±0.06	31.89±1.36
2	O 19.13±0.11	32.14±0.09	28.80±0.16	28.08±0.13
3	O 27.13±0.13	27.33±0.14	28.84±0.11	29.43±0.15
4	32.33±0.07	O 13.93±0.06	50.10±0.13	50.76±1.89
5	40.93±0.06	O 9.86±0.05	43.20±0.06	41.48±1.44

表 4: UCI データの認識エラー率 (平均 ± 標準偏差)

Data Type	CLFDA	LFDA	CFDA	FDA
Iris	14.53±6.97	17.47±6.12	O 5.76±3.91	24.35±5.71
Wine	11.28±4.23	7.86±2.13	O 1.41±2.06	1.54±1.82
Transfusion	23.92±0.41	O 19.83±0.47	26.89±2.66	26.44±2.29
Haberman	32.57±4.44	O 31.94±4.14	34.39±4.45	34.53±4.25

4　おわりに

特徴抽出は，対象を区別できるような情報を観測パターンから取り出す，パターン認識においてとても重要なプロセスである。本論文では特徴抽出法の一種である局所フィッシャー線形判別分析 (LFDA) をもとに，チェルノフ距離に基づいた補正項を加えることによって，より精度を高めることを目的とした特徴抽出手法を提案した。そして認識実験を行い，既存手法と比較し，その有用性を調べた。

今後の課題は，2 クラス 3 クラスター (ABA 型) のデータに対する CLFDA の性能をが安定化手法を開発すること，パターン間距離の評価法を検討することである。

参考文献

[1] 上田修功ほか (1998) 『わかりやすいパターン認識』オーム社

[2] 佐藤真一, 福井和広 (2011)「パターン認識とビジョン」pp.1-4, 16

[3] Yokota, et al., ”Heteroscedastic Gaussian based Correction term for Fisher Discriminant Analysis and Its Kernel Extension”Proc. of International Joint Conference on Neural Networks (IJCNN2013), no. 1188,　pp. 1-3, Aug. 2013

[4] Sugiyama, et al., ”Dimensionality Reduction of Multimodal Labeled Data by Local Fisher Discriminant Analysis”, Journal of Machine Learning Research vol.8, pp. 1029-1036, May. 2007.

[5] X. He, P.Niyogi, ”Locality Preserving Projections”, NIPS’03 Proceedings of the 16th International Conference on Neural Information Processing System, pp. 153-155,　Dec.2003.

Study of GPU accelerated computer vision

Student Number: 13_10694 Name: Shitian Ni Supervisor: Yukihiko Yamashita

1 Introduction

While needs for high computing powers continue to grow to process the exponentially growing amount of data from smart devices around the globe, Moore's law is reaching to its limit. Gordon Moore noted that transistors eventually would reach the limits of miniaturization at atomic levels.

Cores and threads could be put together to work in parallel to accelerate data processing. Therefore, the market trend is to use more and more cores.

Intel's CPU lineup can have up to 72 cores with Xeon and over 200 when used with dual Xeon Phi coprocessors. On the other hand, Nvidia GeForce GTX 1080Ti has 3584 CUDA cores, Nvidia Tesla V100 has 5120 CUDA cores and 640 Tensor cores, far more cores than a CPU can have.

GPUs are designed for manipulating computer graphics and image processing, and their highly parallel structure to manipulate image blocks makes them more efficient than CPUs to do matrix computations which are necessary for modern artificial intelligence deep learning and computer vision tasks.

In this research, we conduct a parallel computing acceleration of an image recognition algorithm called GPT via GPU, which achieves a further acceleration of global projection transform (GPT) enhanced methods proposed by Zhang et al [2] [3].

2 Global Projection Transformation (GPT)

A measure of image matching is based on the canonicalized correlation between two normalized images $f(\boldsymbol{r})$ and $g(\boldsymbol{r})$ given by (1).

$$C(f,g) = \int_{\mathcal{K}} f(\boldsymbol{r})g(\boldsymbol{r})\mathrm{d}\boldsymbol{r}, \tag{1}$$

where $\mathcal{K}$ is the image area and $\boldsymbol{r} = (x,y)^{\mathrm{T}}$ is a position vector. Images need to be normalized to calculate canonicalized correlation. Normalization for an image $f(\boldsymbol{r})$ is defined by the following equations.

$$\int_{\mathcal{K}} f(\boldsymbol{r})\mathrm{d}\boldsymbol{r} = 0, \quad \int_{\mathcal{K}} f(\boldsymbol{r})^2\mathrm{d}\boldsymbol{r} = 1. \tag{2}$$

GPT correlation matching which calculates the normalized correlation after GPT is given by

$$C_{\mathrm{GPT}}(f,g) = \int_{\mathcal{K}} f(\boldsymbol{r})g\left(\frac{A\boldsymbol{r}+\boldsymbol{b}}{1+\langle \boldsymbol{c},\boldsymbol{r}\rangle}\right)\mathrm{d}\boldsymbol{r}. \tag{3}$$

The method is proposed by Yamashita and Wakahara [1] to address projection transformation by extending affine-invariant GAT (Global Affine Transformation) correlation matching. Zhang et al. [2] [3] enhanced GPT with sHOG filters and accelerations by templates and lookup tables.

3 GPU computing

Although templates and lookup tables significantly accelerated the computation speed, further improvements are considered. Massive amount of computation involving image pixel matrix calculations has to be done. In those cases, there would be a 'for' loop going through all image pixels. Consider an image which has 200*200 pixels. If we add value 1 to all pixels, then we need to do 40000 times of calculations in serial in the original code base. But if we use GPU, for example a 2000 CUDA core GPU and if we can spread the pixels to all CUDA cores, based on a simple calculation, we just need 20 times of calculations for each CUDA core being given 20 pixels and do the calculation in parallel.

Notice that tasks performed in parallel should not depend on each other. That is, order in which the tasks are performed should not matter the final result. For example, task_1 is adding 1 to pixel_a, task_2 is adding pixel_a to pixel_b. Performing task_1 before task_2 and performing task_2 before task_1 would result in different pixel_b values. In this kind of cases, operations are related to each other, so they should not be performed in parallel. But because many of those operations going through image pixels do the same tasks, GPU acceleration theoretically helps to improve performance.

In the original code of the GPT matching, the following operations are included

- Calculation of mean of nearest-neighbor interpoint distances between two images
- Determination of optimal GAT components that yield the maximal correlation value
- Calculation of Gaussian weighted mean values
- 8-quantization of gradient direction
- Projection transformation of the image by bilinear interpolation
- Update of the Gauss window function
- Update of correlation

For the parallelizable operations, the followings are some further CUDA strategies:

- Reduce parallel kernel code divergence (if..else..)
- Reduce data transfers between different memories
- Access neighboring data in memory
- Parallel paradigm usage including Map, Stream filtering, Scan, Scatter, Gather, Reduce

These calculations for each pixel are independent to each other, so the computing time can be reduced by assigning the independent calculations to GPU threads.

Furthermore, a part of reference table can be loaded into the device memory as well as shared memory in advance to reduce the memory access time.

Access to device memory is slower than shared memory which is slower than registers. To use share memory instead of device memory, we divide data to several blocks, load the blocks to shared memory, then execute data block calculations separately in parallel.

4 Experimental Results

Figure 1 shows the template image and test images from Boat dataset. Table 1 shows comparisons of calculation times required for these matchings between standard CPU algorithm denoted by Stand. CPU, template and lookup table accelerated CPU algorithm denoted by Accel. CPU, GPU accelerated algorithm and CPU ASIFT algorithm.

The calculation times cost by GPU in Table 1 do not include the time for copying the template tables to GPU memory. The calculation times cost by GPT-based methods are the times required for only one subwindow. Accel. CPU costs about one hundredth of the calculation time required by Stand. CPU, and GPU significantly reduces the calculation time of Stand. CPU further to several thousandths of time.

Incidentally, we used Tokyo Institute of Technology supercomputer TSUBAME 3.0 instance with CPU of 3.47 GHz Intel Xeon-X5690 and GPU of NVIDIA Tesla P100 in this experiment. The programs of Stand. CPU were coded in C++. Accel. CPU enhanced Stand. CPU with templates and lookup tables. The GPU accelerated programs were implemented with CUDA on top of the Accel. CPU. Accel. CPU and GPU have the same calculation results which are the image correlation values which are almost the same as the Stand. CPU results. Stand. CPU results are better than ASIFT.
All the programs are available on

`https://github.com/shitian-ni/CUDA-GPT`

Also, the program of ASIFT-RANSAC using the OpenCV library were executed on C++ platform on CPU.

To further compare computation times of different GPU enhancements, we measured calculation times of sample Graffiti Image 6 again.

Exclude time for parameters initialization and time for copying initial data to GPU memory,

- Accel. CPU calculation time is 5.571 sec
- GPU calculation time is 0.467s

If we use CUDA AtomicAdd function to sum elements one by one in serial instead of reduce method with shared memory,

- GPU elapsed time is 0.490 sec

If time for parameters initialization and time for copying initial data to GPU memory are included,

- Total Accel. CPU calculation time is 7.146 sec
- Total GPU calculation time is 1.227 sec

Calculation times differ from execution to executions based on hardware related issues. But that difference is minor, in range between 0.1 to 0.3 seconds. And calculation time error tends to converge after multiple executions. Besides that, memory copy in GPU and serial Atomic operation overheads are still obvious.

Figure 1: The template image (170 × 136) and test images (340 × 272) from Boat dataset

Table 1: The calculation times of Boat dataset (second).

Test image	Image 2	Image 3	Image 4	Image 5	Image 6
Stand. CPU	102.95	96.76	86.6	84.28	82.39
Accel. CPU	1.82	1.64	1.86	1.85	1.82
GPU	0.227	0.248	0.303	0.263	0.23
ASIFT	7.259	6.786	5.766	5.694	5.419

5 Conclusions

This paper first introduced the GPT correlation matching method and its variations. Then we introduced GPU programming and its use on GPT. GPU implementation has the same results as Accel. CPU and almost the same as Stand. CPU which has the best correlation values on the experiment datasets. On the other hand, GPU acceleration reduced the calculation time of Accel. CPU more than ten times and Accel. CPU itself reduces Stand. CPU computation time to about 1 percent. Future works could be about comparison between GPU accelerated GPT and neural networks. Tests on bigger images could also be done.

References

[1] Y. Yamashita and T. Wakahara, "k-NN classification of handwritten characters using a new distortion-tolerant matching measure," *Proc. of 22nd Int. Conf. on Pattern Recognition*, pp. 262–267, Stockholm, Aug. 2014.

[2] S. Zhang, T. Wakahara, and Y. Yamashita, "Theoretical Criterion for Image Matching Using GPT Correlation," *Proc. of 23rd Int. Conf. on Pattern Recognition*, pp. 544–549, Cancun, Dec. 2016.

[3] S. Zhang, T. Wakahara, and Y. Yamashita, "Image Matching Using GPT Correlation Associated with Simplified HOG Patterns," *Proc. of 7th Int. Conf. on Image Processing Theory, Tools and Applications*, pp. 1–6, Montreal, Nov. 2017.

Nitrogen oxides removal using red mud

Student Number: 14_05590 Name: Siqi WU
Supervisor: Hirofumi HINODE, Kurniawan WINARTO

1. Introduction

Nitrogen oxides (NOx) are considered one of the most significant air pollutants and it causes acid rain, ground-level ozone and global warming. NOx usually relates to NO and NO_2. Half of NOx emitted in the atmosphere come from automobiles, and a significant 20% from electric power plants. Because of the presence of O_2, NOx cannot be easily removed in the lean-burn gasoline or diesel engines using a three-way catalyst. Therefore, selective catalytic reduction with ammonia (NH_3-SCR) or NOx storage-reduction (NSR) is currently the most developed technology to reduce the emission of NOx. However, NH_3-SCR requires large amount of additional reductants, and can easily cause secondary pollution with ammonia.

Red mud, or bauxite residue, is solid waste generated by the Bayer process in aluminum industry. This waste product usually contains a mixture of many oxides. Due to the high pH from 10 to 12, and massive volumes of production of over 20 billion tons a year globally, it has potential impacts on surface and ground water quality.

In this study, red mud was investigated as potential material for NO removal in the excess of O_2.

2. Experimental

Indonesian red mud was used in this study. The composition of red mud is shown in Table 1. [1]

Table 1 Chemical composition of Indonesian red mud

Chemical composition	**Weight%**
Fe_2O_3	33.36
Al_2O_3	24.63
SiO_2	13.8
Na_2O	7.98
TiO_2	1.33
CaO	0.57
MgO	0.05
ZrO_2	0.03
MnO_2	0.05

A series of samples were prepared by calcining red mud powder at different temperatures from 300℃ to 600℃ under air flow. The powder was put into the tube furnace and heated for 5 h, then pelletized, ground, and sieved with 1.0 to 1.4 mm particle size.

Using a 6 mm inner diameter quartz glass tube as fixed-bed flow reactor, the activity of red mud was measured by passing a reactant gas consisted of 1500 ppm NO, 10% O_2, with He as balance gas at a flow rate of 4 ml/s with space velocity 13000 h^{-1}. The reaction temperatures were varied from 150℃ to 550℃.

Subsequently, the NO and NO_2 concentration were measured by NOx analyzer (NOA-305A; Shimadzu Co.). Characterization of samples was done by X-ray diffraction (XRD) to analyze crystalline structure and Fourier Transform Infrared Spectroscopy (FT-IR), for the analysis of surface functional groups.

3. Results and Discussion

Fig.1 shows the performance of a series of samples prepared at different calcination temperature (The number following "RM" shows the calcination temperature of the samples. Uncalcined red mud was named "RM" only.). Samples calcined at 300℃-400℃ showed the highest activities. When the calcination temperature is above 400℃, the performance significantly decreased. The NO removal for RM600 drop below 0 at 450℃-500℃, indicating the removal process of NO was an adsorption, not a decomposition. At lower temperatures, NO was adsorbed in these samples, while at high temperatures, NO was desorbed from these samples, resulting in NO concentration higher than inlet gas.

Fig.2 compares the results of 1st round test and 2nd round test of uncalcined red mud. As shown in the graph, the performance of the samples at 1st round is much better than in the

2nd round. Therefore, we can conclude that the components affecting catalytic activity are influenced by calcination temperature, and these are present in low temperature yet becomes unstable at high temperature.

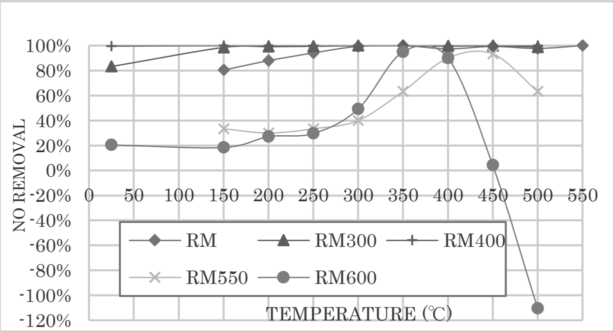

Fig. 1. NO removal of various RM samples

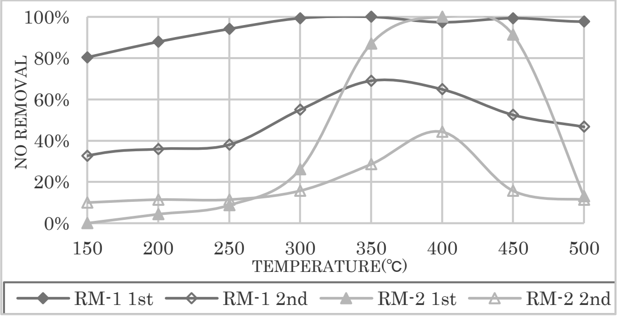

Fig. 2. NO removal of RM samples, 1st and 2nd round test

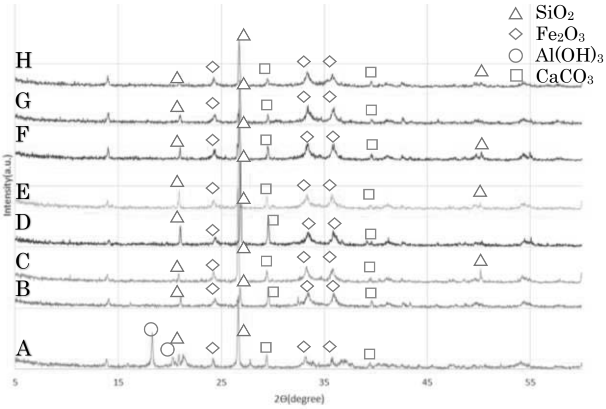

Fig. 3. XRD patterns of various samples. ((A)RM pre-experiment, (B) RM post-experiment, (C) RM300 pre-experiment, (D) RM300 post-experiment, (E) RM400 pre-experiment, (F) RM400 post-experiment, (G) RM600 pre-experiment, (H)RM600 post-experiment)

As shown in Fig.3, RM has more components than RM300, such as $Al(OH)_3$ and other unknown components. However, these components are missing in the post-experiment RM because $Al(OH)_3$ decomposed to Al_2O_3 and water at about 180 °C. Because activity of post-experiment samples decreased, $Al(OH)_3$ might have effect on the experiment outcome.

To verify the adsorption capacity, the adsorption tests were performed at room temperature. Fig. 4 shows the result and for comparison, adsorption using $Al(OH)_3$ was also performed. The adsorption capacity of uncalcined red mud is similar to $Al(OH)_3$, it indicates $Al(OH)_3$ is the effective component in the red mud for NOx adsorption at room temperature. However, the conversion rate in RM400 reached 100%, perhaps there are other metal oxides creating synergistic effect with $Al(OH)_3$.

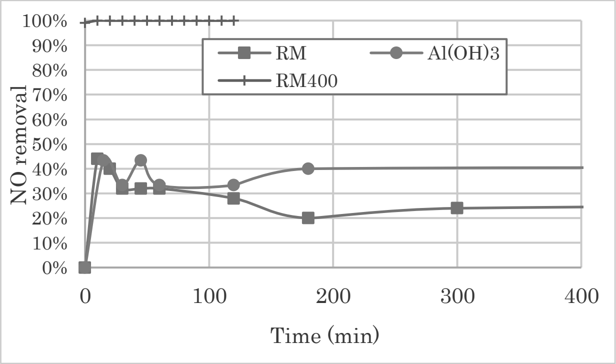

Fig. 4. NO adsorption test results

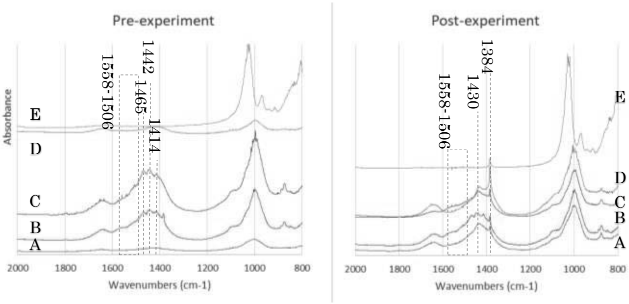

Fig. 5. FT-IR Characterization. (A)RM, (B)RM300, (C) RM400, (D)RM600, (E)$Al(OH)_3$; Peaks $[N_2O_2]^{2-}$: 1442, 1384, NO_2^- :1506-1558

Fig.5 shows the result of FT-IR analysis. The presence of $[N_2O_2]^{2-}$ indicates the occurrence of chemical adsorption during the process.

4. Conclusion

Uncalcined red mud, and red mud calcined at 300℃ or 400 ℃, showed high performances in NOx removal. Considering the energy consumption during the production process, uncalcined red mud is more suitable for industrial use.

In addition, $Al(OH)_3$ accelerates the NO removal due to its adsorption capability. The combination of $Al(OH)_3$ with other metal oxides might generate synergistic effect on the use of uncalcined red mud for NO removal.

Reference

[1] A. Wahyudi; Doctor Thesis, Tokyo Institute of Technology (2017)

STUDY ON MECHANISM OF POTASSIUM REMOVAL FROM PALM KERNEL SHELL BY HYDROTHERMAL TREATMENT

Student Number: 16B07365 Name: Tsamara Tsani Supervisor: Fumitake TAKAHASHI

Keywords: Potassium Removal, Hydrothermal Treatment, Palm Kernel Shell (PKS)

1 Introduction

Palm Kernel Shell (PKS) is one of the abundantly available agricultural waste in Indonesia. Palm oil industry in Indonesia yields 5.9 million tons of PKS annually, which is equal to 54.8 GJ of energy [1]. Despite the energy potential, the utilization of PKS as biofuel is still limited.

Pretreatment of PKS is needed to upgrade the biomass quality in order to achieve an efficient energy conversion through combustion. There are several characteristics of desirable solid biofuel, one of which is low potassium content [2]. At high temperature, potassium content in biomass reacts with silica and produces a sticky and mobile phase which causes slagging that disturb the heat exchange process in the boiler. Therefore, removal of potassium prior to combustion is important to be conducted.

Hydrothermal treatment (HTT) has shown remarkable performance in removing potassium content from other lignocellulosic biomass, such as Empty Fruit Bunch (EFB) [3]. A study also gives a hint toward the utilization of potassium-rich liquid by-product from HTT as liquid fertilizer [4]. However, the mechanism of potassium removal from lignocellulosic biomass by hydrothermal treatment is not fully understood yet. The understanding of potassium existence form in biomass and its removal process by hydrothermal treatment is important to further optimize the extraction effort. This study aims to investigate the potassium existence form and its removal mechanism from lignocellulosic biomass (in this case palm kernel shell) by hydrothermal treatment.

2 Materials and Method

PKS sample used in this work is originated from Indonesia. It was received in dried condition, but mixed with some dirt. The sample were then water washed and oven dried at 70-80°C for 24hr. Experimental and analysis procedures are shown in the flowchart below.

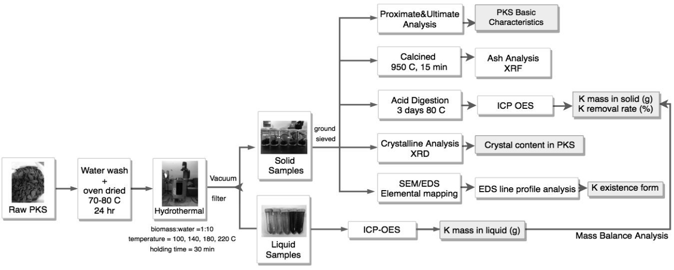

Chart 1 Experiment and analysis flowchart

Hydrothermal treatment was conducted at 100, 140, 180 and 220°C with biomass to water ratio of 1:10 and 30 minutes holding time.

Proximate analysis, ultimate analysis, ash composition analysis (XRF), SEM-EDX line profile analysis, crystalline analysis (XRD), potassium concentration analysis (ICP-OES), and mass balance analysis were conducted in this study.

Potassium (K) removal rate was calculated using the following equation.

$$\text{K removed (\%)} = \frac{ms_{ki} - ms_{kt}}{ms_{ki}} \; x \; 100\%$$

ms_{ki} = mass of potassium in raw PKS
ms_{kt}= mass of potassium in HT-treated PKS at t-temperature

In order to check the existence form of potassium, line profile analysis and crystalline analysis were conducted. Elemental mapping was conducted in prior to line profile analysis. Particles with high potassium content were then selected to undergo line profile analysis. This particle was divided into 4-5 analysis sections shown in picture 1.

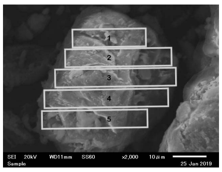

Picture 1 Line profile analysis sections

3 Result

3.1 Potassium Characterization in Raw PKS

Utilizing the data from ICP-OES analysis, it is obtained that potassium concentration in raw PKS is 1441.621 mg/kg or 0.144 wt%. Raw PKS also identified to have 30.6% of ash content, 34.24% carbon content and HHV of 12.95 MJ/kg.

Line profile analysis in raw PKS (picture 2) shows high correlation of Potassium existence with Si (average r=0.7455) and Al (average r=0.7077).

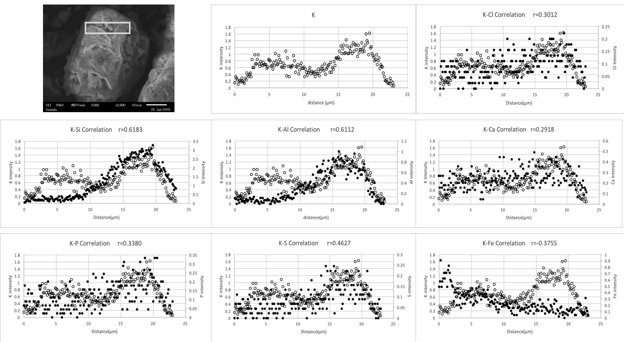

Picture 2 Line profile analysis in section 1 raw PKS

When Si and Al intensity are plotted to one another, it also shows high correlation (average r=0.9437). Therefore, it is predicted that potassium inside raw PKS may exists in the aluminum silicate matrix as K^+ cation. The structure may appear in type of feldspar [6] (picture 3). Potassium also shows positive correlation with Cl (average r= 0.490) and S (average r=0.635). Therefore, potassium is also predicted to exist as KCl and K2SO4 in raw PKS.

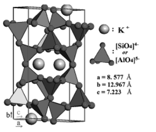

Picture 3 Orthoclase (KAlSi3O8), one of Feldspar structure

XRD crystalline analysis in raw PKS confirms the existence of potassium in the form of KCl and feldspar group structures (orthoclase, anorthoclase and trikalsilite).

3.2 Potassium Removal by Hydrothermal

Potassium removal rate increases with treatment temperature (shown in graph1). It reached the highest removal rate of 60.11% at 220°C treatment.

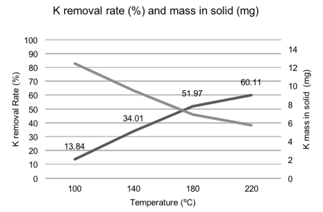

Graph 1 Potassium removal rate and potassium mass remained

The ash and K2O content in the hydrochar also decreased as the temperature increases. However, both of these content slightly increased at 220°C treatment (graph 2). This maybe because hemicelluloses were degraded at 220-315°C [7], thus creates porous structure on the hydrochar (picture 4). These pores absorb back some inorganics thus resulted in higher ash and K2O content.

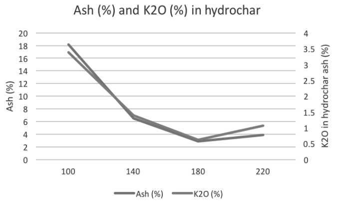

Graph 2 Ash (%) in hydrochar and K2O (%) in hydrochar ash

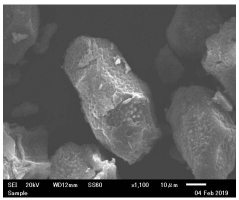

Picture 4 Porous structure of HTT-220

Potassium mass balance analysis was also conducted in this study (graph 3). It confirms the removal of potassium from solid biomass to liquid by product.

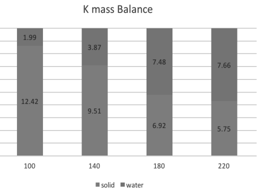

Graph 3 Mass Balance Analysis

XRD pattern of treated PKS at 100 and 140°C confirm the existence of potassium as KCl and feldspar group. However, the KCl peak vanish after treated at 180 and 220°C and left potassium only in the form of feldspar.

4 Conclusion

Potassium is estimated to exist in PKS in the form of KCl, K2SO4, and feldspar ($K(Al,Si)_4O_8$) as cation (K^+). Due to its existence as cation, potassium can be removed by ion exchange using subcritical water in hydrothermal treatment. Potassium removal rate increases with temperature to up to 60.11% at 220°C. However, high porosity created at high temperature has resulted in the slight increase of potassium and ash content in HTT-220 hydrochar.

Catalytic hydrothermal using H2CO3 or other weak acid is purposed for future study to improve the efficiency of potassium removal. The exact plan for solid hydrochar and liquid by-product utilization after hydrothermal treatment also need to be examined thoroughly in the future study.

References

[1] Prastowo Bambang, “Biomass Resource in Indonesia: Indonesia’s Solid Biomass Energy Potential”, German-Indonesia Workshop on Biomass, 2011.

[2] P. McKendry, “Energy production from biomass (part 1): overview of biomass”, Bio resource Technology 83 (2002), pp. 37-46, 2002

[3] Nurdiawati A., Novianti S., Zaini I.N. et al, “Production of Low-Potassium Solid Fuel from Empty Fruit Bunches (EFB) Employing Hydrothermal Treatment and Water Washing Process”, Journal of the Japan Institute of Energy 94 pp. 775-780, 2015.

[4] Novanti S, Nurdiawati A, Zaini Ilman N, et al, “Hydrothermal treatment of palm oil empty fruit bunches: and investigation of solid fuel and liquid organic fertilizer applications”, Biofuels, 2016.

[5] Hiroki Kitamura, Dahlan A.V, et al, “Geochemical form analysis of titanium in municipal solid waste incineration fly ash particles employing correlation analysis of elemental distribution line profiles”, Journal of Japan Society of Civil Engineers, Ser. G (Environmental Research). 73, 2017.

[6] David A.C. Manning, “Mineral sources of potassium for plant nutrition, a review”, Agronomy for Sustainable Development. Springer Verlag/EDP Sciences/INRA, 2010.

[7]Nizamuddin Sabzoi et. al, “Synthesis and Characterization of Hydrochars Produced by Hydrothermal Carbonization of Oil Palm Shell”, The Canadian Journal of Chemical Engineering, November 2015.

Hydraulic Experiment and Numerical Analysis on Tsunami – Storm Surge Entering Through Breakwater Mound

Student Number: 15B08456 Name: Yoshifumi TAKATA Supervisor: Hiroshi TAKAGI

1. Introduction

Installing floodgates and movable breakwaters such as flap gates on the opening of the port are getting attention as effective countermeasures against tsunamis and storm surges [1][2][3]. For instance, a large-sized floodgate "View-O" has been constructed at Numazu port (Fig. 1) in 2004 to prevent the hinterland from tsunamis. It is necessary to assess the inflow of the seawater from the small gaps of the movable gates [4]. In addition seawater may also intrude into the basin through other parts of the port. Especially, the breakwater consists of impermeable caisson and permeable rubble mound. Hence, there is concern that tsunamis and storm surges enter inside the port through the gap op the rocks when difference in water level exists between inside and outside the port. However, such a risk has not been clearly recognized to date. As a result, any practical method for assessing the inflow rate of tsunami or storm surge through the mound has not been established.

This study estimates the inflow discharge through the breakwater mound by carrying out a hydraulic experiment and numerical analysis. The results demonstrate that seawater inevitably enters inside the port from the mound even if the port's opening can be perfectly enclosed by the floodgate before arrival of tsunami or storm surge.

Fig. 1 The floodgate "View-O" at Numazu port

2. Hydraulic experiment and numerical analysis

We conducted a water flume experiment installing a model breakwater composed of an acrylic caisson and a rubble mound (Fig. 2). The average grain diameter of the mound was 11.2 mm, and the void ratio was 40.2%.

A total of 5 different water levels have been tested, and whereby the flow rate through the breakwater mound was measured.

Moreover, we also conducted a numerical analysis in order to reproduce the experimental cases and compared the result from the experiment (Fig. 3). A computational setting known as "porous media" was used to characterize the rubble mound.

From the comparison, we confirmed that Ergun's estimated formula [5] is appropriately determines the coefficients of non-Darcy law; it shows the relationship between hydraulic gradient and inflow rate when relatively fast flow occurs in a porous media.

Based on that, we conducted a numerical analysis on a real scale breakwater model. It assumed that the average rubble diameter of the mound was 50 cm and the void ratio of it was 40%. We tested 16 different water levels between the front and back of the breakwater and calculated the flow rate through the breakwater mound.

Based on our numerical analysis, we derived the equation (1) that estimates the inflow rate from the difference of water level.

$$q = 0.393\sqrt{H} \tag{1}$$

q : inflow rate per unit width [m^3]
H : the difference of water level [m]

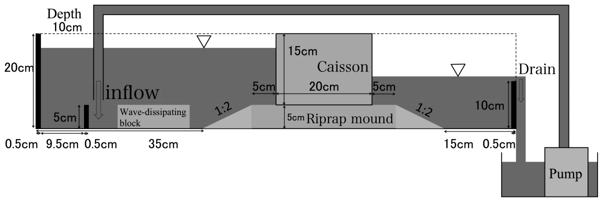

Fig. 2 The experimental equipment

Fig. 3 An example of velocity distribution derived by numerical analysis

3. Calculation in the model port

We calculated the changes in water level using derived Eq. (1) in our model port (Fig. 4). The model port is composed of a port basin (76000 m^2) and a pier (24000 m^2). Additionally, a breakwater (760 m) and a floodgate (40 m) have been placed to surround the port, and the floodgate is closed before tsunami or storm surge arrive.

We generated 4 types (amplitude: 3.3 m, period: 15 min, 30 min, 1 hour and 2 hours) of long waves and compared the changes in water level inside and outside of the port (Fig. 5).

Therefore, it was recognized that water level increased in all cases and seawater inflow through the breakwater mound is not negligible. Especially, the longer the wave period, the more seawater inflow into the port.

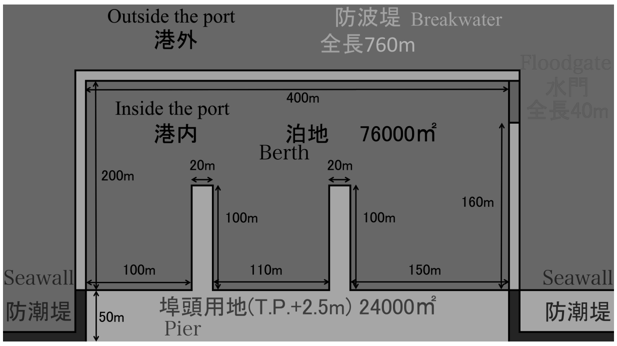

Fig. 4 Configuration of the model port

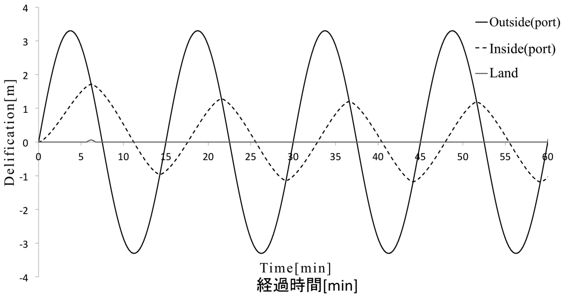

(a)

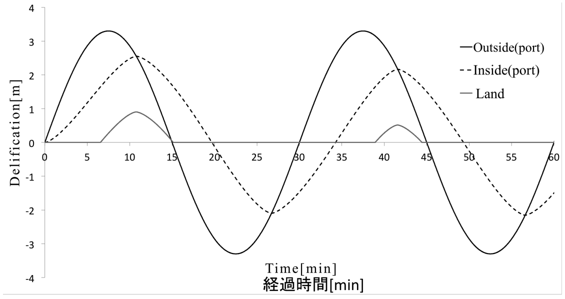

(b)

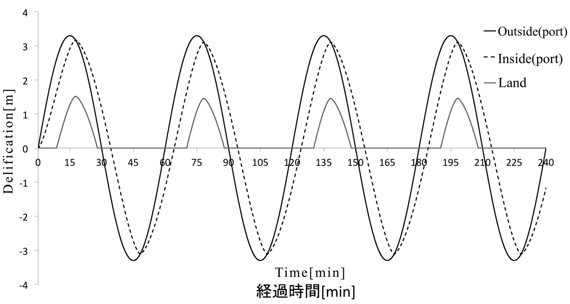

(c)

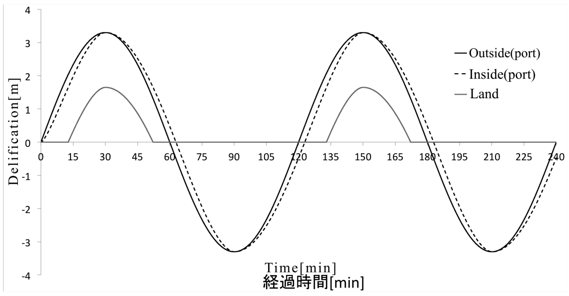

(d)

Fig. 5 Estimated result (a=period: 15 min); (b=period: 30 min); (c=period: 1 hour); (d=period: 2 hour);

4. Conclusion

The comparison between hydraulic experiment and the numerical analysis revealed that Ergun's estimated formula is applicable to determine the coefficient of non-Darcy flow. Following this observation, we derived the evaluation formula of the inflow rate through the breakwater mound when water-level difference appears between inside and outside the port occurs. Finally, the numerical analysis for the model port confirmed that the inflow of the tsunami and storm surge inside the port is unavoidable for the period range of tsunami and storm surge.

References

[1] 中島晋, 高山知司, 小原恒平ら: 津波防御に向けた直立浮上式防波堤の性能設計, 土木学会論文集 B2（海岸工学）, Vol.67, No.2, pp.786-790, 2011.

[2] フラップゲート式可動防波堤開発グループ：フラップゲート式可動防波堤実海域試験（最終報告書概要版）, 22p., 2013.

[3] Fujii N. *et al.* Self-elevating Sea Wall Constructed with Pneumatic Caisson Method, 43rd Conference on Our World in Concrete & Structures, Singapore, 2018.

[4] 高木泰士, 富安良一, 荒木健人ら, 浮上式防潮堤の狭小隙間部から流入する津波・高潮流量の評価手法, 土木学会論文集 B3（海洋開発）, 土木学会, 73(1), 35-42, 2017.

[5] Ergun S. Fluid flow through packed columns. *Chem. Eng. Progress* 48(2), 1952.

Experiment system to examine the effect of cathode temperature on electric field intensity at breakdown

Student Number: 14_01570 Name: Ryoji Ichisaki Supervisor: Kunio Takahashi

1. Introduction

Research on electric breakdown is important to use discharge phenomena and ensure insulation.

In the research on the re-ignition of plasma phenomena, Omata[1] investigated the relation between the arc current before interruption and electric field intensity, i.e. applied voltage divided by distance between electrodes, required for re-ignition. He suggested that the field intensity may be determined by the cathode temperature. However, the actual cathode temperature was not measured.

Murooka[2] investigated the relation between electrodes' temperature and breakdown voltage. However, the change of electrodes' distance due to thermal expansion hasn't been considered. Therefore, it is impossible to measure the field intensity.

The purpose of this study is to design an experimental system capable of changing the cathode temperature and field intensity independently considering thermal expansion.

2. Experimental system

2.1 Overview

The schematic illustration of the proposed experimental system is shown in Fig. 1. a pure tungsten plate (t0.20mm) is used as the anode. A V-shaped filament made of a pure tungsten wire (φ0.10mm) is used as the cathode, and is heated up to a target temperature by a constant DC current. Both of the electrodes are set in an acrylic box, which shielding gas (Ar) is flowed to (5L/min). The cathode temperature is measured by a radiation thermometer (TR-630) through the acryl. In order to set the field intensity, it is required to change the voltage and the distance between electrodes. The voltage is applied by a DC power supply (MATSUSADA MR-600-1.7). The distance is set by using a three-axis micro-stage. A DSLR camera is used for capturing the cathode before and after being heated to measure the thermal expansion of the cathode.

2.2 Constant current power supply

The circuit of the constant current power supply connected to the filament cathode is shown in Fig. 2. The current I flowing through the filament is controlled to satisfy $I \times \mathrm{R}_0 = V_{\mathrm{ref}}$ by FET switching and OP-amp comparator. The variable resistor is used to adjust V_{ref} at the output of the three-terminal regulator. Isolation transformers are used to isolate the circuit from the ground level of the high voltage power supply to prevent damages due to discharged current.

2.3 Actual distance between electrodes

In order to measure the field intensity, the actual electrodes distance is measured by the following procedure.

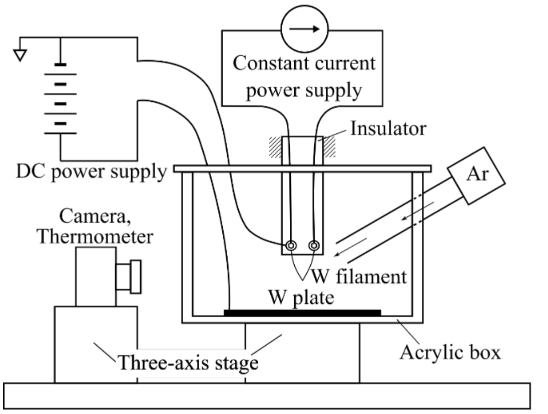

Fig. 1 Schematic illustration of the experimental system

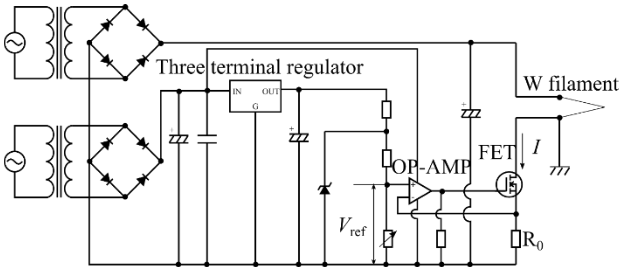

Fig. 2 Circuit of the constant current power supply

(1) Set the initial electrodes' distance d_{int}
(2) Take pictures of cathode before and after heating, as shown in Fig. 3
(3) Obtain the thermal expansion Δl of the cathode from the pictures
(4) Determine the actual electrodes' distance d_{act} by subtracting Δl from d_{int} (as shown in Fig. 4)

3. Experiment

3.1 Experimental procedure

The experiment is conducted by the following procedure.

(1) Set the initial electrodes' distance d_{int} (0.50 ~ 1.25mm)
(2) Set the cathode temperature (room temperature ~ 2100℃)
(3) Increase applied voltage between electrodes until breakdown occurs
(4) Measure the cathode's temperature, breakdown voltage V_{B}, actual electrodes' distance at the breakdown

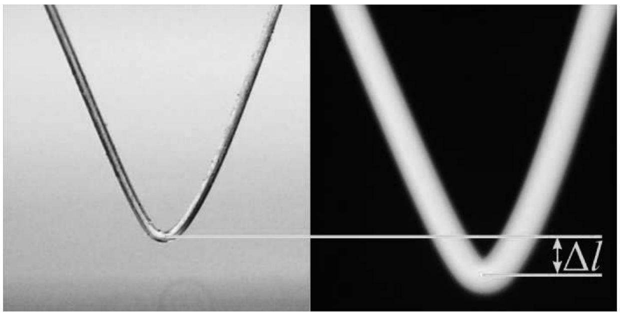

Fig. 3 Pictures of cathode before and after heating

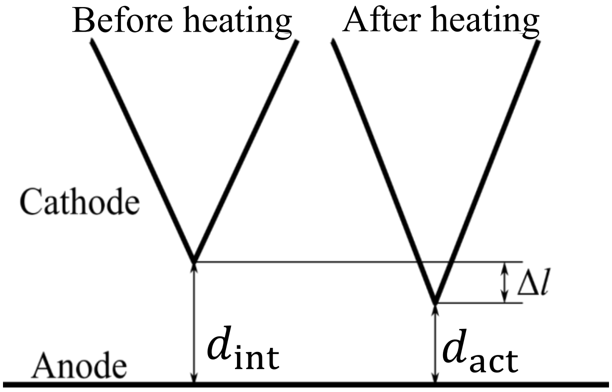

Fig. 4 Relation between d_{int}, d_{act}, and Δl

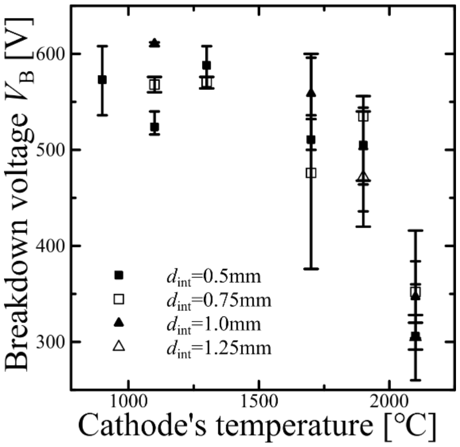

Fig. 5 Cathode temperature vs $\boldsymbol{V}_{\mathbf{B}}$

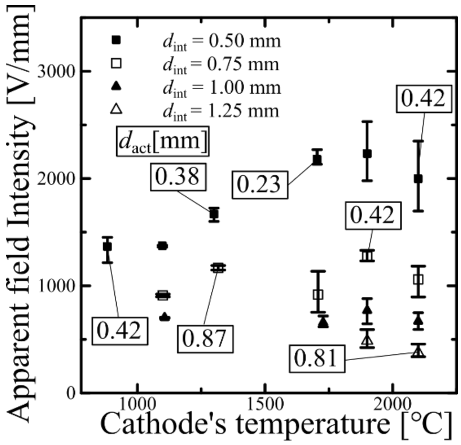

Fig. 6 Cathode temperature vs apparent field intensity

3.2 Experimental result

Relation between the cathode's temperature and the breakdown voltage V_{B} is shown in Fig. 5. It shows a trend that V_{B} decreases as the cathode temperature increases. When the cathode's temperature was around 1500°C, breakdown didn't occur even at the maximum voltage of the power supply (600V).

The apparent field intensity is obtained by dividing V_{B} by actual electrodes distance d_{act}. The relation between the cathode's temperature and the apparent field intensity is shown in Fig. 6. It shows a trend that as the cathode's temperature increases, the apparent field intensity increases under 1500°C, and it decreases over 1500°C.

4. Discussion

The actual electrodes' distance d_{act} of some points are shown in Fig. 6. It shows a trend that the larger d_{act} is, the smaller the apparent field intensity at breakdown is.

According to the research of the effect of electrode-tip's curvature on the field intensity by Nurishi[3], the theoretically analytical field intensity is larger than the apparent field intensity by the effect of the curvature. The effect increases as d_{act} increases. Therefore, by taking into account the effect of cathode's curvature in the field intensity, the experimental points might be compensated upward approaching the analysis result. The amount of the shift is large as apparent field intensity is small. Thus, it is suggested that the analysis field intensity considering the cathode's curvature might be determined by the cathode's temperature.

5. Conclusion

We proposed an experimental system for independently changing the cathode's temperature and apparent field intensity in the range written as below.
-Cathode temperature: room temperature ~ 2100 ℃
-Apparent field intensity: 0 ~2500 V/mm

Experimental results suggest that the electrodes' curvature can't be ignored, and that the actual field intensity may be determined by the cathode's temperature.

6. Reference

[1] T.Omata,'Effects of Arc Current and Voltage between Electrodes on Arc Reignition in DC Arc Discharge", Mate2017, 23rd Symposium on "Microjoining and Assembly Technology in Electronics", 2017, Jan.

[2] Y.Murooka, K.R.Hearne "The Effect of Electrode Temperature on Spark Brearkdown Voltage" The transactions of the Institute of Electrical Engineers of Japan.A

[3] 塗師豪太, 2017 年度学士論文

Image Feature Extraction by Sliding Discrete Fourier Transformation

Student's ID: 15B08321 Name: Sun Xu Supervisor: Yamasita Yukihiko

1 Introduction

In the fields of computer vision, pattern recognition, etc, object recognition has been intensively studied as an important research theme. It is realized by associating feature points in two images. The corresponding feature points in two images must be detected from a unique point. The local feature is described with respect to the feature point, and they can be associated based on the feature.

There are two important points in feature point detection. The first is the exact location of a feature point, and the second is high repeatablity. Many feature point detection methods have been proposed in order to improve locarization and repeatability. One of the detection methods to extract characteristic points that are invariant against rotation and scale change is called "SIFT"(Scale-Invariant Feature Transformation), which is provided complete by David Lowe in 2004.

In SIFT, feature points are extracted using the difference of Gaussian that in an approximated method for Laplacian of Gaussian. This paper proposes to use the sliding discrete Fourier transformation (we denote it by SDFT) to calculate the difference of Gaussian and Laplacian of Gaussian, then applies it to SIFT to detect feature points and confirms the effectiveness by experiment.

2 Mathematical Preparation

Gaussian smoothing is a process of blurring an image using a Gaussian function. It can be applied to noise removal, preprocessing of edge extraction, etc.

Let the coordinates of the image before rotation be (x, y), the coordinates of the image after rotation with rotation angle θ be (x', y'), then rotation of an image is defined by the coordinate transformation with

$$\begin{pmatrix} x' \\ y' \end{pmatrix} = \begin{pmatrix} \cos\theta & -\sin\theta \\ \sin\theta & \cos\theta \end{pmatrix} \begin{pmatrix} x \\ y \end{pmatrix}.$$

Scale change in SIFT means that the convolution of the input image with the two-dimensional Gaussian function with standard deviation σ, that is, Gauss smoothing.

3 Difference of Gaussian to approximate Laplacian of Gaussian

Laplacian of Gaussian is given by

$$G_{DD}(x, y) = -\frac{x^2 + y^2 - 2\sigma^2}{2\pi\sigma^6} \exp\left(-\frac{x^2 + y^2}{2\sigma^2}\right).$$

We denote Laplacian of Gaussian by LoG.

The difference of Gaussian is given by the difference between two images given by Gaussian Smoothing with two different parameters. Let a smoothed image be $L(x, y, \sigma)$, then the difference of smoothed image is given by $D(x, y, \sigma) = L(x, y, k\sigma) - L(x, y, \sigma)$.

Partial differentiation of the Gaussian function with respect to the standard deviation σ has relationship with LoG, which is $\frac{\partial G}{\partial \sigma} = \sigma \Delta G$. Also, by combining differential approximation of partial derivatives, we can have $\sigma \Delta G = \frac{\partial G}{\partial \sigma} \simeq \frac{G(x,y,k\sigma) - G(x,y,\sigma)}{k\sigma - \sigma}$. Then, we know $(k - 1)\sigma^2 \Delta G \simeq G(x, y, k\sigma) - G(x, y, \sigma)$ can express approximation.

4 SIFT

SIFT (scale-invariant feature transformation) can be separated into 5 parts.

The first part is the extreme value detection in scale space. We need to use a lot of smoothing parameters σ to apply to the Laplacian of Gaussian filter. This σ can be regarded as a scale-parameter. And we often use the difference of Gaussian for approximation to search local extrema of an image over scale and space.

The second part is the localization of key points. We calculate detailed cordinates of key point candidates. In SIFT, we use Taylor expansion of the scale space to obtain an extreme value, and delete the key points candidates with a certain threshold value. After that, we use Hessian matrix to delete the key points on edges.

The third part is to calculate the orientations of key points, because we want to obtain rotate-invariant features. Depending on the scale, we extract the points around the keypoint, then calculate the magnitude and the orientation of the gradient in that region. We created a gradient histogram for all directions of 360 degrees with 36 bins, and the maximum direction is taken as the orientation of the key point.

The fourth part is to describe the features. We extract 16×16 areas around the key point. We divide them into 4×4 small blocks. For each small block, we create a gradient histogram with 8 bins. Then, we have 128 values for each key point. A feature vector of the 128 values is constructed.

The fifth part is matching of key points. In SIFT, we use distance to match key points one by one.

5 Gaussian smoothing using sliding discrete Fourier transform

According to [2], we can approximately calculate the convolution between Gaussian function, and second derivatives of Gauss functions, and an input image by $g(n) \simeq \sum_{p=0}^{P} a_p c_p(n)$, $g_D(n) \simeq \sum_{p=1}^{P} b_p s_p(n)$, $g_{DD}(n) \simeq \sum_{p=0}^{P} d_p c_p(n)$, where $c_p(n)$ and $s_p(n)$ are coefficients of SDFT of input $f(n)$, a_p, b_p, and d_p are the coefficients of Fourier series of Gaussian function and its derivatives. They can be calculated in advance. In order to calculate $c_p(n)$ and $s_p(n)$, according to [2], we can use formulas $u(n) = \sum_{k=0}^{n} f(k)e^{i\beta pk}$, $v(n) = u(n) \cdot e^{-i\beta pn}$, $v(n+1) = 2\cos(\beta p)v(n) - v(n-1) + f(n+1) - e^{i\beta p} f(n)$.

6 Experiment

I propose a new feature point extraction method named SIFT-SDFT. The SIFT-SDFT method changes the Gaussian smoothing and DoG in SIFT to Gaussian smoothing and LoG by the sliding discrete Fourier transformation. There is no change in feature description. We will use test images to compare the effect between the SIFT and SIFT-SDFT. We will compare the accuracy of extracted matching and feature point by using digital photo with rotations.

In Figures 1 and 2 we show matching results by two methods.

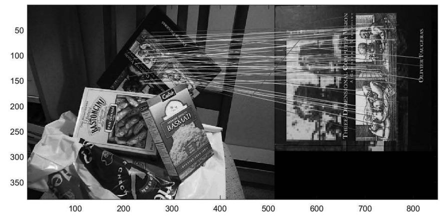

Figure 1: Matching by SIFT

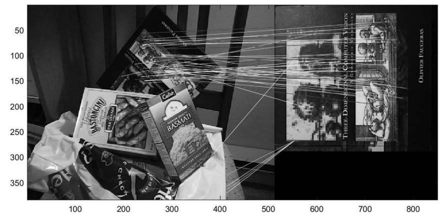

Figure 2: Matching by SIFT-SDFT

Table 1: Matching and extraction accuracy with 90-degree-rotated image

	SIFT	SIFT-SDFT
Matching	99.26%	100.00%
Point extraction	67.59%	82.63%

Table 2: Matching and extraction accuracy with 180-degree-rotated image

	SIFT	SIFT-SDFT
Matching	99.74%	100.00%
Point extraction	63.47%	81.71%

Tables 1 and 2 show the accuracies of matching and extracted feature points.

The number of feature points extracted by the proposed method is fewer than SIFT. The reason is that when SIFT extracts feature points, it enlarges the input image size by 2 times in order to obtain more feature points. The proposed method just uses the original size of input image.

The computation time is longer. Because SIFT-SDFT needs to calculate Gaussian smoothing and LoG seperately while SIFT just calculates Gaussian smoothing once and then takes difference of results of Gaussian smoothing to approximate LoG.

Regarding to the accuracy of matching, both SIFT and SIFT-SDFT have a similar high accuracy. However, regarding to the accuracy of extracted feature points, the proposed method is about 15% better than SIFT.

7 Consideration

This paper proposes the method using sliding discrete Fourier transformation to extract feature points of an image. We confirm the matching and extraction accuracies by proposed method is better than the standard SIFT. Future works are to increase the number of extracted feature points, and to verify the adaptability for projective transformation.

References

[1] David.G Lowe,"Distinctive Image Features from Scale-Invariant Keypoints",Computer Science Department,University of British Columbia,Vancouver, B.C., Canada,January 5,2004.

[2] Yukihiko Yamasita and Toru Wakahara, "An initial search method for region-based image matching", Technical Report of IEICE, vol.118, No.219, PP.119-124, 2018.

食品安全認証の取得有無と日本食品企業の特徴との関係

学籍番号：15B07340　　氏名：周　温文　　指導教官：阿部　直也

1. 研究の背景と目的

食品の安全性を確保し、維持することはどんな時代においても重要性の高い課題だと考えられる。現在の日本では、「安心」かつ「安全」にものを食べるのが当然のことである。しかし、大規模食中毒が多発してきた。例えば、1968年カネミ倉庫社製の食用米ぬか油による食中毒事件、また 2000年にも、雪印乳業（現：雪印メグミルク）の「雪印低脂肪乳」が原因の黄色ブドウ球菌食中毒事件も発生した。これらの事故の原因となるのが生産管理の不十分である。多くの研究では、食品の安全性を向上させる方法として、食品安全認証および管理システム採用に焦点を当てている。

国際食品安全認証は主に三つがある。一つは、潜在的な危険がプロセスを特定して管理する「HACCP 認証」である。もう一つは全てのサプライチェーンやフードチェーン（関係者）をカバーできる「ISO22000 認証」である。最後に管理システムの要件と ISO 技術基準に基づき、特に腐敗しやすい食物のために発行される「FSSC22000 認証」である。日本では食品の安全を守るために食品委員会、厚生労働省、農林水産省などがそれぞれ担当する「リスク評価」、「リスク管理」、「リスクコミュニケーション」の３要素がお互いに働いている。また現在国内の食品安全認証がない。

現在、一部の日本の食品企業は食品安全認証を積極的に取っているが、一部が全く採用しない。食品安全認証の取得有無と日本食品企業の特徴との間にどんな関係があるか。

既存研究のレビューにより、食品企業が食品安全認証を採用する目的は主に三つがある。一つ目はより効率的な生産管理を求めるということである。認証を採用した後で、内部生産のプロセス、手順の定義とモニタリングの改善をできるため、生産効率を向上できる。効率の改善により、企業の生産コストを減らせると考えられる。二つ目は認証の採用により企業の公的なイメージを変えられて販売を促進できるということである。食品安全認証の力を借りて自社製品の安全性などを宣伝し、顧客の購買行動に影響を与えられる。三つ目は国の食品安全に対する政策の要求に応えられるために、食品安全認証を採用しているか。国や企業の実状によって目的が違うが、日本企業のことがまた分析されていない。

２．研究の枠組み

日本における株式会社東京証券取引所、市場第一部（いわゆる東証一部）に上場している 73 社の食品関連企業による「FSSC22000 認証」、「ISO22000 認証」及び「HACCP 認証」の得状態について把握するために収集・使用いたデータおよびその分析枠組みを提示する。東証一部 73 社の会社の 2018 年 IR 情報から、2017 年の売り上げ、営業利益や従業員数を取集し、また各会社のホームページから食品安全認証の情報を収集した。

具体的には各社の認証の取得の有無を確認し、名義尺度の変数とした。また、データの精度を上げるために、食品会社各工場の認証状態を確認し、認証を取っている工場が工場全体に占める割合を算出した。そして、まずはクロスター分析をして、データ全体像を把握した後で、より詳しい結果を求めるために、一元配置分散分析（ANOVA）を用いて、各種の「食品安全認証」と「会社の収益」との関連性を分析する。次に、その結果に基づいて関連性のあるデータに対してさらに多重比較を行う。またχ^2分析を使って、食品カテゴリーにより分類したデータから、企業が認証を採用する目的を検討する。

３．分析の結果及び考察

表. 1研究データ全体像

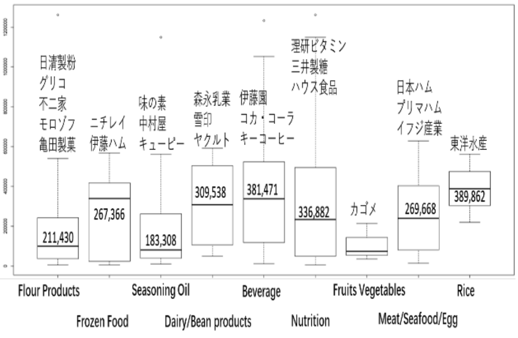

表.2「利益率」と「HACCP 認証」採用割合の検定

	Df	Sum Sq	Mean Sq	F value	Pr(>F)
Performance	2	2.838e+08	0.006068	3.474	0.0364
Residuals	70	3.154e+10	0.001746		

「HACCP 認証」を採用する企業の平均利益率は 4.1%であり、「HACCP 認証」に基づいて管理を行う企業あるいは一部の工場のみ認証を採用する企業の平均利益率は 4.7%であり、また認証を採用しない企業の平均利益率は 7.3%である。つまり、「HACCP」認証を採用しない企業ほうがより高い利益率を生み出している。

理由が主に二つがあると考えられる。一つ目は商品の包装にも「HACCP 認証」の標識を示していないので、企業は「HACCP 認証」の力を借りって宣伝するわけではないと判断できる。そこで、企業は生産の安全性を確保して生産効率を向上させたいために、「HACCP 認証」を導入したと考えられる。また 73 社うちの 5 社は日本国内で、「HACCP 認証」を採用していないが、海外工場や支社が認証を採用している。これはやはり海外（特に欧米、アジアの一部の地域）で水産食品や食肉製品などの製造施設への HACCP の導入が義務化されている。これも「HACCP 認証」を導入する一つの理由である。

また検定結果により、「FSSC22000 認証」や「ISO22000 認証」の採用が「企業収益性」と関係がないということが分かった。

表.3「冷凍食品」と「ISO22000 認証」との分析

認証 商品	なし	あり	合計
取り扱わない	36	27	63
取り扱う	1	9	10
合計	37	36	73
χ^2結果	0.005		

「冷凍食品」の会社は「ISO22000 認証」を採用する傾向がある。冷凍食品は長期保存を目的に冷凍状態で製造・流通・販売されているために、低温にすることで微生物の活動を抑える。麺粉などの商品と比べてより高い生産技術が求められる。つまり、会社は安全性を確保できように「ISO22000 認証」や「HACCP 認証」を採用している。

「肉・海鮮・卵」グループのχ^2結果が 0.06 である。そこで、「肉・海鮮・卵」の会社も「FSSC22000認証」を採用する傾向がある。理由も同じである。

表.4「飲料」と「ISO22000 認証」との分析

認証 商品	なし	あり	合計
取り扱わない	23	31	54
取り扱う	14	5	19
合計	37	36	73
χ^2結果	0.019		

「飲料」の会社は「ISO22000 認証」を採用する傾向がない。実は、飲料が長期保存、品質改良や酸化防止のためにいろいろな化学添加物が加えている。そこで、生産現場の衛生管理や安全保障がもちろん重要だが、化学添加物のコントロールが一番重要なポイントだと考えられる。サンプル中の「飲料」企業の「ISO9001 認証」の採用率は 42%であり、この「ISO9001 認証」は食品の品質を確保する認証である。もう一つの理由としては飲料製品がほとんど個人向けの商品であり、かつ日本の消費者が第三者の食品安全認証に関心を持っていないので、飲料企業が第三者認証を取らない傾向がある。また海外と貿易するために認証をとる視点から、飲料は基本的に日本国内で売っているので、国際の食品安全認証をとる必要がないと考えられる。

4. おわりに

本研究では過去日本の食中毒事件を振り替えながら、食品安全認証の重要性を示した。結果としては日本食品企業は安全性を確保できように第三者安全認証を導入したという可能性が高いと考えられる。食品安全認証と企業の売り上げや、従業員数や営業利益と関連性がないということが分かった。最後に企業が海外や国内の食品安全政策に従って食品安全認証を取っている。

今後の研究では企業のイメージと食品安全認証の関連性について研究を行う。

参考文献

[1]HACCP 認証協会
https://www.th-haccp.com/haccp/
（閲覧日：2019 年 2 月 1 日）
[2] 栗原　伸一. (2011). 入門統計学.オーム社
[3] A.Moore.D. (2004). DairyBeef: Maximizing Quality and Profits

GPU acceleration of initial search method for regional image matching

Student's ID: 15B15829 Name: Moran Lee Supervisor: Yamasita Yukihiko

1 Introduction

Image matching is applied to object detection and pattern recognition, which is one of the most important methods in image processing. Therefore, many image matching methods have been proposed. They can be roughly divided into two types, one is a feature point matching method as extracting feature points from the image and evaluating the consistency of the feature points, and the other is a region matching method as evaluating the consistency of a image region.

Furthermore, depending on the spatial relationship between the template image and the input image, matching can be divided into whole-to-part and whole-to-whole matching. Yamashita and Wakahara proposed a fast initial search method for whole-to-part matching. GPU can be used to further accelerate the method for real time computation. In this paper I propose the implementation method and compare it with CPU calculation.

2 Fast calculation of Gaussian convolution integral

Gaussian smoothing is a process of blurring an image using a Gaussian function. It can be applied to noise removal, preprocessing of edge extraction, etc.

Gaussian smoothing is a convolutional sum given by the following expression $O(n) \simeq \sum_{k=-K}^{K} G(k)I(n-k)$. Since Gaussian function is an even function, the differentiated Gaussian function is an odd function. Therefore, Gaussian function can be approximated by the cosine function ($G(k) \simeq \sum_{p=0}^{P} a_p \cos(\beta pk)$) and differential Gaussian function can be approximated by the sine function($G_d(k) \simeq \sum_{p=1}^{P} b_p \sin(\beta pk)$).

We define the convolutional sum of finite interval trigonometric functions as the following equations, $c_p[n] = \sum_{k=-K}^{K} I[n-k]\cos(\beta pk)$, $s_p[n] = \sum_{k=-K}^{K} I[n-k]\sin(\beta pk)$. Then, we can get a $O(PN)$ algorithm to calculate Gaussian convolutional sum as follows, $[v[n] = e^{i\beta p}v[n-1] + I[n]$, $c_p[n] + is_p[n] = (-1)^p(v[n+K] - v[n-K] + I[n-K])$.

3 Initial search method for regional image matching

The edge direction histogram $D(\theta)$ is weighted sum of the strength of edges in each edge direction in a certain region. It can be described by a Q-th order Fourier series as $D(\theta) = \sum_{q=-Q}^{Q} d_n e^{iq\theta}$. The coefficients can be calculated as $d_q \simeq \frac{I_X(x,y) - iI_Y(x,y)^q}{2\pi(\|I_1(x,y)\|^2+\epsilon)^{\frac{q-1}{2}}}$. In this case, when rotating the reference direction by θ_0, the coefficients d'_q of the rotated histogram can be obtained as $d\prime_q = d_q e^{-iq\theta_0}$.

Using fast calculation of Gaussian convolutional sum and Q-th order Fourier series of edge direction histogram, the feature value calculation of the initial search method for regional image matching can be described as follow.

Algorithm 1 Calculate Feature Values of Region

```
Require: Input Image $I$, a set of scales $S_a$, a set of center points for feature values $T_S$, The regularized coordinates of points where histograms are used $(x_m, y_m)$ $(m = 1, 2, ..., M)$
  for $S \in S_a$ do
    Calculate Gaussian differentiation of $I$ with scale $S/8$.
    Calculate the edge direction histogram $d_q$.
    Calculate Gaussian smoothing of $d_q$ in scales $S$ and $S/4$.
    for $(x, y) \in T_S$ do
      Calculate the orientation(s) of the region with the smoothed coefficient in scale $S$.
      for $\theta_0 \in$(the set of orientions) do
        Calculate cordinates of points where histograms are used.
            $x'_m = S(x_m \cos\theta_0 - y_m \sin\theta_0) + x$
            $y'_m = S(x_m \sin\theta_0 + y_m \cos\theta_0) + y$
        Rotated edge direction histogram in scale $S/4$ and get $M(2Q+1)$-dimensional vector.
        Normalise the obtained vector as its norm is 1 and store it as feature values at the region.
      end for
    end for
  end for
```

The feature values of the target region in the template image and of regions around sample points are calculated. Then, the inner product between feature values in the template image and input image are calculated. The region in input image that maximizes the inner products is given as the matched region.

4 Calculation by GPU

GPU calculation is a kind of SIMD (single instruction multi data) calculation, which means the same task is applied to different cores to process multiple data. GPUs of NVIDIA use warp schedulers to control jobs in the core. Therefore, we need to decrease the branches (if statement) of calculation to increase efficiency of calculation.

GPUs also use cache memory to accelerate calculation. Therefore, the efficiency of calculation can be increased by increasing the cache hit rate. And the best access pattern is given by Figure 1, where the cache hit rate is 100%.

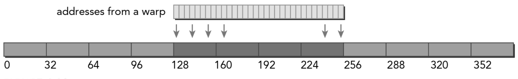

Figure 1: Best memory access pattern

The worst memory access pattern is given by Figure 2, where the cache hit rate is 12.5%.

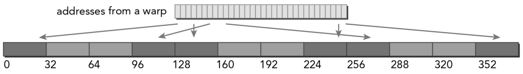

Figure 2: Worst memory access pattern

5 Optimization of initial search method by GPU

In the initial search method for region-based image matching, at first, we calculate Gaussian smoothing of d_q in scale S and $S/4$ at all points. Then we calculate the feature values for sampling region, and sort to find the point which matches the region in the template image best.

Because of the property of the warp scheduler, GPU is not suitable for sorting. Therefore we use CPU to do this job. Because of the same reason, we use CPU to find the point which matches the region best.

Almost all jobs in calculation of all Gaussian smoothing of d_q in scale S and $S/4$ can be calculated in parallel, because the jobs for a point don't have dependency. But the calculation of Gaussian convolution integral at a point is dependent of the result at the former point. Therefore, we divided tasks by rows and tasks for a row is assigned to a core.

But if we assign jobs for a row into a core, the memory access pattern becomes the worst. Therefore I optimize the calculation to increase the cache hit rate. For the purpose, I store results for a row into a column memory structure. Then transpose the data for the next step.

6 Experiment

I use a standard image Lenna (512px×512px) to compare the effect between CPU calculation and optimized GPU calculation of the initial search method for regional image matching introduced before.

At first, I calculate the compute time of CPU calculation (CPU). Secondly, I calculate the normal compute time of GPU calculation (GPU 1). Thirdly, we calculate the compute time of GPU calculation in which memory access is optimized (GPU 2). I calculate compute time of optimized GPU calculation with three scales which can show its efficiency in real world application (GPU 3).

Because the hardware spec affects the calculation efficiency, we use two types of computers to collect experiment data.

Table 1: Comparison of Compute Time(ms)

	940MX(6500U)	1060(7700K)
CPU	742	509
GPU 1	160	66
GPU 2	156	31
GPU 3	136	22

As we can see, the computation time of CPU is at least 5 times more than computation time of GPU. Furthermore optimized calculation has a better efficiency than normal one. Also, it can be calculated within 100 ms for the calculation with three scales, and it will enable 10fps in the initial search. Therefore, the propesd method it can be applied to real-time applications.

7 Conclusion

This paper proposed to accelerate initial search method for regional image matching and realize real-time computing by GPU. We confirm the acceleration and its practicality for real-time processing by experiments. Future works are to increase the hit rate of cache memory in read access, which may further accelerates the method.

References

[1] John Cheng,Grossman,McKercher,(2015)『CUDA C professional programming』,(translated by Sinya Morino) Impress Company, 2015.

[2] Yukihiko Yamasita and Toru Wakahara,"An initial search method for region-based image matching",Technical Report of IEICE, vol.118, no. 219, PP.119-124, 2018.

All-day energy harvesting power system utilizing a thermoelectric generator

Student Number: 15B16421 Name: Yasuki Kadohiro Supervisor: Jeffrey Scott Cross

1 Introduction

After the Great North East Japan earthquake in 2011, distributed energy systems using renewable energy have become popular topics of research [1], and especially, solar power generation systems are being installed worldwide [2]. However, this system has a critical limitation that it cannot generate electricity during the night when people use the most electricity. Energy demand is increasing year by year and it is considered that the energy problem will become the first of the humanity's top ten problems over the next 50 years [3]. Therefore, the systems which can generate electricity not only in the daytime but also in the nighttime is necessary. Moreover, in building applications, hot water is also in demand in addition to electricity so the system should produce hot water too.

Ashwin *et al.* [4] proposed a system combining solar water heating systems and thermoelectric generator (TEG). A TEG is the device which can generate electricity by utilizing the temperature difference between its two surfaces. The temperature difference is made by the concentrated solar thermal energy and the water stored in the tank, and the heat transfers to the water. The system is able to generate electricity and produce hot water. However, the system operates only during the day and cannot generate electricity after the sun goes down.

In this thesis, an all-day energy harvesting power system utilizing a TEG was researched in order to generate electricity both day and night. The proposed system is based on Ashwin's model but the difference is that the system heats water during the day in order to generate electricity at night. Two different systems (System 1 and 2) were designed and developed to investigate the best mechanism for the all-day energy harvesting system. The experimental and analytical study was conducted to investigate the system's potential.

2 Experimental Approach

System 1 was designed based upon Ashwin's model. The schematics of System 2 are shown in Fig 1 and 2. In System 2, two flat aluminum heat pipes (flat aluminum heat pipe 1, 2) are used due to their high heat flux carrying capacity and each of them is thermally coupled to TEG's upper and lower sides by thermally conductive tapes. Metal weights (3087.5g) are placed on TEG and flat aluminum heat pipe 1, 2 in order to reduce the thermal resistance between TEG and flat aluminum heat pipe 1, and 2. A portion of the flat aluminum heat pipe 1 in the water tank 1 is covered by a black absorbing film. Black paint is used as a light absorbing film. A portion of the heat pipe and around TEG are covered by glass wool in order to reduce the heat loss from System 2.

During the daytime, solar radiation passes through Fresnel lens and is concentrated on the flat aluminum heat pipe 1. The heat transfers from the concentrated solar radiation to cold water. Temperature differences of TEG are made by the concentrated solar radiation and cold water. In the experiment, a halogen lamp is used to supply the light since the solar radiation is unstable and the halogen lamp has a similar wavelength as solar radiation. The power is set to $11.29W$, $14.84W$, and $21.17W$. The voltage and water temperature are measured in the experiment.

During the nighttime, cold water (tap water) is poured into the water tank 1. The heat transfers from the hot water to the cold water via the TEG. The temperature difference generates voltage. Temperatures of hot water and cold water are measured in the experiment.

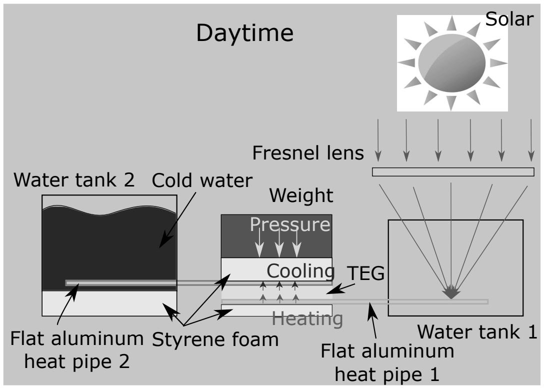

Fig. 1: Schematic of System 2, Daytime (Solar light and Cold water).

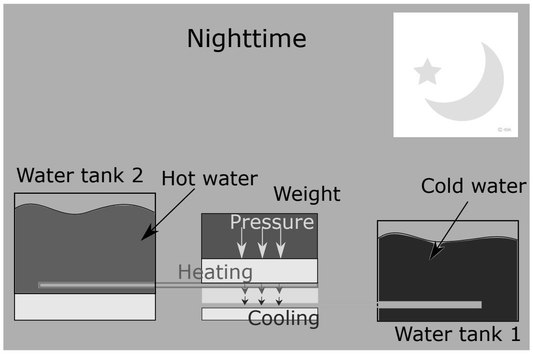

Fig. 2: Schematic of System 2, Nighttime (Hot water and Cold water).

3 Results and Discussion

In the experiment, voltage is measured and from the results, it is observed that System 1 and 2 can constantly generate electricity during the daytime. However, System 1 cannot generate electricity at all at night. System 2 can generate electricity at night but the voltage decreases over time due to the decrease of the temperature differences across the TEG. Therefore, countermeasures are necessary for System 2 to satisfy potential consumers who use electricity for 3 $\sim$ 5 hours at night. Comparing the best case scenarios relating to voltage when there is no heat loss, System 2 has an efficiency of 62 $\sim$ 65% and 60 $\sim$ 65% of the TEG ’ s maximum performance during the day and the night, respectively.

Table 1 shows the comparison of the thermal and electrical efficiency between System 2 and Ashwin's model [4] or System 1. Since Ashwin's model or System 1 cannot generate electricity and the voltage decreases over time in System 2 at night, the electrical efficiency during the nighttime is not shown in Table 1.

Table 1: Comparison of the systems

Results	System 2	Ashwin's model or System 1
$\eta_{electrical}$ (Daytime)	0.68% (14.84W) 0.99% (21.17W)	1.29% (14.84W) 1.87% (21.17W) (System 1)
$\eta_{thermal}$ (Daytime)	65.3% (14.84W) 65.4% (21.17W)	57.6% (20W) 55.0% (40W) (Ashwin's model)
$\eta_{thermal}$ (Nighttime)	48.4% (m_1 =1000g) 37.2% (m_1 =2000g)	-

Here, m_1 is the mass of hot water in the storage tank. As mentioned, System 1 has same structure or mechanism as Ashwin's model. Both systems are concentrating the solar radiation on TEG's hot side directly. In the above table, it is observed that System 1 has higher electrical efficiency than System 2. It can be considered that the mechanism of System 1 (or Ashwin's model) has more advantages than the mechanism of System 2 to generate electricity during the daytime. Here, the results of Ashwin's model are not used since the electrical efficiency depends on not only the mechanism of the system but the performance of the TEG. A different TEG is used in the Ashwin's model, so System 2 is only compared with System 1. In terms of thermal efficiency during the daytime, it is observed that System 2 has higher thermal efficiency than Ashwin's model. It can be considered that the heat loss in the proposed systems (System 1 and 2) is smaller than the heat loss in Ashwin's model. Since System 1 and Ashwin's model did not store heat in the water during the nighttime, the thermal efficiency of System 2 during the nighttime is only shown in the table. In terms of thermal efficiency during the nighttime, it is observed that the thermal efficiency of System 2 is lower when compared to the thermal efficiency of other systems during the daytime. The heat loss must be reduced and it is necessary to make the value of thermal efficiency more than 60% (near to the thermal efficiency during the daytime). However, System 1 and Ashwin's model cannot store heat and generate electricity at night so it is obvious that System 2 has the highest potential for all-day energy harvesting.

4 Conclusions

Three systems have been compared and the results indicate that System 1 or Ashwin's model is the best system to generate electricity and to transfer the heat during the daytime, and System 2 is the best system to generate electricity and to transfer the heat during the nighttime. Comprehensively, System 1 or Ashwin's model cannot produce hot water and generate electricity during the nighttime so it is considered that System 2 is the best system to generate electricity all-day and to produce hot water. From the study, it is proven that System 2 can store 60 $\sim$ 65% of the input solar thermal energy during the daytime and it can recover 35 $\sim$ 50% of the stored thermal energy. Moreover, it is proven that System 2 exhibits an efficiency of 60 $\sim$ 65% of the TEG ’ s maximum performance during the day and the night, respectively. However, the electricity generation is not sufficient at night due to the voltage decrease over time so System 2 must maintain a constant temperature differential as much as possible to generate higher electricity and to satisfy potential consumers.

References

[1] Miguel Esteban, Joana Portugal-Pereira. (2014). Post-disaster resilience of a 100% renewable energy system in Japan. *Energy*, *68*, 756-764.

[2] Omar Ellabban, Haitham Abu-Rub, Frede Blaabjerg. (2014). Renewable energy resources: Current status, future prospects and their enabling technology. *Renewable and Sustainable Energy Reviews*, *39*, 748-764.

[3] Geoff G. X.Wang. (2012). Development of clean energy and environmental technologies to address humanity ’ s top problems. *Frontiers of Chemical Science and Engineering*, *6*(1), 1-2.

[4] Ashwin Date, Abhijit Date, Chris Dixon, Aliakbar Akbarzadeh. (2014). Theoretical and experimental study on heat pipe cooled thermoelectric generators with water heating using concentrated solar thermal energy. *Solar Energy*, *105*, 656-668.

Liquid-Liquid Equilibria of Terbium and Dysprosium with PC-88A as Extractant

Student Number: 15B05506 Name: Junki KURIHARA Supervisor: Ryuichi EGASHIRA, Hiroaki HABAKI

1. Introduction

Rare earth elements (REEs) are used in various industrial products, such as, the electric vehicles and air conditioners, in which Ne-Fe-B magnets containing neodymium, terbium (Tb) and dysprosium (Dy) are used[1][2]. Since the REEs coexist in the ores and the industrial products usually contain multiple REEs, the separation of REEs in the ore or the recovery of them from industrial product wastes must be important technology.

The solvent extraction is commercially used as a method to separate REEs. Although a number of works on the separation of REEs by solvent extraction have been reported, there are only few studies focusing on the equilibria in the single element system of Tb or in the binary element system of Tb and Dy, whose chemical properties are quite similar, making separation difficult.

In this work, the extraction equilibria were studied in the single element system of Tb or Dy, and the binary element system of Tb and Dy, using PC-88A as an extractant.

2. Experimental

Chloride salts of Tb and Dy in analytical grade were used as metal ion sources. PC-88A (2-Ethylhexyl-2-ethylhexylphosphonate) was used as an extractant. **Table 1** shows the experimental conditions for liquid-liquid equilibrium measurement. The feed solutions containing Tb or Dy for the single metal ion system, or Tb and Dy for the binary metal ion system were prepared. The initial molar concentrations of the metal ion in the aqueous phase and the extractant in the organic phase were fixed. The initial *p*H was adjusted using hydrochloric acid. Kerosene was used as a diluent to prepare the organic phase. The aqueous and organic phase of the same volumes were contacted each other in conical flask and shaken for 12 hours to reach equilibrium. Then, the aqueous phase at initial and equilibrium conditions were analyzed to determine the respective *p*Hs and metal concentrations, using *p*H meter (F-74, Horiba) and ICP-AES (SPS7800, Hitachi High-Tech Science Corp.).

3. Results and Discussion

Reaction equilibrium of the trivalent rare earth metal ion between aqueous phase and organic phase with PC-88A, is generally described as,

$$M^{3+} + 3\overline{(\mathrm{RH})_2} \rightleftarrows \overline{M\mathrm{R}_3(\mathrm{RH})_3} + 3\mathrm{H}^+ \qquad (1)$$

where the overbar and $(\mathrm{RH})_2$ stands for the compound in the organic phase and extractant in dimer, respectively. The material balance equation was expressed as,

$$V_{\mathrm{aq},0}C_{M,\mathrm{aq},0}=V_{\mathrm{org,eq}}C_{M,\mathrm{org,eq}}+V_{\mathrm{aq,eq}}C_{M,\mathrm{aq,eq}} \qquad (2)$$

Table 1 Experimental conditions

Initial metal concentration $C_{M,\mathrm{aq},0}$ (M=Tb, Dy)	
-Single element system	0.005 kmol m^{-3}
-Binary element system	0.005 kmol m^{-3} (for each)
Initial *p*H $p\mathrm{H}_0$	0.0~2.0
Concentration of extractant $C_{\mathrm{RH2,org},0}$	0.25 kmol m^{-3}
Aqueous phase volume V_{aq}	2.0×10^{-5} m^3
Organic phase volume V_{org}	2.0×10^{-5} m^3
Extraction temperature	298 K
Extraction time	12 h

The metal concentration in the organic phase $C_{M,\mathrm{org,eq}}$ at equilibrium was obtained using Eq. (2) with $C_{M,\mathrm{aq},0}$ and $C_{M,\mathrm{aq,eq}}$ directly measured. The concentration of extractant in the organic phase at equilibrium was calculated as,

$$C_{\mathrm{RH2,org,eq}}=C_{\mathrm{RH2,org},0}-3C_{M,\mathrm{org,eq}} \qquad (3)$$

Using the equilibrium constant (K_M), Eq. (1) can be rewritten as Eq. (7), where D is the distribution coefficient, defined as,

$$D = C_{M,\mathrm{org,eq}} / C_{M,\mathrm{aq,eq}} \qquad (4)$$

$$\log D\text{-}3 \log C_{\mathrm{RH2,org,eq}} =3p\mathrm{H}+\log K_M \qquad (5)$$

Fractional extraction of metal ion E_M and solvent free metal mol fraction in phase j, $x_{M,j}$ were defined as,

$$E_M=C_{M,\mathrm{org,eq}}/C_{M,\mathrm{aq},0} \qquad (6)$$

$$x_{M,j}=C_{M,j,\mathrm{eq}}/(C_{\mathrm{Dy},j,\mathrm{eq}}+C_{\mathrm{Tb},j,\mathrm{eq}}) \qquad (7)$$

where j stands for aq or org.

Single element system

In all cases, the *p*H at equilibrium became lower than that at initial condition since hydrogen of the extractant was released by the extraction of metal ions.

The plots of E_M in the single systems against the equilibrium *p*H are shown in **Fig. 2**. In the range of low *p*H, both REEs were little extracted into the organic phase.in the range of *p*H of 0 to 0.5, both elements started to be extracted. Change of fractional extraction was significant in the range of *p*H of 0 to 1, and over 90% of REEs were extracted when *p*H was higher than 1.

The terms of the left hand of Eq. (5) were plotted against the *p*H at equilibrium in the case of the single metal ion systems, as shown in **Fig. 2**. According to Eq.

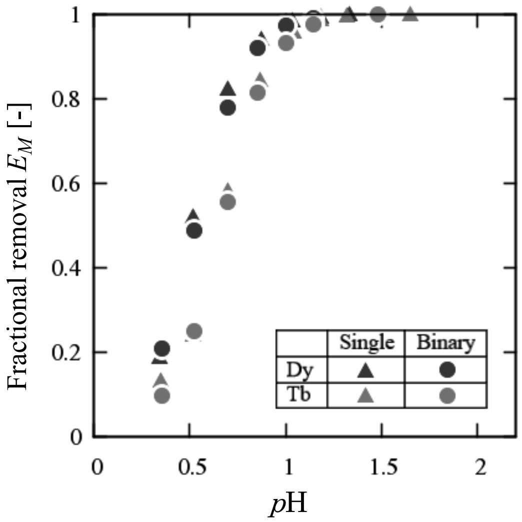

Fig. 1 Fractional removal vs. pH at equilibrium in single or binary element system

(5), the slope of the line of the plots with each metal ion should be 3, and it was found that both reactions of Tb and Dy with PC-88A in the single systems followed Eq. (1). Then, the reaction equilibrium constants of K_{Tb} and K_{Dy} were estimated as 1.34 and 2.99, respectively. The Dy ion was extracted more than Tb because the heavier REEs should be generally extracted more than the lighter ones.

The separation factor between Tb and Dy were obtained as $\beta_{\mathrm{Dy,Tb}}=K_{\mathrm{Dy}} / K_{\mathrm{Tb}}=2.2$. Then, $\beta_{\mathrm{Dy,Tb}}$ was relatively low and the separation between Tb and Dy was found to be relatively difficult by the solvent extraction.

Binary element system

pH change was also observed in the binary element system and the decrease was more significant than that in the single element system because the larger amount of REE was extracted.

The plots of E_M in the binary systems against the equilibrium pH are shown in Fig. 2. Trend of extraction was similar to that in the single system.

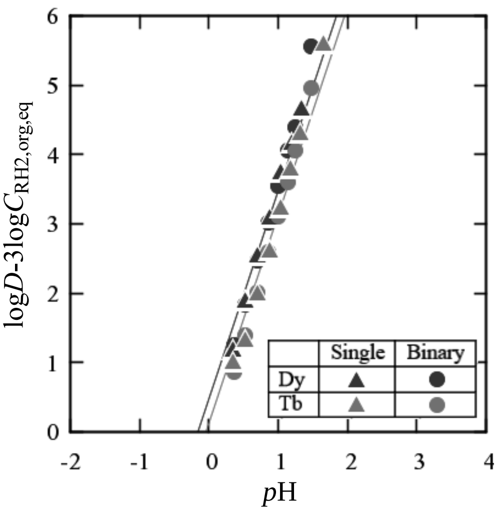

Fig. 2 Slope analysis of terbium and dysprosium in single and binary system

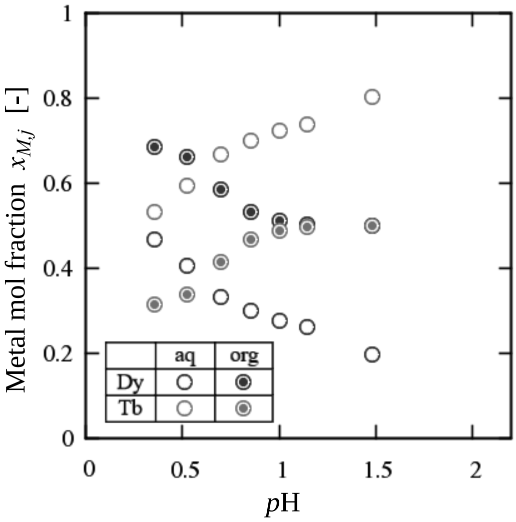

Fig. 3 Mol fraction of each REE in each phase

The extraction equilibria with the binary system containing both Tb and Dy ions are shown in Fig. 2, together with those with the single systems. The results with the binary system were approximately the same as those for the respective metal ions with the single systems, and no effects of the coexisting metal ions were found in this measurement range.

Plots on **Fig. 3** show the mol fraction of each metal in organic phase. Mol fraction of Dy was higher than Tb at the lower pH while almost same mol fraction was obtained at the higher pH. From this result, purification can be obtained when pH is low, but as Fig. 3 shows, REEs are not extracted into organic phase at the lower pH, such as less than 0.5, so the concentrations of both elements should be low.

The mol fraction of each metal in aqueous phase is also shown on Fig. 3. In contrast to the result in organic phase, mol fraction of Tb is higher than that of Dy and the higher pH made the larger difference of mol fraction. When pH is higher than 1, although the difference of mol fraction between the 2 elements was relatively wide, over 90% of elements were extracted into organic phase. From the results shown on Fig. 1, it is declared that batch separation or purification is not enough in this condition, and for the further separation, multistage process should be considered.

4. Conclusions

From the experiment on the single element system, extraction coefficient of terbium and dysprosium and the separation factor were estimated; $K_{\mathrm{Dy}}=2.99$, $K_{\mathrm{Tb}}=1.34$, $\beta_{\mathrm{Dy,Tb}}=2.2$. From the experiment on the binary element system, extraction trends were clarified.

5. Reference

[1] Y. Arai *et al.*, 廃棄物資源循環学会誌, Vol. 22, No. 1, p. 41-49 (2011)

[2] S. Ishihara *et al.*, Chishitsu News, No. 609, p. 4-18 (2005)

Enhancing NH_3 recovery from aquaculture sludge composting by inoculation of the sludge solubilizing bacteria

Student Number: 15B10306 Name: Ryo NAKAGAWA Supervisor: Kiyohiko NAKASAKI

1. Introduction

The accumulation of aquaculture sludge on the bottom of pond could decrease the quality of the water and affect to the shrimp culture. The efficient strategy to treat aquaculture sludge from the pond has not been yet established. Methane fermentation and composting are well known as methods to treat the aquaculture sludge, but their products has low values. Thus, a way to improve the value of the products is important for the improvement of the sustainability of aquaculture industry.

Our laboratory recently proposed a new strategy to recovery of NH_3 gas from the aquaculture sludge by using thermophilic composting [1]. NH_3 gas is free from pathogen and heavy metals, so that it can be used for cultivation of high value micro algae. From the nitrogen mass balance analysis of the sludge composting [1], it was revealed that NH_3 recovery reached 16% of the total N content of the sludge, but 65% of N was remained as un-decomposed organic nitrogen. Thus enhancing the solubilization of sludge is required to increase the ammonia recovery. The objective of this study is to enhance the organic nitrogen degradation in the aquaculture sludge by inoculating the microorganism.

2. Materials and methods

2-1. Composting of shrimp aquaculture sludge

Aquaculture sludge was obtained from the bottom of a shrimp pond in Malaysia. This sludge is fresher than the sludge used in our previous paper[1], so that it contains almost double amount of easily degradable organic matter compare to that sludge. Lab-scale composting experiment was conducted to examine the NH_3 recovery in different temperature conditions (50, 60, and 70°C). The sludge was mixed with sawdust and commercial seeding material with the mixing ratio of 5: 14: 1 in dry-weight base. Total nitrogen content of the sludge, and the content of total dissolved nitrogen and NH_4^+-N in compost sample, and NH_3 gas yield were measured to examine the nitrogen mass balance during composting.

2-2. Isolation of protein-degrading bacteria and inoculation for composting materials

Protein-degrading bacteria was isolated from compost sample in this study by using skim milk agar medium, by selecting colonies which forms clear zone around the colony on the medium. The DNA of the isolated bacteria was extracted and analyzed the sequence. To clarify its ability to enhance the sludge solubilization, the isolated bacteria was suspended in 0.9 w/v% NaCl solution and inoculated to the sludge composting. Lab-scale composting of the sludge was conducted in a same way with 2-1.

3. Results and discussion

3-1. Effect of temperature on solubilization of the sludge

The nitrogen mass balance after composting is exhibited in Fig. 1. The ammonia ($NH_3 + NH_4^+$-N) conversion efficiency of dissolved nitrogen at 70°C was lower than 60°C. These results show that the composting temperature at 60°C is the optimum condition for NH_3 recovery. On the other hand, more than 60% of nitrogen remained in the compost as non-dissolved N. Therefore, enhancing the solubility of nitrogen is needed for NH_3 recovery.

Fig. 1. Nitrogen mass balance before and after composting at different temperatures (50°C, 60°C, and 70°C).

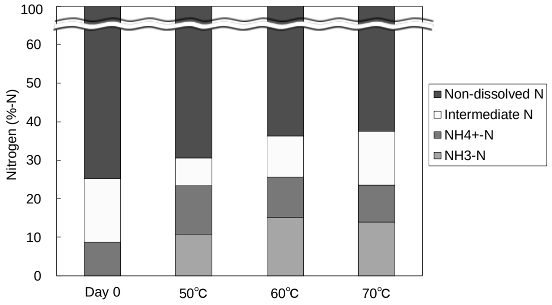

Fig. 1. Nitrogen mass balance before and after composting at different temperatures (50°C, 60°C, and 70°C)

3-2. Effect of inoculation of the R2 isolate

The picture of isolated bacteria (R2) is shown in Fig. 2. It was shown that the clear zone appeared around R2 colony on the skim milk medium. It is suggested that the R2 could degrade the protein and has potential to be used for the inoculation in order to increase the ammonia recovery in the composting.

The nitrogen mass balance of the sludge composting with or without the inoculation of R2 is exhibited in Fig. 3. The solubilization efficiency of non-dissolved nitrogen, which is obtained by the formula:

$((NH_3 + NH_4^+\text{-N} + \text{intermediate N}) / \text{Total N}) \times 100$, at the inoculated condition and un-inoculated condition were 45.3% and 38.0%, respectively. These results revealed that the R2 could be a useful microorganism to increase the ammonia recovery from aquaculture sludge composting by enhancing the sludge solubilization.

Fig. 2. Appearance of the clear zone around R2 isolate on the skim milk agar medium.

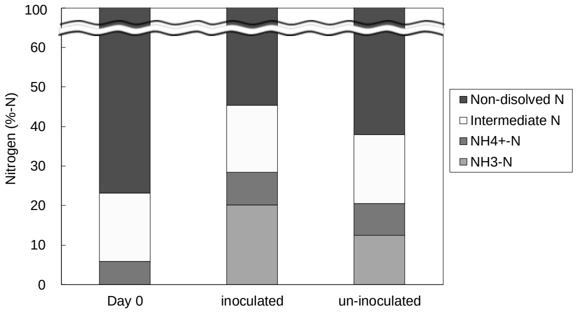

Fig. 3. Nitrogen mass balance before and after composting with and without inoculation of R2 isolate.

4. Conclusion

Protein-degradable bacteria was isolated from the compost sample. Furthermore, NH_3 recovery from composting of aquaculture sludge was improved by enhancing the solubilization of non-dissolved nitrogen in sludge by inoculation of the protein-degrading bacteria.

Reference

[1] Koyama *et al.*(2018) *Bioresour. Technol.*, vol. 265, pp. 207–213

[2] Nakasaki *et al.*(2009) *Bioresour. Technol.*, vol. 100, no. 2, pp. 676–682

New Activation Functions by Simulating Synaptic Plasticity to Enhance Forgetfulness in Neural Network

Student Number: 15B15918 Name: Liu Xiaochen Supervisor: Yukihiko Yamashita

1. Research Background

One of the reasons why these days, artificial intelligence (AI) technologies based on deep learning neural network, can achieve the best result so far in human history might be the neural network somehow works familiar to the network made of natural neurons in human or animal brains. Another reason might be the none liner functions used in neural networks, such as ReLU, somehow works familiar to such a neuron.

As an attempt to make AI behave like human being, I tried to redesign the popular activation function ReLU to simulate a biological neuron better, especially by simulating synaptic plasticity mechanism. What I expect on this simulation is that to find a simple way to simulate and control the forgetfulness of a neural network.

2. Methodology and Theory

2.1. Biological and Artificial Neural Networks

The human brain consists of a tremendous number of nerve cells or neurons which form into extremely complex networks. Neurons communicate via electrical signals, and connection between neurons are called synapses [1].

Each neuron typically receives many thousands of connections from other neurons and all signals from other neurons are integrated or summed together in some way and, roughly speaking, if the resulting signal exceeds some threshold then the neuron will ”fire” or generate a voltage impulse in response [1].

On the other hand, an artificial neural network is an interconnected assembly of simple processing elements, units or nodes, whose functionality are loosely based on the animal neuron [1].

The key effort to simulate the behaviour of biological neuron is to find a mathematical switch function, which can be turned on and off depending on the value of input. One of the most popular approach is an activation function called *Rectified Linear Units* (ReLU), which can be described as

$$f(x) = \max(0, x). \tag{1}$$

where x represents the input signal, and $f(x)$ represents the output signal.

However, ReLU can’t provide further simulations of any other important behaviour of a biological neuron, such as *synaptic plasticity*, for lack of learnable parameters.

2.2. Synaptic Plasticity

Synaptic plasticity is the ability of synapses to strengthen or weaken over time, in response to increases or decreases in their activity [2]. Some widely accepted hypotheses suggest that activity-dependent synaptic plasticity is induced at appropriate synapses during memory formation [3].

Related to synaptic plasticity, typical mechanisms that can be roughly described as consistent stimulation signals transmitted by synapse can increase or decrease the strength of the synapse its self [3].

3. Proposed Method

3.1. Proposed Activation Function

To simulate the connection strength variation between actual neurons, I designed a new activation function that is similar to ReLU function, however, with a learnable parameter a which I called *activate strength*. This activation function can be described as

$$f(x) = \max(0, ax). \tag{2}$$

where a is the *activate strength*. Combined with the newly designed parameter updating method which mentioned in Section 3.2, I call this activation function as *variable ReLU (vReLU)*.

3.2. Parameter Updating Method for vReLU

Because the tradition way for parameter updating, *gradient descent* [5], is not appropriate for synaptic plasticity mechanism simulation, I designed a new algorithm to update the parameter, which can be described as Algorithm 1.

Algorithm 1: vReLU 1

```
Data: Input: $x$
      Old parameter: $a$
Result: Updated parameter: $a$
Set $vr = 10^{-5}$ (for example)
if $x > 0$ then
    $a = a + vr$
else
    $a = a - vr$
end
$a = \max(0, x)$
```

Algorithm 2 is an alternative algorithm I designed which works similar to Algorithm 1, but much more efficient.

3.3. Implementation by PyTorch

In this research, I use PyTorch [4] to implement the newly designed activation functions and the newly designed parameter updating method which was described in Section 3.1 and Section 3.2. However, since

Algorithm 2: vReLU 2

```
Data: Input: $x$
      Old parameter: $a$
Result: Updated parameter: $a$
Set $b = 10^{-5}$ (for example)
$a = 2a \cdot \text{Sigmoid}(bx)$: ($\text{Sigmoid}(x) = \frac{1}{1+\exp(-x)}$)
```

the newly designed parameter updating method works different from the default way of PyTorch, *gradient descent* [5], I find a solution to keep the implementations are compatible with PyTorch default libraries.

Concretely, I implemented each version of the activation function and parameter updating function algorithm into automatic differentiation functions [4], vrelu1 and vrelu2. Because the algorithm used here is not related to differentiation, instead of computing the differentiation of *activate strength* (a), I implemented the code that outputs

$$\text{dif} = (a_{old} - a_{new})/l_r. \tag{3}$$

where dif is the fake 'differentiation' of a and l_r is the learning rate of a typical gradient descent like parameter updating algorithm, such as *mini-batch gradient descent* and *Adagrad* [5]. PyTorch will later updating a automatically by

$$a_{new} = a_{old} - \text{dif} \cdot l_r. \tag{4}$$

or another result near this value, which turns out to be the correct result we want.

After that, I packed these differentiation functions into higher-level standard modules, vReLU1 and vReLU2, which can be easily used in PyTorch.

4. Experiment Models

All experiments start by training a basic convolutional neural network (CNN) model with complete data, which means the data contains all kinds of labels. Then use transfer learning method to train the pre-trained CNN model (all parameters are kept, ReLU layers are replaced by vReLU layers or not) by incomplete data, which means one certain kind of label is removed from the data on purpose.

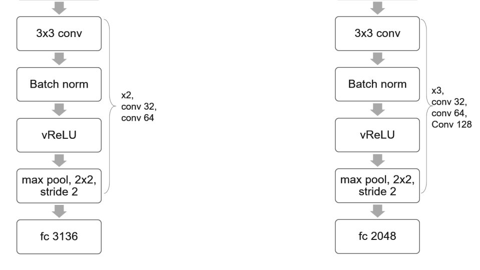

a: MNIST model b: CIFAR10 model

Figure 1: Architecture of CNN

Figure 1 shows the architectures of CNN used in experiments, while Figure 1a shows CNN for MNIST data and figure 1b shows CNN for CIFAR10 data.

5. Result and Analysis

All experiments show similar results. Figure 2 shows the recognition accuracies of label-removed data, which is a typical experiment result. Although the recognition accuracy of a typical CNN model use ReLU also drops during training, the recognition accuracies of models with the proposed vReLU1 and vReLU2 activation functions drop faster. Then we can know that both newly designed activation functions can speed up forgetting.

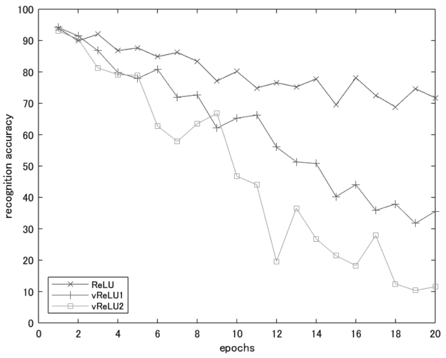

Figure 2: Forgetfulness of CNN with various activation functions on MNIST Data

6. Conclusion

In this thesis, I proposed two new activation functions used in deep learning neural network based on *ReLU*, including new learnable parameters and other parameters. These activation functions use none-gradient descent method to update learnable parameters and were designed to simulate synaptic plasticity mechanism. Experiments shows both of these activation functions can speed up the forgetting of typical CNNs.

For future works, I want to explore real world situations that suitable to apply new activation functions, and find better ways for evaluating the effects on neural network models by the new activation functions. Furthermore, we have to research on different kinds of neural network and optimize method for parameter updating.

References

[1] K. Gurney. *An introduction to neural networks*. CRC press, 2014.

[2] J. R. Hughes. Post-tetanic potentiation. *Physiological reviews*, 38(1):91–113, 1958.

[3] S. J. Martin, P. D. Grimwood, and R. G. Morris. Synaptic plasticity and memory: an evaluation of the hypothesis. *Annual review of neuroscience*, 23(1):649–711, 2000.

[4] A. Paszke, S. Gross, S. Chintala, G. Chanan, E. Yang, Z. DeVito, Z. Lin, A. Desmaison, L. Antiga, and A. Lerer. Automatic differentiation in pytorch. 2017.

[5] S. Ruder. An overview of gradient descent optimization algorithms. *arXiv preprint arXiv:1609.04747*, 2016.

Recovery of Oil from Spent Coffee Grounds by Solvent Extraction for Biodiesel Production

Student ID: 15B12334 Name: Thisang PHAM Supervisor: Ryuichi EGASHIRA, Hiroaki HABAKI

1. Introduction

Coffee is the second most consumed beverage in the world after water [1] and a huge amount of spent coffee grounds (SCG) is generated after brewing coffee. The amount of SCG generated from the instant coffee industry in the world was estimated about 6 million tons per year [2] and various approaches to utilize SCG have been developed, such as fertilizer, wood powder, absorbent and so on. In spite of these applications, most of the SCG are still discarded as waste and the effective utilization of SCG is being studied. Although the utilization of the SCG in the biofuel production was expected as a promising application because of its great sugar content and lipid content, the production method has not been fully studied.

This study aims to apply the solvent extraction technique to the recovery of oil from the SCG for biodiesel production. Then, the overall yield of the oil recovered from SCG was determined and effects of the solvents and extraction temperature on the recovered oil were studied.

2. Experimental

The SCG used in this study were provided in the form of frozen state from AJINOMOTO AGF, INC., and the moisture was firstly removed by leaving the sample at 383K for more than 24 hours. After removing the moisture, the pretreated SCG were used as the feed for the solvent extraction experiments. The coffee grounds from AJINOMOTO AGF, INC., were purchased and used as the virgin coffee grounds (VCG) for the solvent extraction experiments without any pretreatment.

As solvents, hexane, toluene and methanol were used. Hexane was one of the common solvents commercially used to extract food plant oils. Toluene or methanol was selected as an example of aromatic or alcohol compounds. These chemicals were in analytical grade and purchased from Fujifilm Wako Pure Chemical Co.

The procedure of multistage crosscurrent extraction by batchwise operation and experimental conditions are shown in **Figure 1** and **Table 1**, respectively. The feed coffee grounds of VCG or SCG were introduced to the 1st stage as feed, *F*.

The *F* was mixed with 100 mL solvent S_1 and the mixture was shaken in isothermal bath in 24 hours, under the specified temperature. Then, the mixture was separated into the liquid E^*_1 and the wet solid R^*_1. The solvent contained in E^*_1 or R^*_1 was removed by heating at the specified temperature and the solid R_1 and extracted oil E_1 were obtained. R_1 was used as feed for the 2-nd extraction. The same amount of solvent S_k was added in the *k*-th extraction. First, hexane was used as solvent and the extraction was carried out 10 times (*n*=10). Then, the overall yield of the oil extracted from VCG and SCG were determined. Second, the solvent extractions were conducted under different extraction conditions in the cases of *n*=1. Hexane, methanol, toluene were used as solvents and the extraction temperature was changed at 300K, 310K and 320K. Then the influences of solvents and extraction temperature on the yield of the extracted oil were investigated.

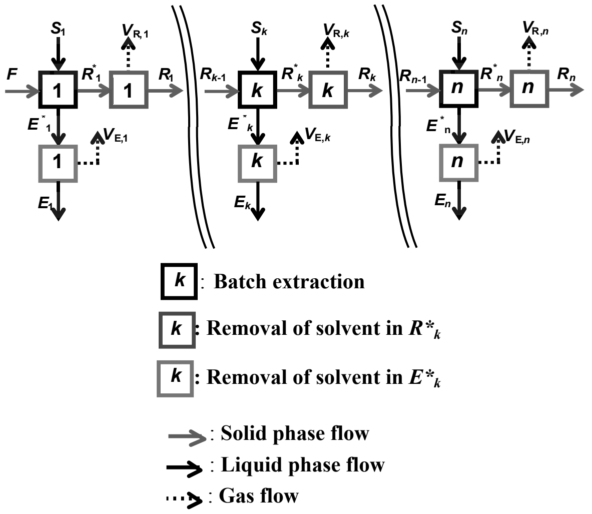

Figure 1 Multistage crosscurrent extraction procedure

Table 1 Experimental conditions

Materials		
Coffee Grounds		VCG SCG
Solvent		Hexane, methanol, toluene
Extraction conditions		
Mass of sample, *F*	[kg]	0.025
Volume of solvent, S_k	[m^3]	1.0×10^{-4}
Extraction time	[hr]	24
n	[–]	1, 10
Extraction temperature, *T*	[K]	300, 310, 320
Conditions of solvent removal in R^*_k E^*_k		
Temperature	[K]	353(methanol, hexane) 383(toluene)
Time	[hr]	10(hexane, methanol removal in E^*_k) 14(toluene removal in E^*_k) 48(solvent removal in R^*_k)

3. Results and discussion

3.1 Definition of oil yield

The yield of the oil extracted after *k*-th extraction was defined as,

$$Y_k = \sum_{i=1}^{k} E_i/F \qquad (1)$$

where, E_i and F were the oil extracted at the i-th extraction and the mass of the feed coffee grounds.

3.2 The yield of oil recovered from VCG and SCG

The provided SCG were dried in the atmosphere at 383K and the mass became constant after more than 24 hours. The ratio of the dried mass to the initial wet mass was obtained as 0.26 kg-dried/kg-wet and the SCG pretreated for more than 24 hours were used as the extraction feed in all cases.

Figure 2 shows the plots of Y_k against the stage number of extraction k with VCG and SCG. In the case of VCG, the solvent extraction was conducted twice. Y_k increased gradually from 0.056 to 0.111 while k ranged from 1 to 8 and had nearly no change with k >8. Y_{10} was 0.111 while the yield of oil extracted at first time Y_1 was more than 0.058, it meant 0.52 of total oil was recovered at the first time extraction. In the case of SCG, the solvent extraction was also conducted twice and their results were mostly the same. Y_k increased gradually from 0.056 to 0.093 (run 2) or 0.089 (run 1) while k ranged from 1 to 8 and had nearly no change with k >8. Y_{10} ranged between 0.089 and 0.093 while the yield of oil extracted at first time Y_1 was more than 0.056, it meant more than 0.60 of total oil was recovered at the first time extraction.

The total recovered oil of VCG is 0.111 higher than that obtained of SCG (0.093). Although the SCG were not obtained from the VCG used in this study and the reason was unclear, some parts of oil might have been taken at the brewing step.

Y_k of VCG and Y_k of SCG were mostly the same at k=1 and different with $k \geq 2$. Although the solubility of oil in hexane was not determined in this study, at the first time extraction (k=1) the solubility limit of oil in hexane might have been exceeded.

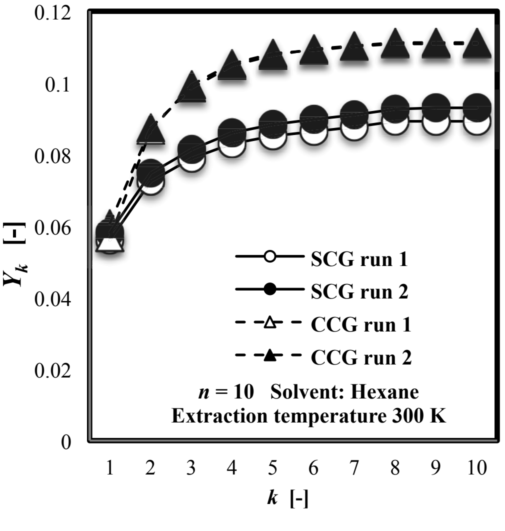

Figure 2 Yield of oil extracted from VCG and SCG

3.3 Influences of solvents and extraction temperature on the yield of oil

Figure 3 shows the influences of solvents and extraction temperature on the yield of oil Y_1. Hexane showed the highest Y_1 followed by toluene and methanol. Y_1 in the cases of hexane and toluene were comparable and Y_1 in the case of methanol was much smaller. This trend was also reported in previous study [3]. The main components of oil must have been triglycerides of free fatty acid C16 or C18 therefore they were soluble more in non-polar solvent. The yield of oil Y_1 increased slightly as temperature increased. Although the effects were insignificant in this measurement range, the solubility increased as the temperature increased.

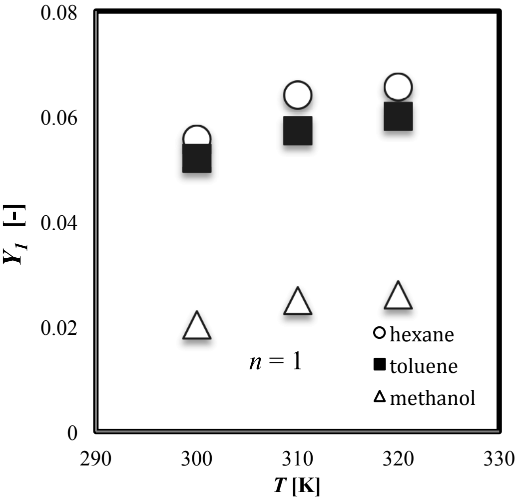

Figure 3 Influences of solvents and extraction temperature on the yield of oil

4. Conclusions

From the experiment on removing moisture from the provided SCG, the ratio of the dried mass to the initial wet mass was obtained as 0.26 kg-dried/kg-wet. From the experiment on determining the overall yield of the oil recovered from VCG and SCG, Y_{10} of VCG was 0.111, Y_{10} of SCG ranged between 0.089 and 0.093. From the experiment on investigating influences of solvents and extraction temperature on the yield of oil, hexane showed the highest Y_1 followed by toluene and methanol. Y_1 increased slightly as extraction temperature increased.

5. References

[1] Angellina., "Cofee, the second most popular drink in the world", Eastwest, 2016 January.

[2] T. Tokimoto et al., "Removal of lead ions in drinking water by coffee grounds as vegetable biomass", Journal of Colloid and Interface Science, 281, 56-61, 2005.

[3] Ioannis et al., "Influence of solvent selection and extraction temperature on yield and composition of lipids extracted from spent coffee grounds", Industrial Crops & Products, 119, 49–56, 2018.

Earth-Moon Transportation System Using a Reusable Vehicle and Fuel Stations

Student Number : 15_11197 Name : Ayu Numata Supervisor : Daisuke Akita

1. Introduction

In the future, new space missions such as deep space exploration and construction of the base will advance more. These developments lead various missions and a large amount of transportation. Actually, the ratio of the mass of payload in the launch rocket is about 1%. Therefore, the transportation cost for the space mission would be increased more than ever.

OTV (Orbital Transfer Vehicle) Network, using R-OTV (Reusable-Orbital Transfer Vehicle), is proposed as a future interplanetary transportation system. This network system consists of orbital fuel stations and R-OTV. The R-OTV is fueled at the station. R-OTV transports the cargo among the orbits. A previous research [1] shows that the cost of OTV network between the Earth orbits is lower than conventional method.

The objective of this study is to construct a model of Earth-Moon OTV network, clarifying the characteristics and superiority of the system with IMLEO (Initial Mass of Low Earth Orbit) and cost assessment.

2. Mission concept

Four transportation models between the low earth orbit (LEO) and the low lunar orbit (LLO) are considered in this study. Model 1 is conventional model using E-OTV (Expendable-OTV). On the other hand, model 2-4 uses R-OTV. Figure 1 shows the mission scenario of the model 2.

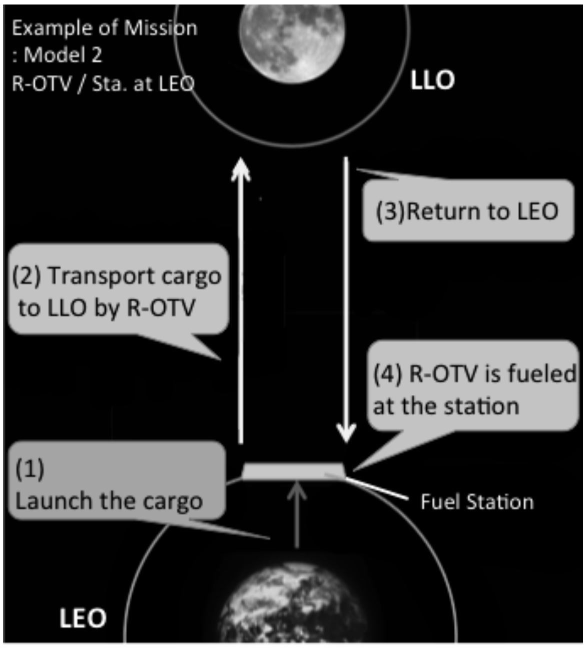

Figure 1: Example of mission model (Model 2)

Model 1: E-OTV / no fuel station
Model 2: R-OTV / fuel station at LEO
Model 3: R-OTV / fuel station at LLO
Model 4: R-OTV / fuel station at LEO&LLO

Assumptions are as follows.

- Transport 136 ton cargo per year.
- R-OTV can be fueled fuel at only the station.
- R-OTV can be used 100 times repeatedly.
- I_{sp} of OTV propulsion is 450s.
- All the orbits are on the same orbital plane.

3. Transportation System Model

Cost assessment needs the mass budget of each model. The mass of OTV is calculated using HASA [2] as shown below.

$$M_{\mathrm{total}} = M_{\mathrm{prop}} + M_{\mathrm{pay}} + M_{\mathrm{engine}} + M_{\mathrm{tnk}} \tag{1}$$

$$M_{\mathrm{prop}} = M_{\mathrm{total}} \left(1 - \mathrm{e}^{-\frac{\Delta V}{I_{\mathrm{sp}} \cdot g}}\right) \tag{2}$$

$$M_{\mathrm{engine}} = 0.0.76(T_{\mathrm{totrk}}) + 0.00033(T_{\mathrm{totrk}})(A_{\mathrm{ratio}})^{0.5} + 130 \ [lb] \tag{3}$$

$$M_{\mathrm{tnk}} = R_{\mathrm{t}} \times M_{\mathrm{prop}} \tag{4}$$

M_{total}[kg] : total mass of OTV
M_{prop}[kg] : propellant mass
M_{pay}[kg] : OTV payload mass
M_{engine}[kg] : engine mass
M_{tnk}[kg] : propellant tank mass
T_{totrk}[lbf] : engine thrust in vacuum
A_{ratio}[-] : expansion ratio of rocket nozzle (=100)
R_{t}[-] : ratio of tank mass / propellant mass

In this study, payload of E-OTV is assumed to be 8 ton, and the total mass of R-OTV is calculated to be the same as that of the E-OTV. The mass of the fuel station is set to be 50 ton by reference to previous research [1].

4. Cost model

Cost is calculated as the sum of the fabrication cost (C_{F}) and the operation cost (C_{O}), excepts the development cost. Operation cost excludes other launch operation cost, but fuel cost. In this study, the C_{O} of E-OTV is set to be unit. (dimensionless quantity). Other costs are relatively evaluated based on C_{O} of E-OTV. Operation cost of R-OTV is proportional to consumed fuel mass, and is calculated as Figure 1. The parameter of this study is the launch cost to investigate its effect.

$$(\mathrm{R}-\mathrm{OTV}\ C_{\mathrm{O}}) = \frac{(\mathrm{R}-\mathrm{OTV}\ M_{\mathrm{Prop}})}{(\mathrm{E}-\mathrm{OTV}\ M_{\mathrm{prop}})} \times (\mathrm{E}-\mathrm{OTV}\ C_{\mathrm{O}}) \tag{5}$$

Table 1: Cost Parameter

	OTV		Fuel Station		Launch
	C_{F}	C_{O}	C_{F}	C_{O}	$C_{\mathrm{F}}+C_{\mathrm{O}}$
Model 1	1 (= Standard)	0.01	10	-	1
Model 2~4	10	(5)			

5. Result of calculations

Figure 2 shows IMLEO breakdown for the 20 years. Figure3 and Figure 4 show the result of cost assessment of Model 1~4.

In Figure 2, there is no large difference between the IMLEO of Model 1, 2 and 4. However, the IMLEO of Model 3 is five times as large as others because the R-OTV is required to carry all the fuel to the station on LLO in Model 3.

In Figure 3, the cost of Model 2 and Model 4 (R-OTV / the fuel station at LEO) are lower than that of Model 1 (E-OTV), because R-OTV can be used repeatedly. However, the R-OTV is more expensive than the E-OTV in the first year because of the initial setup cost for the reusable system.

It is found that the cost of Model 3 is drastically large as shown in Figure 4. That is because the total launch cost is proportional to IMLEO in this study, and the IMLEO of Model 3 is extensively larger than other models. That is because the R-OTV is required to carry all the fuel to the station on LLO in Model 3. Figure 3 also indicates that most of total cost is launch cost. In the near future, the launch cost could be reduced with more inexpensive launch vehicle and the reusable launch vehicles, which are under development around the world. The system proposed hare has potential to reduce the mission cost considerably.

Among the Model 2, 3 and 4, using R-OTV, Model 2 (Sta. only at LEO) has the lowest cost. That is because, in this study, the mission models are considered for the one way transportation only from the earth to the moon. In the future, new missions which take something back to the earth will be necessary. Investigating the superiority of construction of the LLO fuel station in would be necessary such a mission.

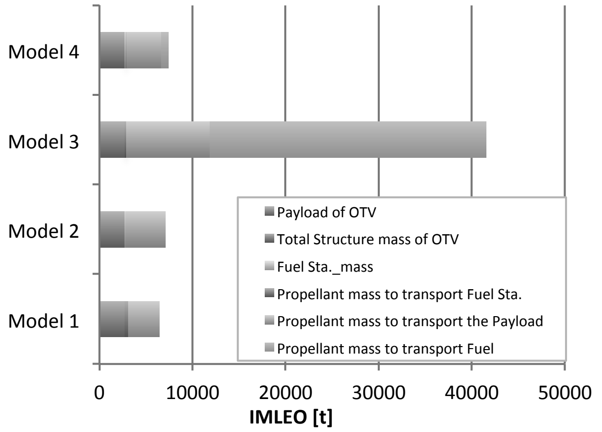

Figure 2: IMLEO Breakdown of the 20 year

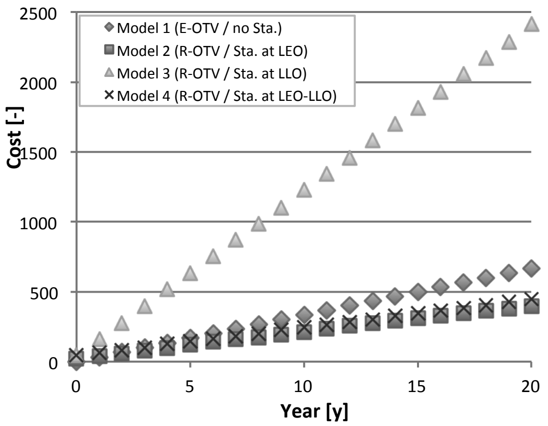

Figure 3: Trend of Total System Cost

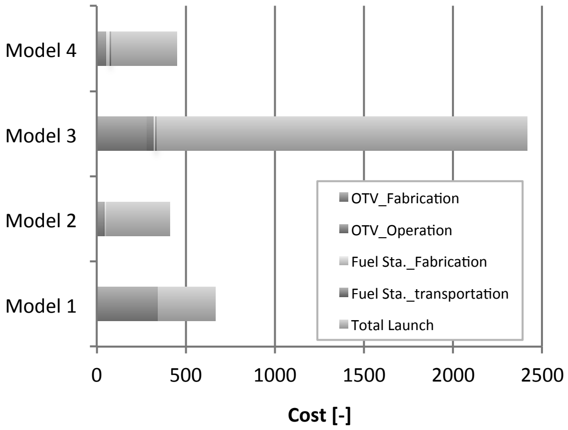

Figure 4: Accumlated Cost Budget for 20 years

6. Conclusions

Cost assessment in this study indicates that R-OTV/fuel station system has lower cost than conventional method of E-OTV. And it is revealed that decreasing the fabrication cost of R-OTV and launch cost are dominant factors to reduce the total mission cost. Future works are as follows.

- The effect of constructing the fuel station on orbits other than LEO and LLO (e.g. Lagrange point)
- The effect of the LLO station for the transportation from the moon to the earth
- Transportation to other plants (e.g. Mars)

Reference

[1] Shinichi Nakasuka, Toru Tanabe, Naoko Sumino (1993), “Fuel Station-Based Transportation Network as a Future Space Infrastructure”, Journal of Space Technology and Science, Vol.8, No.2, pp.22-37

[2]]Gary J. Harloff and Brian M. Berkowitz(1988), “HASA – Hypersonic Aerospace Sizing Analysis for the Preliminary Design of Aerospace Vehicles”, NASA Contractor Report 182226

2次元曲面において熱画像風速測定法(TIV)の結果の表現

学籍番号：15B08315　　氏名：孫 岳　　指導教官：神田 学

1. はじめに

流れは我々の日常生活に大きく関わっている．しかし，普段の流れは複雑な空間構造を有して透明であり，そのままの観測は困難である．流れ,特に気流の可視化を達成するために，計測法として粒子画像流速測定法(PIV)，シミュレーション法として数値流体力学(CFD)が大きく発展している．PIVは，レーザーシートにより，ある平面における微小な粒子の動きを追跡し，流れ及び速度分布を計算する．その結果はレーザーシートの平面に制限されている．CFDはコンピューター上でモデルを作り，流れを数値解析・シミュレーションする手法．高いレイノルズ数や複雑な形状を持つ物体の乱流解析の応用には困難である．

以上の点を踏まえて，PIVのアルゴリズムを利用し，新たな観測手法である熱画像風速測定法（Thermal Image Velocimetry ,TIV）が提案された．この手法は粒子の代わりに，対象物体表面の熱画像を利用し風速を計測するため，直接物体表面の風速場の計算ができる．この手法は非接触的，安価，安全などいくつかの利点があり，シミュレーションと比べ実在する大きく複雑な表面がある物体の観測も可能である．この手法によって，垂直壁の上昇流や地表面の塵旋風(ダストデビル)など観測事例があった，これらの観測事例の対象面は平面であり，カメラの角度によリ射影変換を行い，結果を一つの平面に整理した．

本研究では，発泡スチロール製の円柱体及びマネキンを対象とし．その表面の自然状態での流れをTIVで捉え，更にそれらの3Dモデルと組み合わせることにより，TIVの結果を2次元曲面上に表現することが目的である．

2. 観測概要

本実験で，東京工業大学大岡山キャンパス石川台4号館の屋上で，黒い発泡スチロール製のマネキンと発泡スチロール製で黒く塗った直径300mm，高さ400mmの円柱体を対象に，サーモカメラによる熱画像を撮り，TIV解析を行う．同時に超音波風速計により環境風の風向風速の測定を行う．

3. 解析手法

TIVの結果を2次元平面へ表現するため，結果の風速ベクトルを2次元から3次元まで拡張することが必要である．結果を格納する座標系は熱画像左下を原点とし，元の熱画像のXY座標系を右手系になるように新たなZ軸を定義する．

空気が物体表面を流れるときに乱流が生じ，その乱流によって表面に温度変化の不均一性が発生する．TIVはサーモカメラにより物体表面の温度情報を撮り，さらに時間・空間スケールにおいて解析を行いその変動を求めることで風速ベクトルを計算する．熱画像しか使わないため，風速ベクトルの結果は熱画像平面への投影である．この結果へピクセルのZ座標情報を持ち込み，3次元の風速ベクトルを作ることができる．

これを達成するために，対象物体の3Dモデルを作り，モデルの座標と熱座標の座標が対応できるように座標変換を行う．それから自作したプログラムにより，ピクセルごとのZ座標を計算する．最後に，風速ベクトルの値

は整数に限らないため，その終点の座標を周りの加重平均で計算する．この速度ベクトルと始点の座標を組み合わせ，再描画することで，TIV の結果を対象物体の 2 次元曲面で表すことができる

4. 結果及び考察

Z 座標を計算するときに正射影を採用するので，モデルの境界部分で誤差が生じる．

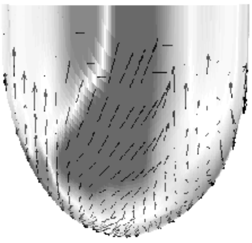

上面図

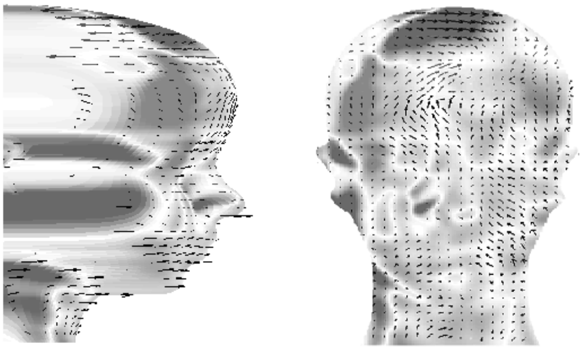

側面図　　正面図

図 1 マネキンの表面温度変動及び風速ベクトルの三面図

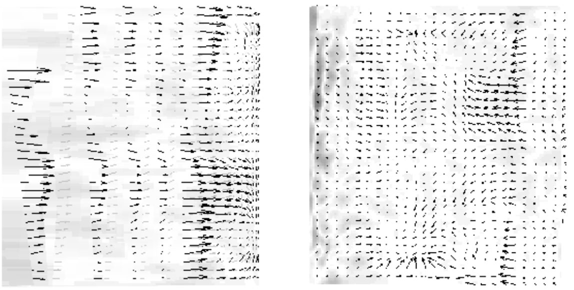

側面図　　正面図

図 2 円柱の表面温度変動及び風速ベクトルの正面図と側面図

TIV の結果を２次元表面へ表現することで，異なる角度から結果を見ることができた．正面で確認しにくい変動も，他の角度から見ると明らかになる．例えば，図１のモデル頂上部分のベクトルや，図２のモデル左側のベクトル．円柱体の表面において，流れの剥離の現象が確認された．

超音波風速計による風速は 1m/s 以上であり，TIV 手法により計算された風速は主に 0.1m/s 以下である．この原因は対象物体のスケールが小さいと考えられる．

5. 結論

TIV の結果を２次元表面へ表現することに成功した．その結果を異なる角度から観察することで１つの角度では気づきにくい変化も発見しやすくなる．しかし，この手法で TIV の精度が上がったことはなく，境界部分でのベクトルは計算に使う情報量は少ないため，定量的な分析には不向きである．

将来もっと大きいスケールの物体へこの手法を運用し，風速の検証を行うことに期待する．また，複数のサーモカメラによる同時観測で境界部分での誤差を減らすことも期待する．

参考文献

[1] Ch Brücker. Digital-particle-image-velocimetry (dpiv) in a scanning light-sheet: 3d starting flow around a short cylinder. Experiments in Fluids, 19(4):255–263, 1995.

[2] Atsushi Inagaki, Manabu Kanda, Shiho Onomura, and Hideaki Kumemura. Thermal image velocimetry. Boundary-layer meteorology, 149(1):1–18, 2013.

[3] Kumemura H. Thermal image velocimetry (tiv) and application to a building wall. 土木学会論文集, 68(4):I1753–I1758, 2012.

[4] Zhang Y. Application of thermal image velocimetry to dustdevil. 東京工業大学修士論文, 2012.

[5] 稲垣厚至. 熱画像風速測定法（tiv）による風の空間分布計測. 水文・水資源学会誌, 29(3):186–195, 2016.

Effect of pull-off angle on adhesion force between side surface of PDMS beam and rigid body

Student Number: 15B11346 Name: Suguru Norikyo Supervisor: Kunio Takahashi

1. Introduction

The gripping device imitating a fine structure of gecko foot-hair is considered to be able to adhere to rough surface even in vacuum. The device's grip and release performance can be gained by controlling tangential force. Mikhail has demonstrated a prototype of the device made of multiple-PDMS-beam structure, and experimentally evaluated its function [1].

Shimahara conducted an experimental study on the relation between pull-off angle and maximum adhesion force of a gel beam contacting with a rigid body [2]. However, Shimahara's experimental results didn't meet those predicted by a theoretical model [3], in which a perfect elastic beam was assumed.

In this study, a PDMS beam (assumed as elastic beam) is used for experimental study of effect of pull-off angle on adhesion force between side surface PDMS beam and rigid body

2. Experiment

In order to clarify the effect of pull-off angle on adhesion force between side surface of a PDMS beam and rigid body. It is necessary to measure the normal force F_n(Fig.1), the tangential force F_t(Fig.1), the displacement of an edge of the beam d, and the length of non-contact area l, experimentally.

We use the experimental system as shown in Fig. 3. The elastic beam is made of a PDMS (Sylgard 184, Dow Corning). The beam is 30 (mm) in length, 15(mm) in width, 5(mm) in thickness, and 10(°)in setting angle. Slide glass (S9213, Matsunami Glass) is used as rigid body.

At the start of the experiment, the slide glass was pressed to the beam vertically until a certain displacement and displaced horizontally until tangential force being 0 (N) (Fig.2). Then, the slide glass was unloaded with pull-off angle constant (Fig.3).

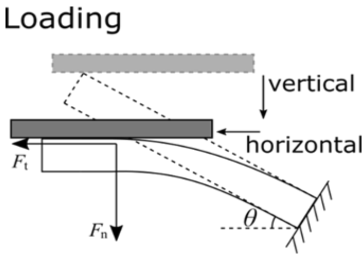

Fig.1 Loading process

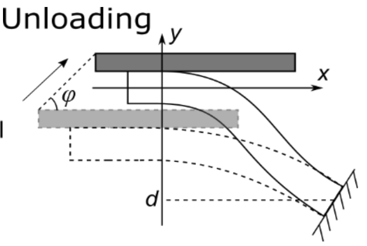

Fig.2 Unloading process

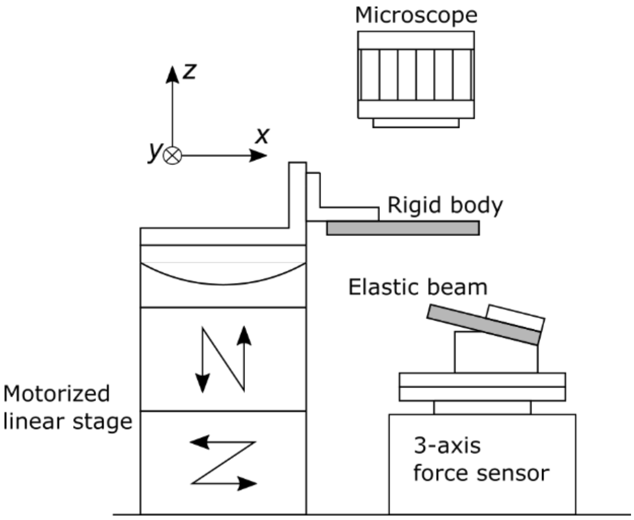

Fig. 3 Experimental system

3. Results

When the pull-off angle $\varphi = 118.0$(°), the normal force is shown in Fig.4. The beam detached from the rigid body after the adhesion force is maximum, and the beam form a new adhesion area. The normal force increases while fluctuating. Finally, adhesion contact between the beam and the rigid body changes from area contact to line contact, and the beam comes to peel off.

These behavior can be observed in the range of pull-off angle φ : 101.6〜146.2(°).

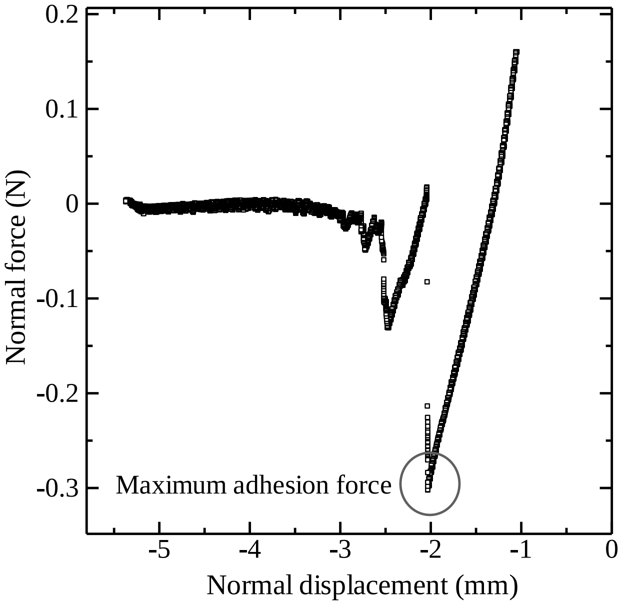

Fig.4 Normal force F_n ($\varphi = 118.0°$)

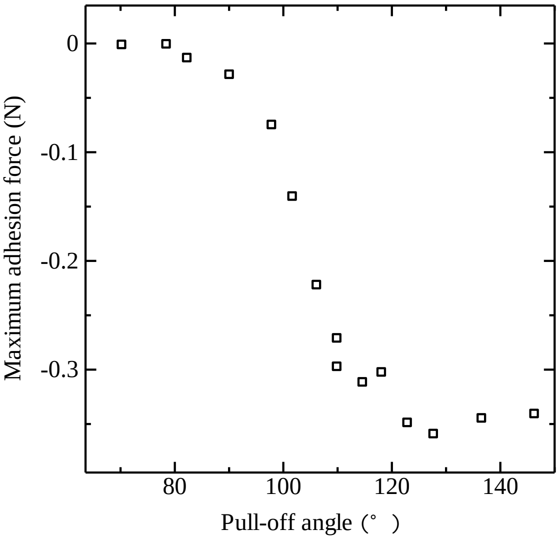

Fig.5 relation between pull-off angle and Maximum adhesion force

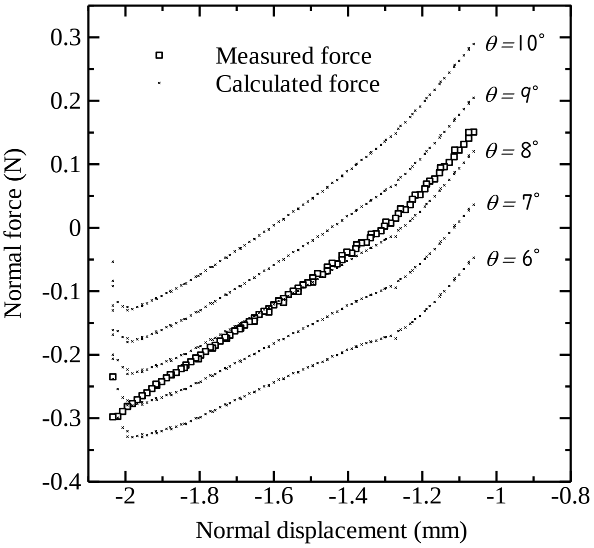

Fig.6 Experimental result and analysis result ($\varphi = 118.0°$)

4. Discussion

The relation between the pull-off angle φ and the maximum adhesion force for each pull-off angle φ is shown in Fig.5. As shown in Fig.5, the maximum adhesion force is nearly 0 (N) when the pull-off angle is less than about 80 (°). The maximum adhesion force changes as the pull-off angle changes between about 80 (°) and about 120 (°). The maximum adhesion force is certain when pull-off angle is larger than about 120 (°).

The maximum adhesion force depends on the tangential force. However, the tangential force does not exceed a certain force by the adhesion area slipping. Therefore, in the previous experiment [2], it is suggested that the range of pull-off angle when the maximum adhesion force is unchanged exists like the result of the experiment (Fig. 5).

According to previous research [2], when the normalized tangential force is positive, the normal force of the model is obtained as

$$\tilde{F}_n = \frac{\tilde{F}_t 2\sqrt{3\tilde{F}_t}\sinh\left(2\sqrt{3\tilde{F}_t}\tilde{l}\right)}{2-2\cosh\left(2\sqrt{3\tilde{F}_t}\tilde{l}\right)+2\sqrt{3\tilde{F}_t}\tilde{l}\sinh\left(2\sqrt{3\tilde{F}_t}\tilde{l}\right)} \times\left(\tilde{d}-\frac{1-\cosh\left(2\sqrt{3\tilde{F}_t}\tilde{l}\right)}{2\sqrt{3\tilde{F}_t}\sinh\left(2\sqrt{3\tilde{F}_t}\tilde{l}\right)}\tan\theta\right)$$

where, the displacement, the length of non-adhesion area, and the force are normalized as $\tilde{d} = d/L$, $\tilde{l} = l/L$, $\tilde{F} = F/(12EI/L^2)$ in the same manner as Shimahara's expressions [2].

As shown in Fig.6, we focus on the force curve of Fig. 5 from the beginning of unloading until the detachment, and apply measured parameters to Shimahara's theoretical model.

The length of non-adhesion area l is described by the difference between the length of the beam L and the length of adhesion area ,which is calculated by the adhesion area divided by the width of the beam. Young's modulus E is estimated to be 1.73 (MPa) by previous research [4].

When setting angle $\theta = 10(°)$, the calculated normal force is larger than measured normal force. Fig.6 shows that calculated normal force decreases as setting angle θ used for calculating decreases. It is suggested that the setting angle θ decreases during unloading.

5. Conclusions

The range of pull-off angle when the maximum adhesion force is changed exists.

It is suggested that setting angle θ changes during peeling by comparing the calculated normal force with the measured normal force.

References

[1] Mikhail Salyukov, et al, "Development of a Multy-Beam Structure by Stacking Comb-Shaped Rubbers", Mate2018, vol24 pp.261-264,2018

[2] Shimahara,S, "Effect of tangential force on adhesion between an elastic beam and rigid body", Master thesis of Tokyo Institute of Technology, 2016

[3] Imai,Y, "弾性梁と剛体平面の接触における梁の長手方向の変形が凝着力に与える影響", Master thesis of Tokyo Institute of Technology, 2018

[4] Mai Ngoc Trung, "The prototype of side-contact type elastic multi-beam using PDMS", Bachelor thesis of Tokyo Institute of Technology, 2016

Application and Comparison of Cooley-Tukey algorithms for Ocean Rendering with Spectral domain approach

Student Number:15_08290 Name: Eungang SON Supervisor: Hiroshi TAKAGI

1 Introduction

Due to the ocean`s highly dynamic behavior, from a silent sea to an intense ocean, it is hard to understand and explain its mechanisms. Representing this visual complex phenomenon is a challenge, and related fields have evolved to deal with this problem. Since 1980, a large number of breakthroughs have emerged in the Ocean Rendering Field. The major idea is to define its phenomenon based on the relative water depth to wave length: deep water and shallow water. The former type of waves is generally used to describe longer wave phenomenon in deep sea, whereas later one illustrates shorter wind waves subject to breaking waves at a nearshore location.

Ocean rendering can be classified into two: spatial/spectral methods incorporated in marine and oceanic flow models, and physically based model which take approximate solutions of the Navier-Stokes Eqauation (NSE) to reproduce the complex dynamic behavior of ocean surface. For rendering, the optical property of the ocean surface is also need to be considered. In rendering stage, several phenomena such as agitation, bubbles, diffraction, and refraction must be calculated. For ocean rendering, these shader techniques are also essential for realistic description.

The advent of Virtual Reality (VR) provides new possibilities in an ocean rendering field. While the traditional rendering can be differntiated into two incompatible types according to its purpose: For accurately focused purpose: such as movie CG, Meteorological research, and expeditiousness focused purpose such as game. VR simulation requires both accuracy and expeditiousness simultaneously. This paper presents a comparison of the frame per second (FPS) of Fourier domain approaches by using Microsoft 4-Dimensional Perlin noise data optimized by various Cooley-Tukey algorithms in VR prerequisite conditions in real-time domain.

2 Methodology

2.1 Cooley-Tukey Algorithm

The basic principle of most Cooley-Tukey algorithms based on the symmetry properties of a complex exponential term in the Discrete Fourier Transform (DFT). DFT converts a finite sequence of equally-spaced samples of a function in a same-lengthy sequence of equally-spaced samples of the discrete-time Fourier transform, which is a complex-valued function of frequency.

$$X(k) = \sum_{n=0}^{N-1} x(n) \cdot e^{-\frac{2\pi i}{N}kn}$$

$$\text{s.t.} \forall k \in \{0, \dots, N-1\}, \forall n \in \{0, \dots, N-1\}$$

N is the data size.

Depending on pure signal input, DFT represents symmetricity.

Even symmetric

$$x_n \in R,\ \forall n \in \{0, \dots, N-1\} \ \rightarrow X_k$$
$$= X^*_{-k \bmod N}$$
$$\forall k \in \{0, \dots, N-1\}, X^* = \bar{X}$$

Also, DFT represents periodical property by input data size N.

$$e^{-\frac{2\pi i}{N}kn} = e^{-\frac{2\pi i}{N}k(n+N)} = e^{-\frac{2\pi i}{N}(k+N)n}$$

Thanks to the properties above, DFT algorithm can be divided into the algorizms, known to be butterfly computation, which can contribute to decreasing computation cost than that of ordinary DFT. DFT algorithm which is optimized by symmetricity is called radix based FFT. All radix based algorithms represent similarly distinguish butterfly computation structural differing only in the core computation of twiddling. We chose the following six types of Cooley-Tukey algorithms for the spectral transform: Radix-2, Twisted Radix-2, Radix-4, Twisted Radix-4, Radix-8, and Split Radix.

2.2 Ocean Rendering

There are mainly two kinds of method are considered in ocean rendering: Deep water rendering, Shallow water rendering and Mixed method . Deep water rendering use theoretical models in marine/ocean science and/or experimental observation data to represent ocean surface. There exist three categories, namely a spatial domain approach, spectral domain approach (Fourier domain approach), and hybrid approach which is combining the two. Spatial domain describes its surface directly in spatial domain by height map which is composed of periodical functions arise from the model oceanic science model. On the other hand, the spectral approach requires wave spectrums to describe its domain and use Fast Fourier Transform (FFT) to transform into the spatial domain. Hybrid methods, which is the combination of the two, generate convincing easily animated surfaces.

Shallow water rendering use NSE to describe ocean surface. There are two methods exist to discretize the NSE in Ocean Rendering. Firstly, Eulerian focus on a 2D or a 3D grid where the fluid moves from cell to cell. On the other hand, Lagrangian approaches focus on each particle which is representing small fluid volumes. Like deep water rendering, Hybrid technics, also developed for strength each virtue by combining these two techniques.

2.3 Spectral Domain Approach

Spectral domain approach uses Fourier Transformation of experimental/observed data which have transformed into the spatial domain. Mastin et al. (1987) proposed the basic concept of spectral domain approach based on Pierson-Moskowitz spectrum theory (1964). Premose and Ashikhmin (2000) used JONSWAP spectrum (1973) which is an revised version of the Pierson-Moskowitz spectrum. Tessendorf (2001) used Phillips spectrum to describe surface of wind waves which was used for scenes of Titanic movie CG. We have used Phillips spectrum for spectral domain rendering.

3 Experimental Result

We have tested FPS and FT (Frame Time) in by transforming prepared 4 dimensional Perlin noise data from the NDVIA corporation into the spatial domain using 8-point Cooley-Tukey algorithms in Philips spectrum (Fig 1) and investigated by the resolution (Figs 2 and 3). (CPU : Intel(R) Core™ i7-4712MQ CPU @ 2.30GHz, 8GB Ram, GPU : NVIDIA GeForce 820M)

Figure 1 Rendered Result

Figure 2 FPS-resolution graph

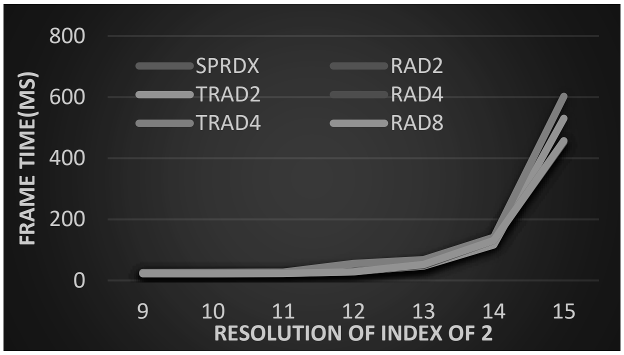

Figure 3 Frame time-resolution graph

4 Conclusion

We investigated FPS spectral domain approach for rendering of specific prepared input data which are optimized by various Cooley Tukey FFT algorithms. The fastest Cooley-Tukey algorithm: Split radix DIF FFT displayed 8 FPS in 4K resolution, which is lower than the minimum requirement(60fps) in VR environments. The result demonstrates the limitation of the technology for the generation of realistc wind waves in VR for now.

References

[1] Soni M. and Kunthe P., “A General Comparison Of FFT Algorithms,” Soni2011AGC, 2011.

[2] Darles E., Crespin B., Ghazanfarpour D., Gonzato J.C.. A Survey of Ocean Simulation and Rendering Techniques in Computer Graphics. Computer Graphics Forum, Wiley, 2011, 30 (1), pp.43-60. <10.1111/j.1467-8659.2010.01828.x>. <hal-00587242>

[3] Tessendorf J.: Simulating ocean waters. In SIGGRAPH course Notes (Course 47) (2001).

籾殻灰の有効利用－$Ca(OH)_2$を鉱化剤としたゼオライトの合成に関する研究

学籍番号：15B15887　名前：陸 遥　指導教員：日野出 洋文, Winarto KURNIAWAN

1. 背景

稲は世界の重要な穀物であり、毎年米の副産物である籾殻は約 1.5 億トンであると報告された(2014)[1]。これは利用可能なバイオマスであり、バイオマス発電に利用されている。発電の固形廃棄物となる籾殻灰はそのまま埋め立てるか、土壌改良、セメント製造の原料などの低価値の方法に利用されている。近年、籾殻灰は約 9 割という高いシリカ含有量のため、ゼオライト合成への応用が注目された[2][3]。

ゼオライトは結晶性のある多孔質アルミノケイ酸塩の総称であり、負電荷の骨格があり、その負電荷を打ち消すため、アルカリ金属又はアルカリ土類金属イオンを含む。それらの陽イオンは交換可能なため、ゼオライトは陽イオン交換能をもち、重金属陽イオン吸着に応用されている。

重金属のカドミウム(Cd)はかつて日本のイタイイタイ病を引き起こした。今でも、中国やタイ国を汚染しているため、本研究で Cd を重金属除去の対象物質とした。

既存の研究[2][3]で籾殻灰からゼオライトの合成中、NaOH が鉱化剤として使われている。ゼオライトの結晶強度や結晶構造は原料だけでなく、鉱化剤にも依存している。本研究では $Ca(OH)_2$ を鉱化剤として、籾殻灰からゼオライトの合成実験を行い、ゼオライトの結晶強度と結晶構造そして陽イオン交換容量(CEC)と Cd 除去能について調べることを目的とした。

2. 実験

2.1 合成実験

本研究に使用した籾殻灰は籾殻を 600 ℃で 4h 加熱して得た。籾殻灰、$Ca(OH)_2$、NaOH、$Al(OH)_3$ を一定の割合で混合し、$Ca(OH)_2$ と NaOH の質量比(Ca/Na)及び合成時間を変えながら、one-step アルカリ水熱合成法[2]を用いて反応温度 90 ℃で、実験を行った。

2.2 キャラクタリゼーション

生成物は XRD で結晶強度と結晶構造を確認し、SEM で表面構造を観察した。CEC は酢酸ナトリウム法[3]を用いて、ICP でナトリウムイオン測定し、算出した。

2.3 吸着実験

吸着剤 1g/L で 100 ppm の Cd 溶液で生成物の除去平衡時間を確認した。30, 50, 100, 150, 200, 300, 400 ppm で除去実験を行い、Langmuir モデルを適用し、生成物の Cd に対する飽和吸着量を推定した。AAS で吸着実験における Cd 濃度を測定した。

3. 結果と考察

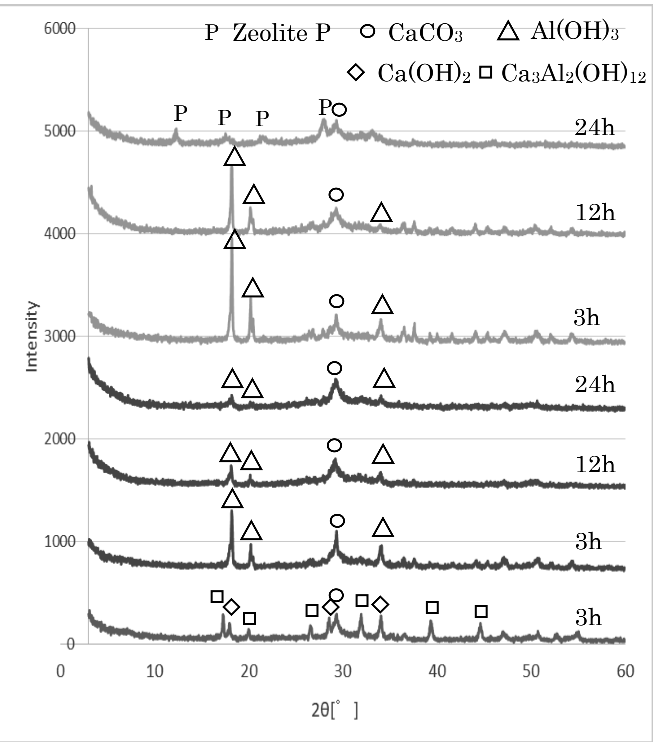

図 1.　生成物の XRD パターン

━ Ca/Na＝1/0　━ Ca/Na＝2/1　━ Ca/Na＝1/2

図 1 から、Ca/Na が 1/0 の場合、$Ca_3Al_2(OH)_{12}$ が主生成物であることが分かった。これは原料

となる $Al(OH)_3$ と $Ca(OH)_2$ から生じた生成物と考えられる。また、未反応の $Ca(OH)_2$ も観測された。Ca/Na が 2/1 と 1/2 の場合、3h と 12h に未反応の $Al(OH)_3$ が観測され、$Al(OH)_3$ の反応が遅いことが分かった。24h の時、Ca/Na が 2/1 の場合は明らかな生成物がなく、Ca/Na が 1/2 の場合は Zeolite P が生成した。また、すべての生成物には $CaCO_3$ が存在し、これは $Ca(OH)_2$ が水熱合成で容器内の CO_2 と反応したものと考えられる。

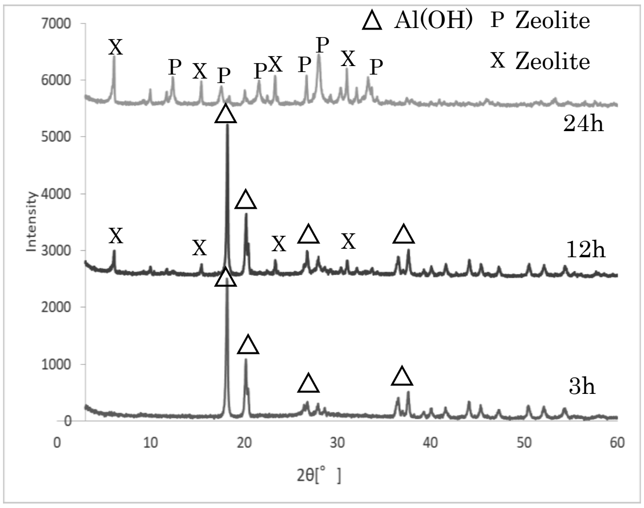

図 2. Ca/Na＝0/1 の場合の生成物 XRD パターン

図 2 から、3h の時と 12h の時は $Al(OH)_3$ 観測できるが、12h の時 Zeolite X が生成したと分かった。24h の時、成長した Zeolite X が観測され、Zeolite P も生成した。これは $Ca(OH)_2$ を鉱化剤とした場合に比べて、Zeolite X が生成し、その生成し始めた時間もより短いと分かった。Zeolite P の回折強度は、Ca/Na が 0/1 の場合が高いことが分かった。

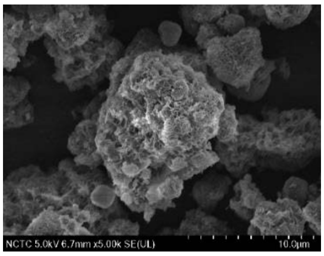

図 3. Zeolite P の SEM 画像

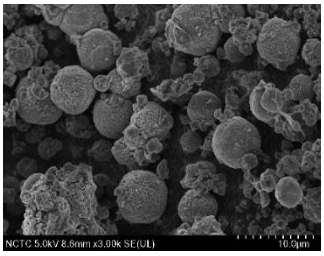

図 4. Zeolite X&P の SEM 画

図 3 と図 4 は Ca/Na=1:2, 24h (Zeolite P) と Ca/Na＝0:1, 12h (Zeolite X&P) の SEM 画像である。図 3 から少量の球状の結晶が観察でき、図 4 から多くの球状と八面体の結晶が観察できる。参考文献[3][4]により、球状結晶は Zeolite P、八面体結晶は Zeolite X と考えられる。

表 1. 生成物の CEC

Samples	CEC (mEq/100g)
Zeolite P	316
Zeolite X&P	445
Na-P Zeolite[4]	395
Na-X Zeolite[3]	503

表 1 から、Zeolite P の CEC は Zeolite X&P より低い値であることが分かった。

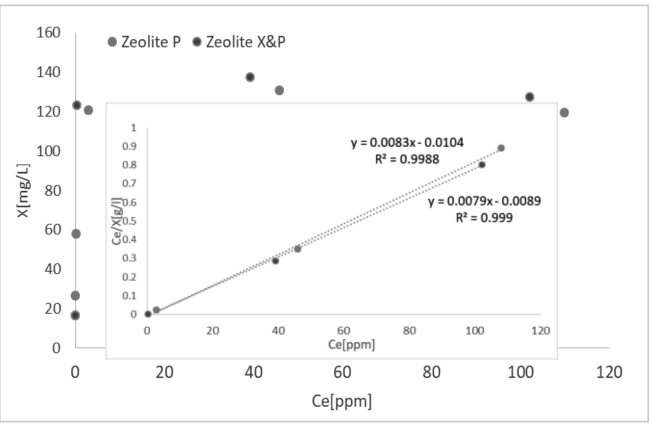

図 5. Zeolite P と Zeolite X&P の Langmuir 吸着等温線

吸着剤 1g/L、100 ppm の Cd 溶液の場合、Zeolite P と Zeolite X&P の吸着平衡時間はそれぞれ 30 と 60 min である。図 5 から、Zeolite P と Zeolite X&P の Cd 飽和吸着量はそれぞれ 120.9 と 126.8 mg/g であり、CEC より低いため、Cd の吸着は陽イオン交換によるものだと考えられる。

4. 結論

$Ca(OH)_2$ を鉱化剤とし、籾殻灰から Zeolite P を合成した。生成物の CEC は 316 mEq/100g、Cd 飽和吸着量は 120.9 mg/g であり、NaOH の場合より CEC の値が低く、合成時間も長いが、Cd に対する吸着速度がより速く、飽和吸着量もほぼ同じである。

参考文献

[1] FAOSTAT, Data.

[2]H. Katsuki, et al. J. Solid State Chem. 182 (2009)

[3]C. Santasnachok, et al. J. Envr. Chem. Eng. 3 (2015)

[4]A. Moirou, et al. Clays & Clay Mine., 48, 5, (2000)

インド・アーメダバードにおけるオートリキシャ旅客特性の解明

学籍番号:15B03625　氏名: 郭　欣　指導教官: 花岡　伸也, 川崎　智也

1. はじめに

インドの急速な発展に伴い、全国範囲における都市化が素早く進んでいる。インドの都市の人口は2008年の3億4,000万人から2030年までに5億9,000万人に増加するのが推定できる。[1]このような都市人口の増加につれ、人々が交通移動の自由の必要性は高まる一方である。しかし、公共交通の発展が経済の発展に追いつかず、そのためオートバイや自動車を含む自家用車の増加がみられている。それに伴い、交通渋滞や大気汚染などの深刻な問題が引き起こされ、人々の日常生活に影響を及ぼしている。特に、大都市では交通問題が手を焼く社会問題となっている。

本研究は、インドのGujarat州で最大の都市、アーメダバードを注目する。アーメダバードでは現在自動車数の増加が市民にとって大きな負担となり、アーメダバードのバスシステムとオートリキシャを含む公共交通機関に解決策を求めるべきだと考えられる。[2]

本研究の目的は4つがある。最初の目的はオートリキシャをBRTSのフィーダーサービスとして使っている旅客の特性を把握することで、２つ目は、BRTSユーザー全般の特性を把握することである。3番目の目的は人々がBRTSとオートリキシャを使う理由を知ることにより、最後の目的はBRTSとautoに対する改善点を把握することである。

前述の目的を満たし、今後アーメダバードでオートリキシャの活用に役立つことを期待している。

2. 研究手段

２０１８年１１月に、アーメダバードにおいてアンケート調査を行った。回答者全員を２つのグループにわけ、１グループはオートリキシャをBRTSのフィーダーサービスとして使うauto userであり、もう１グループは他のフィーダーサービスを使ってBRTS駅に行くnon-auto userである。auto userとnon-auto userの全体はBRTS userであり、平出駿氏が２０１７年の研究でのアンケート調査のサンプルはprivate vehicle userである。

質問票では年齢や教育背景や収入など一般的な個人情報だけではなく、交通モードBRTSとフィーダーサービスに関する質問もアンケート票に記載されている。その中には、交通モードを使う時間帯や利用する理由や改善点などが含まれた。それに、BRTSとオートリキシャに関するコメントに対して５段階評価で1が全く同意していない、５が同意している、と設定されている。

アンケート調査の結果から各質問の結果が違うグループわけに従い、auto userとnon-auto user、またprivate vehicle userとBRTS userの間で比較し、どの質問の結果がauto userとnon-auto userの間で違いとがあるのか、また関係があるのかをT検定とカイニ乗検定をRで計算した数値から判明した。private vehicle userとBRTS userの場合も同じようにRで計算を行った。また、計算結果が異なるため、関係がある質問の結果に関して、各グループの特性を更に対照図形式によって分析した。

3. アンケート調査の結果と考察

3.1 アンケート調査のサンプル数

２日間のアンケート調査の結果より、310サンプルのauto user、300サンプルのnon-auto user、合計610サンプルのBRTS userが収集された。

3.2 カイニ乗検定とT検定の結果

表１　カイニ乗検定の結果①

	auto user & non-auto user	BRTS user & private vehicle user
Age	○	▲
Gender	○	▲
Family member	○	/
Private vehicles	○	/
Employment status	○	▲
Educational background	○	▲
Household income(monthly)	○	▲
Transportation cost(monthly)	○	/
Frequency of using BRTS	▲	/
Time periods of using BRTS (or private vehicle)	○	▲
Trip purpose	○	○
Usage of public transportation app	○	/
Usage of smart card Payment	○	/

(○ :p value > 5%, ▲: p value < 5% , / : no data)

上の表1カイニ乗検定の結果①で示すようにautoを使うかどうかがBRTSの使用頻度との関連性が示されている。更にこの二つのグループの対照図を作り、non-auto userがauto userよりBRTSを使う頻度が高く、時間帯が幅広いことが判明された。

そして、private vehicle userとBRTS userの計算結果では自家用車とBRTSを選択したのは年齢と性別、また雇用状態と月収入、教育背景および出かける時間帯と関係があると表した。この二つのグループの対照図を作り、そこで判明したのはBRTS旅

客の年齢層が１０代と２０代が多く、女性と正式に雇用された人、および月収入が高い人と高学歴を持つ人が自家用車を使う人より少ない。BRTS 旅客がBRTS の利用時間帯が分散である一方、自家用車を使う人たちの出かける時間帯がラッシュアワーに集中することが分かった。

表２　カイ二乗検定の結果②

Comments about BRTS		Mean		P value
		Auto users	Non-auto users	
1	People around me including family, friends and colleagues usually use it.	3.72	4.08	▲
2	Request to operate in early morning and midnight.	3.27	3.55	▲
3	Difficult to get on and off the bus station.	2.28	2.29	○
4	Ticketing system is complicated.	2.18	2.18	○
5	I feel safe to use it.	4.18	4.23	○
Comments about auto				
6	People around me including family, friends and colleagues usually use it.	3.62	3.61	○
7	It tends to get involved in harassments.	1.86	2.08	○
8	It is frequently available.	3.51	3.46	○
9	Auto drivers have bad attitude.	2.83	2.89	○
10	It is small inside, I feel congested.	2.14	2.14	○
11	I feel safe to use it.	3.94	3.88	▲

(○ : p value > 5%, ▲: p value < 5%)

上の表２カイ二乗検定の結果②で示すようにautoを使うかどうかが１番目、２番目と１１番目の三つのコメントに対する態度の違いと関係がある。平出駿氏の研究により private vehicle user が公共交通を使わないことに１番大きな影響を与えていた項目“Subjective norm”であった。周囲の人々の意思決定が本人の意思決定に大きくかかわっていることがわかる。[3] １番目のコメントが示すように、平出駿氏の研究結論はBRTS の旅客でも証明できた。２番目のコメントはnon-auto user がBRTS を広い時間帯で利用するのが推定でき、３番目のコメントを通し auto user がオートリキシャへの信頼性が non-auto user より高いことが判明できた。

表３　交通時間Ｔ検定の結果

	Auto(min)	Non-auto(min)	P value
Access time	mean: 8.56 median: 7	mean: 7.21 median: 5	▲
Egress time	mean: 7.42 median: 5	mean:6.77 median: 5	○
BRTS time	Mean: 30.9 median:25	Mean :27.5 median:25	▲
total travel time	mean: 46.9 median: 42	mean: 41.4 median:38	▲

(○ : t value > 5%, ▲: t value < 5%)

上記の表３が示すように、auto user のアクセス時間と BRTS に乗る時間、および全体のトリップ時間は平均的に non-auto user より長いことが判明できる。今回調査時に聞いた時間は待ち時間が含まれたので、オートリキシャを探すときドライバーとの値段交渉や経路決定などにかける時間がこの時間差が生じた原因だと考えられる。目的地までの距離が短いことにより BRTS を使ったのはイグレスで時間差がない原因だと考えられる。

3.3BRTS とオートリキシャを使う原因と改善点

BRTS を利用する原因として一位となったのは「安い料金」（64.３％）であり、「速度が速い」（55.７％）と「家から行きやすい」（40.８％）のは２位、３位である。他には「居心地が良い」や「家から近い」や「BRTS が安全」などもある。

オートリキシャに関して、auto user にオートリキシャをフィーダーサービスとして使う原因、また non-auto userに使わない原因を聞いた結果、「駅から遠すぎ」（81.６％）と「駅から近すぎ」（85.３％）は各質問の答えで一位である。そこで、駅からの距離の遠近がオートリキシャを BRTS のフィーダーサービスとして使うかどうかの一番の原因だと考えられる。

BRTS の改善点に関して、「バスの頻度」を選択した人が一番多く、37.５％である。オートリキシャの場合では「高い料金」が一番で３７％である。しかし、この二つの答えの中ではが「改善点がない、今のままでいい」と答えた人も少なくない。

4.終わりに

この調査では、アンケート調査から、オートリキシャをBRTS のフィーダーサービスとして使う人の特性分析を行い、オートリキシャがアーメダバードの公共交通での役割を解明した。調査結果により、private vehicle user とBRTS user の間では顕著な差が存在することが判明できた。BRTS 旅客の中に学生の割合が顕著的に高く、自家用車を使う人たちの中で雇用された人が多い。しかし、auto user と non-auto user の間に個人特性に関する明らかな差がなく、BRTS を使う頻度だけに関係あるのを示した。この結果から、公共交通利用者のフィーダーサービスの選択が公共交通と繋がり、将来的に公共交通の進展に伴い変動する可能性が予測できる。

参考文献：

[1] McKinsey Global Institute: India’s urban awakening: Building inclusive cities, sustaining economic growth:2010

[2] AKSHAY MANI, MADHAV PAI,RISHI AGGARWAL: Sustainable Urban Transportation in India: *Role of the Auto-rickshaw sector*:2012

[3] Hiraide, T., Kawasaki, T. & Hanaoka, S., Clarification of public transport usage conditions in Ahmedabad, India. *WIT Transactions on the Built Environment*, 182, WIT Press, 2018.

Adhesion model of side contact for elastic beam with consideration of inflection point

Student Number:15_03938 Name:Saneyuki KATO Supervisor:Kunio TAKAHASHI

1 Introduction

In the research field of manipulation, the development of a grip-and-release device has been focused. Mikhail has developed such device using a two dimension array of side-contact elastic (PDMS) beams[1]. He designed the device by setting every single beam with a fixed tilting-angle and experimentally studied its function. The adhesion force of the device[1] could be controlled by changing tangential force. However, theoretical model required for designing work is still not clear.

On the other hand, an adhesion model of side contact for inextensible elastic beam was proposed [2]. This model assumed the adhesion between an elastic beam and a rigid surface and considered the bending deformation of the beam. According to the experimental results of Mikhail [1], it was observed that inflection point exists during the beams' deformation, which this phenomenon can not be predicted by the previous analytic model [2]. Thus, I propose an adhesion model for side-contact elastic beam with the consideration of inflection point. This study is thought to be a guideline required for designing grip-and-release device using side-contact elastic beams.

2 Modeling

The proposed adhesion model, as shown in Fig. 1, assumes the contact between a side of an elastic beam and a rigid surface. The beam with length L, width W, moment of inertia of the (rectangular) cross-section I, is assumed as Bernoulli-Euler beam. It partially adheres to the surface, so that the non-adhesion length (referred to as non-adhesion area) is defined as l. In this model, a pure bending deformation is assumed without any axial deformation, and no deformation occurs in the adhesion area. The boundary between the non-adhesion area and adhesion area is perpendicular to the rigid surface, and the angle θ of the beam base is constant.

By considering bending deformation, the deflection angle φ of the beam within the non-adhesion area caused by the force F applied to the beam can be calculated as,

$$\frac{d\varphi}{d\tilde{s}} = \pm 2\sqrt{\tilde{F}\{\cos(\varphi-\alpha)+C\}}, \tag{1}$$

where, $\tilde{F} = F/(\Delta\gamma W)$, $\tilde{s} = s/\sqrt{2EI/\Delta\gamma W}$, are the normalized force and (neutral axial) length, respectively. E is Young's modulus of the beam, $\Delta\gamma$ is the work of adhesion, and C is a curvature parameter to be determined from boundary condition.

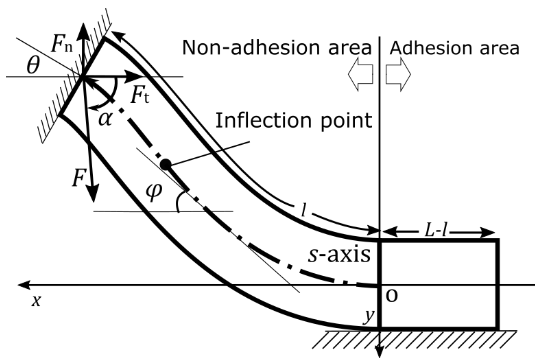

Fig. 1: Schematic image of the contact between side surface of an elastic beam and a flat rigid surface

The total energy U_{T} of the contact system, defined as the sum of bending energy, surface energy and potential energy of external force, can be expressed as,

$$\tilde{U}_{\mathrm{T}} = 2\tilde{F}\int \cos(\varphi-\alpha)d\tilde{s} + (\tilde{F}\cos(\alpha)-1)(\tilde{L}-\tilde{l}) + \tilde{F}C\tilde{l} \tag{2}$$

where, $\tilde{U}_{\mathrm{T}} = U_{\mathrm{T}}/\sqrt{2EI\Delta\gamma W}$, $\tilde{L}$, $\tilde{l}$ are the normalized energy, total length, and non-adhesion length of the beam, respectively. It is assumed that the beam move statically. Here, we can obtain the equilibrium equation of the contact system as

$$\frac{\partial \tilde{U}_{\mathrm{T}}}{\partial C} = \{1-\tilde{F}\cos(\alpha)-\tilde{F}C\}\frac{\partial \tilde{l}}{\partial C} = 0. \tag{3}$$

Since the total energy of the system is stable if second-order differential value of the total energy is positive. Eqs.(1) and (3) yields

$$\frac{d\varphi}{d\tilde{s}} = \pm 2\sqrt{1+\tilde{F}\{\cos(\varphi-\alpha)-\cos(\alpha)\}}. \tag{4}$$

The non-adhesion length $\tilde{l}$, horizontal displacement $\tilde{x}$ and vertical displacement $\tilde{y}$ of the beam base are expressed as follows.

$$\tilde{l} = \frac{1}{2}\int \pm\frac{d\varphi}{\sqrt{1+\tilde{F}\{\cos(\varphi-\alpha)-\cos(\alpha)\}}} \tag{5}$$

$$\tilde{x} = \frac{1}{2}\int \pm\frac{\cos(\varphi)d\varphi}{\sqrt{1+\tilde{F}\{\cos(\varphi-\alpha)-\cos(\alpha)\}}} \tag{6}$$

$$\tilde{y} = \frac{1}{2}\int \pm\frac{-\sin(\varphi)d\varphi}{\sqrt{1+\tilde{F}\{\cos(\varphi-\alpha)-\cos(\alpha)\}}} \tag{7}$$

Consequently, for the beam without inflection point, the integration interval is from 0 to θ, whereas for the beam with inflection point, the integration interval is from 0 to φ_c and φ_c to θ. φ_c is the deflection angle at the inflection point.

3 Result and discussion

Fig.2 shows the relation between the total energy of the beam and the curvature parameter. $\Delta\widetilde{U}_\mathrm{T}$, as shown in Fig.2, denotes the gap between the total energy of the beam when it deforms with an inflection point comparing to that in equilibrium without an inflection point. When the energy gap $\Delta\widetilde{U}_\mathrm{T}$ is zero, the beam exhibits a fransition from its deformation without an inflection point to that with an inflection point. But the beam detaches from the object afterward since no energy equilibrium exists. When the energy gap exists, the beam does not exhibit the fransition. Therefore, as long as a constant force applied, a transition would not happen from the beam without an inflection point to that with an inflection point. In this paper, since detachment from grip is of our interest, we only discuss the beam without inflection point.

When the tangential force $\widetilde{F}_\mathrm{t}$ is kept constant, the maximum value of the normal force $\widetilde{F}_\mathrm{n}$ becomes the maximum adhesion force as long as the system is at equilibrium. Consequently, the maximum adhesion force can be controlled by the tangential force, and for this device, griping and detaching performances can be achieved by manipulating the tangential force.

We have also examined the relationship between the maximum adhesion force and the angle of the beam base θ, as shown in Fig.3. It is observed that as θ decreases the maximum adhesive force increases. Therefore, the smaller the angle of the beam base is, the heavier object the beam can grip. However, when the beam length L is sufficiently long, the influence of the beam base angle on the adhesion force become less as the tangential force increases. Or in other words, the release range becomes larger as the base angle of a sufficiently long beam becomes larger. Consequently, the beam can grip and release objects of various weights by selecting appropriate value of the base angle. However, we should be careful that the maximum adhesion force would decrease when the base angle is large, and the beam length is short. Therefore, the larger the beam base angle is, the longer the beam length is required.

The smaller the beam base angle is, the more heavy object the beam can grasp. On the other hand, the larger the beam base angle is, the lighter object the beam can release. But, when the beam length is sufficiently long, the influence of the beam base angle on grip and release becomes less as the tangential force increases.

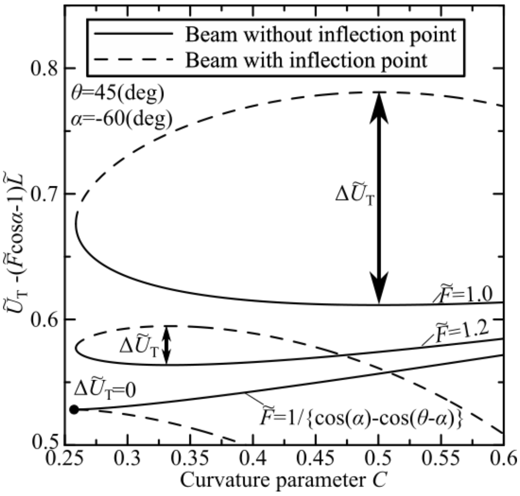

Fig. 2: Total energy equilibrium depends on curvature parameter

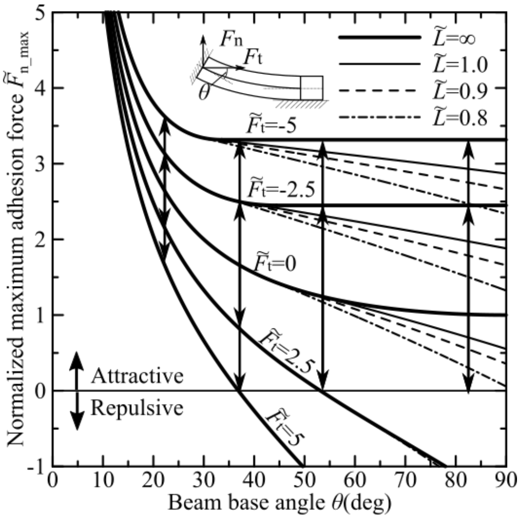

Fig. 3: Maximum adhesion force depends on angle of beam base

4 Conclusion

An adhesion model utilizing a side contact of an elastic beam was proposed, and the behavior of the beam was studied with considerations of its inflection point. The beams with and without inflection point were carefully analyzed, and the results showed that there is no transition from the beam without inflection point to that with inflection point. The relationship between the adhesion force and the angle of the beam base was also discussed, and concluded that the smaller the beam base angle is, the more heavy object the beam can grasp and, the larger the beam base angle is, the lighter object the beam can release.

The proposed model is required for designing a grip-and-release device using an array of side-contact elastic beams.

References

[1] M. Salioukov et.al., Mate vol.24 pp. 261-264, 2018, Jan.

[2] L. W. He et.al., Journal of Applied Physics,vol.112, no.1,pp.013516- 1-6,Jul. 2012.

公共交通指向型開発のための都市成長モデルの開発

学籍番号:15_09852　氏名:董　思繁　指導教員:花岡　伸也, Alvin Christopher Galang Varquez

1. はじめに

国際連合が発表した「世界都市人口予測・2018 年改訂版」により，2018 年の世界都市人口率は 55%であり, 2050 年に 68%増加すると予測されている。そのうちの 90%近くがはアジアとアフリカに発生すると予測されている。急激な都市化により，都市部の森林、緑地の減少，汚染，交通渋滞などいろいろ問題が起こっている。これらの問題を避けて，より持続可能な都市発展を求めるために，都市成長モデルを用い，将来都市の成長状況と土地利用転換の傾向を把握する必要性がある。

SLEUTH モデル(Clarke.K.C,1997)はその背景に応じて開発された都市成長シミュレーションモデルである。SLEUTH モデルは過去のデータから将来の都市成長パターンを把握できることを前提し，6 つの入力レーヤー(斜面，土地利用，排除，都市，交通，陰影)は全て研究エリアの過去の地図から得る GIF イメージと要求されているため，地域の要因に制限されなく，世界範囲で広く使える特性がある。モデルは今まですでに世界で 100 個以上の都市に利用され，パフォーマンスを検証された。しかしながら，モデルの交通レーヤーの入力は道路の地図だけがあり，道路発展の都市成長への影響しか考えていない。これは持続可能な都市開発に足りないと考えられるため，本研究では公共交通機関の発展を考慮し，公共交通指向型開発（Transit Oriented Development，TOD）の下の都市成長を予測できるように， 1) 排除レーヤーで TOD が反映できる最適なピクセル値を探る; 2) 駅を新しい入力レーヤーとして加えて，道路に沿う開発より駅周辺の都市成長に優先させるの二つの手法で SLEUTH モデルを再開発する。

2. 研究手法

本研究では, TOD の典型例と考えられるつくばエクスプレス線の中の茨城県にある 6 つの駅を研究エリアとして, 1997, 2006 ,2009 ,2014 年のデータから 2014〜2050 年の都市成長状況を予測した。

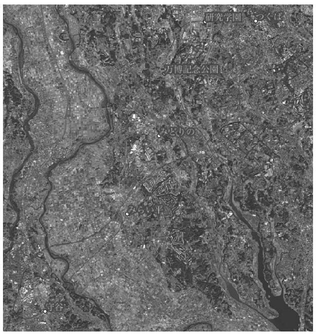

図 1. 研究エリア(35.94° ~36.09° , 139.99° ~140.12°)

2.1 排除レーヤーの最適ピクセル値を発見

排除レーヤーはピクセルの値により海、川のような都市化不可能な地域を定義する役割がある。 新しい排除レーヤーはもとのデータの上に駅の地図を加え，駅の影響を考慮するために，駅エリアを一番都市化される可能性高いようにピクセル値に 0，川部に 100 を与え，その他の地域の値は 0〜70 の間に 5 を間隔として 15 回繰り返してモデルを実行した。

2.2 新しい入力レーヤーを作る

SLEUTH モデルの中に既存のシミュレーションルールに基づいて，もともとの道路に沿う都市発展より駅周辺の成長を優先させる。また，駅の開業による都市開発は駅を中心として駅

周辺に発散する特徴があるため，円型で拡散する成長に工夫をした(図 2)。

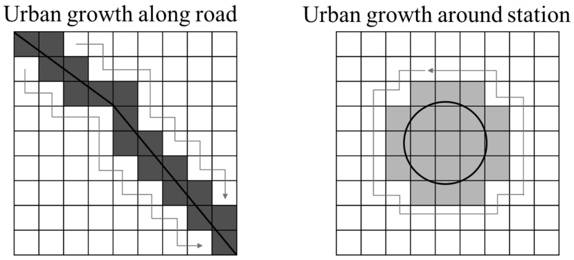

図 2．道路と駅の都市成長の特徴

3．結果

3.1 排除レーヤーの最適ピクセル値を発見

異なるピクセル値を持つ新しい排除レーヤーを用いてシミュレーションした 2014 年の結果を実際の土地利用状況と比べて，それぞれの精度を検証した（図 3)。その他の地域のピクセル値が 50 のとき，モデルの精度が一番高いと見え，86.04%と検証された。

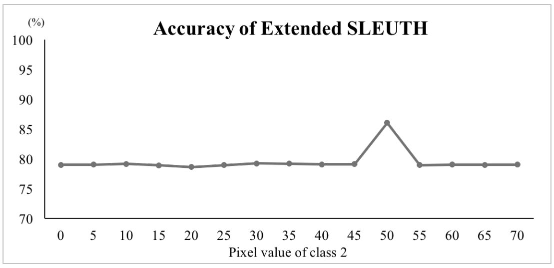

図 3．ピクセル値が異なるときのモデルの精度検証

また，2050 年の都市成長確率アウトプットから，15 つのケースの間に，ピクセル 50 の場合に駅周辺の成長率とほかの地域の成長率の差が一番大きく見える(図 4)。

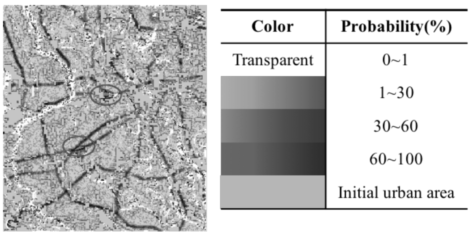

図 4．ピクセル値 50 のときの 2050 年都市成長率結果

3.2 新しい入力レーヤーを作る

駅を考慮した新モデルと駅考慮しない旧モデル両方を実行し，2050 年の土地利用状況の結果を比べた。駅エリアの都市ピクセルの数を数え，全体の都市ピクセルに対する比率を計算した結果，新モデルの駅周辺都市比率は 0.0226 で，オリジナルモデルのほうは 0.0220 であった。さらに，新モデルとオリジナルモデル両方の 2014 年のアウトプットを用いて精度検証した結果，それぞれの精度は 84.92%と 84.67%であった。

4．おわりに

結果によって，排除レーヤーにおいてのピクセル値はそれぞれ川部 100，駅エリア 0，その他の地域 50 の時に，TOD の影響を一番大きく体現できると考えられる。また，駅レーヤーを加えた新 SLEUTH モデルにおいて，都市の発展はオリジナルモデルと比べてより駅に集中することが実現できた。さらに，TOD 影響を考慮した後に，より精度高い予測ができると考えられる。

本研究では駅周辺の都市成長に優先性を与えることによって SLEUTH モデルを公共交通指向型の都市開発に発展した。この結果を用いて，研究エリアの将来の都市発展の成長可能性と起こりうる問題が見込まれ，持続可能な都市を作るために参考になると考えられる。排除レーヤーでピクセル値の与えにより駅エリアの発展に加重をしたことと新しい入力レーヤーを作ったことから SLEUTH モデルの柔軟性とポテンシャルを検証できた。また，公共交通システムの発展は将来の都市成長に関わる重要な要因と考えられているため，これからの研究において，TOD の影響を表す数式モデルを SLEUTH に結合し，より精度が高いシミュレーションを求めることに工夫をするべきである。

参考文献

[1] United Nations, 2018, 2018 Revision of World Urbanization Prospects

Exploring Europa by Plume Breaking

Student Number: 15_15137 Name: Juyon Yamazaki Supervisor: Daisuke Akita

1. Introduction

Beneath the icy surface of Jupiter's moon Europa is perhaps the most promising place to look for present-day environments suitable for life. Due to Europa's eccentric orbit, heat created by tidal flexing is considered to cause the ice to melt and form a huge amount of salty ocean. Therefore, many missions have proposed to explore Europa to find out its habitability. Since image captured by Hubble Space Telescope revealed water vapor erupting from near south pole, it now brings us great opportunity to study the characteristics of Europa's subsurface ocean without digging thick icy surface anymore. However, this phenomenon is yet poorly understood that the location of the vent is not precisely known and is difficult to predict this sporadic event.

2. Mission Concept

It is impossible to land near the vent by detecting the plume unless the phenomenon is well known. Therefore, we propose a mission that detects the plume by using numbers of a small size lander.

Fig.1 shows the mission scenario and the concept of the lander. In order to detect plume, lander is injected to the polar orbit all of which cover the area (latitudes between -80~ -50 [deg] and longitudes between 120 ~ 250 [deg]) [1] where the vent is known to be found roughly from mothership orbiting Europa. When a lander encounters(detects) plume, it would decelerate due to the force of plume that flight trajectory would change dynamically (We call this "Plume Breaking"). The mothership would track the lander and reveals plume's characteristics by using radar in the meantime. Lander is supposed to be very light to get enough deceleration not to crash. Our mission considers the lander's ballistic coefficient near 0.1 [kg/m^2]. Zylon is used for heat protection and high elastic metal is used to keep its body. Payloads should be light enough.

Our goal is to estimate the feasibility of this mission which is,

- Is it possible to make the lander encountering plume get enough deceleration by plume force and touch down on surface under the speed 200 [m/s]?
- Can the lander touch down inside the area of the plume or outside but not far from the area?
- How many landers are required for this mission?

Unknown for the characteristics of the plume, modeling the plume is necessary.

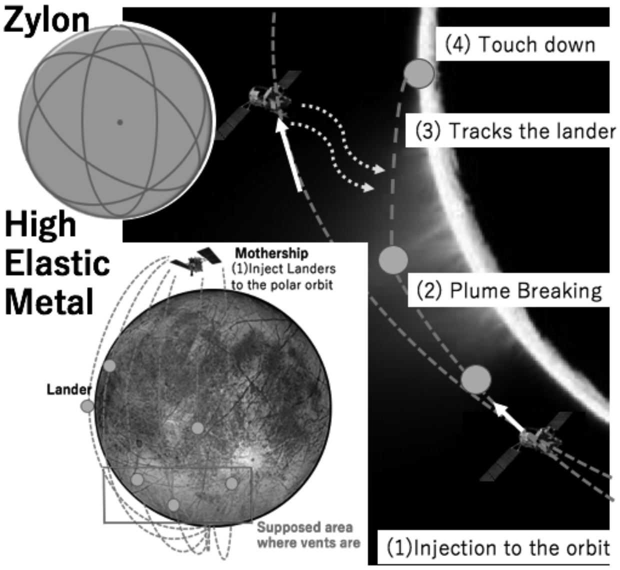

Fig.1 Mission Scenarios, Lander Concept

3. Modeling Plume

The model we considered are shown in Fig.3. Vents are consisted of multiple narrow vents, and each vent erupts water vapor by angle of 2θ.

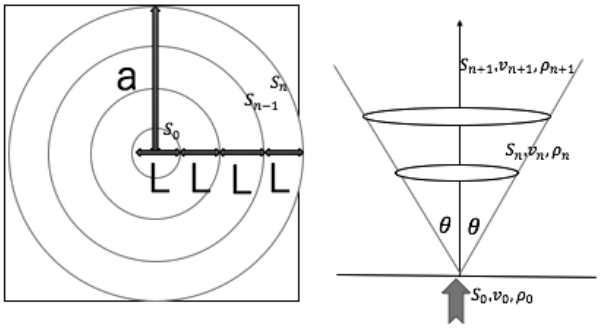

Fig.2 Plume model

We assume the flow is compressive and isentropic, only the gravity of Europa works as the force. The initial state gives,

$$a = (2n - 1)L + 2nw_{plume} \quad (1\text{-}1)$$

$$\textstyle\sum_k^n S_k = 2\pi wna - \pi wn(n - 1)l - \pi w^2 n^2 = S_{plume} \quad (1\text{-}2)$$

The equation of mass flow and energy conservation gives,

$$\dot{m} = \rho S v = const. \quad (1\text{-}3)$$

$$\frac{1}{2}u^2 - \frac{u_E}{R+h} + \frac{\gamma}{\gamma-1}\frac{P_0}{\rho_0}\left(\frac{\rho}{\rho_0}\right)^{\gamma-1} = const. \quad (1\text{-}4)$$

$$P = P_0\left(\frac{\rho}{P_0}\right)^{\gamma} \quad (1\text{-}5)$$

Isentropic flow gives Eq. (1-5). As shown in Fig.2, plume will spread in a circle whose radius is the tangent of the height, however the area can be solved in a different way between certain height from this calculation.

$$S = 2\pi n^2\{l + w\}\{h\tan\theta + w/2\} \qquad (2h\tan\theta \leq L) \quad (1\text{-}6)$$

$$S = \pi(a + h\tan\theta + w/2)^2 \qquad (2h\tan\theta \geq L) \quad (1\text{-}7)$$

We used the initial state of the plume's velocity and area as v_0 as 560 [m/s^2][2], S_0=S_{plume}=1.5×10^5[m^2][2], the mass flow for 7.0×10^3 [kg/s] [2], and the width of each ring w_{plume} as 10 [cm] [3]. a, θ, $\dot{m}$ are the parameter of this model because these depends on Europa's activity which is impossible to predict.

a[m]: radius of plume area
L[m]: distance between ring
S_k[m^2]: the area of k's ring
v [m/s]: velocity of plume
γ: Specific heat ratio of plume
μ_E[m^3/s^2]: Europa's gravitational constant number
h [m]: height

n: number of ring
θ [deg]: eruption angle
ρ [kg/m^3]: density of plume
S [m^2]: area of plume
r [m]: radius of Europa
$\dot{m}$ [kg/s]: mass flow

4. Motion Equation

Motion of the lander is considered in polar coordination shown in Fig.3. The Force taken into account for the motion is the gravity of Europa and air force of plume. The motion equations of the lander are given by Eq. (2-1~4)

$$\frac{d\gamma}{dt} = (\frac{\mu_E}{r^2} - \frac{v}{r})cos\gamma \quad (2\text{-}1)$$

$$\frac{dv}{dt} = \frac{\mu_E}{r^2}sin\gamma - \frac{1}{2}\rho v^2\frac{1}{\beta} \quad (2\text{-}2)$$

$$\frac{dr}{dt} = vsin\gamma \quad (2\text{-}3)$$

$$\frac{d\theta}{dt} = \frac{vcos\gamma}{r} \quad (2\text{-}4)$$

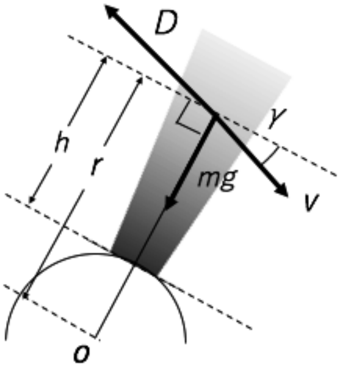

Fig.3 Motion equations model

t [s]: Time from Plume entry
v [m/s]: velocity
γ [deg]: flight path angle
θ [deg]: Longitude
ρ [kg/m^3]: density of plume
r [m]: distance from the center of Europa
μ_E [m^3/s^2]: Europa's gravitational constant
β [kg/m^2]: ballistic coefficient

Eq. (2-1~4) is numerically calculated by 4th order Runge-Kutta method with time step of 0.01 [s]. ρ is given by solving Eq. (1). β , r are the parameter of the trajectory. It should be noted that the lander may perhaps not be in the plume and at that time, the air force of plume should not be taken into account. This happens when the lander has flown away from the area of plume or when the height of the lander satisfies Eq. (1-5) and the lander in the position surrounded by plume (See position 2 shown in Fig.4).

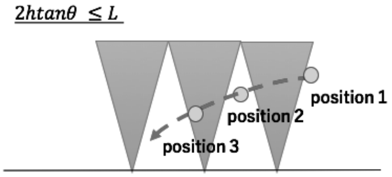

Fig.4 Position of the lander

5. Trajectory Results

From chapter3 and chapter4, there are five parameters to simulate the lander's trajectory. However, 2 parameters from chapter4 can be controlled manually. Therefore, β =0.1, r=500 [m] are chosen since the smaller ballistic coefficient gives more plume force to break (plume breaking) from Eq. (2-1), and the lower height gives thicker plume from Eq. (1-4) which then results to above.

From Eq. (1-1,5,6), if height is low, the radius of plume area affects much more than the angle of eruption. However, the mass flow is the strongest to affect plume. Hence, we assumed the lander's touch down speed and the distance from the plume area is affected by the mass flow and the radius of plume area.

Fig.5 shows the lander's distance from plume area and the last speed when $\dot{m}$ = 7000×1 [kg/s]. Fig.5 reveals that the larger the radius of plume area, the further the lander would land from the area of plume area. though if it is small, the lander would not land in the area of plume but land far. In this case, we cannot make landers to land inside the plume. The speed is poorly reduced that it would crash into the surface. This case brings worse mission scenarios. However, we can obtain the characteristics of plume by tracking the trajectory of landers using the mothership.

Fig.5 shows the lander's distance from plume area and the last speed when $\dot{m}$ = 7000×100 [kg/s]. Fig.6 reveals what Fig.5 reveals that the smaller the radius of the plume area, the closer landers can land from the area of the plume and the greater landers get the reduction of speed. We should pay attention to the speed that this differs from Fig.5's. In some conditions, landers can manage to soft-land and conduct some scientific mission sending results to the mothership. This case brings preferable mission scenarios.

From Fig.6, we can estimate the number of landers its needed for to achieve mission succeed. $a = 2.4$ [km] is the maximum which satisfies the condition of last speed. Since the area where plume vents are supposed to be has 1758 [km] to be covered, the required number of landers for the case of Fig.6 is roughly 370. If $a \geq 2.4$ [km], it would become hard for soft-landing even though we can get the characteristics of plume with fewer landers. If $a \leq 2.4$ [km], more numbers of landers are needed to fully cover the area though landers can soft-land and conduct scientific missions.

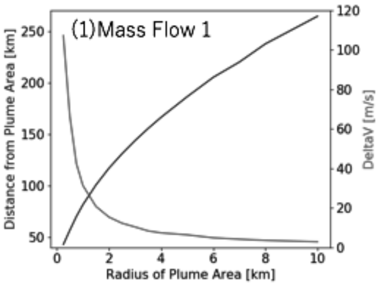

Fig.5 Distance and Touch down speed ($\dot{m}$ = 7000×1 [kg/s].)

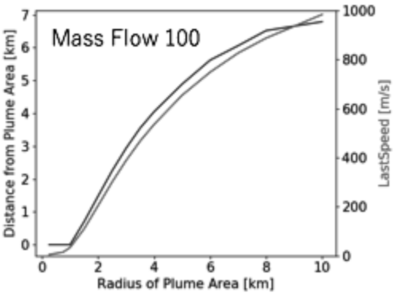

Fig.5 Distance and Touch down speed ($\dot{m}$ = 7000×100[kg/s].)

6. Conclusion

Recently found plume in Europa gives us great opportunity for scientific discoveries however not yet understood. We suggested the mission that can help finding plumes and even land near or inside the plume area by simple and cheap way.When mass flow is given as 7000×100 [kg/s], provided that more than 370 landers were brought for the exploration, landers can detect plume and land near the area of plume in some conditions. Regadless of the characteristics of plume, we can obtain it. However, the model and the assumption would make the result shown above uncertain. There is still room for improvement if we take into consideration more precisely to model plume.

7. References

[1] Alyssa R. Rhoden (2015) "Linking Europa's plume activity to tides, tectonics, and liquid water", Cornell University
[2] Lorenz Roth (2014) "Transient Water Vapor at Europa's South Pole", Science Vol.343, Issue. 6167-10
[3] Jurgen Schmidt (2008) "Slow dust in Enceladus' plume from condensation and wall collisions in tiger stripe fractures", Nature Vol.451, Issue. 685-688

Development and Calibration of Radio Sensor using Off-the-shelf Software-defined Radio for Location Fingerprinting

Student Number:15B05127 Name:Jiang Haichen Supervisor:Jun-ichi TAKADA, Azril Haniz

1 Introduction

Recently, with the fast spread of wireless local area networks (WLANs) and mobile devices, localization systems have become significantly important by the increasing needs of location based services (LBS). Global Positioning Systems (GPS) is usually used to provide precise location of subjects in open area. On the contrary, Indoor localization systems can not use the satellite signals due to complex influence of many obstacles inside buildings [1].

Fingerprint positioning technology, one of the popular positioning technologies for indoor localization systems, utilizes specific signal characteristics such as received signal strength (RSS) with specified reference locations as the offline database. In practice, the target's location fingerprints are matched with the closet offline location fingerprints to estimate its location. In order to enable students and amateurs to apply this approach, a cheap and easy-to-use device which can collect a variety of different fingerprint values is necessary [2].

In this thesis, LimeSDR, an off-the-shelf software-defined radio (SDR) with flexibility and low cost, will be introduced and researched for the stability and reliability of collecting particular signal characteristics which is needed for indoor localization systems.

The objective of this thesis is to figure out whether LimeSDR can be used in measuring specific location fingerprints accurately based on the measurement result after calibration.

2 Development environment of LimeSDR

The radio sensor which is used to measure the location fingerprint is constructed using LimeSDR and GNU Radio.

2.1 Architecture of LimeSDR

LimeSDR is a cheap and powerful SDR with two receiver and transmitter channels receptively which offer great flexibility compared to other SDRs with only a single receiver and transmitter channel. In this research, since only the development of a receiver is considered, we will omit explanation regarding the transmitter, this section will explain how LimeSDR receives signal data from two channels which can be utilized for fingerprinting collection.

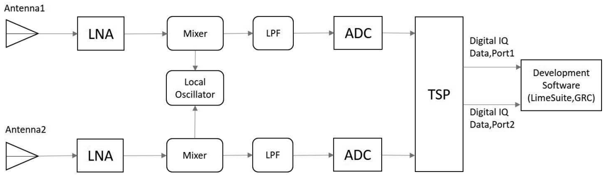

Figure 1: Block diagrams for LimeSDR to process Rx signals.

Figure 1 shows the block diagrams of LimeSDR as a signal receiver. Firstly RF signals are received by two antennas, and then are amplified with low noise amplifiers (LNA). In the next stage, the signals are fed into mixers with another signal generated from the local oscillator to convert the signals into baseband signals and then passed through low pass filters (LPF). Then the analog baseband signals are converted into digital IQ signals by Analog-to-Digital Converters (ADC), and then finally processed by a transceiver signal processor (TSP). In the TSP, the received signal is further adjusted by applying IQ imbalance, gain and DC offset correction. Finally, I (In-phase) and Q (Quadrature) data of baseband signals is transferred to a computer by a USB3.0 connection and processed by software like GNU Radio Companion (GRC) or LimeSuite which also can set the configuration of LimeSDR [3].

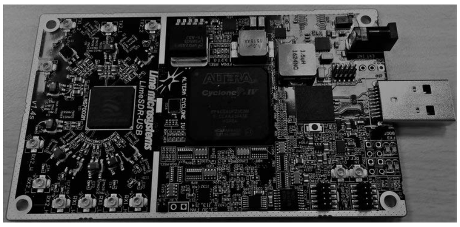

Figure 2: LimeSDR

2.2 GNU Radio

GNU Radio is a free and open-source software development toolkit that provides signal processing blocks to implement software radios. In this research, the LimeSDR source block was employed to control some parameters like RF frequency, RX gain, and also receive samples from the LimeSDR. Then, the File Sink block was employed to store the received raw IQ data into a binary file for further processing.

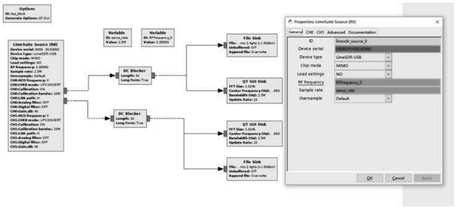

Options
ID: top_block
Generate Options: QT GUI

LimeSuite Source (RX)
Device serial: 0009...5C6300C
Device type: LimeSDR-USB
Chip mode: MIMO
Load settings: NO
RF frequency: 2.3999G
Sample rate: 2.5M
Oversample: Default
CH0:NCO frequency: 0
CH0:CMIX mode: UPCONVERT
CH0:Calibration: ON
CH0:Calibration bandw.: 10M
CH0:LNA path: H
CH0:Analog filter: OFF
CH0:Digital filter: OFF
CH0:Gain,dB: 40
CH1:NCO frequency: 0
CH1:CMIX mode: UPCONVERT
CH1:Calibration: ON
CH1:Calibration bandw.: 10M
CH1:LNA path: H
CH1:Analog filter: OFF
CH1:Digital filter: OFF
CH1:Gain,dB: 40

Variable
ID: samp_rate
Value: 2.5M

Variable
ID: RFfrequency_0
Value: 2.3999G

DC Blocker
Length: 32
Long Form: True

File Sink
File: ...mo-2.4ghz-1-(-30dbm)
Unbuffered: Off
Append file: Overwrite

QT GUI Sink
FFT Size: 1.024k
Center Frequency (Hz): ...99G
Bandwidth (Hz): 2.5M
Update Rate: 10

File Sink
File: ...mo-2.4ghz-2-(-30dbm)
Unbuffered: Off
Append file: Overwrite

Properties: LimeSuite Source (RX)

ID: limesdr_source_0
Device serial: 0009070105C6300C
Device type: LimeSDR-USB
Chip mode: MIMO
Load settings: NO
RF frequency: RFfrequency_0
Sample rate: samp_rate
Oversample: Default

Figure 3: Operating layer of GNU Radio

3 Measurement and evaluation

3.1 Measurement Method by LimeSDR

To make sure LimeSDR could be used for indoor localization system, we have to ensure that it can accurately measure the location fingerprint from received signals which are transmitted from a commercial device. In this research, two types of fingerprints, RSS and phase-difference fingerprint are considered. RSS represents the power of the received signal, and phase-difference fingerprint is calculated by taking the phase-difference between two receiver channels. Therefore, it is necessary to evaluate the accuracy in measuring RSS and phase-difference in this research.

As shown in Figure 4, a Sine wave with various value of power and frequencies in Bluetooth low-energy (BLE) channels will be generated by a Signal Generator (SG) and divided into two separated signals by a power splitter. Then LimeSDR receives two individual signals and convert them into digital IQ data for laptop to process into the desired fingerprints. Here, the signals were converted into 0.5MHz low IF (Intermediate Frequency) signals instead of baseband signals by setting corresponding RF frequency in GNU Radio to avoid the DC offset error, and the sampling frequency of the LimeSDR was set to 2.5MHz. Each type of measurement was conducted for 20 times consecutively, and the whole process was repeated twice to check reproducibility.

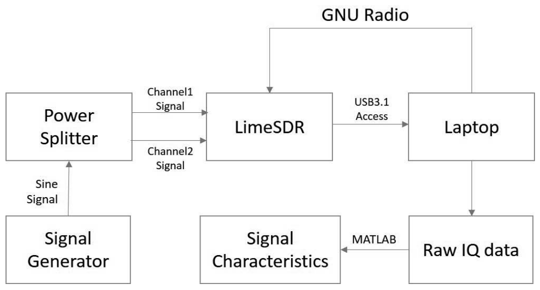

Figure 4: Measuring Environment

Table 1: Setting of configuration of input sine signal from SG

Frequency	2.402GHz 2.426GHz 2.480GHz
Power	-30dBm

3.2 Measurement result

The measurement results are shown in Table 2, including phase difference between RX channels, output power of two RX channels and IQ phase difference of individual channel.

Table 2: Average measured results with original configuration by LimeSDR

Frequency	Output Power in channel1(dBm)	Output Power in channel2(dBm)	Phase difference between channels(degree)
2.402GHz	-56.48	-56.43	32.50
2.426GHz	-56.29	-56.20	33.74
2.480GHz	-55.67	-55.63	36.75

The measurement results showed that there were significant errors in the measured power and phase-difference, which should ideally be 30dBm and 0degrees, respectively.

4 Calibration and conclusion

In order to calibrate the system and eliminate the errors, we performed the following steps. Firstly, we employed the automatic IQ calibration function in GNU Radio to reduce the IQ phase difference for each channel. Then the transmission loss due to the power splitter and cables was measured by a vector network analyzer (VNA) and subtracted from the measured data. We also applied a fixed phase-offset to channel2 based on the first measurement results to eliminate the phase-difference between channels. The result is shown in the Table 3.

Table 3: Average Measured results after calibration

Frequency	Output Power in channel1(dBm)	Output Power in channel2(dBm)	Phase difference between channels(degree)
2.402GHz	-29.97	-29.96	0.15
2.426GHz	-29.95	-29.99	0.24
2.480GHz	-30.03	-30.04	0.28

Compared with Table 2, the results with calibration was more accurate, which proves that collecting fingerprint values with calibration is necessary. Therefore, in this work, LimeSDR was successful in accurately measuring location fingerprints, and will be utilized as radio sensors in indoor localization systems as future work.

References

[1] Y. Gu, A. Lo and I. Niemegeers, ”A survey of indoor positioning systems for wireless personal networks,” in IEEE Communications Surveys & Tutorials, vol. 11, no. 1, pp. 13-32, First Quarter 2009.

[2] H. Liu, H. Darabi, P. Banerjee and J. Liu, ”Survey of Wireless Indoor Positioning Techniques and Systems,” in IEEE Transactions on Systems, Man, and Cybernetics, Part C (Applications and Reviews), vol. 37, no. 6, pp. 1067-1080, Nov. 2007.

[3] LimeMicro, LMS7002M Datasheet. [Online] Available: `https://wiki.myriadrf.org//LimeMicro:LMS7002M\_Datasheet\#RXTSP\_structure`

Separation of acetonitrile from pharmaceutical wastewater using solvent extraction

Student Number: 15B06836   Name: Kaito Sawada   Supervisor: Ryuichi Egashira, Hiroaki Habaki

1. Introduction

Acetonitrile is an important compound in the chemical industry, especially used in the pharmaceutical industry, and is generally produced as a by-product of acrylonitrile. Since the price of acetonitrile is unstable due to demand fluctuation of acrylonitrile and most of acetonitrile used in the pharmaceutical industry has been discharged, the recovery and recycle of acetonitrile is recently attracting much attentions. On the other hand, acetonitrile forms an azeotropic mixture with water [1] and it is impossible to separate the mixture by the ordinary distillation. Then, some separation methods have been studied, such as pressure swing distillation [2], extractive distillation, solvent extraction [3], and so on.

In this study, the application of the solvent extraction to recovery of acetonitrile from pharmaceutical wastewater was studied. Then, the liquid-liquid equilibrium was experimentally measured with hydrocarbons as solvent and the recovery of acetonitrile was investigated.

2. Experimental

Heptane and toluene were selected from alkane and aromatic compounds, respectively, and used as solvents. The experimental conditions of liquid-liquid equilibrium measurements were listed in **Table 1**. In advance, the aqueous solution at the specified mass fraction of acetonitrile and the mixture of heptane and toluene at the specified ratio were prepared, and they were contacted in the conical flask at 298 K in the isothermal bath for 48 hours to be equilibrated. The mass ratio of the feed and solvent was fixed at unity. After equilibration, both phases were analyzed by gas chromatograph GC2010 and Karl Fischer titrator 758 KFD Titrino to determine the compositions of both phases. In cases of analysis of the aqueous solution by Karl Fischer titrator, it was occasionally difficult to determine the mass fraction of water, and then it was calculated using the mass balance relationship.

Table 1 experimental conditions

Shaking	[h]	48
Settling	[h]	1
Shaking temperature	[K]	298
Acetonitrile aq.	[-] (mass fraction)	0.1~0.9
Solvent (Heptane: Toluene)		1:0, 3:1, 1:1, 1:3, 0:1
Solvent/Feed ratio	[-]	1
Mass (respectively)	[kg]	2.0×10^{-2}

3. Results and Discussion

In Water-Acetonitrile-Heptane-Toluene ternary and quaternary system, basically it forms liquid-liquid 2 phases. But three liquid phases are formed when solvent is heptane 50, 75 %, feed is higher than acetonitrile mass fraction 40 %. Since it is said that industrial operation is difficult if it becomes three phases, these samples in three phases are not measured in this study. In addition, these didn't form emulsion, therefore it is easy to separate them. From these results, it was found that separation operation is possible.

Component *i, j* contains Water, Acetonitrile, Heptane and Toluene as W, A, Hp and T respectively. material balance is given by

$$\sum_i^N x_i = 1 \quad \textbf{(1)} \qquad \sum_i^N y_i = 1 \quad \textbf{(2)}$$

$$R_0 x_{i,0} + E_0 y_{i,0} = \mathrm{R} x_i + E y_i \quad \textbf{(3)}$$

where, E, R is each mass of extract phase and raffinate phase after extraction. E_0, R_0 is mass of feed solution and solvent. x_i is mass fraction in raffinate phase. y_i is mass fraction in extract phase. $x_{i,0}$ is initial mass fraction in feed, about component *i*.

Water in raffinate phase is calculated by equation **(1)**. Regarding the extract phases, the mass fraction of acetonitrile are adjusted so that the total is 1, using equation **(2)**. Using equation **(3)**, Data is out of this equation a lot is removed.

Distribution coefficient m_i about component *i*, Separation selectivity $\beta_{i,j}$ of component *i* relative to component *j* is given by

$$m_\mathrm{i} = \frac{y_\mathrm{i}}{x_\mathrm{i}} \quad \textbf{(4)}$$

$$\beta_{\mathrm{i,j}} = \frac{m_\mathrm{i}}{m_\mathrm{j}} \quad \textbf{(5)}$$

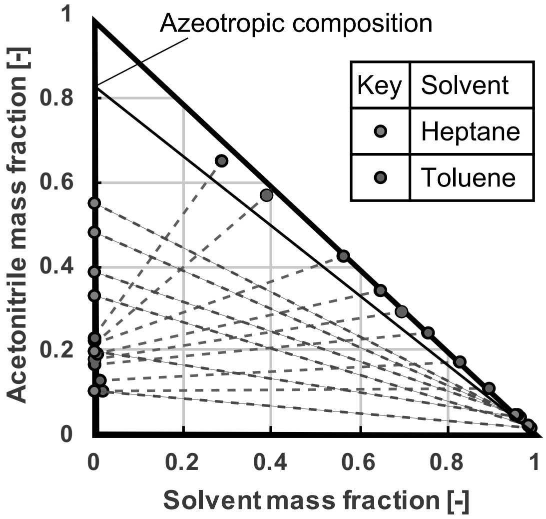

Fig. 1 Phase Diagram of Liquid-liquid equilibrium ternary system

Fig. 1 is phase diagram of Water-Acetonitrile-Solvent liquid-liquid equilibrium. In Water-Acetonitrile-Heptane ternary system, it is found that it has solubility for heptane and acetonitrile, heptane and water. In Water-Acetonitrile-Toluene ternary system, It is found that only toluene and water have solubility. In addition, the azeotropic composition in the case of removing the solvent is indicated by a black solid line in the figure. It was suggested that it is possible to exceed the azeotropic composition after the extraction operation with any solvent.

Fig. 2 shows effects of Initial feed mass fraction of acetonitrile to the distribution coefficient of acetonitrile with solvent of mixture heptane and toluene. The more Toluene mass fraction is in solvent, the higher m_A is. It is thought that the reason for this is that toluene has a higher polarity than heptane, acetonitrile also relatively high polarity, so more acetonitrile moves extract phase. And, effect of x_A was not clear.

Fig. 3 shows separation selectivity of acetonitrile compare to water with solvent of mixture heptane and toluene. For heptane 100% solvent, when $x_{A,0}$ is 0.1 and 0.2, the mass fraction of water reached 10 ppm order, so it cannot measured.

The more Heptane mass fraction is in solvent, the higher $\beta_{A,W}$ is. Moreover, Any solvent $\beta_{A,W}$ decrease as $x_{A,0}$ rises. It is thought that the reason for those features is the large effect of the distribution coefficient of water.

4. Conclusion

From the results, it was found that acetonitrile could be separated from water using solvent extraction.

The distribution coefficient of acetonitrile increased as the polarity of solvent increased.

On the other hand, the selectivity of separation of acetonitrile against water decreased as the polarity of solvent increased.

5. Reference

[1] J. Gmehling, J. Menke, et al. Azeotropic Data for Binary Mixtures, (1994).

[2] Repke J U, Klein A, et al. Pressure swing batch distillation for homogeneous azeotropic separation[J]. Chemical Engineering Research and Design,85(4):492-501, (2007).

[3] Acosta J, Rodríguez I, et al. Recovery of acetonitrile from aqueous waste by a combined process: Solvent extraction and batch distillation Sep. Purif. Technol. 2006, 52, 95– 101, (2006)

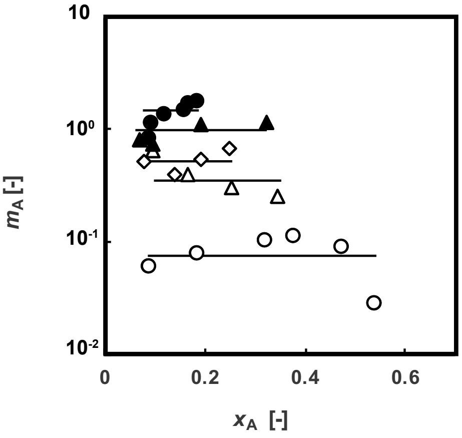

Key	Solvent	mass fraction of Heptane
○	Hp	1
△	Hp+T	0.75
◇	Hp+T	0.5
▲	Hp+T	0.25
●	T	0

Fig. 2 Distribution coefficient of acetonitrile with solvent of mixture heptane and toluene

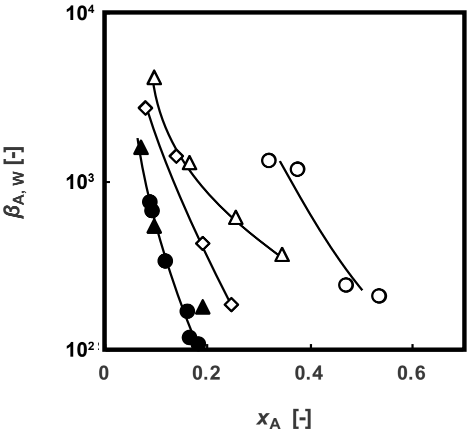

Fig. 3 Separation selectivity of acetonitrile compare to water with solvent of mixture heptane and toluene

無線ネットワークセル設計のためのニューラルネットワークを用いた電波伝搬損失予測

学籍番号: 15B05044　氏名: Jin Yongri　指導教官: 高田 潤一、 齋藤 健太郎

1　はじめに

近年移動通信分野におけるデータトラフィックが急速に増加している. Cisco 社の調査によると世界のデータトラフィック量は 2021 年には 2016 年の 7 倍に達すると予測されている [1]. また将来は Internet of Things (IoT) システムの普及により様々な無線通信機器が利用されるようになると考えられており， 効率的な無線ネットワークの構築が重要になってきている. 無線ネットワークを構築するにはエリア内の各地点の伝搬損失を把握する必要があるが，既存の伝搬損失推定式は市街地や屋内環境など複雑な特徴を持つサイトの伝搬損失を予測する事に向いていない．一方で，実験によりあらゆる地点の伝搬損失を測定するのは労力やコストの観点から困難である．そこで本稿では，エリア内で離散的に得られた伝搬損失データから Artificial Neural Network (ANN) を用いてエリア全体の伝搬損失特性を予測する手法を提案する．屋内環境でレイトレーシングのシミュレーションを行い，得られたシミュレーション結果からエリア全体の伝搬損失特性を予測する実験を行った．提案手法による予測の平均絶対偏差は約 7dB であった．今後は提案手法の無線ネットワーク設計への利用が期待される.

2　ANN を用いた電波伝搬損失予測手法

2.1　レイトレーシング (RT)

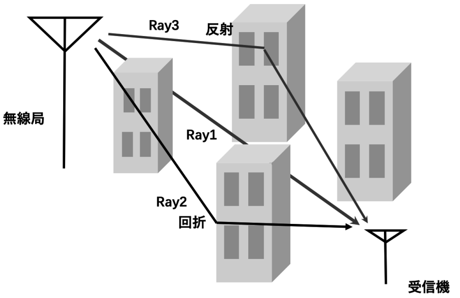

図 1: 電波伝搬

レイトレーシングシミュレーションとは電波を光に見立て, 幾何光学的原理に基づき, 反射点を幾何学的に捜索するイメージング法, 送信点から全角度に均一に出射されるレイを幾何学的に軌跡をトレースするレイラウンチング法を用いてレイを追跡する方法である [2] . 図 1 のように伝搬の過程で生じる反射, 透過, 回折などをフリスの伝達公式より求まる自由空間伝搬損, フレネルの反射係数,UTD からの回折係数から計算し, 受信レベルを求めることで, 式 1 から 送信点から受信点における伝搬損失が求まる. P_T は送信レベルで, P_R は受信レベル,PL は伝搬損失をデシベル (dB) で表している.

$$PL = P_{\mathrm{T}} - P_{\mathrm{R}} \tag{1}$$

本シミュレーションでは表 1 のようにダイポール型のアンテナを使用し, 周波数は 5.2GHz に設定した上, 無線局の送信電力は 200mW, 送信アンテナと受信アンテナの高さはそれぞれ 1.5m に設定した.

表 1: レイトレーシングシミュレーションの設定

電波周波数	5.2 GHz
送信電力	200mW
TxRx 高さ	1.5m
アンテナー種類	ダイポール

2.2　ニュートラルネットワーク

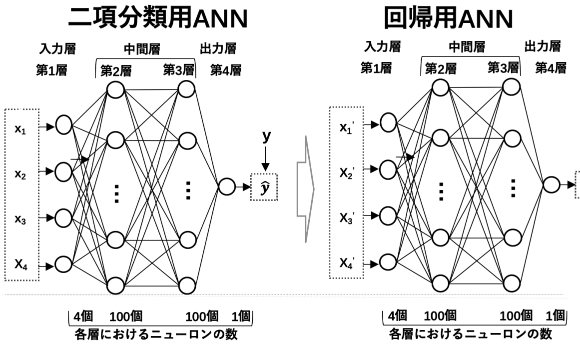

図 2: 計算に用いた ANN のモデル

本提案手法は図 2 で示すように 2 項分類用と回帰用の ANN からなる. 2 項分類用の ANN はエリア内かエリア外を予測し, 回帰用の ANN は伝搬損失を推定する.

RT シミュレーションでは反射, 回折の回数などの拘束条件により, 二種類の伝搬損失結果が得られる. 得られた結果の一つは受信点で電波の受信ができた時の連続的な値で, もう一つは受信電力が閾値以下の場合もしくは有効伝搬経路が発見されなかった時の離散的な値である. よって ANN 回帰分析モデルをそのまま用いることはできない. RT シミュレーションの伝搬損失の結果に基づき, 電波が届いた連続的な結果にはエリア内, 電波を感知できなかった離散的な結果にはエリア外というラベルをつけることでもう一つのデータセットを作成する.

先ず Tx, Rx の座標とエリア内もしくはエリア外のインディケーターでできたデータセットから教師あり学習をさせることで, 二項分類 ANN モデルの学習を行う. 次に Tx と Rx の座標とその間の伝搬損失で構成したデータセットを用いて, 教師あり学習をさせることで, 回帰用の ANN モデルを作る. そして伝搬損失を知らない任意の二点の間で二項分類用の ANN を用いて伝搬が届くかどうかを予測する. 電波が届くと予測されたら, 回帰分類モデルを使い, 二点間の伝搬損失を予測することができる.

3 実験

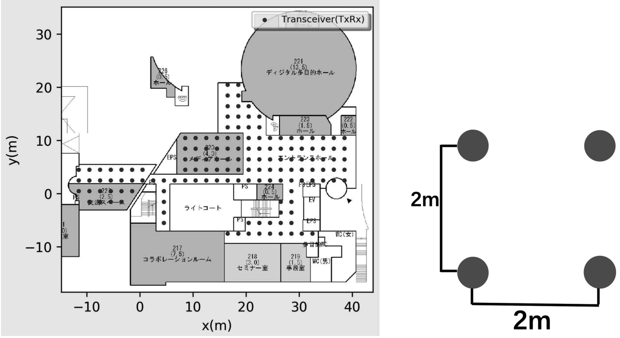

(a) (b)

図 3: 無線局の配置

シミュレーションの環境は東京工業大学西 9 号館の一階のロビーを想定した. シミュレーションでは電波を受信するレシーバー (Rx), 電波を送信するトランスミッター (Tx) 両方の機能をもつトランシーバーを用いた. 本研究では構造計画研究所により開発された Raplab ソフトウェア・ツールを用いて RT シミュレーションを行った. 図 3 で示すように $2m \times 2m$ 間隔でトランシーバーをエリア内に均一に配置し, レイトレーシングシミュレーションによって異なる二点間の伝搬損失サンプルを 101904 セット得た.

結果の 80%を用いて ANN モデルをトレーニングし, 残りの 20%を用いて ANN モデルのパーフォマンスを検証した [3].

4 結果と考察

二項分類用 ANN モデルでは, トレーニングにおいて 97.5%, テストにおいては 97.3%まで正確率上げることができた. 回帰用のモデルでは平均絶対偏差はトレーニングで 7dB, テストサンプルでは 6.7dB のパフォーマンスが得られた. 両モデルにおいてトレーニングとテスト二種類のサンプルセットでほぼ同じパフォーマンスが見られることから, 過剰適合は起きず, 汎化能力を持っていると言える.

一つの例として無線局を座標 (20,10) においた場合, 二項分類モデルを用いれば図 4 で示しているように各場所において電波を受信できる確率分布が得られる. 受信率が 50%以上のエリアのみ抽出し, 回帰用のモデルにインプットすることで, 図 5 で示すように各場所における伝搬損失分布が求まる. 図 5 から廊下の角等を曲がる事で急激に伝搬損失が大きくなり, また通信エリア外の領域が現れる事が分かる.

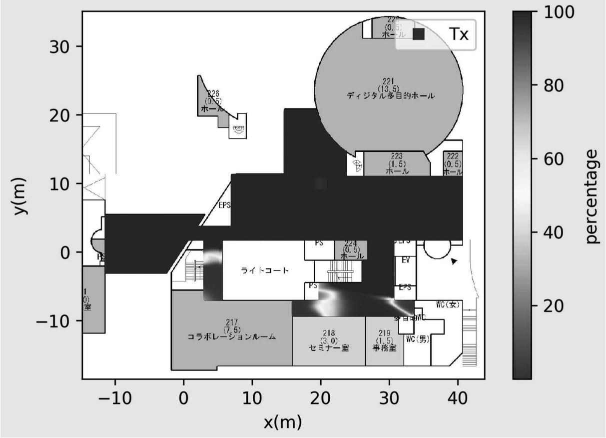

図 4: 二項分類結果の分布図

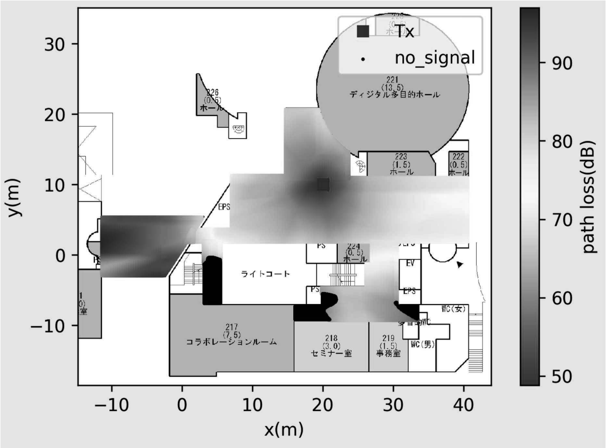

図 5: 伝搬損失分布図

5 まとめ

本研究ではレイトレーシングシミュレーション結果を用いてニュートラルネットワークをトレーニングし, その ANN モデルを使い, エリアにおける任意の二点間の伝搬損失を予測することができた. このモデルを更に活用することで, 効率的に無線ネットワークの構築ができると考えている.

今後の課題として, ANN モデルから予測する伝搬損失を実測値と比較することで, リアル環境でのパフォーマンスを検証する必要がある.

参考文献

[1] Cisco. ”Visual networking index: Global mobile data traffic forecast,” update 20142019, white paper.

[2] Z, Yun and F. Iskander , ”Ray Tracing for Radio Propagation Modeling: Principles and Applications,” in IEEE Access, vol. 3, pp. 1089-1100, 2015.

[3] A. Nielsen, ”Neural Networks and Deep Learning” Determination Press,pp. 34-59,2015.

[4] Yao Yiyun.”Path loss prediction by using machine learning for wireless LAN site planning” 東京工業大学環境社会理工学院 修士論文 [未公開]. Feb, 2017.

指向性チャネルモデルに基づく伝搬パラメータからの大型アレーMIMOシステムのチャネル容量評価

学籍番号: 15B09438　氏名: 趙 恒偉　指導教官: 高田 潤一、 齋藤 健太郎

1　はじめに

近年、ネットワークを利用した様々なアプリケーションサービスの普及に伴い、高速移動無線通信システムに対する需要が高まっている。そのようなシステムにおいて、高いデータレートの実現を目的とした Multi-Input Multiput-Output (MIMO) 伝送が主要技術の 1 つとして注目されている。更に、次世代通信規格である第 5 世代においては、マッシブ MIMO と呼ばれる大型アレーアンテナによる指向性合成も導入される。一方、MIMO チャネルの評価に用いられている双角度 (double directional) チャネルパラメタは、アレーアンテナの素子間隔を半波長以下として測定する必要があるため、比較的小型のアレーアンテナとなり角度分解能が制約されることから、大型のアレーアンテナに適用できるとは限らない。そこで、本研究では、小型アレーアンテナで測定した角度パラメタを用いて大型アレーアンテナのチャネル応答を予測し、実際に大型アレーアンテナで測定した結果と比較することによって、予測可能な範囲を評価することを目的とする。

2　MIMO チャネル構成

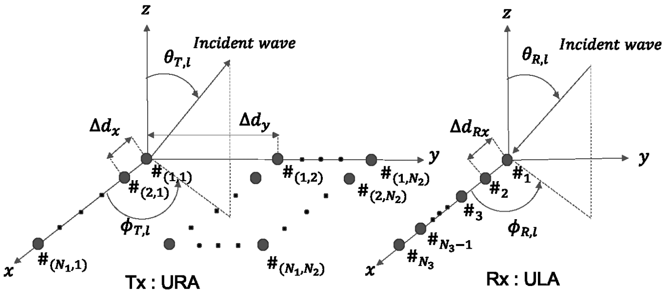

図 1: **URA x ULA MIMO チャネルモデル**

図 1 において、送信アンテナ URA では x 方向に Δ_x 間隔で N_1 素子、y 方向に Δ_y 間隔で N_2 素子、受信アンテナ ULA では x 方向に Δ_{Rx} 間隔で N_3 素子がある。また、アンテナにおいてはそれぞれ L 個の狭帯域平面波が放射・到来するとし、各波は図 1 に定める [2] 放射方位角 $\phi_{\mathrm{T},l}$、放射天頂角 $\theta_{\mathrm{T},l}$、到来方位角 $\phi_{\mathrm{R},l}$、到来天頂角 $\theta_{\mathrm{R},l}$、伝搬時間 τ_l、伝搬における複素振幅の変化を持つ $\alpha_l (1 \le l \le L)$。さらに、中心周波数を f_c として Δ_f 間隔で全 N_4 点の伝達関数のサンプリングを行う。このとき測定される伝達関数 y_{k_1,k_2,k_3,k_4} は以下のように表される。ただし、$0 \le k_r \le (N_r - 1) \quad (1 \le r \le 4)$ は送受信アンテナと周波数のサンプル点の番号である。

$$y_{k_1,k_2,k_3,k_4} = \sum_{l=1}^{L} \left[s_l \prod_{r=1}^{4} e^{j\mu_l^{(r)}(k_r)} \right] + n_{k_1,k_2,k_3,k_4} \tag{1}$$

また、s_l は位相基準点間の複素伝達関数、$\mu_l^{(r)}$ は位相遅延、n_{k_1,k_2,k_3,k_4} はガウスノイズである。s_l と $\mu_l^{(r)}$ はそれぞれ以下のように表される。

$$s_l = \alpha_l f_{\mathrm{dep}} \left(\mathbf{\Omega}_{l\mathrm{dep}} \right) f_{\mathrm{arr}} \left(\mathbf{\Omega}_{l\mathrm{arr}} \right) \tag{2}$$

$$\mu_l^{(1)} \left(k_1 \right) = \frac{2\pi}{\lambda} \left(k_1 - 1 \right) \Delta d_x \sin\theta_{T,l} \cos\phi_{T,l} \tag{3}$$

$$\mu_l^{(2)} \left(k_2 \right) = \frac{2\pi}{\lambda} \left(k_2 - 1 \right) \Delta d_y \sin\theta_{T,l} \sin\phi_{T,l} \tag{4}$$

$$\mu_l^{(3)} \left(k_3 \right) = \frac{2\pi}{\lambda} k_3 \Delta d_{Rx} \sin\theta_{R,l} \cos\phi_{R,l} \tag{5}$$

$$\mu_l^{(4)} \left(k_4 \right) = 2\pi \left(k_4 - \frac{N_4}{2} \right) \Delta_f \tau_l \tag{6}$$

f_{dep}，　f_{arr} は送受に用いるアンテナの複素放射電界パタン、α_l は伝搬利得である。また、$\mathbf{\Omega}_{ldep}$，　$\mathbf{\Omega}_{larr}$ は以下のように定義される。

$$\mathbf{\Omega}_{l\mathrm{dep}} \equiv \left[\phi_{T,l}, \theta_{T,l} \right], \mathbf{\Omega}_{l\mathrm{arr}} \equiv \left[\phi_{R,l}, \theta_{R,l} \right] \tag{7}$$

ここで、以下のようなパラメータを定義し、式 1 で表されるデータをベクトル化する。ここで、$\mathbf{A} \in C^{N \times L}$ はマルチパス応答ベクトルで、L はマルチパスの数である。また、記号 $\diamond$ は列ごとのクロネッカー積を示し、$N = N_1 N_2 N_3 N_4$ である。

$$\mathbf{a} \left(\mu_l^{(r)} \right) = \left[e^{j\mu_l^{(r)}(0)} e^{j\mu_l^{(r)}(1)} \ldots e^{j\mu_l^{(r)}(N_r - 1)} \right]^T \in C^{N_r} \tag{8}$$

$$\mathbf{A} \left(\mu^{(r)} \right) = \left[\mathbf{a} \left(\mu_1^{(r)} \right) \cdots \mathbf{a} \left(\mu_L^{(r)} \right) \right] \in C^{N_r \times L} \tag{9}$$

$$\mathbf{A} = \mathbf{A} \left(\mu^{(1)} \right) \diamond \mathbf{A} \left(\mu^{(2)} \right) \diamond \mathbf{A} \left(\mu^{(3)} \right) \diamond \mathbf{A} \left(\mu^{(4)} \right) \in C^{N \times L} \tag{10}$$

3　屋外 MIMO チャネル測定

3.1　測定諸元

本研究では、石垣市で実施した屋外伝搬測定によって取得された実測値を使用する。測定諸元及び測定環境をそれぞれ表 1, 図 2 に示す。また、本研究の全測定は同じ測定環境で測定した。図 2 は Tx と Rx の測定位置を表している。さらに、パラメータ推定のために小間隔円形アレーアンテナを用いて測定を行った。また、推定されたパラメータ [3] を用いて、測定で使用した大間隔 URA x ULA の MIMO チャネルを構成し、構成後の結果と実際に大型アレーアンテナで測定した場合の結果の比較を行う。

表 1: チャネルサウンダの詳細

パラメータ	値
キャリア周波数	11 GHz
信号帯域幅	400 MHz
送信電力	10 mW
波長	2.73 cm
周波数間隔 (ΔF)	195.31 KHz
サブキャリア数 (N)	2048
遅延分解能 $(\Delta\tau)$	2.5 ns
最大遅延 $(\tau_{\max})$	5.12 μs
アレーアンテナ	Tx: 12 素子 (二重分極) Rx: 12 素子 (二重分極) 高さ: Tx:3m, Rx:8m

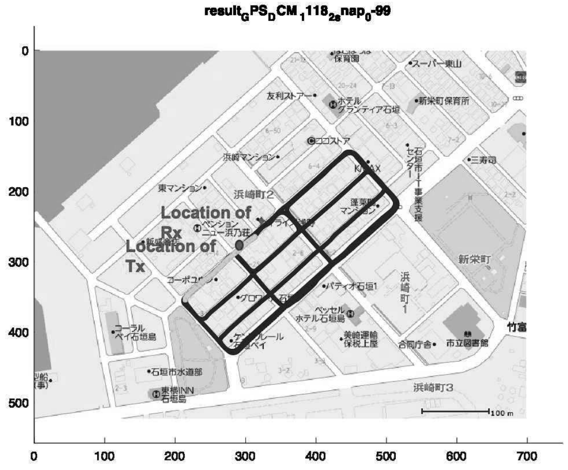

図 2: 測定において **Tx** と **Rx** の位置

表 2: 測定の設定

測定	Tx	Rx
URA x ULA 測定	URA:12 素子 高さ:3m 間隔:5.46cm	ULA:12 素子 方向:南南西 200° 間隔:5.5cm

3.2 結果と考察

小型アレーアンテナを使用して測定したデータに対してパラメタ推定を行った結果を使用し、大型アレーアンテナのチャネル応答を予測した結果を、実際に大型アレーアンテナで測定した結果と比較した。なお、チャネル特性の合成に当たっては、素子アンテナの校正用指向性データがないため、遅延電力スペクトルのピークが実測値と一致するようにスケーリングを行った。更に、両者の比較は固有値分布を指標として行う。はじめに全 2048 サブキャリアにおいて計 12 個の固有値を算出する。その後、サブキャリア毎に各固有値の CDF を求めることにより評価を行う。結果を図 3 に示す。なお、実線は測定データ、破線は推定結果を表している。

図 3 より、測定データと合成データの固有値分布はおおむね一致していることが分かる。また、低い固有値の分布は、測定データと合成データでほぼ同じ傾向がある。しかし、図 3 では、2 番目と 3 番目の固有値分布において、測定データと合成データの間に少し 1 ～ 1.5dB の差がある。その原因は多分 LoS の方向性によるものである。図 2 に示した Tx と Rx の位置では、LoS の方向は建物の表面と平行であり、建物の表面近くの敷設材によって LoS のレベルが変わる可能性が考えられる。

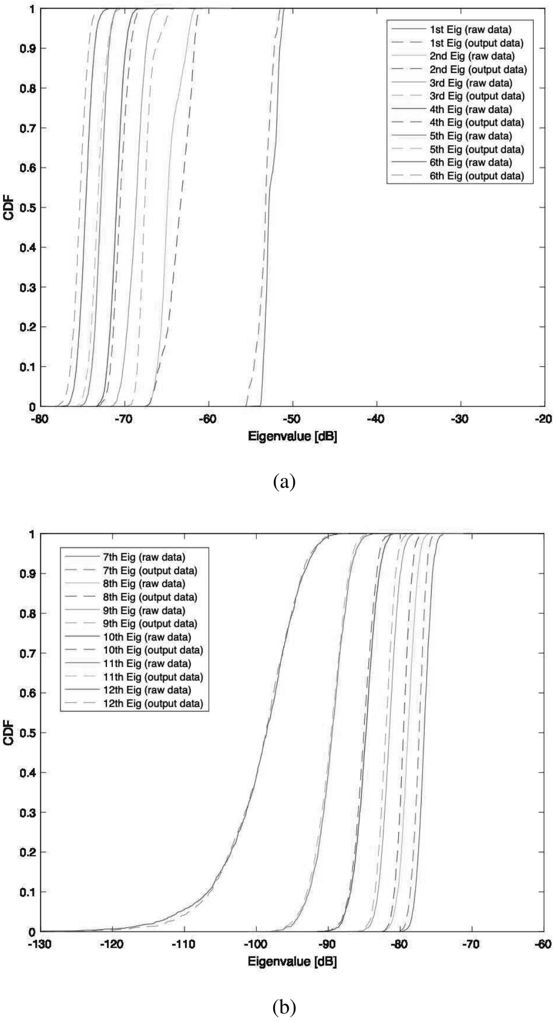

(a)

(b)

図 3: 全サブキャリアにおける各固有値の CDF グラフ

4 おわりに

本研究では、小型アレーアンテナを用いて測定した伝搬路パラメタを利用し、大型アレーアンテナのチャネル応答を予測し、その結果を実際の測定結果と比較した。比較の結果、今回予測した事例においては、両者は十分によく一致しており、推定されたパラメタを用いたチャネルモデルがアンテナの大きさをある程度大きくしても適用可能であることが明らかになった。

今後、他の観測点でも比較評価を行う。

参考文献

[1] Dwi Joko Suroso, Kentaro Saito, Jun-ichi Takada. ”On Investigation of Directional Channel Model for Large Spacing Array MIMO: Eigenvalues Comparison of Measurement and Channel Synthesis”. *IEICE Technical Report*, pp.1-6, Feb. 2018.

[2] Kentaro Saito, Yunyi Yao, Jun-ichi Takada. ”Parameter estimation refinement of MIMO propagation channel by nonlinear conjugate gradient approach”. *IEICE Communications Express*, vol. 7, no. 9, pp. 328-333, Sep. 2018. DOI:10.1587/comex.2018XBL0083.

[3] Minseok Kim, Jun-ichi Takada, Kentaro Saito. ”Multi-dimensional Radio Channel Measurement, Analysis and Modeling for High Frequency Bands (invited)”. *IEICE Transactions on Communications*, vol. E101-B, no. 2, pp. 293-308, Feb. 2018.

Development of Channel Sounder for SHF Band Channel Measurement by Virtual Planar Array

Student No. : 15B05713 Name: Kang CheChia Supervisor: Jun-ichi Takada, Kentaro Saito

1 Introduction

In the 5th generation mobile communication system (5G), the wide range of frequency bands from 2GHz to 60 GHz is expected to be utilized for mobile communication to increase the network bandwidth drastically. However, because the radio propagation characteristics significantly depend on the frequency band, it is indispensable to clarify the dependency through a comparable measurement campaign for system design. In [1], SHF band channel characteristics was investigated by the virtual uniform circular array (UCA) method. However, it had the limitation of the degree of freedom of the array structure. In this paper, I developed a virtual array measurement system by using a three-dimensional positioner. The developed system has the advantage that the arbitrary structure of arrays can be formed for the channel measurement. 3-dimensional channel measurement was conducted in 12 GHz band in an indoor environment and the measurement accuracy was investigated.

2 Signal Model of Virtual Array Channel Sounding[2]

The signal model received by the VA based channel sounder is shown as follows. In the measurement, the positioner changes the receiving antenna position at M points, and the frequency transfer function is measured at each point. Assuming the number of frequency sample is N, the measured data is a MN×1 vector.

For an incident wave from Direction of Arrival (DoA) θ, the propagation length difference $d_m(\theta)$ from the reference point in position m is:

$$d_m(\theta) = -(\vec{u}(\theta) \cdot \vec{r_m}) \tag{1}$$

where $\vec{u}(\theta)$ is the incident wave vector of DoA θ, and $\vec{r_m}$ is the position vector of the m-th antenna position. Assuming that incident waves are plane waves, the ideal array response, and the ideal signal distribution of the antenna array is:

$$\mathbf{a}_a(\theta) = [a_1(\theta), a_2(\theta), ..., a_{\mathrm{M}}(\theta)]^T \tag{2}$$

$$a_m(\theta) = \mathrm{e}^{\frac{-j2\pi f_n}{\mathrm{C}} d_m(\theta)} \tag{3}$$

where $\mathbf{a}_a(\theta)$ is the array response of the antenna array with DoA θ with its elements $a_i(\theta)$, f_n is the nth subcarrier frequency of estimating signal, and C is the speed of light. Array response represents the theoretical receiving signal of the array.

Then in the beamforming (BF) algorithm, assume the evaluation function $P_{BF}(\theta, \tau)$ as follows

$$P_{BF}(\theta,\tau) = |\mathbf{a}^H(\theta,\tau)\mathbf{x}|^2 \tag{4}$$

$$\mathbf{a}(\theta,\tau) = \mathbf{a}_a(\theta) \otimes \mathbf{a}_d(\tau) \tag{5}$$

$$\mathbf{a}_d(\tau) = [\mathrm{e}^{-2\pi f_1 \tau}, ..., \mathrm{e}^{-2\pi f_{\mathrm{N}} \tau}] \tag{6}$$

$$\mathbf{x} = [x_{11}, x_{12}, ..., x_{mn}, ..., x_{\mathrm{MN}}]^T \tag{7}$$

where $\mathbf{a}(\theta, \tau)$ represents the theoretical receiving signal when the plane wave arrives with DoA θ and propagation delay τ, which is the product of $\mathbf{a}_a(\theta)$ and $\mathbf{a}_d(\tau)$. $\mathbf{a}_d(\tau)$ is the united complex amplitude of antenna array with propagation delay τ. $\otimes$ here denotes the kronecker product. x_{mn} is the received signals of the i^{th} antenna, j^{th} frequency sample. As $P_{BF}(\theta, \tau)$ is swept over all candidate DoA θ, and delay of arrival τ, it will reach peaks while the candidate approaches the observed parameters.

3 Development of Virtual Array based Channel Sounder

Figure 3 shows the structure diagram of the VA system composed by SURUGA SEIKI positioner and R&S vector network analyzer (VNA) with a personal computer as it's host. The PC and positioner is connected by the serial port, and LAN cable was used to connect the PC to the VNA. Both antennas are connected to the VNA by a coaxial cable while the receiver is fixed on the positioner with an acrylic holder. The accuracy of the positioner is 10μm and the position repeatability is $\pm 3\mu$m space[3].

To perform the measuring campaign automatically, the software of this work is designed in C++ language to hold control of the system.The PC first should establish a serial communication with the positioner, and a control library for instruments called VISA is used to connect with the VNA, then the transmit parameters for the positioiner were set e.g. the number of antenna elements, spacing distance, and center coordinate, and parameters for the VNA e.g. sweeping band, number of subcarriers, and transmit signal power. For each measurement position, the PC sends moving and trigger commands to both devices, and collects data after the measurement at that point is completed. The data is named accordingly based on the position information.

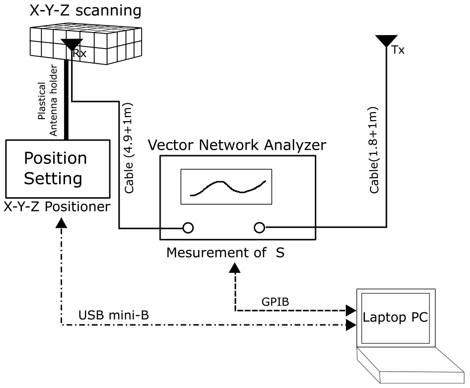

Figure 1: Structure diagram of VA system.

4 Measurement Experiment

4.1 Measurement setup

Table 1: Measurement parameters

Frequency band	12.80 GHz to 12.95 GHz
Frequency points	201
Virtual Array with element spacing	Cubic array (10 × 10 × 10) 10mm
Antenna	Horn antenna (10dBi)
Transmit power	10 dBm

Table 1 shows the basic data of measurement. This research measured DoA azimuth and elevation, and delay spectrum of both axes with virtual cubic array system and 2 horn antennas. Tx site was 1.19 m away from the floor, and the center height of Rx site was 2.15 m. To keep LOS within the main lobe of antenna, Tx antenna pointed northward while Rx pointed southward. Figure 2 shows the top view of whole environment, where DOA= 0 is westward,i.e., the plus direction of Rx's X-axis. Tx antenna was located 3.42m apart from the Rx antenna, at the direction whose azimuth was 110° and elevation was $-17.25°$. It took 10 seconds to suppress the vibration of antenna holder. The surroundings was a room full of small objects.

4.2 Data processing

Using the channel transfer function (CTF) output by VNA with the BF algorithm, the DoA power spectrum can be obtained as Figure 3, in which not only LOS but also several signals were detected. For the signals traveled 12 m more than LOS signal did, it's known as the mix of double-bound reflect rays.

5 Conclusion

The VA system was successful in distinguishing incident EM wave form LOS in 12.8 GHz band. However, the reflected waves wasn't distinguishable form the sidelobe of LOS wave with matched filtered result. To deal with the problem, measuring with more antenna elements again could be helpful in angle domain, extending the measuring bandwidth is effective in delay domain on the other hand. This two solutions definitely take more measuring time, so, it's important for future usage measuring 32 GHz band to reduce vibration suppressing time.

References

[1] W. Fan, I. Carton, J. O. Nielsen, K. Olesen, and G. F. Pedersen, "Measured Wideband Characteristics of Indoor Channels at Centimetric and Millimetric Bands," *EURASIP Journal on Wireless Communications and Networking.* vol. 2016(1), p. 58, 2016.

[2] Andreas F. Molisch. "Channel Sounding" in *Wireless Communications*, 2^{n}d ed, Chichester, U.K.: IEEE., 2011, pp.145-164.

[3] SURUGA SEIKI. "Standard Type : SXM30." Internet: https://jpn.surugaseiki.com/products/series/SXM30, 2018[Feb. 12, 2019].

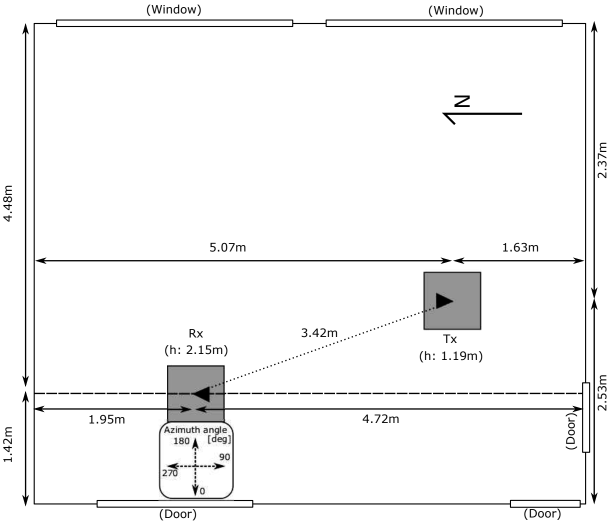

Figure 2: Top view of cubic array measurement.

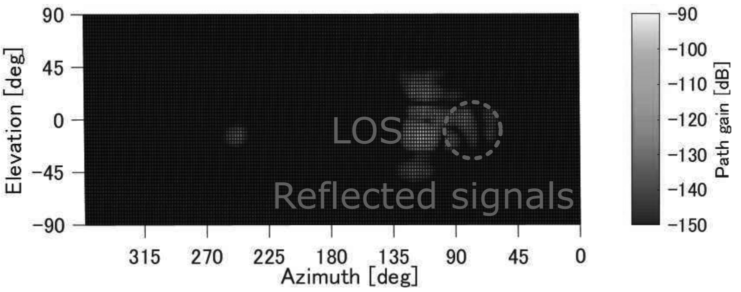

Figure 3: DOA estimation with cubic array.

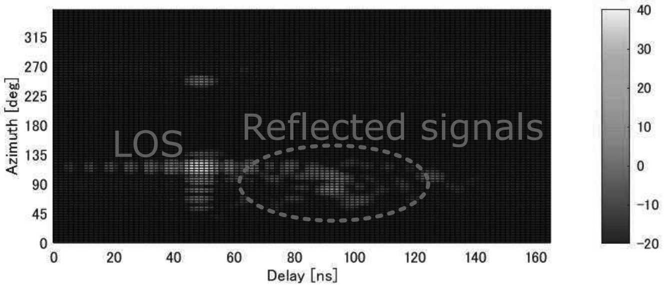

Figure 4: DOA estimation with cubic array.

Selection guidelines Windmill and Generators for Small Wind Power Generation System Considering Maximum Power Point Tracking

Student Number: 15B11754 Name: Hayashi Honoka Supervisor: Kunio Takahashi

1. Introduction

Movement to make small-scale wind power generation system has been increasing. There is a need for maximum power point (MPP) tracking with less consuming electric power, because one unit of small-scale wind power generation system generates only a small amount of energy. small-scale wind power generation system consists of windmill, generator, boost convertor, and electric storage device. The boost convertor performs MPP tracking (MPPT) and efficiently stores electricity while boosting up the voltage. Prototype of autonomous boost converter for solar power generation has been made [1]. By scanning I-V characteristics of solar cell, boost converter automatically detects and tracks MPP. However, since windmill takes time to reach a steady state 対象, the method of using scanning is not suitable. The relation among the wind speed, the rotation number of the drag type windmill and the torque was experimentally investigated [2]. However, since there is only one generator, generator dependency cannot be verified. Also, experiment apparatus is a possibility that the wind tunnel is too small to keep wind speed. Therefore, there is a possibility that experimental result could not be reproduced. Therefore, this paper experimentally investigates the relation of wind speed, electric current, voltage of small wind power generation system by using sufficiently large wind tunnel and several generators, and consider selection guidelines Windmill and Generators for Small Wind Power Generation System Considering Maximum Power Point Tracking

2. Experiment apparatus

A schematic diagram of the experimental apparatus is shown in Fig.1. We prepare the same shape of windmill with different number of blades. The projected area varies depending on the number of blades. And also prepare a commercial wind turbine (SMG-1001). Wind tunnel has a cross sectional area of 50cm × 50cm which has sufficient size for windmill of diameter 10cm to 20 cm. Three power generators with equivalent output power and different rated voltages have been prepared. Torque applied for generator is measured by the torque meter (UTMII, UNIPULSE). The I-V characteristic of generator changes depending on the load resistance shown in Table.1. We measure the torque, rotational speed, and voltage while varying resistance, wind speed and blade number, as shown in table 1. The current value divides the measured voltage by the load resistance. Measurement was continued for over 10 seconds. Measurements are repeated twice.

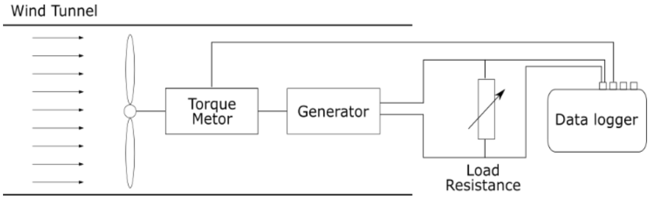

Fig. 1 Experimental apparatus

Table. 1 Various elements

Number of blade	8,12,16,20
Rated voltage of generator	3,7,13[V/1000rpm]
Wind speed *U*	7.2[m/s],6.0[m/s],4.8[m/s], 3.6[m/s],2.4[m/s],1.2[m/s]
Load resistance *R*	5M[Ω]over, 5080[Ω], 1980[Ω], 1000[Ω], 488[Ω], 198[Ω], 101[Ω],74[Ω],51[Ω], 32[Ω],22[Ω],16[Ω],10[Ω], 5.3[Ω],3.6[Ω],1.2[Ω]

3. Results and discussions

3.1. I-V characteristic depending on type of windmill

Fig.2 shows I-V characteristic depending on the type of windmill at the wind speed of 6.0m/s. The I-V characteristics is linear when 20 blades. As the number of blades decreases, in the region where the load resistance is low, it is not linear.

Fig.3 shows relation between torque and voltage depending on the type of windmill at wind speed of 6.0m/s. The relationship between voltage and torque is linear when 20 blades, and as the number of blades decreases, in the region where the resistance is low, it is not linear.

These shows the same trend. It can be considered that when the number of blades of the windmill becomes small, windmill becomes impossible to output torque enough to rotate the generator stably.

3.2. I-V characteristics depending on wind speed

Fig.4 shows the I-V characteristic of the 16 blades due to wind speed. The I-V characteristics is linear when U=7.2m/s. As the wind speed decrease, in the region where the resistance is low, I-V characteristic is not linear. When the wind speed decreases, the torque output by the windmill decreases.

Fig.5 shows relation between torque and voltage of the 16 blades due to wind speed. The relationship between voltage and torque is linear when, wind speeds is 7.2 m/s and as wind speeds decrease, in the region where the resistance is low, it is not linear.

Therefore, when the wind speed decreases, sufficient torque can't be output to rotate the generator, possibly causing the output current to drop.

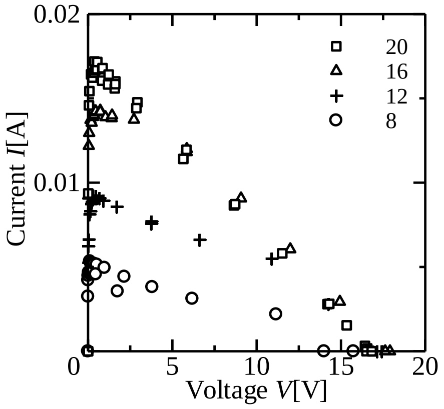

Fig. 2 I-V characteristic depending on windmill

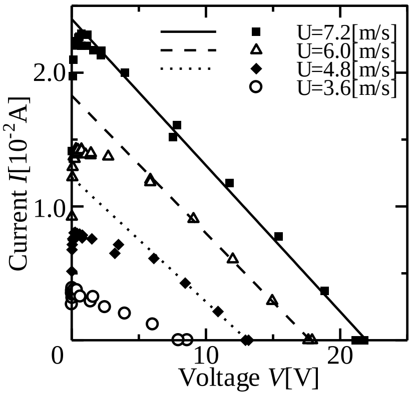

Fig. 4 I-V characteristic depending on wind speed

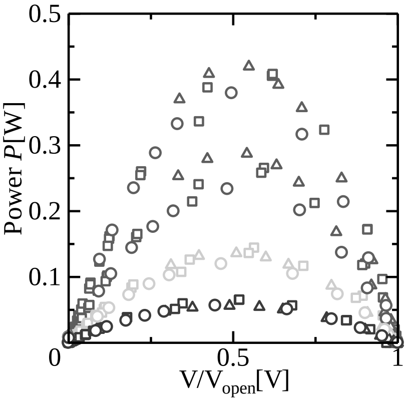

Fig. 6 P-V/V$_{\text{open}}$ characteristics of the commercial wind turbine

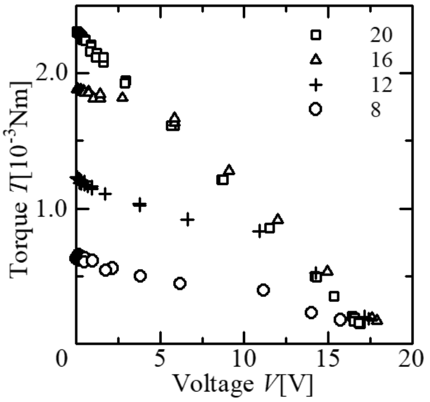

Fig. 3 Relation between Torque and voltage depending on windmill

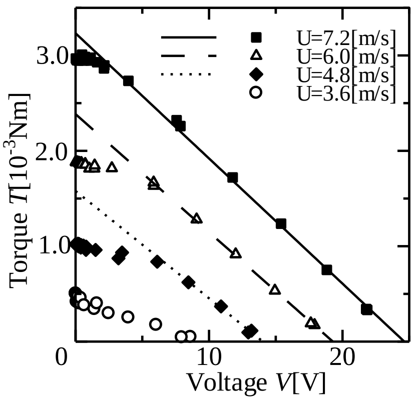

Fig. 5 Relation between Torque and voltage depending on wind speed

3.3. P-V characteristics depending on type of generator

The open voltage is represented by V$_{\text{open}}$. The rated voltages of the generators prepared this time are different. For the reason the output voltage of each generator was normalized by V$_{\text{open}}$. Fig.6 shows the P-V/V$_{\text{open}}$ characteristics of the commercial wind turbine. By setting the normalized voltage on the horizon axis and the output power on the vertical axis and plotting the experimental result of each generator, the profiles appear to be the same. Since the profiles are the same, MPP has the same value. So, MPP does not depend on the rated voltage.

Therefore, there is a possibility that the generator can be selected according to the voltage targeted by the boost convertor or the storage element.

3.4. I-V characteristics and MPP

If I-V characteristics can be approximated linearly, the voltage of the MPP(V$_{\text{MPP}}$) is expressed by the following equation with the open voltage(V$_{\text{open}}$).

$$V_{\text{MPP}} = \frac{1}{2} V_{\text{open}}$$

This suggests that when the I-V characteristic is within the range which can be linear approximation, MPPT can be performed by measuring V$_{\text{open}}$ and taking half of V$_{\text{open}}$. This can be realized with lower power than the method using the scan of reference [1].

If I-V characteristics can't be approximated linearly, V$_{\text{MPP}}$ is not half of V$_{\text{open}}$. Therefore, if the I-V characteristic is nonlinear, MPPT cannot be done with a method that takes half the voltage of V$_{\text{open}}$. In such a case, it is necessary to re-select the number of blades of the windmill and the generator.

4.Conclusion

- In a drag type wind turbine, the output torque increases as the number of blades increases
- If the torque output from the windmill is large enough to rotate the generator, the I-V characteristic of the generator can be linearly approximated
- We suggest possibility if I-V characteristic can be linear approximation, MPP tracking with low power.

5.Acknowledgement

I would like to thank Prof. Chihiro Yoshimura for providing the wind tunnel. Also I would like to thank Prof. Atsushi Inagaki for his corporation on measure wind speed.

6.References

[1] R.Asami, Master's thesis, Tokyo Institute of Technology, “Prototype of an autonomous energy harvesting system using boost converter”

[2] Y. Tokuda, Graduation Thesis, Tokyo Institute of Technology, “the Relation between Wind Velocity, Rotation Speed and Torque of Drag Type Wind Turbine for Small Wind Power Generation

Orbital Transfer System for Microsatellites using Laser Propulsion

Student number: 15-07830 Name: Shun Suzuki Supervisor: Daisuke Akita

1. Introduction

Microsatellites, say less than 100 [kg], are being actively developed by universities and enterprise for the cost-effective space-based observation or telecommunication. Figure 1 shows the increase in the number of the microsatellite launches. However, it is often launched in a piggyback manner with a primary large satellite in order to reduce the launching cost as shown in Fig. 2. Therefore, the microsatellites generally cannot choose the date & time and launching orbit. In addition, microsatellites are difficult to have a propulsion system.

Laser propulsion is expected as a method of promoting spacecrafts of the future because of the high-efficiency propulsion, which is realized by a remote laser system separated from the accelerating target satellite. However, the laser satellite with a sufficient power to propel usual satellites have not been put into practical use. This study shows the capability of an orbital transfer system for the microsatellite by a space-based laser propulsion.

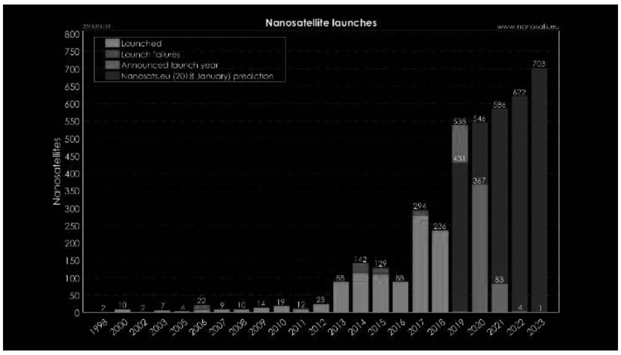

Fig. 1 Increase in number of microsatellites [1]

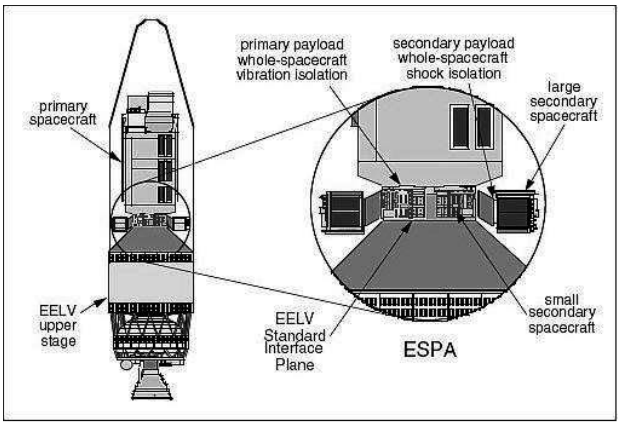

Fig. 2 Piggyback satellites inside rocket fairing [2]

2. Mission concept

Figure 3 to 5 show the mission concept. In this study, a space-based ablative laser propulsion is selected not to require high performance for the laser station as shown in Fig. 3.

1. A Laser Station is launched to an orbit of 400 [km] altitude.
2. Laser is irradiated from the laser station to the ablator attached to the accelerating target satellite.
3. An ablation jet is generated from the surface of the ablator and propelled by its reaction force.

Figure 4 and 5 show the two cases of orbital transfer mission supposed in this study, altitude change mission and orbital inclination change mission, respectively.

This study investigates the followings.

1. Required power and number of the laser station.
2. Orbital transfer capability and applicable satellite scale.

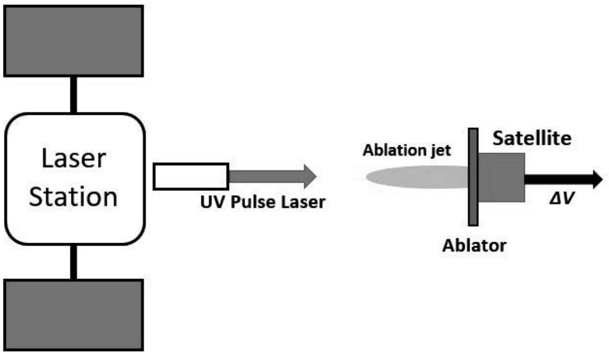

Fig. 3 Mission concept

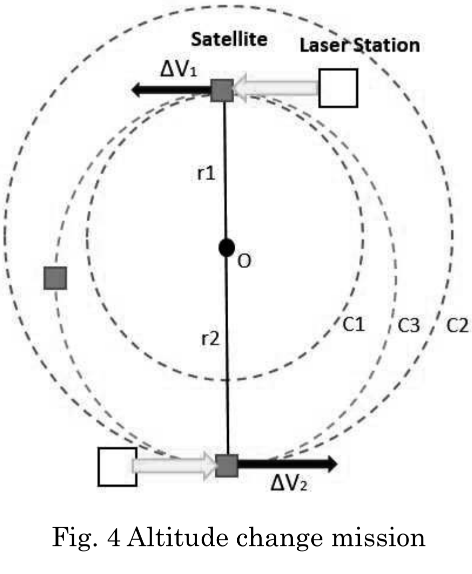

Fig. 4 Altitude change mission

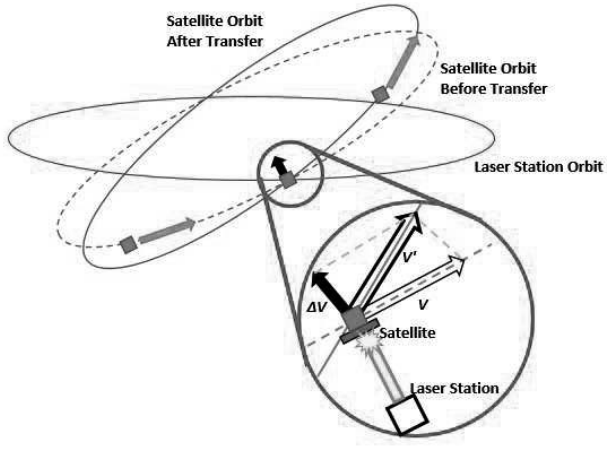

Fig. 5 Orbital inclination change mission

3. Modeling of Laser Propulsion

The orbital transfer by the laser propulsion is calculated using the equations below.

$$C_m = \frac{f}{P_{\text{laser}}} \qquad (1)$$

$$I_{\text{sp}} \cdot C_m = \frac{2}{g} \cdot \eta_{\text{AB}} \qquad (2)$$

$$\Delta \text{V} = \text{g} \cdot I_{\text{sp}} \cdot \ln \frac{m_0}{m_T} \qquad (3)$$

$$\Delta \text{V} = \frac{f}{m} \cdot \Delta t \qquad (4)$$

C_m	[N/MW]	: Momentum coupling coefficient.
f	[N]	: Thrust.
P_{laser}	[W]	: Incident laser optical power.
I_{sp}	[s]	: Specific Impulse.
g	[m/s^2]	: standard acceleration of gravity.
η_{AB}		: Ablation efficiency.
Δt	[s]	: Irradiation time.
m	[kg]	: Satellite mass

The most important parameter for laser propulsion is the momentum coupling coefficient C_m. In principle, Al powder and POM powders can be mixed in proportions to obtain C_m values desired in the range $30 < C_m < 770$ [N/MW]. η_{AB} is the energetic efficiency of the ablation process, ordinarily 50 [%]. Table 1 shows the nominal parameter setting. The laser power is a control parameter.

Table 1 Nominal Parameter setting

C_m [N/MW]	100
η_{AB} [%]	50
Initial mass [kg]	100
Initial altitude [km]	400
Irradiation time [sec]	500

4. Results

Figure 6 Shows relationship between the number of laser stations and duration for the altitude change mission. The number of the laser station is assumed to be proportional to the laser power. In this case, considering changing from altitude of 400 [km] to 800 [km], altitude changes are made only by Hofmann transfer. Altitude of laser station are arranged at regular intervals. Laser power is the minimum value that gives the necessary ΔV. The total mass of the laser station decreases with the number of them. However, it slow down at the number of station of about 7.

Figure 7 shows relationship between C_m and fuel consumption in the case of Fig. 5. The change in the inclination angle is 30 [deg]. It shows that the mission could be completed with a reasonable C_m and fuel consumption.

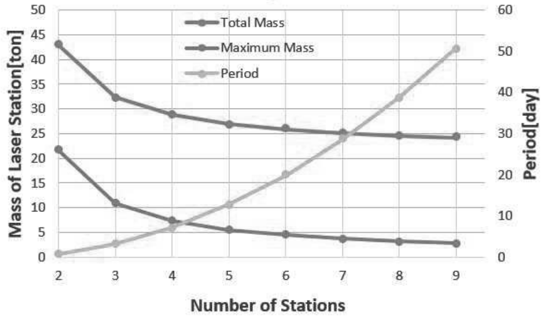

Fig. 6 Number of stations vs. mass of total laser stations and mission period

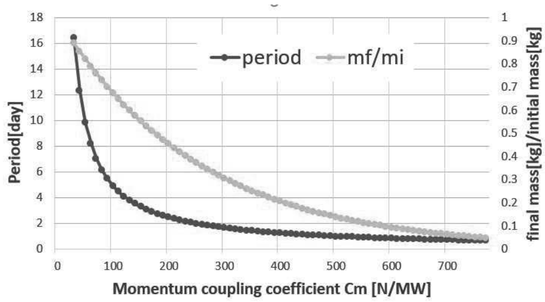

Fig. 7 C_m vs. period and fuel consumption

5. Conclusion

This study shows the capability of the laser propulsion for the microsatellite. The laser pointing accuracy would be the most difficult point to realize a practical space-based laser propulsion.

References

[1]"Nanosatellite & Cubesat Database | Missions, constellations, companies, technologies, and more". https://www.nanosats.eu/#info (acessed 2019-02-28)

[2]"STP-1-eoPortal Directory-Satellite Missions" https://earth.esa.int/web/eoportal/satellite-missions/s/stp-1 (acessed 2019-02-28)

全球情報を用いた都市幾何形状情報作成手法の提案

ID : 13B09805　　Name : 富沢哲郎　　Supervisor : 神田学, Alvin C. G. Varquez

1. 序論

近年、発展途上国を中心に人口増加に伴う都市化が急速に進んでおり、人口 1000 万人以上のメガシティの34都市のうち28都市が発展途上国圏に集中している。そのような急速な都市化に伴い、大気汚染や熱中症といったような、人体を害する数々の気象的な問題が生じていることがGrimmond S. (2007)により報告されている。そのような問題の対策のためにも、ウェザーモデルを用いて都市の気象シミュレーションを行う必要性は都市に関わらず高まっていると考えることができる。

都市の気象シミュレーションに都市幾何形状を考慮することは、WRF に代表されるメソスケールモデルやLESに代表されるマイクロスケールモデルのどちらにおいても重要である。例えば、居石ら(2018)は、LESを用いて2mの高解像度で都市街区の3次元的な空間構造を考慮した気象場の解析を行い、その数値解析の結果は観測で得られた値とおおよそ分布が一致していることを報告している。しかし、建物情報を得るためのコストの高さから、都市幾何形状情報は一部の先進国の大都市に限られている。

本研究の目的は、全球配備された情報を用いた低コストでの高解像度都市幾何形状情報推定のための手法の確立である。都市気象学の技術をグローバルに展開するために、グローバルに入手可能な情報を用いて、価格や手間の観点で低コストであることを目指した。また同時に、メソスケール、マイクロスケールのどちらの研究にも対応できるよう高解像度であることにも重きを置いた。

また、上記の手法に基づいて、人口1000万人以上の世界30メガシティの$25\mathrm{km}^2$の領域における、都市の幾何パラメータを算出することも目的とした。

2. 手法

本研究では以下に示すいずれもグローバルに入手可能な 3 種類の情報を組み合わせることで、全球整備可能な高解像度都市幾何形状情報(個別建物高さ情報、平均建物高さ$\mathrm{H_{ave}}$、最高建物高さ$\mathrm{H_{max}}$)作成を試みた。

① 地図情報から得た建物占有面積情報
Open Street Map (OSM) からダウンロードした建物占有面積情報

② ステレオマッチングにより得た数値表層モデル(DSM)
商用の 50cm 解像度衛星ステレオ画像、NASAにより無償で提供されるステレオマッチングツールであるThe Ames Stereo Pipeline (ASP) を用いてDSMを作成した。

③ 汎用衛星情報である数値標高モデル(DEM)
ALOS World 3D-30m (AW3D30) 及びGlobal Multi-resolution Terrain Elevation Data 2010 (GMTED2010) を用いた。

まず、DSM と地図情報から得た建物占有面積情報から、25mバッファーポリゴンを作成しバッファーポリゴン内のDSMの最小ピクセル値$\mathrm{H_{minimum}}$を ArcGIS のゾーン統計ツールを用いて算出し、その値を建物が設置する地形のDTMと推定した。また、同様に建物占有面積情報ポリゴン内のDSMの平均ピクセル値$\mathrm{H_{average}}$を計算し、平均ピクセル値$\mathrm{H_{average}}$から最小ピクセル値$\mathrm{H_{minimum}}$を差分することで建物占有面積ポリゴン毎の建物高さ情報$\mathrm{H_{bld}}$を算出した。

しかし、本研究で作成したDSMには、高層建物であると、左右画像間の視差が大きすぎることや、太陽光線によるハレーションによる影響が大きく、標高データを算出できない問題が生じた。

上記の問題を打開するため、DSM が計算されない建物においては、汎用衛星情報である数値標高モデル(DEM)を用いて建物高さの推定を行った。具体的には、DSMであるAW3D30から、地物の影響が良く排除されている

GMTEDmin を差分することで建物高さの推定を行った。

以上をまとめた、本研究で提案する手法のフローチャートを図1に示す。

3. 結果と考察

東京とジャカルタの研究対象地域にて、前述の手法により得られた個別建物高さ情報に関して、商用の個別建物高さ情報との比較及び検証を行った。

図2,3に得られた散布図を示す。いずれの結果からも本研究で提案した手法では、強い相関があるが、建物高さを過小評価していることが分かった。DSMを作成する際に、ステレオマッチングでは建物による急激な高度変化に対応できず、地形標高データを高く見積もってしまうSmooth effectのためであると考えられる。

4. 結論

商用50cm高解像度ステレオ衛星画像と無償のステレオマッチングツールによるステレオマッチングで作成したDSM及び、汎用衛星情報から得られるDEMや無償公開されている建物占有面積情報、いずれもグローバルに入手可能なデータを用いて高解像度な都市幾何形状情報を低コストで作成することができた。

提案した手法を基に、メソスケールの気象シミュレーションだけでなく、LESに代表されるようなマイクロスケールの都市気象シミュレーションに最新の都市の幾何形状を含んだ研究が可能になることが期待出来る。

個別建物高さ情報に関しては、領域ベース法以外のマッチングアルゴリズムを試みることでDSM向上を図り、個別建物高さ情報の更なる精度向上が期待される。

建物占有面積情報に関してはOSMのみを使用した場合、都市によってデータ量の差が出てしまうため、Google Mapのような他の地図情報の使用や、衛星画像から画像分類で算出により更なる向上が期待される。

参考文献

[1] S. Grimmond: Urbanization and Global Environmental Change: Local Effects of Urban Warming (2007)

[2] A. Manuel et al: Generation and Quality Assessment of Stereo-Extracted DSM From GeoEye-1 and WorldView-2 Imagery (2014)

[3] A. Abdalla et al: Comparison of Matching Algorithms for DSM Generation in Urban Areas from Ikonos Imagery (2010)

[4]居石ら: 全球・都市の将来シナリオを考慮した都市街区の温熱環境予測 (2018)

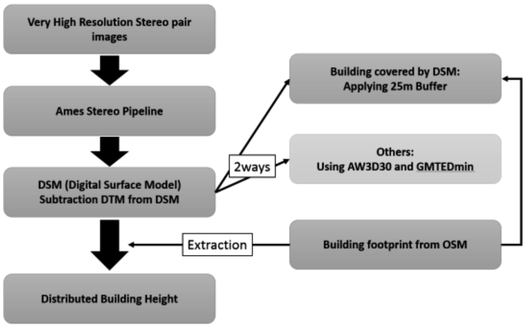

図1　提案する手法の全体像

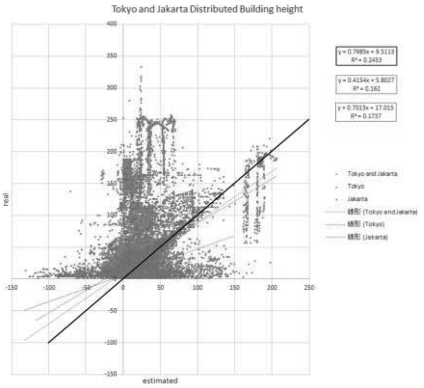

図2　個別建物高さの比較

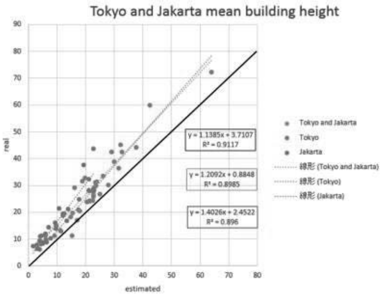

図3　平均建物高さの比較

A study on separation of Lithium and Cobalt from mixture solution

Student Number : 15_00153　Name : Daisuke AKAZAWA
Supervisor : Hirofumi HINODE, Winarto KURNIAWAN

1. Introduction

Lithium-ion batteries are the major type of rechargeable batteries and are used in mobile devices and electric or hybrid cars. The cathode of this battery contains cobalt (Co) and lithium (Li). Cobalt is a kind of rare metals because only few countries have the resources. Moreover, lithium is valuable metal because future rechargeable battery will also use lithium. Both elements are predicted to have a shortage in 4-6 years. Currently some companies recycle cobalt and lithium by organophosphorus solvent extraction. Around 80% of cobalt is recycled, however, recycling lithium is not feasible because the system is complex and expensive [1)].

Other simple recovery methods such as adsorption and chemical precipitation were reported. Researchers tried to separate cobalt and lithium using natural zeolites, however both metals were not adsorbed [2)]. Though the use of synthetic zeolites (zeolite-A) in cobalt and lithium recovery has not been reported, zeolite-A, which has higher cation exchange capacity can be promising. Research has been done utilizing sodium hydroxide to precipitate cobalt, and then remaining solution was passed through an ion-exchange resin to separate lithium and sodium [3)]. They could recover 99% of cobalt, but they had to concentrate lithium to recover it.

The research objective of this study is to develop the low-cost recycle methods by using synthetic zeolite or precipitation. Potassium hydroxide (KOH) and potassium periodate (KIO_4) were used to precipitate Co and Li, respectively.

2. Experimental

2.1 Zeolite-A Elemental Analysis

Determination of the elements contained initially in zeolite-A was done by X-ray Fluorescence (XRF). To measure lithium content in zeolite-A, 50 mg of zeolite-A and 1.5 g of ammonium sulfate were mixed in 20 mL of deionized water for 3 hours, followed by filtration. Lithium content was determined from the filtrate analyzed using Inductively Coupled Plasma - Atomic Emission Spectrometry (ICP-AES).

2.2 Zeolite-A Ion-Exchange Test

Preparation of the mixture solutions of Co^{2+}(100 ppm), Li^+(100 ppm) and NH_4^+(0/50/100 ppm) were done by solving their respective sulfates salts. Ion-exchange test was done by stirring 20 mL of the solution and zeolite-A in Erlenmeyer flasks for 3 hours in 25°C of water bath. The zeolite was then filtered and the concentration of Co and Li were measured using ICP-AES.

The zeolite-A used in this research contains Na^+ ions. Zeolite-A was pretreated to replace Na^+ with NH^{4+} and H^+ ions which are reportedly easier to separate from the solution after ion-exchange.

2.3 NH_4^+ exchanged Zeolite Ion-Exchange test

NH_4^+ exchanged zeolite was prepared by mixing 1.0 g of zeolite-A and 2.0 g of ammonium sulfate in 40 mL of deionized water in Erlenmeyer flask for 3 hours. The process is repeated 3 times. Then, the ion-exchange experiment similar to zeolite-A was done.

2.4 H^+ exchanged Zeolite Adsorption test

H^+ exchanged zeolite was prepared by heating NH_4^+ exchanged zeolite at 350°C for 120 mins. Then, the ion-exchange experiment similar to zeolite-A was done.

2.5 Precipitate Recovery Test

The mixture solution of Co^{2+} (1000 ppm) and Li^+ (1000 ppm) were made by dissolving their respective sulfates salts. Then, as shown in Fig.1, about 200 mg of potassium hydroxide pellets were added into 40 mL of the mixture solution, stirred, followed by filtration. The precipitate was recovered, dried, and analyzed using XRD. Then after which, the precipitate was dissolved in nitric acid and hydrogen peroxide and the analyzed using ICP-AES.

For other set of experiment, 0.288 M of KIO_4 solution in 20% KOH was prepared. The filtrate and KIO_4 solution were mixed at 2:5 volume ratio, heating it in the oven at 90°C for 30 mins. Then, the solution was filtered by Teflon membrane filter. The precipitate was dissolved in nitric acid and hydrogen peroxide, then analyzed using ICP-AES.

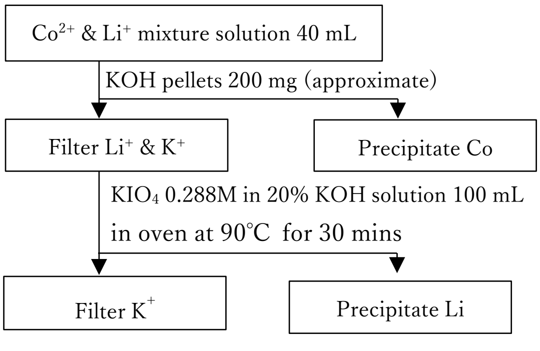

Fig.1 The process of the precipitation test

3. Result and Discussion

Fig. 2 shows the mass ratio of lithium and cobalt adsorbed to zeolite-A, and Fig.3 shows NH_4^+ exchanged zeolite and H^+ exchanged zeolite.

According to the elemental analysis, zeolite-A has Na^+ as exchangeable cation. Fig.2 shows almost all Co^{2+} adsorbed by zeolite-A, while less than 20% of Li^+ adsorbed. Addition of NH_4^+ into the solution resulted in lower separation performance. From this result, it can be concluded that zeolite-A can separate cobalt and lithium, however Na^+ are released to the solution. Na^+ is difficult to separate from Li^+, so NH_4^+ and H^+ exchanged zeolites were used because they have easily separable cations.

However, as Fig.3 shows, NH_4^+ exchanged zeolite has less selectivity and H^+ exchanged zeolite has low capacity for both Co^{2+} and Li^+. NH_4^+ exchanged zeolite may have a potential to separate without releasing interrupting ions.

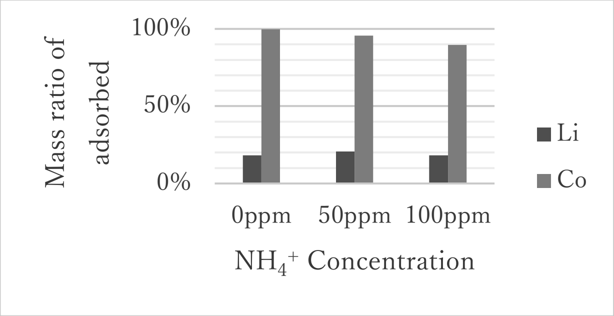

Fig.2 Zeolite-A adsorption test

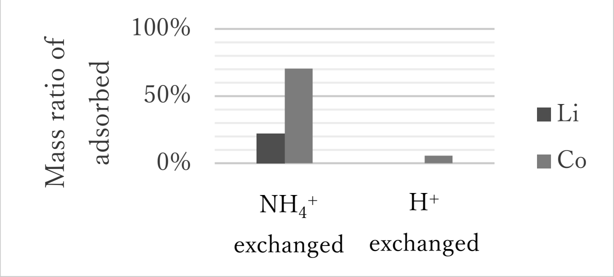

Fig.3 NH_4^+ and H^+ exchanged zeolite

Table 1 shows the recovery ratio by precipitation methods. Almost all of cobalt and 88% of lithium were recovered. This recovery rate is enough for recycling.

Table 1 Recovery ratio by precipitation method

	Li	Co
Precipitated by KOH	0%	99%
Precipitated by KIO4	88%	<1%
Loss	12%	<1%

Fig.4 shows the XRD result of precipitation by KOH. The peaks show that the precipitate is cobalt hydroxide ($Co(OH)_2$). Table 2 shows the mass ratio of the cations in the precipitation by KOH. The precipitation have high purity, which means that cobalt was successfully recovered.

Table 2 also shows the mass ratio of the cations in the precipitation by KIO_4. Although lithium can be concentrated, the precipitation still has much amount of potassium. Further research on method to minimize potassium content is still needed.

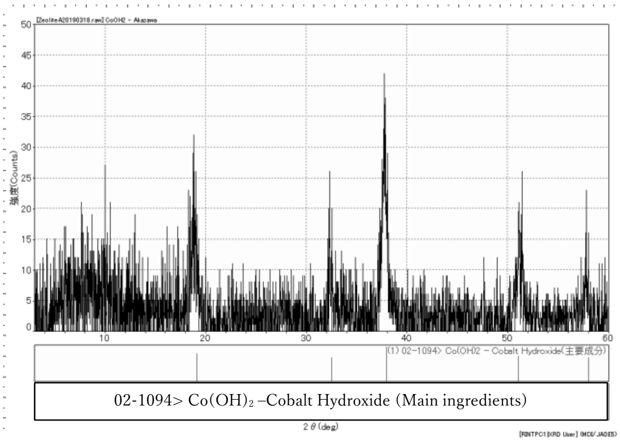

Fig.4 The XRD result of precipitation by KOH.

Table 2 The mass ratio of the cations in precipitation

	Li	Co	K
By KOH	<1%	>99%	<1%
By KIO_4	16%	<1%	84%

4. Conclusion

Zeolite-A was able to separate cobalt and lithium from a simulated mixture solution, but it releases Na^+, which is hard to separate. NH_4^+ exchanged zeolite has less selectivity, but it may have the potential to separate cobalt and lithium without releasing interrupting cations. H^+ exchanged zeolite has low capacity so it cannot be used for recycling cobalt and lithium.

KOH precipitation method can recover almost 100% of cobalt in the form of cobalt hydroxide. In KIO_4 precipitation method, we can recover 88% of lithium, however the precipitation contains high amount of potassium. To obtain pure lithium precipitation, further research is needed.

References

1)JOGMEC, ‘EV 電池および電池材料（Ni, Co, Li）の市場動向‘, 2019, http://mric.jogmec.go.jp/reports/current/20190604/113521/

2)Chandra Wahyu Purnomo・Endhy Kesuma・Sang Kompiang Wirawan・Hirofumi Hinode, ‘The Development of Lithium Ion Recovery Method by Activated Carbon and Natural Zeolite-based Adsorbent’, 2017

3) 吉塚 和治・西浜 章平, ‘有価廃棄物からのレアメタルの統合的抽出分離回収システムの開発‘, 2012

サプライチェーンを考慮した東京都市圏物流施設の年類型別立地分析

Transition of logistics facilities' location choices considering supply chain in Tokyo Metropolitan Area

学籍番号: 15_00756　名前: 衣然　指導教員: 花岡伸也

１．背景と目的

東京都市圏は、東京都区部を中心とする都市圏であり、世界最大の人口と経済規模を持っている。一般に交通調査において定義される東京都市圏に含まれる１都６県（茨城県、栃木県、群馬県、埼玉県、千葉県、神奈川県、東京都）は、面積は全国の 8.6%に過ぎないが、人口は 33%、実質県内総生産と実質最終消費支出は全国の約 38%を占める 1)。このような圏域において、産業・経済や人々の暮らしと密接に関係がある物流を把握することが重要である。また、一般的に中流施設は短期的に立地が変化するため立地誘導施策の影響を受けにくい一方で、特に工場等の上流施設は、歴史的な経緯で立地している等、物流効率や用地確保以外の要因で立地している可能性がある。施設の創設年で分けて立地選択分析を行うことも重要である。

近年、物資流動調査などの集計データで物流施設の立地問題をモデル化することで、物流施設の立地傾向を分析し、立地促進政策に示唆を与える研究が多数存在する 2)3)4)。さらに東京都市圏を対象には物流施設をサプライチェーン上の位置で分類した研究 5)や、物流施設の立地選好とサプライチェーン上の位置との関係を分析し、実際に上流・中流・下流で分類した施設によって立地が異なることを示した研究 4)もあるが、施設創設年で分けた分析は行われていない。。

本研究では、第五回東京都市圏物資流動調査のデータを用いて、サプライチェーン上の位置によって分類した物流施設を年類型別で再分類し、立地選択モデルを構築する。さらに、構築したモデルの推定結果を用いて年類型別に物流に関連する施設の立地選好とサプライチェーン上の位置との関係を解明することを目的とする。

２．研究手法

中道ら 4)は、第５回東京都市圏物資流動調査から物資流動 origin-destination（以下 OD）の搬出先あるいは搬入元の情報を用いて搬出搬入票の中で「店舗」、「飲食店・宿泊・娯楽施設」、「住宅・文教施設等」、「工事現場」を最終消費者と定義し、「倉庫」、「集配送センター・荷捌き場」、「トラックターミナル」、「その他の輸送中継施設」、「物流施設（詳細不明）」を物流施設と定義し、「工場」を工場と定義し、「事務所施設」を事務所と定義した。主な搬出先が最終消費者である施設を下流施設と定義し、ほかに工場及び主な搬出先が工場である施設を上流施設と定義し、ほかに主に物流施設に配送している施設を中流施設と定義し、主に事務所に配送している施設をサプライチェーン分類と立地研究の対象外にした。

選択肢であるメッシュの効用は式(1)に表す

$$V_{i,j} = \sum_k \beta_k L_{i,k} \qquad (1)$$

$$P_i^r = \frac{exp(\overline{v_j}^r + ln\,M_i)}{\sum_j exp(\overline{v_j}^r + ln\,M_j)} = \frac{exp(V_i^r)}{\sum_j exp(V_j^r)} \qquad (2)$$

$V_{i,j}$:施設 j に対するゾーン i の観測可能な効用

P_i^r: セグメント r の物流施設がゾーン（3 次メッシュ）i を選択する確率

$\overline{v_j}^r$：ゾーン i 内の立地可能な敷地ロットの平均効用とそのばらつきを表す効用関数（確定項）

V_i^r：ゾーン i の効用関数

以上によって、式 5 のロジットモデルの効用関数は、以下のように定式化される。

$$V_i^r = \sum_k \beta_k^r x_{ki} + lnS_i \qquad （式 3）$$

x_{ki}：ゾーン i 内の敷地の平均的な立地効用を表す k 番目の変数（立地要因変数）

β_k^r：パラメータ

このモデルのパラメータ推定においては、規模変数の項 lnS_i の係数を 1 に固定し、β_k^rを通常のロジットモデルと同様に推定している。本研究では、第 5 回東京都市圏物資流動調査の調査範囲である茨城県南部中部、栃木県南部、群馬県南部、千葉県、神奈川県、東京都の１都６県の中で可住地面積 0 以上の三次メッシュを研究範囲とする。三次メッシュ数は合計 19844 個である。

中道ら 4)は推定ソフトウェア(R)の能力、及び作業効率を考慮し、物流施設の立地している区画とそれ以外のメッシュを無作為に 199 区画を抽出し、合計 200 区画の要素を有する部分選択肢集合を抽出し、選択肢としたが、兵藤・坂井・河村(2015)6)によると、メッシュ総数 17961 のモデルであったが、R のマトリックス計算機を用いることで、全選択肢を扱っても標準的な PC で、十数秒で問題なくパラメータ推定が行えたということのため、本研究では全メッシュ(19844 個)をモデルの選択肢としてモデルの構築を試みる。本研究では、中道ら 4)で採用していた説明変数を参考に選定を行った。本研究は、全メッシュを選択肢とし、サンプルごと配送先重心を計算するには計算量が膨大になるため、意思決定者の配送先重心への距離を除き、それ以外を説明変数とした。

３．結果と考察

年類型の定義について、15 年ずつ等間隔で分類することにしたが、空港、港のような数十年前から位置変更がほぼない変数以外の統計データについて、例えば人口データの場合、公表されている人口のメッシュ統計は 1970 年からであり、さらに前の年代は 1970 年の人口を使用せざるを得ない。一方、新しく立地した物流施設の分析はより重要となり、さらに、1985 年以降は日本の景気循環 7)を考慮する必要がある。そのため 1985 年以降の年類型は 10 年間隔とした。

表１．年類型とサプライチェーン分類別の物流施設サンプル数

	~1954	1955~1969	1970~1984	1985~1994	1995~2004	2005~2013	合計
上流施設	541	1446	1847	1253	1094	570	6751
中流施設	58	126	257	259	358	218	1276
下流施設	168	365	542	446	513	314	2348

1955 年以前の施設から 2005 年以降の施設までモデルを立ち上げ、パラメータ推定を行った。表 2 と表 3 は物流施設のパラメータ推定結果の一部である。本研究は中道ら 4)と同じように、R 言語の GLM 関数を使用し分析を行った。主に参考するパラメータは、推定値、p 値、AUC、尤度比である。0.05 以上の p 値を持つ変数に帰無仮説を採択し、物流施設の立地選択に無相関と判断する。

各変数の物流施設に対する相関性は以下の通りである。

・人口：1970 年から 1995 年までの上流施設に対し少ないほど立地しやすく、1955 年以前の上流施設と下流施設に対し多いほど立地しやすい 1995 年以降ほぼ立地に影響はない。

・通勤圏内労働人口：1970 年以降の上流施設と 1995 年以降の中流施設と 1970 年から 1995 年までの下流施設に対し多いほど立地しやすく、1955 年以前の上流施設と下流施設に少ないほど立地しやすい。

・素材系業界への接近性：すべての上流施設に対し立地選択要素の一つである。素材系業界の付近に上流施設を立地誘導すべきである。

・加工組立関連への接近性：1995 年以前の上流施設に立地選択要素の一つである。1985 年から 1995 年までの中流施設に対し離れて立地する傾向がある。

・生活関連業界への接近性：1970 年から 1985 年までの上流施設と 1995 年から 2005 年までの中流施設に対し立地選択要素の一つである。

・全製造業への接近性：1970 年前と 1985 年から 2005 年までの上流施設と 1985 年から 1995 年までの中流施設に対し正の相関を持つ。加工組立関連、生活関連業界、全製造業はそれぞれ物流施設に重要視とされる時期があったが 2005 年以降はほぼ有意性を持たない。

・卸売業市場への接近性：1970 年以降の下流施設と 1955 年後の中流施設に対し正の相関を持つ。下流や中流施設は最終消費者を主な搬出先とするためと考える。

・業務地接近性：すべての施設に対し接近するほど立地しやすい。

・最寄 IC への距離：1995 年から 2005 年までの上流施設と 1955 年から 1970 年までと 1995 年以降の中流施設に対し近いほど立地しやすい。

表２．施設創設年が 2005 年以降の施設の推定結果

	2005年以降	上流			中流			下流		
		推定値	p値		推定値	p値		推定値	p値	
	定数項	-14.8392	0.0000	***	-19.8412	0.0000	***	-13.1716	0.0003	***
1	人口	0.1057	0.3100		-0.2658	0.0507	.	0.2411	0.0929	.
2	通勤圏内労働人口	0.3818	0.0012	**	0.5996	0.0019	**	0.2813	0.0638	.
3	素材系業界への接近性	0.0119	0.0406	*	0.0004	0.9681		0.0149	0.0564	.
4	加工組立関連への接近性	0.0043	0.5987		-0.0115	0.3783		-0.0016	0.8766	
5	生活関連業界への接近性	0.0146	0.5953		-0.0116	0.8006		-0.0660	0.0662	.
6	全製造業への接近性	0.0078	0.5375		0.0122	0.5287		0.0042	0.8032	
7	卸売業市場への近接性	0.0331	0.3876		0.1662	0.0037	**	0.1511	0.0016	**
8	業務地近接性	0.4791	0.0000	***	0.4306	0.0001	***	0.3383	0.0004	***
9	一般消費地の近接性夜間人口	-0.2303	0.1612		0.0734	0.7530		-0.5740	0.0105	*
10	最寄ICへの距離	0.0073	0.5445	.	-0.0643	0.0216	*	-0.0114	0.5261	
11	最寄空港への距離	-0.0641	0.8041		-0.7392	0.0262	*	-0.2241	0.4961	
12	最寄港湾への距離（東京神奈川）	0.0051	0.9839		-0.0155	0.9594		-0.2680	0.3645	
13	最寄港湾への距離（千葉）	0.0566	0.6875	.	0.1457	0.5525		0.2773	0.1699	
14	最寄港湾への距離（ひたちなか）	0.0507	0.7644		0.4289	0.1040		0.1003	0.6460	
15	道路延長	0.1728	0.0722	.	0.3103	0.0521	.	0.3993	0.0110	*
16	住宅地域割合	-0.6106	0.0917	.	-0.7149	0.2378		-0.2117	0.6692	
17	商業地域割合	-1.6992	0.0104	*	-0.6235	0.4543		-1.3046	0.1022	
18	準工業地域割合	1.3191	0.0036	**	1.9090	0.0026	**	1.8326	0.0014	**
19	工業地域割合	2.1835	0.0001	***	0.4406	0.6729		2.6001	0.0002	***
20	工業専用地域割合	1.1690	0.0055	**	0.2341	0.7458		1.5122	0.0098	**
21	市街化調整区域割合	0.3230	0.1534		0.4863	0.2361		0.5000	0.1374	
22	都市計画区域割合	-0.5594	0.4139		0.7866	0.4540		1.1810	0.1609	
23	地価	-0.0680	0.0099	**	-0.0834	0.0613	.	0.1394	0.0353	*
24	臨海部ダミー	0.0821	0.7194		-0.5320	0.1000		-0.3875	0.1538	
25	郊外部ダミー	0.4062	0.0333	*	0.4731	0.0955	.	0.3460	0.1309	
26	工業団地ダミー	0.9600	0.0000	***	0.7981	0.0008	***	0.4470	0.0226	*
	サンプル数	570			218			314		
	初期対数尤度	-2363.351			-1072.328			-1492.246		
	最終対数尤度	-1896.938			-822.9378			-1195.496		
	選択肢数	19844			19844			19844		
	AUC	0.8464032			0.8848054			0.859426		
	尤度比	0.197			0.233			0.199		

表 3. 施設創設年が 1985 年から 2005 年までの施設の推定結果

[1995,2005)							[1985,1995)						
	上流		中流		下流			上流		中流		下流	
	推定値		推定値		推定値			推定値		推定値		推定値	
	-17.1701	***	-13.8355	***	-11.9669	***		-16.6907	***	-10.3657	**	-18.2453	***
1	0.0567		-0.0284		0.1194		1	-0.0634	*	-0.0684		0.0141	
2	0.2286	**	0.3067	*	0.0781		2	0.2678	***	0.2468		0.3052	*
3	0.0103	*	0.0052		0.0079		3	0.0147	***	-0.0049		0.0079	
4	0.0230	***	0.0057		0.0152	.	4	0.0136	*	-0.0465	***	0.0081	
5	0.0165		0.0712	*	0.0198		5	-0.0097		-0.0412		0.0479	
6	0.0258	**	0.0002		-0.0089		6	0.0274	**	0.0395	*	-0.0053	
7	0.0622	*	0.1992	***	0.2050	***	7	0.0033		0.1006	.	0.1378	***
8	0.5209	***	0.5868	***	0.5173	***	8	0.5548	***	0.5014	***	0.5712	***
9	-0.0819		-0.2106		-0.2292	.	9	0.1140	*	-0.2437	*	0.0034	
10	-0.0180	*	-0.0494	**	-0.0125		10	0.0040		-0.0186		0.0004	
11	-0.2793		-0.6724	*	-0.0125		11	-0.2648		0.6755	.	-0.1429	
12	0.4371	*	0.0281		-0.1010		12	0.2491		-0.6820	*	0.2197	
13	0.2525	*	0.0586		0.4105	*	13	0.1275		0.0154		0.3938	*
14	0.0476		0.4257	*	-0.1709		14	0.1342		-0.2908		-0.3880	*
15	0.0837	.	-0.0047		-0.0284		15	0.0936	*	0.0331		0.0537	
16	-1.1570	***	-0.5063		0.0074		16	-1.3937	***	0.6024		-1.1382	**
17	-2.6843	***	-1.9305	**	-2.7349	***	17	-3.2352	***	-0.5185		-3.5523	***
18	0.2321		0.4388		0.8675	.	18	0.3248		2.5988	***	-0.2675	
19	1.1166	*	0.6694		0.2902		19	-0.1887		2.9018	***	-0.0442	
20	0.9902	**	0.1729		0.3140		20	0.1157		1.3204	*	-0.4559	
21	0.1513		0.3641		0.2353		21	0.0283		0.3528		-0.0789	
22	-0.1716		-1.4266		-1.7478	.	22	-1.0005	*	-1.8581		0.6223	
23	-0.0286		-0.0643	.	-0.0433		23	-0.0310	.	0.0039		0.0225	
24	0.0168		-0.0723		-0.2230		24	0.0246		0.7132	*	0.0526	
25	0.1259		0.3107		-0.1560		25	0.3064	*	1.0167	**	0.3985	*
26	0.7778	***	0.7606	***	0.6320	***	26	0.7561	***	0.2402		0.4686	**
	1094		358		513			1253		259		446	
	-3720.892		-1555.283		-2204.942			-4122.196		-1186.71		-2023.28	
	-2902.588		-1192.861		-1796.484			-3357.934		-946.4381		-1687.665	
	19844		19844		19844			19844		19844		19844	
	0.8385542		0.879899		0.8423762			0.8182699		0.8698953		0.837487	
	0.22		0.233		0.185			0.185		0.202		0.166	

- 最寄空港への距離：1955 年から 1985 年までの中流施設と 1955 年から 1970 年までの下流施設に対し遠いほど立地しやすく、1995 年以降の中流施設に対し近いほど立地しやすい。
- 最寄港湾（東京と神奈川湾）への距離：1995 年から 2005 年までの上流施設に対し遠いほど立地しやすく、1955 年から 2005 年までの中流施設と 1955 年から 1970 年の下流施設に対し近いほど立地しやすい。
- 最寄港湾（千葉湾）への距離：1995 年から 2005 年までの上流施設と 1985 年から 2005 年までの下流施設に遠いほど立地しやすい。
- 最寄港湾(ひたちなか湾)への距離：1995 年から 2005 年までの中流施設に対し遠いほど立地しやすく、1985 年から 1995 年までの下流施設に対し近いほど立地しやすい。
- 道路延長：1970 年から 1995 年までの上流施設と 2005 年後の下流施設に長いほど立地しやすい。交通系の変数の各年類型の推定結果は一致しないものが多数で、過去の傾向を参考し立地誘導することが難しいと考える。また、"遠いほど立地しやすい"という結果はあるが、実際わざと港湾や空港に離れる場所に立地する理由は考えられないので、ほかの要素に影響されていると考えられる。
- 住宅地域割合：1955 年から 2005 年の上流施設と 1985 年から 1995 年までの下流施設に対し割合が低いほど立地しやすい。物流施設は住宅地域と離れて立地してきたが、近年、こういう傾向がなくなっている。
- 商業地域割合：1955 年以降の上流施設と 1970 年から 2005 年までの中流施設に対し割合が低いほど立地しやすい。
- 準工業地域割合：2005 年以降と 1970 年前の上流施設とすべての中流施設と 2005 年以降と 1955 年以前の下流施設に割合が高いほど立地しやすい。
- 工業地域割合：1995 年以降と 1985 年以前の上流施設と 1970 年から 1995 年までの中流施設と 2005 年以降と 1955 年から 1985 年までの下流施設に対し割合が高いほど立地しやすい。
- 工業専用地域割合：1995 年以降と 1985 年以前の上流施設と 1985 年から 1995 年までの中流施設と 2005 年後と 1970 から 1985 年までの下流施設に対し割合が高いほど立地しやすい。用途地域は物流施設の立地選択にとって重要な参考である。
- 地価：2005 年以降の下流施設に対し高いほど立地しやすく、2005 年以降と 1970 年から 1985 年までの上流施設に対し安いほど立地しやすい。工場などの上流施設は利益を上げるために、地価の安いところに立地するのに対し、下流施設は地価が高いが最終消費者が多い場所に立地すると考えられる。
- 臨海部ダミー：1985 年から 1995 年までの中流施設と 1955 年前の下流施設に対し臨海部に傾向がある。
- 郊外部ダミー：2005 年以降と 1985 年から 1995 年までの上流施設と 1985 年から 1995 年までの中流施設と 1970 年から 1995 年までと 1955 年以前の下流施設に対し郊外部に立地する傾向がある。
- 工業団地ダミー：1955 年以降の上流施設と 1995 年以降と 1955 年から 1985 年までの中流施設と 1970 年以降の下流施設に対し工業団地に立地する傾向がある。

4. 結論

推定結果から、以下の結論が得られた。

(1) 工業団地や用途地域との相関性は年類型別に異なる傾向を示し、最近の施設は、すべての施設に対し有意性を持つため、立地誘導の時重点的に考慮する必要がある。

(2) 上流施設と下流施設の立地誘導に、地価を考慮する必要がある。

(3) 同じサプライチェーンの位置の施設でも各業種への近接性は年類型によって異なる傾向を示すことから、現時代の需要に適応する施策が必要となる。

(4) 最近の中流施設は空港の近くに立地する傾向があることから、中流施設の立地誘導政策に空港を考慮する必要がある。

本研究は、グループ数が過多にならないように物流施設を FF 施設、FL 施設 [4)]のような搬入搬出先で分類していない。今の段階ではまだ工場、多機能事務所など具体的な施設種類に立地に言及することができない。今後の課題としては、物流施設を搬入搬出先で分類し、正確に当時の施設の特徴を表す適切な年類型別で立地選択分析をする必要がある。

参考文献

1) 東京都市圏交通計画協議会：東京都市圏の望ましい物流の実現に向けて, 2015.
2) 荻野保克・遠藤弘太郎(2007)：立地選択モデルを用いた東京都市圏における物流施設の立地ポテンシャル分析」, 土木計画学研究・論文集，No.24pp.103-110.
3) 篠原丈実，福田大輔，兵藤哲朗：Spatial Sample-Selection Model を用いた物流施設の立地先・立地量の同時決定行動の分析，土木計画学研究・講演集, Paper No. 7311.
4) 中道久美子・川崎智也・花岡伸也・呂田子：サプライチェーンを考慮した東京都市圏物流施設の立地分析, 土木計画学研究・講演集, Vol.57, 2018.
5) 中道久美子・川崎智也・花岡伸也・渡邊雄太郎：東京都市圏におけるサプライチェーンの観点からの物流施設分類とその品目別分析, 土木学会論文集 D3, Vol.74, No.5, pp.1005-1018, 2018.
6) 兵藤哲朗・坂井孝典・河村和哉：東京都市圏物資流動調査による空間相関を考慮した物流施設立地選択モデルの検討, 土木学会論文集 D3, Vol.71, No.4, pp156-167, 2015.
7) 内閣府：景気基準日付.

都市近郊における農業の特徴の二時点比較：千葉県を事例として

学籍番号：15_02494　遠藤奈美　指導教員：阿部直也

1.　背景・目的

近年の日本が抱える少子高齢化や人口の都市集中による農村地域の空洞化などの影響から、農村地域において人手不足が叫ばれていることは周知の事実である。事実、農林水産省の農業構造動体調査（[１]）によると日本の総農業経営体数、農業従事者数はともに年々減少し続けている。

一方で、農業の組織経営体数は年々増え続けており、また最近では都市内やその近郊における農業の役割や重要性について注目が集まっている。

本研究の目的は、これらの新しい話題に注目しながら、最新のデータの分析結果および既存研究を用いて、二時点での地域の状況を比較する事により近代農業の流れを明らかにする事である。

研究対象地域とした千葉県は、東京に隣接した都市的地域、都市から離れた農村地域など様々なタイプの農業があり、農家個数は年々減少しているものの産出額はキープされており、各々の地域での近代農業事情に合った変化を観測することができる。

2.　関連情報と既存研究

2-1. 都市近郊農業

都市農業は都市化地域とその近郊で行われている農業のことであり、兼ねてから循環型社会におけるその働きは注目されてきた。近年は、その立地の良さを生かした販売方法、地産地消が注目されている。図２は農林水産省の2011年、2001年の東京都における農産物の販売ルートである。10年間で農協経由でない市場外流通の割合が大幅に増えている事がわかり、農家の販売ルートとしての農協依存度が減少していることを表している。このような変化に伴い、自己販売経路を確立している都市農家では野菜を中心とした作物の多様化が進んでいる。

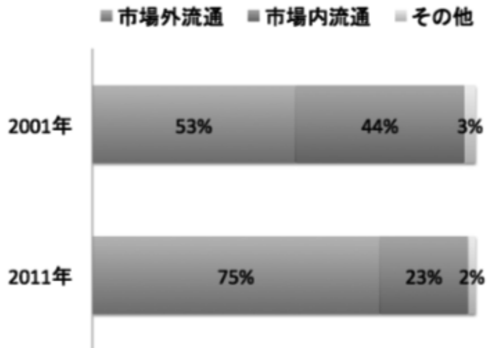

図１、東京都農業の販売経路（[２]）

2-2. 農村地域の構造変化

農村地域における高齢化や後継者不足などによる空洞化から、作業委託や借地経営が増えている。こうした状況に対処するため、各都道府県に設置された農地中間管理機構に依る農地の集積転売は同機構発足時の2014年からわずか3年で7.7倍にもなっている。具体的事例として、かつて集落が盛んだった新潟県上越市三和区での大規模借地経営への移り変わりについて細山（2011）は言及している（[３]）。

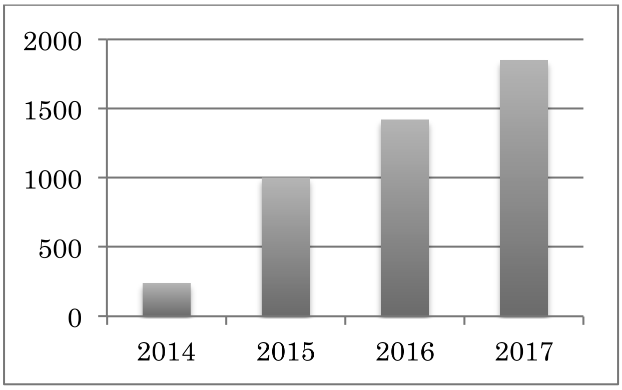

図２．農地集積機構の実績(100万ha)

3.　研究手法、データ

研究手法ならびにデータは比較対象の既存研究（[４]）を参考に、データは農林水産省の統計データである農林業センサスの2015年のものを用いた。また、分析対象とした区分は、千葉県の昭和25年当時の市区町村区分に従った341旧市区町村とした。

具体的な分析方法は、第一に、同県内の各地域の農業の特性を表す15の変数（表1）を用いた主成分分析を行い、その後に主成分スコアを用いたクラスター分析を行い類型化した。その上で、各知育区分における農業形態の変化の有無を、既存研究の成果と照らし合わし、地図上の比較検討を行なった。

表１．分析に用いた変数

1	本業農家（65歳未満農業専業、主業農家）戸数
2	総経営耕地面積
3	本業農家率
4	同居後継者いる農家率
5	１戸あたり経営耕地面積
6	経営耕地面積3ha以上農家率
7	経営耕地面積3ha以上農地シェア
8	販売金額1,000万円以上農家率
9	60歳未満農業就業人口率
10	雇用（常雇用、臨時雇用）農家率
11	販売金額１位が稲作の農家率
12	販売金額１位が野菜の農家率
13	販売金額１位が畜産の農家率
14	水田流動化係数（借地、全作業委託、収穫委託の割合）
15	水田率

4. 分析結果と考察

クラスター分析で類型化された各地域区分(341 区分)のグループについて 2005 年と 2015 年の２時点間の比較をした結果、各グループの変数に対する値の平均値がそれぞれ大きく異なり、それぞれのグループに農業的特徴が見られた。

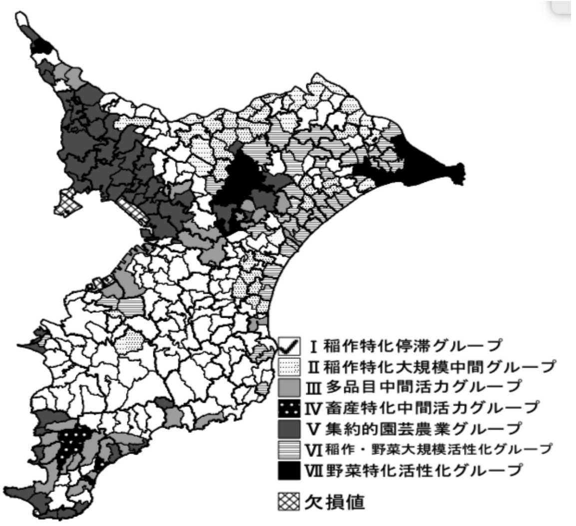

図２. 既存研究による色分け
（文献[５]70 頁より抜粋）

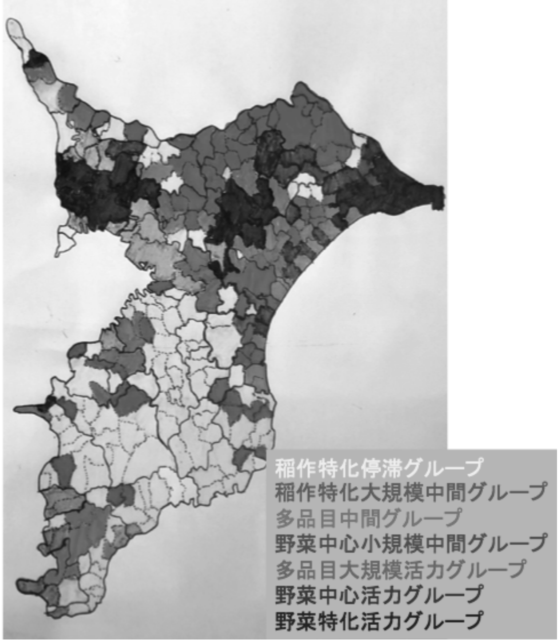

図３. 本研究による色分け

既存研究との対応を図る為、主成分１が表す 65 歳未満就業者立や販売金額 1000 万以上などの農業活性化度に応じてグループ１から７までを昇順に並べたところ、グループ１、２は概ね合致していたが、グループ５の一部がグループ６になるなどの変化も見られた。

各グループにおける各変数の平均値を算出し、作成したマップとも照らし合わせながら比較した。特徴的だったのは、都市的地域を中心とした小規模野菜特化農業以外のほぼ全ての地域で農地の集約が見られたこと、また野菜特化度の上昇した都市的地域、および農地集積の流れが見られた農業最活性化地域における 1,000 万円以上販売農家率の増加である。

概ね同様の地域を含んでいたグループ１、２に関しては、どちらも停滞地域ではあるが、農地集積が進んでいるデータが得られた。ただ、変化の大きさには差が見られ、グループ２の方が大きかった。

グループ５からグループ６に移った地域に関しては、野菜特化度合いが大きく増加し、都市農業的傾向通りの変化を遂げていることが確認された。

5. 結論、今後の課題

5-1. 結論

本研究の目的であった「農地集積、法人化、都市農業などによる近代農業の変化の流れを明らかにする」という事に対しては、農業活性化地域地域での農地集積やその規模増加に伴う販売金額 1,000 万円以上農業経営体率の増加、また都市的地域での野菜特化傾向（都市農業に適した作物）及び販売金額 1,000 万円以上農家率の増加から農地集積や大規模経営化、都市的地域における都市農業的特徴を持った農業経営体の増加を観測し、街頭地域における近代農業の流れを明らかにした。一方で、後継者不足、や平均年齢の増加にも関わらず近代農業的変化の見られない農業停滞地域があることも明らかにした。

5-2. 今後の課題

今回の比較研究では、２時点間データをそれぞれのグループごとに比較したので、千葉県における農業の地域特性および変化の大まかな流れを把握することはできたが、一つ一つの市区町村を対応させて逐次比較をすることはできず、各グループに含まれる地区町村が異なる事による誤差が生じることは避けられなかった。そこで、さらなる研究としては土地を対応させた平均値を含めた考察が挙げられる。

＜参考文献＞

[１]農林水産省、農業構造動体調査、令和元年 6/28 公表
http://www.maff.go.jp/j/tokei/kouhyou/noukou/index.html

[２]農林水産省「都市農業をめぐる情勢について」、平成 28 年 10 月
http://www.maff.go.jp/j/nousin/kouryu/tosi_nougyo/attach/pdf/t_gaiyo-2.pdf

[３] 細山隆夫、「大区画圃場地域における大規模借地経営の存立状況と農地団地化」、農業経営研究第３号、2011

[４] 溝田俊之、農山村地域の農業構造分析と施策への提言、平成 20 年度地域活性化のための農業集落データ分析委託事業報告書、65 頁、2009
http://www.aafs.or.jp/sogo/h20_itaku.pdf

Comparative analysis of network transportation costs for truck platooning and existing driving

（トラック隊列走行と単独走行のネットワーク輸送費用の比較分析）

Student ID : 13B00715　Name : Hyunsoo LEE　Academic advisor : Shinya HANAOKA, Tomoya KASAWAKI

1. Introduction

Truck transportation plays a key role in Japan's logistics transportation because it accounts for about 90% on a ton basis [1]. However, the shortage of drivers and soaring fuel costs has become serious recently [2]. And, truck platooning is one means for solving the problem because it is effective in reducing fuel consumption and labor costs [3]. However, many studies on it have so far focused on the effects of introduction and there are few studies on detailed transport cost comparative analysis. Therefore, the objectives of this study are as follows. (1) Compare and analyze the transportation costs of the virtual network of existing driving and truck platooning (Analysis 1). Verify with actual highway data (Analysis 2). Next, truck platooning will be explained. It means that many trucks form a platoon and travel while maintaining the distance between vehicles while sharing the driving situation via communication [4]. And, platooning operated by only one driver and no driver in the following trucks is called autonomous truck platooning. In case of existing driving, transportation is performed directly between each logistics base. However, in case of truck platooning, trucks form or release platooning at platooning center and move in a platoon between platooning center.

2. Analysis

A model based on the virtual network is created. Next, transportation costs are compared to find out the boundary conditions and a comparative analysis is made on the way to operate, number of trucks, and vehicle separation distance. Finally, verification on an actual highway is performed by adapting the model.

2-1. Model

There are three cases like existing driving (Case0), truck platooning (Case1), autonomous truck platooning (Case2). The model for the cost is as follows.

(Cost)[円/回]

$$= \textit{Labor cost} + \textit{Fuel cost} + \textit{Highway tolls} + \textit{Other expenses}$$

$$\textit{Labor cost} = \{T_m + (t_w + t_f + t_{wr} + t_r) \times n\} \times c_l \quad (1)$$

$$\textit{Fuel cost} = (D_m - \alpha \times n \times d_{AB}) \times cp \quad (2)$$

$$\textit{Highway toll} = u_h \times n \quad (3)$$

$$\textit{Other expenses} = (c_i + c_t + c_m + c_x) \times n \quad (4)$$

Tm:sum of all driver's driving hours [h], tw,twr:waiting time for matching (forming/releasing platooning) [h], tf,tr:time for forming/releasing platooning [h], n:number of trucks, cl:driver's labor cost per hour [yen/h], Dm:sum of all truck's transportation distance [km], α:average of fuel savings, dab:transportation distance in platoon [km], p:unit price of fuel [yen/ℓ], c:fuel consumption per km [ℓ/km], uh:usage fee for highway per unit [yen/unit], ci:insurance money [yen], ct:tax [yen], cm:vehicle maintenance cost [yen], cx:consumable goods [yen].

2-2. Comparative analysis (Analysis 1)

Next, this model will be used to calculate the boundary conditions and write a graph while changing variables. Fig 1 shows the boundary conditions (difference between Case0 and Case1, Case0 and Case2) in a graph. In this graph, Db means average distance between logistics bases [km].

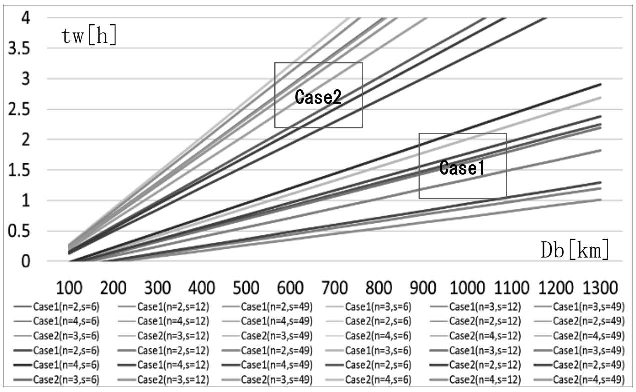

Fig 1. Boundary conditions

And, the boundary conditions are compared.

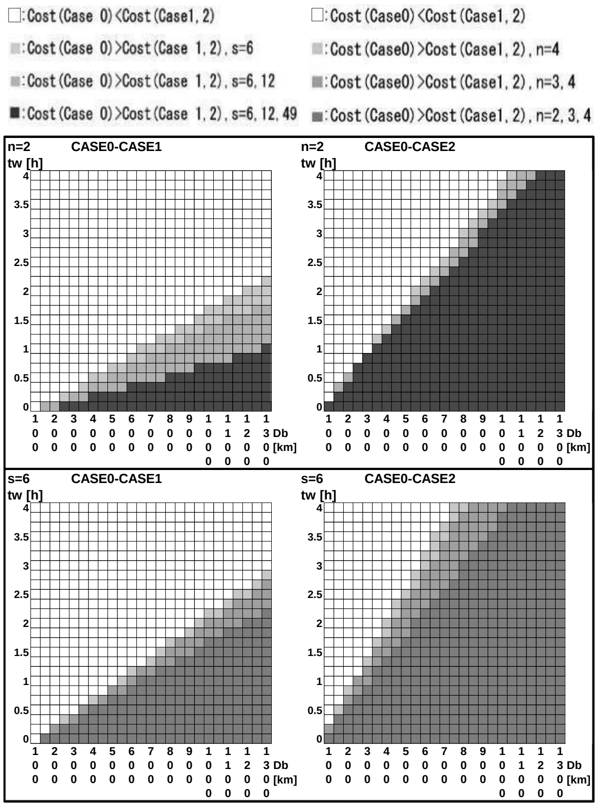

Fig 2. Comparison of boundary conditions

This is example figure in which the comparison of the boundary conditions was performed with the number of trucks(n) or the vehicle separation distance fixed. The meaning of each color is on the top of Fig 2. s means vehicle separation distance. As a result of fixing n (2,3,4 vehicles) and s (6,12,49m), there are 6 results. For example, in case of two trucks and 6m of s are presented in Fig 2.

2-3.Verification (Analysis 2)

From now on, actual data will be used to verify whether platooning is actually effective or not on actual expressway. This verification is performed based on the calculation results of Hirata(2019) [5]. This study was based on actual data to determine how many platoons(maximum) could be formed between Tokyo and Aomori on the Tohoku Expressway. (Inbound:2043 vehicles, Outbound:1550 vehicles). However, since the trucks form a platoon on the road while driving in this data, the calculation was conducted according to this study(Gather at the platoon center to form or release a platoon). The total cost reduction is calculated from the difference between the cost of existing driving and truck platooning. In addition, because this data calculates the maximum number of trucks that can form platooning, it may include the possibility that the cost will increase due to platooning. Therefore, verification is performed in the following two cases. (1) If the trucks are disadvantage when forming platooning, it is assumed that they do not form platooning (Verification 1). (2) All trucks that can form platooning form platooning (Verification 2). The result of verification 1 means that the profit obtained by platooning is maximum. At vehicle separation distance(s) is 6 m, which is vehicle separation distance based on minimum safety time for platooning communication, where the profit is maximum, the result of verification 1 is shown in Fig 3.

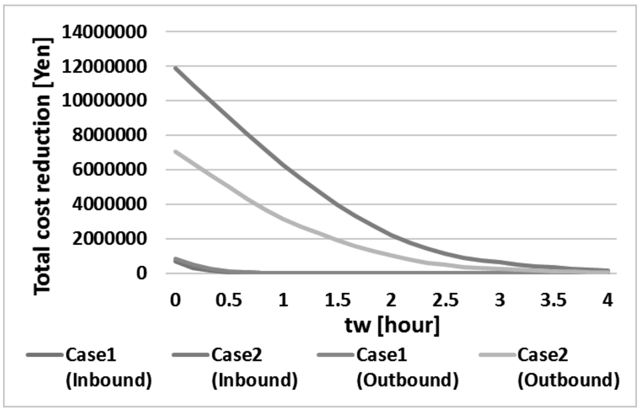

Fig 3. Result of verification 1

Next, Similarly, at s is 6 m, the result of verification 2 is shown in Fig 4.

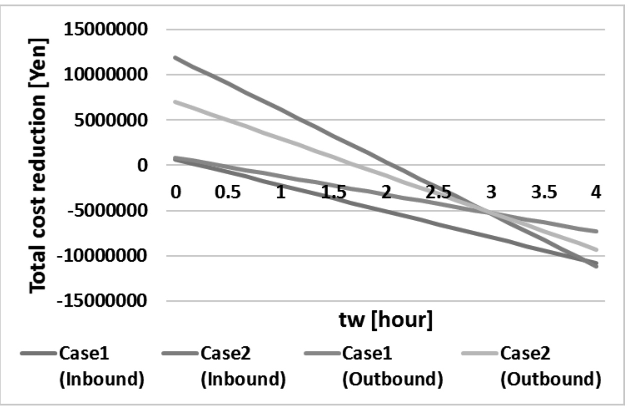

Fig 4. Result of verification 2

3. Conclusion

According to the purpose of the study, the conclusions are as follows. First, under the conditions in the area under each of the graphs in Fig 1, it is likely that the cost of transportation becomes lower when truck platooning than existing driving. Next, Case1 is sensitive to s because the graph changes drastically due to changes in s (to reduce s is important), Case2 is sensitive to n(to increase n is important). However, Case2 is much more advantageous than Case1. Then, it is considered that there is a high possibility that the cost of transportation becomes lower when truck platooning than existing driving on the Tohoku Expressway between Tokyo and Aomori. Because, significant total cost reduction can be obtained when tw is small enough (especially in Case2, total cost reduction is more than about 10 times of Case1). In particular, it is important to focus on adjusting the tw with proper scheduling and introducing autonomous truck platooning that is quite effective. Finally, Future issues are explained. As the number of trucks increases, tw is expected to increase, so reflect that change. Also, it is considered that there was a possibility that the accuracy of the calculation was slightly reduced due to a difference in the calculation method in the verification (On the road or Platooning center). Therefore, the model is improved so that it can be calculated even on the road.

References

[1] 全日本トラック協会 (2018)., 日本のトラック輸送産業現状と課題2018., pp.4.

[2] 国土交通省 (2015)., 物流をめぐる状況～物流の現状及び物流政策の取組状況等～., pp.34.

[3] Watanabe (2019)., ヨーロッパにおける大型貨物車を利用した貨物輸送に関する取組の実態と課題., 2019年ＩＢＳフェローシップ発表会.

[4] European Automobile Manufacturers' Association (2017)., What is truck platooning?.

[5] Hirata, Abe (2019)., 都市間物流データを活用したトラック隊列走行の車両マッチングポテンシャルの推計～東北自動車道を対象として～., 日本物流学会誌., 27., 91-98.

Numerical Analysis for Precise Estimation of Wave Pressure and Overtopping around Coastal Dike

Student Number: 15_13747 Name: Takumi Mizuochi Supervisor: Hiroshi Takagi

1. Introduction

Dike is a part of coastal protection system that are constructed along coast to protect human lives and assets from storm surges, tsunamis, and waves. The design standard for coastal structures requires wave pressures and overtopping flow rate being below the allowable magnitude during the lifetime of the structure. A number of estimation formula and diagram have been proposed to date, which are mostly determined by hydraulic experiments. However, in recent years, a sophisticated CFD (computational fluid dynamics) is attracting attention in analyzing wave pressures and overtopping rate. This study attempts to demonstrate the validity of CFD analysis results for wave pressure and overtopping flow comparison with experiments.

2. Wave Pressure

The author performed the CFD and compared the results with the previous experimental data (Takagi and Nakajima, 2007), which measured wave pressures acting on an upright breakwater. Figure.1 shows the geometry and the breakwater model considered in this experiment and numerical analysis. In the experiment the rubble mound was a porous structure, whereas in numerical analysis this part was treated as an impermeable body. Three different wave conditions (Table.1) were posed from the offshore inlet boundary. Waves mostly reflected on the dike, while a slight water mass overtopped the crest of the structure. Wave pressure is measured by three pressure gauges, installed at depth of 6, 10, 14cm on the front surface of the dike. In both experiments and numerical analysis, the input wave height and period were first determined under the case without any structures in order to examine how high wave passes the location of the breakwater. An open source software OpenFOAM was used for the computation and a solver called interFoam was adopted to solve two-phase flow using VOF (Volume of Fluid) method.

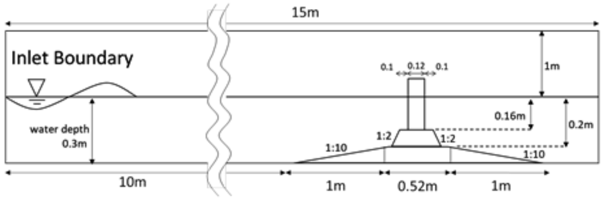

Fig.1 Geometry of experimental and numerical analysis

Table.1 Incident wave

Case No.	Period (s)	Height (m)
1	1.0	6.0
2	1.0	8.0
3	1.4	10.0

3. Wave Pressure comparison

Figure.2 shows the example of pressure in experiment and numerical analysis, and Figure.3 shows comparison between wave pressure in experiment and numerical analysis. These data shows that, at shallow water depth, the temporal changes and minimum and maximum pressures are almost similar. However, as the water depth becomes deeper, difference in wave pressure between the simulated and experimental value increased.

This difference in this results may be associated with energy loss in the porous body. And another reason for this difference is that the larger the wave height, the more complicated the flow turbulence occurs in front of the breakwater. In this study, the analysis did not use a particular turbulence model, so it may not be possible to reproduce these complicated flow.

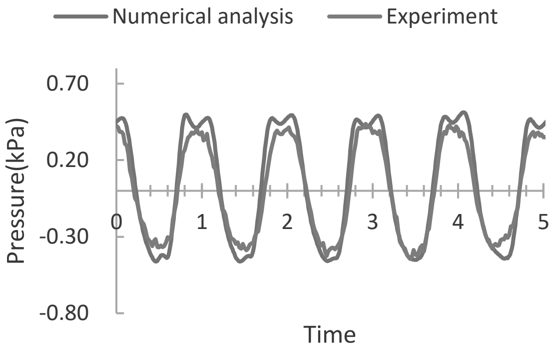

Fig.2 Example of pressure in numerical analysis and experiment (Case No.1, pressure gauge sets 6cm depth)

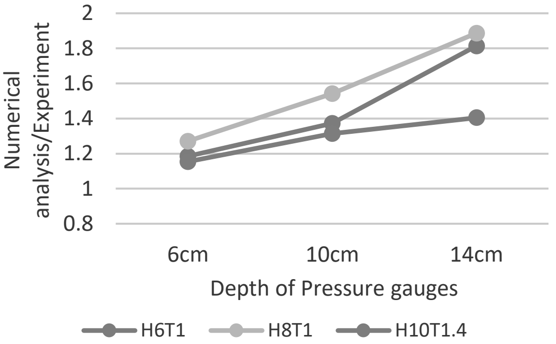

Fig.3 Comparison between wave pressure in experiment and numerical analysis

4. Flow rate of the Overtopping wave

A comparison was made between the flow rate derived from the overtopping wave diagram by Goda *et al.* (1975) as shown in Figure.4 and that obtained by numerical analysis for the upright dike. Numerical analysis performed using interFoam. Figure.5 show the geometry of numerical analysis for the wave overtopping test. The flow rate is estimated by measuring the volume of the water phase stored in the reservoir behind the dyke. The wave height and period of incident wave were adjusted in the condition without the slope and dike, resulting in the values shown in Table.2. Figure.6 shows the example of change in volume per unit width of liquid phase stored in the reservoir.

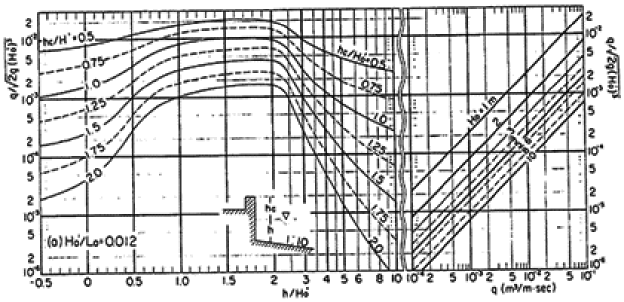

Fig.4 The diagram of flow rate of wave overtopping (Goda *et al.*, 1975)

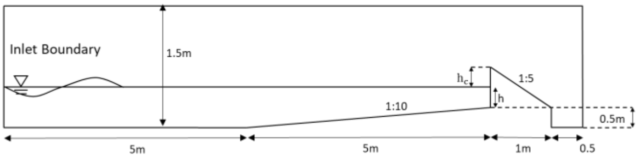

Fig.1 Geometry of experimental and numerical analysis

Table.2 Input wave and water depth detail

Case No.	Period (s)	Wave height (m)	Depth h (m)
0	2.92	0.160	0.50
1	2.47	0.114	0.557
2	2.18	0.089	0.589
3	1.97	0.073	0.609
4	1.81	0.062	0.623
5	1.58	0.047	0.641
6	1.50	0.042	0.647
7	1.43	0.038	0.652
8	1.31	0.032	0.660
9	1.21	0.028	0.666

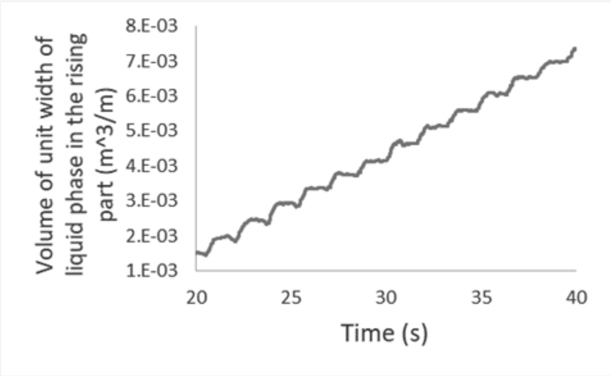

Fig.6 example of change in volume per unit width of liquid phase stored in the reservoir (Case No.5)

5. Flow rate of the Overtopping wave comparison

Figure.7 shows comparison flow rate overtopping wave between numerical analysis and diagram in Goda *et al.* (1975).

Case No.0~3, the calculation doesn't converge, so the flow rate of the overtopping wave couldn't set to a sufficient wave number. But, before the wave hit dike when the landing water depth was smaller than the wave height it was confirmed that the overtopping flow was small because the wave broken and the wave height of the reflected wave did not occur.

In case No.4~9, it was confirmed that the overtopping amount tends to decrease as the wave height decreases.

All cases show higher flow rate compare to flow rate overtopping wave between numerical analysis and diagram (Goda *et al.*, 1975).

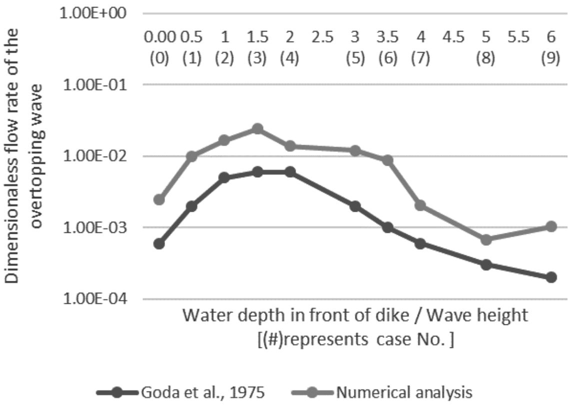

Fig.7 comparison of overtopping rate between numerical analysis and diagram in Goda *et al.,* (1975)

6. Conclusion

By comparing results of the previous experiment and research, wave simulation by OpenFOAM, incorporating interFoam solver, demonstrates the ability to estimate wave pressures and overtopping around upright dike at a reasonable accuracy.

However, OpenFOAM tends to overestimate the wave pressure acting on upright dike. The flow rate of overtopping wave also tends to be overestimated by 3~5times.

In this study, all numerical analysis were carried out without a turbulent model due to a numerical stability problem. If a sophisticated turbulent model is incorporated, the accuracy of the estimation is expected to improve.

It is also expected that more accurate analysis will be possible by expanding from the two to the three dimensional numerical analysis.

References

[1] Goda Y. *et al.*, Laboratory Investigation on the Overtopping Rate of Seawalls by Irregular Waves, *Report of the port and harbor research institute* Vol.14, No.4, pp3-44, 1975 (in Japanese)

[2] Takagi H. and Nakajima C., Estimation error in the analytical prediction of standing wave pressures acting upon breakwaters, *Journal of Hydraulic, Coastal and Environmental Engineering, JSCE,* Vol.63, No.4, pp291-294, 2007 (in Japanese)

[3] 岩垣雄一，山口正隆，Stokes 波とクノイド波の適用限界について，海岸工学講演会講演集，第 14 巻，pp8-16，1967

Analysis of characteristics and benefits of sharing service users

Student No.: 15_13411 Name: Hidehiko MATSUDA
Supervisor: Naoya ABE

1. Introduction

In recent years, widely recognized sharing services such as Uber (mobility hailing), Times (car), Airbnb (accommodation), AirCroset (clothing) have gotten social popularity and its penetration into society looks certain to some extent. There are three factors for the trend, 1. increasing demand for community participation; 2. internet penetration; 3. global recession (Botsman & Rogers, 2010). The sharing services are often categorized into two types (Belk, 2010). The first type is conventional reuse or recycle of goods, involving the transfer of ownership from one to other. This type with transfer of ownership means mainly used goods trading. Therefore, trading in a thrift shop or flea market is included in this type. In Japan, the market for flea market apps has grown rapidly in recent years with the advent of flea market apps such as Mercari. The second type is access-based consumption (ABC) without having the ownership of goods and/or services. ABC is a consumption behavior that involves using goods or services for a certain period of time and paying for them, which is also known as a service of subscription. Therefore, rental services, car sharing services and Airbnb's services fall into this type.

According to a previous study (Benoit et al, 2017), people use these sharing services for five reasons, for saving money, communicating with other people, experience extraordinary, reduction for risk and responsibility, environmental protection. But less studies have been conducted in Japan for the same argument.

1.1. Research objectives

In previous studies, classification and positioning of economic behavior as sharing and motivation that people share are mainly discussed. But discussion on the characteristics of people who use sharing services is not enough. Based on these, this research aims at the following two

- To identify trends in what life stages people share with what types of sharing.
- To understand the relationship between personal characteristics and the benefits of using sharing services.

2. Methodology

2.1. Data & Sample

Data collection was done using online-based questionnaire survey platform SurveyMonkey® from 30-31 January 2020. The questionnaire survey was distributed to a total of 502 respondents which are residents of Kanto region, Japan. The summary of demographic information of the respondent is shown in Table 1. And table2 shows the correspondence table of two type of sharing services.

Table 1. Demographic summary of the respondents (n = 502)

	Respondent Profile	Frequency	Percentage (%)
Gender	Male	249	49.7
	Female	252	50.3
Age	<18	5	1
	18-29	115	23
	30-44	155	31
	45-60	165	33
	>60	61	12

Table 2. Two types of sharing and sharing services

Type with transfer of ownership
- Trading at recycle shop (off-line)
- Trading at flea market app. (on-line)

Type with access-based consumption
- Car sharing (ex. Times , Uber)
- Space sharing (ex. Airbnb)

3. Result & Discussion

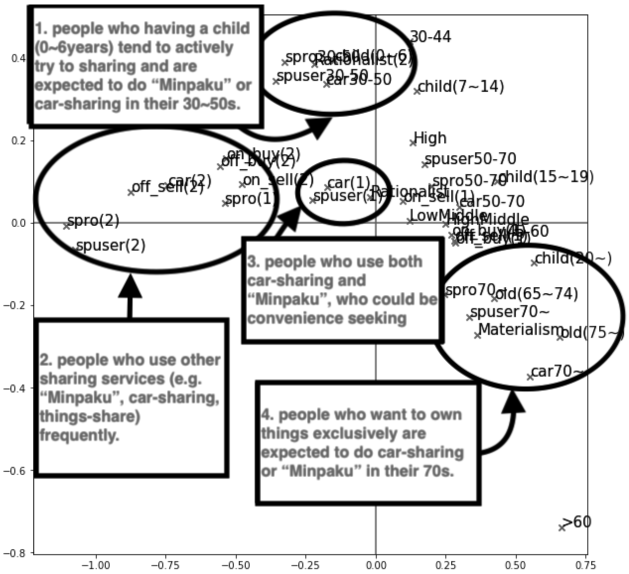

Fig1. Respondent's characteristics and usage of sharing services (correspondence analysis)

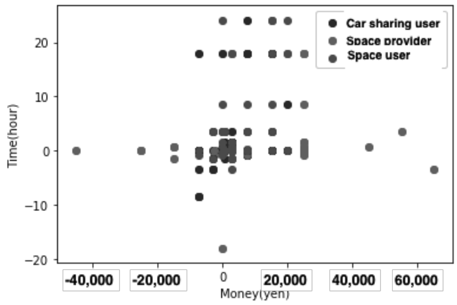

Fig 2. Subjective time and monetary benefits recognized by either sharing services users or provider

Fig1 shows the relationship between personal characteristics and sharing usage. This figure reveals four main findings. First one is that people who having a child (0~6years) tend to actively try to sharing and are expected to do "Minpaku" or car-sharing in their 30~50s.

Second one is that people who use other sharing services (e.g. "Minpaku", car-sharing, things-share) frequently.

Third one is that "rationalists" relatively use car-sharing and space-sharing.

And fours one is that people who want to own things exclusively are expected to do car-sharing or "Minpaku" in their 70s.

Fig2 shows the time and economic benefits of sharing services from the user's subjective judgement. Many people feel both time and money benefit through car sharing and using "Minpaku" But "Minpaku" providers differ in economic benefits. It will be a difference whether they are successful as an inn.

And from the point of view of the relationship between personal characteristics and benefits of sharing services, in both sharing, car sharing and using "Minpaku", people whose income is relatively low fell the benefit financially, while high-income individuals benefit from time. And housewife's benefit from the time, perhaps because they can quickly find better accommodations when choosing a family vacation inn. There may be many attractive lodgings for families registered in the private lodging service.

4. Conclusion

The study revealed the relationship between personal characteristics and the use of sharing services, and the relationship between personal characteristics and benefits.

In conclusion, it was found that age, income, the presence of children, and the presence of elderly people affect people's values for things, and the usage and benefits of sharing services.

As a future task, mobility sharing services such as Uber are not major in Japan, so it will be necessary to analyze sharing in overseas countries where such mobility sharing services are widespread.

5. References

1. Belk, R. (2010). Sharing: Table 1. *Journal of Consumer Research*, *36*(5), 715–734. https://doi.org/10.1086/612649
2. Botsman R, Rogers R. 2010. What's mine is yours: the rise of collaborative consumption. Harper Business: New York, NY.
3. Benoit, S., Baker, T. L., Bolton, R. N., Gruber, T., & Kandampully, J. (2017). A triadic framework for collaborative consumption (CC): Motives, activities and resources & capabilities of actors. *Journal of Business Research*. https://doi.org/10.1016/j.jbusres.2017.05.004

ドップラーライダーで観測された建物後流(ストリーク)の研究

学籍番号：15_05191　氏名：桐谷 蒼介　指導教官：神田 学　稲垣 厚志

1. 始めに

地表付近における大気の流れは、人工排熱や汚染物質の輸送・攪拌という重要な役割を担っている。そのため、近年都市域で頻発している環境問題には大気の運動が深く関わっており、その仕組みを解明することは必要不可欠である。

大気の流れ場の空間構造をモニタリングするには、ドップラーライダーが極めて有効である。都市では図 1 のようなストリーク構造(筋状の弱風域が一定間隔で並ぶ構造)が頻繁に観測される。また、八木ら(2011)が東京都目黒区東京工業大学に設置されたドップラーライダーを用いて行った研究では、高層ビル群後流域に最大で観測領域 8km 全域に渡ってストリークが伸びているのが確認された(図 1a)。

このようなストリークは、風の収束による局所的な上昇流が地表付近の遅い流れを輸送することで形成される。そのため物質輸送にも関係し、またこのような建物後流のストリークによって他のストリークの位置も決定されている可能性がある。都市で普遍的に見られるストリーク構造の研究はこれまで多く行われてきたが、建物から伸びるストリークの分析は行われてこなかった点で本研究は新しい。

2. 観測概要

東京工業大学に設置されたドップラーライダーの、2011 年 8 月 19 日から 2013 年 2 月 3 日までに観測された PPI スキャン(観測半径 4275m、視線方向分解能 50m、スキャン速度 3 degrees/s、俯角 0.5°で全周を水平スキャンする)のデータを用いた。観測領域の南西縁(武蔵小杉周辺)には、高さ 160~190m の高層ビル群があり、そこから伸びるストリークが頻繁に観測される。本研究ではこの建物から発生するストリーク(図 1a)を対象に分析を行う。

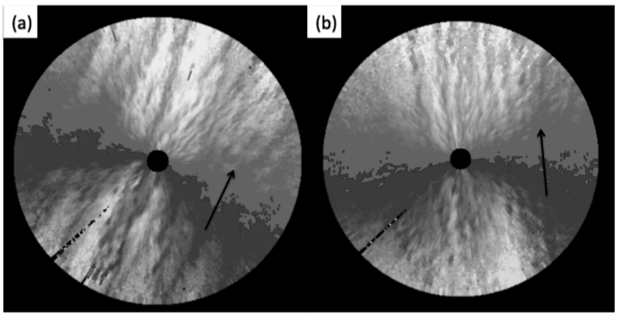

図 1：ストリーク例 (a)有り (b)無

風向を矢印で示す。

3. 解析手法

本研究では目視による観察と分類によってストリークを分析し、特徴をまとめた。最初に 2 時間おきのスキャンからストリークの有無(図 1)を分類し、ストリークの出ているものに対してストリークの挙動、長さなどについてさらに分類をした。

4. 結果と考察

ストリークの発生頻度には、風が強い時ほど発生しやすい傾向にあった(図 3)。ストリークが発生しているスキャンを時系列で見ていくと、そのストリークのほとんどは図 4 に示すように、数分程度の周期で左右交互に蛇行して伸びていくような構造を持っていた。振動する流体現象の非定常性を表す無次元量ストローハル数 St は、式(1)のように定義されるが、大気におけるカルマン渦(チェジュ島等)においては St=0.15 となる(参考文献[4])。ストリークの波長(λ)と水平風速から計算した時間スケールと、St=0.15 から逆算した振動周期を比較すると(図 5)、大気が安定な夜間におけるストリークで両者の値が比較的一致している。

ストリークは、風速場全体の揺れに合わせて更に長い周期で揺れることがある。日中はほとんどの場合で揺れが見られ、2 本のストリークが合流する挙

動(図 6a)がよく見られた。逆に夜間は、揺れが見られないことの方が多く、30 分間の平均場においても、観測領域 8km 全域に渡ってストリークが伸びる(図 6b)こともあった。

$$St = \frac{D}{UT} \qquad \text{式(1)}$$

D は流れの代表長さ、U は水平風速である。

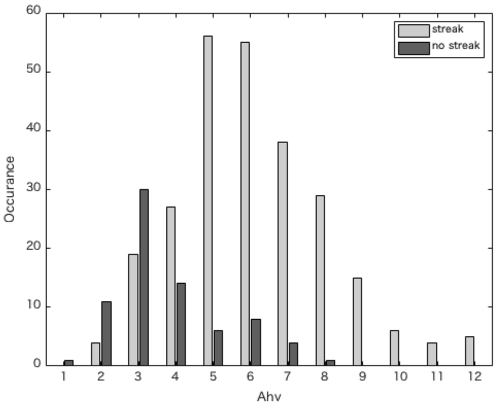

図 3.風速に対するストリークの頻度分布

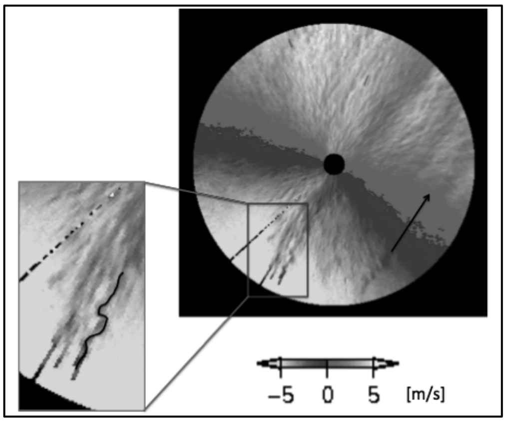

図 4 蛇行するストリーク

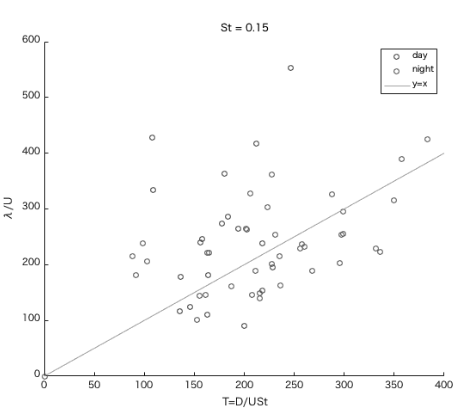

図 5. St=0.2 における各スキャンの振動周期

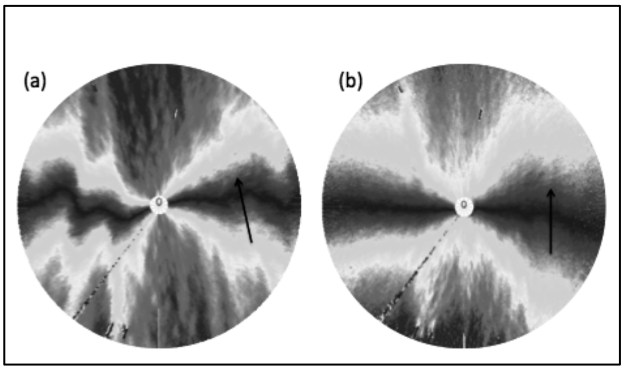

(a)ストリークの合流 (b)非常に長いストリーク

図 6：30 分間(１５スキャン分)の平均場

5. まとめ

建物後流ストリークを観察すると、蛇行しながら伸びていく様子が確認でき、夜間のストリークはカルマン渦の周期と比較的一致していた。都市域の流れ場にもカルマン渦のような流れが存在することが示唆されたと言える。今後の課題として、画像認証技術の導入などによるストリークの定量的な評価や、さらなる大気パラメーターとの関連性を検証して行きたい。

参考文献

[1] 八木綾子, 稲垣厚至, 神田学, 藤原忠誠, 藤吉康志. ドップラーライダーによる都市上空の流れ分類. 土木学会論文集 B1(水工学), Vol. 69, No. 4, pp. I 1753–I 1758, 2013.

[2] 八木綾子, 稲垣厚至, 神田学, 藤原忠誠, 藤吉康志. ドップラーライダーを用いた筋状乱流構造の間隔に関する研究. 土木学会論文集 B1(水工学), Vol. 71, No. 4, pp. I 415–I 420, 2015.

[3] 坪木和久，若浜五郎. 1台のドップラーレーダーを用いた風速場の測定法:最小二乗法を用いたVAD解析.低温科学 物理篇, Vol.47:73 – 88 1989

[4] Ito, Niino. Atmospheric Kármán Vortex Shedding from Jeju Island, East China Sea: A Numerical Study

GDPと人口によるグローバル都市成長モデルの改良

学籍番号:15B03536　　氏名:HE ZUO　　指導教官:神田 学、 Alvin Varquez

1. はじめに

20世紀後半、人間社会は高度成長の時代を迎えた。急速な都市化によって、人間社会は地球温暖化、生物多様性の減少、ヒートアイランドなど、様々な環境問題に直面している。都市化がもたらす気候変動などの問題に対する緩和策、対応策を練るため、グローバルな時空間都市成長分布予測はとても重要であるが、まだ難しい問題と見られている。

2. 既存研究と本研究の目的

都市成長予測モデルSLEUTH(K.Clark et al. [1])は、傾斜、土地利用、除外地域、都市地域、交通網、山岳、六つのローカル空間的情報を用いて、都市化の時空間分布を予測する。さらにZhou et al.[2]は、SLEUTHに基づいた全球時空間都市成長確率を予測する手法GUSPSを提案したが、欠点として、将来の経済社会発展方向を考慮できない。

GDP、人口は都市成長過程を制御するマクロな指標だと考えられるため、本研究はGDPと人口が都市成長に与える影響を探究し、GUSPSの空間分布予測を、共通社会経済経路(SSP)から抽出するGDP人口予測によって修正して、それから空間分布を再調整することを目的にしている。(図1)

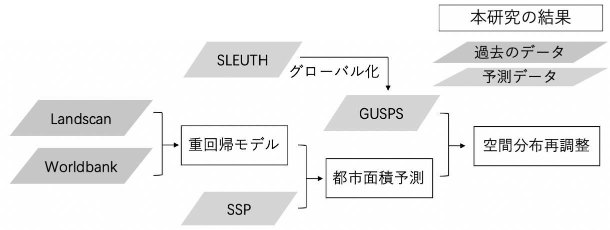

図1 本研究のフロー

3. GDPと人口が都市成長に与える影響

3.1 過去の時系列データ

データセットLandScan は30秒の空間解像度(約1km^2)で空間的人口分布を提供している。本研究は、LandScanで人口が1000を上回る格子を都市格子と定義し、過去の都市面積を算出する。

World Bank Open Dataは世界銀行より公開されており、過去の国レベルGDP、人口データを提供している。

LandScanから過去の都市面積を抽出する際、年ごとの変動が大きい。そのばらつきを抑えるため、i年の都市面積Uについて式1で平滑化を行なう。従って2001年から2016年まで、16年分のデータを準備した。なお、小さい都市の成長は政策に敏感に反応するため、分析対象を全球から抽出した合計114個大都市圏や首都にする。

$$\mathrm{Smoothing}(\mathrm{U}_i) = \mathrm{U}_{i-1}\times 0.25 + \mathrm{U}_i\times 0.5 + \mathrm{U}_{i+1}\times 0.25 \qquad \text{式 1}$$

3.2 国レベルGDP、人口データ使用の妥当性

北京、ロスアンゼルスにおいて、都市レベルと国レベルのGDP、人口成長率それぞれを[0,1]の範囲に正規化した成長曲線がほぼ一致している。つまり都市レベルと国レベル成長率の比は不変である。各対象都市において、この比例が常に一定値を保つと仮定すると、比例係数は3.3節で使用する重回帰式の係数Coefに考慮されるため、国レベルデータの使用は妥当である。

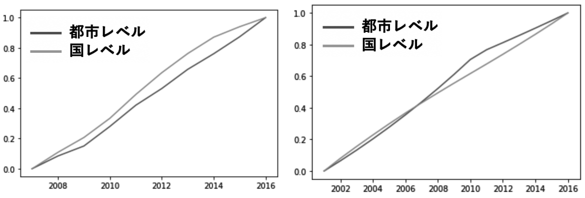

図2 北京の 左)GDP 右)人口 成長を正規化した曲線

3.3 重回帰モデルの作成

以下の制約に従い、114個都市それぞれを対象に重回帰分析を行なう。

- 都市面積成長率を従属変数にする
- GDP成長率、人口成長率を独立変数にする
- GDP成長率と都市成長率は負でない相関がある
- 人口成長率と都市成長率は負でない相関がある
- GDPが増加しない、かつ人口が増加しない場合、都市面積は一定値を保つ

次に、時間スケールが変数の相関に影響する可能性を考慮し、timestepを設置する。任意のXが$(i-timestep)$年からi年までの成長率$\mathrm{d}(\mathrm{X}_i)$を式2で定義する。従って、任意のtimestepに対して、回帰式は式3となる。

$$\mathrm{d}(\mathrm{X}_i) = \frac{\mathrm{X}_i - \mathrm{X}_{i-timestep}}{\mathrm{X}_{i-timestep}} \qquad \text{式 2}$$

$$d(Urban_i) = Coef_{GDP}\times d(GDP_i) + Coef_{POP}\times d(POP_i) \qquad \text{式 3}$$

(ただし　$Coef_1 \geq 0,$　　$Coef_2 \geq 0,$　　POPは人口)

また、成長率が負にならないように、都市面積、GDP、人口の成長率を正規化線形関数(ReLU) で処理しておく。Li et al. [3]、Mertes et al. [4]などの研究でも負の成長の解消を勧めた。

3.3 重回帰分析の結果

一つの対象都市に対して、timestepが1から12まで、12回重回帰分析を繰り返し、最も高い決定係数を持つ式をその都市に対する最適解とする。一部の結果を表1で示す。

切片を0にする制約によって、28個対象都市は負の決定係数を示した。係数Coefが0の場合、その都市において該当の変数が都市成長に与える影響が微小だと思われる。

都市名	timestep	決定係数	$Coef_{GDP}$	$Coef_{POP}$
北京	9	0.32	0.11	0
東京	8	0.63	0.21	3.32
ロサンゼルス	4	0.38	0.33	0

表 1　重回帰分析結果の一部

4.　SSP シナリオによる修正

共通社会経済経路(SSP)は将来社会経済発展の可能性を、緩和策、適応策の困難性に応じて５種類に分類した。そのうち、SSP1 は最も良いシナリオ、持続可能な開発を代表している。SSP3 は最も悪いシナリオ、地域の分断を代表している。

第 3 章で求めた回帰式に SSP1、3 の GDP、人口データを代入した予測結果の例を図 3 で示す。GUSPS データセットから都市格子を判定する都市化確率の閾値を 50%に設定した。次に 2050 年 GUSPS データセットの予測結果を再分布する例を図 4 で示す。

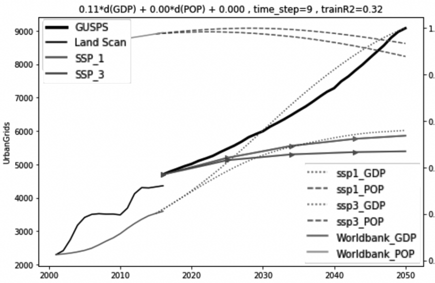

図 3 北京の予測結果

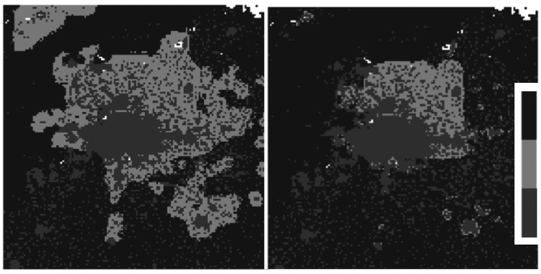

図 4. 北京(a) GUSPS (b) SSP1 による再分布

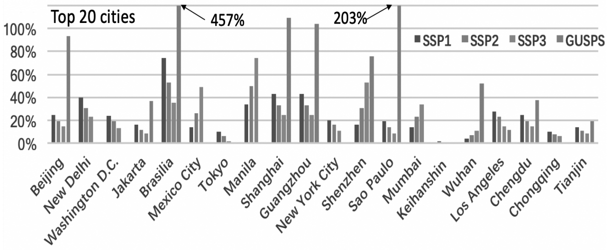

図 5.　2016~2050 年トップ 20 位まで都市の成長率[%]予測

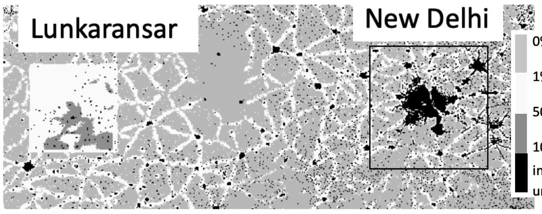

図 6.　GUSPS データセットから見る New Delhi とその周辺

5.　最終結果

まず、2016 年から 2050 年まで、全対象都市の総合都市面積成長率について、GUSPS は 43%の成長率を示した。SSP1~5 を利用した回帰モデルはそれぞれ 47%、39%、37%、33%、63%の成長を示した。これは適切な範囲だと考えられる。

つぎに、トップ 20 位までの都市(図 5)を見ていくと、GUSPS から飛躍的な成長を予測された都市において、回帰モデルでは控えめな成長になっている。一方で、8 個の都市において GUSPS から全く成長が認められないものの、回帰モデルからは多少成長すると予測された。

特に注目したい点は、インド人口上位５位までの都市すべてにおいて、GUSPS はまったく成長しないと示唆した。インドの首都 New Delhi でさえ、都市化確率が閾値の 50%を超える格子が現れなかった。かわりに、周辺都市の Lunkaransar から飛躍的な都市拡張が予測された(図 6)。つまり、SLEUTH モデルから見るインドの都市成長は主に小さい都市で進めると思われ、大都会に偏るような都市集積効果は認められていない。回帰モデルの方は、それでも現在の大都市は成長すると予測した。

上述の結果を踏まえて、本研究の回帰モデルは GUSPS と比べ、折衷的な予測だと考えられる。

6.　考察と結論

本研究はトップダウンの手法で、まず全球主要な都市それぞれを対象に、GDP、人口が都市成長に与える影響を条件付きの重回帰分析で求めた。

本来、都市レベルデータを入手できなければ、それに基づいたモデル作成が難しい。本研究は、都市レベルと国レベルの GDP、人口成長率の比が各対象都市において不変であると仮定したことによって、数多くの都市に回帰分析を応用できた。

しかし、この仮定が成り立たない都市について、回帰モデル予測精度の低下が予想される。他に、回帰モデルに様々な制約を設けた結果、決定係数が低くなり、特に切片を 0 にする制約は、負の決定係数に導いた。

GUSPS データセットの改良手法として、本研究は既存の大都市圏で適切な結果を得たものの、全地域の改良はまだ未解決である。

7.　参考文献

[1] K C Clark et al.　*"A Self-Modifying Cellular Automaton Model of Historical Urbanization in the San Francisco Bay Area"*

[2] Zhou Yuerong et al. "High-resolution global urban g*rowth projection based on multiple applications of the SLEUTH urban growth model"*

[3] Li Xuecao et al. *"Projecting Global Urban Area Growth Through 2100 Based on Historical Time Series Data and Future Shared Socioeconomic Pathways"*

[4] Mertes et al. *"Detecting change in urban areas at continental scales with MODIS data"*

Image super-resolution by a convolutional neural network using a difference image for learning

Student number : 14_00990 Name : Haruki Ikenoue Supervisor : Yukihiko Yamashita

1 Introduction

As the performance of information processing terminals improves, the resolution of displays is increasing. On the other hand, since the resolutions of images and videos produced in the past are low, the outline blurring is conspicuous when the processing to increase the resolution is not performed. In order to improve this visibility, the image super-resolution (SR) is used to restore the edges of a low-resolution (LR) image as clearly as possible to obtain a high-resolution (HR) image. In recent years, image SR by a convolutional neural network has been used. The methods have been devised, and researches are being conducted to obtain a more accurate restoration by adjusting the number of layers and the structure of the network. The amount of calculation using deep learning increases as the structure of the network becomes more complicated. In this research, I try to improve the restoration accuracy by using a pre-processed LR image as an input image for Super-Resolution Convolutional Neural Network (SRCNN) [1], which has a relatively simple structure among convolutional neural networks. As a result, the accuracy is improved without complicating the network structure.

2 Image interpolation

The basic method of generating an image with a large number of pixels from an image with a small number of pixels is based on interpolation. [2] There are various image interpolation methods and each of them has its own characteristics. The nearest neighbor method is an interpolation method in which the pixel value of the input image closest to the position of the pixel to be interpolated is used for it when interpolating the input image. While its calculation is simple, there is a problem that jaggies are likely to occur. The bi-linear method is a method by calculating with linear interpolation using 4 pixels around the target pixel. Although the processing by the bi-linear interpolation method is less likely to cause jaggies on the contour than the nearest neighbor method, the edges may be blurred. The bi-cubic interpolation method is an interpolation method that uses 16 pixels around the target pixel and performs interpolation by a cubic expression. The bi-cubic interpolation method can obtain a sharper image than the bi-linear interpolation method, but the amount of calculation increases. It also has the property that the edges may be blurred. The Lanczos-n method is a method of referencing and weighting pixels with a distance of not greater than n around the target pixel to interpolate them.

3 Convolutional neural network

The convolutional neural network [3] is a technique to improve the accuracy of image recognition by performing convolution processing using a movement-invariant filter as the weight of the neural network. By performing the convolution process, it becomes possible to perform image processes such as edge detection and image leveling inside the network. Since it also has the function to detect features similar to the features of the filter from the input image [4], it is possible to perform the image super-resolution by combining a LR feature extraction filter and a HR feature extraction filter.

4 Network learning using difference images

In this research, in order to improve the accuracy of the convolutional neural network, I propose to simply extract the features from the enlarged low-resolution image and perform learning using it. As a method to obtain the amount of features, the difference between the LR enlarged images obtained by using different enlargement methods is used. The difference image obtained by this method contains many high-frequency components that are easily lost when the image is enlarged. On the contrary, the low-frequency component that is easily restored does not contain very much. Figure 1 visualizes the difference between the original image and the interpolated image, and the difference between the images interpolated by different two methods. A gray filter was used to improve visibility. It can be seen that the difference between the different interpolation methods is similar to the difference between the original image and the interpolated image.

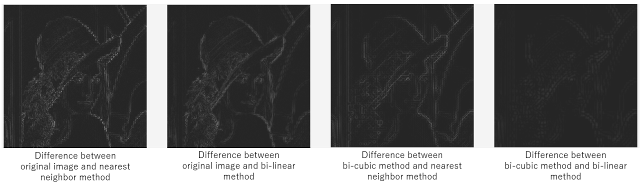

Figure 1: Comparison of difference images

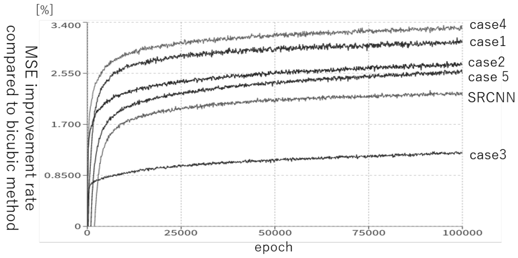

Figure 2: Learning result

5 Experiment

I conduct experiments to compare SRCNN, which is trained using the training data of difference between LR images and HR images, and SRCNN, which used the training data of LR difference images and HR images, which is the proposed method. The images used for learning were 800 data from the DIV2K dataset, and calculations were performed up to 100000 epoch. Table 1 shows Method A and Method B used for image upscaling. Case 5 is a network that inputs a LR enlarged image and predicts the difference. Figure 2 shows the learning result, and Figure 3 shows the result of super-resolution. The vertical axis of Figure 2 shows the improved ratio of MSE between HR image and SR result to the MSE between HR image and the LR image by the bi-cubic method. From the results, the learning using the difference image increases the gradient of accuracy at the initial stage of learning and the prediction accuracy after learning. It is considered that the gradient at the initial stage of learning by using the difference image is large because the low frequency components are not useless at the stage. Regarding the improvement of accuracy after learning, the proposed methods other than case 3 generally provide good results. Therefore, we can say that the difference between blurred images with similar properties is an excellent feature for super-resolution. It can be considered that the features of the bi-cubic and Lanczos-4 methods used in case 3 were the worst because the restorations of high-frequency components were superior to other interpolation methods. As a result of the experiments, good results were obtained from the super-resolution using the convolutional neural network with the proposed method. However, case 4 does not provide the best result. Regarding the Lenna image, the prediction result of case 4 was lower than that of the conventional SRCNN. This is because the feature extraction was not successful.

Table 1: Upscaling methods

	Method A	Method B
case1	4x bi-cubic	4x nearest neighbor
case2	4x bi-cubic	4x bi-linear
case3	4x bi-cubic	4x Lanczos-4
case4	4x bi-cubic	8x bi-cubic

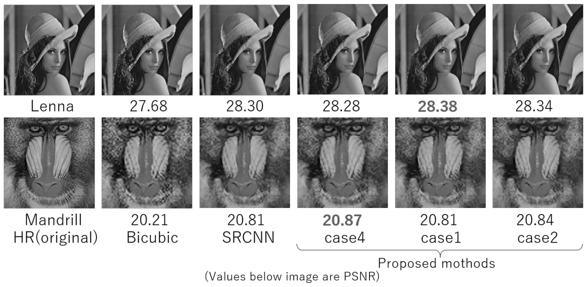

Figure 3: result of super-resolution

6 Conclusion

In this study, I proposed to train the convolutional neural network using the difference image to improve the accuracy of SR without changing the structure of the convolutional neural network. It was confirmed that the proposed method improves the accuracy of super-resolution by experiments.

Since it is not preferable that the accuracy of the prediction result and the training result differ depending on the method, we have to improve the method to generate the difference image so that the method to acquire the difference image can stably retain the features.

References

[1] Chao Dong, Chen Change Loy, Member, IEEE, Kaiming He, Member, IEEE, and Xiaoou Tang, Fellow, IEEE ”Image Super-Resolution Using Deep Convolutional Networks”, arXiv:1501.00092v3 [cs.CV], 31 Jul 2015

[2] Masanao Koeda, Etsuko Ueda, Takayuki Nakamura ”Introduction to Image Processing with OpenCV”, Kodansha, 2014 (in Japanese)

[3] Atushi Fujita ”Deep learning learned in C++”, Excite Japan Co. Ltd., 2017 (in Japanese)

[4] Takayuki Okatani ”Machine Learning Professional Series - Deep learning”, Kodansha, 2015 (in Japanese)

EFFECT OF PH REGULATION ON PIG MANURE COMPOSTING

Student number: 14_12986 Name: Nobuaki HOJO Supervisor: Kiyohiko NAKASAKI

1. Introduction

Composting is a biotechnology to effectively utilizes organic waste by converting it to the compost and recycle to farmland. Among organic wastes, livestock manure is considered to be particularly suitable for composting because it does not contain impurities that are not suitable for composting, and does not contain toxic substances such as heavy metals. For this reason, most of the livestock manure has been treated by composting, but pig manure is difficult to compost because of its acidity. As a countermeasure, neutralization with alkaline agent such as lime has been applied. However, there are regulations that do not recognize agricultural products as "organically grown product" if they are grown using compost that has been neutralized with chemicals. Therefore, there has long been a need to develop a new method for composting of acidified pig manure. The aim of this study was to confirm whether a new method of inoculating organic acid-degrading microorganisms can promote composting of pig manure.

2. Materials and Methods

2.1. Preparation of Composting material

For the raw materials of composting, pig manure, sawdust, and Alles G were mixed at a dry weight ratio of 5:14:1. For the organic acid-degrading bacteria, yeast *Pichia kudriavzevii* RB1 strain and filamentous fungus TR1 strain isolated in the laboratory were used. Yeast RB1 strain was cultured on potato dextrose (PD) agar medium at 30°C for 2 days, and one colony was picked and suspended into liquid PD medium and cultured at 30°C for 2 days before composting experiment. The filamentous fungus TR1 strain was cultured in PD liquid medium at 30°Cfor 3 days. After culturing, the cells were washed with physiological saline and then inoculated.

There are four composting experimental Runs: Run A using the composting material itself, Run B inoculated with yeast RB1 strain as the composting material, Run C with lime added to the composting material, and Run D inoculated with the filamentous fungus TR1 strain. The inoculation concentrations of the cells in Run B and Run D were adjusted to 10^9 CFU/g-ds and 1.94 mg/g-ds, respectively, and the lime in Run C was added so that the pH of the raw material was 9.

2.2. Composting operation

The composting device was shown in Fig. 1. Distilled water was added to the compost raw material to adjust the moisture content to 55%, and 12 g of the raw material was put into a mini-reactor to start composting. The air flow rate to the mini reactor was 5.5mLmin. For Runs A and C, the composting temperature was raised from 30°C to 60°C at a rate of 2.5°C/ h and then maintained at 60°C. By contrast, in Run B and D, the temperature was maintained at 30°C for 3 days and 4 days after the start of composting respectively, to wait for the growth of the inoculated microorganism. Thereafter, the temperature was raised to 60°C in a same matter with other Runs. The composting period was 10 days in all runs. The exhaust gas from the mini-reactor was collected in a 10 L gas bag, and the CO_2 concentration was measured every 24 hours. The CO_2 evolution rate was measured from the CO_2 concentration and the aeration rate, and the conversion of carbon, which corresponds to the degree of organic matter decomposition, was calculated from the cumulative value.

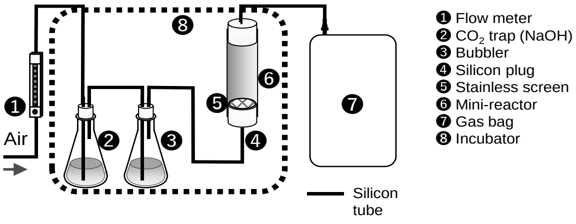

Fig. 1. Experimental devices

2.3. Measurement of physicochemical and microbiological properties

The pH of the compost was measured using a pH meter; samples were prepared as water-soluble extracts using distilled water at a 1:9 ratio and treated with a homogenizer. The moisture content (%) was measured after drying at 105 °C for 24 h in a dry oven. Organic acid concentration of the compost was analyzed by using HPLC. The bacterial cell densities were determined using a Real-time PCR. The bacterial DNA was extracted from the compost sample and the bacterial community was analyzed by next generation sequencing (NGS).

3. Results and discussion

3.1. Courses of CO_2 evolution rate and conversion of carbon during composting

Figure 2 shows the time course the CO_2 evolution rate and conversion of carbon. In Run A, CO_2 was not generated indicating no organic matter degradation. By contrast, CO_2 evolution was vigorous in Run B, C and D from day 1. Conversion of carbon at day 10 was almost 0 in Run A, while around 50% in other Runs. This result clearly indicates that the organic matter degradation of inoculated Runs (Run B and D) was as high as lime-added Run (Run C). Therefore, the effectiveness of microbial inoculation was confirmed.

3.2. Courses of concentration of pH and organic acid concentration

The time course of pH in composting is shown in Fig. 3. In Run A and C, only the initial and final values are shown. In Run A, the pH remained unchanged from the initial value of around 5.5. In Run C, lime was added at the beginning to adjust the temperature to around 9, but even at the end of composting, a weak alkaline condition of 8.5 or more was maintained. These results corresponded well to the fact that organic matter was not degraded at all in Run A and was vigorous in Run C. In both Run B and C, the pH increased after the start of composting, but the rate of increase was particularly fast in Run B, which is not shown in detail here, but yeast is a filamentous fungus. It was considered that the growth rate was faster than that of yeast. In both Run B and C, the pH finally became a weak alkaline value around 8. The pH rose faster in Run B as compared with Run C. The reason for this maybe yeasts grows faster than filamentous fungi, although the details are not given here.

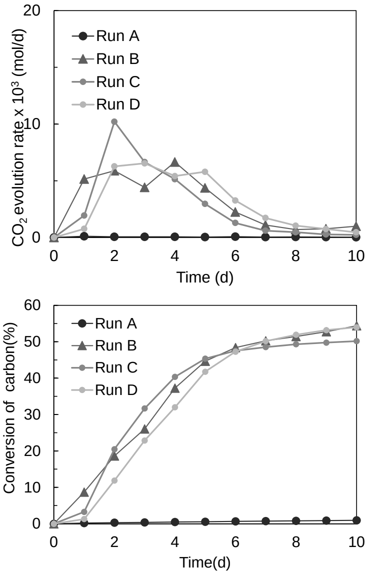

Fig. 2. Courses of CO$_2$ evolution rate and conversion of carbon during composting.

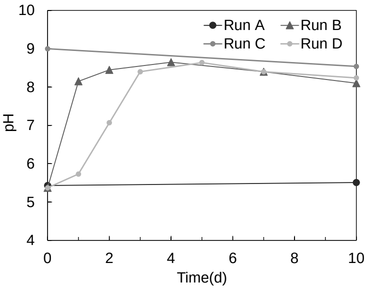

Fig. 3. Courses of pH during composting.

Figure 4 shows the course of the organic acid concentration during composting of Run B and C. Lactic acid and propionic acids were observed while acetic acid and butyric acid were not detected in all Runs. At the beginning of composting, the concentration of lactic acid was remarkably higher than propionic acid. The concentration of both organic acids quickly decreased in the early stage of composting. This is probably owing to the organic acid degradation by the inoculated microorganisms. The change in organic acid concentration corresponded well with the increase of pH values. It should be noted that the pH reached to the weak alkaline condition, although it should not rise above neutral level only by the removal of organic acids. This is probably due to the accumulation of ammonia as a result of protein degradation in the pig manure.

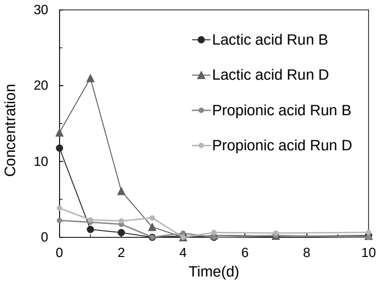

Fig. 4. Courses of concentration of organic acid during composting.

3.3. Courses of bacterial cell density and microbial community during composting

Figure 5 shows the time course of total bacterial cell density during composting of Run B and D. In all composting, the cell density reached a maximum value around day 2 or 3, and then decreased in the latter half of the composting period. However, a high value of 10^9CFU/g-ds or more was maintained throughout the composting period, confirming that organic matter degradation was active.

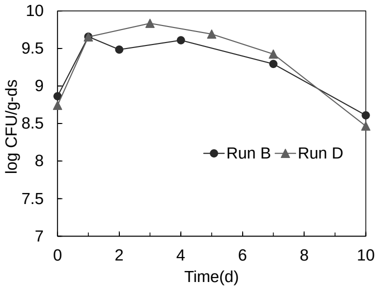

Fig. 5. Courses of concentration of total bacteria during composting.

Although details are not shown here, microbial community analysis showed that the abundance of *Bacillales* rapidly proliferated after 4 days, suggests that this microorganism has high organic matter degradation activity in high temperature. *Clostridiaceae* also showed high abundance throughout composting, but this spore-forming bacteria was also abundant in raw material under room temperature conditions. Therefore, the role of *Clostridiaceae* in pig manure composting is still questionable and needs further investigation to clarify it.

4. Conclusion

The yeast strain RB1 and filamentous fungus strain TR1 used in this experiment were effective in degrading organic acids, increasing pH, and maintaining the activity of composting microorganisms when inoculated in the early stage of pig manure composting. The promotion effect was as high as lime addition. Since lime cannot be used to compost for the production of organically grown vegetables, these microbial inoculants was found to be effective for composting of acidified raw material instead of lime addition.

外国人観光客の避難所利用に対する日本人の受容意識

学生番号:15B03482 氏名:厳　鮮詠(オム　ソンヨン)　指導教員:花岡 伸也

1. はじめに

日本は島国で、地震や水害などの多くの自然災害の影響を受けた国である。過去における災害の中で、たくさんの高齢者や外国人の被害が報告されている。災害への影響を最小限に抑えるために、災害リスク管理が重要である。日本は 2011 年に 621 万人に止まっていた訪日外国人数は、2019 年には約 5 倍増の 3188 万人を記録した。その背景にはビザ緩和、航空運賃の低価格化、日本文化・商品への高い関心などがある。[1]
訪日外国人の急増に伴い、災害に対する十分な備えが必要である。しかしながら、過去の災害事例から外国人への対応の課題が挙げられている。例えば、「言葉が分からずどこに行けば良いか分からなかった」など言語の問題で外国人の避難が遅くなる可能性がある。外国人に対する情報提供の取り組みをして、外国人の視点で避難所利用しやすくする必要である。また、訪日外国人観光客は、自国における被災経験や防災教育の有無などにより、日本人の特徴と異なり、災害対応時の情報収集と対応行動が日本人と異なる。それで、避難所で外国人と日本人避難者とトラブルになる可能性がある。[2]

そこで、本研究では外国人観光客の避難所利用に対する日本人の受容意識を分かるため、アンケート調査を行い、調査結果を分析と考察をする。

2. クロス集計とカイ二乗検定

クロス集計はアンケート調査の2つ質問項目の関係を調べる手法である。回答数の交差頻度を通して、統計的有意性を検証する。カイ二乗検定は二つ変数間の関係が相互独立関係なのかを検証する方法である。実際に出た観察頻度と統計的に期待できる期待頻度の間でどれだけの差があるかをカイ二乗検定を通して、統計的に検証する。期待頻度は行と列の各頻度の和を掛け合わせた上で総頻度数で割ったものである。カイ二乗値は観察頻度と期待頻度の差を二乗した後、期待頻度で割った値である。カイ二乗値は期待頻度より観測頻度が大きいほど大きくなり、カイ二乗値が大きいほど p 値は小さくなり、二つの変数間の関連性は高くなる。そこで、仮説を設定できる。

帰無仮説(H_0＝二つの変数は相互独立関係である)

対立仮説(H_1＝二つの変数は相互独立関係ではない)

カイ二乗値に応じた p 値によって、帰無仮説を棄却し、対立仮説を採用するか、対立仮説を棄却して帰無仮説を採択するかを決める。帰無仮説を棄却すると二つの変数は相互独立関係ではないことだと判断される。

本研究では、外国人に対する認識と避難所選択の多方面から分析したくて、外国人に対する認識と外国人との社会的接触などアンケート調査項目と有意性を調べるためにクロス集計とカイ二乗検定法を用いる。

3. コンジョイント分析

コンジョイント分析とは、製品またはサービスが持っている要因に、回答者が与える価値いわば効用値を求める。また、求められた効用値で複数の要因間の相対重要度の把握できる手法である。30年以内に首都直下地震が発生する可能性が高いと言われてる。首都直下型地震が発生して、避難所に避難するシナリオを想定する。本研究では、避難所選択の相対重要度を分かるためコンジョイント分析の手法を用いる。避難所の要因は避難所まで移動時間、間仕切りの有無、 外国人避難者の有無の3つである。要因の各水準は2つで移動時間は 10 分以内と 10 分以上、間仕切りの有無はありとなし、外国人避難者の有無はいるといないである。求めた各要因の水準の効用値が正の値のものは回答者から好まれているであり、負の値のものは好まれていないことを示す。これを見ると、それぞれの水準が回答者によってどのように評価されているのかを分かる。コンジョイント分析の中で、本調査では選択型コンジョイント分析を用いて分析する。選択型コンジョイント分析は、二つの選択肢が提示され、そこから良いと思うものを1つ選ぶ方法である。

4. 調査結果の分析

アンケート調査は避難所に避難した経験がある日本人300人、避難所に避難した経験がない日本人300人を対象で2021年1月22日から25日までWEB調査を実施した。設問項目は基本情報、避難所選定の重要度、避難シナリオ上避難所選択、自分のコミュニティで外国人の受け入れに同意、外国人との社会的関係、人生に対する満足度、外国人専用の避難所を設置する必要などを設問した。そこで、日本人が外国人に対する認識を分かるために自分のコミュニティで外国人の受け入れに同意するかしないかの結果と外国人との付き合うがあるかの外国人との社会的接触に有意性を調べるために、調査結果をクロス集計とカイ二乗検定を行う。

自分のコミュニティで外国人の受け入れと外国人との付き合いの有無連関性を調べるためにクロス集計を実施した。

表1. クロス集計とカイ二乗検定の結果

		外国人との付き合いの有無		
		あり	なし	全体
自分のコミュニティで外国人の受け入れに同意	同意しない	38 (29.5%) (6.3%)	91 (70.5%) (15.2%)	129 (100%) (21.5%)
	どちらといえない	90 (31.7%) (15%)	194 (68.3%) (32.3%)	284 (100%) (47.3%)
	同意する	100 (53.5%) (16.7%)	87 (46.5%) (14.5%)	187 (100%) (31.2%)
	全体	228 (38%)	372 (62%)	600 (100%)
$x^2(p)$		27.805(0.001^{***})		

$p^* < 0.05$, $p^{**} < 0.01$, $p^{***} < 0.001$

表1によると、自分のコミュニティで外国人の受け入れに同意しない人は外国人と付き合いがないのが一番高い頻度を見せた。分析結果、カイ二乗値は 27.805、p値は 0.001 である。有意水準 0.05 でp値により、帰無仮説棄却し、対立仮説が採択する。従って、外国人の受け入れと外国人との付き合いの有無は相互独立関係ではないから連関性があると判断される

上記の3で述べた避難シナリオ上避難所選択の調査結果を選択型コンジョイント分析を通して、回答者の避難所選択の選好度を調べる。

表2. 避難シナリオ上避難所選択肢

	移動時間	間仕切りの有無	外国人の有無
避難所1	10 分未満	ある	いない
避難所2	10 分未満	ない	いる

表2は、避難所選択肢の一つの例である。避難所の要因を移動時間、間仕切りの有無、外国人の有無である。各要因を見て、自分が選好する避難所を選べる。

タグチ直交表を用いて避難所の選択肢を最適化した避難所の4つを比較する6つのシナリオの結果をコンジョイント分析をする。

コンジョイント分析を通して属性の効用値を求められる。

表3. コンジョイント分析の結果

	答え	効用値	重要度
移動時間	10 分未満	0.5766	28.5%
	10 分以上	−0.5774	
間仕切りの有無	ある	1.0601	52.4%
	ない	−1.0609	
外国人の有無	いる	−0.3846	19.1%
	いない	0.3839	

表3は、回答者の600人が6つのシナリオで避難所選択の結果をコンジョイント分析の結果である。効用値が正数の場合は回答者が選好することで負数の場合は選好しないことである。移動時間は短い方で自分の近い避難所を選好する。間仕切りの有無はある方を選好して、避難所で自分だけの空間とかプライベートを重視する。最後に避難所で外国人の有無については外国人がない方を選好する。効用値で避難所の要因の重要度を分かる。重要度を見ると避難所の選択で重要だと思うことを分かる。間仕切りの有無が52．4%で一番高かった。回答者は避難所を選択するときに自分の空間があるかプライベートが守られるかを重視する。理由として、災害で住むどころがなくなって自分の家のようなどころが必要だと思う。避難所で外国人の有無の重要度を見ると19．1%で低かった。

クロス集計の結果で外国人との関係有無と外国人の認識は連関性があるだと判断されたから外国人と付き合いがある人と付き合いがない人と分けてコンジョイント分析をすると重要度の変化があるか調べる。

表4. 外国人との付き合いによる避難所選択の重要度

	外国人との付き合いがある	外国人との付き合いがない
移動時間	29.2%	28.2%
間仕切りの有無	54.6%	51.2%
外国人の有無	16.2%	20.6%

表 4 を見ると、外国人との関係がある人は避難所の外国人有無の重要度が 16.2%で低くなる。外国人との関係がない人は 20.6%で高くなる。この結果で外国人と社会的接触が高いほど外国人に対する認識も高いことを分かる。避難所で外国人の有無に気にしないである。

5. おわりに

外国人観光客の避難所利用に対する日本人の受容意識を分かるため今回のアンケート調査と調査の結果を分析をした。クロス集計の結果で外国人との社会的接触が高い人、すなわち外国人との付き合いがある日本人は自分のコミュニティーで外国人を受け入れることに同意していることが分かった。

人々は避難のとき避難所を選ぶ際に自分のプライバシーを重視して外国人観光客の受容については重要度が低かった。クロス集計の結果を用いて、外国人と社会的接触の高い人の避難所選択のコンジョイント分析の結果を見ると、外国人たちと避難所で一緒に暮らすことを理解する。

参考文献

[1]日本政府観光局（JNTO）「訪日外国人旅行者統計」https://www.jnto.go.jp/jpn/statistics/since2003_visitor_arrivals.pdf.

[2]Rajarshi Dasgupta, et al.：A rapid indicator-based assessment of foreign resident preparedness in Japan during Typhoon Hagibis, International Journal of Disaster Risk Reduction 51 (2020) 101849.

[3]真城 知己：「SPSS によるコンジョイント分析」, 東京図書 (2001).

[4]John R. Hauser：Note on Conjoint Analysis, MIT Sloan Management (2015) 2-18.

[5]宮城県農業・園芸総合研究所情報経営部：マーケティングに活用される分析手法-選択型コンジョイント分析 (2014) 27-39.

EXPERIMENTAL INVESTIGATION ON ACCURACY OF SURFACE TENSION DETERMINED BY SESSILE DROP SHAPE

Student Number: 15_14445 Name: Yuino MUROZONO Supervisor: Kunio TAKAHASHI

1 Introduction

The wettability of liquid to solids, such as wax, solder and surfactants, is evaluated by contact angle and surface tension. The contact angle of liquid is measured by the sessile drop and the surface tension is often measured by the pendant drop. But, the surface tension is easily affected by atmosphere and impurities. So, we need a method to determine the surface tension and contact angle simultaneously from a sessile drop observation.

A theoretical method to determine the surface tension from the shape of a droplet on a plane surface using a diagram has been proposed [1] [2], but the applicability of this method has not been sufficiently investigated.

In this study, the accuracy of the method [2] for determining the surface tension from the shape of a droplet on a plane is experimentally investigated using photographs of the droplet.

2 Surface tension determined by sessile drop shape

A droplet on a solid plane is assumed to be axisymmetric, as shown in Figure1. The vertex of the droplet on the axis of symmetry is the origin (O), the r-axis is perpendicular to the axis of symmetry, and the z-axis is in the direction of gravity of the axis of symmetry. Take the l-axis along the droplet surface from the origin (O), and let θ be the angle with the r-axis at any point P on the droplet surface. The coordinates of point P can be expressed by z and r.

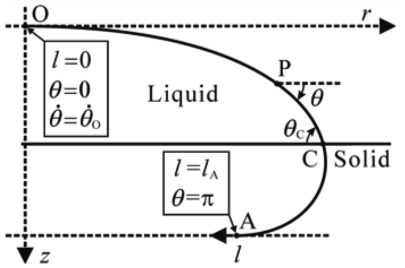

Figure 1Model of sessile drop and definition of coordinates [1]

Variables with a length dimension are nondimensionalized as $\tilde{z}=z/l_{\mathrm{T}}$ using $l_{\mathrm{T}}=\sqrt{\frac{\gamma_{\mathrm{l}}}{\rho g}}$, where γ_{l} and ρ are the surface tension and the density of the liquid, respectively. And g is the gravity acceleration. The liquid shape depends on the nondimensionalized curvature at the top of the liquid $\tilde{\dot{\theta}}_{\mathrm{O}}$. If we measure r, z and θ of arbitrary point on the liquid surface, we can determine $\tilde{\dot{\theta}}_{\mathrm{O}}$ from z/r and θ using a figure, we can determine $\tilde{z}$ from the $\tilde{\dot{\theta}}_{\mathrm{O}}$ and θ using another figure, and finally, we can determine the surface tension as $\gamma_{\mathrm{l}}=\rho g\left(\frac{z}{\tilde{z}}\right)^2$. The details of this method are expressed in Refs.[1] and [2].

3 Experimental investigation on accuracy of surface tension determined by sessile drop shape

3.1 Observation or droplet shape

A plate of PTFE (polyethylene terephthalate) is cleaned up with pure water and completely dried up. It is placed on a vibration isolation table, so that the surface of the plate is horizontal. Micro-ruler sheets are pasted on the side-surface of the plate. A droplet of pure water is placed on a clean surface of the PTFE plate. A camera is put about 20cm aside of the droplet, so that the optical axis of the camera is also horizontal.

3.2 Surface tension measurement results and discussion of their accuracy

Figure 2 shows the image of the droplet. Image data taken by the camera are imported to a drawing software. Grid lines are introduced on the image adjusting to the scale of the ruler. After the image is locked, another line is introduced on the image independently, whose tilt angle is θ. By moving the tilt line to contact on the liquid surface, the contact point is sought. r and z of the contact point are listed for some θ in Table 1. The surface tension is determined using the method [1,2] and listed also in the table.

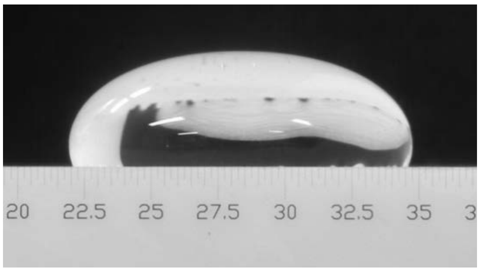

Figure 2 Side view photograph of sessile drop.

Table 1 Surface tension measurement results

θ	r	z	z/r	γ_l
30	4.675	1.025	0.219	65.5014
45	5.625	1.725	0.307	66.7205
60	6.125	3.400	0.385	68.0744
75	6.300	2.825	0.448	56.2697
90	6.425	3.550	0.553	67.0948
Mean				64.7322

Since the ideal surface tension of pure water is about 72 [mN/s], the error is about -10.1%. Since the surface tension of a liquid is reduced by dust and other contaminants, this method is sufficiently useful for evaluating the wettability of a liquid.

Other liquids of medium and small volumes were also considered. As a result, the error in the accuracy of the surface tension measurement was around 10%, indicating its usefulness.

The data of z/r and $\tilde{\theta}_0$ for all θ are plotted on the figure used in the method [1,2]. The evaluated values of $\tilde{\theta}_0$ are all in a narrow range. It suggests that the surface tensions are successfully determined for these θ. However, for smaller θ, the deviation of the evaluated $\tilde{\theta}_0$ seems increased. The effect of the error in the measurement on the evaluation is investigated by giving an intentional error of 0.025 mm for z and r. The effect is found not so critical for the determination of the surface tension in the measurements of the present study.

Since the experiments carried out in the present study are limited, further investigation would be required for more detailed discussion.

4 Conclusion

The accuracy of the surface tension values obtained by the method [1,2] is examined. The error was around 10%, and it is found that the accuracy is sufficiently useful for the evaluation of wettability.

References

[1] 高橋、他、「大体積の平面上液滴の形状情報から液体の表面張力を決定する手法の提案とその 適用性の検討」，溶接学会論文集 38 巻 (2020), pp.193-198

[2] 高橋、他、「重力下の平面上液滴 (Sessile drop) 形状から図を用いて表面張力と接触角を同時 決定する非反復的手法」，溶接学会論文集 39 巻 (2021), pp.32-38